



Chemical Composition and Nutritional Characterization of Cotton Seed as Potential Feed Supplement

Marili F. Zubair^{1*}  , Olalekan Sulyman Ibrahim¹ , Olubunmi Atolani² , and Abdulmumeen Amao Hamid² 

¹Department of Industrial Chemistry, Faculty of Physical Sciences, University of Ilorin, Ilorin, Nigeria

²Department of Chemistry, Faculty of Physical Sciences, University of Ilorin, Ilorin, Nigeria

Abstract: The potential of cotton seeds to serve as animal feed in reducing feed-food competition between humans and animals was examined in this research. Proximate analysis, mineral characterization, and fatty acid composition of the seed were determined using standard analytical techniques. The protein content of cotton seeds found to be $24.81 \pm 0.42\%$ was observed to be above the protein requirement of 18% by rabbits and chicken and 12% for goats and sheep. The combination source of carbohydrates, protein, and fat in which cotton seed is endowed offers an adequate nutritional diet for animals. Carbohydrate and crude fat accounted for $19.30 \pm 0.1\%$ and $24.81 \pm 0.42\%$, respectively, making cotton seed a valuable source of lipids, protein, and carbohydrate, all major nutrients needed to maintain animals' proper maintenance. The most abundant mineral was potassium (K), at 126.70 ± 5.77 mg/g, which can help maintain body weight. It could assist in the modulation of electrolyte and water balance in the system. Quality assessments indicate that cotton seed, when properly processed, can serve as an affordable alternative to soybean, maize, and groundnut and is currently used as the major sources of animal protein and energy, thereby reducing the competition between feed and food.

Keywords: Feed food, proximate analysis, mineral characterization, fatty acid composition.

Submitted: April 04 2021. **Accepted:** August 23, 2021.

Cite this: Zubair M, Ibrahim S, Atolani O, Hamid A. Chemical Composition and Nutritional Characterization of Cotton Seed as Potential Feed Supplement. JOTCSA. 2021;8(4):977-82.

DOI: <https://doi.org/10.18596/jotcsa.906949>.

***Corresponding Author. E-mail:** marilizub@unilorin.edu.ng. Tel No: +2348030661412.

INTRODUCTION

The increasing world population has set the pace for competition for food between humans and animals, thereby deepening the global food shortage crisis (1). In addition, major food-producing countries such as Nigeria and India are experiencing low agricultural yields due to banditry, kidnapping of farmers, uncontrolled grazing on farmland, and unfriendly agricultural government policies. These burdens increase the demand for food crops such as soybeans, a vital source of protein, which are hugely craved by animal production farmers and human beings.

To meet the increasing global demand for food, it is essential to explore the inherent potential in

underutilized and undervalued nutritionally dense lesser-known plant sources (2). Nah and Chau (2010) (3) reported that there is a thousand lesser-known biomass that might substantially add to the array of available nutrient sources, particularly animal protein needs.

It is already established globally that human needs for food and animal feed production compete for the already limited resources available (4). To eradicate this competition for the same resources and avoid increasing the pressure on natural resources, alternative raw materials needed for animal feed production need to be researched. One strategy is the use of underutilized waste seeds. Hence, the current work explores the potential of cotton seeds

to serve as an alternative to animal protein and fat requirements.

Cotton seed, an often-discarded waste material after cotton fiber has been removed from the pod, is readily available and affordable locally. Hence, the reason for characterizing them in animal production, especially in developing countries where protein needs are a problem, and demand for food often drives the price of goods.

In this regard, recent studies have shown that underutilized plant materials are a potentially sustainable and suitable source of food, particularly for animal production (2). Nweze *et al.* (2011) (5) reported that the performance of broiler chickens fed African porridge fruits (*Tetrapluera tetraptera*) and the dressed weight of broilers fed a *Tetrapluera tetraptera* feeding regime were better than those fed other diets.

Similarly, Ade-Omowaye *et al.* (2015) (6) carried out research into the nutritive potential of some underexplored legumes in Nigeria. *Mallotus subulatus* was found to be rich in protein, making it an alternative source of protein for animal feeding. Harouna *et al.* (2018) (7) exploited the use of different species of wild *Vigna* plants in animal feed production; their findings indicate that the species can be judiciously used as a food replacement in animal feedstocks. Research further reported that the species are underutilized because their potential is still obscured.

With a dearth of information on available alternative sources of animal feed ingredients, this study hopes to evaluate the proximate, mineral, and fatty acid contents of underutilized seeds of cotton seed (*Gossypium hirsutum*).

MATERIALS AND METHODS

Sample Preparation

A fully matured sample of cotton seed was collected fresh from a farm in Ogbondoroko, Afon area of Kwara State, Nigeria. The plant material was identified at the Herbarium of Plant Biology, University of Ilorin, Ilorin, Nigeria, where a voucher specimen was deposited. The seeds were deshelled, pulverized, dried, and kept safe until needed for analysis.

Methods

Proximate analyses

Proximate analysis was carried out to determine the moisture content, ash content, crude fiber, crude fat, crude protein, and carbohydrate contents. The standard procedure of the Association of Official Analytical Chemists was used to determine the listed parameters (8).

Mineral Characterization

The mineral contents of cotton seed were determined by atomic absorption spectrophotometry (AAS) according to the methods of Birt *et al.*, 2002 (8).

The digested sample was analyzed for mineral contents by an atomic absorption spectrophotometer (Hitachi model 170-10). The absorption measurement of the elements for cotton seed was read out.

Extraction and Physicochemical Analysis of the Seed Oil

Oil extraction was carried out using n-hexane (1000 mL) according to the method of Atolani *et al.* (2016). Two hundred grams of sample material of ground dried seeds was extracted using a Soxhlet extractor at 55 °C for 7 hours. The oil was obtained using a rotary evaporator at 40 °C, according to standard methods described by Zubair *et al.* (2018) (9).

GC-MS Characterization of the Seed Oils

The esterified oil from the seeds was analyzed using a gas chromatograph (6890N, Agilent Technologies Network) coupled to an Agilent technology inert XL EI/CI mass selective detector (MSD) (5975B, Agilent Technologies Inc., Palo Alto, CA). Constituents were identified primarily based on the comparison of retention time with those of the authentic standards and further confirmed by comparing mass fragmentation patterns with those of the NIST library (10).

RESULT AND DISCUSSION

Proximate Analysis

In this research, we obtained data that point to the potential of underutilized cotton seeds in Nigeria as an alternative plant feed ingredient to reduce feed-food competition between animals and humans for scarce, limited food crops such as soybean and groundnut seeds.

The proximate analysis results of cotton seed are presented in Table 1. The oil content was found to be $24.81 \pm 0.42\%$, this is very close to the value of 30.31% reported for soya beans by Bayero *et al.*, (2019) (11) and $48.33 \pm 0.14\%$ for ground nut as reported by Kamuhu *et al.*, (2019) (12), this implies the seeds can equally serve as a major source of fat and oil for industry, freeing up the convectional groundnut oil and soybean oil consumed at home, thereby reducing home-industrial competition for vegetable oil. Fat and oil are one of the primary energy sources available to humans and animals and a source of fat-soluble vitamins A, D, E, and K (13). The seed has a moisture content of $7.49 \pm 0.21\%$ and falls within the range of the WHO/FAO recommended standard; the low moisture content implies that the seed's shelf life would be high (14).

The food ash content indicates that the mineral composition of food, macro-, and micronutrients aids proper digestion of food; the ash content was found to be 5.85 ± 0.00 , this was also more than the ash content in soybean (4.61 %), groundnut (2.37 ± 0.04 %) and maize (1.35 %) (12) indicating the seed is rich in minerals. Ruminant animals need highly desirable fiber-rich plants for proper gut functions. The high fiber content (18.71 ± 0.26) justifies cotton seed as an alternative source of feed ingredients, particularly in ruminant animals such as cattle, goats, sheep, and rabbits. This value is higher than the 3.7 ± 0.03 reported value by Atasi *et al.* (2009) (15) and 9.80 ± 0.19 by Kamuhu *et al.*, (2019) (12) for groundnut seed, commonly used in animal feeds but coveted by humans.

The available protein in the body complements the restoration of damaged tissue and the supply of

energy. The high protein level in soya and groundnut seeds is a significant reason for animal feeding as a source of protein, thereby creating the problem of feed-food competition that this research hopes to solve. The protein content of cotton seed was found to be $24.81 \pm 0.42\%$, which is more than the enough protein requirement of 18% by rabbits, (16), 12% for goats and sheep (17), and 18% for chicken (18). The combination source of carbohydrates, protein, and fat will offer an adequate nutritional diet for animals. Carbohydrates accounted for $19.30 \pm 0.1\%$, making cotton seed a valuable source of lipids, protein, and carbohydrates, all major nutrients needed to maintain proper animal maintenance. This clearly indicates that cotton seed, when properly processed, can serve as an alternative to soybean, the primary current source of animal protein, helping to reduce the tension between feed-food competition.

Table 1: The proximate composition of cotton seed.

Class of food	% Composition		
	Cotton seed	Soybean	Ground nut
Moisture	7.49 ± 0.21	8.13	5.11 ± 0.05
Crude Protein	24.37 ± 0.28	39.24	22.02 ± 0.23
Crude Fiber	18.71 ± 0.26	6.84	9.80 ± 0.19
Ash	5.85 ± 0.00	4.61	2.37 ± 0.04
Lipid	24.81 ± 0.42	30.31	48.33 ± 0.14
Carbohydrate	19.30 ± 0.10	5.08	12.37 ± 0.44
	This study	Ref (11)	Ref (12)

Mineral Characterization

Table 2 shows the values obtained for mineral characterization of the seed. The seeds were analyzed for minerals such as Mg, K, Na, Zn, Ca, and Fe. Minerals are known for their vital roles in enhancing the proper utilization of food by both plants and animals (19).

The most abundant minerals were found to be potassium (K) at 126.7 ± 05.77 mg/g. Potassium assists in regulating water and electrolyte balance in the body system (20). The sodium content was 12.5 mg/g. Low sodium content helps to regulate acid-base balance and prevent nerve and muscle contraction. High sodium content has been reported to induce hypertension (21).

Magnesium (Mg) plays a crucial role in the stability of the nucleic acid structure. A moderate level of Mg content (7.45 mg/g) will aid in the absorption of electrolytes in the body (22).

Calcium (Ca) is needed for strong bone and dental formation: proper blood clotting and normal functioning of the nervous system. Deficiency of calcium has been reported to include rickets and decaying of the teeth. Excess calcium affects phosphorus usage in the body of animals, another final vital nutrient; hence, a moderate level of the

content found in the seed (7.4 ± 0.02 mg/g) is desirable for animals (23).

Iron (Fe) aids oxygen binding to hemoglobin and control of infection (24). Fe and zinc were found in trace amounts (0.1 ± 0.01 mg/g and 0.1 ± 0.00 mg/g, respectively). Zinc (Zn) assists in wound healing. Excess zinc can induce anemia, and deficiency can cause dermatitis (25).

These mineral compositions of cotton seed further show its nutritive potential as a replacement feed ingredient in animals.

Physicochemical Characterization of Cotton seed

Physicochemical characteristics are vital in determining the appropriate use of seeds. Crucial traits such as the acid value are often used to judge the edibility potential of uncommon seeds. Table 3 gives the quality assessment of cotton seed. The percentage yield of $24.81 \pm 0.42\%$ indicates that it is a vital source of oil. The acid value was found to be 41.14 ± 0.32 mg KOH/g, which compared favorably to the value of 65.50 mg KOH/g for maize seed oil (26). This further indicates that cotton seed oil can serve as a replacement for feed ingredients, thereby helping to reduce the food-feed competition that has currently been seriously experienced. The

saponification value of cotton seed oil was 183.40 ± 0.12 mg/KOH, which is below the standard stated by the International Codex for edible oils compared with a reference standard of 196-205 mg/KOH. This implies that the oils obtained would not be an excellent feedstock for soap-making but somewhat reserved for dietary needs. The iodine value shows the extent of the degree of unsaturation in a molecule. A high degree of unsaturation is desired in edible oils. Polyunsaturated fatty acid-rich oil was reported to mitigate several health challenges, as it prevents clogging of the arteries. Cotton seed shows an iodine value of 157.2 ± 1.55 I₂100 g⁻¹ oil; these

high iodine values mean that the oils contained highly unsaturated fatty acids. The level of unsaturation was further confirmed by GC-MS characterization (Table 4), with a total unsaturation level of 58.54%. Physicochemical analysis revealed that the oil is stable and rich in phytochemicals, as evidenced by the lower free fatty acid content. Higher free fatty acids have been associated with the autooxidation of fat and oil. The lower free fatty acids also indicate a longer shelf life of cotton seed oil and make it an ideal candidate ingredient to reduce food-feed competition between humans and animals.

Table 2: The Mineral Characterization of Cotton seed oil.

Minerals	% Composition
Na	12.60 ± 0.10
K	126.70 ± 5.77
Ca	6.9 ± 0.06
Mg	7.4 ± 0.02
Zn	0.1 ± 0.00
Fe	0.1 ± 0.01

Table 3: Quality parameters of cotton seed oil.

Parameter	Cotton seed oil
% Yield	24.81 ± 0.42
Saponification value (mg KOH/g)	183.40 ± 0.12
Acid value (mg KOH/g)	41.14 ± 0.32
% Free fatty acid	2.11 ± 0.01
Peroxide value (meq kg ⁻¹)	4.16 ± 0.04
Iodine value (I ₂ 100 g ⁻¹ of oil)	157.2 ± 1.55
Physical state at ambient temperature (25°C)	Liquid

Fatty Acid Methyl Ester Composition of Cotton seed oil

Gas chromatography-mass spectrometry (GC-MS) analysis of cotton seed oil revealed the presence of ten (10) compounds, as shown in Table 4.

The relative abundances of the compounds were in the order linoleic acid (30.22%) > palmitic acid (25.32%) > vaccenic acid (22.27%) > oleic acid (4.92%) > stearic acid (4.19%). The least abundant fatty acids were 7,10-hexadecadienoic acid (0.73%), myristic acid (0.53%), stearolic acid (0.24%), 7-hexadecenoic acid (0.19%) and tridecanoic acid (0.18%) (Table 4). Literature appraisals have revealed the crucial roles these fatty acids play in nutrition.

Linoleic acid, a polyunsaturated fatty acid, is credited to prevent food spoilage (27). Field *et al.* (2009) (28) reported that vaccenic acid, another PUFA found in cotton seed oil, demonstrated a beneficial reduction in cell and tumor growth.

Sales-Campos *et al.* (2013) (29), in a mini-review, attributed the reduction of inflammation enhancement of bactericidal and fungicidal action and inhibition of cancer proliferation amongst other bioactive functions to the presence of oleic acid.

The role of cotton seed oil rich in polyunsaturated fatty acid (PUFA) PUFAs in the management of cardiovascular-related ailment cannot be overemphasized (6, 30). The high prevalence of PUFAs in cotton seed oil implies a positive health benefit to the animals.

Table 4: Fatty acid composition of cotton seed oil.

S/N	Fatty acid	Saturation	% Composition
1	Tridecanoic acid	13:0	0.18
2	Oleic acid	18:1	4.92
3	Palmitic acid	16:0	25.32
4	7,10-Hexadecadienoic acid	16:2	0.73
5	Stearolic acid	18:1	0.24
6	Linoleic acid	18:2	30.22
7	Vaccenic acid	18:1	22.27
8	Stearic acid	18:0	4.19
9	Myristic acid	14:0	0.53
10	7-Hexadecenoic acid	16:1	0.19
Total Saturation			41.46
Total Monounsaturations			27.62
Total Polyunsaturations			30.95
Total Unsaturation			58.54

CONCLUSION

This study indicates that cotton seed, if properly processed, can serve as an alternative to soybean, maize, and groundnut currently used as the primary sources of animal protein and energy, thereby reducing the tension between feed-food competition. Many seeds are available cheaply in Nigeria and many other tropical countries and are often discarded as waste after the fiber has been removed. Processing the seeds into animal feed is viable, as cotton seed possesses many nutritional benefits, making it a good alternative in animal feed. The seed is an endowed source of carbohydrates, protein, and fat with other nutritional benefits. Carbohydrates and crude fat accounted for $19.30 \pm 0.1\%$ and $24.81 \pm 0.42\%$, respectively, making cotton seed a valuable source of lipids, protein, and carbohydrates, all significant nutrients needed to maintain proper animal maintenance. The combination source of carbohydrate, protein and fat demonstrated by cotton seed will offer adequate nutritional diet for animals. This clearly indicate that cotton seed when properly processed can serve as alternative to soybean, groundnut and maize currently been used as the major source of animal protein, thereby reducing the tension between feed-food competition.

REFERENCES

- Hodges J. Cheap food and feeding the world sustainably. *Livestock Production Science*. 2005;92(1):1-16. [<DOI>](#).
- James S, Nwabueze TU, Onwuka GI, Ndife J, Usman MAa. Chemical and nutritional composition of some selected lesser known legumes indigenous to Nigeria. *Heliyon*. 2020;6(11):e05497. [<DOI>](#).
- Nah S-L, Chau C-F. Issues and challenges in defeating world hunger. *Trends in food science & technology*. 2010;21(11):544-57. [<DOI>](#).
- Muscat A, de Olde E, de Boer IJ, Ripoll-Bosch R. The battle for biomass: A systematic review of food-feed-fuel competition. *Global Food Security*. 2019;100330. [<DOI>](#).
- Nweze B, Nwankwegu A, Ekwe O. The performance of the broilers chickens on African porridge fruit (*Tetrapleura tetraptera*) pod under different feeding regimes. *Asian Journal of Poultry Science*. 2011;5(4):144-9. [<DOI>](#).
- Ade-Omowaye B, Tucker G, Smetanska I. Nutritional potential of nine underexploited legumes in Southwest Nigeria. *International Food Research Journal*. 2015;22(2):798.
- Harouna DV, Venkataramana PB, Ndakidemi PA, Matemu AO. Under-exploited wild *Vigna* species potentials in human and animal nutrition: a review. *Global food security*. 2018;18:1-11. [<DOI>](#).
- Birt D, Boylston T, Hendrich S, Lane J, Hollis J, Li L, et al. AOAC. 2002. Official Methods of Analysis of The Association of Official Analytical Chemist, Inc., Washington, USA. AOAC. 2005. Official Methods of Analysis of The Association of Official Analytical Chemist, Inc., Washington, USA.
- Zubair MF, Atolani O, Ibrahim SO, Oguntoye OS, Abdulrahim HA, Oyegoke RA, et al. Chemical and biological evaluations of potent antiseptic cosmetic products obtained from *Momordica charantia* seed oil. *Sustainable Chemistry and Pharmacy*. 2018;9:35-41. [<DOI>](#).
- Atolani O, Olabiyi ET, Issa AA, Azeez HT, Onoja EG, Ibrahim SO, et al. Green synthesis and characterisation of natural antiseptic soaps from the oils of underutilised tropical seed. *Sustainable Chemistry and Pharmacy*. 2016;4:32-9. [<DOI>](#).
- Bayero A, Datti Y, Shuaibu M, Nafisatu A, Asma'u A, Dikko M, et al. Phytochemical screening and antibacterial activity of the root bark extracts of

- Neocarya macrophylla. ChemSearch Journal. 2019;10(2):41-5. [<URL>](#).
12. Kamuhu R, Mugendi B, Kimiywe J, Njagi E. Proximate analysis of raw and roasted groundnut (*Arachis hypogaea* L.): Red Valencia and manikanta varieties. International Journal of Food Science and Nutrition. 2019;4(4):191-4. [<URL>](#).
 13. Sikkens EC, Cahen DL, Koch AD, Braat H, Poley J-W, Kuipers EJ, et al. The prevalence of fat-soluble vitamin deficiencies and a decreased bone mass in patients with chronic pancreatitis. Pancreatology. 2013;13(3):238-42. [<DOI>](#).
 14. Akintayo E, Bayer E. Characterisation and some possible uses of *Plukenetia conophora* and *Adenopus breviflorus* seeds and seed oils. Bioresource technology. 2002;85(1):95-7. [<DOI>](#).
 15. Atasie V, Akinhanmi T, Ojiodu C. Proximate analysis and physico-chemical properties of groundnut (*Arachis hypogaea* L.). Pakistan Journal of Nutrition. 2009;8(2):194-7.
 16. Marín-García P, Ródenas L, Martínez-Paredes E, Cambra-López M, Blas E, Pascual J. A moderate protein diet does not cover the requirements of growing rabbits with high growth rate. Animal Feed Science and Technology. 2020;264:114495. [<DOI>](#).
 17. Luo J, Goetsch A, Nsahlai I, Sahlu T, Ferrell C, Owens F, et al. Metabolizable protein requirements for maintenance and gain of growing goats. Small Ruminant Research. 2004;53(3):309-26. [<DOI>](#).
 18. Beski SS, Swick RA, Iji PA. Specialized protein products in broiler chicken nutrition: A review. Animal Nutrition. 2015;1(2):47-53. [<DOI>](#).
 19. Abdel-Salam A. Functional foods: Hopefulness to good health. American Journal of Food Technology. 2010;5(2):86-99. [<DOI>](#).
 20. Borges S, Da Silva AF, Majorca A, Hooge D, Cummings K. Physiological responses of broiler chickens to heat stress and dietary electrolyte balance (sodium plus potassium minus chloride, milliequivalents per kilogram). Poultry science. 2004;83(9):1551-8. [<DOI>](#).
 21. Mishra S, Ingole S, Jain R. Salt sensitivity and its implication in clinical practice. Indian heart journal. 2018;70(4):556-64. [<DOI>](#).
 22. Sissi C, Palumbo M. Effects of magnesium and related divalent metal ions in topoisomerase structure and function. Nucleic acids research. 2009;37(3):702-11. [<DOI>](#).
 23. Pravina P, Sayaji D, Avinash M. Calcium and its role in human body. International Journal of Research in Pharmaceutical and Biomedical Sciences. 2013;4(2):659-68.
 24. Prashanth L, Kattapagari KK, Chitturi RT, Baddam VRR, Prasad LK. A review on role of essential trace elements in health and disease. Journal of dr ntr university of health sciences. 2015;4(2):75. [<DOI>](#).
 25. Lansdown AB, Mirastschijski U, Stubbs N, Scanlon E, Ågren MS. Zinc in wound healing: theoretical, experimental, and clinical aspects. Wound repair and regeneration. 2007;15(1):2-16. [<DOI>](#).
 26. Amos-Tautua B, Inengite A, Abasi C, Amirize G. Evaluation of polycyclic aromatic hydrocarbons and some heavy metals in roasted food snacks in Amassoma, Niger Delta, Nigeria. African Journal of Environmental Science and Technology. 2013;7(10):961-6. [<URL>](#).
 27. Shin S, Bajpai V, Kim H, Kang S. Antibacterial activity of eicosapentaenoic acid (EPA) against foodborne and food spoilage microorganisms. LWT-Food Science and Technology. 2007;40(9):1515-9. [<DOI>](#).
 28. Field CJ, Blewett HH, Proctor S, Vine D. Human health benefits of vaccenic acid. Applied Physiology, Nutrition, and Metabolism. 2009;34(5):979-91. [<DOI>](#).
 29. Sales-Campos H, Reis de Souza P, Crema Peghini B, Santana da Silva J, Ribeiro Cardoso C. An overview of the modulatory effects of oleic acid in health and disease. Mini reviews in medicinal chemistry. 2013;13(2):201-10. [<DOI>](#).
 30. Molendi-Coste O, Legry V, Leclercq IA. Why and how meet n-3 PUFA dietary recommendations? Gastroenterology research and practice. 2010;2011. [<DOI>](#).



Improvement of The CO₂ Sensitivity of HPTS Along With ZnO/CuO Nanoparticles: A Comparative Study Between Core-Shell and Hybrid Structures

Sibel Oğuzlar^{1*}  

¹Dokuz Eylül University, Center for Fabrication and Application of Electronic Materials, 35390, Izmir, Turkey

Abstract: Semiconductor metal oxide materials have gained huge attention in gas sensors owing to their high sensitivity to many target gases. Herein, ZnO/CuO core-shell and ZnO/CuO hybrid, which were synthesized by different sol-gel methods and formed in two different crystal structures, were used as an additive material to enhance the response range of 8-hydroxypyrene-1, 3, 6-trisulfonic acid (HPTS) for the sensing of gaseous carbon dioxide. Metal oxide materials were characterized by using XPS, XRD, FTIR, SEM, UV-Vis, and PL spectroscopy. The HPTS dye along with the ZnO/CuO hybrid material displayed a higher CO₂ gas sensitivity as 94% ratio ($I_0/I_{100}=16.90$) and Stern-Volmer constant (K_{SV}) value and extended linear response range compared to the HPTS-based sensing thin films along with ZnO/CuO core-shell material and additive-free form. ZnO/CuO core-shell and hybrid structures were used for enhancing of carbon dioxide sensitivity of the HPTS dye.

Keywords: Photoluminescence, optical-based carbon dioxide sensor, HPTS, metal oxide, ZnO/CuO core-shell / hybrid.

Submitted: June 02, 2021. **Accepted:** August 23, 2021.

Cite this: Oğuzlar S. Improvement of The CO₂ Sensitivity of HPTS Along With ZnO/CuO Nanoparticles: A Comparative Study Between Core-Shell and Hybrid Structures. JOTCSA. 2021;8(4):983-94. .

DOI: <https://doi.org/10.18596/jotcsa.947087>.

***Corresponding author:** e-mail: sibel.oguzlar@deu.edu.tr.

INTRODUCTION

Detection of carbon dioxide (CO₂) has great significance in various applications like clinical analysis, chemical analysis, and environmental monitoring (1,2). For this reason, it is very critical to measure CO₂ values accurately, continuously, and precisely. The CO₂ can be measured by infrared (IR) spectrometry (3), severinghaus glass electrode (4), and optical sensors (5-7). Recently, the usage of optical-based sensors for the quantitative determination of CO₂ presents many advantages according to other detection methods and reduced noise interference, electrical isolation, remote sensing, and the possibility of miniaturization. The working principle of most optically based carbon dioxide sensors is based on the colorimetric or fluorometric changes of the pH indicators. Reham et al. reported a scheme for sensing CO₂ with a low

concentration range by detecting the dual luminescence of the upconverting nanoparticles emission together with bromothymol blue (BTB) (1). A pH-sensitive indicator dye as di-OH-aza-BODIPY was presented by Schutting et al. (8). Schutting and co-workers also introduced new pH indicators based on diketo-pyrrolo-pyrrole (DPP) dye, which becomes highly soluble in polymers and organic solvents with the addition of dialkylsulfonamide groups for optical CO₂ sensors (9).

Borchert and colleagues reported an optochemical CO₂ sensor using a colorimetric pH indicator α -naphthathalene that was included into the plastic matrix together with a phosphorescent reporter dye PtTFPP and a phase transfer agent tetraoctyl- or cetyltrimethylammonium hydroxide (10). Among the used dyes in optical-based CO₂ sensors, the most commonly used pH-sensitive fluorescent dye

has been the trisodium salt of the 1-hydroxy-3, 6, 8 pyrenetrisulfonic acid (HPTS) or ion pair form of HPTS. HPTS has distinct emission and absorption bands in the visible light area (6). Fluorescent HPTS dye, which is pH sensitive, has previously been used in many carbon dioxide sensor studies (11–15). pH-sensitive and fluorescence-based HPTS dye embedded in an organically modified silica (ORMOSIL) glass matrix were utilized for CO₂ gas monitoring (16). Bültzingslöwen et al. presented an optical sol-gel based carbon dioxide sensor with a fast and reversible response in a wide concentration range (0-100% CO₂) based on the luminescent dye HPTS (11). Ertekin et al. presented a new fiber optic detection device using the fluorescence HPTS dye in ion pair form in a capillary reservoir, encapsulated in an ethylcellulose matrix (17).

It can be concluded from these studies that the researchers employed hydrophobic polymers; ethylcellulose, silicon, poly (1-trimethylsilyl-1-propyne), polyethylene, polymethyl methacrylate, and sol-gel as matrix materials with or without additives either in the thin film, composite, micro-nanofiber, and/or micro-nano particle forms. Oter and et al. reported the ionic liquids and perfluorocompounds in the same matrix for more sensitive determination of CO₂ gas with the signal change of bromothymol blue (BTB). They reported that the electrospun nanofibers offered enhanced sensitivity extending to 98% relative signal change (18). By the way, Ongun and et al. presented two novel coordination polymers for usage as sensor additives with HPTS with the result of I₀/I₁₀₀ value as 6.80 and 10.33 for CP1 and CP2, respectively (19). However, further studies for the usage of new matrix materials are still required to enhance the sensitivity and stabilization of the sensors to develop fluorescent optics-based CO₂ sensors, the specific properties of both the sensitive dye and the matrix material need to be viewed and improved.

Semiconducting metal oxides (SMO) are promising candidate materials for gas sensing applications due to their easy production methods, high sensitivity to many target gases, low cost and is highly compatible with other processes (20). Nanomaterials are already established in the field of gas detection due to their high sensitivity, especially due to their large surface/volume ratio. Recently, many heterojunctions containing ZnO and other metal oxides have become a new and popular application to improve electronic tape structure and improve gas detection performance. For example, studies have been conducted on ZnO/TiO₂, NiO/ZnO, CuO/NiO/ZnO, ZnFe₂O₄/ZnO, CuO/ZnO structures (21).

The use of CuO and ZnO materials together among the related metal oxides can increase the change of conductivity, thus increasing the gas sensitivity of the materials. However, it has been shown in the

studies that the formation of p-CuO/n-ZnO heterostructures increases the gas detection performance (22). Zhyrovetsky et al. reported optical-based gas detection properties of several metal oxide nanoparticles like ZnO, ZnO:Cu, ZnO:Sn, ZnO:Au, ZnO:Ni, TiO₂, SnO₂, ZnO:Pt, WO₃ in several gas environments such as O₂, N₂, H₂, CO, CO₂ (23). The sensor based on the p-CuO/n-ZnO heterojunction fabricated by Ramachandran and co-workers exhibited the enhancement for gas-sensing performance to the ethanol (24). Wang et al. presented that CuO/ZnO composite nanostructure has more CO gas detection capability than single phase ZnO nanowires (25). According to the literature, many gas sensor studies containing metal oxide are based on electrical measurement. The advantage of the luminescence-based measurement used as an alternative in the absence of electrical contact between the resulting impurities and nanostructures. In addition, real-time information about the variation of certain additives in the photoluminescence spectra can be observed. However, the effect of adsorbed gases on the photoluminescence of metal oxide powders has not yet been adequately studied.

In this study, the CuO/ZnO hybrid and CuO/ZnO core-shell particles have been synthesized by the complex-directed hybridization and sol-gel approaches, respectively, and were characterized as morphological, structural, and optical properties. As far as we know, the CuO/ZnO particle additives were previously not used for the enhancement of carbon dioxide sensitivity of the HPTS ion pair dye. The aim of this study is to improve the emission-based response of HPTS dye to CO₂ gas with the synthesized metal oxide additive in our laboratories. Herein, the carbon dioxide-induced emission response of the highly sensitive dye-doped thin film in the PMMA matrix was measured along with a range of different CO₂ concentrations. Upon exposure to different concentrations of CO₂, the sensitivity values of I₀/I₁₀₀ were 10.16 and 16.90 for core-shell ZnO/CuO and hybrid ZnO/CuO immobilized PMMA thin films, respectively.

EXPERIMENTAL SECTION

Reagents

All utilized chemicals were of analytical purity. The CO₂ sensitive and pH indicator fluorescent dye, 8-hydroxypyrene-1,3,6-trisulfonic acid trisodium salt (HPTS) was used in the ion pair form as synthesized before (26). The trisodium salt of HPTS and TOABr were mixed as 1:4 ratio in 1% sodium carbonate solution and CH₂Cl₂ (1:1). Based on the formation of the ion pair, the organic and aqueous phases were separated with a separating funnel and the organic solvent was evaporated to obtain the ion pair. The HPTS dye, additive tetrabutylammonium hydroxide (TBAOH) was supplied from Fluka. The ionic liquid 1-butyl-3-methylimidazolium tetrafluoroborate

(BMIMBF₄), dioctylphthalate (DOP), polymethyl methacrylate (PMMA), and the solvents of ethanol and tetrahydrofuran (analytical grade) were obtained from Sigma. Nitrogen and carbon dioxide gases were 99.9% purity and supplied from Tinsa Gas, Izmir, Turkey. Copper(II) acetate dihydrate (Cu(CH₃CHOO)₂×2H₂O), Zinc acetate dihydrate (Zn(CH₃COO)₂×2H₂O), sodium hydroxide (NaOH), boric acid (H₃BO₃) were supplied from Sigma Aldrich.

Instrumentation

The phase structure of the synthesized powders was investigated by an X-ray diffractometer (XRD, Thermo Scientific ARL X-ray diffractometer, Cu-K α , 1.5405 Å, 45kV, 44mA). X-ray photoelectron spectroscopy (XPS, Thermo Scientific K-Alpha) with a monochromatic Al-K α (1486.7 eV) X-ray source and a beam size of 400 μ m diameter was studied to determine the elemental composition of metal oxide samples. Functional groups of powders were evaluated by Fourier transform infrared spectroscopy (FTIR, Thermo Scientific Nicolet I10). UV-visible diffuse reflectance spectroscopy (UV-vis DRS) measurement was performed to identify absorbance spectra with Thermo Scientific Evolution 600. Microstructure images for morphological characterization were studied with scanning electron microscopy (SEM, COXEM EM-30 Plus) at different magnifications. The steady-state photoluminescence (PL) emission, excitation, and decay time measurements were carried out by FLSP920 Fluorescence Spectrometer, Edinburgh Instruments. The CO₂ and N₂ gases were blended in the 0–100% concentration range by a Sonimix 7000A gas blending system for carbon dioxide detection measurements. Mixtures of gases were introduced into the sensing membrane via a diffuser needle under ambient conditions after the gases were humidified at a constant relative humidity level of 100%. The humidification of the gases was accomplished by bubbling the gas stream through thermostated wash bottles filled with water at 25 °C at a constant relative humidity level of 100%.

Synthesis of ZnO/CuO Particles via Two Methods

The ZnO/CuO hybrid and ZnO/CuO core-shell particle (1:1 ratio) samples were synthesized

similarly, as based on the literature (27,28). 0.25 M (Zn(CH₃COO)₂×2H₂O) and 0.25 M (Cu(CH₃CHOO)₂×2H₂O) solutions were stirred with the addition of NaOH pellets to prepare the ZnO/CuO hybrid composites. Upon keeping the final solution 12h at 120 °C, the calcination process applied as 400 °C for 2.5 h. To prepare the ZnO/CuO core-shell structure, 1 M (Zn(CH₃COO)₂×2H₂O) solution was prepared with the addition of NaOH pellets. The obtained final powders with drying at 75 °C for 2h were added into the 0.35 M (Cu(CH₃CHOO)₂×2H₂O) solution. After waiting for 18 h, bluish precipitates were dried at 100 °C for 1 h to obtain core-shell particles. Both of the synthesized particles were characterized and used as additive materials to enhance the response of the HPTS indicator dye for CO₂ gas sensing measurements.

Thin Film Preparation

The PMMA based carbon dioxide sensing thin films were made by stirring 120 mg of PMMA, 96 mg of plasticizer (DOP), 24 mg of [BMIM][BF₄], 2 mg of HPTS ion pair dye, and 10 mL of THF/EtOH (1:1) mixture in presence and absence of additive materials; 5 mg ZnO/CuO hybrid and 5 mg ZnO/CuO core-shell metal oxide particles. Table 1 presents the compositions of the utilized cocktails. The solutions were mixed under magnetic stirring to provide homogeneity. The obtained polymeric cocktail compositions were spread onto a 125 mm Mylar™ type polyester support to obtain thin films. The sensing films were cut to 1.2×3.0 cm and placed crosswise in the quartz cuvette and then emission/excitation-based spectra were taken. All sensing composites contain 25% of polymeric matrices [BMIM] [BF₄], optimized in our previous studies (29). The used ionic liquid increased the stability of the sensing slides and carbon dioxide solubility due to their unique properties such as their reversible solubility with gases. This high solubility results from the formation of Lewis acid-base complexes between the CO₂ anion (electron-pair acceptor) and the ionic liquid (electron-pair donor). The ZnO/CuO hybrid nanocomposite and ZnO/CuO core-shell metal oxide samples were encoded as ZCO-HC and ZCO-CS, respectively.

Table 1: Cocktail compositions used as CO₂-sensing agents.

Dye	Coctail Name	PMMA (mg)	THF (mL)	DOP (mg)	TBAOH (μ L)	Ionic liquid (mg)	Additive / ZCO-H (mg)	Additive / ZCO-CS (mg)
HPTS (2 mg)	HPTS_Additive free	120	2.00	96	200	24	-	-
	HPTS_ZCO-H	120	2.00	96	200	24	5	-
	HPTS_ZCO-CS	120	2.00	96	200	24	-	5

RESULTS AND DISCUSSION

Characterization of Synthesized Nanoparticles

The structural changes of the produced particles were examined by XRD. Figure 1 (a) shows XRD patterns for both ZCO-H and ZCO-CS particles, respectively. The recorded patterns exhibit all of the major peaks of a monoclinic CuO phase (JCPDS:48-1548) and also a hexagonal wurtzite ZnO phase (JCPDS:36-1451) for both samples (27,28). The variation in peak positions and their corresponding

intensities can be attributed to the change of synthesized methods as a hybrid structure and also the core ZnO and CuO shell in the ZnO/CuO.

Additionally, FTIR analysis was carried out to determine the molecular structure of the synthesized particles. Figure 1 (b) indicates the FTIR spectra of both the ZCO-H and ZCO-CS powders. All relevant peaks according to the obtained spectra are shown in Table 2.

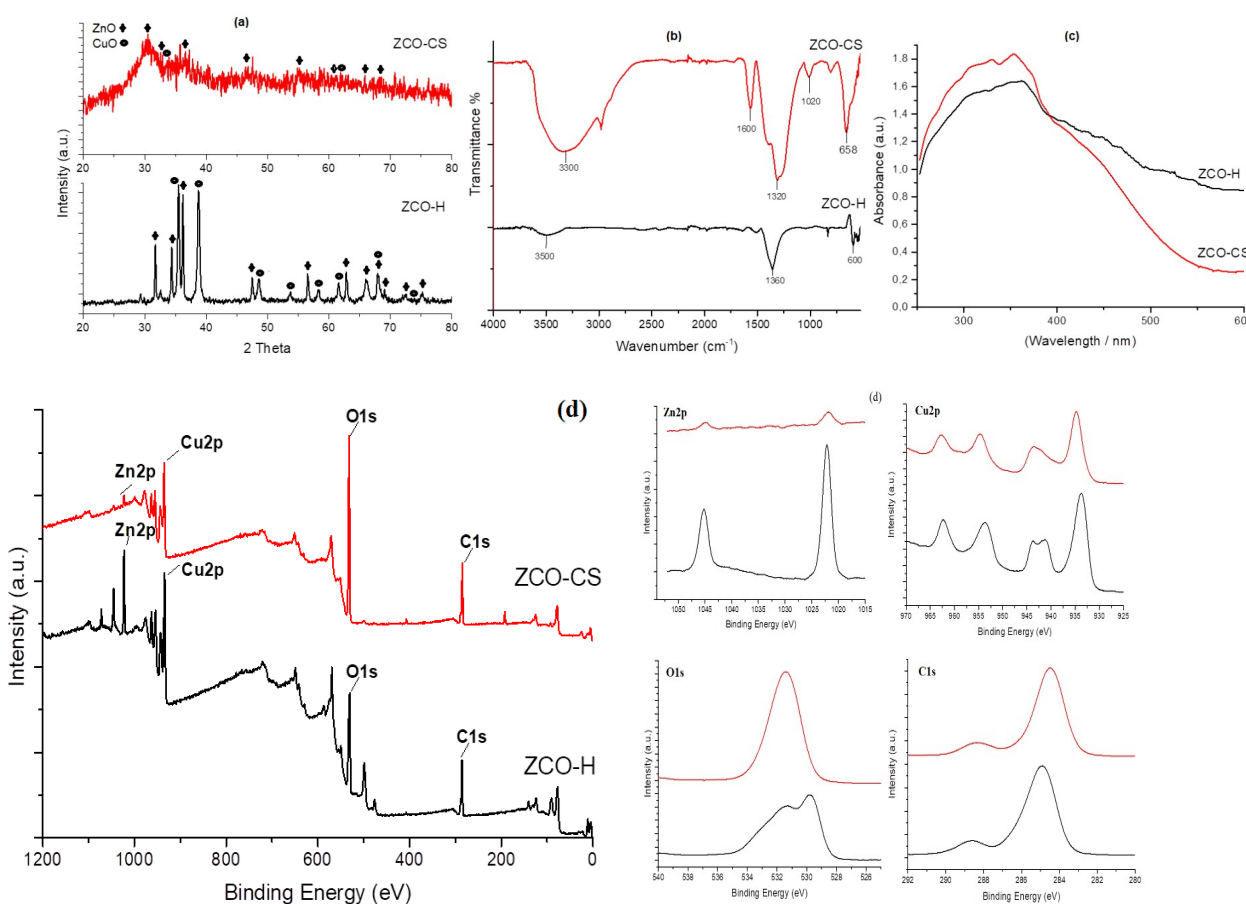
Table 2: FTIR spectra data for ZCO-H and ZCO-CSO powders.

Sample	Wavelength/cm ⁻¹	Vibration Type
ZCO-H / ZCO-CS	3000 - 3700	O-H stretching vibration modes
	1100 - 1500	C-H bending (symmetrical)
	1500 - 1750	O-H bending vibration modes
	400 - 700	u(M-O) stretching modes

The absorbance spectra (See Fig. 1 (c)) measurements were performed by using UV-Vis DRS. As it is seen from the spectra, both samples exhibit strong absorption with a maximum of around 350 nm in the UV range.

of binding energies and atomic weight (%) values of available elements. The binding energy (BE) peaks around 1022 eV for the Zn2p, 934 eV for the Cu2p, 531 eV for the O1s, and 285 eV for the C1s were in evidence for both ZCO-H and ZCO-CS that are presented in Figure 1 (d).

The XPS analysis was studied to clarify the surface chemical structure of all prepared particles in terms



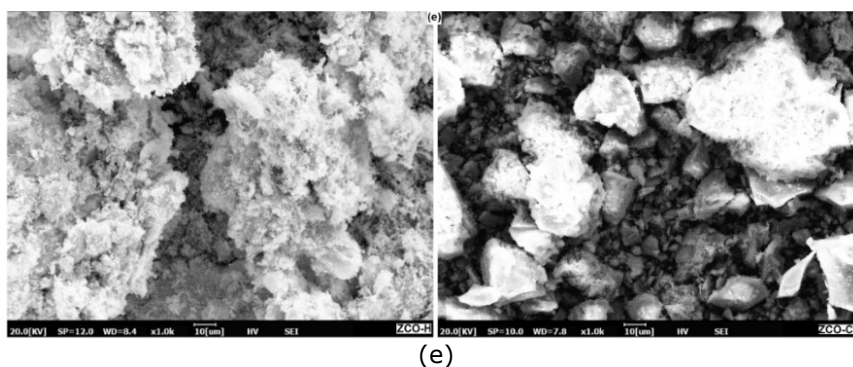


Figure 1: a) XRD patterns, b) FTIR spectra, c) UV-Vis. Spectra, d) XPS spectra, e) SEM images of both ZCO-H and ZCO-CSO particles.

According to the information given in the literature, while the binding energy for Cu2p shifts to lower energy than pure CuO, and the binding energy for Zn2p shifts to higher binding energy than pure ZnO upon to the ZnO/CuO structure formation. This binding energy change in XPS measurement is mainly assigned to the difference in electronegativity between the metal ions (30). The fact that the electronegativity value of Cu²⁺ is 2.0 and this value of Zn²⁺ is 1.7 causes the electrons to remove from Zn²⁺ to Cu²⁺. So the electron-shielding effect of Cu²⁺ is improved and the main peak of Cu2p shifts at lower binding energy, while the main peak of Zn2p shifts to higher binding energy (31).

Considering this information, when both materials are examined, the highest shift in both Zn2p and Cu2p values according to binding energies of pure CuO and ZnO (31) was observed for ZCO-H. Meanwhile, the XPS spectra of O 1s can be placed on peaks with the binding energy of 529.78 eV and 531.29 eV for ZCO-H. According to the former studies, the 529.78 eV peak is attributed to the lattice oxygen (O₂⁻) on the metal oxide structure, while the 531.29 eV peaks belong to the presence of O²⁻ at the surface. By the way, it has been reported that the sensor sensing performance is due to the adsorbed oxygen on the surface of the material reacting with the target gas (31) (See Table 3).

Table 3: Binding energy (BE) and atomic weight % values according to XPS survey analysis of all samples.

Name	ZCO-H		ZCO-CS	
	Peak BE	Weight %	Peak BE	Weight %
Zn2p	1022.15	15.18	1021.88	3.67
Cu2p	933.48	40.05	934.53	36.71
O1s	531.29	25.20	531.18	37.58
C1s	285.87	19.57	285.12	22.04

The SEM micrographs were performed to search for the morphology and microstructure of the hybrid and core/shell particles and the results were shown in Fig. 1 (e). According to the obtained results, the particles are agglomerated. However, some large particles present in the structure and aggregation of nanoparticles can be assigned to the high surface area and surface energy of ZnO particles. In ZnO/CuO particles, the formation of p-n heterojunctions between p-type CuO and n-type ZnO along with pores and voids also contributes to

sensitivity. Previous reports presented that the interface between CuO and ZnO plays an important role in gas sensitivity. In our study, ZCO-H material has much finer pores and voids in the structure.

Emission and Excitation Spectra of HPTS and the Utilized Metal Oxide Powders

The excitation and emission spectra of HPTS dye, ZCO-H, and ZCO-CS particles were shown individually in Figure 2.

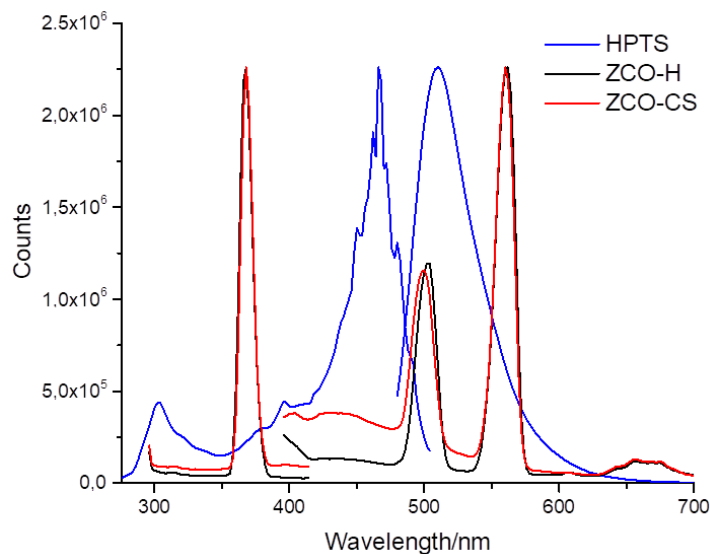


Figure 2: The excitation and emission spectra of the PMMA embedded HPTS, ZCO-H, and ZCO-CS.

In accordance with the literature, HPTS dye exhibited an excitation peak at 380, 405, and 467 nm and also an emission peak at 515 nm when it is embedded in the PMMA matrix (32). The existence of different excitation wavelengths indicates whether the structure is protonated or unprotonated. However, when the dye is exposed to CO₂ gas, the peak at 405 nm increases, whereas the peak at 467 nm decreases with an isobestic point at 419 nm.

The presence of additives significantly increased the CO₂-induced sensitivity of HPTS, increasing the I_0/I_{100} parameter from 6.36 to 10.16 and 16.90 for sensing agent dye along with the ZCO-CS and ZCO-H additives, respectively. So, in this study, we measured the excitation and emission spectra of HPTS dye and the additives of ZCO-H and ZCO-CS heterostructures independently in order to clarify the reasons lying behind the enhancement to CO₂-induced sensitivity (See Fig. 2). Both ZCO-H and ZCO-CS have strongly absorbed between 300 and 420 nm and emitted in a wide range of 400 to 700 nm that covers the excitation band of HPTS. This result enables an energy transfer between the synthesized metal oxide particles and the HPTS dye.

The mechanism underlying the strong emission and absorption capabilities of the ZnO/CuO heterostructure involves bandgap excitation by energetic photons that produce holes in the crystalline valence band and exciton pairs with electrons in the conduction band. Also, the p-n hetero formation plays an important role in improving the detection performance (21,24). However, it can also be attributed to the larger depletion layer on the CuO/ZnO surface, which results from the formation of p-n heterojunctions between the p-CuO and n-type ZnO particles (24).

CO₂ Induced Response of HPTS Based Sensing Slides

Figures 3, 4, and 5 reveal CO₂-induced variations of the excitation and emission spectra of HPTS-based sensing thin films in the absence and the presence of the ZCO-CS and ZCO-H additives, respectively. Intensity-based emission/excitation measurements were performed upon exposure of sensing PMMA-based thin films to 0, 10, 20, 40, 60, 80, and 100% gaseous CO₂ after humidification of the gas.

Herein, the effects of synthesized ZCO-H and ZCO-CS particles on the CO₂ sensitivity of HPTS dye were investigated. It was expected an enhancement in the performance of the dye is expected by the formation of the p-n heterojunction, which reveals a wide depletion region properties of the additives. As a result, HPTS based thin films showed high sensitivity and good linearity in certain concentration ranges along with the additives.

In this study, the Stern-Volmer constant was used for quantitative measurements of photoluminescence-based quenching (Eq. 1):

$$\frac{I_0}{I} = 1 + K_{sv} [CO_2] \quad (\text{Eq. 1})$$

where I_0 and I are the emission intensities of without and with a quencher, respectively; $[CO_2]$ is the carbon dioxide concentration, K_{sv} is the collisional quenching constant, called the Stern-Volmer constant. The equation indicates that I_0 / I increases directly proportional to the concentration of the quencher (33).

Figure 3 indicates the CO₂-induced spectral behavior of the additive-free HPTS embedded in PMMA thin

film for the 0-100% [CO₂] concentration range. In the case of excitation at 467 nm, the decrease of the emission intensities was observed at 515 nm. The I₀/I₁₀₀ value which shows the sensitivity of the sensor has been recorded as 6.36 with a linear response, which can be characterized by the equation $y = 0.0084x + 1$ and R² value of 0.9818. However, the I₀/I₁₀₀ values of the sensing films in presence of ZCO-CS and ZCO-H additives were

enhanced to 10.16 and 16.90, respectively (see Table 2). This result can be assigned to the absorption and emission abilities of the ZnO/CuO particles as well as the large surface-to-volume ratio and the defects in the ZnO/CuO system (34). All of the HPTS based sensing slides exhibited good carbon dioxide sensitivity (I₀/I₁₀₀), regression coefficients, and K_{SV} values for the concentration range of 0-100% p[CO₂].

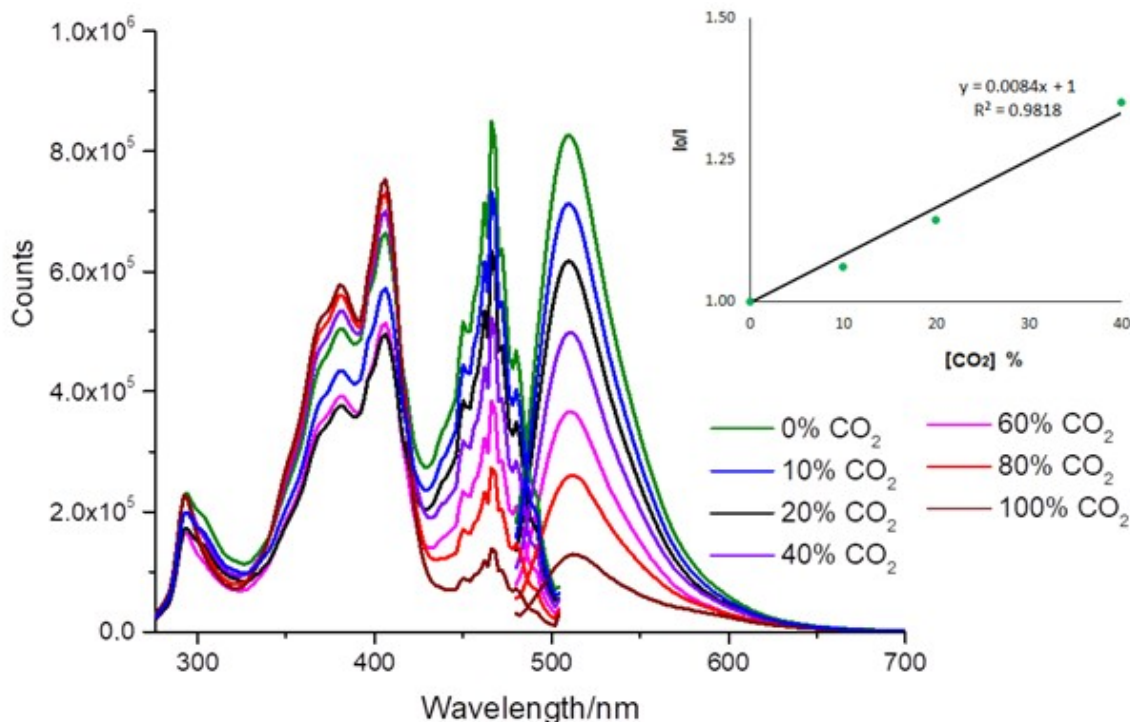


Figure 3: Emission and excitation spectra of additive-free-HPTS upon to exposure 0.0%, 10.0%, 20.0%; 40.0%; 60.0%; 80.0%; 100.0% CO₂(g).

Figures 4 and 5 show the CO₂-induced spectral behavior of HPTS with ZCO-CS and ZCO-H additives embedded in PMMA thin film for the 0-100% [CO₂] concentration range, respectively. The insets of Figures 4 and 5 show the linear response for the 0-40% [CO₂] concentration range. When comparing

the CO₂-induced response of the HPTS-based used composites, ZCO-H showed a superior linear response and a considerably higher slope than ZCO-CS, which can be characterized by the equation $y = 0.0102x + 1$ and R² value of 0.9951.

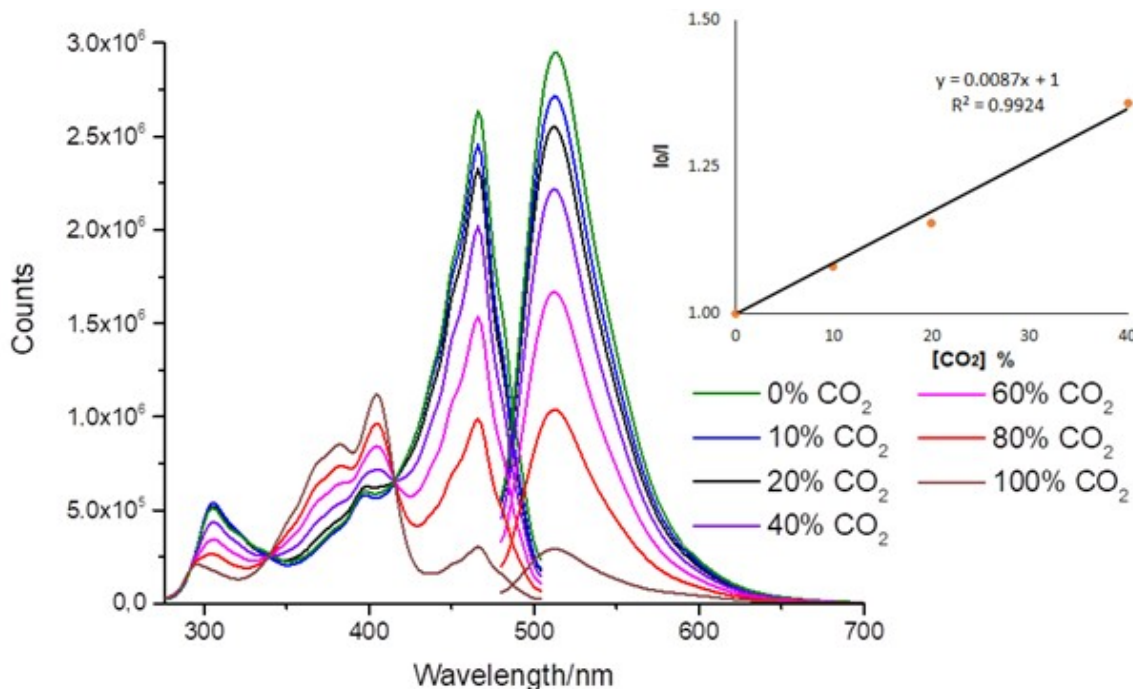


Figure 4: Emission and excitation spectra of HPTS as including ZCO-CS upon to exposure 0.0%, 10.0%, 20.0%; 40.0%; 60.0%; 80.0%; 100.0% CO₂(g).

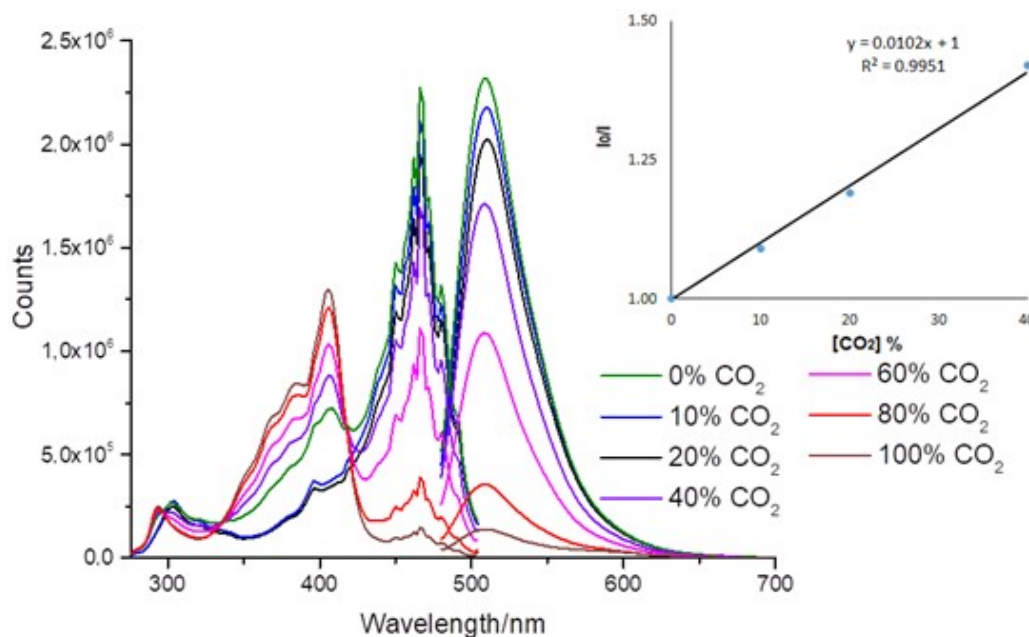


Figure 5: Emission and excitation spectra of HPTS as including ZCO-H upon to exposure 0.0%, 10.0%, 20.0%; 40.0%; 60.0%; 80.0%; 100.0% CO₂(g).

Figure 6 presents comparative calibration plots of composites used for the 0-100% [CO₂] concentration range. Comparing the CO₂-induced variations of the composites used, HPTS_ZCO-H

exhibited a quite high slope between 0-100% pCO₂ and linear response for the 0-40% [CO₂] concentration range.

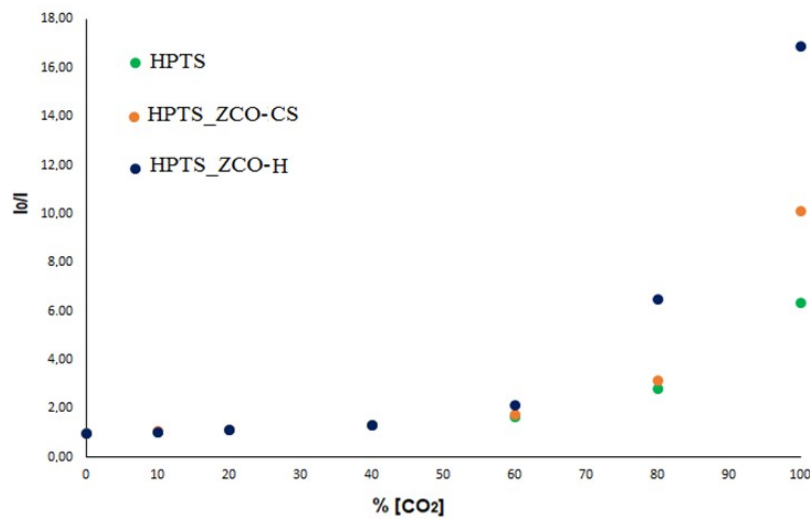


Figure 6: The CO₂-induced response of the additive-free HPTS and HPTS along with ZCO-H and ZCO-CS additives for the 0-100% [CO₂] range.

The use of additive metal oxide materials remarkably increased the CO₂-induced sensitivity of HPTS, enhancing the parameter of I₀/I₁₀₀ from 6.36 of additive-free to 10.16, 16.90 for composites including, ZCO-CS, ZCO-H, respectively (See Table 4). The presence of too many free electrons on the surface of the semiconductor material allows a large number of oxygen species to be adsorbed by trapping the free electrons. Due to the presence of too many oxygen species on the ZnO/CuO structure surface, much more CO₂ gas reaches the surface, which leads to an increase in gas sensitivity. Apart from this, the presence of the ZnO/CuO heterostructure provides more reactive part and surface area, so it absorbs more CO₂ gas molecules (24).

Among the prepared HPTS-based sensing slides, the highest K_{SV} value of HPTS_ZCO-H underlines extreme sensitivity to CO₂, making ZnO/CuO proportion attractive for the detection of trace

amounts of carbon dioxide. Wang et al. reported that sensitivity decreased in the case of reducing the Zn proportion in the structure (31). Lavin and co-workers also present that ZnO content in ZnO/CuO heterojunction enhances the photocatalytic efficiency of the structure (21). In our study, unlike the ZCO-CS, the Zn amount is higher for the ZCO-H heterostructure (confirmed by XPS). So the higher sensitivity of the ZCO-H structure along with HPTS dye can be attributed to the equilibrium of the interaction. When the CuO and ZnO materials are incorporated, electrons can be moved from n-type ZnO to p-type CuO until the system is equilibrated, which indicates the strong interaction between both materials.

This result indicates that HPTS dye with ZCO-H (K_{SV} = 1.02 × 10⁻² %⁻¹) has appropriated candidates for sensitive CO₂ sensing whereas the lower K_{SV} value of HPTS_ZCO-CS (K_{SV} = 8.7 × 10⁻³ %⁻¹) (see Table 4).

Table 4: Photoluminescence-based properties and CO₂ sensitivity of HPTS dye in PMMA thin film with additives ZCO-CS and ZCO-H.

Cocktail name	Equation (Concentration range of 0–40 % [CO ₂])	K _{sv}	Regression coefficient, R ²	I ₀ /I ₁₀₀
Additive-free	y = 0.0084x + 1	8.4 × 10 ⁻³	0.9818	6.36
ZCO-CS	y = 0.0087x + 1	8.7 × 10 ⁻³	0.9924	10.16
ZCO-H	y = 0.0102x + 1	1.02 × 10 ⁻²	0.9951	16.90

Decay Time Measurements

We measured and interpreted CO₂-induced decay time values of the HPTS dye including ZCO-H and ZCO-CS additives to clarify the CO₂ sensitivity upon excitation at 468 nm pulsed laser. The recorded decay time values were shown in Table 5. In

addition, measuring the decay times of the thin films give us significant information for the interaction mechanism between fluorophore and quencher. The decay curves of the HPTS_ZCO-H and HPTS_ZCO-CS for 0-100% [CO₂] concentration were indicated in Figure 7. The decay time values of

HPTS_ZCO-H and HPTS_ZCO-CS decreased from 4.51 ns to 2.57 ns and from 4.52 ns to 3.89 ns when exposure to carbon dioxide, respectively.

Table 5: The decay time values of ZCO-H and ZCO-CS in the PMMA matrix.

Sample	To (0% CO ₂)	Decay Time (ns)	Std. Dev. (ns)	Rel. (%)	To (100% CO ₂)	Decay Time (ns)	Std. Dev. (ns)	Rel. (%)
HPTS_ZCO-H	T ₁	4.05	0.01	95.96	T ₁	0.42	0.01	34.96
	T ₂	15.45	0.06	4.04	T ₂	3.73	0.05	65.04
	T_{avr}	4.51 ns			T_{avr}	2.57 ns		
HPTS_ZCO-CS	T ₁	4.10	0.01	93.89	T ₁	0.75	0.02	21.04
	T ₂	11.04	0.02	6.11	T ₂	4.73	0.03	78.96
	T_{avr}	4.52 ns			T_{avr}	3.89 ns		

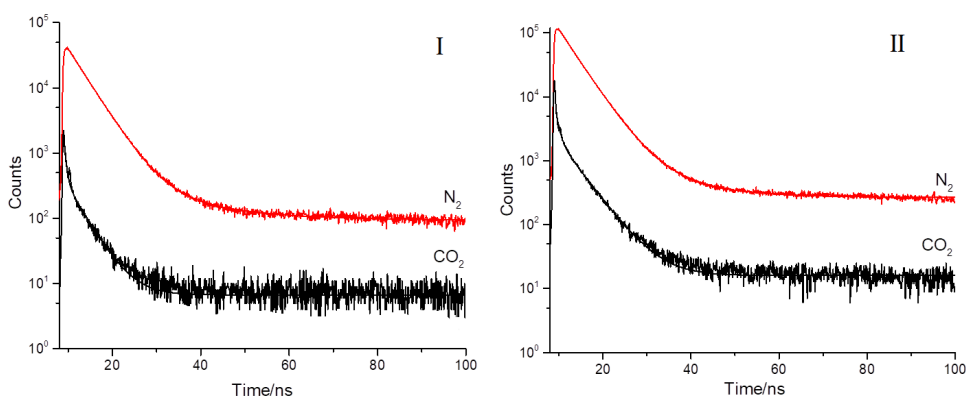


Figure 7: Decay curves of **I:** HPTS_ZCO-H **II:** HPTS_ZCO-CS.

The obtained results can be evaluated as electrical conductivity and charge mobility, resulting in a decrease in decay time values. In metal oxide semiconductors, the adsorbed or diffused gas reduces the carrier density and creates potential barriers between the oxide grains that cause a reduction in electrical conductivity. The same charge mobility that affects the conductivity also affects the luminescence and the decay time values decrease (35).

CONCLUSION

In this study, HPTS dye was used along with additives of ZnO/CuO heterostructures for the first time and thus HPTS dye has been shown to increase its sensitivity to CO₂ gas. The carbon dioxide sensitivities of the HPTS along with these additives are tuned via changing the proportion of ZnO and CuO. Although the I₀/I₁₀₀ value of core-shell ZnO/CuO immobilized in PMMA thin film was 10.16, hybrid ZnO/CuO showed better sensitivity with the value of 16.90 upon to CO₂. The results show that the generation of heterojunction between ZnO and CuO in the synthesized ZnO/CuO structure makes free electrons, which facilitates the adsorption of CO₂ molecules on the surface and facilitates morphology and defects.

ACKNOWLEDGMENT

Characterization measurements were performed at Dokuz Eylul University, Center for Fabrication and Applications of Electronic Materials. I want to thank all.

CONFLICT OF INTEREST

The author declares that there are no conflicts of interest.

REFERENCES

1. Ali R, Saleh SM, Meier RJ, Azab HA, Abdelgawad II, Wolfbeis OS. Upconverting nanoparticle based optical sensor for carbon dioxide. *Sensors and Actuators B: Chemical*. 2010 Sep;150(1):126–31. <DOI>.
2. Chu C-S, Lo Y-L, Sung T-W. Review on recent developments of fluorescent oxygen and carbon dioxide optical fiber sensors. *Photonic Sens*. 2011 Sep;1(3):234–50. <DOI>.
3. Swickrath M, Anderson M, McMillin S, Broerman C. Application of Commercial Non-Dispersive Infrared Spectroscopy Sensors for Sub-ambient Carbon Dioxide Detection. In: 42nd International Conference on Environmental Systems [Internet]. San Diego, California: American Institute of

- Aeronautics and Astronautics; 2012 [cited 2021 Aug 24]. <DOI>.
4. Shimizu Y, Yamashita N. Solid electrolyte CO₂ sensor using NASICON and perovskite-type oxide electrode. *Sensors and Actuators B: Chemical*. 2000 Jun;64(1-3):102-6. <DOI>.
 5. Malins C, MacCraith BD. Dye-doped organically modified silica glass for fluorescence based carbon dioxide gas detection. *Analyst*. 1998;123(11):2373-6. <DOI>.
 6. Zeyrek Ongun M. Tuning CO₂ sensitivity of HPTS by ZnO and ZnO@Ag nanoparticles. *Journal of Photochemistry and Photobiology A: Chemistry*. 2020 Sep;400:112664. <DOI>.
 7. Neurauter G, Klimant I, Wolfbeis OS. Microsecond lifetime-based optical carbon dioxide sensor using luminescence resonance energy transfer. *Analytica Chimica Acta*. 1999 Feb;382(1-2):67-75. <DOI>.
 8. Schutting S, Jokic T, Strobl M, Borisov SM, Beer D de, Klimant I. NIR optical carbon dioxide sensors based on highly photostable dihydroxy-aza-BODIPY dyes. *J Mater Chem C*. 2015;3(21):5474-83. <DOI>.
 9. Schutting S, Borisov SM, Klimant I. Diketo-Pyrrolo-Pyrrole Dyes as New Colorimetric and Fluorescent pH Indicators for Optical Carbon Dioxide Sensors. *Anal Chem*. 2013 Mar 19;85(6):3271-9. <DOI>.
 10. Borchert NB, Kerry JP, Papkovsky DB. A CO₂ sensor based on Pt-porphyrin dye and FRET scheme for food packaging applications. *Sensors and Actuators B: Chemical*. 2013 Jan;176:157-65. <DOI>.
 11. von Bültzingslöwen C, McEvoy AK, McDonagh C, MacCraith BD, Klimant I, Krause C, et al. Sol-gel based optical carbon dioxide sensor employing dual luminophore referencing for application in food packaging technology. *Analyst*. 2002;127(11):1478-83. <DOI>.
 12. Nivens D. Multilayer sol-gel membranes for optical sensing applications: single layer pH and dual layer CO₂ and NH₃ sensors. *Talanta*. 2002 Sep 12;58(3):543-50. <DOI>.
 13. Wolfbeis OS, Kovács B, Goswami K, Klainer SM. Fiber-optic fluorescence carbon dioxide sensor for environmental monitoring. *Mikrochim Acta*. 1998 Sep;129(3-4):181-8. <DOI>.
 14. Neurauter G, Klimant I, Wolfbeis OS. Fiber-optic microsensor for high resolution pCO₂ sensing in marine environment. *Fresenius' Journal of Analytical Chemistry*. 2000 Mar 2;366(5):481-7. <DOI>.
 15. Oter O, Polat B. Spectrofluorometric Determination of Carbon Dioxide Using 8-Hydroxypyrene-1,3,6-trisulfonic Acid in a Zeolite Composite. *Analytical Letters*. 2015 Feb 11;48(3):489-502. <DOI>.
 16. McEvoy AK, Von Bültzingslöwen C, McDonagh CM, MacCraith BD, Klimant I, Wolfbeis OS. Optical sensors for application in intelligent food-packaging technology. In: Glynn TJ, editor. Galway, Ireland; 2003 [cited 2021 Aug 24]. p. 806. <DOI>.
 17. Ertekin K. Characterization of a reservoir-type capillary optical microsensor for pCO₂ measurements. *Talanta*. 2003 Feb 6;59(2):261-7. <DOI>.
 18. Oter O, Sabancı G, Ertekin K. Enhanced CO₂ Sensing with Ionic Liquid Modified Electrospun Nanofibers: Effect of Ionic Liquid Type. *sen lett*. 2013 Sep 1;11(9):1591-9. <DOI>.
 19. Zeyrek Ongun M, Oğuzlar S, Köse Yaman P, Öter Ö. Tuning CO₂ sensing properties of HPTS along with newly synthesized coordination polymers (CPs). *Spectrochimica Acta Part A: Molecular and Biomolecular Spectroscopy*. 2021 Dec;263:120224. <DOI>.
 20. Arafat MM, Dinan B, Akbar SA, Haseeb ASMA. Gas Sensors Based on One Dimensional Nanostructured Metal-Oxides: A Review. *Sensors*. 2012 May 30;12(6):7207-58. <DOI>.
 21. Lavín A, Sivasamy R, Mosquera E, Morel MJ. High proportion ZnO/CuO nanocomposites: Synthesis, structural and optical properties, and their photocatalytic behavior. *Surfaces and Interfaces*. 2019 Dec;17:100367. <DOI>.
 22. Fan C, Sun F, Wang X, Majidi M, Huang Z, Kumar P, et al. Enhanced H₂S gas sensing properties by the optimization of p-CuO/n-ZnO composite nanofibers. *J Mater Sci*. 2020 Jun;55(18):7702-14. <DOI>.
 23. Zhyrovetsky VM, Popovych DI, Savka SS, Serednytski AS. Nanopowder Metal Oxide for Photoluminescent Gas Sensing. *Nanoscale Res Lett*. 2017 Dec;12(1):132. <DOI>.
 24. Mariammal RN, Ramachandran K. Study on gas sensing mechanism in p-CuO/n-ZnO heterojunction sensor. *Materials Research Bulletin*. 2018 Apr;100:420-8. <DOI>.
 25. Wang JX, Sun XW, Yang Y, Kyaw KKA, Huang XY, Yin JZ, et al. Free-standing ZnO-CuO composite nanowire array films and their gas sensing properties. *Nanotechnology*. 2011 Aug 12;22(32):325704. <DOI>.

26. Oter O, Ertekin K, Derinkuyu S. Ratiometric sensing of CO₂ in ionic liquid modified ethyl cellulose matrix. *Talanta*. 2008 Jul 30;76(3):557-63. [<DOI>](#).
27. Yang C, Cao X, Wang S, Zhang L, Xiao F, Su X, et al. Complex-directed hybridization of CuO/ZnO nanostructures and their gas sensing and photocatalytic properties. *Ceramics International*. 2015 Jan;41(1):1749-56. [<DOI>](#).
28. Mahajan P, Singh A, Arya S. Improved performance of solution processed organic solar cells with an additive layer of sol-gel synthesized ZnO/CuO core/shell nanoparticles. *Journal of Alloys and Compounds*. 2020 Jan;814:152292. [<DOI>](#).
29. Ongun MZ, Oter O, Sabancı G, Ertekin K, Celik E. Enhanced stability of ruthenium complex in ionic liquid doped electrospun fibers. *Sensors and Actuators B: Chemical*. 2013 Jul;183:11-9. [<DOI>](#).
30. Chen W, Qiu Y, Zhong Y, Wong KS, Yang S. High-Efficiency Dye-Sensitized Solar Cells Based on the Composite Photoanodes of SnO₂ Nanoparticles/ZnO Nanotetrapods. *J Phys Chem A*. 2010 Mar 11;114(9):3127-38. [<DOI>](#).
31. Wang X, Li S, Xie L, Li X, Lin D, Zhu Z. Low-temperature and highly sensitivity H₂S gas sensor based on ZnO/CuO composite derived from bimetal metal-organic frameworks. *Ceramics International*. 2020 Jul;46(10):15858-66. [<DOI>](#).
32. Choi MF. Spectroscopic behaviour of 8-hydroxy-1,3,6-pyrenetrisulphonate immobilized in ethyl cellulose. *Journal of Photochemistry and Photobiology A: Chemistry*. 1997 Apr;104(1-3):207-12. [<DOI>](#).
33. Ratterman M, Shen L, Klotzkin D, Papautsky I. Carbon dioxide luminescent sensor based on a CMOS image array. *Sensors and Actuators B: Chemical*. 2014 Jul;198:1-6. [<DOI>](#).
34. Dey A. Semiconductor metal oxide gas sensors: A review. *Materials Science and Engineering: B*. 2018 Mar;229:206-17. [<DOI>](#).
35. Aydin I, Ertekin K, Demirci S, Gultekin S, Celik E. Sol-gel synthesized Sr₄Al₁₄O₂₅:Eu²⁺/Dy³⁺ blue-green phosphorous as oxygen sensing materials. *Optical Materials*. 2016 Dec;62:285-96. [<DOI>](#).



Antimalarial Evaluation of the Chemical Constituents Isolated from *Dendrocalamus asper*

Kok Tong Wong¹ , Hasnah Osman^{1*}  , Thaigarajan Parumasivam² ,
Jafri Malin Abdullah³⁻⁵ , Mohd. Zaheen Hassan⁶ ,
and Mohamad Nurul Azmi^{1*}  

¹School of Chemical Sciences, Universiti Sains Malaysia, Minden 11800 Penang, Malaysia

²School of Pharmaceutical Sciences, Universiti Sains Malaysia, 11800 Minden, Penang, Malaysia

³Department of Neurosciences, School of Medical Sciences, Jalan Hospital USM, 16150 Universiti Sains Malaysia Health Campus, Kota Bharu, Kelantan, Malaysia

⁴Brain and Behaviour Cluster, School of Medical Sciences, Universiti Sains Malaysia Health Campus, 16150, Kota Bharu, Kelantan, Malaysia

⁵Department of Neurosciences & Brain Behaviour Cluster, Hospital Universiti Sains Malaysia, Universiti Sains Malaysia Health Campus, 16150, Kota Bharu, Kelantan, Malaysia

⁶College of Pharmacy, King Khalid University, Abha, KSA

Abstract: Bamboo shoots of *Dendrocalamus asper* is essential for human health because of the high content of dietary fiber, low sugar, negligible amount of fat, and rich vitamin and mineral content. The bamboo shoots' chemical constituents were evaluated against the *P. falciparum* strain 3D7 as a potential antimalarial drug. One new metabolite, (11Z,13E,17E,19Z)-dimethyl-15,16-dibutoxytricont-11,13,17,19-tetraenedioate (**1**) along with four known compounds; β -sitosterol (**2**), methyl-4-hydroxybenzoate (**3**), 1-methoxy-4-(methoxymethyl)benzene (**4**) and 4-hydroxybenzaldehyde (**5**) were isolated from the crude extract of *Dendrocalamus asper* using chromatographic methods: MPLC, UPLC/MS, analytical and preparative HPLC. Among these, compounds **1**, **3**, and **4** showed promising antimalarial activity with IC₅₀ between 0.8-2.2 μ g/mL. The molecular docking between the most potent compound **3** and dihydrofolate reductase-thymidylate synthase (DHFR-TS) was done to understand and explore the ligand-receptor interactions and hypothesize the compound's refinements.

Keywords: *Dendrocalamus asper*, antimalarial, *P. Falciparum*, Molecular docking, dihydrofolate reductase-thymidylate synthase (DHFR-TS).

Submitted: March 28, 2021. **Accepted:** August 25, 2021.

Cite this: Wong K, Osman H, Parumasivam T, Abdullah J, Hassan M, Azmi M. Antimalarial Evaluation of the Chemical Constituents Isolated from *Dendrocalamus asper*. JOTCSA. 2021;8(4):995-1002.

DOI: <https://doi.org/10.18596/jotcsa.904529>.

***Corresponding authors. E-mail:** mnazmi@usm.my / ohasnah@yahoo.com

INTRODUCTION

Malaria is a tropical blood-borne protozoan disease caused by parasites of the genus *Plasmodium*, and spread by female *Anopheles* mosquitoes. There are five types of *Plasmodium* causing malaria viz; *P. ovale*, *P. knowlesi*, *P. malariae*, *P. vivax*, and *P. falciparum* (**1**). The World Health Organisation

(WHO) reported that in 2018, there were 228 million malaria cases that occurred worldwide. It resulted in 405,000 deaths and approximately 70% of the global deaths involving children under-five from malaria (**2**). Even though Malaysia does not have any domestic malaria (indigenous) cases recorded since 2018, it remains one of the most significant health challenges to other southeast

Asian countries (2). The main drawback of malaria's current treatment are the development of multiple drug resistance and the non-specific targeting to intracellular parasites. This, in turn results in the requirement of high-dose anti-parasitic drugs and subsequent intolerable toxicity. Hence, there is a need for novel chemotherapeutic agents.

The tropical rain forest is rich in biological and chemical resources, which have a huge potential as defense agents against pests, diseases, and predators (3). Two natural compounds, quinine, isolated from the stem of *Cinchona sp.* and artemisinin, isolated from the herbal plant *Artemisinin annua* are phenomenal, and have contributed greatly to reducing deaths due to malaria all over the world (4,5). Malaysia is one of the world's most thriving center of biodiversity with its tropical rainforests. Many of the rainforest plant based phytomedicines are used as an alternative treatment for malaria (6). Among these, the *Dendrocalamus asper* (bamboo) from the family of Poaceae is a tall arborescent grass, which plays an essential role in construction, reinforcing fibers in paper, medicines, and food sources (7). Bamboo shoots are young, edible plants with health benefits, including healthy weight loss, antibacterial and anti-carcinogenic activities.

To date, no antimalarial studies have been reported on the bamboo plant. Therefore, this research reports new potential antimalarial agents, and phytochemical investigations of the extract from bamboo shoots of *Dendrocalamus asper*. The evaluation of the antimalarial activity of all the isolated compounds are herein reported.

EXPERIMENTAL SECTION

Plant material

Bamboo shoots of *Dendrocalamus asper* (DAPB52014) were collected at Pos Brook Village, Gua Musang, Kelantan, Malaysia. The bamboo shoots were identified by Assistant Botanist, Mr. Deraman, M., from South Kelantan Development Authority (KESEDAR).

General

All chemicals were obtained from QRec (Asia) and Merck (Germany). Thin-layer chromatography (TLC) were performed on alumina plates pre-coated with silica gel (Merck 60 F₂₅₄). The spots were determined under UV radiation ($\lambda_{\text{max}} = 254$ nm). SiO₂-MPLC was performed using CombiFlash Companion (Teredyne ISCO). Preparative reverse phase HPLC was performed using a Waters 600 pump system with Waters 2998 photodiode array detector and Senshu pack pegasil ODS column (20 X 250 mm). Analytical HPLC was performed using

an Empower system with Waters 2996 detector with senshu pack column (4.6 X 250 mm) and Waters 717 plus autosampler. One- and two-dimensional nuclear magnetic resonance (NMR) spectra were recorded using a JEOL ECA-500 spectrometer at Chemical Biology Building, RIKEN, Wakoshi, Saitama, Japan using CDCl₃ and methanol-*d*₄ as solvents. Infrared (IR) spectrum was recorded on a Perkin-Elmer System FTIR-ATR spectrometer at the School of Chemical Sciences, USM. The chemical ionization mass spectrometry (CI-MS) was recorded by using a Bruker Micro TOF-QII LCMS at the Department of Chemistry, National University of Singapore. The measurement was carried out in positive-ion mode. Mass resolution: 17,500 (FWHM), temperature compensated, mass range: 50-20,000 *m/z*, acquisition rate: 20 Hz (2 GHz sampling rate).

Extraction, separation, and isolation

The dried bamboo shoot (1.29 kg) was extracted with three different types of solvents, one after the other on the same bamboo shoot. First, *n*-hexane was used in the extraction. After the extraction, the bamboo shoot was evaporated to dryness. It was then extracted with dichloromethane. After which the sample was evaporated to dryness and finally extracted with methanol. The recovered extractants were evaporated using a rotary evaporator to obtain the crude extract. The dry weight of *n*-hexane extract (BSH) was 19.4 g, the dichloromethane extract (BSD) was 30.9 g, and the methanol extract (BSM) was 80.9 g. **Figure 1** shows the structure of compounds isolated from the *n*-hexane and dichloromethane extracts.

n-hexane extract (BSH)

BSH extract (16.5 g) was separated by SiO₂-MPLC eluted with *n*-hexane:acetone stepwise gradient (100:0, 99:1, 98:2, 95:5, 90:10, 80:20, 50:50, 0:100) to obtain 8 fractions. Fr.5 (2.08 g) was subjected to the SiO₂-MPLC with *n*-hexane/ethyl acetate gradient system (ethyl acetate: 0–100%) to afford five fractions (Fr.5.1 to Fr.5.5). Fr.5.4 (200.7 mg/ 432.3 mg) was subjected to the SiO₂-MPLC using *n*-hexane/ethyl acetate in a stepwise gradient (ethyl acetate 0-100%) to afford six fractions (Fr.5.4.1 to Fr.5.4.6). Fr.5.4.5 (18.2 mg) was purified by preparative reverse phase HPLC using an isocratic solvent system of MeCN/H₂O (80/20) to yield compound **1** (*t*_R 12.5 min, 2.1 mg, 0.013%) as a yellowish oil.

Further analysis of Fr.5.4.3 afforded compound **2** (27.0 mg, 0.164%) as a white solid. Fr.6 (1.53 g) was subjected to the SiO₂-MPLC using hexane/ethyl acetate gradient system (ethyl acetate: 0–100%) to afford five fractions (Fr.6.1 to Fr.6.5). Purification of Fr.6.3 (50.5 mg) by preparative reverse phase HPLC using an isocratic

solvent system of MeCN/H₂O (20/80) yielded compound **3** (*t_R* 42.1 min, 3.9 mg, 0.024%) as a white powder. This fraction also afforded compound **4** (*t_R* 21.6 min, 3.7 mg, 0.022%) as a white powder through the preparative reverse phase HPLC using an isocratic solvent system of MeCN/H₂O (20/80).

From spectroscopic analyses, compound **1** was found to be a new compound. While compounds **2**, **3** and **4** were identified as β -sitosterol, methyl-4-hydroxybenzoate, and 1-methoxy-4-(methoxymethyl)benzene, respectively, by comparing with the spectroscopic data in the literature (8-11).

(11*Z*,13*E*,17*E*,19*Z*)-dimethyl-15,16-dibutoxytriconta-11,13,17,19-tetraenedioate (**1**) (*t_R* 12.5 min, 2.1 mg, 0.013%) as yellowish oil. FT-IR (ATR) ν_{\max} cm⁻¹: 3013 (C-H *sp*²), 2927 (C-H *sp*³), 1712 (C=O), 1221 (C-O), 1093 (C-H in plane bending), 751 (C-H out-of-plane bending); **¹H-NMR (500MHz, CDCl₃)**: δ_{H} 0.87 (3H, t, *J* = 6.5 Hz, 4'-CH₃), 2.15 (2H, q, *J* = 5.5 Hz and 6.9 Hz, 10-CH₂), 2.28 (2H, t, *J* = 7.5 Hz, 2-CH₂-), 3.62 (2H, s, 1'-OCH₂-), 3.64 (3H, s, -OCH₃), 4.13 (1H, m, 15-OCH-), 5.43 (1H, dt, *J* = 6.4 Hz and 10.9 Hz, H-11), 5.64 (1H, dd, *J* = 6.9 Hz and 15.2 Hz, H-14), 5.95 (1H, t, *J* = 11.5 Hz, H-12) and 6.46

(1H, dd, *J* = 10.9 Hz and 15.5 Hz, H-13); **¹³C-NMR (125 MHz, CDCl₃)**; δ_{C} 14.3 (C-4'), 22.8 (C-3'), 25.1 (C-3), 25.6 (C-4), 28.0 (C-10), 29.3 (C-5), 29.4 (C-6), 29.5 (C-7), 29.6 (C-8), 31.7 (C-2'), 34.3 (C-2), 37.5 (C-9), 51.7 (-OCH₃), 70.8 (C-1'), 73.1 (C-15), 126.1 (C-13), 127.9 (C-12), 133.3 (C-11), 136.0 (C-14), and 174.5 (C-1); CI-MS: *m/z* 647.4 [M+H]⁺ {calcd 646.5 for (C₂₀H₃₅O₃)₂} and *m/z* 585.2 [M-31]⁺ {calcd 585.9 for (C₁₉H₃₂O₂)₂}.

Dichloromethane extract (BSD)

A part of BSD (5.12 g) was separated by SiO₂-MPLC using CHCl₃/MeOH in a stepwise gradient (CHCl₃/MeOH 100:0, 99:1, 98:2, 95:5, 90:10, 80:20, 50:50, 0:100) to obtain eight fractions. Fr.5 (414.2 mg) was subjected to the SiO₂-MPLC with CHCl₃/MeOH gradient system (methanol: 0-100%) to afford eight fractions (Fr.5.1 to Fr.5.8). Then, Fr.5.4 (0.414 g/ 2.380 g) was subjected to the SiO₂-MPLC using *n*-hexane/EtOAc in a stepwise gradient (EtOAc 0-100%) to afford eight fractions (Fr.5.4.1 to Fr.5.4.8). TLC analysis of Fr.5.4.3 yielded compound **5** (203.3 mg, 3.9707 %) as a white powder. Based on the spectral data and comparison with the literature report (12,13), compound **5** was identified as 4-hydroxybenzaldehyde.

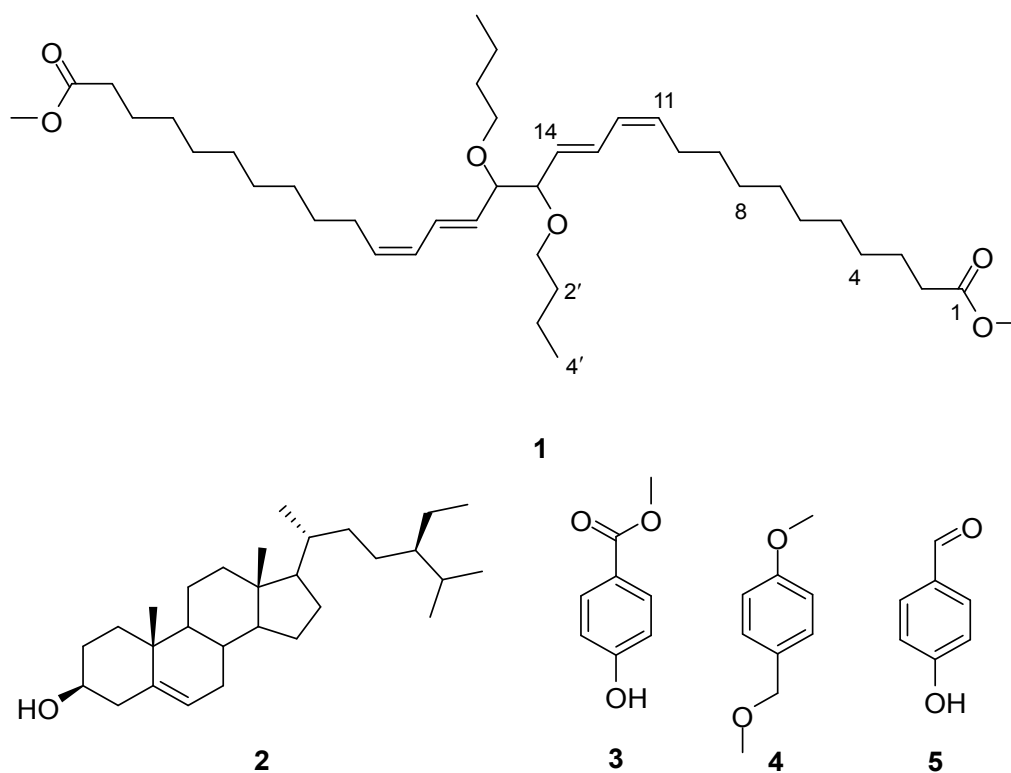


Figure 1: Compounds **1-5** isolated from *Dendrocalamus asper*. Compound **1** to **4** is from the BSH extract and compound **5** is from the BSD extract.

Antimalarial activity

Plasmodium falciparum 3D7 were cultured at 37 °C under 5.0% CO₂ and 5% O₂ in 3% hematocrit t-type A human red blood cells (Japanese Red Cross Society) in RPMI1640 (Thermo Fisher Scientific), supplied with 0.4% glucose, 20 µg/mL hypoxanthine, 24 µg/mL gentamicin, and 0.25% AlbuMax-II [14,15]. The, *P. falciparum* growth assay was performed by suspending 100 µL of 0.3%-parasitized red blood cells (as above) and 2% hematocrit in a 96-well plate for 72 h; the plates were frozen overnight at -70 °C and then thawed at room temperature for 4 h. An amount of 150 µL of the reaction mixture (166 mM sodium L-lactate, 166 µM 3-acetylpyridine adenine dinucleotide, 208 µM Nitro Blue Tetrazolium Chloride, 150 µg/mL diaphorase (22.5 U/mL), 0.8% Tween 20, 116 mM Tris-HCl, pH 8.0) was then freshly prepared and added into the wells to analyze LDH activity. After 10 minutes of incubation at room temperature, the plates were shaken to ensure mixing and the absorbance at 650 nm using a plate reader (PerkinElmer) was recorded.

Molecular docking

Molecular docking studies were performed using AutoDock v. 4.2.2 to identify appropriate binding modes and conformation of the ligand molecule. The crystal structure of *Plasmodium falciparum* DHFR-TS complexed with pyrimethamine (PDB code: 3QG2) was retrieved from the RCSB protein data bank as a PDB format (<https://www.rcsb.org/structure/3QG2>) (16). Preparation of protein was carried out following the steps described elsewhere (17). All hetero atoms and water molecules were deleted using PyMol (version 1.3) software packages whereas, energy minimization of the protein was carried out using Swiss-Pdb viewer software (version 4.1.0). The structures of all the ligands were drawn using Chemdraw Ultra 13.0 and converted into 3D structures using Hyperchem Pro 8.0 software (www.hyper.com). Autodock Tools (ADT) version 1.5.6 (www.autodock.scrips.edu) was used to prepare the molecular docking. The active site was considered as a rigid molecule, while the ligands were treated as being flexible. Finally, rigid docking simulation was performed by AutoDock software considering the center grid box size of 27x6x67 in the x, y and z coordinates. The best binding conformation was selected from the docking log (.dlg) file for each ligand and further interaction analysis was done using PyMol and Discovery Studio Visualizer 4.0.

RESULTS AND DISCUSSION

Chemistry

Extraction followed by chromatographic fractionation of *Dendrocalamus asper* yielded one new compound; (11Z,13E,17E,19Z)-dimethyl-15,16-dibutoxytricycanta-11,13,17,19-tetraenedioate (**1**), and four known compounds; β -sitosterol (**2**) (18), methyl-4-hydroxybenzoate (**3**) (19,20), 1-methoxy-4-(methoxymethyl)benzene (**4**) (21) and 4-hydroxybenzaldehyde (**5**) (22) (**Figure 1**). The last four known compounds have not been previously isolated from this plant species. The structure of **1** was elucidated by FTIR, 1D and 2D NMR, and CI-MS.

The FTIR of compound **1** exhibited transmission bands at 3013, and 2927 cm⁻¹ due to the C-H *sp*² and C-H *sp*³ stretching. Besides that, the transmission band at 1712 cm⁻¹ indicated the presence of the carbonyl group (C=O) stretching of the methylated fatty acid ester moiety attached to compound **1**. Also, the band at 1221 cm⁻¹ was attributed to the C-O bond stretching vibration, while the band at 1093 cm⁻¹ was assigned to the in-plane bending of the C-H bond.

The ¹H NMR spectrum of compound **1** exhibits four signals at δ_H 6.46 ppm (1H, dd, *J* = 10.9 Hz and 15.5 Hz), 5.95 ppm (1H, t, *J* = 11.5 Hz), 5.64 ppm (1H, dd, *J* = 6.9 Hz and 15.2 Hz), 5.43 ppm (1H, dt, *J* = 7.5 Hz and 10.9 Hz) which represents the four vinylic protons, H-13, H-12, H-14, and H-11. H-11 and H-14 protons are bonded to an *sp*³ hybridized carbon, C-10, and C-15, respectively. So, they are shielded and absorb upfield compared to H-12 and H-13. H-13 has two nearby non-equivalent protons that split its signal, the *trans* protons of H-12 and H-14. H-14 splits the H-13 signal into a doublet, and H-12 proton splits the doublet into two doublets, forming doublet of the doublet. At the same time, H-12 has two nearby non-equivalent protons, the *cis* proton H-11, and *trans* proton H-13. H-13 is more deshielded than H-12 due to the hydrogen in a *cis*-isomer being slightly more upfield and *trans* hydrogen being more downfield to the left of the spectrum. Two singlet signals located at δ_H 3.64 (3H) and δ_H 3.62 (2H) were assigned to the -OCH₃ and 1'-OCH₂. The ¹³C NMR of compound **1** shows the presence of 20 signals. The signals for twelve methylene carbons (C-2, C-3, C-4, C-5, C-6, C-7, C-8, C-9, C-10, C-1', C-2', and C-3') can be observed at δ_C 34.3, 25.1, 25.6, 29.3, 29.4, 29.5, 29.6, 37.5, 28.0, 70.8, 31.7, and 22.8, respectively. Meanwhile, the signal for carbonyl carbon, C-1 showed a resonance at δ_C 174.5. The ¹H-¹H COSY and HMBC correlations of compound **1** are shown in **Figure 2**. The HMBC spectrum reveals the aliphatic proton, H-14 at δ_H 5.64, correlated with C-12 (δ_C 127.9) and C-15 (δ_C 73.1). The signal for methyl proton (4'-CH₃) showed cross-peak with C-2' (δ_C 31.7)

and C-3' (δ_c 22.8). Besides, the singlet methoxy proton ($-\text{OCH}_3$) at δ_H 3.64 assigned to $-\text{OCH}_3$ (δ_c

51.7) showed HMBC correlation with the carbonyl carbon, C-1 (δ_c 174.5).

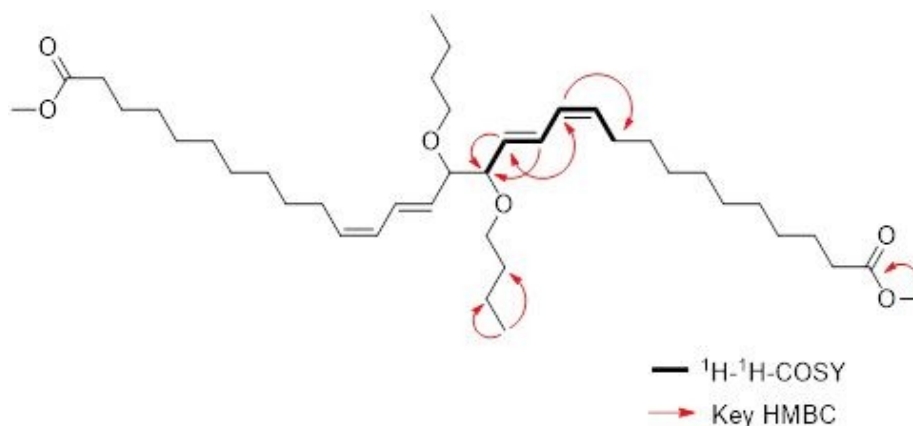


Figure 3. Key COSY/ HMBC correlations of compound **1**.

The nominal APCI-MS spectra of compound **1** were in good agreement with the molecular formula $(\text{C}_{20}\text{H}_{35}\text{O}_3)_2$ showing a base peak at m/z 646.4 $[\text{M}+\text{H}]^+$ {calcd 646.5 for $(\text{C}_{20}\text{H}_{35}\text{O}_3)_2$ }. The ion peak at m/z 585.6 arise due to the $(\text{C}_{19}\text{H}_{32}\text{O}_2)_2$ fragment, by the loss of two methoxy radicals

$[\text{M}+\text{H}-62]^+$ (**Figure 3**). Based on the spectroscopy data (IR, 1D- and 2D-NMR) and mass spectrometric data, compound **1** is a new diester isolated for the first time from the plant and its chemical name is (11Z,13E,17E,19Z)-dimethyl-15,16-dibutoxytriconta-11,13,17,19-tetraenedioate.

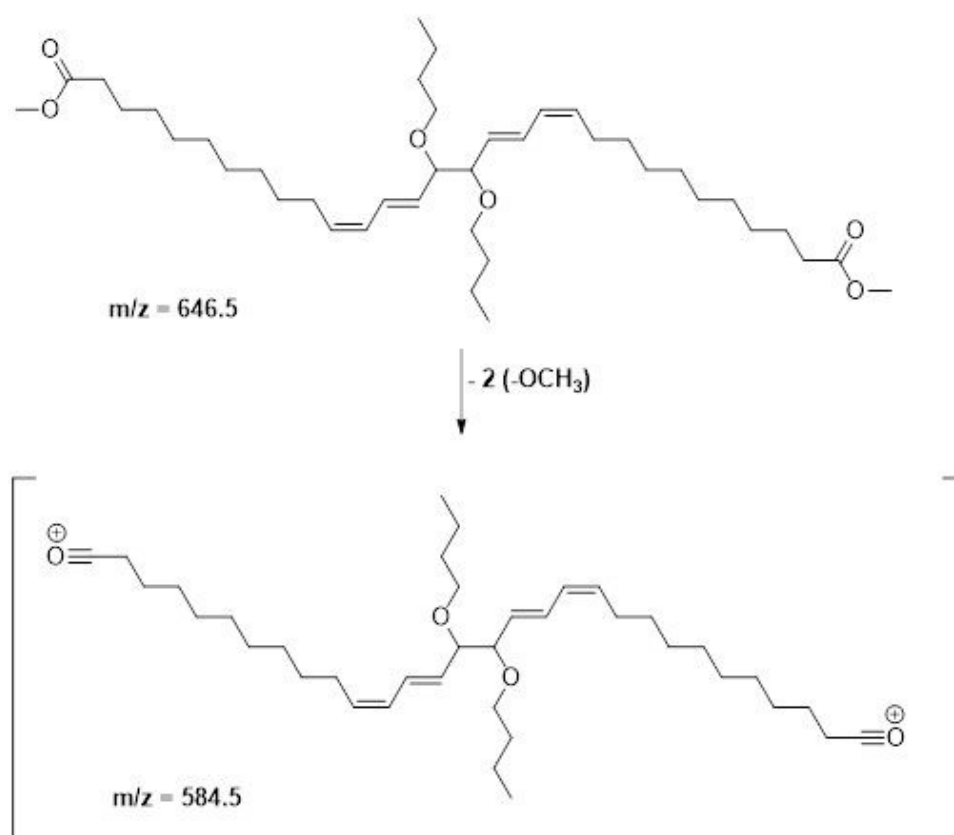


Figure 3. The fragmentation of compound **1** leading to the ion peak m/z 584.5.

Antimalarial activity

All the five isolated chemical constituents of *Dendrocalamus asper* were evaluated for their

potential antimalarial properties against the *P. falciparum* strain 3D7 (**Table 2**). Compound **3** was the most active compound against the *P.*

falciparum with the IC₅₀ value of 5 µM (~0.82 µg/mL). Meanwhile, compounds **1** and **4** showed moderate antimalarial activity with the IC₅₀ values of 3 µM (~2.2 µg/mL) and 7 µM (~1.1 µg/mL),

respectively. However, compounds **2** and **5** showed weak antimalarial activity with 50 % inhibition (IC₅₀) value > 24 µM (>10 µg/mL) and > 82 µM (>10 µg/mL), respectively.

Table 2. Growth inhibitory activity of compounds **1-5** against *P. falciparum* 3D7.

Compound	IC ₅₀	
	µg/mL	µM
1	2.2	3
2	>10	>24
3	0.8	5
4	1.1	7
5	>10	>82
Chloroquine (control)	0.01	0.05

Results are mean values of duplicate independent assays

Molecular docking studies

To gain further evidence regarding the mode of action of the potent compounds (i.e **1**, **3** and **4**) a molecular docking study was carried out on *P. falciparum* enzyme dihydrofolate reductase-thymidylate synthase (DHFR-TS), which is a potential drug target for malaria (16). All the three compounds **1** (-4.20 kcal/mol), **3** (-5.4 kcal/mol), and **4** (-5.2 kcal/mol) showed good interactions with the enzyme DHFR-TS in terms of binding interactions. It was also observed that all the three compounds **1,3**, and **4** occupied the same binding

site and formed similar type of interactions with the active site residues (**Figure 4**). The results of binding studies of the most active compound **3** clearly indicate that the compound exhibited significant interactions at the active site by forming two hydrogen bonds with LEU164 and TYR170 residues (docking score of -4.16 kcal/mol). A π-π stacking was also observed between the phenyl ring of compound **3** and PHE58. The results of molecular docking studies revealed that the antimalarial activity of compound **1, 3** and **4** might be due to DHFR-TS inhibition.

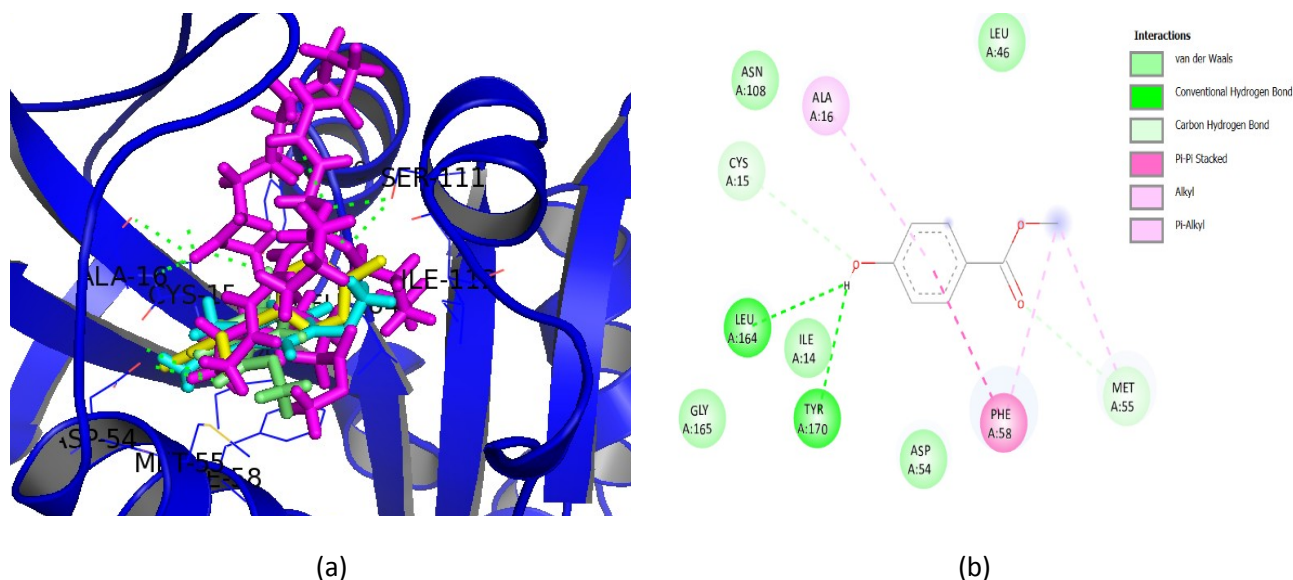


Figure 4. (a) Docking poses of compound **1** (magenta), **3** (lime), **4** (cyan) and reference ligand pyrimethamine (yellow) at the active site of *P. falciparum* DHFR-TS (PDB ID: 3QG2) showing hydrogen bondings (green). (b) 2D binding interactions of the most active compound **3** showing two hydrogen bonds (green) with LEU164 and TYR170 residues at the active site.

CONCLUSION

Five bioactive principles were isolated from bamboo shoot extracts, of which one new metabolite, compound **1**, and three known metabolites, which are compounds **2-4** were

isolated from *n*-hexane extract, whereas one known metabolite, compound **5** was obtained from dichloromethane extract. Among these, compound **3** was highly active against *P. falciparum* with IC₅₀ value of 0.82 µg/mL.

ACKNOWLEDGMENT

The authors would like to acknowledge the financial support from the Ministry of Higher Education of Malaysia (MyPhD – MyBrain15) and the USM RUT grant (1001/Pkimia/8011072). Wong, K.T. also extends his appreciation to Prof Osada, H., Nogawa, T., and Futamura, Y. from Chemical Biology Research Group, RIKEN Center for Sustainable Resource Science, Wako, Saitama, Japan for providing laboratory facilities and technical assistance under short-term International Program Associate (IPA). We also like to thank Zhang J.L. for his contribution to this project. We also like to thank Awang, K. for the assistance in the confirmation of spectroscopic analysis & interpretation.

REFERENCES

- Al-Adhroey AH, Nor ZM, Al-Mekhlafi HM, Amran AA, Mahmud R. Antimalarial activity of methanolic leaf extract of *Piper betle* L. *Molecules*. 2010; 16(1): 107-18. [<DOI>](#).
- World Health Organisation. 2019 World Malaria Report. Geneva, Switzerland: WHO, 2019. (Accessed 01.03.2020). [<URL>](#).
- Jantan I. Medicinal plant research in Malaysia: Scientific interests and advances. *Malaysian J. Health Sci*. 2004; 2(2):27-46.
- Schwikkard S, Van Heerden F. Antimalarial activity of plant metabolites. *Nat. Prod. Rep*. 2002; 19(6): 675-92. [<URL>](#).
- Klayman DL. Qinghaosu (artemisinin): an antimalarial drug from China. *Science*. 1985; 228(4703): 1049-55. [<DOI>](#).
- Nik Abdul Rahman NN, Furuta T, Kojima S, Takane K, Mohd MA. Antimalarial activity of extracts of Malaysian medicinal plants. *J. Ethnopharmacol*. 1999; 64(3): 249-54. [<DOI>](#).
- Kant P. Should bamboos and palms be included in CDM forestry projects? IGREC working paper, No. IGREC-07:2010, Institute of Green Economy, New Delhi, 2010. [<URL>](#).
- Chaturvedula VSP, Prakash I. Isolation of stigmasterol and β -sitosterol from the dichloromethane extract of *Rubus suavissimus*. *Int. Curr. Pharm. J*. 2012; 1(9): 239-42. [<DOI>](#).
- Aliba MO, Ndukwe IG, Ibrahim H. Isolation and characterization of β -sitosterol from methanol extracts of the stem bark of large-leaved rock fig (*Ficus Abutilifolia* Miq). *J. Appl. Sci. Environ. Manage*. 2018; 22(10): 1639-42. [<DOI>](#).
- Chang YC, Chang FR, Wu YC. The constituents of *Lindera glauca*. *J. Chin. Chem. Soc*. 2000; 47(2): 373-80. [<DOI>](#).
- Bhaskar G, Solomon M, Babu G, Muralidharan D, Perumal PT. A simple and an efficient indium trichloride catalyzed benzyl etherification. *Indian J. Chem., Sect B*. 2010; 49B: 795-801. [<URL>](#).
- Panyo J, Matsunami K, Panichayupakaranant P. Bioassay-guided isolation and evaluation of antimicrobial compound from *Ixora megalophylla* against some oral pathogens. *Pharm. Biol*. 2016; 54(9): 1522-27. [<DOI>](#).
- Magano J, Chen MH, Clark JD, Nussbaumer T. 2-(Diethylamino)ethanethiol, a new reagent for the odorless deprotection of aromatic methyl ethers. *J. Org. Chem*. 2006; 71(18): 7103-5. [<DOI>](#).
- Hayase H, Watanabe N, Lim CL, Nogawa T, Komatsuya K, Kita K, Osada H. Inhibition of Malaria Parasite Growth by Quinomycin A and its derivatives through DNA-Intercalating Activity. *Biosci, Biotechnol, Biochem*. 2015; 79(4): 633-5. [<DOI>](#).
- Gamo FJ, Sanz LM, Vidal J, De Cozar C, Alvarez E, Lavandera JL, Vanderwall DE, Green DV, Kumar V, Hasan S, Brown JR, Peishoff CE, Cardon LR, Garcia-Bustos JF. Thousands of chemical starting points for antimalarial lead identification. *Nature*. 2010; 465(7296): 305-10. [<DOI>](#).
- Vanichtanankul J, Taweechai S, Yuvaniyama J, Vilaivan T, P Chitnumsub, Kamchonwongpaisan S, Yuthavong Y. Trypanosomal Dihydrofolate Reductase Reveals Natural Antifolate Resistance. *ACS. Chem. Biol*. 2011; 6(9): 905-11. [<DOI>](#).
- Matin MM, Hasan MS, Uzzaman M, Bhuiyan MMH, Kibria SM, Hossain ME, Roshid MHO. Synthesis, spectroscopic characterization, molecular docking, and ADMET studies of mannopyranoside esters as antimicrobial agents. *J. Mol. Struct*. 2020; 1222, 128821-33. [<DOI>](#).
- Ahmad F, Ali M, Alam P. New phytoconstituents from the stem bark of *Tinospora cordifolia* Miers. *Nat. Prod. Res*. 2010;24(10): 926-34. [<DOI>](#).
- Tian JK, Sun F, Cheng YY. Chemical constituents from the roots of *Ranunculus*

ternatus. *J. Asian Nat. Prod. Res.* 2006; 8(1-2): 35-9. [<DOI>](#).

20. Vijayan N. Structural and optical characterization on solution grown methyl *p*-hydroxybenzoate single crystals. *Indian J. Chem., Sect A.* 2007; 46(1): 70-3. [<URL>](#).

21. Tsai CY, Sung R, Zhuang BR, Sung KS. TiCl₄ -activated selective nucleophilic substitution

of *tert*-butyl alcohol and benzyl alcohol with *p*-donating substituents. *Tetrahedron.* 2010; 66(34): 6869-72. [<DOI>](#).

22. Kim H, Ralph J, Lu F, Boudet AM, MacKay JJ, Sederoff RR, Ito T, Kawai S, Ohashi H, Higuchi T. NMR analysis of lignins in CAD-deficient plants. Part 1. Incorporation of hydroxycinnamaldehydes and hydroxybenzaldehydes into lignins. *Org. Biomol. Chem.* 2003; 1(2): 268-81. [<DOI>](#).



Synthesis and Spectral Characterization of 6-*O*-Octanoyl-1,2-*O*-isopropylidene- α -D-glucofuranose Derivatives

Puja Devi¹ , Mohammed M. Matin^{1*}  , Md. Mosharef H. Bhuiyan¹ , and Md. Emdad Hossain² 

¹University of Chittagong, Faculty of Science, Department of Chemistry, 4331, Chittagong, Bangladesh.

²Jahangirnagar University, Wazed Miah Science Research Centre (WMSRC), Savar, 1342, Dhaka, Bangladesh.

Abstract: Site selective acylation of monosaccharides and oligosaccharides is essential for the preparation of both natural and novel synthetic carbohydrate compounds, synthetic intermediates, postglycosylation modifications, and for the preparation of therapeutic agents, including research tools for glycobiology. Hence, site-selective octanoylation of 1,2-*O*-isopropylidene- α -D-glucofuranose was conducted. Under low temperature in anhydrous pyridine, direct unimolar octanoylation of this glucofuranose without any catalyst exhibited selectivity at the C-6 hydroxyl group. The C-6 *O*-octanoylglucofuranose, thus obtained, was then used to prepare three 3,5-di-*O*-acyl esters in a similar direct method to get novel esters of glucofuranose. Characterization of all the glucofuranose esters by 1D and 2D spectroscopic technique is also discussed herein.

Keywords: Bisacetone D-glucose, HMBC, Site-selective acylation, Sugar esters.

Submitted: April 30, 2021. **Accepted:** August 25, 2021.

Cite this: Devi P, Matin MM, Bhuiyan M, Hossain M. Synthesis and Spectral Characterization of 6-*O*-Octanoyl-1,2-*O*-isopropylidene- α -D-glucofuranose Derivatives. JOTCSA. 2021;8(4):1003-24.

DOI: <https://doi.org/10.18596/jotcsa.929996>.

***Corresponding author. E-mail:** mahbubchem@cu.ac.bd, Tel: +880-1716-839689, Fax: +880-31-2606014.

INTRODUCTION

Carbohydrate-derived fatty acid esters, also known as sugar esters (SEs), have attracted interest due to their non-ionic surfactant (1) and biological activities (2-5). In general, the combination of hydrophilic sugar moieties and hydrophobic acid(s) produced the sugar esters and showed high stability, biodegradability under aerobic or anaerobic conditions, and low stimulatory effects with no taste (6-7). These properties attracted their use in food (e.g., gelatinization of starch), cosmetics, and pharmaceutical industries (8-9). One of the crucial features is their HLB (hydrophilic-lipophilic balance). This HLB can be manipulated, if necessary, via altering fatty acid(s) and monosaccharide moiety (glycon part) (10). Maintaining this HLB a plethora SEs has been synthesized for a long time, searching for effective bio-surfactant and potential

biodegradable drugs (11-13). Their environmental acceptability, renewability, and low cost make SEs surfactants an excellent alternative to petrochemically derived similar types of products. Apart from the well-known surfactant and drug, SEs are found ubiquitously and well documented for other health-protective effects such as antimicrobial, anti-inflammatory, antimutagenic, etc. (14-16). In plants, SEs can carry not only sugars but also long-chain fatty acids into the plant cells. Thus, synthesis and application of monosaccharide-based SEs are essential for both medicinal and biological chemists (17-19).

Of the SEs, several glucofuranose esters of alkyl-fumarates were found suitable for use as active substances in treating psoriasis or other hyperproliferative, inflammatory, or autoimmune disorders (20). To control the solubility of SEs

sometimes sugar acetals and alkyl derivatives are also used (21). Protected glucofuranose, i.e., bisacetone D-glucose has been used as an intermediate for the synthesis of many natural and synthetic novel bioactive compounds (22-24). For example, D-glucofuranose-derived Seprilose (GW 80126) is used to inhibit prostaglandin E2 synthesis (25). Kobayashi and co-workers (26) also utilized D-gluco-1,4-furanose to synthesize its 6-*O*-palmitoyl derivative **1** (Figure 1) by enzymatic technique. Catelani et al. (27) synthesized several 3-*O*-acyl-1,2-*O*-isopropylidene-D-glucofuranose derivatives

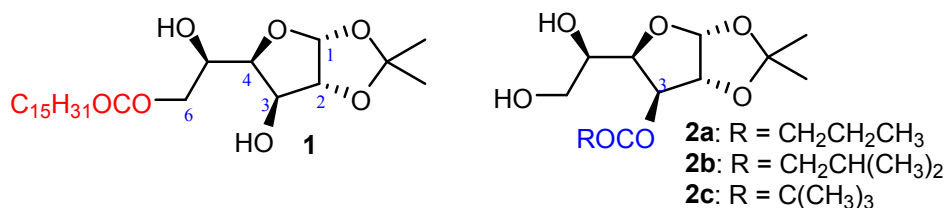


Figure 1. Structure of glucofuranose ester **1** and **2**.

Synthesis of site-selective monosaccharide esters faces unique synthetic difficulties as compared to other biomolecules. The basic problem is the availability of several hydroxyl (OH) groups in monosaccharides of almost the same reactivity as many reagents (33). Again, most of these secondary OH groups have similar reactivity and lead to mono-, di-, and poly-ester formation (34-36). Investigations for selective and site-selective conversion/protection of monosaccharides have been conducted for the last 100 years. Many methods were developed using a minor inherent reactivity variation of hydroxyl groups in useful ways (34, 37-38). For instance, in glucopyranoside and mannopyranoside, the OH group at C-4 was found intrinsically more reactive than the OH groups present in other positions under several conditions (39). However, in most cases, the 1° OH group showed higher reactivity than the 2° hydroxyl groups (40-41). The most common esterification/protection methods for monosaccharides are (i) direct method (42-43), (ii) catalyst mediated acylation (44-45), (iii) protection-deprotection method (46-47), (iv) enzymatic (48), and (v) microwave-assisted method (49). A direct acylation technique was employed in the present study, maintaining some important reaction conditions with some advantages over other methods (12-13).

Site-selective octanoylation of 1,2-*O*-isopropylidene- α -D-glucofuranose and its 3,5-di-*O*-acyl esters are described in the present article. Especial emphasis is given to their 1D and 2D spectroscopic characterization.

EXPERIMENTAL

Materials and general methods

All the reagents (D-glucose, octanoyl chloride,

2a-c) for bioactivity tests found that several such acyl glucofuranoses were highly potent enhancers for erythroid tumor cells. It was found that the combination of glucofuranose with various ester groups like acetyl and benzoyl groups increased its antimicrobial activities, and in some cases, the results are comparable to the standard drugs (28-29). Overall, an intrinsic interest was observed to synthesize glucofuranose derived compounds, many of which are used as drugs (e.g., Seprilose) (30-32).

pentanoyl chloride, hexanoyl chloride, 4-chlorobenzoyl chloride etc.) and related solvents were purchased from a commercial supplier (analytical grade). Reduced pressure and temperature (40 °C, Büchi rotavapor, Switzerland) were maintained for evaporations. Electrothermal melting point apparatus is used for melting points and reported without corrections. Silica gel GF₂₅₄ plates were used for thin-layer chromatography (TLC) detection. For purification, silica gel G₆₀ was used in column chromatography (CC). During CC purification different proportion of *n*-hexane (PE)/ethyl acetate (EA) was used, and these solvents were distilled before use. FT-IR spectra were recorded on an FT-IR spectrometer (PerkinElmer, Spectrum Two) without solvent (neat). CDCl₃ solutions of the samples were used for scanning ¹H (400 MHz) and ¹³C (100 MHz) NMR spectra. During characterization, the position of the proton and carbon signals for each compound was confirmed with the help of their different types of 2D spectra.

Preparation of 1,2-*O*-isopropylidene- α -D-glucofuranose (**4**)

Initially, bisacetone D-glucose **3** was prepared from the reaction of dry D-glucose with freshly dried CH₃COCH₃ and dry copper sulfate following reported method (50) in moderate yield (46%, solid, mp 107-109 °C [(50) mp. 108-109 °C]. The bisacetone D-glucose (5.0 g, 19.209 mmol) was then dissolved in a mixture of methanol-water (70:15 mL) with stirring followed by the addition of 10% H₂SO₄ (3.6 mL) at normal temperature. The stirring was continued for 5 h when the reaction mixture was neutralized with saturated aqueous potassium carbonate (K₂CO₃) solution. The reaction mixture was concentrated to dryness and slowly extracted with organic solvent (EA) with occasional heating. The combined EA layer was dried (MgSO₄) and

subjected for concentration. The thick syrup thus obtained was passed through the silica gel column. Elution with petroleum ether (PE)/EA (1:9) furnished the title compound **4** as a white solid (3.215 g, 76%), mp 158-160 °C [literature (51) melting point 159-160 °C].

Preparation of 1,2-O-isopropylidene-6-O-octanoyl- α -D-glucofuranose (**5**)

To a solution of monoacetonide **4** (1.5 g, 6.812 mmol) in dry C_6H_5N was slowly added octanoyl chloride (1.218 g, 7.488 mmol) at ice-cooled temperature. Stirring of the reaction mixture was continued at this temperature for 9 h and then at 22-25 °C temperature for 3 h. The reaction was quenched with ice-water. Then it was added with DCM for extraction (dichloromethane, 8×3 mL). The combined DCM solution was washed with 5% aqueous HCl, saturated aqueous $NaHCO_3$ solution and NaCl solution followed by drying with $MgSO_4$, and concentration under diminished pressure. Purification of the thick residue thus obtained was achieved by passing the syrup through silica gel column (PE/EA, 1:1) and obtained a clear solid compound **5** (1.772 g, 73%) as needles, mp 90-92 °C (ethyl acetate-*n*-hexane). R_f = 0.66 (*n*-hexane/EA = 1/2); FT-IR (neat) ν_{max} (cm^{-1}): 3180-3465 (OH), 1710 (CO), 1377 ($C(CH_3)_2$); 1H NMR (400 MHz, $CDCl_3$) δ_H ppm: 5.98 (d, J = 3.6 Hz, 1H, H-1), 4.55 (d, J = 3.6 Hz, 1H, H-2), 4.42-4.47 (m, 1H, H-6a), 4.38 (d, J = 1.6 Hz, 1H, H-3), 4.22-4.28 (m, 2H, H-5 and H-6b), 4.09-4.11 (m, 1H, H-4), 2.89-2.98 (br s, exchangeable with D_2O , 2H, 2×OH), 2.39 (t, J = 7.6 Hz, 2H, $CH_3(CH_2)_5CH_2CO$), 1.63-1.68 (m, 2H, $CH_3(CH_2)_4CH_2CH_2CO$), 1.51 (s, 3H, $C(CH_3)_2$), 1.34 (s, 3H, $C(CH_3)_2$), 1.26-1.32 (m, 8H, $CH_3(CH_2)_4(CH_2)_2CO$), 0.90 (t, J = 6.4 Hz, 3H, $CH_3(CH_2)_6CO$); ^{13}C NMR (100 MHz, $CDCl_3$) δ_C ppm: 174.5 (CO), 111.9 ($C(CH_3)_2$), 105.0 (C-1), 85.2 (C-2), 79.3 (C-4), 75.6 (C-3), 69.4 (C-5), 66.0 (C-6), 34.2, 31.6, 29.0, 28.8, 24.8, 22.6 ($CH_3(CH_2)_6CO$), 26.8, 26.2 ($C(CH_3)_2$), 14.0 ($CH_3(CH_2)_6CO$). All the positions of proton and carbons were determined by combined analyses of 1D and several 2D spectra.

General procedure for preparation of 3,5-di-O-acyl derivatives **6-8** of 6-O-octanoyl- α -D-glucofuranose **5**

Selected three acyl halides (2.2 eq.) were added separately drop-wise to an ice-cooled and well-stirred solution of diol **5** (0.2 g, 0.578 mmol) in dry C_6H_5N . A catalytic amount of DMAP was added to the solution. Stirring was continued, and reaction temperature was allowed to rise to 22-25 °C. Stirring continues for 10-12 h. Decomposition of excess acyl halide(s) was accomplished by the addition of a small amount of frozen water. An organic solvent like dichloromethane (DCM) was added and collected several times from a separating funnel. The combined DCM layer was washed with dilute aqueous HCl solution, then with aqueous $NaHCO_3$ solution, and finally with NaCl solution in

water. This DCM layer was dried with $MgSO_4$ and concentrated in a rotavapor. This gave a thick syrup, which was finally purified employing column chromatography (CC). In CC, elution was performed with different proportions of *n*-hexane and ethyl acetate (10:0 to 6:1). After CC, the desired 3,5-di-O-acylates **6-8** were obtained in satisfactory yields.

1,2-O-Isopropylidene-6-O-octanoyl-3,5-di-O-pentanoyl- α -D-glucofuranose (**6**):

Colorless thick mass; yield 91%; R_f = 0.50 (PE/EA = 5/1); FT-IR (neat) ν_{max} (cm^{-1}): 1747, 1741, 1733 (CO), 1375 ($C(CH_3)_2$); 1H NMR (400 MHz, $CDCl_3$) δ_H ppm: 5.93 (d, J = 3.6 Hz, 1H, H-1), 5.33 (d, J = 2.4 Hz, 1H, H-3), 5.24 (ddd, J = 7.2, 5.6 and 2 Hz, H-5), 4.61 (dd, J = 12.4 and 2.0 Hz, 1H, H-6a), 4.47 (dd, J = 7.2 and 3.2 Hz, 1H, H-4), 4.44 (d, J = 2.8 Hz, 1H, H-2), 4.14 (dd, J = 12.4 and 5.6 Hz, 1H, H-6b), 2.30-2.34 (m, 4H, $2 \times CH_3(CH_2)_2CH_2CO$), 2.26 (t, J = 7.5 Hz, 2H, $CH_3(CH_2)_5CH_2CO$), 1.54-1.62 (m, 6H, $2 \times CH_3CH_2CH_2CH_2CO$ and $CH_3(CH_2)_4CH_2CH_2CO$), 1.53 (s, 3H, $C(CH_3)_2$), 1.25-1.39 (m, 15H, $C(CH_3)_2$, $2 \times CH_3CH_2(CH_2)_2CO$ and $CH_3(CH_2)_4(CH_2)_2CO$), 0.88-0.94 (m, 9H, $2 \times CH_3(CH_2)_3CO$ and $CH_3(CH_2)_6CO$); ^{13}C NMR (100 MHz, $CDCl_3$) δ_C ppm: 173.3, 172.4, 172.3 (CO), 112.4 ($C(CH_3)_2$), 105.2 (C-1), 83.3 (C-4), 76.8 (C-2), 74.6 (C-3), 67.4 (C-5), 63.1 (C-6), 34.2, 33.8, 33.6, 31.7, 29.1, 28.9, 26.7, 26.6, 24.9, 22.6, 22.2(2) ($2 \times CH_3(CH_2)_3CO$ and $CH_3(CH_2)_6CO$), 26.8, 26.3 ($C(CH_3)_2$), 14.0, 13.7(2) ($2 \times CH_3(CH_2)_3CO$ and $CH_3(CH_2)_6CO$).

3,5-Di-O-hexanoyl-1,2-O-isopropylidene-6-O-octanoyl- α -D-glucofuranose (**7**):

Clear syrup; yield 88%; R_f = 0.52 (PE/EA = 5/1); FT-IR (neat) ν_{max} (cm^{-1}): 1736, 1739, 1722 (CO), 1374 ($C(CH_3)_2$); 1H NMR (400 MHz, $CDCl_3$) δ_H ppm: 5.91 (d, J = 3.2 Hz, 1H, H-1), 5.31 (d, J = 2.8 Hz, 1H, H-3), 5.23 (ddd, J = 7.0, 5.4 and 1.6 Hz, H-5), 4.59 (dd, J = 12.2 and 1.6 Hz, 1H, H-6a), 4.45 (dd, J = 7.1 & 3.2 Hz, 1H, H-4), 4.42 (d, J = 2.4 Hz, 1H, H-2), 4.12 (dd, J = 12.2 & 5.4 Hz, 1H, H-6b), 2.11-2.44 (m, 6H, $2 \times CH_3(CH_2)_3CH_2CO$ and $CH_3(CH_2)_5CH_2CO$), 1.56-1.74 (m, 6H, $2 \times CH_3(CH_2)_2CH_2CH_2CO$ and $CH_3(CH_2)_4CH_2CH_2CO$), 1.53 (s, 3H, $C(CH_3)_2$), 1.34 (s, 3H, $C(CH_3)_2$), 1.22-1.33 (m, 16H, $2 \times CH_3(CH_2)_2(CH_2)_2CO$ and $CH_3(CH_2)_4(CH_2)_2CO$), 0.87-0.92 (m, 9H, $2 \times CH_3(CH_2)_4CO$ and $CH_3(CH_2)_6CO$); ^{13}C NMR (100 MHz, $CDCl_3$) δ_C ppm: 173.3, 172.4, 172.3 (CO), 112.5 ($C(CH_3)_2$), 105.1 (C-1), 83.3 (C-4), 76.8 (C-2), 74.6 (C-3), 67.4 (C-5), 63.1 (C-6), 34.1, 34.0, 33.8, 31.6, 31.2(2), 29.1, 28.9, 24.8, 24.4, 24.2, 22.6, 22.2(2) ($2 \times CH_3(CH_2)_4CO$ and $CH_3(CH_2)_6CO$), 26.8, 26.2 ($C(CH_3)_2$), 14.0, 13.8(2) ($2 \times CH_3(CH_2)_4CO$ and $CH_3(CH_2)_6CO$).

3,5-Di-O-(4-chlorobenzoyl)-1,2-O-isopropylidene-6-O-octanoyl- α -D-glucofuranose (**8**):

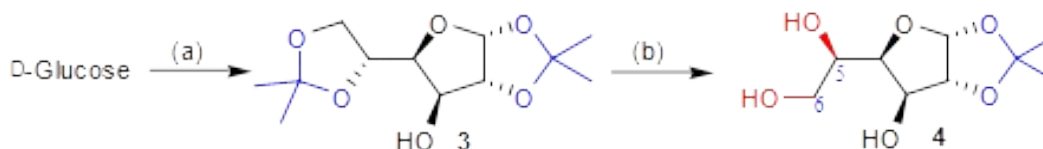
Pale-yellow semi-solid; yield 94%; R_f = 0.59 (PE/EA = 5/1); FT-IR (neat) ν_{max} (cm^{-1}): 1745, 1708, 1701 (CO), 1381 ($C(CH_3)_2$); 1H

NMR (400 MHz, CDCl₃) δ_H ppm: 7.90 (d, J = 8.4 Hz, 2H, Ar-H), 7.82 (d, J = 8.8 Hz, 2H, Ar-H), 7.43 (d, J = 8.4 Hz, 2H, Ar-H), 7.38 (d, J = 8.4 Hz, 2H, Ar-H), 6.04 (d, J = 3.6 Hz, 1H, H-1), 5.60 (ddd, J = 7.2, 5.6 and 2.8 Hz, H-5), 5.54 (d, J = 2.8 Hz, 1H, H-3), 4.68-4.72 (m, 2H, H-4 & H-6a), 4.66 (d, J = 3.2 Hz, 1H, H-2), 4.37 (dd, J = 12.4 & 5.6 Hz, 1H, H-6b), 2.30 (t, J = 7.5 Hz, 2H, CH₃(CH₂)₅CH₂CO), 1.61 (s, 3H, C(CH₃)₂), 1.52-1.59 (m, 2H, CH₃(CH₂)₄CH₂CH₂CO), 1.37 (s, 3H, C(CH₃)₂), 1.19-1.29 (m, 8H, CH₃(CH₂)₄(CH₂)₂CO), 0.87 (t, J = 6.4 Hz, 3H, CH₃(CH₂)₆CO); ¹³C NMR (100 MHz, CDCl₃) δ_C ppm: 173.5 (C₇H₁₅CO), 164.2, 164.1 (2 \diamond 4-Cl.C₆H₄CO), 140.0, 139.9, 131.2(2), 131.0(2), 128.9(2), 128.8(2), 127.8, 127.4 (Ar-C), 112.7 (C(CH₃)₂), 105.2 (C-1), 83.2 (C-4), 76.9 (C-2), 76.1 (C-3), 68.8 (C-5), 63.1 (C-6), 34.1, 31.6, 29.0, 28.9, 24.9, 22.6 (CH₃(CH₂)₆CO), 26.8, 26.3 (C(CH₃)₂), 14.0 (CH₃(CH₂)₆CO).

RESULTS AND DISCUSSION

Regioselective octanoylation of monoacetonide- α -D-glucofuranose **4**

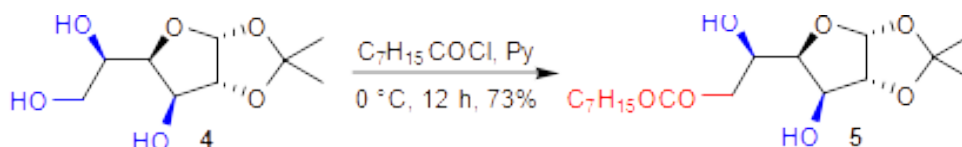
The present study mainly describes the synthesis and spectroscopic characterization of 6-*O*-octanoyl- α -D-glucofuranose **5** and its three derivatives **6-8**. In this respect, initially, 1,2:5,6-di-*O*-isopropylidene- α -D-gluco-1,4-furanose (**3**) was prepared from D-glucose. Treatment of D-glucose with anhydrous acetone, a catalytic amount of conc. H₂SO₄ and CuSO₄, according to the literature procedure (Scheme 1), gave **3** in moderate yield (46%) (19, 50). At this stage, removing the 5,6-*O*-acetonide group was conducted selectively by treating bisacetonide **3** with 15% H₂SO₄ in methanol for 5 h, which upon CC purification was furnished pure crystals of monoacetonide **4** (76%), mp 158-160 °C (Scheme 1). Its FT-IR, ¹H, and ¹³C NMR showed similarity with the published data (51).



Scheme 1: (a) Dry acetone, anhydrous CuSO₄, conc. H₂SO₄, rt, 24 h, 46% (50); (b) 15% H₂SO₄, MeOH-H₂O, 25 °C, 5 h, 76% (51).

Having monoacetonide **4** in hand attempt was made for its mono-octanoylation. Thus, treating **4** with unimolar octanoyl chloride in basic pyridine at reduced temperature (0 °C) for 12 h followed by CC purification gave a solid mp 90-92 °C in 73%

(Scheme 2). Its FT-IR showed one broad characteristic band at 3180-3465 cm⁻¹ for the OH group. Also, a sharp characteristic band at 1710 cm⁻¹ (CO) indicates the molecule's partial octanoylation.



Scheme 2. Selective octanoylation of glucofuranose **4**.

In its ¹H NMR spectrum, additional fifteen protons appeared at δ 2.39 (t, 2H), 1.63-1.68 (m, 2H), 1.26-1.32 (m, 8H), and 0.90 (t, 3H), which corresponded to an octanoyl group of protons. The appearance of a broad singlet at δ 2.89-2.98 corresponding to two protons of two OH groups supported the addition of only one octanoyl group in this solid. Also, the seven protons of glucofuranose skeleton appeared in their anticipated positions (Figure 2). In ¹³C NMR eight extra carbons were found at δ 174.5 (CO), 34.2, 31.6, 29.0, 28.8, 24.8, 22.6 [CH₃(CH₂)₆CO] and 14.0 [CH₃(CH₂)₆CO]. The relative position of each proton and carbon signal was ascertained by analyzing its 2D COSY (Figure 3a), DEPT-135 (Figure 3b), and HSQC. Now, the

position of attachment of the octanoyl group was ascertained in two ways. Firstly, reasonable downfield shifting of both the H-6 protons (δ 4.42-4.47 and 4.22-4.28) than that of its starting compound **4** (19, 51) suggested that an octanoyl group was added at the C-6 position of the glucofuranose skeleton. Secondly, in its HMBC spectrum (Figure 3c), the only carbonyl carbon interacts with both the protons of H-6a,b, which significantly confirmed that the C₇H₁₅CO was added to the primary OH (C-6) position. Thus, corroboration of FT-IR, ¹H and ¹³C NMR, DEPT-135, 2D COSY, HSQC, and HMBC spectra confirmed the structure assigned as **5**.

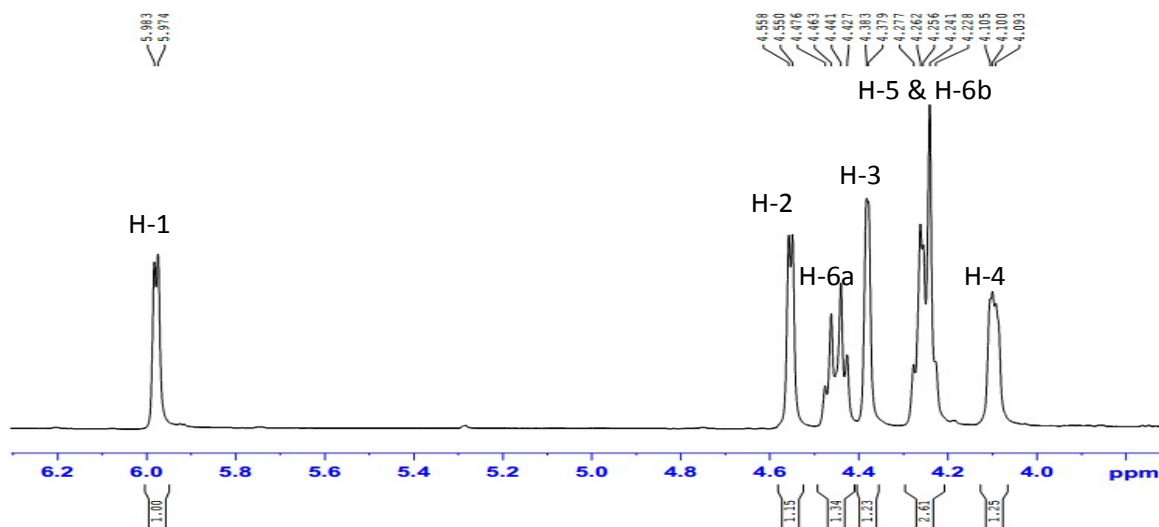
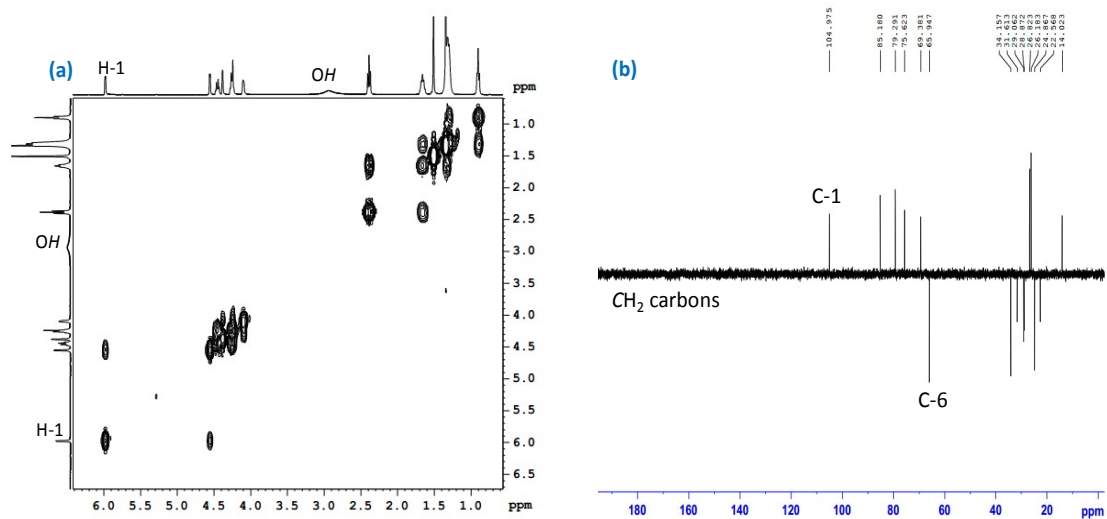


Figure 2. ^1H NMR spectrum of 6-*O*-octanoate **5** indicating glucofuranose proton signals.



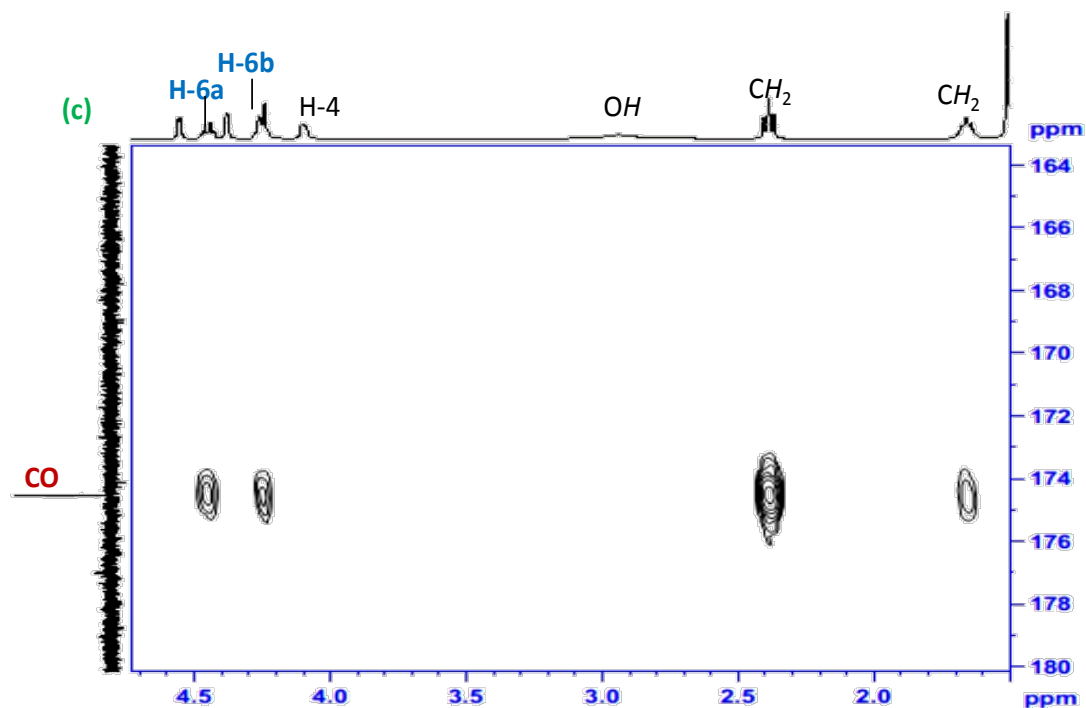
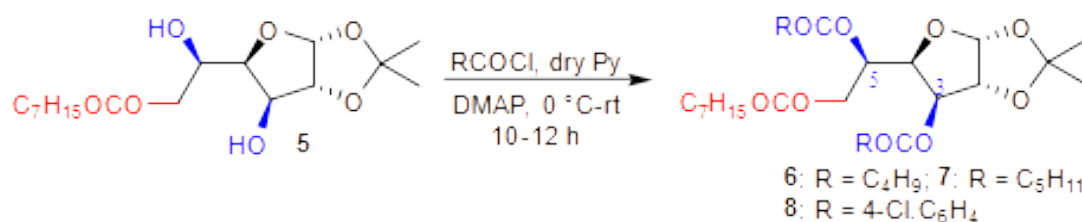


Figure 3: (a) 2D COSY, (b) DEPT-135, and (c) HMBC spectra of 6-*O*-octanoate **5**.

The successful synthesis of compound **5** thus indicated that the necessary conditions for site-selective 6-*O*-octanoylation in the direct method are- (i) use of bulky acylating agent, (ii) use of unimolar acylating agent, and (iii) reaction need to conduct at low temperature (0 °C). An analogous methodology has also been reported by Sindona et al. (52) with other acylating agents and yields vary from 15% to 93%.

Synthesis of 2,5-di-*O*-acyl esters 6-8 of octanoate **5**

For more evidence in favor of 6-*O*-octanoate **5** formation and to prepare newer glucofuranose esters, **5** was converted into three 3,5-di-*O*-acyl esters using three different acylating agents. First of all, dihydroxy compound **5** was reacted with pentanoyl chloride in dry C₆H₅N for 10 h, and a thick syrup was obtained in 91% (Scheme 3).



Scheme 3. Derivatization of octanoate **5** (**6** = 91%; **7** = 88%; **8** = 94%).

In its FT-IR spectrum, carbonyl characteristic peaks appeared at 1747, 1741, and 1733 cm⁻¹ while the hydroxyl stretching band completely disappeared (Figure 4), indicating the pentanoylation of the molecule. A total of thirty-nine protons resonated in the aliphatic region of its ¹H NMR spectrum. Of

these 6 protons are due to one isopropylidene group, and fifteen protons are for one octanoyl group that already exists in the molecule. The additional eighteen protons than its starting **5** were indicative of the attachment of two C₄H₉CO groups in the molecule.

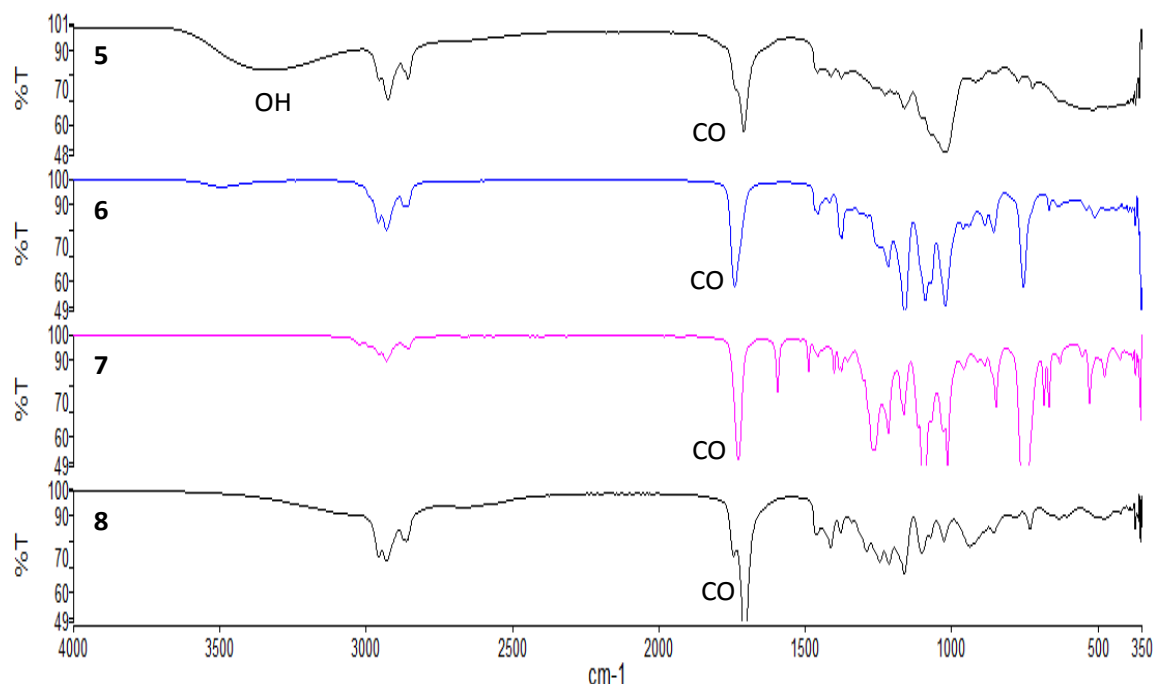


Figure 4. Comparative FT-IR peaks of all the synthesized glucofuranose esters **5-8**.

For confirmation, its ^{13}C NMR was analyzed, where an additional two CO and fourteen aliphatic carbon signals were present. In its HMBC, protons present at 3 and 5 positions were found to interact with two carbonyl carbons at δ 172.4 and 172.3, respectively, and thus, the new two pentanoyl groups must be attached at the same 3 and 5 positions. The considerable downfield shift of H-3 (δ 5.33) and H-5 (δ 5.24) as compared to its precursor **5** (δ 4.38 and 4.22–4.28, respectively) confirmed this fact. Thus, the structure of this compound was unambiguously assigned as **6**.

In the next step, dimolar hexanoylation of octanoate **5** in dry DMF for 12 h (Scheme 3) furnished a syrup in 88% yield. No band in the OH was observed in its FT-IR spectrum. Instead, it exhibited characteristic bands at 1736, 1739, and 1722 cm^{-1} (CO) (Figure 4). The ^1H NMR spectrum gave peaks for additional characteristic twenty-two protons compared to its precursor compound **5**. In its ^{13}C NMR carbonyl carbon signals at δ 173.3, 172.4 and 172.3, and aliphatic carbon signals at δ 34.1, 34.0, 33.8, 31.6, 31.2(2), 29.1, 28.9, 24.8, 24.4, 24.2, 22.6, 22.2(2), 26.8, 26.2, 14.0 and 13.8(2) were confirmative of the addition of two $\text{C}_5\text{H}_{11}\text{CO}$ groups in this compound in addition to one isopropylidene and one octanoyl group. HMBC spectrum showed multiple bond correlations between carbonyl carbons and H-3, H-5, and H-6a,b (Figure 5). As the octanoyl group is already attached to the C-6 position, hexanoyl groups must be attached with 3 and 5 positions. Complete analysis of its all 1D and 2D spectra established its structure as **7**.

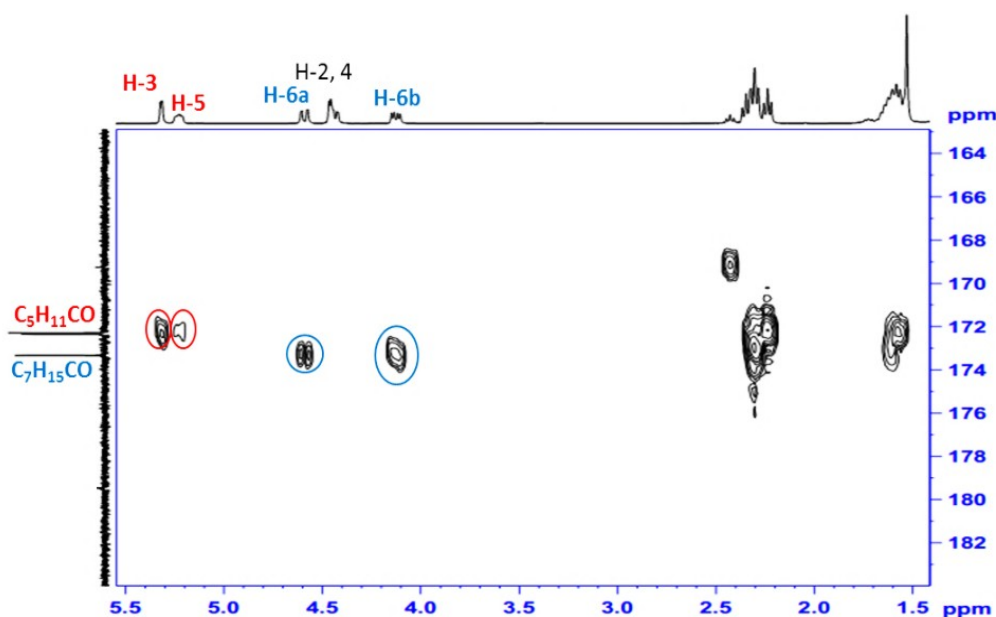


Figure 5. HMBC correlation between CO and H-3, H-5 and H-6a,b in **7**.

Finally, dimolar 4-chlorobenzoylation of octanoate **5** in dry pyridine for 10 h gave a semi-solid which resisted crystallization (Scheme 3). The disappearance of OH band and presence of CO characteristic bands at 1745, 1708, and 1701 cm^{-1} were informative of the desired dichlorobenzoylation of this compound (Figure 4). To confirm this observation, initially, its proton NMR spectrum was analyzed, where new eight aromatic protons resonated at δ 7.90 (2H), 7.82 (2H), 7.43 (2H), and 7.38 (2H) indicating the attachment of two 4-chlorobenzoyl groups in the molecule. A doublet at δ 6.04, assigned for H-1, with small coupling constant 3.6 Hz indicated *cis*-relationship with H-2. As H-2 is β -oriented H-1 must be β -oriented i.e. above the plane. Also, C-3 and C-5 protons resonated at highly down fields (at δ 5.54 and 5.60, respectively). Like compound **6-7**, its carbonyl signals at δ 164.2 and 164.1 showed heteronuclear multiple bond correlation with H-3 and H-5, respectively, thereby confirming that 4-chlorobenzoyl groups were added at these C-3 and C-5 positions. Thus, its structure was established as **8**.

CONCLUSION

A convenient and straightforward site-selective octanoylation method for monoacetone protected α -D-glucopyranose is described. The necessary condition for such a reaction was using an unimolar acylating agent and a lower reaction temperature, and the absence of any catalyst. The regioselective 6-O-octanoate **5**, thus obtained, was converted into corresponding three di-O-acyl esters **6-8** successfully. All these synthetic compounds were characterized well with 1D and 2D spectroscopic techniques. The biological activities, computer-aided *in silico* thermodynamics, binding energy and

ADMET properties, and structural basis for such bioactivities will be reported shortly.

ACKNOWLEDGMENT

We highly acknowledge the financial support from the Ministry of Science and Technology, Bangladesh (Phys 535, 2020-21) to conduct this research work.

REFERENCES

1. Plat T, Linhardt RJ. Syntheses and applications of sucrose-based esters. *J Surfact Deterg.* 2001 Oct;4(4):415-21. [<DOI>](#).
2. Zhao L, Zhang H, Hao T, Li S. In vitro antibacterial activities and mechanism of sugar fatty acid esters against five food-related bacteria. *Food Chemistry.* 2015 Nov;187:370-7. [<DOI>](#).
3. Lucarini S, Fagioli L, Campana R, Cole H, Duranti A, Baffone W, et al. Unsaturated fatty acids lactose esters: cytotoxicity, permeability enhancement and antimicrobial activity. *European Journal of Pharmaceutics and Biopharmaceutics.* 2016 Oct;107:88-96. [<DOI>](#).
4. Shao S-Y, Shi Y-G, Wu Y, Bian L-Q, Zhu Y-J, Huang X-Y, et al. Lipase-Catalyzed Synthesis of Sucrose Monolaurate and Its Antibacterial Property and Mode of Action against Four Pathogenic Bacteria. *Molecules.* 2018 May 8;23(5):1118. [<DOI>](#).
5. Matin MM, Bhattacharjee SC, Chakraborty P, Alam MS. Synthesis, PASS prediction, in vitro antimicrobial evaluation and pharmacokinetic study of novel n-octyl glucopyranoside esters. *Carbohydrate Research.* 2019 Nov;485:107812.

[<DOI>](#).

6. Tarahomjoo S, Alemzadeh I. Surfactant production by an enzymatic method. *Enzyme and Microbial Technology*. 2003 Jul;33(1):33–7. [<DOI>](#).
7. Szűts A, Pallagi E, Regdon G, Aigner Z, Szabó-Révész P. Study of thermal behaviour of sugar esters. *International Journal of Pharmaceutics*. 2007 May;336(2):199–207. [<DOI>](#).
8. Marshall DL, Bullerman L. Antimicrobial properties of sucrose fatty acid esters. *Carbohydrate polyesters as fat substitutes*. 1994;149–67. ISBN: 0824790626.
9. Kabara JJ, Conley AJ, Swieczkowski DM, Ismail IA, Jie MLK, Gunstone FD. Antimicrobial action of isomeric fatty acids on group A *Streptococcus*. *J Med Chem*. 1973 Sep;16(9):1060–3. [<DOI>](#)
10. Kobayashi T, Takahashi T, Adachi S. Synthesis of 6-O-Octanoyl-1,2-O-isopropylidene- α -D-glucopyranose by Lipase-catalyzed Esterification in an Organic Solvent. *J Oleo Sci*. 2012;61(2):75–9. [<DOI>](#).
11. Allen DK, Tao BY. Carbohydrate-alkyl ester derivatives as biosurfactants. *J Surfact Deterg*. 1999 Jul;2(3):383–90. [<DOI>](#).
12. Matin MM, Chakraborty P, Alam MS, Islam MM, Haneef U. Novel mannopyranoside esters as sterol 14 α -demethylase inhibitors: Synthesis, PASS predication, molecular docking, and pharmacokinetic studies. *Carbohydrate Research*. 2020 Oct;496:108130. [<DOI>](#).
13. Matin MM, Bhuiyan MMH, Kabir E, Sanaullah AFM, Rahman MA, Hossain ME, et al. Synthesis, characterization, ADMET, PASS predication, and antimicrobial study of 6-O-lauroyl mannopyranosides. *Journal of Molecular Structure*. 2019 Nov;1195:189–97. [<DOI>](#).
14. Kumar N, Goel N. Phenolic acids: Natural versatile molecules with promising therapeutic applications. *Biotechnology Reports*. 2019 Dec;24:e00370. [<DOI>](#).
15. Matin MM, Islam N, Siddika A, Bhattacharjee SC. Regioselective Synthesis of Some Rhamnopyranoside Esters for PASS Predication, and ADMET Studies. *Journal of the Turkish Chemical Society Section A: Chemistry*. 2021 Feb 28;8(1):363–74. [<DOI>](#).
16. Matin MM, Bhuiyan MMH, Azad AKMS, Akther N. Design and synthesis of benzyl 4-O-lauroyl- α -L-rhamnopyranoside derivatives as antimicrobial agents. *105267/j.ccl*. 2017;31–40. [<DOI>](#).
17. Yang X-D, Li Z-Y, Mei S-X, Zhao J-F, Zhang H-B, Li L. Two new phenylpropanoid esters of rhamnose from *Lagotis yunnanensis*. *Journal of Asian Natural Products Research*. 2003 Sep;5(3):223–6. [<DOI>](#).
18. Matin MM, Iqbal MdZ. Methyl 4-O-(2-chlorobenzoyl)- α -L-rhamnopyranosides: Synthesis, Characterization, and Thermodynamic Studies. *Orbital: Electron J Chem*. 2021 Mar 30;13(1):19–27. [<DOI>](#).
19. Matin MM, Bhuiyan MMH, Azad AKMS, Rashid MHO. Synthesis of 6-O-Stearoyl-1, 2-O-isopropylidene- $[\alpha]$ -D-glucopyranose derivatives for antimicrobial evaluation. *Journal of Physical Science*. 2015;26(1):1.
20. Nilsson H, Andersen J. New glucopyranose esters and glucopyranose esters of alkyl-fumarates useful for treating psoriasis and other hyperproliferative, inflammatory and autoimmune disorders [Internet]. Copenhagen; WO 2007/006308 A1, 2007. [<URL>](#).
21. Rong YW, Zhang QH, Wang W, Li BL. A Simple and Clean Method for O-Isopropylideneation of Carbohydrates. *Bulletin of the Korean Chemical Society*. 2014 Jul 20;35(7):2165–8. [<DOI>](#).
22. Luginina J, Vasiljevs D, Ivanovs I, Mishnev A, Turks M. Diastereoselective aza-Michael addition for synthesis of carbohydrate-derived spiropiperazinones. *Monatsh Chem*. 2019 Jan;150(1):21–8. [<DOI>](#).
23. Dhavale DD, Matin MM, Sharma T, Sabharwal SG. Synthesis and evaluation of glycosidase inhibitory activity of octahydro-2H-pyrido[1,2-a]pyrimidine and octahydro-imidazo[1,2-a]pyridine bicyclic diazasugars. *Bioorganic & Medicinal Chemistry*. 2004 Aug 1;12(15):4039–44. [<DOI>](#).
24. Dhavale DD, Matin MM. Selective sulfonylation of 4-C-hydroxymethyl- β -l-threo-pento-1,4-furanose: synthesis of bicyclic diazasugars. *Tetrahedron*. 2004 May;60(19):4275–81. [<DOI>](#).
25. Arora S. Solvent-free synthesis of 1,2:5,6-di-O-isopropylidene-3-O-3'-(N',N'-dimethylamino-n-propyl)- α ,D-glucopyranose and 1,2:5,6-di-O-isopropylidene-3-O-heptyl- α ,D-glucopyranose [Internet]. Philadelphia; 1995. [<URL>](#).
26. Kobayashi T, Ehara T, Mizuoka T, Adachi S. Efficient synthesis of 6-O-palmitoyl-1,2-O-isopropylidene- α -D-glucopyranose in an organic solvent system by lipase-catalyzed esterification. *Biotechnol Lett*. 2010 Nov;32(11):1679–84. [<DOI>](#)
27. Catelani G, Osti F, Bianchi N, Bergonzi MC, D'Andrea F, Gambari R. Induction of erythroid differentiation of human K562 cells by 3-O-acyl-1,2-O-isopropylidene-D-glucopyranose derivatives.

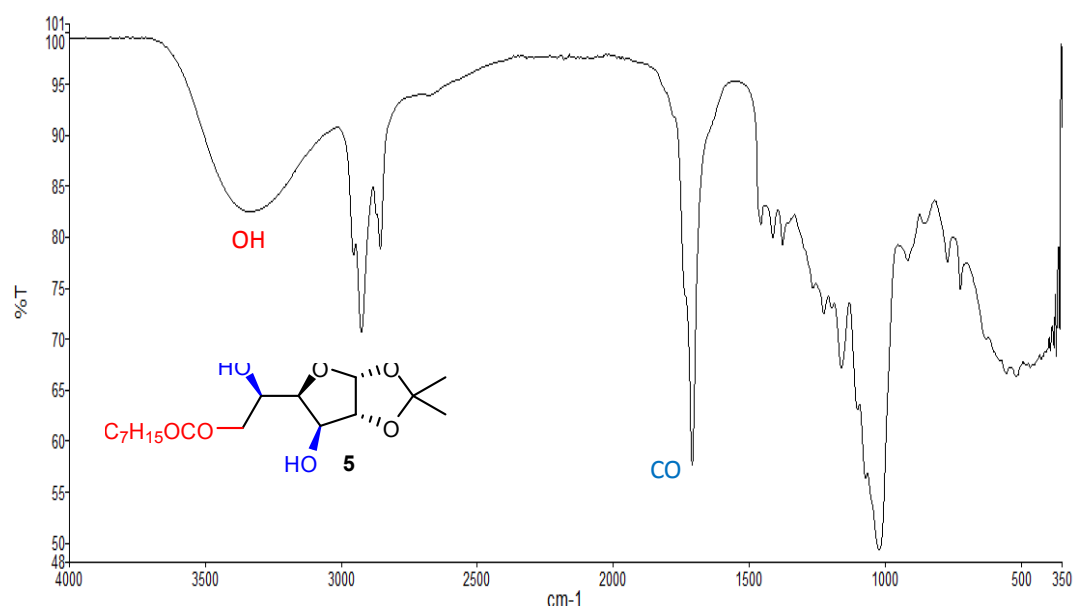
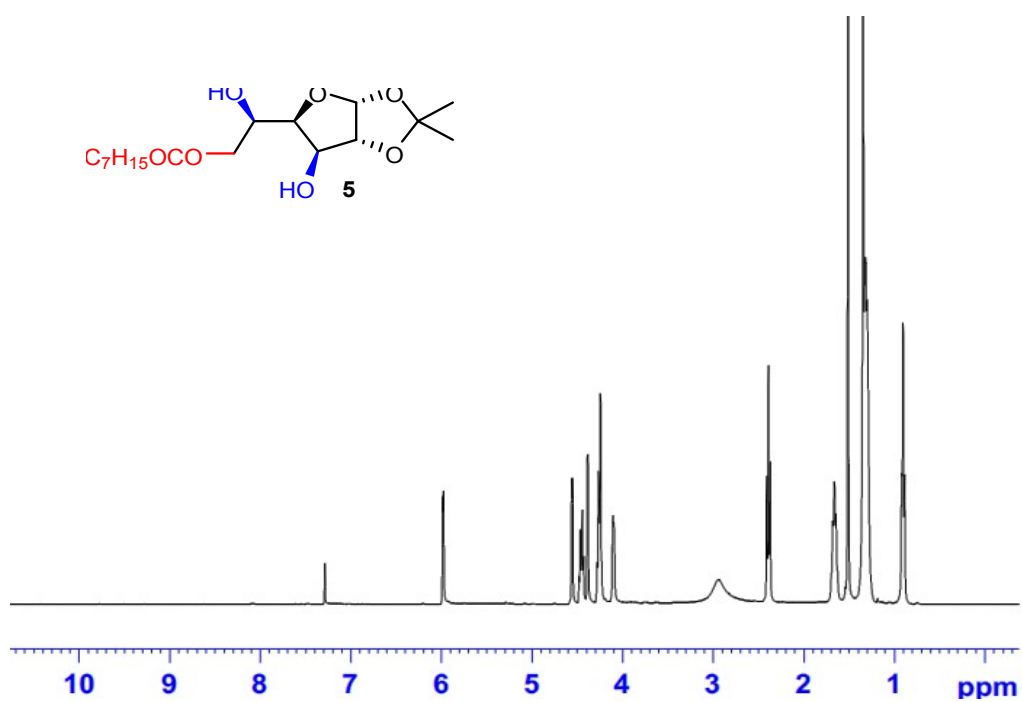
- Bioorganic & Medicinal Chemistry Letters. 1999 Nov;9(21):3153-8. [<DOI>](#).
28. Matin M, Bhuiyan M, Azad A, Bhattacharjee S, Rashid M. Synthesis and antimicrobial studies of 6-O-lauroyl-1, 2-O-isopropylidene- α -D-gluco-furanose derivatives. *Chem Biol Interface*. 2014;4(4):223-31.
29. Matin M, Bhuiyan M, Debnath D, Manchur M. Synthesis and comparative antimicrobial studies of some acylated d-glucofuranose and d-glucofuranose derivatives. *Int J Biosci*. 2013 Aug 22;3(8):279-87. [<DOI>](#).
30. Kolodiazhnyi OI, Grishkun EV. Asymmetric Induction In The Reaction Of Nonsymmetrical Phosphinic And Phosphinous Acid Chlorides With Derivatives Of D-Glucofuranose. Phosphorus, Sulfur, and Silicon and the Related Elements. 1996 Aug 1;115(1):115-24. [<DOI>](#).
31. Ridley D, Smal M. Preparation of arenesulfinic esters of 1,2:5,6-Di-O-cyclohexylidene- α -D-glucofuranose, and their conversion into optically active sulfoxides. *Aust J Chem*. 1982;35(3):495. [<DOI>](#).
32. Sheville J, Berndt D, Wagner T, Norris P. Crystal structure of 1,2:5,6-di-O-isopropylidene-3-O-(phenylacetyl)-D-glucofuranose. *Journal of Chemical Crystallography*. 2003;33(5/6):409-12. [<DOI>](#).
33. Matin MM, Hasan MdS, Uzzaman M, Bhuiyan MdMH, Kibria SM, Hossain MdE, et al. Synthesis, spectroscopic characterization, molecular docking, and ADMET studies of mannopyranoside esters as antimicrobial agents. *Journal of Molecular Structure*. 2020 Dec;1222:128821. [<DOI>](#).
34. Dimakos V, Taylor MS. Site-Selective Functionalization of Hydroxyl Groups in Carbohydrate Derivatives. *Chem Rev*. 2018 Dec 12;118(23):11457-517. [<DOI>](#).
35. Sugihara JM. Relative Reactivities of Hydroxyl Groups of Carbohydrates. In: *Advances in Carbohydrate Chemistry* [Internet]. Elsevier; 1953 [cited 2021 Aug 26]. p. 1-44. [<URL>](#).
36. Haines AH. Relative Reactivities of Hydroxyl Groups in Carbohydrates. In: *Advances in Carbohydrate Chemistry and Biochemistry* [Internet]. Elsevier; 1976 [cited 2021 Aug 26]. p. 11-109. [<URL>](#).
37. Lawandi J, Rocheleau S, Moitessier N. Regioselective acylation, alkylation, silylation and glycosylation of monosaccharides. *Tetrahedron*. 2016 Oct;72(41):6283-319. [<DOI>](#).
38. Jäger M, Minnaard AJ. Regioselective modification of unprotected glycosides. *Chem Commun*. 2016;52(4):656-64. [<DOI>](#).
39. Kurahashi T, Mizutani T, Yoshida J. Effect of intramolecular hydrogen-bonding network on the relative reactivities of carbohydrate OH groups †. *J Chem Soc, Perkin Trans 1*. 1999;(4):465-74. [<DOI>](#).
40. Jiang L, Chan T-H. Regioselective Acylation of Hexopyranosides with Pivaloyl Chloride. *The Journal of organic chemistry*. 1998;63(17):6035-8.
41. Matin MM. Synthesis of some silyl protected 1, 4-galactonolactone derivatives. *Journal of Applied Sciences Research*. 2006;2(10):753-6.
42. Matin MM, Priyanka Chakraborty P. Synthesis, PASS Predication, Antimicrobial, DFT, and ADMET Studies of Some Novel Mannopyranoside Esters. *JASPE*. 2020 Oct 30;7(2):572-86. [<DOI>](#).
43. Matin M, Azad A. Synthesis of some protected 6-O-acyl-galactopyranose derivatives. *J Appli Sci Res*. 2006;2(12):1199-202.
44. Kabir A, Matin MM. Regioselective acylation of a derivative of L-rhamnose using the dibutyltin oxide method. *J Bangladesh Chem Soc*. 1994;7(1):73-9.
45. Kabir A, Matin MM. Regioselective monoacylation of a derivative of L-rhamnose. *JOURNAL-BANGLADESH ACADEMY OF SCIENCES*. 1997;21:83-8.
46. Matin M, Nath A, Saad O, Bhuiyan M, Kadir F, Abd Hamid S, et al. Synthesis, PASS-Predication and in Vitro Antimicrobial Activity of Benzyl 4-O-benzoyl- α -l-rhamnopyranoside Derivatives. *IJMS*. 2016 Aug 27;17(9):1412. [<DOI>](#).
47. Matin M, Ibrahim M. Synthesis of some methyl 4-O-octanoyl- α -L-rhamnopyranoside derivatives. *JACR*. 2010;6(10):1527-32. [<URL>](#).
48. Staroń J, Dąbrowski JM, Cichoń E, Guzik M. Lactose esters: synthesis and biotechnological applications. *Critical Reviews in Biotechnology*. 2018 Feb 17;38(2):245-58. [<DOI>](#).
49. Richel A, Laurent P, Wathelet B, Wathelet J-P, Paquot M. Microwave-assisted conversion of carbohydrates. State of the art and outlook. *Comptes Rendus Chimie*. 2011 Feb;14(2-3):224-34. [<DOI>](#).
50. Furniss B, Hannaford A, Smith P, Tatchell A. Vogel's textbook of practical organic chemistry. New. ed., 5. ed., rev. [Nachdr.]. Furniss B, Vogel A, editors. Harlow: Pearson/Prentice Hall; 1996. 1514 p. ISBN: 978-0-582-46236-6.

51. Gramera RE, Park A, Whistler RL. A Convenient Preparation of 1,2-Mono-O-isopropylidene- α -D-glucopyranose. *J Org Chem.* 1963 Nov;28(11):3230-1. [<DOI>](#).

Sindona G. Nonionic surfactants. Regioselective synthesis of fatty acid esters of α - and β -glucopyranose. *Lipids.* 1997 May;32(5):559-63. [<DOI>](#).

52. De Luca D, De Nino A, Liguori A, Procopio A,

SUPPLEMENTARY DATA

Synthesis, and Spectral Characterization of 6-O-Octanoyl-1,2-O-isopropylidene- α -D-glucofuranose Derivatives**Figure S1.** FT-IR (neat) spectrum of compound **5**.**Figure S2.** ¹H NMR (400 MHz, CDCl₃) spectrum of compound **5**.

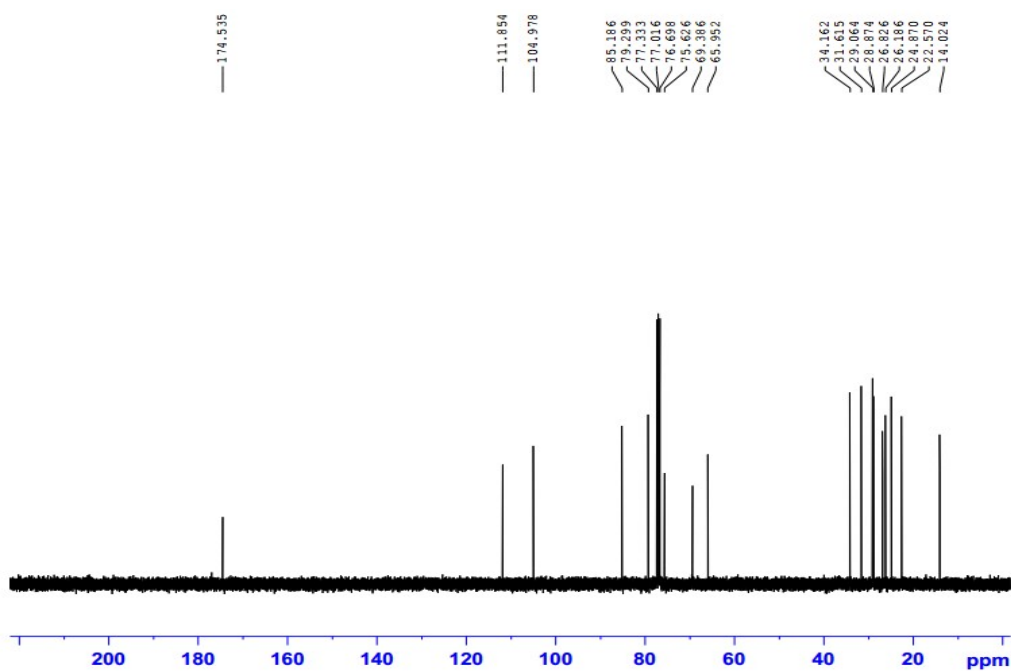


Figure S3. ^{13}C NMR (100 MHz, CDCl_3) spectrum of compound **5**.

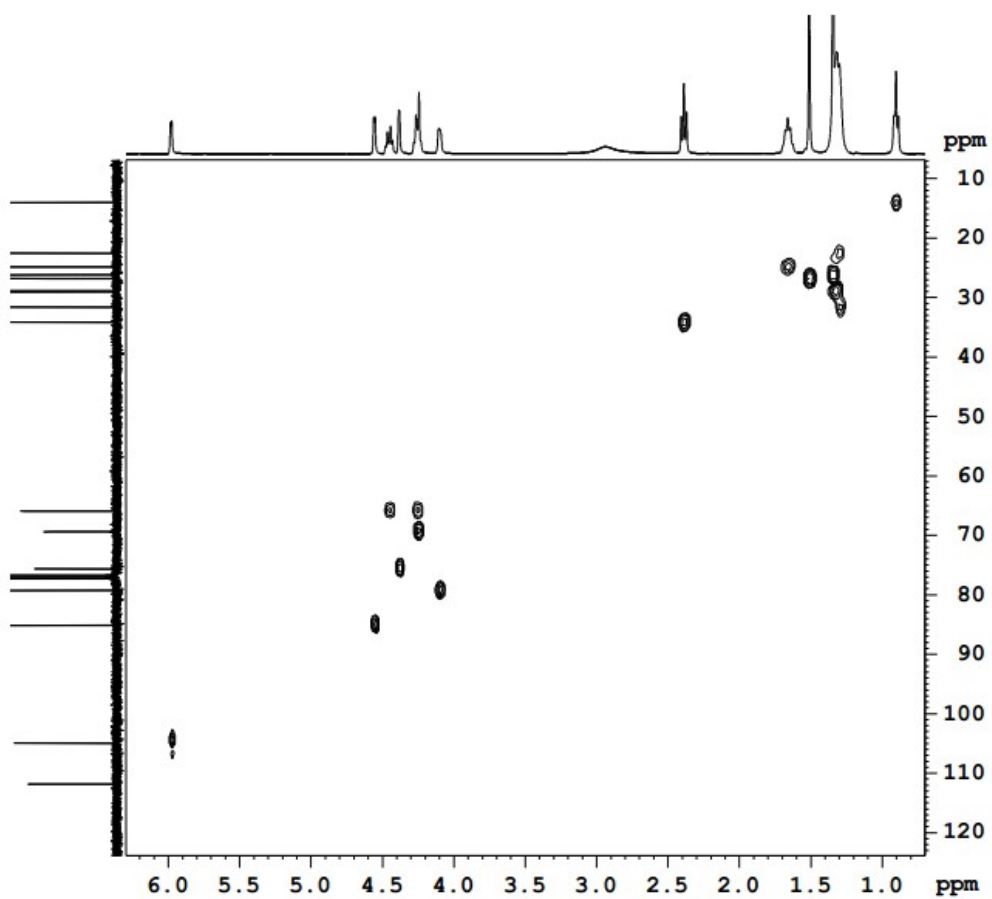


Figure S4. 2D HSQC spectrum of compound **5**.

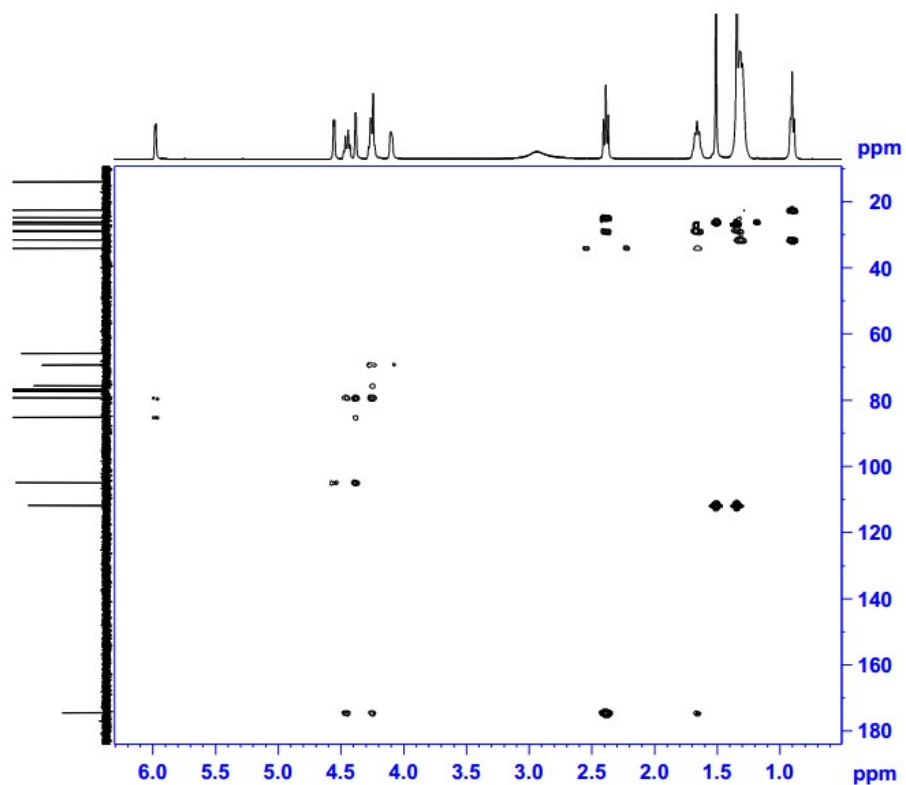


Figure S5. 2D HMBC spectrum of compound **5**.

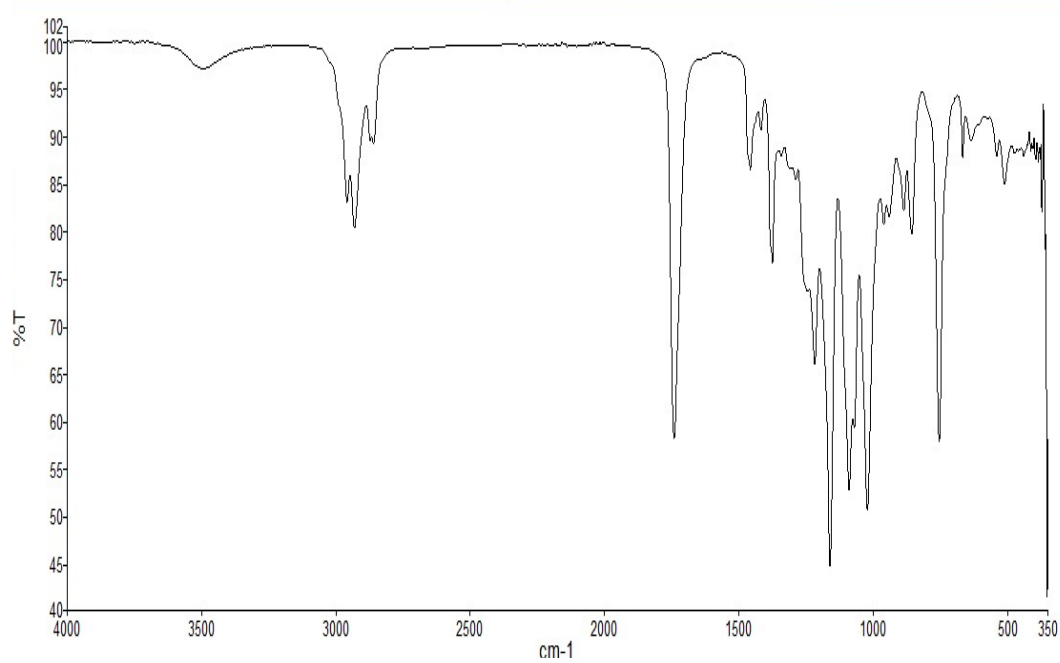


Figure S6. FT-IR (neat) spectrum of compound **6**.

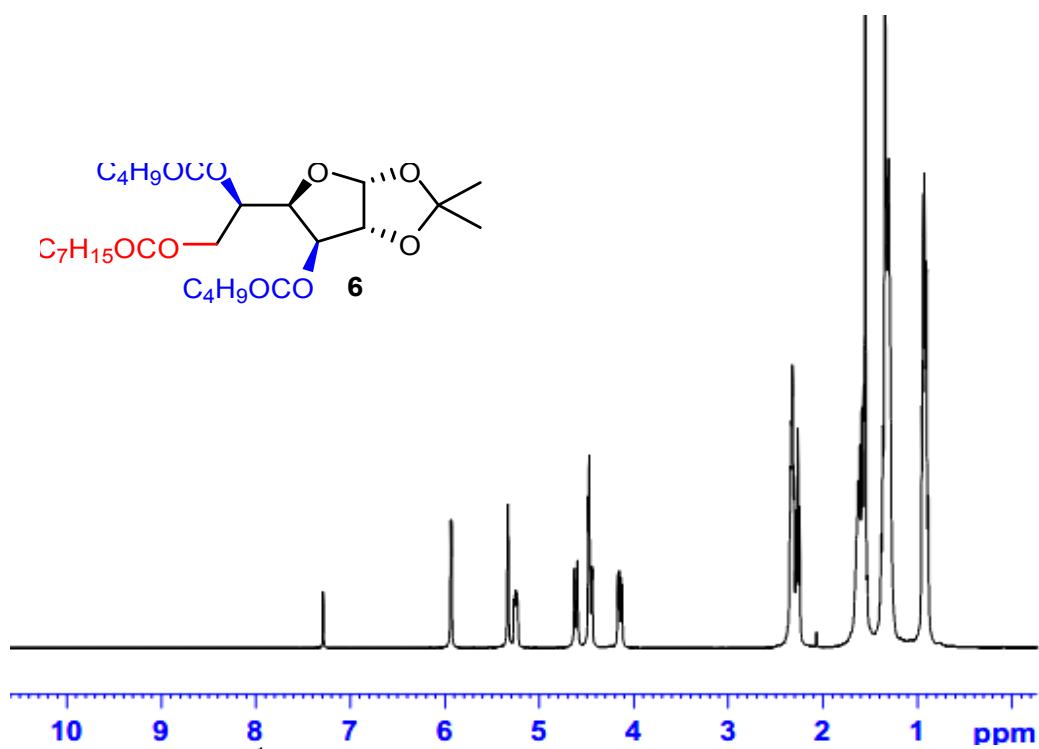


Figure S7. 1H NMR (400 MHz, $CDCl_3$) spectrum of compound **6**.

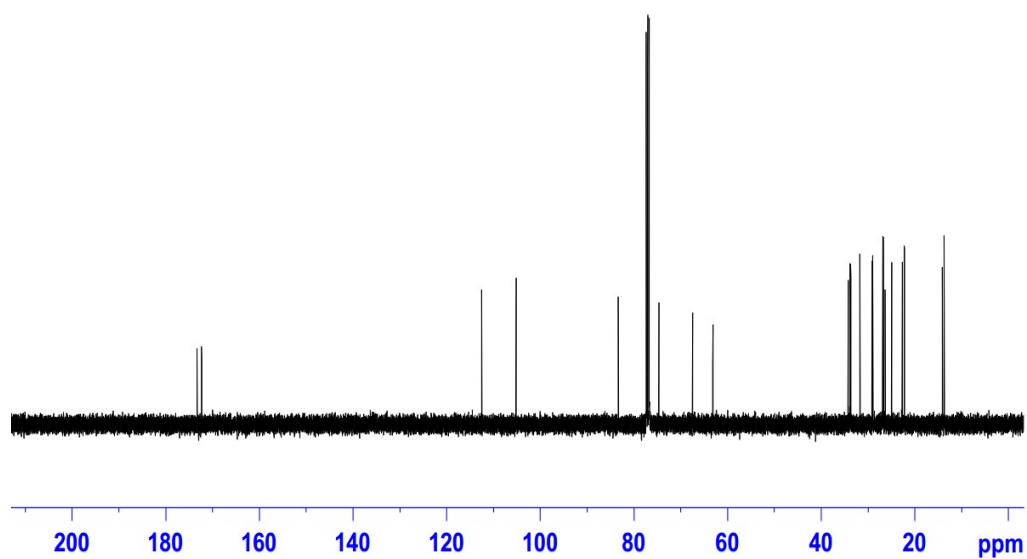


Figure S8. ^{13}C NMR (100 MHz, $CDCl_3$) spectrum of compound **6**.

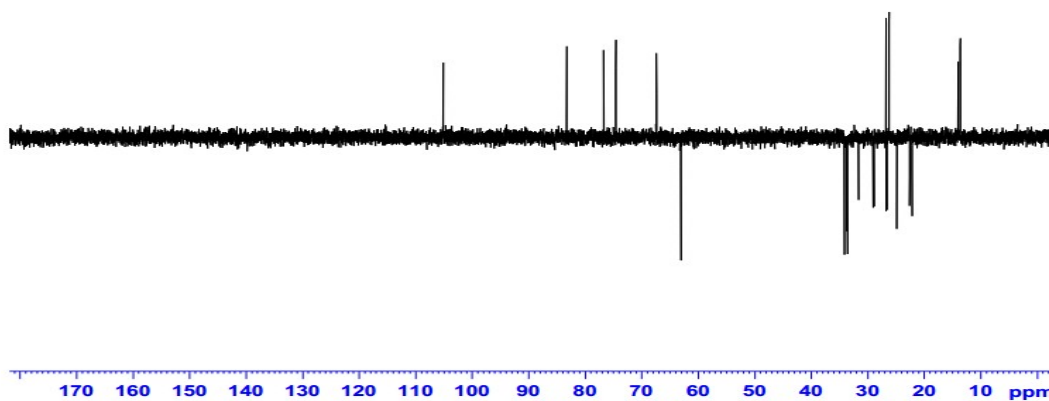


Figure S9. DEPT-135 spectrum of compound **6**.

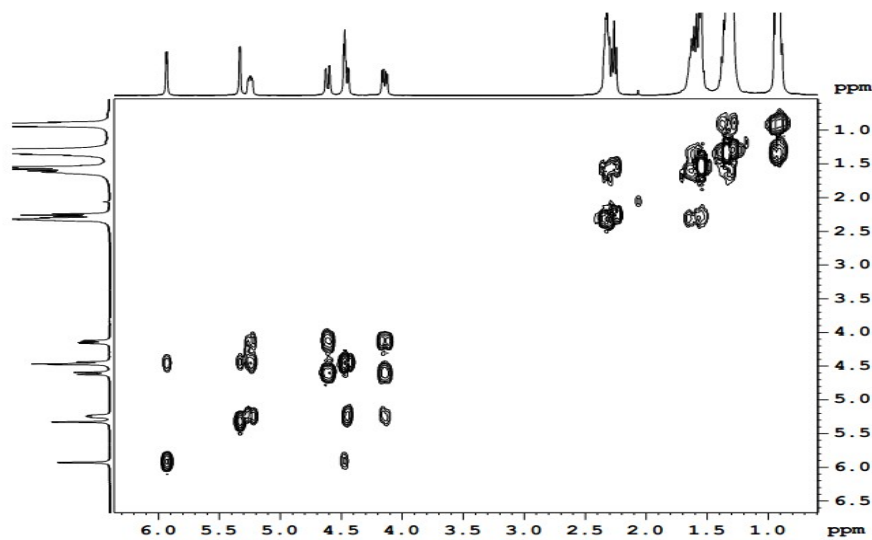


Figure S10. 2D COSY spectrum of compound **6**.

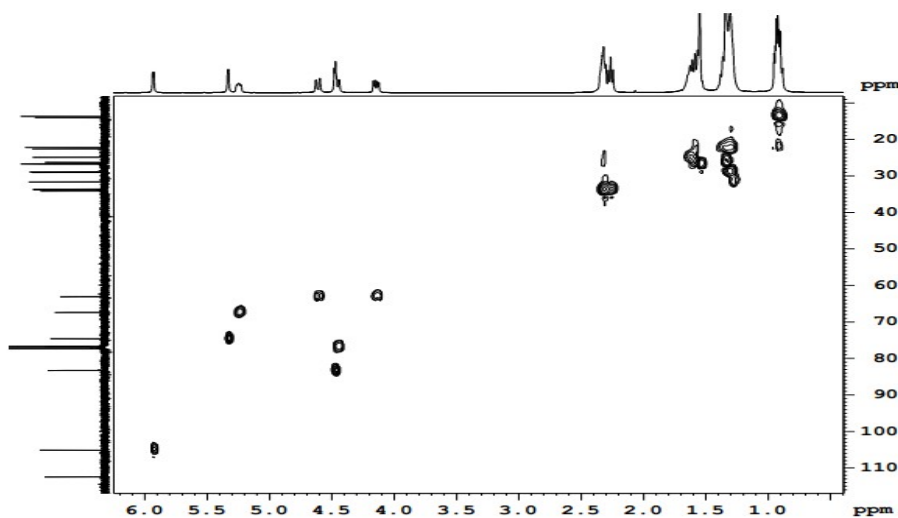


Figure S11. 2D HSQC spectrum of compound **6**.

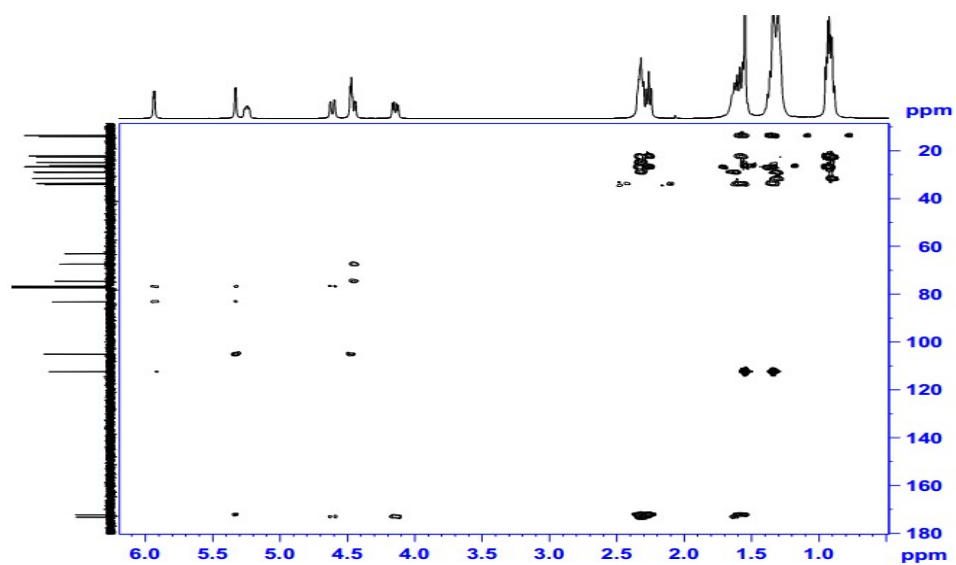


Figure S12. 2D HMBC spectrum of compound **6**.

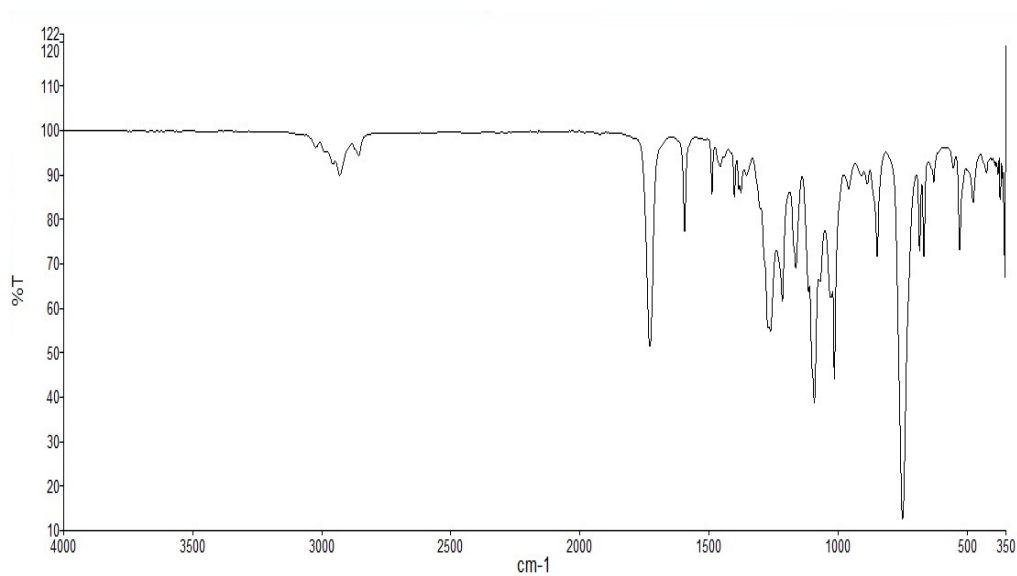


Figure S13. FT-IR (neat) spectrum of compound **7**.

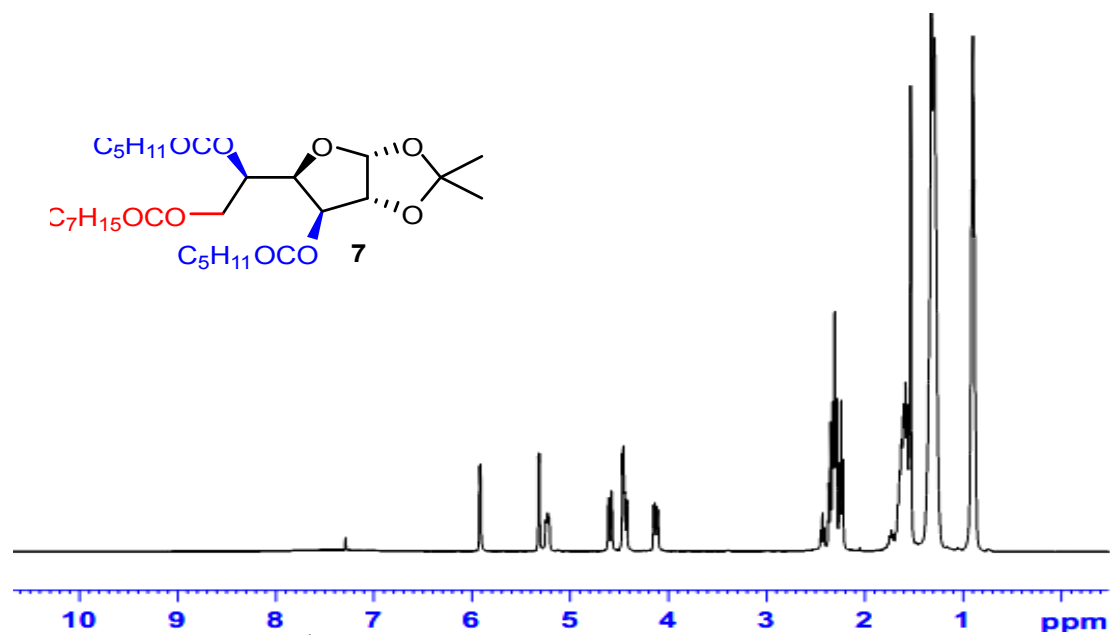


Figure S14. ¹H NMR (400 MHz, CDCl₃) spectrum of compound 7.

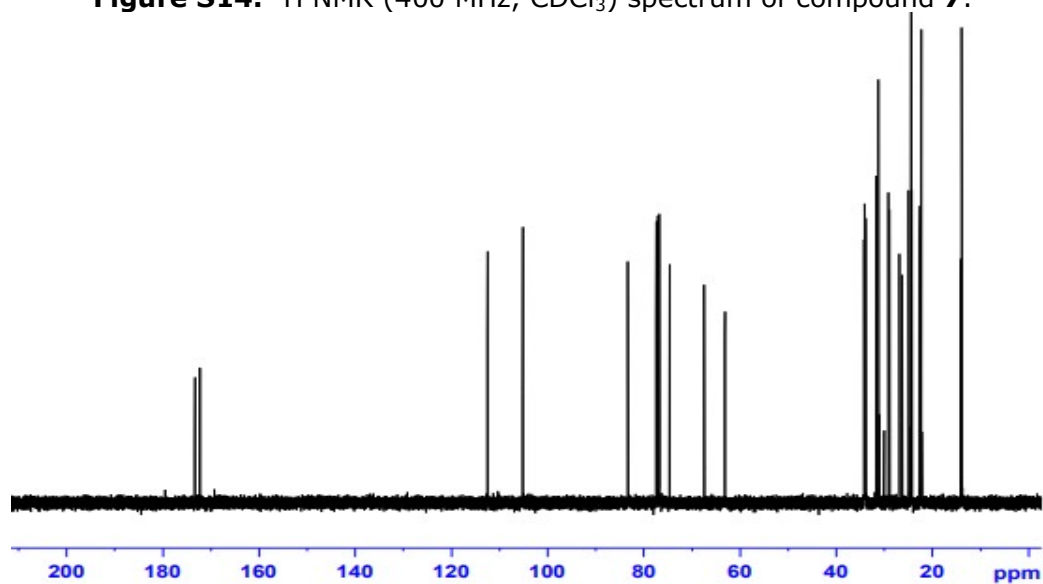


Figure S15. ¹³C NMR (100 MHz, CDCl₃) spectrum of compound 7.

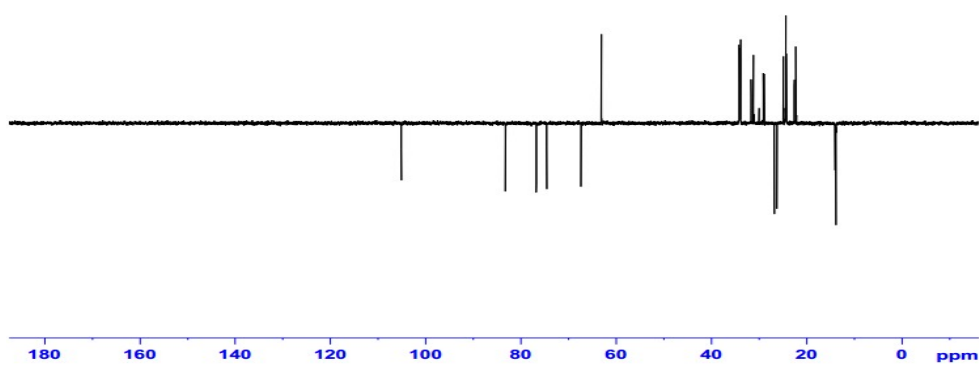


Figure S16. DEPT-135 spectrum of compound 7.

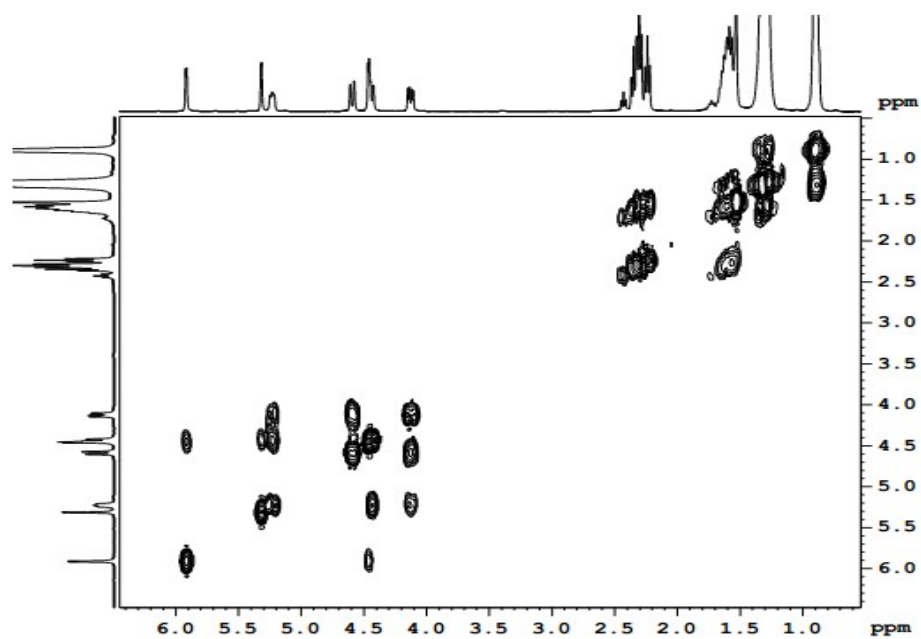


Figure S17. 2D COSY spectrum of compound **7**.

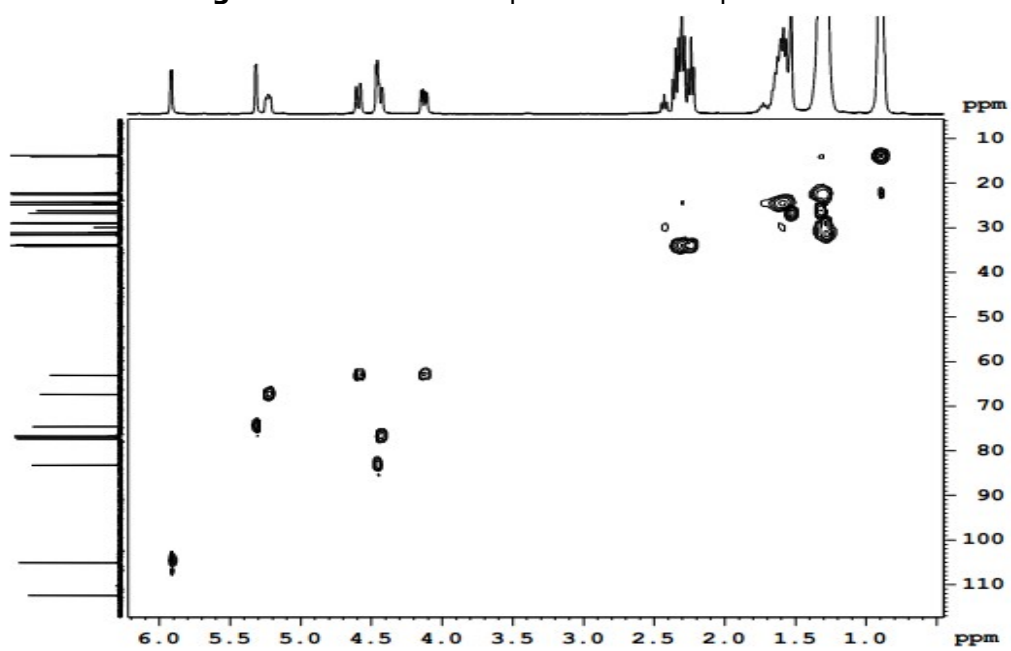


Figure S18. 2D HSQC spectrum of compound **7**.

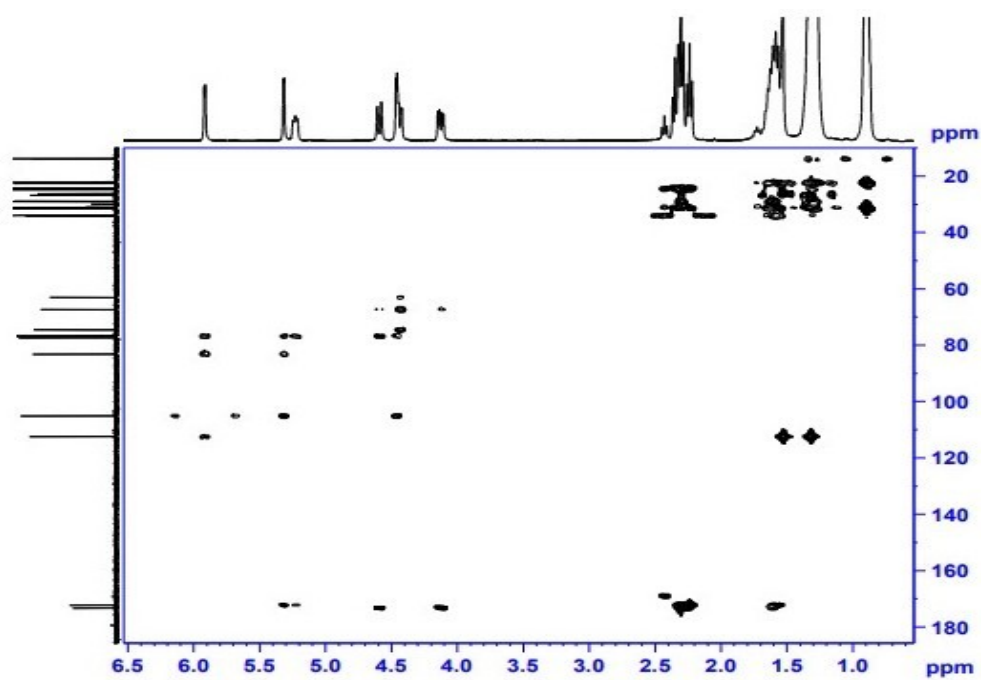


Figure S19. 2D HMBC spectrum of compound **7**.

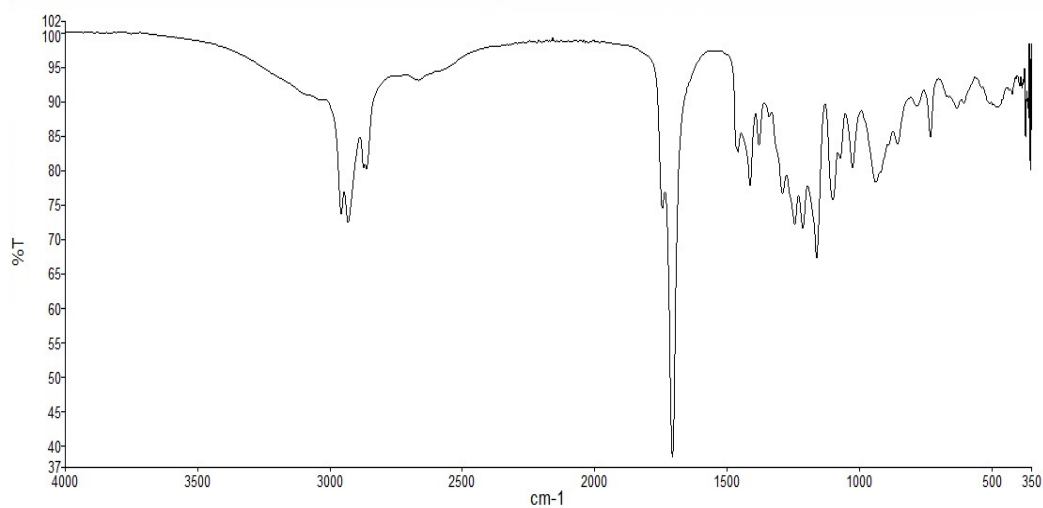


Figure S20. FT-IR (neat) spectrum of compound **8**.

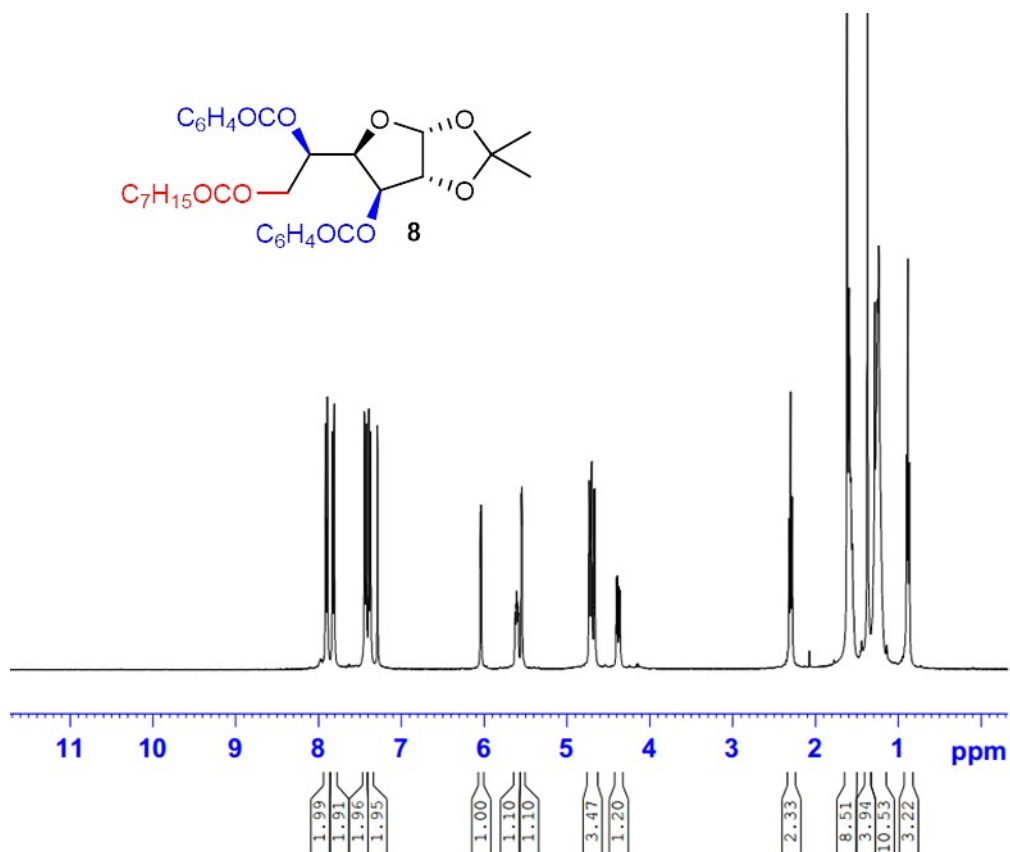


Figure S21. ^1H NMR (400 MHz, CDCl_3) spectrum of compound **8**.

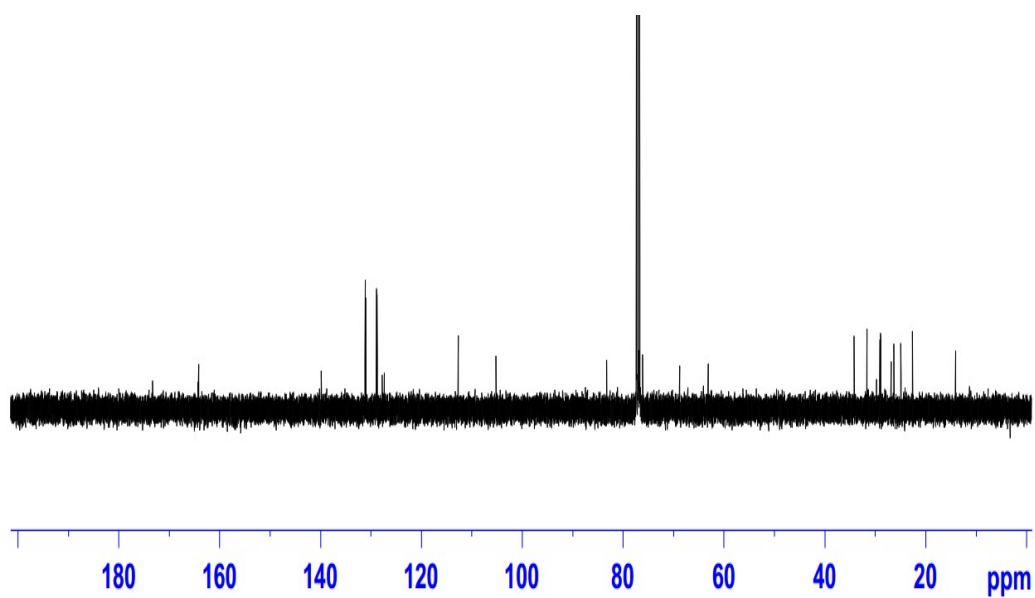


Figure S22. ^{13}C NMR (100 MHz, CDCl_3) spectrum of compound **8**.

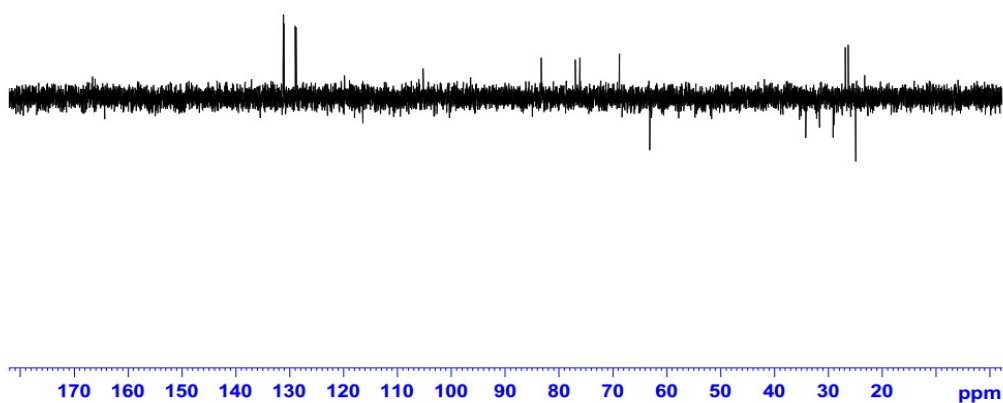


Figure S23. DEPT-135 spectrum of compound **8**.

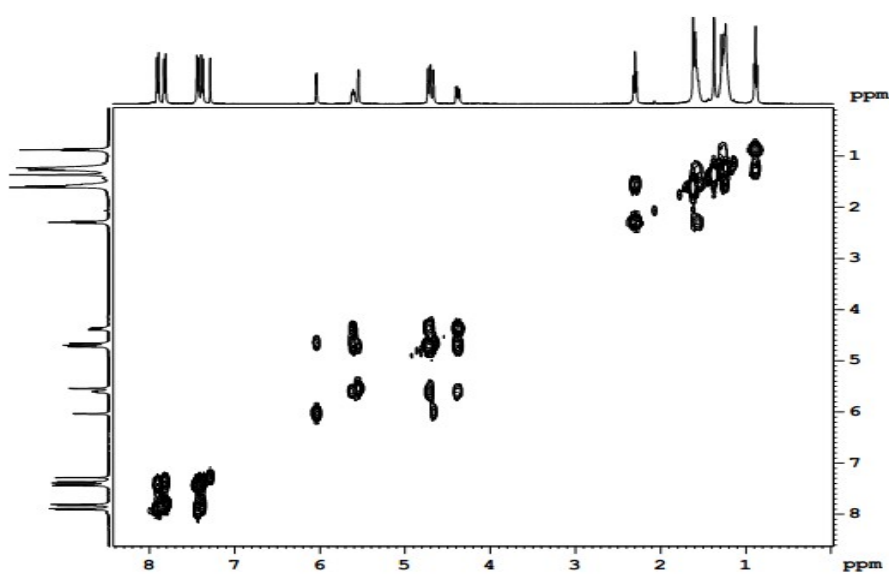


Figure S24. 2D COSY spectrum of compound **8**.

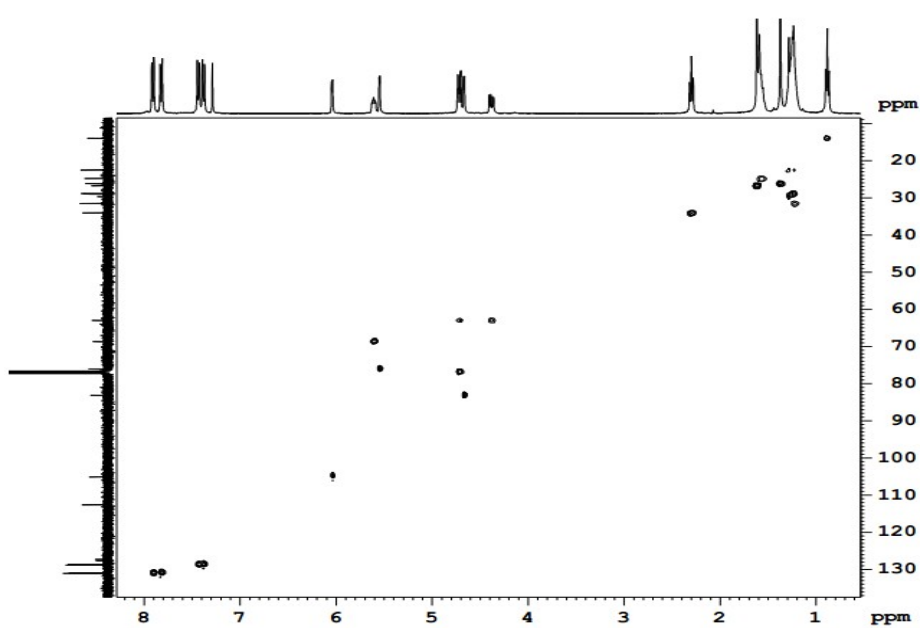


Figure S25. 2D HSQC spectrum of compound **8**.



Anticancer Activities of a Metal-Free Phthalocyanine on MCF-7 and MDA-MB-231 Cells and Singlet Oxygen Production as a Photosensitizer in PDT

Mevlûde Canlıca^{1*}  , İdil Çetin² 

¹Yıldız Technical University, Faculty of Science and Art, Department of Chemistry, Davutpasa Campus, 34220 Esenler, Istanbul, TR

² Istanbul University, Faculty of Science, Department of Biology, 34459, Vezneciler, Istanbul, TR

Abstract: Cancer, which is often described as an uncontrollable rapid proliferation of cells, is currently the leading cause of death in the world together with cardiac disease. Therefore, the main purpose of the current research work was to study the anticancer effects of a first-time-synthesized phthalocyanine (Pc) as photosensitizer in PDT against cancer and evaluate its effects on human cells in vitro. Quantum yields of singlet oxygen photogeneration were in air using the relative method with standard-ZnPc as reference and DPBF as chemical quencher for singlet oxygen. The concentration of DPBF was prepared almost 3×10^{-5} molar to avoid chain reactions induced by DPBF in the presence of singlet oxygen. Solutions of Pc as sensitizer (absorbance = 2.0 at the irradiation wavelength) containing DPBF were prepared in the dark and irradiated in the Q band region using the setup described. DPBF degradation at 417 nm was monitored with UV-Vis spectrophotometry. For in vitro studies, nine different MFPC-1 concentrations (0.2 μ M- 0.4 μ M- 0.8 μ M- 1.6 μ M- 3.2 μ M- 6.4 μ M- 12.8 μ M- 25.6 μ M- 51.2 μ M) applied to MCF-7 and MDA-MB-231 breast cancer cell lines for 24 hours and MTT assay was carried out. After determination of optimum concentration, mitotic index, and apoptotic index values of cell lines were determined with administration of these concentrations. Singlet oxygen quantum yield (Φ_{Δ}), which is a measure of the efficiency, of MFPC-1 was found 0.50, although MFPC-1 is being metal-free phthalocyanine. For in vitro studies after the application of different concentrations to MCF-7 and MDA-MB-231 for 24 hours, the optimum concentration was determined as 12 μ M for both cell lines by the MTT assay. After application of the determined optimum concentration for 24, 48 and 72 hours, there was a significant decrease in the mitotic index values and significant increase in the apoptotic index values of both MCF-7 and MDA-MB-231 breast cancer cell lines.

Keywords: Metal-free phthalocyanine, singlet oxygen, in vitro, breast cancer, cell kinetic.

Submitted: November 27, 2020. **Accepted:** August 27, 2021.

Cite this: Canlıca M, Çetin İ. Anticancer Activities of a Metal-Free Phthalocyanine on MCF-7 and MDA-MB-231 Cells and Singlet Oxygen Production as a Photosensitizer in PDT. JOTCSA. 2021;8(4):1025-34.

DOI: <https://doi.org/10.18596/jotcsa.832628>.

***Corresponding author.** E-mail: mcanlica@yahoo.com, Tel: +902123834161.

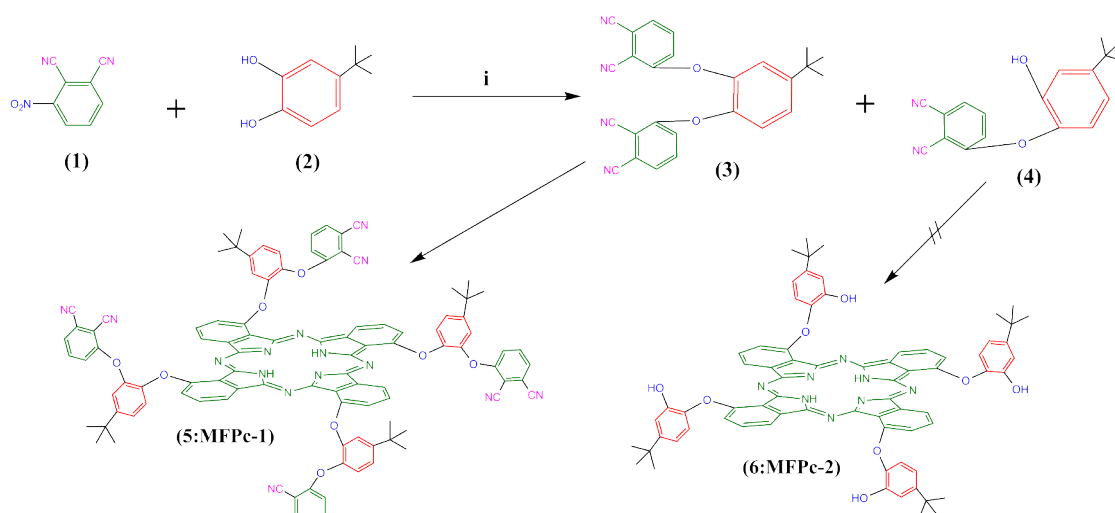
INTRODUCTION

Phthalocyanine (Pc) was discovered by accident in 1907 as a by-product in the synthesis of o-cyanobenzamide (1). Pcs are macrocyclic compounds that consist of 4 pyrrole subunits that are linked by azomethine bridges in a 16-membered ring with 18n electron system which is responsible for the intense blue/green color (2). Pcs can be modified to suit a specific application either by

changing the peripheral group and non-peripheral group or by changing the central metal (3). Therefore, they are useful in a wide range of areas such as in medicinal and material science as gas sensors (4) photodynamic therapy sensitizers (5) nonlinear optical materials (6). In medicine, Pcs were used in clinical photodiagnosis due to photosensitizer properties (7,8). For PDT, the first official approval and clinical were concurrently reported in 1993 and 1996, and it can be alternative

due to be a safe in cancer treatment, respectively (9-11). PDT has advantages over other cancer treatment modalities, such as surgery, radiotherapy, and chemotherapy. PDT consist of light, photosensitizer, and cancer tissue which is based on the generation of singlet oxygen (1O_2) and a Pc can do this as a photosensitizer that leads to cancerous cell death upon the wavelength of irradiation between 650 and 900 nm (12-15).

In the present study, we have obtained Pc(MFPC-1) substituted with electron-donating group including di-tert-butyl while 3,3'-(4-tert-butyl-1,2-phenylene)bis(oxy)diphthalonitrile was recrystallized from methanol. This is not surprised since the first accidental synthesis of Pcs by Braun and Tcherniac (16). Here, we report the production of singlet oxygen as possible photosensitizer based on PDT. We also present here antiproliferative effect of the MFPC-1 obtained on cancer cells (17,18).



Scheme 1. Synthetic pathway. i: DMSO, K_2CO_3 , 3 days, room temperature.

EXPERIMENTAL SECTION

Materials and Methods

3-nitrophthalonitrile **1** and 1,2-dihydroxy-4-tert-butylbenzene **2** were purchased from Alfa Aesar and Sigma-Aldrich, USA, respectively. The materials, instruments and methods that are used for synthesis, photophysical (fluorescence quantum yield) and photochemical studies (singlet oxygen quantum yield) as previously published in the literature (19-25).

Synthesis

A reaction was started so that can obtain 3,3'-(4-tert-butyl-1,2-phenylene)bis(oxy) diphthalonitrile **3** (24,25) from 4-tert-butylbenzene-1,2-diol **2** (2.40 g, 14.45 mmol) and 3-nitrophthalonitrile **1** (5.00 g, 28.90 mmol) in the present anhydrous potassium carbonate (11.98 g, 86.68 mmol) in dimethylsulfoxide (15 mL) under Ar atmosphere, after stirring for 4 h at 60 °C. The reaction mixture was stirred at room temperature for 3 days and was subsequently poured into water (500 mL). The beige to yellow powdery product was filtered off. It was observed to give a green color in a flat-bottomed flask while being crystallized from ethanol (150 mL), yielding a MFPC-1. Then, it was purified via column chromatography using a gradient of tetrahydrofuran and methanol as the eluent, respectively. Pc was obtained as a deep green powder with mp > 200 °C and is soluble in THF, DMSO, and DMF. The other

data such as FTIR and UV-Vis spectrum are given as follows.

Yield 0.021 g. UV-Vis (DMSO), λ_{max}/nm (log ϵ): 724 (4.67), 695 (4.67), 660 (4.35), 632 (4.25), 320 (4.68). FT-IR (ATR), μ_{max}/cm^{-1} : 2958 (Ar-CH), 2906/2865(Aliph. -CH), 2237 (C≡N), 1575 (C=C), 1275/1245 (C-O-C). 1H -NMR (DMSO- d_6), δ ,/ppm: 7.85–7.00 (36H, Ar-H), 1.35 (36 H, t-butyl). Anal. calcd. for $C_{104}H_{74}N_{16}O_8$: C, 74.54; H, 4.45; N, 13.37 found: C, 74.58; H, 4.45; N, 13.45%. MALDI-TOF-MS: m/z calcd. 1674.59 amu; found 1678.00 amu $[M+4H]^+$.

Photophysical Studies

Fluorescence quantum yield (Φ_F)

Relative Φ_F was calculated by a comparative method using a standard reference, using Equation 1.

$$\Phi_F = \Phi_{F(Std)} \frac{F \times A_{Std} \times n^2}{F_{Std} \times A \times n_{Std}^2} \quad (\text{Eq. 1})$$

Photochemical Studies

Singlet oxygen quantum yield (Φ_Δ)

Singlet oxygen quantum yield was also determined by chemical procedure according to to Eq. (2).

$$\theta_A = \frac{\theta_A^{Std} \times R_{DPBF} \times I_{abs}^{Std}}{R_{DPBF}^{Std} \times I_{abs}} \quad (\text{Eq. 2})$$

Cell Studies

Cell culture

The MCF-7 and MDA-MB-231 cells used in the experiments were purchased by our research laboratory from American Type Culture Collection (ATCC Manassas, VA, USA). Cells were cultured in DMEM (Invitrogen, Carlsbad, CA, USA) supplemented with 10% (v/v) fetal bovine serum (FBS; Invitrogen, Carlsbad, CA, USA), 100-unit mL⁻¹ penicillin and 100 µg mL⁻¹ streptomycin at 37 °C and 5% CO₂ (26).

Cell viability

The antiproliferative effect of MFPC-1 on MCF7 and MDA-MB-231 cells were determined by the MTT (3-(4, 5-dimethylthiazol-2-yl)-2, 5-diphenyltetrazolium bromide) assay. Cells were plated in 96-well plates with 3x10⁴ cells/200 µL medium for 24 h at 37 °C. MFPC-1 was applied to the cells at 0,2 µM- 0,4 µM- 0,8 µM- 1,6 µM- 3,2 µM- 6,4 µM- 12,8 µM- 25,6 µM- 51,2 µM concentrations for 24 hours. At the end of the experimental period the medium in each well was removed and 40 µL MTT solution (5 mg/mL in phosphate buffered saline/PBS) was added into each well and cells were incubated at 37 °C for 4 h. Then, 16 µL of dimethylsulfoxide (DMSO) was added into each well and cells were shaken thoroughly for 1 h on a shaker. The absorbance of the samples was measured against a background control as a blank using an Elisa reader at 450-690 nm (18).

Mitotic index (MI)

For evaluation of MI, cells were planted in 24-well plates. Each well contained 3x10⁴ cells for both cell lines. Cells were incubated 24 hrs after cell seeding. Cells were treated with 12.8 µM concentration for 24, 48 and 72 hours. At the end of this experimental period, for fixation, Carnoy fixative was used and the cells were made clear with the Feulgen method and stained with Giemsa. For analyzing MI, metaphases, anaphases and telophases stages of cell division were evaluated. For calculating of MI, approximately 3000 cells were counted (27).

Apoptotic index (AI)

The AI represents the percentage of fragmented nuclei. DAPI (6-diamidino-2-phenylindole) was used to determine the apoptotic nucleus. It is a blue fluorescent dye. Cells were cultured in 6-well culture dishes and fixed with methanol: FTS mixture after the experimental process until staining was performed. Washing was carried out to remove the dye. For washing, PBS was used. A fluorescent microscope was used to identify apoptotic cells. For calculating of AI, approximately cells in 100 microscopic fields were evaluated (27).

Statistics

All parameters of cell kinetics were evaluated according to the controls and each other. Therefore, in order to analyze the results, one-way Anova test, Dunnett's test and Student's t-test were used. These statistical analyses were performed using SPSS statistics software (V22.0 IBM, Armonk, NY, USA). In the tests p < 0.05 level of significance was accepted.

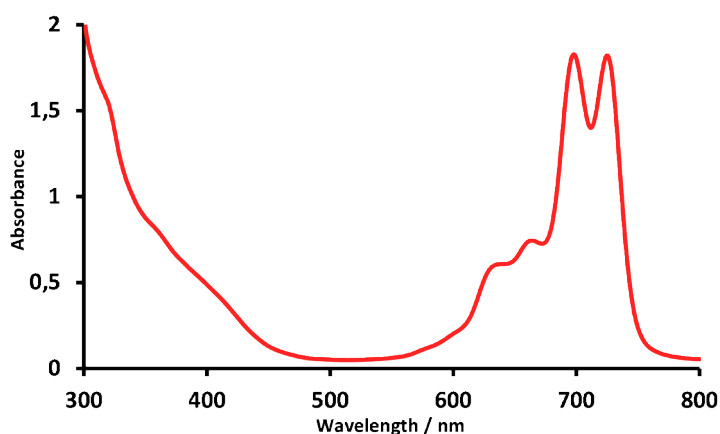


Figure 1: UV-Vis spectrum for MFPC-1 in DMSO.

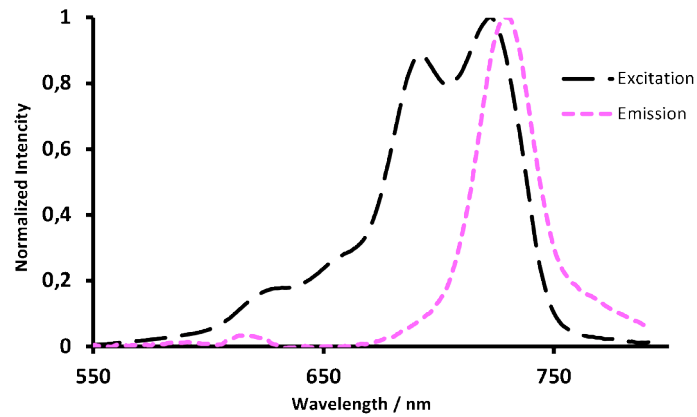


Figure 2: The excitation spectrum (long dashed line, black), emission spectrum (square line, pink), excitation wavelength 617 nm.

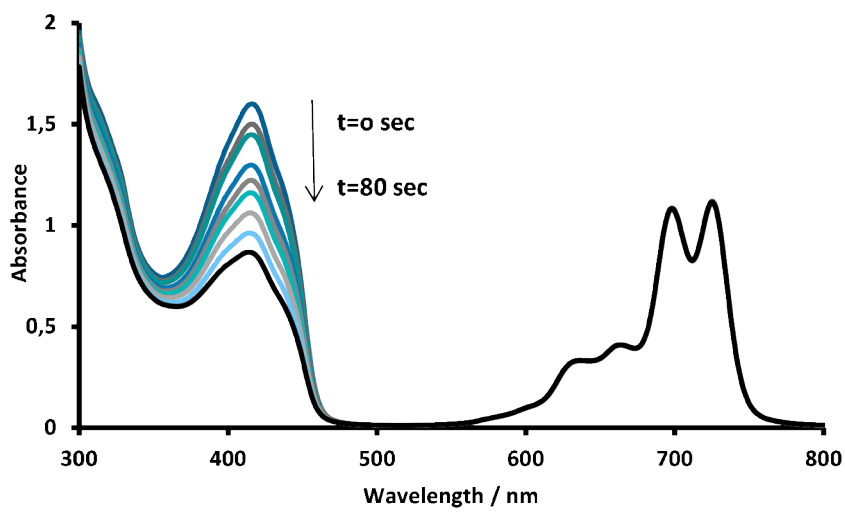


Figure 3: Singlet oxygen generation spectrum at 417 nm.

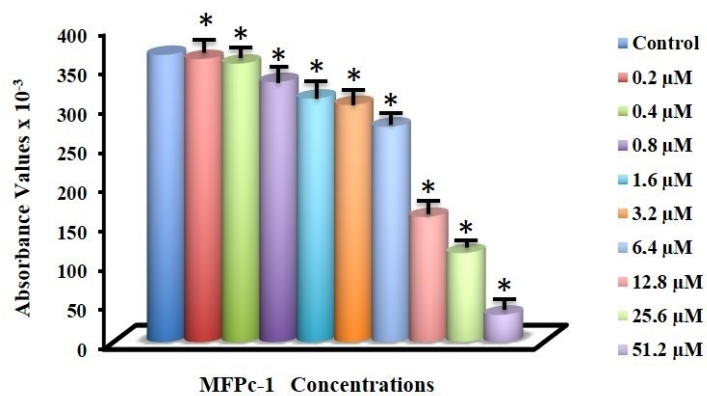


Figure 4: Absorbance values of mitochondrial dehydrogenase activity of MCF-7 cells treated with different MFPC-1 concentrations for 24 h (450-690 nm) ($p < 0.05$).

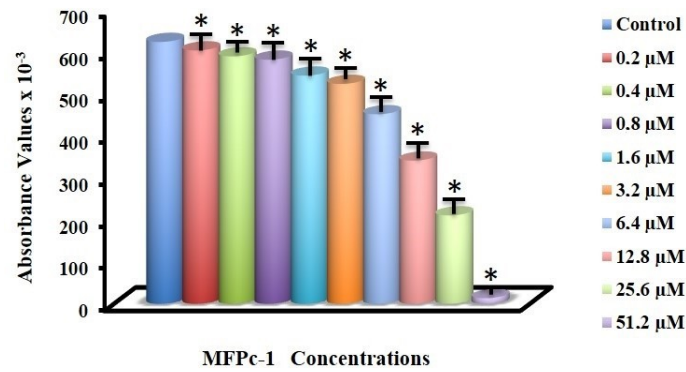


Figure 5: Absorbance values of mitochondrial dehydrogenase activity of MDA-MB-231 cells treated with different MFPc-1 concentrations for 24 h (450-690 nm) ($p < 0.05$).

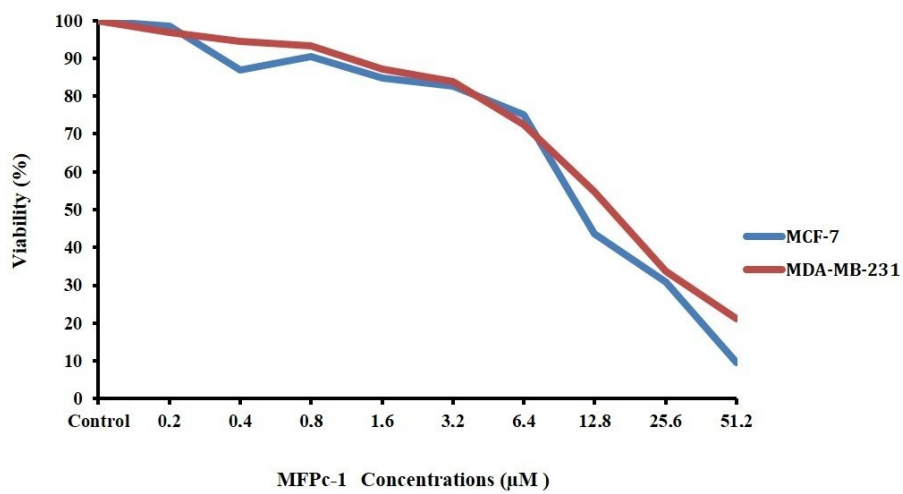


Figure 6: Percent viability values of MCF-7 and MDA-MB-231 cells treated with different concentrations of MFPc-1 for 24 hours ($p < 0.05$).

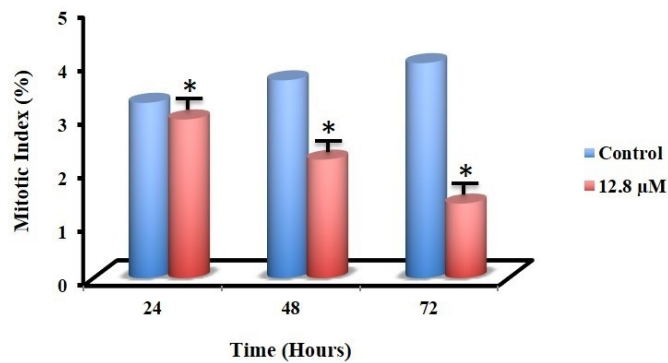


Figure 7: Mitotic index values of MCF-7 cells treated with 12.8 μM concentration of MFPc-1 for 24, 48 and 72 h ($p < 0.05$).

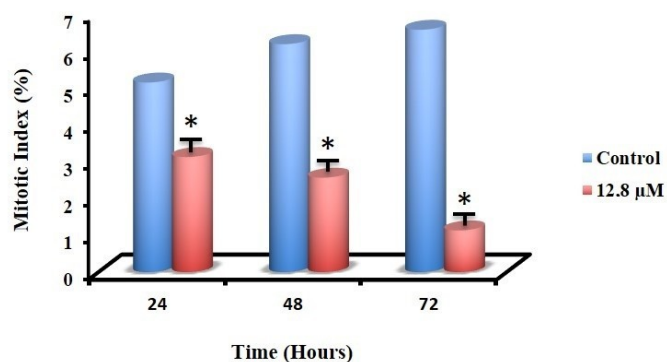


Figure 8: Mitotic index values of MDA-MB-231 cells treated with 12.8 μM concentration of MFPC-1 for 24, 48 and 72 h ($p < 0.05$).

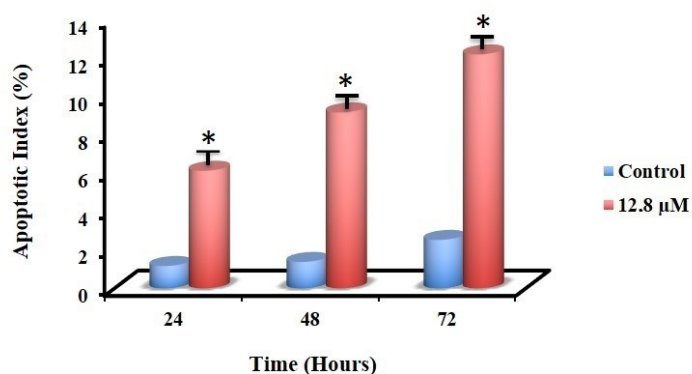


Figure 9: Mitotic index values of MCF-7 cells treated with 12.8 μM concentration of MFPC-1 for 24, 48 and 72 h ($p < 0.05$).

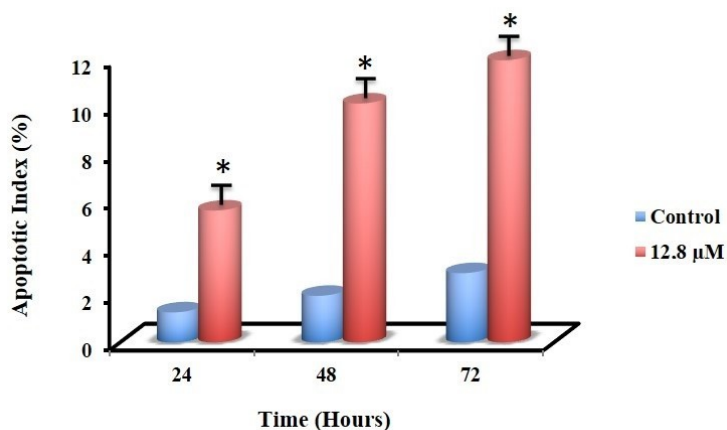


Figure 10: Mitotic index values of MDA-MB-231 cells treated with 12.8 μM concentration of MFPC-1 for 24, 48 and 72 hours ($p < 0.05$).

Table 1: The photophysical and photochemical data in DMSO.

Compound	λ_{Abs}	λ_{Ems}	λ_{Exc}	λ_{Stokes}	Φ_{F}	Φ_{Δ}	ISC
MFPC-1	695/724	729	690/722	5	0.18	0.50	0.32
Std-ZnPc ^a	672	682	672	10	0.18	0.67	0.15

^aData from refs. (28, 29).

RESULTS

We obtained a novel Pc even if it is by chance. Characterization of this Pc was carried out using FT-IR, UV-Vis spectroscopy, mass spectrometry, and elemental analysis. In the UV-Vis spectrum of a Pc, there are two peaks as characteristic called Q band and B (Soret) band. As shown in Figure 1, B band and Q band of MFPC-1 were recorded at 320 nm and at 695/724 nm with D_{4h} symmetry in DMSO at room temperature, respectively. The shape of Q band was typical for metal-free Pcs. On the other hand, the Q band is attributed to $n \rightarrow n^*$ transitions from the HOMO to the LUMO of the Pc ring whereas the B band is observed due to the transitions between the deeper n levels and the LUMO.

Fluorescence excitation and emission peaks for MFPC-1 are shown in Figure 2 and the data are listed in Table 1. Fluorescence emission peak was observed at 719 nm in DMSO. The Q band in emission spectrum and excitation spectrum, is typical of Pcs (30). While the observed Stokes shift of the MFPC-1 is lower than that of unsubstituted Std-ZnPc. Fluorescence quantum yield value is 0.18 just like a typical metal Pc, this means it is losing less energy.

Singlet oxygen is generated by a Type II reaction and is explained transform to from triplet oxygen energy level with the Jablonski Diagram (Kindly see Supplementary inf. Figure S1, at the end) the generation of singlet oxygen via the Type II process involving a spin coupling interaction with oxygen in its triplet ground-state. The efficiency is known as their singlet oxygen quantum yield (Φ_{Δ}) which is described as the number of molecules of singlet oxygen generated per number of photons absorbed by the sensitizer (here MFPC-1). DPBF is used to determine the singlet oxygen quantum yield which is a good acceptor because it reacts rapidly with singlet oxygen (31). The spectral changes were examined during the photolysis of the MFPC-1 in the presence of DPBF were measured over time (0–80 sec) by UV-Vis spectroscopy. In Figure 3, the spectrum of MFPC-1 shows no change at 417 nm in the Q band, this means the compound is not degraded. The Φ_{Δ} value is 0.50 and is considerably high for metal-free Pcs. This result is considerably good compared to substituted metal-free phthalocyanines published in the literature (32). This may be due to the effect electron-donating of *t-butyl* groups to Pc ring.

Cell proliferation values belong to MCF-7 cells decreased from 365.333×10^{-3} to 360×10^{-3} for 0.2 μM ; to 354.286×10^{-3} for 0.4 μM ; to 330.857×10^{-3} for 0.8 μM ; to 309.714×10^{-3} for 1.6 μM ; to 301.75×10^{-3} for 3.2 μM ; to 274×10^{-3} for 6.4 μM ; to 159.25×10^{-3} for 12.8 μM ; to 113.25×10^{-3} for 25.6 μM and 34.714×10^{-3} for 51.2 μM (Figure 4). Cell proliferation values belong to MDA-MB-231 cells

decreased from 622.5×10^{-3} to 602.375×10^{-3} for 0.2 μM ; to 588.25×10^{-3} for 0.4 μM ; to 580.375×10^{-3} for 0.8 μM ; to 542.5×10^{-3} for 1.6 μM ; to 522.625×10^{-3} for 3.2 μM ; to 450.625×10^{-3} for 6.4 μM ; to 340.5×10^{-3} for 12.8 μM ; to 210.25×10^{-3} for 25.6 μM and 13.5×10^{-3} for 51.2 μM (Figure 5).

After the administration MFPC-1 concentrations for 24 h, cell proliferation values of MCF-7 and MDA-MB-231 cells decreased significantly depending on concentration. The differences between the control and all experimental groups were significant ($p < 0.05$). Cell viability values of MCF-7 cell line are 98,54%, 86,98%, 90,56%, 84,78%, 82,6%, 75%, 43,6%, 30,9%, 9,5 for MCF-7 cells; 96,77%, 94,49%, 93,23%, 87,15%, 83,95%, 72,39%, 54,69%, 33,78%, 21,17% for MDA-MB-231 cells respectively for 0,2 μM - 0,4 μM - 0,8 μM - 1,6 μM - 3,2 μM - 6,4 μM - 12,8 μM - 25,6 μM - 51,2 μM concentrations (Figure 6).

Administration of 12,8 μM concentration of MFPC-1 to MCF-7 and MDA-MB-231 cells caused a decrease in mitosis. MI values decreased from 3.27% to 2.96% at 24 h; from 3.69% to 2.21% at 48 h and from 4.01% to 1.39% at 72 h for MCF-7 cells (Figure 7); decreased from 5.14% to 3.12% at 24 h; from 6.18% to 2.56% at 48 h and from 6.57% to 1.13% at 72 h for MDA-MB-231 cells (Figure 8). MI values of MCF-7 and MDA-MB-231 cells decreased significantly with time as a result of MFPC-1 administration. This decrease was statistically significant ($p < 0.05$).

Administration of 12.8 μM concentration of MFPC-1 to MCF-7 and MDA-MB-231 cells caused apoptotic cell death. AI values increased from 1.16 to 6.12 at 24 h; from 1.37 to 9.16 at 48 h and from 2.52 to 12.18 at 72 h for MCF-7 cells (Figure 9); increased from 1.27 to 5.58 at 24 h; from 1.97 to 10.11 at 48 h and from 2.93 to 11.94 at 72 h for MDA-MB-231 cells (Figure 10). Apoptotic index values of MCF-7 and MDA-MB-231 cells increased significantly with time as a result of MFPC-1 administration. This increase was statistically significant ($p < 0.05$).

CONCLUSION

We have explored the photophysical and photochemical properties of a 4-*tert*-butylbenzene substituted metal-free phthalocyanine. MFPC-1 is a novel material and its findings suggest that MFPC-1 exerts potent anticancer effects and shows that it can potentially be used as a photosensitizer in PDT. In this study, antiproliferative effects of MFPC-1 on MCF-7 cell line derived from estrogen receptor-positive human breast epithelial carcinoma and MDA-MB-231 cell line derived from estrogen receptor-negative human metastatic breast carcinoma were investigated. For this purpose, the anticancer effects of MFPC-1 were evaluated using

different cell kinetics parameters (cell viability, mitotic index and apoptotic index).

Among these parameters, MTT analysis (cell viability) is an effective and fast method used to determine cytotoxicity in vitro. In various studies using phthalocyanine, MTT analysis has been used to determine cytotoxicity (33, 34). In present study as a result of MTT analysis for both cell lines, 12,8 μM concentration was determined as LD₅₀ (Lethal Dose 50) that caused the death of half of the cells.

Although the mitotic index parameter is not widely used, it is a laborious and reliable method used in determining cell kinetics. Apoptotic index is one of the frequently used methods in cell kinetics studies. The 12.8 μM concentration used in this present study resulted in a significant reduction in mitotic index values and significant increase in apoptotic index values in both cell lines and similar results were seen.

These parameters showed that MFPC-1 has similar effects in both cell lines. Similar sensitivities to the compound for both cell lines have suggested that the mechanisms causing cell death are independent of the presence of the hormone receptor.

ACKNOWLEDGMENTS

This work was funded by the TUBITAK-BİDEB-2219 international postdoctoral research scholarship programme, number: 1059b191401081, and the yildiz technical university in istanbul, turkey and the university of illinois at urbana-champaign in the usa. The author is thankful to Prof. Kenneth K. Suslick for providing lab space to synthesize the compounds used in this study.

CONFLICT OF INTERESTS

The authors declare no conflict of interests.

REFERENCES

1. L'Her M, Pondaven A. Electrochemistry of Phthalocyanines. In: Kadish K, Smith K, Guillard R, editors. The Porphyrin Handbook. California, USA: Academic Press; 2003. p. 104–69. ISBN: 0-12-393220-3.
2. van Staden J (Koos) F. Application of phthalocyanines in flow- and sequential-injection analysis and microfluidics systems: A review. *Talanta*. 2015 Jul;139:75–88. [<DOI>](#).
3. Kumar KVA, Raghavendra S, Rao SV, Hamad S, Dharmaprakash SM. Structural, linear and nonlinear optical study of zinc tetra-tert-butyl phthalocyanine thin film. *Optik*. 2015 Dec;126(24):5918–22. [<DOI>](#).
4. Morishige K, Tomoyasu S, Iwano G. Adsorption of CO, O₂, NO₂, and NH₃ by Metallophthalocyanine Monolayers Supported on Graphite. *Langmuir*. 1997 Sep 1;13(19):5184–8. [<DOI>](#).
5. Oluwole DO, Prinsloo E, Nyokong T. Photophysical properties of nanoconjugates of zinc(II) 2(3)-mono-2-(4-oxy)phenoxy)acetic acid phthalocyanine with cysteamine capped silver and silver-gold nanoparticles. *Polyhedron*. 2016 Nov;119:434–44. [<DOI>](#).
6. Sheng N, Yuan Z, Wang J, Chen W, Sun J, Bian Y. Third-order nonlinear optical properties of sandwich-type mixed (phthalocyaninato)(porphyrinato) europium double- and triple-decker complexes. *Dyes and Pigments*. 2012 Dec;95(3):627–31. [<DOI>](#).
7. Allen CM, Sharman WM, Van Lier JE. Current status of phthalocyanines in the photodynamic therapy of cancer. *J Porphyrins Phthalocyanines*. 2001 Feb;05(02):161–9. [<DOI>](#).
8. Detty MR, Gibson SL, Wagner SJ. Current Clinical and Preclinical Photosensitizers for Use in Photodynamic Therapy. *J Med Chem*. 2004 Jul;47(16):3897–915. [<DOI>](#).
9. Dougherty TJ, Mang TS. Characterization of intratumoral porphyrin following injection of hematoporphyrin derivative or its purified component. *Photochem Photobiol*. 1987 Jul;46(1):67–70. [<DOI>](#).
10. Canti G, Lattuada D, Morelli S, Nicolin A, Cubeddu R, Taroni P, et al. Efficacy of photodynamic therapy against doxorubicin-resistant murine tumors. *Cancer Letters*. 1995 Jul;93(2):255–9. [<DOI>](#).
11. Lofgren LA, Hallgren S, Nilsson E, Westerborn A, Nilsson C, Reizenstein J. Photodynamic Therapy for Recurrent Nasopharyngeal Cancer. *Archives of Otolaryngology - Head and Neck Surgery*. 1995 Sep 1;121(9):997–1002. [<DOI>](#).
12. Furuyama T, Miyaji Y, Maeda K, Maeda H, Segi M. Extremely Photostable Electron-Deficient Phthalocyanines that Generate High Levels of Singlet Oxygen. *Chem Eur J*. 2018 Dec 14;chem.201805082. [<DOI>](#).
13. Dougherty TJ. Photosensitizers: therapy and detection of malignant tumors. *Photochem Photobiol*. 1987 May;45(s1):879–89. [<DOI>](#).
14. Dougherty TJ, Grindey GB, Fiel R, Weishaupt KR, Boyle DG. Photoradiation Therapy. II. Cure of Animal Tumors With Hematoporphyrin and Light. *JNCI: Journal of the National Cancer Institute*. 1975 Jul;55(1):115–21. [<DOI>](#).

15. Macdonald IJ, Dougherty TJ. Basic principles of photodynamic therapy. *J Porphyrins Phthalocyanines*. 2001 Feb;05(02):105–29. [<DOI>](#).
16. Braun A, Tcherniac T. Über die Producte der Einwirkung von Acetanhydrid auf Phthalamid. *Ber Deutsch Chem Ges*. 1907;40:2709.
17. Stuchinskaya T, Moreno M, Cook MJ, Edwards DR, Russell DA. Targeted photodynamic therapy of breast cancer cells using antibody-phthalocyanine-gold nanoparticle conjugates. *Photochem Photobiol Sci*. 2011;10(5):822. [<DOI>](#).
18. Cetin I, Topcul MR. In vitro antiproliferative effects of nab-paclitaxel with liposomal cisplatin on MDA-MB-231 and MCF-7 breast cancer cell lines. *J BUON*. 2017;22(2):347.
19. Fery-Forgues S, Lavabre D. Are Fluorescence Quantum Yields So Tricky to Measure? A Demonstration Using Familiar Stationery Products. *J Chem Educ*. 1999 Sep;76(9):1260. [<DOI>](#).
20. Fu J, Li X, Ng DKP, Wu C. Encapsulation of Phthalocyanines in Biodegradable Poly(sebacic anhydride) Nanoparticles. *Langmuir*. 2002 May;18(10):3843–7. [<DOI>](#).
21. Ogunsipe A, Maree D, Nyokong T. Solvent effects on the photochemical and fluorescence properties of zinc phthalocyanine derivatives. *Journal of Molecular Structure*. 2003 May;650(1–3):131–40. [<DOI>](#).
22. Tau P, Ogunsipe AO, Maree S, Maree MD, Nyokong T. Influence of cyclodextrins on the fluorescence, photostability and singlet oxygen quantum yields of zinc phthalocyanine and naphthalocyanine complexes. *J Porphyrins Phthalocyanines*. 2003 Jun;07(06):439–46. [<DOI>](#).
23. Seotsanyana-Mokhosi I, Kuznetsova N, Nyokong T. Photochemical studies of tetra-2,3-pyridinoporphyrazines. *Journal of Photochemistry and Photobiology A: Chemistry*. 2001 May;140(3):215–22. [<DOI>](#).
24. Canlıca M, Topçul MR, Çetin İ. In vitro antiproliferative effect of four ball-type phthalocyanines linked by t-butylcatechol and high singlet oxygen production. *Journal of Coordination Chemistry*. 2020 Dec 1;73(23):3291–305. [<DOI>](#).
25. Hsiao S-H, Yang C-P, Chu K-Y. Synthesis and Properties of Poly(ether imide)s Having Ortho - Linked Aromatic Units in the Main Chain. *Macromolecules*. 1997 Jan 1;30(2):165–70. [<DOI>](#).
26. Cetin I, Topcul M. Triple Negative Breast Cancer. *Asian Pacific Journal of Cancer Prevention*. 2014 Mar 30;15(6):2427–31. [<DOI>](#).
27. 1. Topcul M, Cetin İ, Ozbas Turan S, Kulusayin Ozar M. In vitro cytotoxic effect of PARP inhibitor alone and in combination with nab-paclitaxel on triple-negative and luminal $\frac{1}{2}$ A breast cancer cells. *Oncol Rep*. 2018 Apr 12;527–35. [<DOI>](#).
28. Kuznetsova N, Gretsova N, Kalmykova E, Makarova E, Dashkevich S, Negrimovskii V, et al. Relationship between the photochemical properties and structure of pophyrins and related compounds. *Russ J Gen Chem*. 2000;70:133–40. [<URL>](#).
29. Jacques P, Braun AM. Laser Flash Photolysis of Phthalocyanines in Solution and Microemulsion. *Helv Chim Acta*. 1981 Sep 23;64(6):1800–6. [<DOI>](#).
30. Freyer W, Mueller S, Teuchner K. Photophysical properties of benzoannelated metal-free phthalocyanines. *Journal of Photochemistry and Photobiology A: Chemistry*. 2004 Apr;163(1–2):231–40. [<DOI>](#).
31. Bonnett R. Chemical Aspects of Photodynamic Therapy [Internet]. 0 ed. CRC Press; 2000 [cited 2021 Aug 28]. 324 p. [<URL>](#). ISBN: 978-0-429-18201-3.
32. Canlıca M. 3,5-di-tert-butyl substituted phthalocyanines: Synthesis and specific properties. *Journal of Molecular Structure*. 2020 Aug;1214:128160. [<DOI>](#).
33. Manisova B, Binder S, Malina L, Jiravova J, Langova K, Kolarova H. Phthalocyanine-mediated Photodynamic Treatment of Tumoural and Non-tumoural cell lines. *Anticancer res*. 2015;35(7):3943–51. [<URL>](#).
34. Mehraban N, Musich P, Freeman H. Synthesis and Encapsulation of a New Zinc Phthalocyanine Photosensitizer into Polymeric Nanoparticles to Enhance Cell Uptake and Phototoxicity. *Applied Sciences*. 2019 Jan 24;9(3):401. [<DOI>](#).

Supporting Information For

Anticancer activities of a metal-free phthalocyanine on MCF-7 and MDA-MB-231 cells and singlet oxygen production as a photosensitizer in PDT

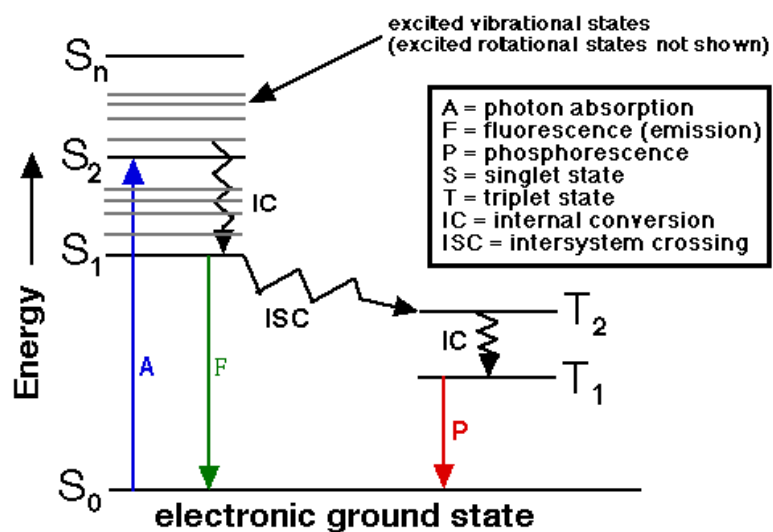


Figure S1: Jablonski diagram.



Biosynthesis of Bimetallic Ag-Au (core-shell) Nanoparticles Using Aqueous Extract of Bay Leaves (*Laurus nobilis* L.)

Numan Hoda^{1*}  , Leyla Budama Akpolat² , Firdevs Mert Sivri³ ,
and Duygu Kurtuluş⁴ 

¹. Akdeniz University, Department of Material Science and Engineering 07058 Antalya, Turkey

². Akdeniz University, Department of Chemistry 07058 Antalya, Turkey

³. Suleyman Demirel University, Department of Basic Pharmaceutical Sciences, 32200 Isparta, Turkey

⁴. Gebze Technical University, Department of Nanoscience and Nanoengineering 41400 Kocaeli, Turkey

Abstract: The green synthesis of bimetallic nanoparticles using plant extracts is attracting an increasing attention in the nanoparticle production field since, besides being available for the production of bimetallic nanoparticles, it is cost-effective, eco-friendly, and it is available for large scale production. The required agents to reduce and stabilize metal nanoparticles during synthesis already exist in plant extracts as phytochemicals. The study highlights the synthesis of gold, silver, and silver-gold (bimetallic) nanoparticles at room temperature using an aqueous extract of dried bay leaves and their physical and chemical characterizations for their potential applications. We have synthesized Ag, Au, and Ag-Au nanoparticles using the aqueous bay leaves extract. The nanoparticles were characterized by UV-Vis spectroscopy, X-ray diffraction (XRD), transmission electron microscopy (TEM), and Fourier transform infrared spectroscopy (FT-IR). According to UV-Vis spectroscopic results, it is concluded that Ag-Au bimetallic nanoparticles synthesized in the extract have a core-shell arrangement. XRD measurements revealed that all nanoparticles (Ag, Au, and Ag-Au) are in fcc structure. The nanoparticles' average sizes were measured as 10 ± 7 , 23 ± 4 , and 8 ± 3 nm for Ag, Au, and Ag-Au nanoparticles, respectively, as determined from the TEM images. The results offer that besides Ag and Au nanoparticles, bimetallic Ag-Au nanoparticles synthesized in an aqueous extract of dried bay leaves may play a prominent role in the field of nanotechnology, especially in nanomedicine.

Keywords: Green synthesis, bimetallic nanoparticles, bay leaf.

Submitted: February 23, 2021. **Accepted:** August 27, 2021.

Cite this: Hoda N, Budama Akpolat L, Mert Sivri F, Kurtuluş D. Biosynthesis of Bimetallic Ag-Au (core-shell) Nanoparticles Using Aqueous Extract of Bay Leaves (*Laurus nobilis* L.). JOTCSA. 2021;8(4):1035-44.

DOI: <https://doi.org/10.18596/jotcsa.885558>.

***Corresponding author. E-mail:** nhoda@akdeniz.edu.tr.

INTRODUCTION

Bimetallic nanoparticles often display different or better catalytic, optical and magnetic properties and surface energy than their monometallic counterparts due to the synergism between two metallic nanoparticles (1-4). These nanoparticles' structures can be divided into alloys and core-shell structures (5). Alloy structure may be defined as merely a "mixture of at least two different metal

atoms in one nanoparticle," and core-shell structure consists of nanoparticles having a monometallic core surrounded by another metallic layer (shell) (Figure 1). Among core-shell nanoparticles, the Au-Ag combination is one of the most studied bimetallic nanostructures due to their surface plasmon resonance (SPR) tunability features for applications such as sensing, imaging, and nanophotonics (5-8). Ag-Au core-shell nanoparticles can be prepared by a number of

methods such as seed-growth (9,10), pulsed laser ablation (11), green approach (12,13), etc. Among them, green approach is one of the emerging fields in nanoscience and nanotechnology, because of being eco-friendly, biocompatible, low-cost, and energy-efficiency (13–16). There are many publications on the synthesis of bimetallic nanoparticles of Au-Ag using plant extracts such as Neem (*Azadirachta indica*) leaf broth (14), Persimmon (*Diospyros kaki*) leaf (17), *Anacardium occidentale* (18), mushroom (13), mahogany (*Swietenia mahogani* JACQ.) leaf (19), *Cacumen platycladi* leaf (20), cruciferous vegetable (21), *piper pedicellatum* (22), and sago pondweed (*Potamogeton pectinatus* L.) (23). The synthesis of nanoparticles in plant extracts is a bottom-up approach in which metal salts are used as precursors. Biomolecules present (carbohydrates, proteins, sugars, etc.) can be responsible for reducing metal ions into metal nanoparticles. For example, Mondal et al. (19) reported that bimetallic Au-Ag nanoparticles were produced using mahogany leaf extract. Also, they claimed that limonoids, one group of the phytochemical constituents of the mahogany leaf, were reducing and stabilizing agents for the formation of stable nanoparticles. Bimetallic nanoparticles are synthesized by simultaneous or sequential reduction in plant extracts. In simultaneous reduction, two metal ions are added into plant extract together (co-reduction), leading to the formation of alloy or core-shell structure (14,19). Sequential reduction involves the addition of two metal ions into plant extracts successively, and it is the most promising method to synthesize core-shell bimetallic nanoparticles. In this method, one of the two metal ions is added first and reduced to form nanoparticle as core and second metal ions are deposited by reduction onto preformed nanoparticle (core) to form shell. While there are limited publications concerning synthesis of Ag-Au (core-shell) structured bimetallic nanoparticles using plant extracts in literature (24), there are many researches on the synthesis of Au-Ag (core-shell) or alloy structured bimetallic nanoparticles using plant extracts (14,17,18). Ag-Au (core-shell) bimetallic nanoparticles are used in many applications such as a sensing and medical imaging etc. (25,26). Therefore, it is worth studying the synthesis of Ag-Au (core-shell) bimetallic nanoparticles that are biocompatible, in green and eco-friendly way.

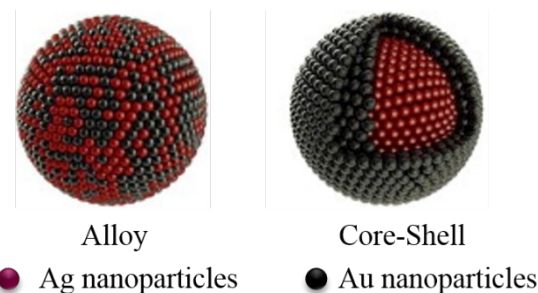


Figure 1: A schematic representation of alloy and core-shell structure of bimetallic nanoparticles.

Laurus nobilis L., commonly known as bay leaves, is a Laureacea family member, being one of the native species to the Mediterranean region (27). It is an evergreen tree cultivated in many countries with the moderate and subtropical climax, such as Italy, Turkey, Mexico, Spain, and the USA (28). It can also be used as a spicy fragrance and flavor in traditional dishes (29); it is also used to treat the symptoms of gastric secretion, flatulence, and rheumatic complaints (30). Aqueous extract of bay leaves contains constituents such as sugars, organic acids, acylated kaempferol glycosides, sesquiterpene lactones, megastigme glycosides, (+)-catechin, (-)-epicatechin, (+)-gallocatechin, (+)-epigallocatechin, and procyanidins (B2, B4, B5 and B7, etc.), which can reduce metallic ions to form nanoparticles and stabilize them (31–36). A few researches on the synthesis of nanoparticles using bay leaves extract are seen in literature in the last few years (37–39). For example, Vijakumar et al. (2016) synthesized ZnO nanoparticles using aqueous bay leaves extract and characterized them by UV-Vis spectroscopy, FTIR, XRD, TEM, SEM, and EDX. After characterization, they further investigated ZnO nanoparticles synthesized for their antibacterial activity, cytotoxicity, and anticancer activity. They found that ZnO nanoparticles synthesized effectively inhibited the biofilm growth of *S. aureus* and *P. aeruginosa* at 75 mg.mL⁻¹, showed no cytotoxic effect on normal murine RAW264.7 macrophage cells, and were influential in inhibiting the viability of human A549 pulmonary cancer cells at higher concentrations of 80 mg.mL⁻¹. The present work's primary purpose is to synthesize Ag, Au, and bimetallic Ag-Au nanoparticles using aqueous bay leaves extract and characterize them for their further applications. There is no publication on the synthesis of Ag-Au bimetallic nanoparticles using bay leaves extract to the best of our knowledge.

EXPERIMENTAL

Material and Method

Silver nitrate, AgNO₃ (Aldrich), and sodium tetrachloroaurate(III) (NaAuCl₄.2H₂O) were used as purchased. In the extraction processes,

deionized water was used. All other reagents were purchased from commercial sources and were used after the usual drying and/or distillation without further purification. Bay leaves were purchased from the local market and confirmed that they are gathered in the Mediterranean coast of Antalya, Turkey, and dried in shadow.

Preparation of aqueous leaves extract

After washing with tap water, the leaves were washed twice with deionized water and spread to dry for three days at room temperature and ground. The ground leaves were sieved, and the fraction of 0.650-1.00 mm was used for extraction. 2.5 gram of leaves powder was taken into an Erlenmeyer flask, and 100 mL of deionized water was added and then refluxed for 5 min. After cooling to room temperature, the mixture was sieved with 0.350 mm mesh to remove large

particles, and then it was centrifuged with 4500 rpm for 15 min. The supernatant was collected and stored at 4 °C for further studies.

Synthesis of nanoparticles

0.01 M, 1 mL of AgNO_3 , and HAuCl_4 were added to 10 mL of extracts to synthesize Ag and Au nanoparticles separately, and the mixtures were stirred for 24 h in a dark condition at room temperature. For the synthesis of Ag-Au core-shell nanoparticles, 0.01 M, 1 mL of AgNO_3 has initially been added to 10 mL of extract and was allowed to be reduced and stabilized by phytochemicals present in the extract. Then, the corresponding portion of HAuCl_4 was added and allowed to complete the reaction. The green synthetic steps of the Au-Ag bimetallic nanoparticles are shown in Figure 2.

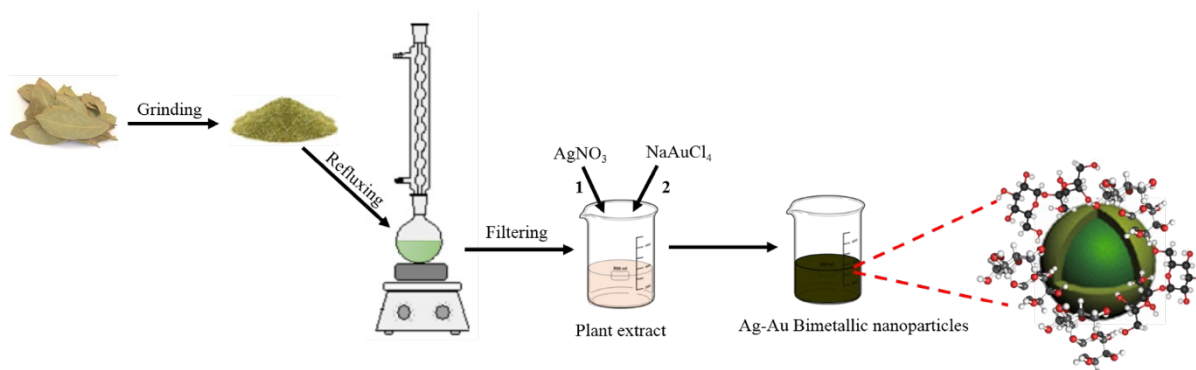


Figure 2: Schematic diagram of green synthesis of Ag-Au bimetallic nanoparticles using aqueous extract of bay leaves (*Laurus nobilis L.*).

Characterization of synthesized nanoparticles

UV-visible spectra of extracts containing Ag, Au, and Ag-Au nanoparticles were recorded with the wavelength range from 200 to 800 nm using a Perkin Elmer Lambda 35 UV/Vis spectrometer operating at a resolution of 1 nm. X-ray (XRD) patterns of synthesized nanoparticles were obtained using Rigaku MiniFlex X-ray diffractometer with monochromatic Cu-K α incident beam ($\lambda=0.154056$ nm) with nickel monochromator the range between 10° and 90° at 2 θ angle. The morphologies and the synthesized nanoparticles' sizes were examined through Transmission Electron Microscopy (TEM) Zeiss Leo 906E TEM instrument by evaluating TEM images with Adobe Photoshop 7. A total of 200 particles were counted and averaged for corresponding particle sizes. Fourier transforms infrared (FT-IR) spectra were recorded with ATR-FTIR using Perkin Elmer Two spectrometer at room temperature at 4 cm^{-1} resolution.

RESULTS AND DISCUSSION

The synthesis of Ag, Au, and Ag-Au (core-shell) nanoparticles was performed in an aqueous bay leaf extract. After adding any precursor into an extract and stirring, an immediate change in color of solutions was observed, confirming nanoparticles' formation by reduction reactions. As indicated in the inset of Figure 3, the color of extracts turned into dark-yellow, purple, and grayish-black for Ag, Au, and Ag-Au nanoparticles, respectively. Also, Figure 3 shows the UV-Vis spectra of synthesized nanoparticles. The absorption peaks at 425 nm (Figure 3b) and 542 nm (Figure 3c) belong to the SPR absorption of Ag and Au nanoparticles. SPR bands are highly dependent on the shape and size of the nanoparticles (40). The absorption peak observed at 542 nm is the characteristic peak for spherical gold nanoparticles (12).

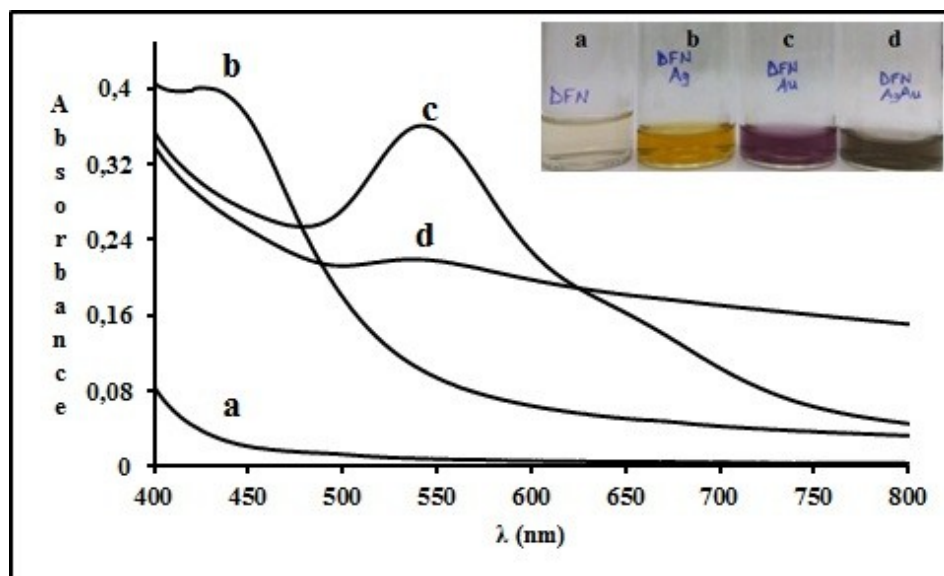


Figure 3: UV spectra of extract and nanoparticle solutions (a, b, c, and d represent bay leaf extract, Ag, Au, and Ag-Au nanoparticles in extract, respectively).

Experimental absorption spectra and calculated spectra for the Au-coated Ag nanoparticles (using full Mie equations and the dielectric data for the alloys) were compared by Mulvaney (41) to investigate whether the optical spectra alone can reveal whether alloying has taken place during deposition of a second metal onto a seed metal particle. According to Mulvaney's work (1996), Ag-Au bimetallic nanoparticles' alloyed structure has a single plasmon band between the corresponding bands of monometallic Ag and Au nanoparticles regarding content ratios of corresponding metals. As Au content increases in the bimetallic nanoparticle, a continuous red-shift in the band position is observed. In the case of core-shell structures (Ag-core, Au-shell) Ag (core) plasmon band is strongly damped but does not shift, and Au's thick coating on the Ag core shows a plasmon band close to the band of monometallic Au nanoparticle. As Au content (correspondingly thickness of the shell) increases, damping in the Ag (core) band increases. In our case for Ag-Au synthesized nanoparticles, the SPR absorption observed at 538 nm (Figure 3d) confirming the Ag-Au bimetallic nanoparticles are in core-shell arrangement. Because, in the UV-Vis spectrum of Ag-Au bimetallic nanoparticles, the disappearance of absorption peak for Ag nanoparticles and still observing absorption peak at almost the same position as in monometallic Au nanoparticles strongly suggest that Ag nanoparticles formed core and Au formed the shell. Also, the complete disappearance of absorption peak for Ag nanoparticles depends on the thickness of the shell since, when the shell is sufficiently thick, only absorption corresponding to shell could be observed, but when the thickness of the shell is not enough to shield UV-Vis waves, any absorption

from the core could occur (41). The results are in good agreement with the works on Ag-Au core-shell bimetallic nanoparticles (12-16,24,27-30,35-38,42). In general, during synthesizing bimetallic nanoparticles of Ag and Au by co-reduction, if monometallic nanoparticles of Au and Ag form separately, the solution will be just a physical mixture of the corresponding nanoparticles; just two absorption bands will be observed at the same position and intensity with the monometallic counterparts. Nevertheless, when any intensity change is observed at the absorption maxima, it can result from the formation of core-shell arrangement. In alloy arrangement for bimetallic nanoparticles, only one absorption peak is observed between two maxima of the corresponding monometallic nanoparticles, and the peak of maximum observed depends on the concentration of the precursors (41,42).

The crystalline natures of the synthesized nanoparticles were confirmed by X-ray diffraction (XRD) analysis. Powders of nanoparticles were obtained by vacuum drying of extracts containing nanoparticles using a rotary evaporator. The XRD patterns of powders are given in Figure 4. As illustrated in Figure 4a, the XRD pattern of Ag nanoparticles shows four distinct diffraction peaks at 38.1° , 43.9° , 64.5° and 77.1° representing (1 1 1), (2 0 0), (2 2 0), and (3 1 1) crystal planes of a face centered cubic (fcc) lattice of silver consistent with the JCPDS data [No. 04-0783]. In Au nanoparticle diffraction pattern (Figure 4b), the peaks at 38.1° , 44.2° , 64.4° and 77.4° correspond to the (1 1 1), (2 0 0), (2 2 0) and (3 1 1) facets (1,28,30,36) of the face-centered cubic crystal structure, respectively. The ratio between peak intensities gives the predominant orientation, and

in the Au nanoparticle diffraction pattern, the ratio of intensities of (2 0 0) and (1 1 1) peaks is much lower than the usual value (0.52), suggesting that the (1 1 1) plane is the predominant orientation (27). In the case of Ag-Au bimetallic nanoparticles (Figure 4c), diffraction peaks appeared at 38.1° (111), 44.1° (200), 64.4° (220), and 77.1° (311),

confirming that Ag-Au bimetallic nanoparticles are in fcc structure. Unassigned peaks in all the XRD patterns can be attributed to the crystallization of the bioorganic phase on nanoparticles' surface. Similar results were reported in some works in the literature, too (12,13,21).

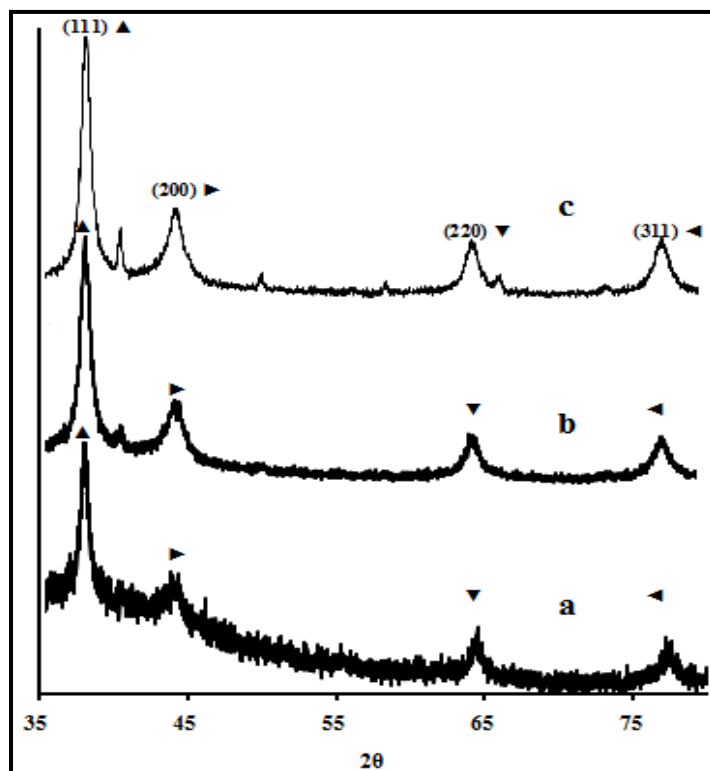


Figure 4: XRD patterns of nanoparticles synthesized (a, b and c represent Ag, Au and Ag-Au nanoparticles, respectively).

The TEM images of nanoparticles synthesized in bay laurel leaves extract are given in Figure 5, and these images can help us analyze the size and shape of the nanoparticles. Figure 5(a), 5(b), and 5(c) are the images of nanoparticles of Ag, Au, and Ag-Au (core-shell), respectively. The shape of the nanoparticles is spherical primarily, but for Au nanoparticles, a few hexagonal and triangular shapes were observed in TEM images not given here. While Ag-Au nanoparticles' size ranges between 1 nm and 17 nm with a mean diameter of 8 ± 3 nm, Au nanoparticles' size ranges between 12 and 33 nm with a mean diameter of 23 ± 4 nm and Ag nanoparticles' size ranges between 1 nm and 31 nm with a mean diameter of 10 ± 7 nm. The size

of core-shell Ag-Au nanoparticles is smaller than that of Au and Ag nanoparticles synthesized. Gopinath et al. synthesized Ag, Au and Ag-Au bimetallic nanoparticles by using the *Gloriosa superba* leaf extract and they reported that mean size of Ag-Au bimetallic nanoparticles as 10 nm (43) which is close to our findings. In another study, Chavez and Rosas synthesized Ag-Au Core-shell bimetallic nanoparticles using the extract of *Hamelia patens* plant and they found that the particle size distribution ranging from 10 to 50 nm being the average particle size was 32 nm (44) which is four folded of our findings. The size of nanoparticles synthesized using plant extracts may depend on plant types.

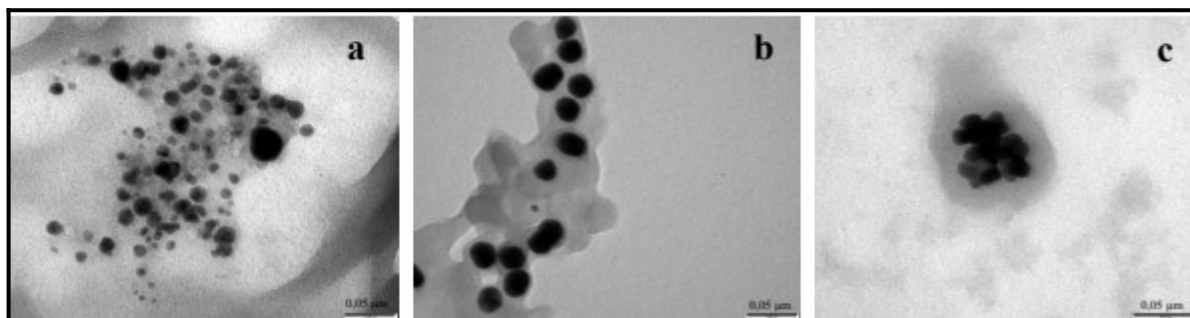


Figure 5: TEM images of the **a)** Ag, **b)** Au, and **c)** Ag-Au nanoparticles in bay leaf extract.

Fourier Transform Infrared Spectroscopy (FT-IR) measurements of pure and nanoparticle-containing powdered samples of bay leaf extract were carried out to identify the possible interactions between the nanoparticles (Ag, Au, and Ag-Au) and bioactive molecules, which might be effective in the synthesis and stabilization of the nanoparticles in the extracts. The FT-IR spectra obtained from the pure extract powders display absorption peaks at different positions for various functional groups at 3342, 2921, 2856, 1711, 1606, 1438, 1373, 1206, 1040, and 775 cm^{-1} as seen in Figure 6. The bands at 3342 cm^{-1} and 1040 cm^{-1} can be attributable to O-H stretching vibrations indicating hydroxyl groups' presence in the structure of biomolecules present in the powder of extract (45). The bands observed at around 2921 cm^{-1} and 2850 cm^{-1} are from stretching vibration of C-H (46). The stretching vibrations of the C=O group from ketones are observed at 1722 cm^{-1} . While the

band observed at 1616 cm^{-1} corresponds to stretching of C-O bond of amide-I, the weak band at 1440 cm^{-1} corresponds to $-\text{C}=\text{C}-$ vibrations from aromatic skeletal compounds (47). The bands at 1373 and 775 cm^{-1} are assigned to C-H bending vibration for $-\text{CH}_3$ symmetrical deformation and N-H's bending vibration, respectively. The band at 1206 cm^{-1} can be attributed to in-plane bending vibration of the $-\text{OH}$ group of phenols (48). While the characteristic IR band of amine and amino-methyl stretching groups appeared at 1438 cm^{-1} , C-N vibrations appeared at 1373 cm^{-1} (49). When the spectrum of pure extract and spectra of nanoparticle-containing powdered extract samples are compared, there are only minor shifts of about $\pm 1-5 \text{ cm}^{-1}$ except for the band at 1040 cm^{-1} which shifted to 1032 cm^{-1} for Au and Ag-Au containing samples. As explained above, many functional groups are responsible for reducing or stabilizing the nanoparticles in the extract.

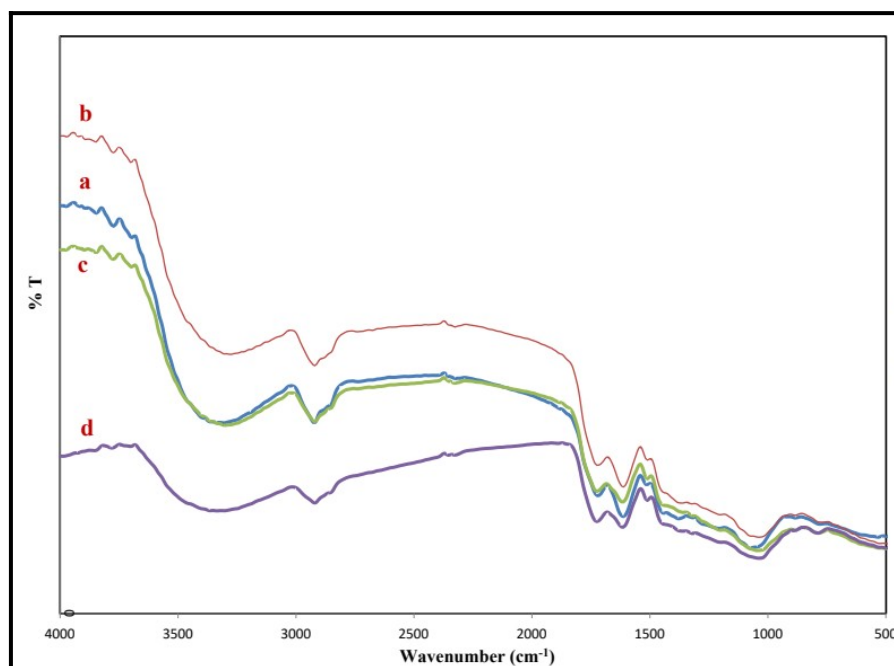


Figure 6: FTIR Spectra of **a:** bay leaf extract, **b:** Ag nanoparticles, **c:** Au nanoparticles, **d:** Ag-Au bimetallic nanoparticles in the bay leaf extract.

CONCLUSION

This study focused on producing nanoparticles of Ag, Au, and Ag-Au (bimetallic) in the aqueous bay leaf extract. The nanoparticles were prepared by a green, eco-friendly, fast, low cost, and large-scale applicable method. The synthesized nanoparticles were characterized by TEM, UV, XRD, and FT-IR. It was observed that Ag-Au bimetallic nanoparticles synthesized in the extract are in the core-shell structure according to UV spectral results. XRD characterization of nanoparticles showed that all nanoparticles synthesized are in FCC structure. TEM technique was used to identify the size and shape of the nanoparticles. TEM measurements indicated that the nanoparticles' shape is primarily spherical, but a few hexagonal and triangular shapes were observed for Au nanoparticles. The nanoparticles' average sizes were measured as 10 ± 7 , 23 ± 4 , and 8 ± 3 nm for Ag, Au, and Ag-Au nanoparticles, respectively. FT-IR measurements showed that the extract's biomolecules are responsible for reducing Ag^+ and Au^{3+} ions to Ag^0 and Au^0 to form nanoparticles and stabilize them in the extract. The present study confirmed that Ag, Au, and Ag-Au nanoparticles could be successfully synthesized in the aqueous bay leaf extract. These nanoparticles have potential usage in various applications, including the biomedical field.

ACKNOWLEDGMENTS

We sincerely thank the Scientific Research Projects Unit of Akdeniz University for supporting this work through project number FDK-2015-757 and FBA-2014-83.

REFERENCES

- Ding K, Cullen DA, Zhang L, Cao Z, Roy AD, Ivanov IN, et al. A general synthesis approach for supported bimetallic nanoparticles via surface inorganometallic chemistry. *Science*. 2018 Nov 2;362(6414):560-4. [<DOI>](#).
- Sankar M, Dimitratos N, Miedziak PJ, Wells PP, Kiely CJ, Hutchings GJ. Designing bimetallic catalysts for a green and sustainable future. *Chem Soc Rev*. 2012;41(24):8099. [<DOI>](#).
- Alonso DM, Wettstein SG, Dumesic JA. Bimetallic catalysts for upgrading of biomass to fuels and chemicals. *Chem Soc Rev*. 2012;41(24):8075. [<DOI>](#).
- Ferrando R, Jellinek J, Johnston RL. Nanoalloys: From Theory to Applications of Alloy Clusters and Nanoparticles. *Chem Rev*. 2008 Mar 1;108(3):845-910. [<DOI>](#).
- Chen HM, Liu RS, Jang L-Y, Lee J-F, Hu SF. Characterization of core-shell type and alloy Ag/Au bimetallic clusters by using extended X-ray absorption fine structure spectroscopy. *Chemical Physics Letters*. 2006 Apr;421(1-3):118-23. [<DOI>](#).
- Chatterjee K, Sarkar S, Jagajjanani Rao K, Paria S. Core/shell nanoparticles in biomedical applications. *Advances in Colloid and Interface Science*. 2014 Jul;209:8-39. [<DOI>](#).
- Kim K, Kim KL, Choi J-Y, Lee HB, Shin KS. Surface Enrichment of Ag Atoms in Au/Ag Alloy Nanoparticles Revealed by Surface-Enhanced Raman Scattering of 2,6-Dimethylphenyl Isocyanide. *J Phys Chem C*. 2010 Mar 4;114(8):3448-53. [<DOI>](#).
- Zhang L, Zhang J, Wang F, Shen J, Zhang Y, Wu L, et al. An Au@Ag nanocube based plasmonic nano-sensor for rapid detection of sulfide ions with high sensitivity. *RSC Adv*. 2018;8(11):5792-6. [<DOI>](#).
- Srnová-Šloufová I, Lednický F, Gemperle A, Gemperlová J. Core-Shell (Ag)Au Bimetallic Nanoparticles: Analysis of Transmission Electron Microscopy Images. *Langmuir*. 2000 Dec;16(25):9928-35. [<DOI>](#).
- Xu S, Zhao B, Xu W, Fan Y. Preparation of Au-Ag core-shell nanoparticles and application of bimetallic sandwich in surface-enhanced Raman scattering (SERS). *Colloids and Surfaces A: Physicochemical and Engineering Aspects*. 2005 May;257-258:313-7. [<DOI>](#).
- Mallik K, Mandal M, Pradhan N, Pal T. Seed Mediated Formation of Bimetallic Nanoparticles by UV Irradiation: A Photochemical Approach for the Preparation of "Core-Shell" Type Structures. *Nano Lett*. 2001 Jun 1;1(6):319-22. [<DOI>](#).
- Vinod M, Gopchandran KG. Ag@Au core-shell nanoparticles synthesized by pulsed laser ablation in water: Effect of plasmon coupling and their SERS performance. *Spectrochimica Acta Part A: Molecular and Biomolecular Spectroscopy*. 2015 Oct;149:913-9. [<DOI>](#).
- Philip D. Biosynthesis of Au, Ag and Au-Ag nanoparticles using edible mushroom extract. *Spectrochimica Acta Part A: Molecular and Biomolecular Spectroscopy*. 2009 Jul;73(2):374-81. [<DOI>](#).
- Shankar SS, Rai A, Ahmad A, Sastry M. Rapid synthesis of Au, Ag, and bimetallic Au core-Ag shell nanoparticles using Neem (Azadirachta

indica) leaf broth. Journal of Colloid and Interface Science. 2004 Jul;275(2):496–502. [<DOI>](#).

15. Kalaiarasi R, Jayalakshmi N, Venkatachalam P. Phytosynthesis of nanoparticles and its applications. Plant Cell Biotechnology and Molecular Biology. 2010;11(1/4):1–16.

16. Dwivedi AD, Gopal K. Biosynthesis of silver and gold nanoparticles using *Chenopodium album* leaf extract. Colloids and Surfaces A: Physicochemical and Engineering Aspects. 2010 Oct;369(1–3):27–33. [<DOI>](#).

17. Song JY, Kim BS. Biological synthesis of bimetallic Au/Ag nanoparticles using Persimmon (*Diopyros kaki*) leaf extract. Korean J Chem Eng. 2008 Jul;25(4):808–11. [<DOI>](#).

18. Shen Y DS, Mathew J, Philip D. Phytosynthesis of Au, Ag and Au–Ag bimetallic nanoparticles using aqueous extract and dried leaf of *Anacardium occidentale*. Spectrochimica Acta Part A: Molecular and Biomolecular Spectroscopy. 2011 Jun;79(1):254–62. [<DOI>](#).

19. Mondal S, Roy N, Laskar RA, Sk I, Basu S, Mandal D, et al. Biogenic synthesis of Ag, Au and bimetallic Au/Ag alloy nanoparticles using aqueous extract of mahogany (*Swietenia mahogani* JACQ.) leaves. Colloids and Surfaces B: Biointerfaces. 2011 Feb;82(2):497–504. [<DOI>](#).

20. Zhan G, Huang J, Du M, Abdul-Rauf I, Ma Y, Li Q. Green synthesis of Au–Pd bimetallic nanoparticles: Single-step bioreduction method with plant extract. Materials Letters. 2011 Oct;65(19–20):2989–91. [<DOI>](#).

21. Jacob J, Mukherjee T, Kapoor S. A simple approach for facile synthesis of Ag, anisotropic Au and bimetallic (Ag/Au) nanoparticles using cruciferous vegetable extracts. Materials Science and Engineering: C. 2012 Oct;32(7):1827–34. [<DOI>](#).

22. Tamuly C, Hazarika M, Borah SCh, Das MR, Boruah MP. In situ biosynthesis of Ag, Au and bimetallic nanoparticles using *Piper pedicellatum* C.DC: Green chemistry approach. Colloids and Surfaces B: Biointerfaces. 2013 Feb;102:627–34. [<DOI>](#).

23. AbdelHamid AA, Al-Ghobashy MA, Fawzy M, Mohamed MB, Abdel-Mottaleb MMSA. Phytosynthesis of Au, Ag, and Au–Ag Bimetallic Nanoparticles Using Aqueous Extract of Sago Pondweed (*Potamogeton pectinatus* L.). ACS Sustainable Chem Eng. 2013 Dec 2;1(12):1520–9. [<DOI>](#).

24. Kasthuri J, Veerapandian S, Rajendiran N. Biological synthesis of silver and gold nanoparticles using apiin as reducing agent. Colloids and Surfaces B: Biointerfaces. 2009 Jan;68(1):55–60. [<DOI>](#).

25. Boote BW, Byun H, Kim J-H. Silver–Gold Bimetallic Nanoparticles and Their Applications as Optical Materials. J Nanosci Nanotech. 2014 Feb 1;14(2):1563–77. [<DOI>](#).

26. Hamidi-Asl E, Dardenne F, Pilehvar S, Blust R, De Wael K. Unique Properties of Core Shell Ag@Au Nanoparticles for the Aptasensing of Bacterial Cells. Chemosensors. 2016 Aug 29;4(3):16. [<DOI>](#).

27. Nagaonkar D. Sequentially Reduced Biogenic Silver-Gold Nanoparticles With Enhanced Antimicrobial Potential Over Silver And Gold Monometallic Nanoparticles. AML. 2015 Apr 10;6(4):334–41. [<DOI>](#).

28. Di Leo Lira P, Retta D, Tkacik E, Ringuelet J, Coussio JD, van Baren C, et al. Essential oil and by-products of distillation of bay leaves (*Laurus nobilis* L.) from Argentina. Industrial Crops and Products. 2009 Sep;30(2):259–64. [<DOI>](#).

29. Sellami IH, Wannas WA, Bettaieb I, Berrima S, Chahed T, Marzouk B, et al. Qualitative and quantitative changes in the essential oil of *Laurus nobilis* L. leaves as affected by different drying methods. Food Chemistry. 2011 May;126(2):691–7. [<DOI>](#).

30. Gómez-Coronado DJM, Barbas C. Optimized and Validated HPLC Method for α - and γ -Tocopherol Measurement in *Laurus nobilis* Leaves. New Data on Tocopherol Content. J Agric Food Chem. 2003 Aug;51(18):5196–201. [<DOI>](#).

31. Dall'Acqua S, Viola G, Giorgetti M, Loi MC, Innocenti G. Two New Sesquiterpene Lactones from the Leaves of *Laurus nobilis*. Chem Pharm Bull. 2006;54(8):1187–9. [<DOI>](#).

32. De Marino S, Borbone N, Zollo F, Ianaro A, Di Meglio P, Iorizzi M. Megastigmane and Phenolic Components from *Laurus nobilis* L. Leaves and Their Inhibitory Effects on Nitric Oxide Production. J Agric Food Chem. 2004 Dec;52(25):7525–31. [<DOI>](#).

33. Fiorini C, David B, Fourasté I, Vercauteren J. Acylated kaempferol glycosides from *Laurus nobilis* leaves. Phytochemistry. 1998 Mar;47(5):821–4. [<DOI>](#).

34. Sakar M, Engelshowe R. Monomere und dimere Gerbstoffvorstufen in Lorbeerblättern (*Laurus*

- nobilis L.). Z Für Lebensm-Unters Forsch. 1985;180(6):494-5.
35. Baytop T. Therapy with medicinal plants in Turkey (past and present). Istanbul: Nobel Tip Kitabevi; 2000.
36. Jha A, Prasad K. Understanding the involved mechanism in plant-mediated synthesis of nanoparticles. In: Rai M, Posten C, editors. Green biosynthesis of nanoparticles: mechanisms and applications. Wallingford, Oxfordshire; Boston, Massachusetts: CABI; 2013. p. 122-31. ISBN: 978-1-78064-223-9.
37. Dias MI, Barros L, Dueñas M, Alves RC, Oliveira MBPP, Santos-Buelga C, et al. Nutritional and antioxidant contributions of *Laurus nobilis* L. leaves: Would be more suitable a wild or a cultivated sample? Food Chemistry. 2014 Aug;156:339-46. <DOI>.
38. Sinha SN, Paul D. Eco-friendly green synthesis and spectrophotometric characterization of silver nanoparticles synthesized using some common Indian spices. Int J Green Herbal Chem. 2014;3:401-8.
39. Vijayakumar S, Vaseeharan B, Malaikozhundan B, Shobiya M. *Laurus nobilis* leaf extract mediated green synthesis of ZnO nanoparticles: Characterization and biomedical applications. Biomedicine & Pharmacotherapy. 2016 Dec;84:1213-22. <DOI>.
40. Khalil M, Mahmoud I, Hamed M. Green synthesis of gold nanoparticles using *Laurus nobilis* L. leaf extract and its antimicrobial activity. Int J Green Herbal Chem. 2015;4(3):265-79.
41. Mulvaney P. Surface Plasmon Spectroscopy of Nanosized Metal Particles. Langmuir. 1996 Jan;12(3):788-800. <DOI>.
42. Yang Y, Shi J, Kawamura G, Nogami M. Preparation of Au-Ag, Ag-Au core-shell bimetallic nanoparticles for surface-enhanced Raman scattering. Scripta Materialia. 2008 May;58(10):862-5. <DOI>.
43. Gopinath K, Kumaraguru S, Bhagyaraj K, Mohan S, Venkatesh KS, Esakkirajan M, et al. Green synthesis of silver, gold and silver/gold bimetallic nanoparticles using the *Gloriosa superba* leaf extract and their antibacterial and antibiofilm activities. Microbial Pathogenesis. 2016 Dec;101:1-11. <DOI>.
44. Chavez K, Rosas G. Green Synthesis and Characterization of Ag@Au Core-shell Bimetallic Nanoparticles using the Extract of *Hamelia patens* Plant. Microsc Microanal. 2019 Aug;25(S2):1102-3. <DOI>.
45. Mukherjee P, Roy M, Mandal BP, Dey GK, Mukherjee PK, Ghatak J, et al. Green synthesis of highly stabilized nanocrystalline silver particles by a non-pathogenic and agriculturally important fungus *T. asperellum*. Nanotechnology. 2008 Feb 20;19(7):075103. <DOI>.
46. Dubey SP, Lahtinen M, Sillanpää M. Green synthesis and characterizations of silver and gold nanoparticles using leaf extract of *Rosa rugosa*. Colloids and Surfaces A: Physicochemical and Engineering Aspects. 2010 Jul;364(1-3):34-41. <DOI>.
47. Kumar VA, Ammani K, Jobina R, Subhaswaraj P, Siddhardha B. Photo-induced and phytomediated synthesis of silver nanoparticles using *Derris trifoliata* leaf extract and its larvicidal activity against *Aedes aegypti*. Journal of Photochemistry and Photobiology B: Biology. 2017 Jun;171:1-8. <DOI>.
48. Groiss S, Selvaraj R, Varadavenkatesan T, Vinayagam R. Structural characterization, antibacterial and catalytic effect of iron oxide nanoparticles synthesised using the leaf extract of *Cynometra ramiflora*. Journal of Molecular Structure. 2017 Jan;1128:572-8. <DOI>.
49. Nezamdoost T, Bagherieh-Najjar MB, Aghdasi M. Biogenic synthesis of stable bioactive silver chloride nanoparticles using *Onosma dichroantha* Boiss. root extract. Materials Letters. 2014 Dec;137:225-8. <DOI>.



Fabrication and Characterization of Gelatin/Chitosan Hydrogel Membranes

Thi Sinh Vo^{1*}  , Tran Thi Bich Chau Vo² , Truong Sinh Nguyen¹ , and Tran Trung Tien¹ 

¹School of Mechanical Engineering, Sungkyunkwan University, Suwon 16419, Korea.

²Department of Industrial Management, Can Tho University, Can Tho, Vietnam.

Abstract: The gelatin/chitosan (GEL/CTS, GC) membranes have been fabricated well by a simple in-situ method. The as-prepared GC membranes were characterized by morphological surface (scanning electron microscopy, SEM), chemical (Fourier-transform infrared spectroscopy, FT-IR), crystallinity (X-ray diffraction, XRD), thermal (thermal gravimetric analysis, TGA), mechanical (tensile test), hydrophilic (water contact angle), and swelling properties to elucidate the changes in their chemical structures and morphologies. The morphological structure of the GC membranes was found to be very smooth, non-rough and homogeneous. The FT-IR and XRD studies manifest that the GC membranes have good interaction and compatibility between GEL and CTS in the hydrogel mixture. The prepared GC membranes also obtain better thermal, mechanical and swelling properties comparing to the raw CTS molecule. These results suggest that the nontoxic GC membrane can become a preferred hydrogel membrane in the field of wound dressing or tissue-engineering applications.

Keywords: Chitosan, gelatin, swelling, hydrogel membrane.

Submitted: May 25, 2021 . **Accepted:** September 20, 2021.

Cite this: Vo TS, Vo TTBC, Nguyen TS, Tien TT. Fabrication and Characterization of Gelatin/Chitosan Hydrogel Membranes. JOTCSA. 2021;8(4):1045-56.

DOI: <https://doi.org/10.18596/jotcsa.942478>.

***Corresponding author. E-mail:** vtsinh92@skku.edu.

INTRODUCTION

As known, polymeric membrane system was extensively applied in different research fields and practical applications (1-5), at the same time that remarkable factors of a polymeric membrane almost regard to possibly physical, chemical and interface properties. Hence, they are necessary to conduct considerable modification methods that can obtain better desired results corresponding to multiple researches. Especially, hydrogel membrane-based superabsorbent has effective swelling behaviors that can be due to the hydrophilic functional groups (i.e., carboxyl, amino, and hydroxyl groups) contained available on the polymer chains (6-14). At the same time, the hydrogel membranes are also considered as hydrophilic membranes with three-dimensional cross-linked networks being applied for plenty of

biomedical applications. These hydrogel membranes significantly swell in an aqueous medium that can be mainly due to their cross-linked networks, meaning they do not disintegrate in water at physiological pH and temperature (15). Furthermore, the hydrogel membranes reach lots of advantages, e.g., high water content and soft elastic property, boost granulation and epithelialization due to the moist environment (16), promote the healed wound without any damage (17), respectively. Thus, the hydrogel membrane is widely used in the fields of drug delivery, agriculture, purification, hygiene, and food industry. The development and expansion of eco-friendly membrane has been researched and explored intensively to protect environment; concomitantly, multiple natural sources are recently concerned (10-14).

Notably, single-network hydrogel membranes show slow response and weak mechanical property at swelling, while multiple-network membranes (i.e., interpenetrating polymer networks) can be designed to overcome this drawback (18). So far, plenty of hydrophilic polymer sources have been used to produce the appropriate hydrogel membranes, counting natural (proteins and polysaccharides) and synthetic (contain hydrophilic functional groups, i.e., carboxyl, amino, and hydroxyl groups, etc.) polymer sources; especially for commonly natural polymers, e.g., gelatin and chitosan. Specifically, chitosan (CTS) is considered to be an eco-friendly and widely-used compound of chitin N-deacetylation, which is also a potential candidate in numerous fields such as drugs, catalysis, food, etc. (1, 2, 6-8). Besides, the CTS is known as a biomedical material source owing to its wound-healing ability, biodegradability, biocompatibility, hemostasis, antimicrobial activity, etc. (19-21), which leads to being a valuable biomedical material – CTS molecule. Concomitantly, the CTS is soluble in weak acid solvents (i.e., lactic acid, acetic acid, etc.) but insoluble in a water medium, although it has a crystalline structure with several hydrogen bonds (22). Indeed, several researchers presented possible modifications on basic of the CTS molecule regarding to available chemical features to be expanded in the material systems of beads, fibers and membranes, owing to its good solubility in a weak acid medium (1, 2, 23-27). By the way, gelatin (GEL) is a biocompatible protein with a very high bio-absorptivity and low antigenicity in a living body (28, 29), and its outstanding property regards to a sol-gel transition under an aqueous medium. Several various membranes have been produced on natural material sources of the CTS and GEL molecules to be applied in biomedical applications (2, 26, 28). Nonetheless, these membranes were mostly successfully prepared by casting method using GEL/CTS (GC) solution in acetic acid solvent, which is known as a common solvent to dissolve the CTS molecules. However, the odor feature of this acid solvent is one of the disadvantages to be

utilized in the fabrication of GC membranes. Hence, the lactic acid solvent is selected to replace the acetic acid solvent and overcome this disadvantage in this study, at same time that the incorporation of GEL and CTS molecules is also considered as a nontoxic hydrogel membrane, owing to natural polymer sources.

Herein, the lactic acid solvent is employed to fabricate GC hydrogel membranes based on a simple in-situ method. Moreover, the morphological surface, crystallinity, thermal, mechanical, hydrophilic, and swelling properties of the as-prepared GC membranes are specifically investigated with different weight ratios of GEL/CTS to probably elucidate the changes in their chemical structures and morphologies. Thereby, we hope that these nontoxic GC membranes can become a promising hydrogel membrane in the fields of wound dressing or tissue-engineering applications.

EXPERIMENTAL SECTION

Materials

CTS (deacetylation degree = ~90%) and lactic acid ($\text{CH}_3\text{CH}(\text{OH})\text{COOH}$, 85 – 90%) are obtained from Sigma Aldrich. GEL is purchased from Samchun Chemical Co.. Deionized water is directly offered from a Milli-Q ultrapure system.

Fabrication of GC Membranes

A CTS stock solution with a concentration of 2% is fabricated by mixing CTS in 100 mL of aqueous lactic acid (2.5%, v/v) and stirring overnight. Then GEL is added and stirred in 20 mL of distilled water at 50 °C, mixed into the CTS solution, and agitated at 50 °C with the different weight ratios (GEL:CTS, wt/wt = 8:2; 6:4; 5:5; 4:6 and 2:8). The GC solution with different weight ratios is spread over the bottom of Petri dishes (100 mm diameter), and resultant GC membranes are air-dried for 1 day (room temperature). The fabrication process of the GC hydrogel membrane is described in Figure 1.

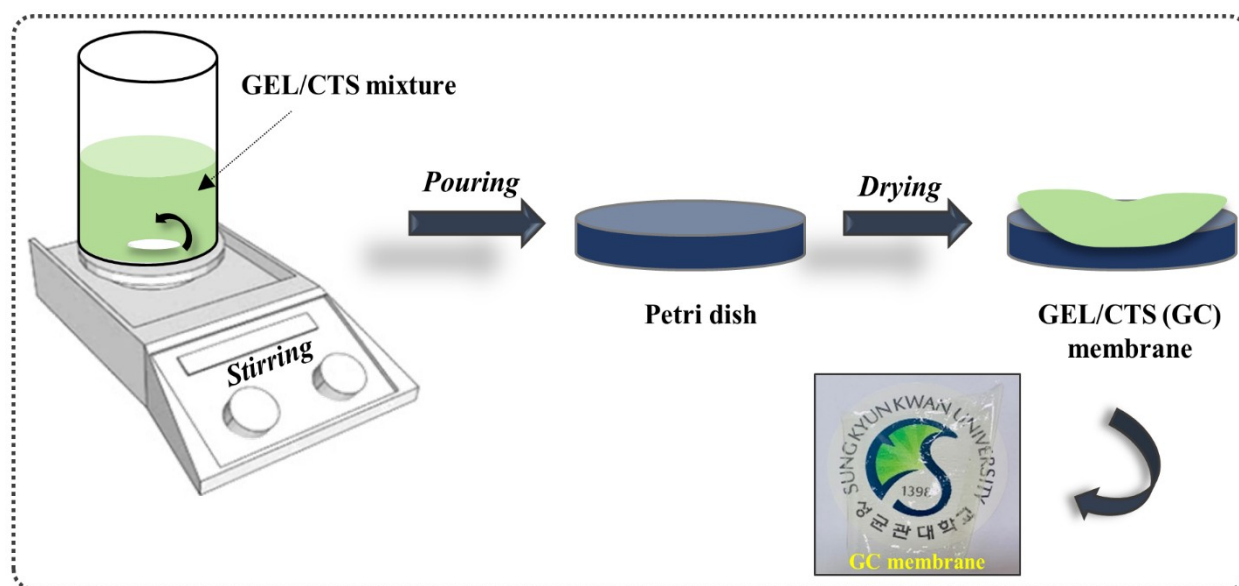


Figure 1: Fabrication process of GC hydrogel membrane.

Swelling Study

The swelling property of the prepared GC membranes is performed by immersing and sealing into an aqueous solution. Specifically, the as-prepared GC membranes are cut and measured the weight (2 cm x 2 cm, W_0) by a four-digit analytical balance. Next, the cut membranes are immersed and sealed into distilled water at room temperature. After preset times ($t = 5 - 60$ min), the membranes are taken out and weight was measured (W_1). Finally, the swelling rate (SW, %) of the membrane is calculated from an equation: $SW (\%) = [(W_1 - W_0)/W_0] \times 100$.

SEM Analysis

The morphological structures of the GC membranes (i.e., top-surface and cross-section) are captured from scanning electron microscopy (SEM) (FESEM JSM-7600F) at different magnifications.

FT-IR and XRD Analysis

The chemical and crystalline characterization of the GC membranes are analyzed by a Fourier-transform infrared (FT-IR) spectrometer and an X-ray diffraction (XRD). FT-IR spectroscopy is measured in the $4000-500$ cm^{-1} wavenumber region by an FT-IR spectrometer with the KBr method (Nicolet 380 spectrometer). Wide-angle XRD analysis is performed in the 2θ range of $5-70^\circ$ via an X-ray diffractometer (D8 ADVANCE, Bruker Corporation).

Thermal Gravimetric Analysis

Thermal gravimetric analysis (TGA) is conducted on a Seiko Exstar6000 instrument with a temperature range of $30-700$ $^\circ\text{C}$ at a heating rate of 10 $^\circ\text{C}\cdot\text{min}^{-1}$ for the samples.

Contact Angle Measurement

In order to determine the hydrophilic properties of the GC membranes, a drop technique is applied to investigate the water contact angle [SEO Phoenix MT(M)] by using a distilled water drop (volume = 5 μL). The contact angle values are calculated by analyzing the captured drop images based on the ImageJ® program.

Tensile Analysis

The strength and strain of the tensile test (original size of membrane = 1 cm x 5 cm) are carried out by a universal tensile machine (UTM model 5565, UK) with 250 N of load cell and 10 $\text{mm}\cdot\text{min}^{-1}$ of pulling rate. Prior to the tensile test, the membranes are stored for more than one day at room temperature.

RESULTS AND DISCUSSION

Characterization of GC Membranes

As known, several researchers (30-32) have used acetic acid solvent, which is known as a common solvent to dissolve the CTS molecules; however, the odor nature of this solvent is seen as a disadvantage to be utilized in the fabrication of GC membrane. Thus, the lactic acid solvent is chosen to replace acetic acid in this study as well as to overcome this disadvantage.

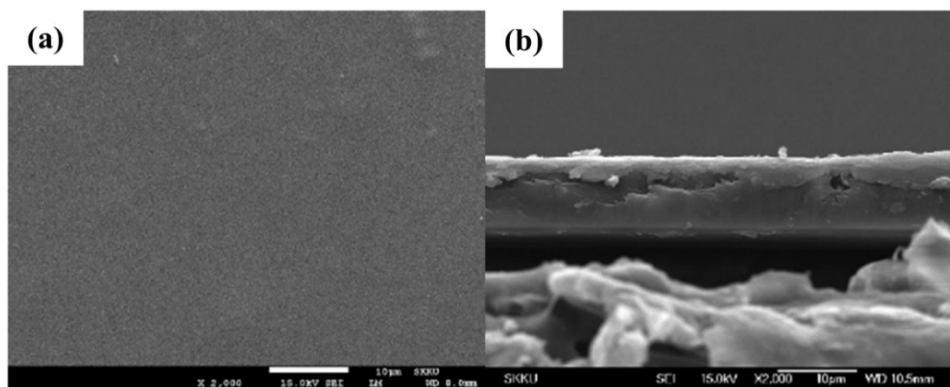


Figure 2: SEM images of top-surface (a) and cross-section (b) of GC_5/5 membrane.

For a hydrogel membrane, the morphological structure is also concerned to be one of the significant factors to evaluate its performance corresponding to the aim study (2). In this study, the morphological structure of GC membranes is detected by SEM images (Figure 2), indicating that the top-surface (Figure 2a) and cross-section (Figure 2b) morphologies of the GC_5/5 membrane are relative smooth surface and non-rough without

the pores. Thereby, this smooth morphology is owing to the GC hydrogel formation in the membrane, manifesting that the CTS and GEL molecules are well dispersed in the molecular level, as well as the homogeneous characterization of this GC mixture. As such, the smooth surface and homogeneous feature of the GC hydrogel membrane are truly useful in the field of wound dressing or tissue engineering applications.

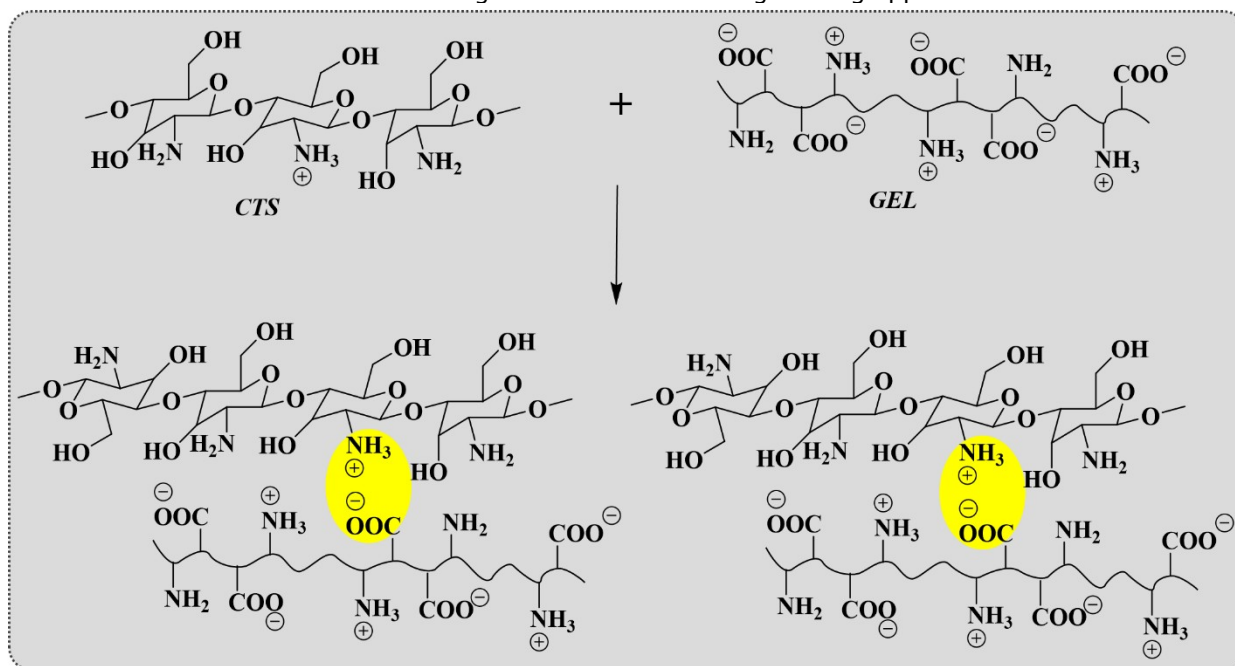


Figure 3: Ion exchange in lactic acid solvent and possible reaction mechanism between CTS and GEL.

Figure 3 indicates that in the GEL/CTS spectrum, the C=O groups of GEL absorbed with the N-H groups of CTS resulting in strong hydrogel bonds, leading to a far more miscible GEL/CTS component. To further understand the chemical characterization of the membrane, FT-IR spectra of CTS, GEL, and GC membrane are shown in Figure 4a. The peaks at 3500-3000 cm^{-1} can belong to the O-H and N-H stretching of CTS, and the peak at 1560 cm^{-1} regards to the C-N deformation vibration (amide II) of CTS (33, 34). The peaks at the amide I (C=O) band (1645 cm^{-1}) and the amide II band are very

weak that can be due to the higher deacetylation degree of CTS (33, 34). For GEL spectra, the N-H bending vibrations of the amide I, II, and III bands can be observed at 1655 cm^{-1} , 1510 cm^{-1} , and 1324 cm^{-1} , respectively (35). Moreover, the vibrational peak of the GC membrane relating to amino groups at 1560 cm^{-1} has disappeared after GEL/CTS polymerization, while prominent peaks at 1650 cm^{-1} are observed clearly in the GC membrane spectra. Thereby, these are probably explained as based on the amidation reaction between carboxyl and amino occurring in CTS and GEL mixture (Figure 3).

Besides, the peaks at 3500–3000 cm^{-1} have also become broader in the GC membrane spectra regarding their hydrogen bonding interaction occurred in that GC hydrogel mixture. At the same time, the shifted peaks of C=O and C–O–C are observed from 1645 cm^{-1} to 1539 cm^{-1} , and from 1068 cm^{-1} to 1058 cm^{-1} in the GC membrane spectra, respectively. Thereby, the chemical interactions of GEL and CTS molecules have happened in this hydrogel mixture, similarly to the above-mentioned SEM analysis. In addition, Figure 4b manifests the XRD pattern of the CTS, GEL, and GC membrane. These show that the primary

diffraction peaks are observed at $\sim 20^\circ$ in their XRD patterns, suggesting good interaction and compatibility between GEL and CTS in the hydrogel membrane. Concomitantly, the peak intensity ratio of GC membrane is reduced with a supplement of GEL component into the mixture, resulting in a decrease in CTS crystallinity probably because of the incorporation of the amorphous nature of GEL into this mixture. Besides, a small reduction in the GC membrane crystallinity can be due to the hydrogen bonding interactions between the GEL and CTS molecules in the mixture regarding their good compatibility (36, 37).

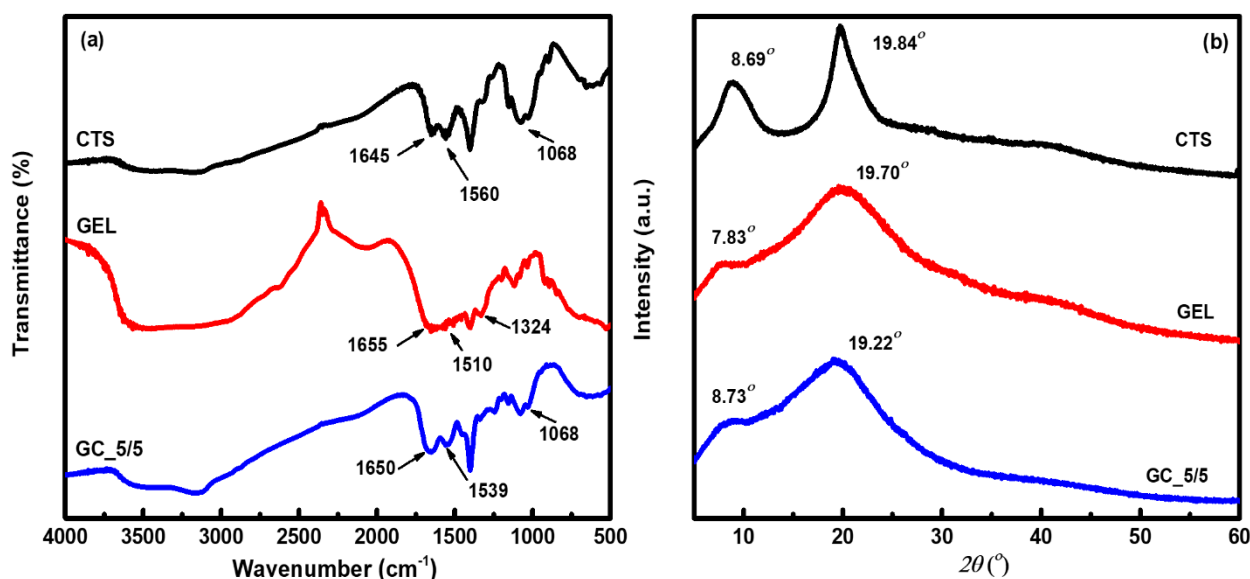


Figure 4: FTIR (a) and XRD (b) spectra of CTS, GEL, and GC_5/5 membrane.

Furthermore, the thermal property of a material is also concerned as a significant factor to be investigated in this study. In Figure 5, it illustrates the thermograms of CTS, GEL, and GC membrane. Their loss of initial weight at $\sim 50^\circ\text{C}$ is attributed to their loss of moisture in all samples. In addition, the CTS curve shows lower thermal stability than that of the GC membrane. Specifically, the second degradation of the CTS curve is observed at 295°C , while that of the GC membrane is at 319°C . Thereby, it probably relates to incorporating the amorphous nature of GEL into the mixture, as well as the GEL degrades faster than the GC membranes. Besides, the DTG peaks of the GC

membrane are similar to CTS peaks, while those of GEL are not similar to the GC membrane (Figure 5b) that can be due to the difference in crystal structure and hydrogen bonding network between GEL and CTS. Also, it indicates that the as-prepared membranes with CTS and GEL are well dispersed at the molecular level. As a result, combining these materials to form a hydrogel membrane is stable more in thermal property compared with pure materials. Overall, there are good interactions and compatibility between the GEL and CTS molecules in this hydrogel mixture through the aforementioned analyses.

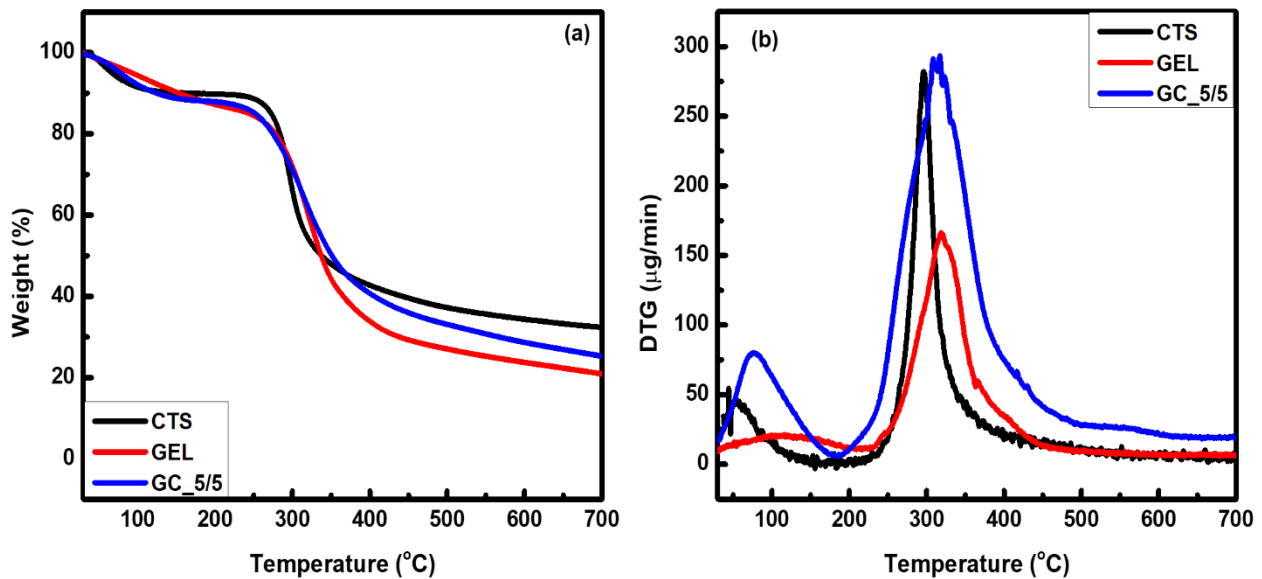


Figure 5: TGA (a) and DTG (b) curves of CTS, GEL, and GC_5/5 membrane.

Mechanical Property of GC Membranes

In addition to the above-suggested chemical, crystalline and thermal characterizations, a material's mechanical property is also seen as a rather important factor in this study. Actually, the hydrogel membranes reach lots of advantages, e.g., soft elastic property and promote the healed wound without any damage (17). Herein, the prepared GC membranes are used to directly investigate their mechanical property based on the values of stress at break and strain at break through the tensile test (Figure 6). It is obvious that the values of stress at break of the GC membranes are high with the decrease of weight ratio of GEL/CTS; it is the opposite for those of strain at break. Specifically, the GC_2/8 membrane has the highest stress and lowest strain values; on the other hand, those values are opposite for the GC_8/2 membrane. Additionally, the GC_5/5 membrane shows a higher value of stress at break comparing to the GC_6/4 and GC_8/2 membranes (i.e., the stress value range from GC_5/5 to GC_6/4 membranes: 0.26 MPa; the stress value range from GC_5/5 to GC_8/2 membranes: 0.62 MPa); on the other hand, the stress value range of GC_5/5 membrane is lower

little comparing to the GC_4/6 and GC_2/8 membranes (i.e., the stress value range from GC_5/5 to GC_4/6 membranes: 0.10 MPa; the stress value range from GC_5/5 to GC_2/8 membranes: 0.30 MPa). Furthermore, the GC_5/5 membrane shows a lower strain value compared to the GC_6/4 and GC_8/2 membranes (i.e., the strain value range from GC_5/5 to GC_6/4 membranes: 0.37%; the strain value range from GC_5/5 to GC_8/2 membranes: 0.81%), while the strain range of GC_5/5 membrane is higher little comparing to the GC_4/6 and GC_2/8 membranes (i.e., the strain value range from GC_5/5 to GC_4/6 membranes: 0.14%; the strain value range from GC_5/5 to GC_2/8 membranes: 0.26%). It indicates that the prepared GC membranes with various weight ratios of GEL/CTS are flexible and reach different stress and strain values. Besides, physical strength is seen as an important factor in biomedical applications. These show that the as-prepared GC membranes can be truly useful in the applications of biomedical fields, at same time that the GC_5/5 membrane can be selected as a promising membrane to apply in the fields of wound dressing or tissue-engineering applications.

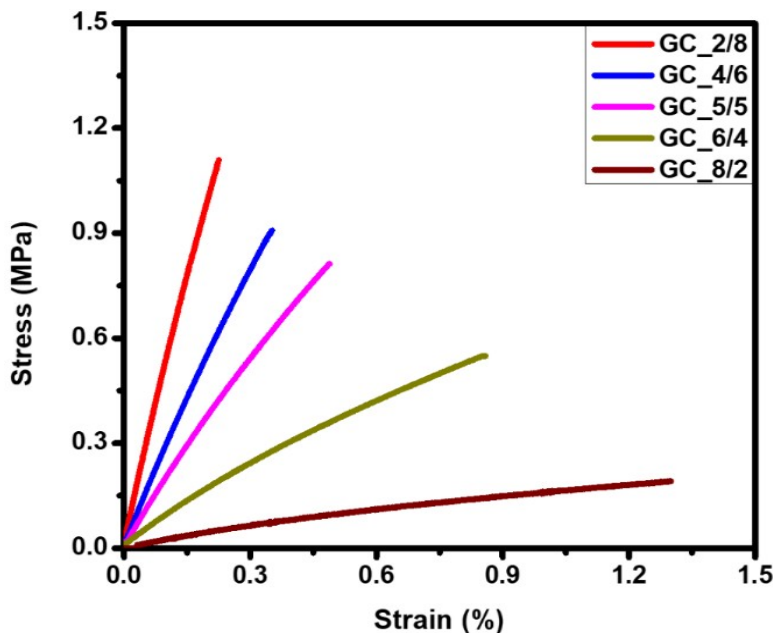


Figure 6: Stress-strain curves of the as-prepared GC membranes.

Hydrophilic Property of GC Membranes

As known, the hydrogel membranes reach lots of advantages, e.g., high water content, boost granulation, and epithelialization due to the moist environment (16). At the same time, the wettability and hydrophilic properties of a solid surface based on a liquid can be predicted from the use of contact angle. Herein, the hydrophilic property of the as-prepared GC membrane surface is also investigated through the water contact angle method. Specifically, the picture of a water droplet on the

CTS surface is captured and shown in Figure 7a, resulting in that its water contact angle is obtained at 119.6°, as well as the hydrophobic nature of the CTS surface. On the other hand, the water contact angle of the as-prepared GC membrane surface significantly decreases with the increase of the GEL/CTS weight ratio (i.e., from 68.0° to 32.3°) (Figure 7b-f) (38). These results further support the swelling test of the as-prepared GC membranes as well.

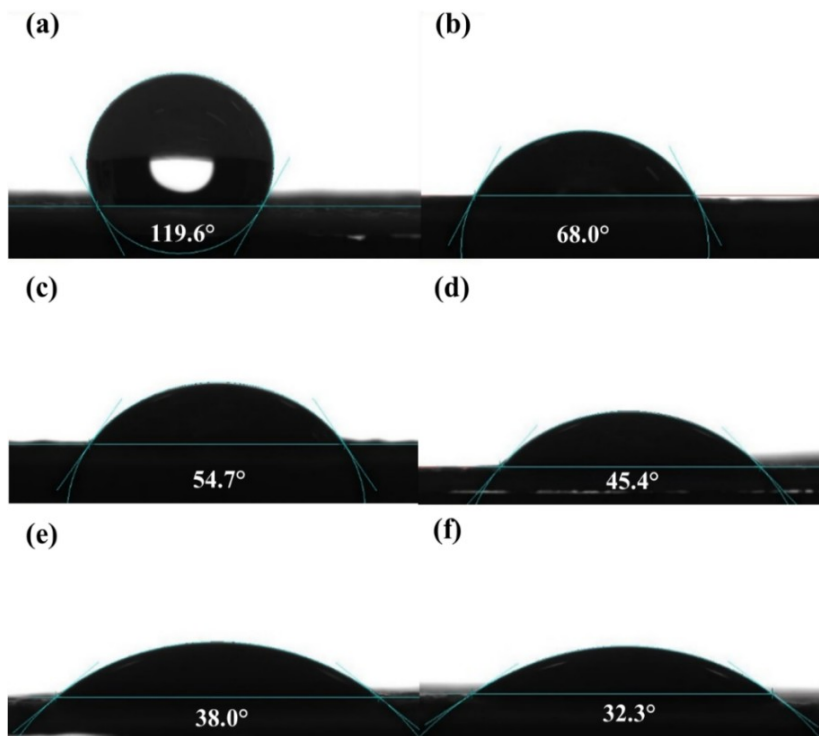


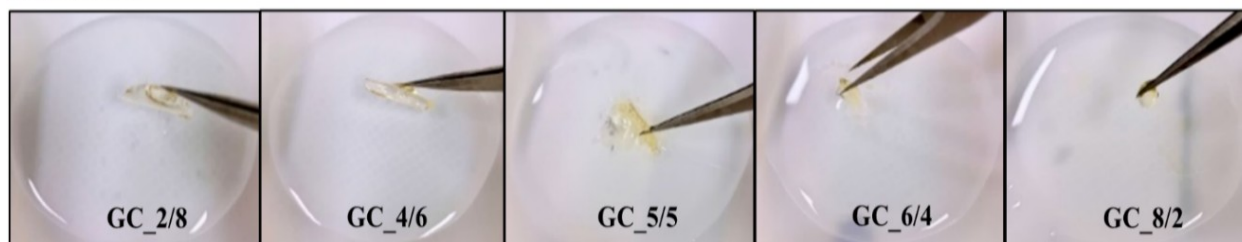
Figure 7: Contact angles of CTS (a), GC (b – f) membranes: GC_2/8; GC_4/6; GC_5/5; GC_6/4 and GC_8/2, respectively.

Swelling Property of GC Membranes

Basically, the hydrogel membranes significantly swell in an aqueous medium that can be mainly due to their interacted networks, meaning they do not disintegrate in water at physiological pH and temperature (15). In addition to the above-mentioned hydrophilic properties, the swelling property of the as-prepared GC membranes is conducted by immersing into distilled water at different times (i.e., 5 – 60 min, r.t). For visual observation of the swelling studies (Figure 8), after

30 and 60 min immersing, GC_8/2 and GC_6/4 membranes are almost soluble into the aqueous solution, in contrast for GC_5/5; GC_4/6, and GC_2/8 membranes. These show that the GC membranes can maintain stable swelling ability with a low weight ratio of GEL/CTS, which involves stronger intermolecular hydrogen bonds among the GC membranes. At the same time, these results are similar to the above-mentioned hydrophilic property of the membranes as well.

After 30 min



After 60 min

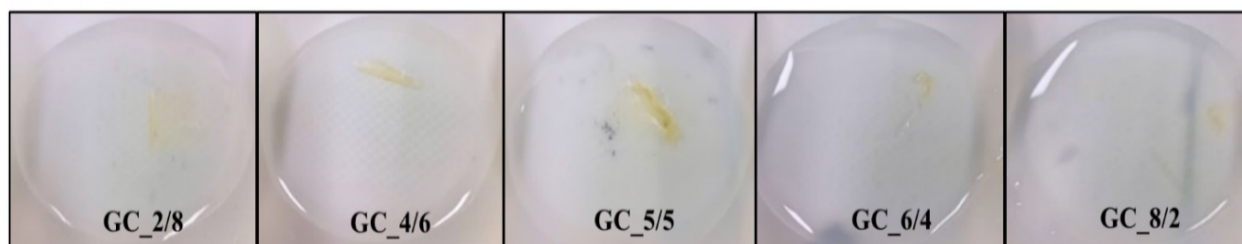


Figure 8: Swelling of all GC membranes after different immersing times.

Besides, each membrane's swelling rate at various immersing times is also concerned to be further investigated, as shown in Figure 9. Specifically, the swelling property of the GC membranes increases with the weight ratio of GEL/CTS within 5 – 60 min of immersing and sealing time period (i.e.: 51.6 – 211.3% / GC_2/8 membrane; 87.7 – 248.3% / GC_4/6 membrane; 107.3 – 270.4% / GC_5/5 membrane; 148.2 – 390.9% / GC_6/4 membrane; and 134.0 – 438.2% / GC_8/2 membrane). The main reason is that the addition of GEL can cause the hydrogel membrane structure to become looser, and the molecular chains in the system is more easily extended (39). Besides, the swelling rate range of each hydrogel membrane has significantly raised from 5 to 60 min of immersing and sealing time period (i.e.: 159.7% / GC_2/8 membrane; 160.6% / GC_4/6 membrane; 163.1% / GC_5/5 membrane; 242.7% / GC_6/4 membrane; and 304.2% / GC_8/2 membrane). The results suggest that the swelling property of each membrane increases rapidly from 5 to 60 min. However, it slows down gradually after 45 min, indicating that the swelling equilibrium of each membrane reaches at 45 min. In general, the GC membranes manifest a good swelling behavior since the incorporation of GEL molecule, which is one of the common hydrophilic polymers. Concomitantly, the water-

absorbing capacity of the hydrogel membranes is higher than their own weight. Additionally, the GC_5/5 membrane shows lower much swelling rate comparing to the GC_6/4 and GC_8/2 membranes (i.e.: the swelling rate range from GC_5/5 to GC_6/4 membranes: 41.0% / 5 min, 84.9% / 10 min, 105.9% / 30 min, 110.2% / 45 min and 120.5% / 60 min; the swelling rate range from GC_5/5 to GC_8/2 membranes: 26.7% / 5 min, 120.2% / 10 min, 149.9% / 30 min, 69.8% / 45 min and 167.8% / 60 min); on the other hand, the swelling rate range of GC_5/5 membrane is higher little comparing to the GC_4/6 and GC_2/8 membranes (i.e.: the swelling rate range from GC_5/5 to GC_4/6 membranes: 19.6% / 5 min, 22.7% / 10 min, 17.1% / 30 min, 22.3% / 45 min and 22.1% / 60 min; the swelling rate range from GC_5/5 to GC_2/8 membranes: 55.7% / 5 min, 58.8% / 10 min, 40.1% / 30 min, 46.8% / 45 min and 59.2% / 60 min). As a result, the GC membranes can maintain stable swelling ability with a low weight ratio of GEL/CTS, which involve to stronger intermolecular hydrogen bonds among the GC membranes. At the same time, the GC_5/5 membrane is chosen as a stable membrane to can apply for wound dressing or tissue-engineering applications.

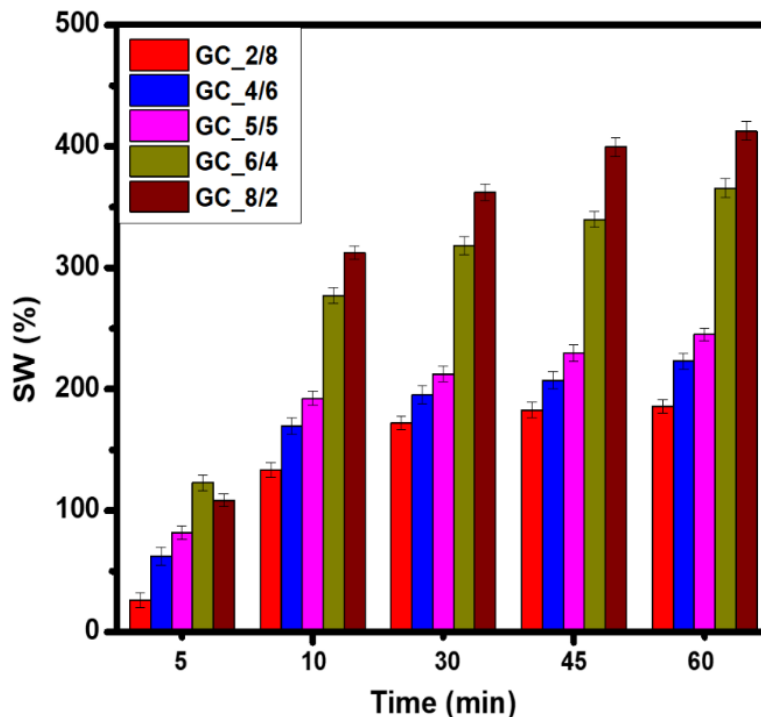


Figure 9: Swelling behavior of all GC membranes at room temperature.

CONCLUSION

In summary, GC membranes with various weight ratios of GEL/CTS have been successfully prepared by a simple in-situ method. The surface morphology of the as-prepared GC membranes, is found to be very smooth and homogeneous. For chemical and crystalline characterization of the as-prepared GC membranes, indicating that the incorporation of GEL in the membrane has decreased the crystallinity of CTS as well as appearing interaction between these molecules based on FT-IR and XRD studies. Besides, combining these natural polymer sources to form a hydrogel membrane is more stable in thermal property than pure materials. In addition to the above-mentioned characterizations, the hydrophilic property of GC membranes is investigated through contact angle measurements, resulting in their contact angle values significantly decrease with the increase of weight ratio of GEL/CTS (i.e., from 68.0° to 32.3°). For the mechanical property of the GC membranes, the values of stress at break are high with the decrease of weight ratio of GEL/CTS, but it is the opposite for the values of strain at break. At the same time, the prepared GC membranes with various weight ratios of GEL/CTS are flexible and reach different stress and strain values. Moreover, the swelling equilibrium of each membrane has reached at 45 min, as well as the GC membranes can maintain a stability in the swelling ability according to the low weight ratio of GEL/CTS, which involves to both the stronger intermolecular hydrogen bonds among the hydrogel membranes and the addition of GEL in the hydrogel membranes. These results suggest that the GC membrane can

become a promising material (i.e., special for GC_5/5 membrane) in the field of wound dressing or tissue-engineering applications, at same time that the incorporation of GEL and CTS molecules is also considered as a nontoxic hydrogel membrane, owing to natural polymer sources.

REFERENCES

1. Vo TS, Vo TTBC, Suk JW, Kim K. Recycling performance of graphene oxide-chitosan hybrid hydrogels for removal of cationic and anionic dyes. *Nano Convergence*. 2020;7, 4:1-11. <DOI>.
2. Vo TS, Hossain MM, Jeong HM, Kim K. Heavy metal removal applications using adsorptive membranes. *Nano Convergence*. 2020;7, 36:2-26. <DOI>.
3. Vo TS, Vo TTBC. Preparation and Characterization of Bis-Propargyl-Succinate, and its Application in Preliminary Healing Ability of Crosslinked Polyurethane using "Azide-Alkyne" Click. *Journal of Engineering Science and Technology Review*. 2020;13(4):110-6. <DOI>.
4. Vo TS, Vo TTBC, Tien TT, Singh NT. Enhancement of mechanical property of modified polyurethane with bis-butyl succinate. *Journal of the Turkish Chemical Society Section A: Chemistry*. 2021;8(2):519-26. DOI: <DOI>.
5. Vo TS, Vo TTBC. A Self-Healing Material Based on Microcapsules of Poly(Urea-Formaldehyde)/Bis-

- Propargyl-Succinate Containing in Polyurethane Matrix. *Journal of the Turkish Chemical Society Section A: Chemistry*. 2021;8(3):787–802. <DOI>.
6. Velmurugan N, Kumar GG, Han SS, Nahm KS, Lee YS. Synthesis and Characterization of Potential Fungicidal Silver Nano-Sized Particles and Chitosan Membrane Containing Silver Particles. *Iranian Polymer Journal*. 2009;18(5 (107)):383–92.
7. Ti Feng J, Zhou J, Zhou J, Gao L, Xing Y, XuHui L. Synthesis and Characterization of Chitosan-based Schiff Base Compounds with Aromatic Substituent Groups. *Iranian Polymer Journal*. 2011;20(2):123–36.
8. KSV Krishna R, K Madhusudana R, Kumar PN, Il-Doo C. Novel Chitosan-based pH Sensitive Micro-networks for the Controlled Release of 5-Fluorouracil. *Iranian Polymer Journal*. 2010;19(4):265–76.
9. Gbenezbor OP, Adeosun SO, Lawal GI, Jun S, Olaleye SA. Acetylation, Crystalline and Morphological Properties of Structural Polysaccharide from Shrimp Exoskeleton. *Engineering Science and Technology, an International Journal*. 2017;20(3):1155–65. <DOI>.
10. Peng Z, Li Z, Shen Y. Influence of Chemical Cross-Linking on Properties of Gelatin/Chitosan Microspheres. *Polymer-Plastics Technology and Engineering*. 2012;51(4):381–5. <DOI>.
11. Zamani A, Taherzadeh MJ. Effects of Partial Dehydration and Freezing Temperature on the Morphology and Water Binding Capacity of Carboxymethyl Chitosan-Based Superabsorbents. *Industrial & Engineering Chemistry Research*. 2010;49(17):8094–9. <DOI>.
12. Adair A, Kaesaman A, Klinpituksa P. Superabsorbent materials derived from hydroxyethyl cellulose and bentonite: Preparation, characterization and swelling capacities. *Polymer Testing*. 2017;64:321–9. <DOI>.
13. Olad A, Pourkhiyabi M, Gharekhani H, Doustdar F. Semi-IPN superabsorbent nanocomposite based on sodium alginate and montmorillonite: Reaction parameters and swelling characteristics. *Carbohydrate Polymers*. 2018;190:295–306. <DOI>.
14. Rop K, Mbui D, Njomo N, Karuku GN, Michira I, Ajayi RF. Biodegradable water hyacinth cellulose-graft-poly(ammonium acrylate-co-acrylic acid) polymer hydrogel for potential agricultural application. *Heliyon*. 2019;5(3):e01416. <DOI>.
15. Pal K, Banthia AK, Majumdar DK. Preparation and characterization of polyvinyl alcohol-gelatin hydrogel membranes for biomedical applications. *AAPS PharmSciTech*. 2007;8(1):E1–5. <DOI>.
16. Fan L, Yang H, Yang J, Peng M, Hu J. Preparation and characterization of chitosan/gelatin/PVA hydrogel for wound dressings. *Carbohydrate Polymers*. 2016;146:427–34. <DOI>.
17. Gonzalez JS, Maiolo AS, Hoppe CE, Alvarez VA. Composite Gels Based on Poly (Vinyl alcohol) for Biomedical Uses. *Procedia Materials Science*. 2012;1:483–90. <DOI>.
18. Dragan ES. Design and applications of interpenetrating polymer network hydrogels. A review. *Chemical Engineering Journal*. 2014;243:572–90. <DOI>.
19. Tokura S, Ueno K, Miyazaki S, Nishi N. Molecular Weight Dependent Antimicrobial Activity by Chitosan. In: *New Macromolecular Architecture and Functions*. Berlin, Heidelberg: Springer Berlin Heidelberg; 1996. p. 199–207. <DOI>.
20. Ceylan S, Alatepeli B. Evaluation of PVA/Chitosan Cryogels as Potential Tissue Engineering Scaffolds; Synthesis, cytotoxicity and genotoxicity investigations. *Journal of the Turkish Chemical Society Section A: Chemistry*. 2020;8(1):69–78. <DOI>.
21. Dwivedi A, Bharti P, Shukla S. Surface assimilation and corrosion inhibition characteristic of water soluble Polyvinyl Alcohol on mild steel surface in 0.5M HCl solution. *Journal of the Turkish Chemical Society Section A: Chemistry*. 2021;8(1):217–28. <DOI>.
22. Okuyama K, Noguchi K, Miyazawa T, Yui T, Ogawa K. Molecular and Crystal Structure of Hydrated Chitosan. *Macromolecules*. 1997;30(19):5849–55. <DOI>.
23. Jayakumar R, Prabakaran M, Reis RL, Mano JF. Graft copolymerized chitosan—present status and applications. *Carbohydrate Polymers*. 2005;62(2):142–58. <DOI>.
24. Jayakumar R, Reis RL, Mano JF. Chemistry and Applications of Phosphorylated Chitin and Chitosan. *E-Polymers*. 2006;6(1):1–16. <DOI>.
25. Jayakumar R, Reis RL, Mano JF. Synthesis and Characterization of N -methylenephenyl Phosphonic Chitosan. *Journal of Macromolecular Science, Part A*. 2007;44(3):271–5. <DOI>.
26. Kołodziejaska I, Piotrowska B, Bulge M, Tylingo R. Effect of transglutaminase and 1-ethyl-3-(3-dimethylaminopropyl) carbodiimide on the solubility

- of fish gelatin–chitosan films. *Carbohydrate Polymers*. 2006;65(4):404–9. <DOI>.
27. Sendemir-Urkmez A, Jamison RD. The addition of biphasic calcium phosphate to porous chitosan scaffolds enhances bone tissue development in vitro. *Journal of Biomedical Materials Research Part A*. 2007;81A(3):624–33. <DOI>.
28. Arvanitoyannis IS, Nakayama A, Aiba S. Chitosan and gelatin based edible films: state diagrams, mechanical and permeation properties. *Carbohydrate Polymers*. 1998;37(4):371–82. <DOI>.
29. Achet D, He XW. Determination of the renaturation level in gelatin films. *Polymer*. 1995;36(4):787–91. <DOI>.
30. Fan M, Hu Q, Shen K. Preparation and structure of chitosan soluble in wide pH range. *Carbohydrate Polymers*. 2009;78(1):66–71. <DOI>.
31. Lu S, Song X, Cao D, Chen Y, Yao K. Preparation of water-soluble chitosan. *Journal of Applied Polymer Science*. 2004;91(6):3497–503. <DOI>.
32. Qin C, Li H, XIAO Q, Liu Y, Zhu J, Du Y. Water-solubility of chitosan and its antimicrobial activity. *Carbohydrate Polymers*. 2006;63(3):367–74. <DOI>.
33. Borzacchiello A, Ambrosio L, Netti PA, Nicolais L, Peniche C, Gallardo A, et al. Chitosan-based hydrogels: Synthesis and characterization. *Journal of Materials Science: Materials in Medicine*. 2001;12(10):861–4. <DOI>.
34. Guan YL, Shao L, De Yao K. A study on correlation between water state and swelling kinetics of chitosan-based hydrogels. *Journal of Applied Polymer Science*. 1996;61(13):2325–35. <DOI>.
35. Xiao C, Lu Y, Gao S, Zhang L. Characterization of konjac glucomannan-gelatin blend films. *Journal of Applied Polymer Science*. 2001;79(9):1596–602. <DOI>.
36. Cheng M, Deng J, Yang F, Gong Y, Zhao N, Zhang X. Study on physical properties and nerve cell affinity of composite films from chitosan and gelatin solutions. *Biomaterials*. 2003;24(17):2871–80. <DOI>.
37. Zhai M, Zhao L, Yoshii F, Kume T. Study on antibacterial starch/chitosan blend film formed under the action of irradiation. *Carbohydrate Polymers*. 2004;57(1):83–8. <DOI>.
38. Delmar K, Bianco-Peled H. The dramatic effect of small pH changes on the properties of chitosan hydrogels crosslinked with genipin. *Carbohydrate Polymers*. 2015;127:28–37. <DOI>.
39. Tomić SL, Mičić MM, Dobić SN, Filipović JM, Suljovrujić EH. Smart poly(2-hydroxyethyl methacrylate/itaconic acid) hydrogels for biomedical application. *Radiation Physics and Chemistry*. 2010;79(5):643–9. <DOI>.



Extractive Desulfurization Using Piperidinium Based Ionic Liquids with Lewis Acids

Assim A. Sabah^{1*}  

¹ Department of Science, College of Basic Education, University of Mosul, Mosul, Iraq

Abstract: This work includes the preparation of ionic liquid 1,4-dimethylpiperidinium iodide [MMPip]I and its salts with ferric chloride as Lewis acid in different molar proportions [MMPip]I/nFeCl₃ (n=1,2,3). The prepared compounds were diagnosed by spectroscopic and physical methods such as ¹H-NMR, FT-IR, elemental analysis (CHN) and other techniques. The thermal stability of these compounds was studied to use in the extractive desulfurization process (EDS). The efficiency of these compounds in removing sulfur compounds from the petroleum model was examined using dibenzothiophene (DBT) with a concentration of 1000 ppm dissolved in the solvent of normal hexane. The results showed that the compounds used had an acceptable efficiency of up to 30% despite using medium amounts of the extracted agent relative to the oil model; these compounds have a promising future in extractive sulfur removal processes.

Keywords: Piperidine ionic liquids, desulfurization, thermal study, lewis acid.

Submitted: July 07, 2021. **Accepted:** September 20, 2021.

Cite this: Sabah A. Extractive Desulfurization Using Piperidinium Based Ionic Liquids with Lewis Acids. JOTCSA. 2021;8(4):1057-88.

DOI: <https://doi.org/10.18596/jotcsa.963930>.

***Corresponding author. E-mail:** assimsabah@uomosul.edu.iq.

INTRODUCTION

Desulfurization is one of the chemical processes used to remove sulfur from raw materials in industry or final products. These processes are critical because they provide a large portion of the sulfur used in other fields and other sulfur-free materials to reduce toxic and polluting emissions to the environment, such as SO_x emissions that cause acid rain (1-3). The fuel refining process necessarily requires the removal of sulfur from the oil hardships. The Environmental Protection Agency has imposed global restrictions on the specifications of the fuels used in transportation (EPA)(4). The optimum allowable sulfur content in diesel and gasoline is 15-30 ppm, which was previously 500 ppm in most countries, and is now being reduced to 10 ppm (5). Thus, one of the critical processes in oil refineries is the removal of sulfur from oil. The price of oil production is determined by the sulfur content, which influences the price of crude oil and processing costs (1, 6-8).

Ionic liquids (ILs) with a high distribution coefficient for sulfur compounds, a low cross solubility for hydrocarbons, a low viscosity, and a fast separation phase after mixing and extraction are ideal. Unfortunately, natural ionic fluids perform less efficiently in liquid-liquid extraction for typical sulfur compounds such as dibenzothiophene (DBT). However, ionic liquids have a high distribution coefficient. In mixtures, the distribution coefficient is somewhat low; in other words, liquids are not ideal solvents for extraction desulfurization, especially with heavy oil, and the (EDS) process efficiency is lower. Because oxidizing sulfur compounds have a much higher distribution coefficient, the efficiency of the ionic liquid extraction process increases if organic sulfur compounds have previously been oxidized to sulfoxides and sulfonates (9-11).

Desulfurization by extracting fuel with ionic liquids instead of conventional organic solvents is an exciting alternative to extremely clean diesel oils. The use of different ionic liquids have been

investigated within (EDS) (cations such as imidazolium, pyridinium, quinolinium, and pyrrolidinium, anions such as alkyl sulfate, alkyl phosphate, halogens, ethanoate, and thiocyanate), the treatment carried with (DBT) dissolved in dodecane as a model fuel. The results showed that the extraction efficiency of the cationic ions is in the following order: methylpyridinium \geq pyridinium \approx imidazolium \approx pyrrolidinium. Methylpyridinium cation showed the highest sulfur removal, up to (80%) per batch (12-16).

In practical experiments with the (EDS) process, it was found that ionic liquids containing Lewis acids such as FeCl_3 , AlCl_3 and CuCl gave promising good results for the selective extraction process for aromatic sulfur compounds even when used in thermal conditions of up to 70°C due to their solid presence (17, 18). In the (EDS) process, many ionic liquids mixed with Lewis acids were tested in different molar ratios, for example, the mixture between the ionic liquid (1-n-butyl-3-methylimidazolium $[\text{BMIM}]\text{Cl}$) and with aluminium chloride AlCl_3 as Lewis acid in molar ratios $[\text{BMIM}]\text{Cl} : \text{AlCl}_3$ (0.35:0.65) where the bilayer system was formed with the petroleum model at room temperature. It was also tested in the (EDS) process of real diesel. In the extraction process, the ionic liquids containing Lewis acids showed higher efficiency than their counterparts, non-containing Lewis acids (18, 19). Also, ionic liquids containing ZnCl_2 were tested in the oxidative desulfurization process (ODS), $[\text{BMIM}]\text{Cl} / n\text{ZnCl}_2$ ($n=1,2,3$), using the fuel model with concentrations of 500 ppm and 1000 ppm of (DBT). The results showed that the desulfurization efficiency decreases with the increase in the percentage of ZnCl_2 . These may be attributed to the strong binding of zinc chloride with the cation in ionic liquid; and its lack of participation in the desulfurization process (20). On the contrary, we

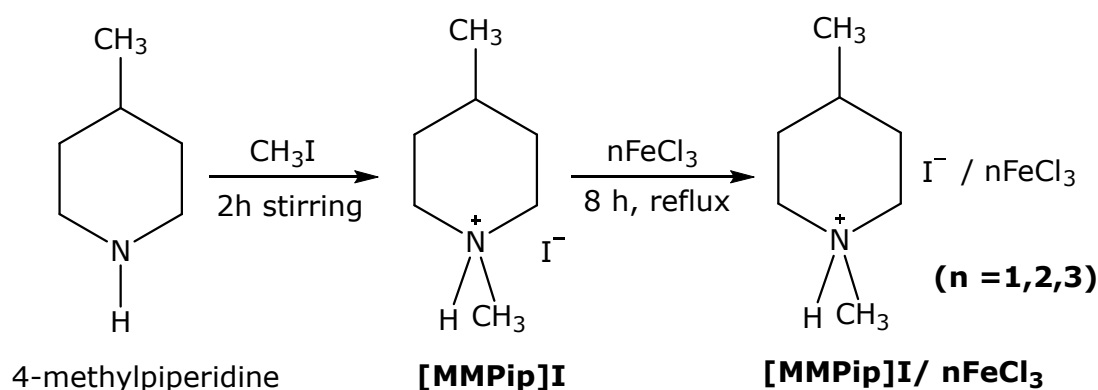
notice the increase in extraction efficiency when using FeCl_3 when increasing the ratio of ferric chloride to ionic liquid $n\text{FeCl}_3 / [\text{BMIM}]\text{Cl}$ ($n=1,2,3$), which is due to the increase in acidity and the closer association of aromatic sulfur compounds with ionic liquids of higher ferric chloride (15, 18). The use of ionic liquid alone or Lewis acid alone did not show high efficiency in the (EDS) process. However, when using the mixing technique between them, the efficiency was higher. Therefore, the process of mixing them is beneficial, as an ionic liquid containing FeCl_3 showed higher efficiency when compared with their counterparts containing AlCl_3 or CuCl under the same experimental conditions (15, 21).

MATERIALS AND METHODS

All chemicals are of high purity and from certified international companies and used without any additional treatment.

Preparation of ionic liquids systems

The ionic liquids (molten salts) were prepared as mentioned in the literature (22-26), the ionic liquid 1,4-dimethylpiperidinium iodide $[\text{MMPip}]\text{I}$ was prepared through the reaction of 4-methylpiperidine dissolved in absolute ethanol with the gradual addition of methyl iodide with continuous stirring for two hours with cooling, the reaction is exothermic. At the end of the reaction, evaporation followed by a rotary evaporator at 80°C concentrated the solution and removed the remaining solvent. After that, the ionic liquid $[\text{MMPip}]\text{I}$ reacted with FeCl_3 in different molar proportions through mixing them with reflux for 4 hours and disposing of the used solvent (absolute ethanol) by rotary evaporator for 4 hours. Scheme 1 shows the preparation of the ionic liquids systems.



Scheme 1: Preparation of ILs systems.

Extractive desulfurization using ILs Systems

1000 ppm of sulfur content has been prepared by dissolving (DBT) in *n*-hexane (as model oil). In the process (EDS), the optimum conditions were determined by treating the prepared ionic liquid

systems to several conditions of temperature, time and concentration of the extracted material. Conical flask 100 mL used in a shaker by adding 10 mL of the (DBT) model oil with a specified concentration of ionic liquid dissolved in 5 mL DMSO, 211DS Shaking

Incubator used to control the operating conditions of the experiment. Analyzing the results of sulfur removal ratio was done by using absorption to create a standard calibration curve and determine the wavelength ($\lambda_{\max} = 285 \text{ nm}$) at the highest absorption intensity, as shown in Figure 5. The percentage of sulfur removed was calculated through the following relationship:

$$S_{\text{removal}} \% = \frac{\text{Conc.}_i - \text{Conc.}_t}{\text{Conc.}_i} \times 100$$

Where Conc._i = initial concentration of sulfur (1000 ppm) represented by concentration of organic sulfur compound (DBT), Conc._t = sulfur concentration at certain time in a specific conditions (DBT) concentration.

Characterization and analysis data

Several physical and spectral methods were used; the $^1\text{H-NMR}$ was investigated by Bruker Avance DPX 400 MHz using DMSO-d_6 as solvent. Trio-1000 equipment was used for mass spectroscopy; the elemental analysis was investigated by Flash EA 1112 Series Thermo Electron Corporation. The FT\IR measured by JASCO Canvas 4200, Avanta 2.02 software for atomic absorption by SensAA GCB scientific equipment system. METTLER Toledo TGA\ DSC used for thermal analysis at 30-950 °C with a ramping heat rate of 10 °C/min under air, STARE evaluation software. The sulfur content was measured by Shimadzu UV-Vis 1800 spectrometer at ($\lambda_{\max} = 285 \text{ nm}$). Table (1) shows some physical properties of prepared compounds.

Table 1: Some physical properties of prepared compounds.

No.	Compound	Conductivity*	m.p. °C	Color
1	[MMPip]I	100	85	Off white
2	[MMPip]I/FeCl ₃	90	70	Brown
3	[MMPip]I/2FeCl ₃	90	68	Dark brown
4	[MMPip]I/3FeCl ₃	90	68	Dark brown

* Conductivity ($\text{ohm}^{-1} \cdot \text{mol}^{-1} \cdot \text{cm}^2$) at (25 °C) and (10^{-3} M) by using water as solvent

RESULTS AND DISCUSSION

Characterization data

The characterization of the cation in the ionic liquids [MMPip]⁺ by $^1\text{H-NMR}$ (DMSO-d_6 , 400 MHz): $\delta 0.9409$ (3H-CH₃, d, $J = 11.52 \text{ Hz}$), $\delta 1.6512$ (5H-CH₂CH₂, m), $\delta 2.7547$ (3H-CH₃, s), $\delta 3.0718$ (4H-2CH₂, m), $\delta 8.2942$ (1H-NH, br).

[MMPip]I (**1**) Anal. Calcd. for $\text{C}_7\text{H}_{16}\text{IN}$: C, 34.87; H, 6.69; N, 5.81. Found: C, 35.89; H, 6.84; N, 5.61.

[MMPip]I/FeCl₃ (**2**) Anal. Calcd. for $\text{C}_7\text{H}_{16}\text{Cl}_3\text{FeIN}$: C, 20.85; H, 4.00; Cl, 26.37; Fe, 13.85; N, 3.47.

Found: C, 19.25; H, 3.76; Cl, 27.66; Fe, 14.65; N, 3.22.

[MMPip]I/2FeCl₃ (**3**) Anal. Calcd. for $\text{C}_7\text{H}_{16}\text{Cl}_6\text{Fe}_2\text{IN}$: C, 14.87; H, 2.85; Cl, 37.61; Fe, 19.75; N, 2.48. Found: C, 13.05; H, 2.66; Cl, 39.05; Fe, 21.55; N, 2.22.

[MMPip]I/3FeCl₃ (**4**) Anal. Calcd. for $\text{C}_7\text{H}_{16}\text{Cl}_9\text{Fe}_3\text{IN}$: C, 11.55; H, 2.22; Cl, 43.84; Fe, 23.02; N, 1.92. Found: C, 9.75; H, 1.98; Cl, 42.76; Fe, 24.25; N, 1.75. Figure 1 shows the $^1\text{H-NMR}$ of [MMPip]I (**1**).

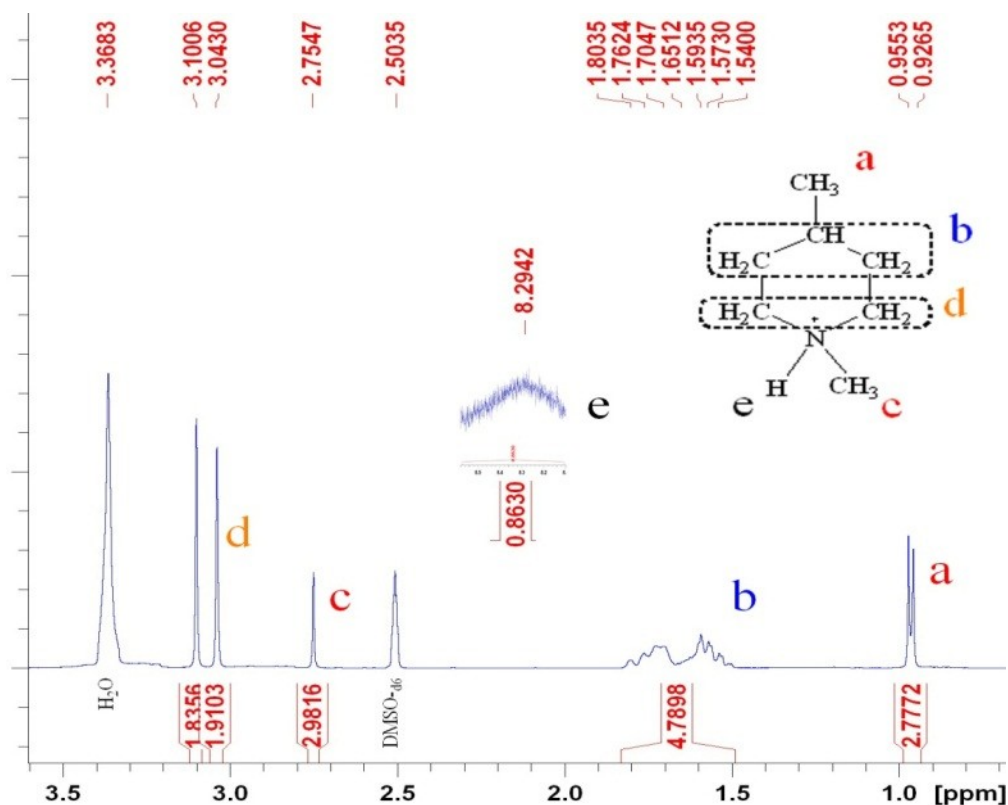


Figure 1: The $^1\text{H-NMR}$ of [MMPip]I (1) (400 MHz, DMSO-d_6).

The infrared spectrum measured the ionic liquid (organic salt) and the ionic liquid mixture with FeCl_3 . The results showed that the presence of Lewis acid makes slight displacements of some bands, and it may change the band's intensity (26-28). For example, a band appeared at 975 cm^{-1} due to the in-plane bending frequency of the (C-H) group and is shifted to a lower position when ferric chloride is

present (20, 29). The bands observed at 1072 cm^{-1} , 1454 cm^{-1} belong to (C-N str. or C-C str.) and (C-H, scissoring bending) respectively (20, 30). The other bands investigated are 2472 cm^{-1} ($\text{N}^+\text{-CH}_3$ str.), 2734 cm^{-1} ($\text{N}^+\text{-H}$ str.), 2954 cm^{-1} (C-H symmetric str.). Figure 2 shows the IR spectra of ILs systems (20).

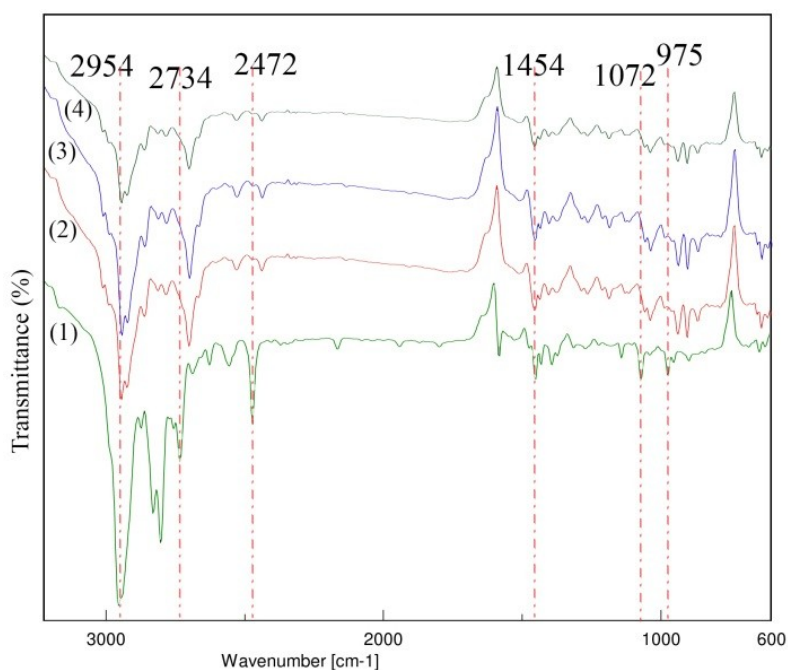


Figure 2: IR spectra of the IL systems: (1) [MMPip]I; (2) [MMPip]I/ FeCl_3 ; (3) [MMPip]I/ 2FeCl_3 ; (4) [MMPip]I/ 3FeCl_3 .

Thermal study data

The thermal stability of [MMPip]I and its mixtures with ferric chloride was studied. A noticeable decrease in the melting point of compounds containing ferric chloride was revealed. The study was under thermal conditions (30-950 °C) and a temperature rampage rate (15 °C/min). The results showed that the ionic liquid [MMPip]I is stable at temperatures up to 250 °C; as shown in Figure 3, the thermal degradation process occurs in one main

stage (21, 31, 32). Although the presence of ferric chloride increases the presence of moisture water in the compound, as the results showed, the moisture water loses by cycling to 110 °C. Thus, the [MMPip]I/nFeCl₃ compounds have two main stages of thermal degradation. However, all mixes are relatively stable at the temperature of experimental conditions of the process (EDS). Figure 4 shows the thermal gravimetric analysis of the compounds.

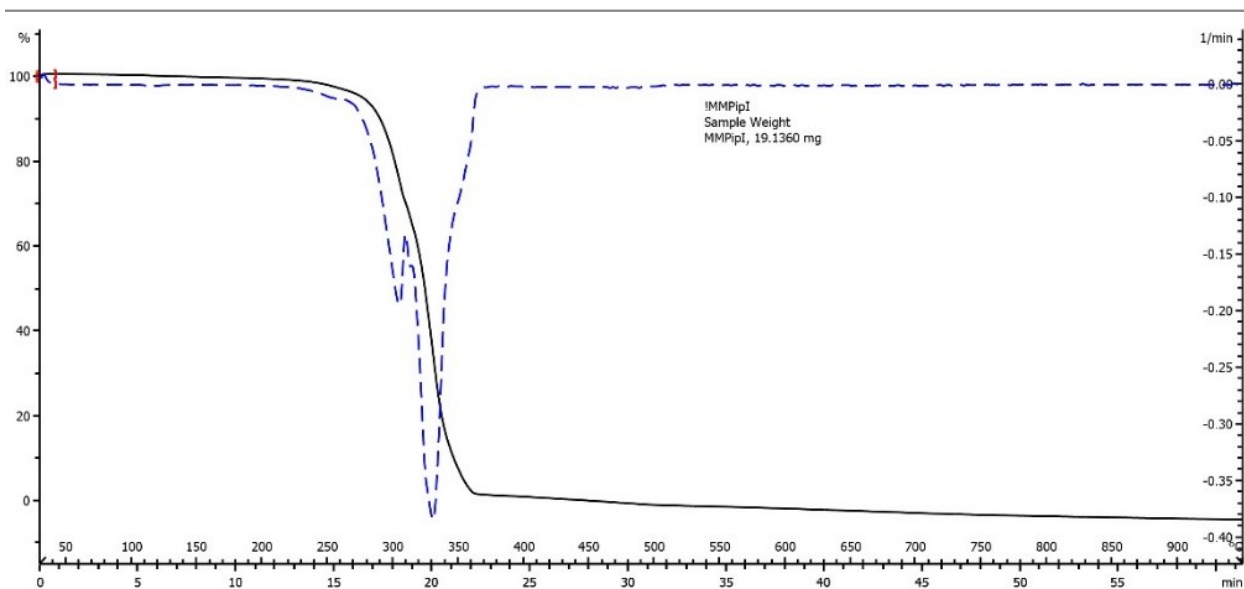


Figure 3: TGA and DTA of [MMPip]I.

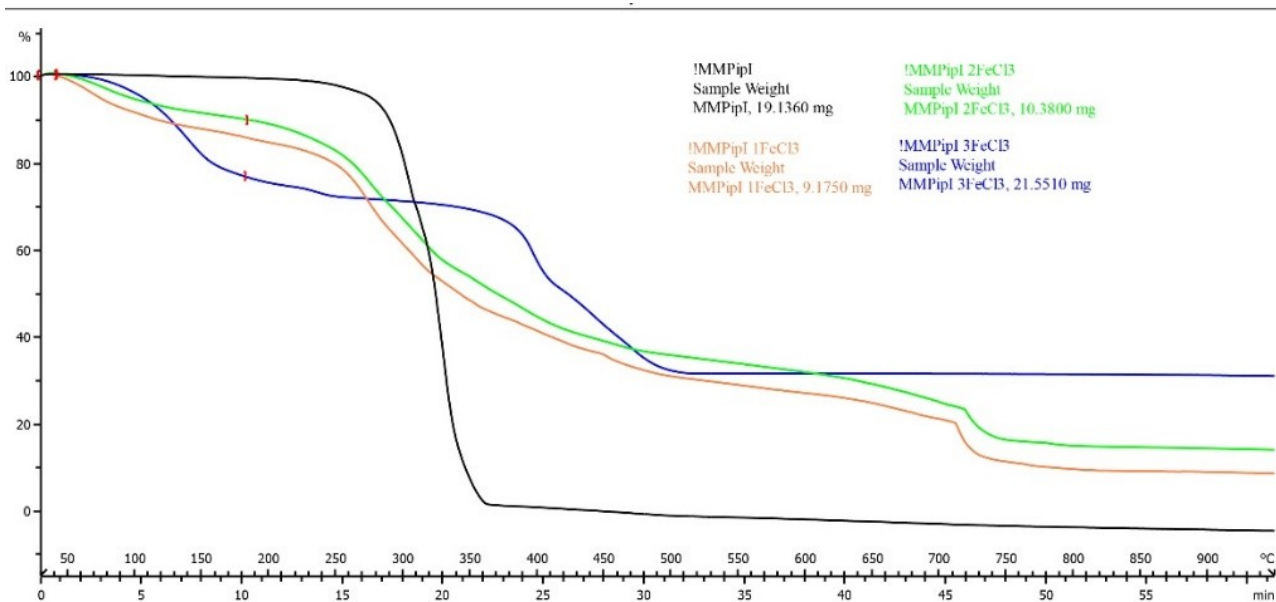


Figure 4: TGA analysis of [MMPip]I and its FeCl₃ mixtures.

Data for desulfurization analysis

Completing the standard curve by measuring the compound (DBT) absorbance for several standard

concentrations (250, 500, 750, and 1000 ppm), as shown in Figure 5.

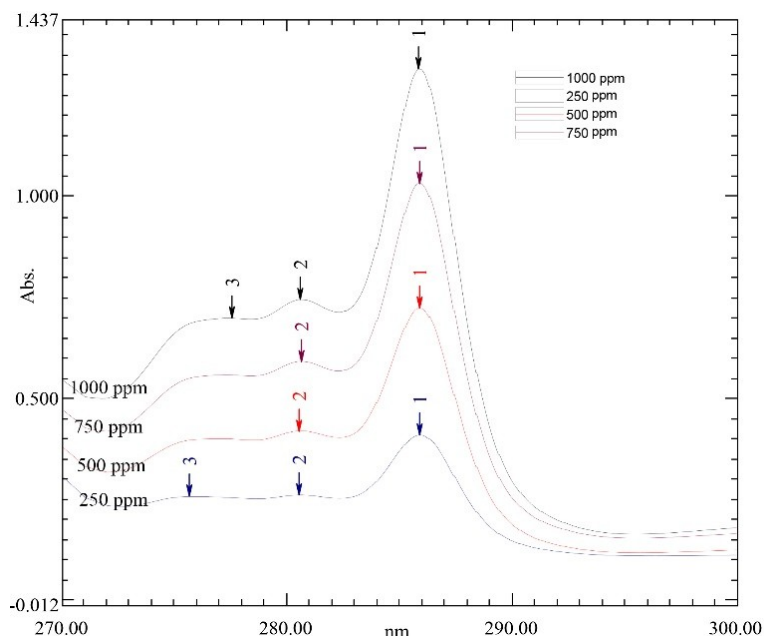


Figure 5: DBT absorbance with different concentrations.

The optimum conditions for the (EDS) process were determined by treating the model oil with prepared compounds for extraction at multiple temperatures (15, 30, 45 °C) using a fixed weight of the extracted materials (0.05 g) and 30 minutes. The results showed an increase in the removal efficiency with an increase in temperature. These results have good similarities to the literature (18, 20, 33), noting that there was no significant increase in efficiency when the temperature was increased from 30 °C to 45 °C, and it is preferable to use the laboratory temperature because it is more controllable, as shown in Figure 6. After stabilizing the temperature,

the optimum time was verified under 30 °C and using the weight of the extracted substance (0.05 g). The results showed that the removal process increases with the increase of time, which have slightly different from the literature (20), and there is no significant difference between 60 minutes and 90 minutes, as the equilibrium is almost stable after 60 minutes and as illustrated in Figure 7. Finally, the efficiency was tested using many different weights, as the results showed that with the increase in the amount of extracted material, the extraction efficiency increases Figure 8.

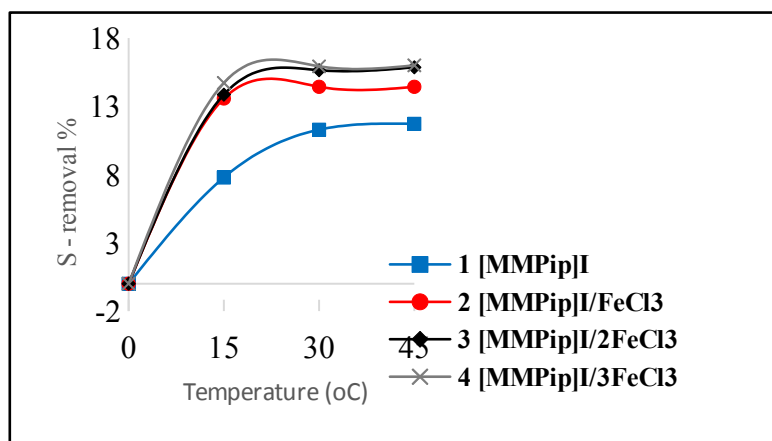


Figure 6: Effect of temperature: extractant used 0.05 g, 30 min.

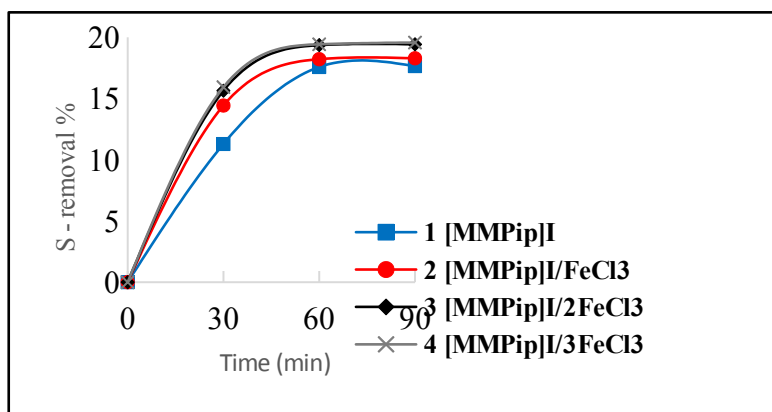


Figure 7: Effect of time: extractant used 0.05 g, 30 °C.

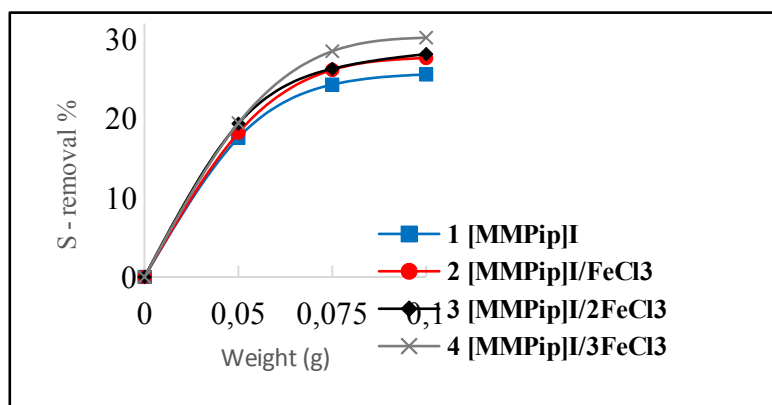


Figure 8: Effect of extractant weight: 60 min, 30 °C.

Through these results, it is noted that the increase in temperature from 30 °C to 45 °C and the increase in the time for the extraction process after 60 minutes does not significantly affect the efficiency of the extraction process, while the increase in the weight of the extracted material (ionic liquid or ionic liquid containing Lewis acid) is more considerable and more clearly. By comparing the results, we find that the highest percentage of sulfur removal is when using 0.1 g of compound (I), which is rather good when compared to efficiency results of up to 100%, but by using high amounts of the extracted substance to the oil model (18, 20). It also noted that the efficiency of the removal ratio increases with the increase in the ratio of ferric chloride to the ionic liquid, which is consistent with the published research (19, 34, 35).

The proposed mechanism for the extraction of organic sulfur compounds is through the interactions between the n electrons of organic sulfur compounds (DBT) with n electrons of the ionic liquid and their interaction with the metallic element in Lewis acid (36, 37). The results showed that ionic liquid mixed with Lewis acid has a higher extraction efficiency than the ionic liquid alone and higher than the use of Lewis acid alone, and the extraction process is more selective for aromatic sulfur compounds (17, 20, 21).

CONCLUSION

The pyridinium base's ionic liquid and salt were prepared with ferric chloride as Lewis acid, and their efficiency was tested in extracting the organic sulfur compounds from the petroleum model. It was found that the best extraction factor among the compounds used is [MMPip]I/3FeCl₃, where the percentage of sulfur removal from the oil model was (30%) under the optimal conditions (10 mL of model oil of 1000 ppm DBT, 0.1 g of extractant, 60 min at 30 °C). Compared with the previous work, these results are considered promising due to the use of acceptable quantities of the extracted agent relative to the quantity of the oil model used. It also noticed that the extraction efficiency increased with the increase in Lewis acid (ferric chloride) ratio to the ionic liquid under the same experimental conditions for the extraction process.

ACKNOWLEDGEMENT

The author is grateful to the University of Mosul for their support of scientific research and the Department of Chemistry at the University of Liverpool for helping to carry out some of the required research measurements.

REFERENCES

- Corma A, Martínez C, Ketley G, Blair G. On the mechanism of sulfur removal during catalytic cracking. *Applied Catalysis A: General*. 2001 Feb;208(1-2):135-52. <DOI>.
- Ito E, van Veen JAR. On novel processes for removing sulphur from refinery streams. *Catalysis Today*. 2006 Sep;116(4):446-60. <DOI>.
- Mei H, Mei BW, Yen TF. A new method for obtaining ultra-low sulfur diesel fuel via ultrasound assisted oxidative desulfurization☆. *Fuel*. 2003 Mar;82(4):405-14. <DOI>.
- Xie Y, Chowdhury M, Bhavsar P, Zhou Y. An integrated modeling approach for facilitating emission estimations of alternative fueled vehicles. *Transportation Research Part D: Transport and Environment*. 2012 Jan;17(1):15-20. <DOI>.
- Armstrong JP, Hurst C, Jones RG, Licence P, Lovelock KRJ, Satterley CJ, et al. Vapourisation of ionic liquids. *Phys Chem Chem Phys*. 2007;9(8):982. <DOI>.
- Yang RT. Desulfurization of Transportation Fuels with Zeolites Under Ambient Conditions. *Science*. 2003 Jul 4;301(5629):79-81. <DOI>.
- Babich I. Science and technology of novel processes for deep desulfurization of oil refinery streams: a review★. *Fuel*. 2003 Apr;82(6):607-31. <DOI>.
- Agarwal P, Sharma DK. Comparative Studies on the Bio-desulfurization of Crude Oil with Other Desulfurization Techniques and Deep Desulfurization through Integrated Processes. *Energy Fuels*. 2010 Jan 21;24(1):518-24. <DOI>.
- Song Z, Zhou T, Qi Z, Sundmacher K. Systematic Method for Screening Ionic Liquids as Extraction Solvents Exemplified by an Extractive Desulfurization Process. *ACS Sustainable Chem Eng*. 2017 Apr 3;5(4):3382-9. <DOI>.
- Domańska U, Wlazło M. Effect of the cation and anion of the ionic liquid on desulfurization of model fuels. *Fuel*. 2014 Oct;134:114-25. <DOI>.
- Lu X, Yue L, Hu M, Cao Q, Xu L, Guo Y, et al. Piperazinium-Based Ionic Liquids with Lactate Anion for Extractive Desulfurization of Fuels. *Energy Fuels*. 2014 Mar 20;28(3):1774-80. <DOI>.
- Zhao H, Baker GA, Wagle DV, Ravula S, Zhang Q. Tuning Task-Specific Ionic Liquids for the Extractive Desulfurization of Liquid Fuel. *ACS Sustainable Chem Eng*. 2016 Sep 6;4(9):4771-80. <DOI>.
- Flieger J, Flieger M. Ionic Liquids Toxicity - Benefits and Threats. *IJMS*. 2020 Aug 29;21(17):6267. <DOI>.
- Zhao Y, Bostrom T. Application of ionic liquids in solar cells and batteries: a review. *Current Organic Chemistry*. 2015;19(6):556-66. <URL>.
- Kulkarni PS, Afonso CAM. Deep desulfurization of diesel fuel using ionic liquids: current status and future challenges. *Green Chem*. 2010;12(7):1139. <DOI>.
- Holbrey JD, López-Martin I, Rothenberg G, Seddon KR, Silvero G, Zheng X. Desulfurisation of oils using ionic liquids: selection of cationic and anionic components to enhance extraction efficiency. *Green Chem*. 2008;10(1):87-92. <DOI>.
- Dharaskar SA, Wasewar KL, Varma MN, Shende DZ. Extractive Deep Desulfurization of Liquid Fuels Using Lewis-Based Ionic Liquids. *Journal of Energy*. 2013;2013:1-4. <DOI>.
- Ko NH, Lee JS, Huh ES, Lee H, Jung KD, Kim HS, et al. Extractive Desulfurization Using Fe-Containing Ionic Liquids. *Energy Fuels*. 2008 May 1;22(3):1687-90. <DOI>.
- Bösmann A, Datsevich L, Jess A, Lauter A, Schmitz C, Wasserscheid P. Deep desulfurization of diesel fuel by extraction with ionic liquids. *Chem Commun*. 2001 Nov 22;(23):2494-5. <DOI>.
- Zhang L, Wang J, Sun Y, Jiang B, Yang H. Deep oxidative desulfurization of fuels by superbase-derived Lewis acidic ionic liquids. *Chemical Engineering Journal*. 2017 Nov;328:445-53. <DOI>.
- Zhang M, Zhu W, Xun S, Li H, Gu Q, Zhao Z, et al. Deep oxidative desulfurization of dibenzothiophene with POM-based hybrid materials in ionic liquids. *Chemical Engineering Journal*. 2013 Mar;220:328-36. <DOI>.
- Buttrus NH, Sabah AA, Taqa AA, Englert U. 3-Allyl-1-methyl-1 H -benzotriazol-3-ium iodide. *Acta Crystallogr E Struct Rep Online*. 2012 Sep 15;68(9):o2735-o2735. <DOI>.
- Singh SK, Savoy AW. Ionic liquids synthesis and applications: An overview. *Journal of Molecular Liquids*. 2020 Jan;297:112038. <DOI>.
- Brown LC, Hogg JM, Swadźba-Kwaśny M. Lewis Acidic Ionic Liquids. In: Kirchner B, Perlt E, editors. *Ionic Liquids II* [Internet]. Cham: Springer International Publishing; 2017 [cited 2021 Sep 20]. p. 185-224. (Topics in Current Chemistry Collections). <URL>

25. Zeng S, Liu L, Shang D, Feng J, Dong H, Xu Q, et al. Efficient and reversible absorption of ammonia by cobalt ionic liquids through Lewis acid–base and cooperative hydrogen bond interactions. *Green Chem.* 2018;20(9):2075–83. [<DOI>](#).
26. Mohammed EH, Ameen AM, Sabah AA, Mustafa TS, Sulyman SAA, Younus NG. Synthesis and Characterization of Mn (II), Fe (III), Co (II), Ni (II), and Cu (II) 1, 3-Dimethylbenzotriazolium Salt Complexes and Their Uses for Decreasing of Sulfur in Diesel Oil. *Indian Journal of Heterocyclic Chemistry.* 2020;30(04):565–70.
27. Kore R, Kelley Steven P, Aduri P, Rogers RD. Mixed metal double salt ionic liquids comprised of [HN₂₂₂]₂ [ZnCl₄] and AlCl₃ provide tunable Lewis acid catalysts related to the ionic environment. *Dalton Trans.* 2018;47(23):7795–803. [<DOI>](#).
28. Fainleib A, Grigoryeva O, Starostenko O, Vashchuk A, Rogalsky S, Grande D. Acceleration effect of ionic liquids on polycyclotrimerization of dicyanate esters. *Express Polymer Letters.* 2016;10(9):722.
29. Chen X, Guo H, Abdeltawab AA, Guan Y, Al-Deyab SS, Yu G, et al. Brønsted–Lewis Acidic Ionic Liquids and Application in Oxidative Desulfurization of Diesel Fuel. *Energy Fuels.* 2015 May 21;29(5):2998–3003. [<DOI>](#).
30. Chan JW, Taylor DS, Zwerdling T, Lane SM, Ihara K, Huser T. Micro-Raman Spectroscopy Detects Individual Neoplastic and Normal Hematopoietic Cells. *Biophysical Journal.* 2006 Jan;90(2):648–56. [<DOI>](#).
31. Montanino M, Carewska M, Alessandrini F, Passerini S, Appetecchi GB. The role of the cation aliphatic side chain length in piperidinium bis(trifluoromethanesulfonyl)imide ionic liquids. *Electrochimica Acta.* 2011 Dec;57:153–9. [<DOI>](#).
32. Salminen J, Papaiconomou N, Kumar RA, Lee J-M, Kerr J, Newman J, et al. Physicochemical properties and toxicities of hydrophobic piperidinium and pyrrolidinium ionic liquids. *Fluid Phase Equilibria.* 2007 Dec;261(1–2):421–6. [<DOI>](#).
33. Sabah AA. Synthesis and Characterization of Some Transition Metals Complex Salts of Pyridinium Iodide Ionic Liquids: Application on Extractive Desulfurization. *Journal of the Turkish Chemical Society Section A: Chemistry.* 2021 Jul 23;8(3):763–74. [<DOI>](#).
34. Song Z, Zhou T, Zhang J, Cheng H, Chen L, Qi Z. Screening of ionic liquids for solvent-sensitive extraction—with deep desulfurization as an example. *Chemical Engineering Science.* 2015 Jun;129:69–77. [<DOI>](#).
35. Wang S, Li P, Hao L, Deng C, Ren W, Lü H. Oxidative Desulfurization of Model Diesel Using a Fenton-Like Catalyst in the Ionic Liquid [Dmim]BF₄. *Chem Eng Technol.* 2017 Mar;40(3):555–60. [<DOI>](#).
36. Wang Q, Lei L, Zhu J, Yang B, Li Z. Deep Desulfurization of Fuels by Extraction with 4-Dimethylaminopyridinium-Based Ionic Liquids. *Energy Fuels.* 2013 Aug 15;27(8):4617–23. [<DOI>](#).
37. Ren Z, Zhou Z, Li M, Zhang F, Wei L, Liu W. Deep Desulfurization of Fuels Using Imidazole Anion-Based Ionic Liquids. *ACS Sustainable Chem Eng.* 2019 Jan 22;7(2):1890–900. [<DOI>](#).

Extractive Desulfurization Using Piperidinium Based Ionic Liquids with Lewis Acids

Assim A. Sabah^{1*}

Supporting Information

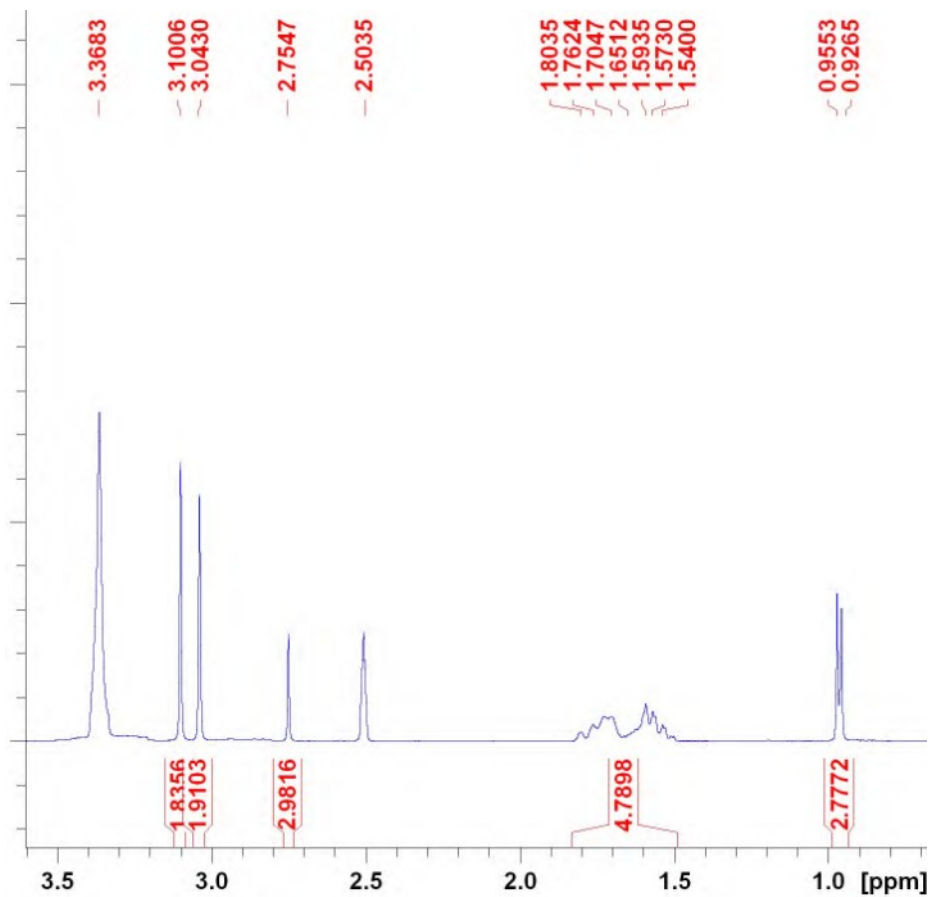


Figure S1: 1H-NMR of [MMPip]I ionic liquids.



Figure S2: Pictures of the prepared compounds.

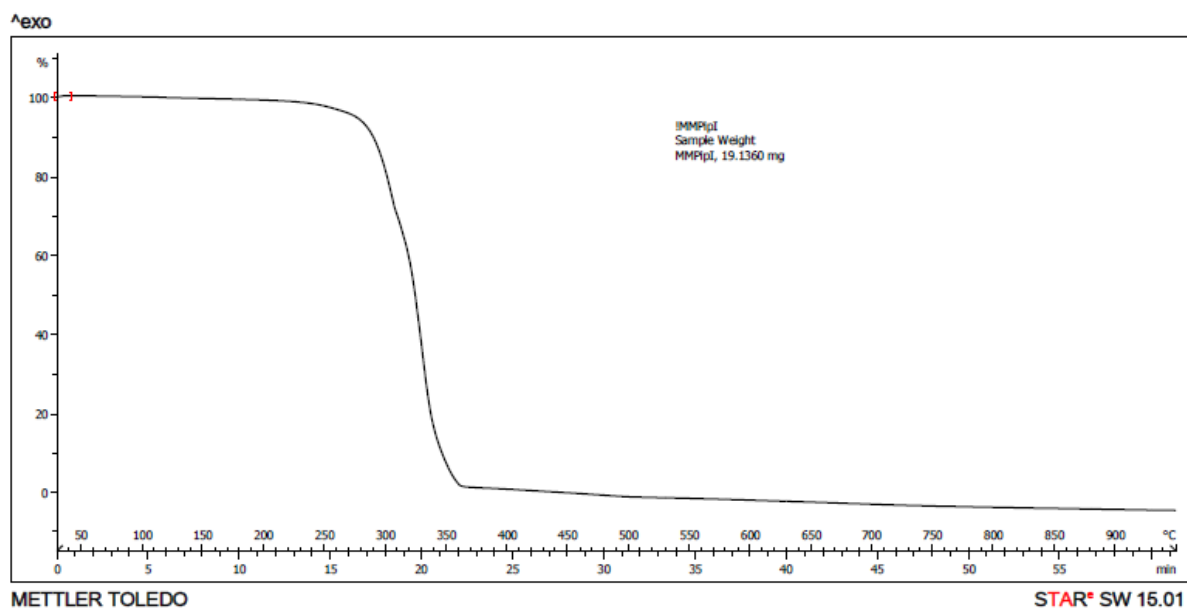


Figure S3: TGA analyses of [MMPip]I ionic liquids.

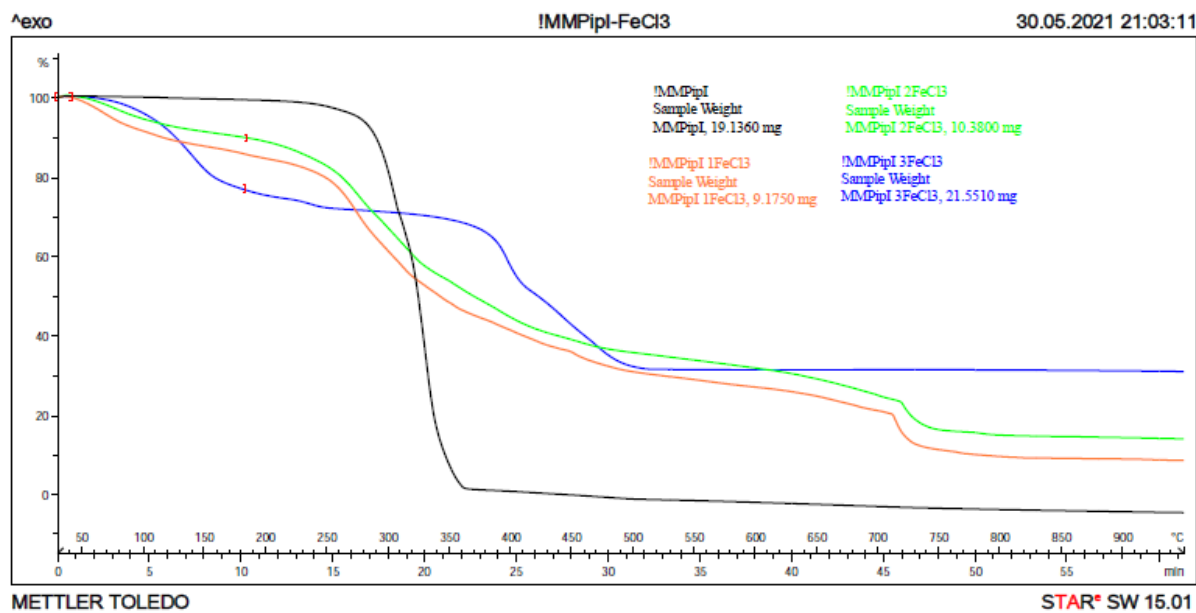


Figure S4: TGA analysis of prepared compounds.

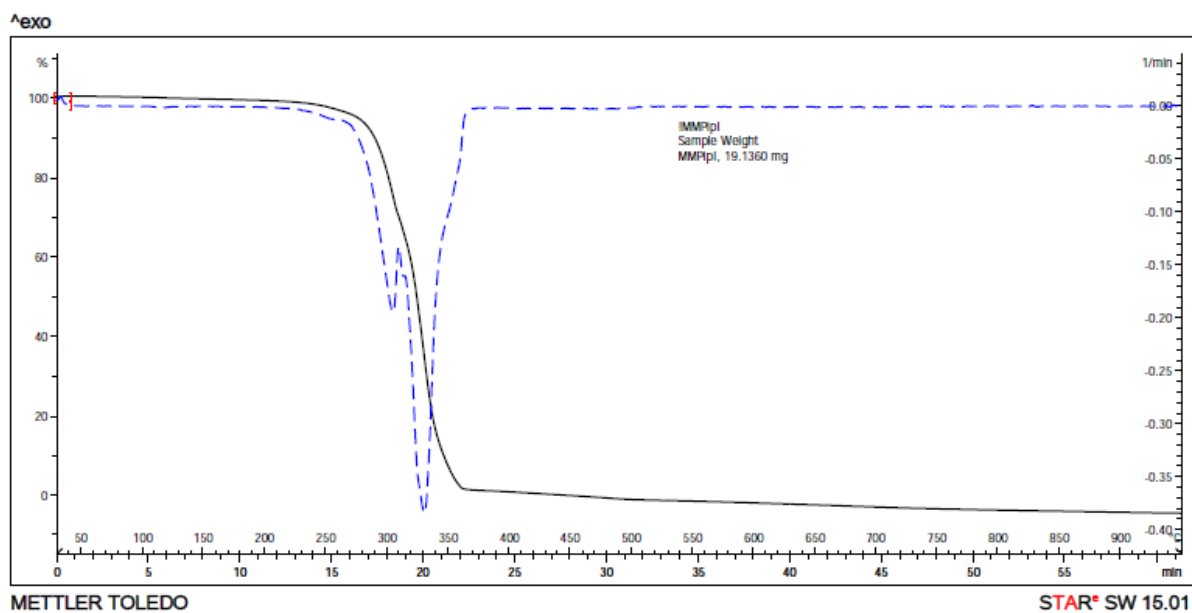


Figure S5: TGA and DTA analyses of [MMPip]I ionic liquids.

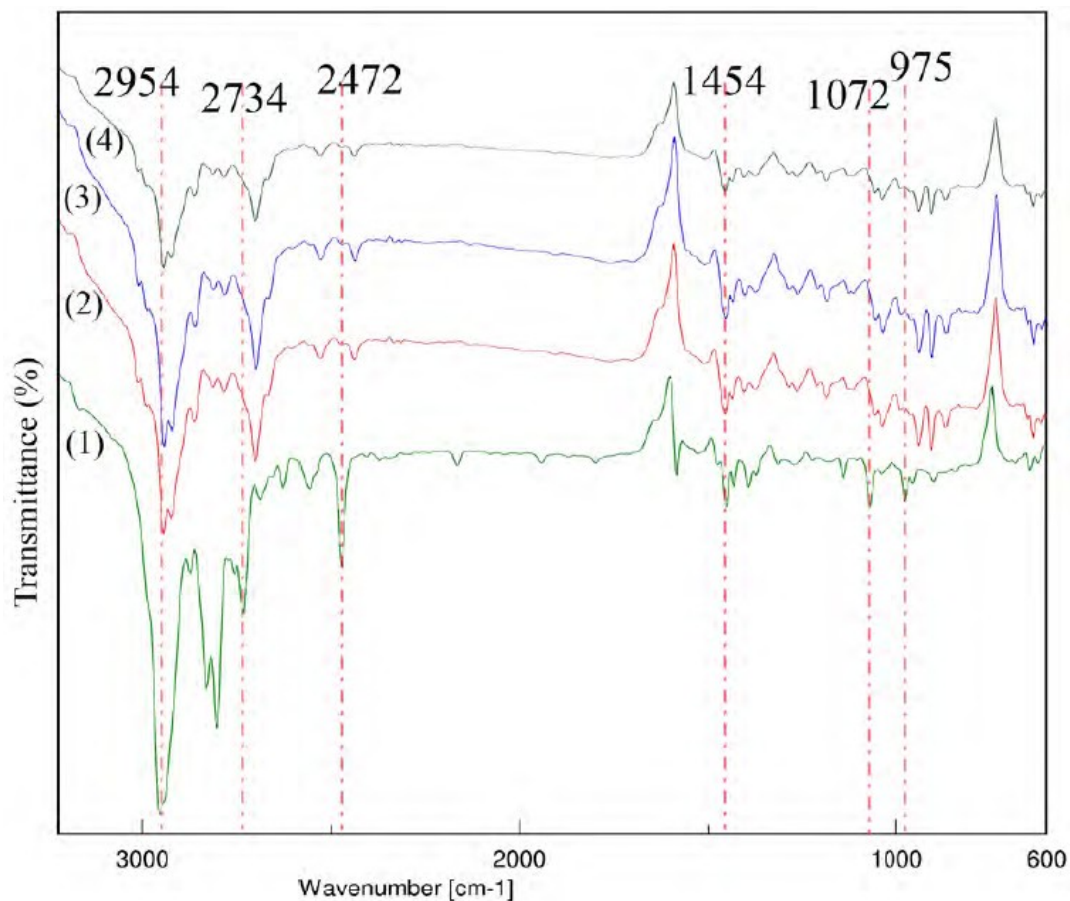


Figure S6: FT-IR spectrum of prepared compounds.

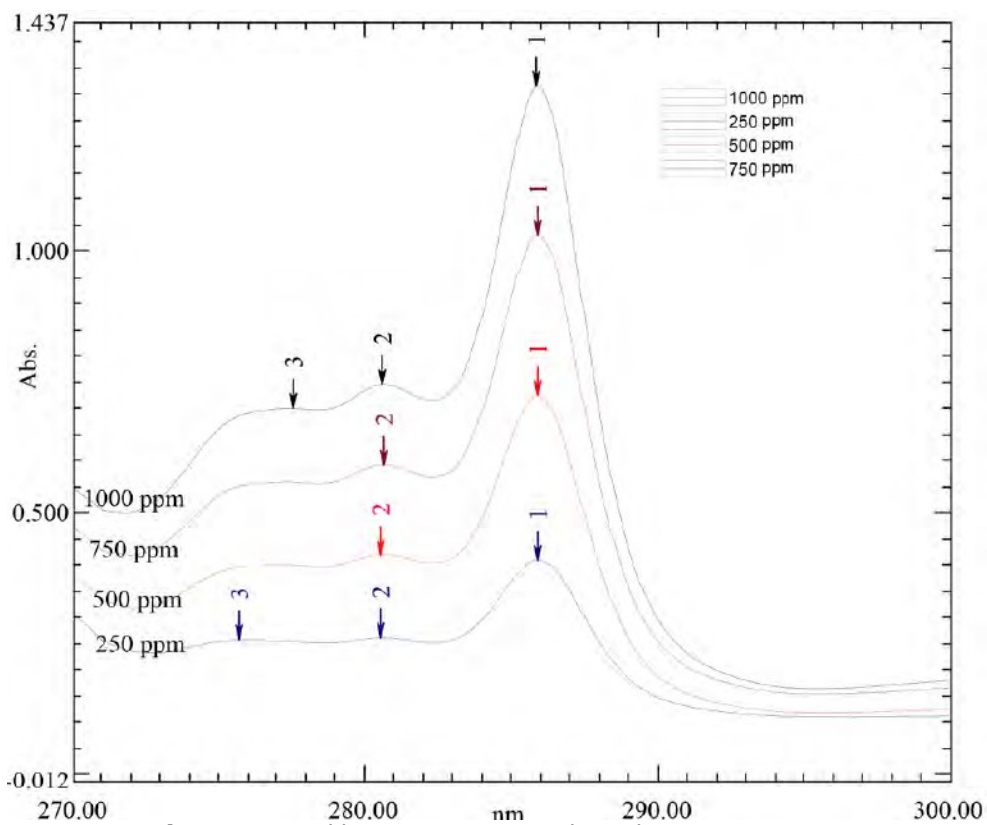


Figure S7: Calibration curve standard solutions spectrum.

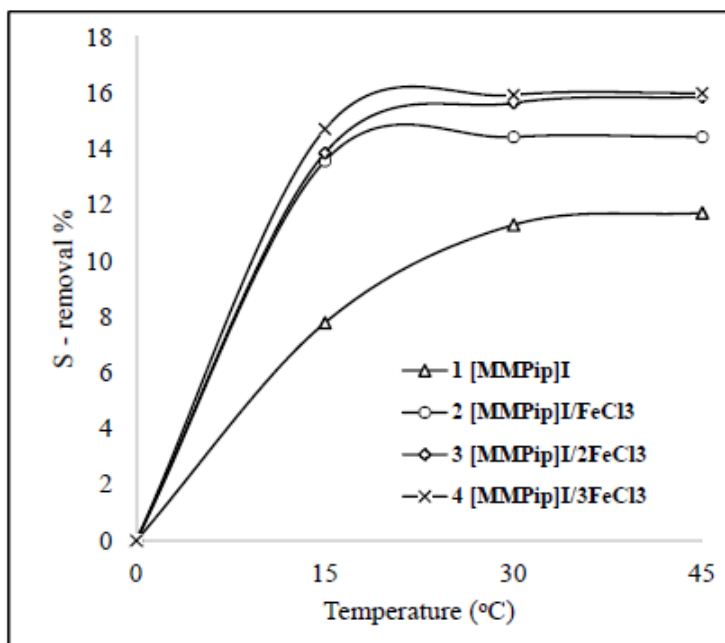


Figure S8: Effect of temperature: extractant used 0.05 g, 30 min.

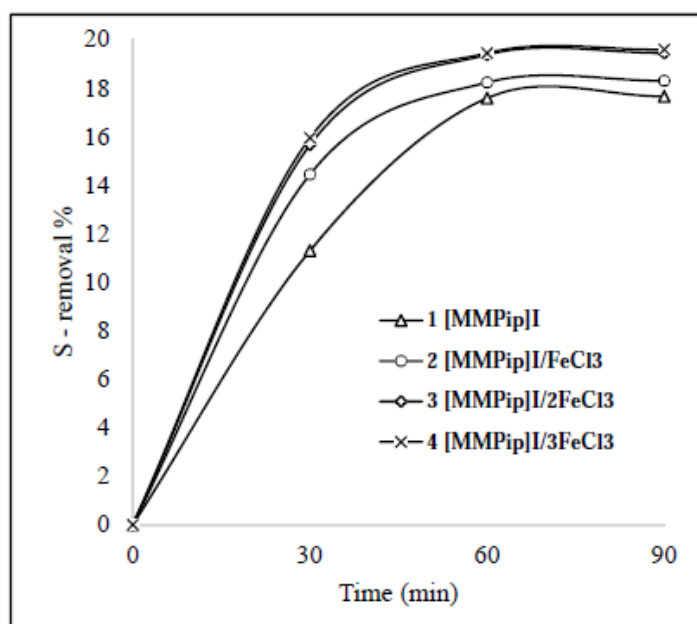


Figure S9: Effect of time: extractant used 0.05g, 30 °C.

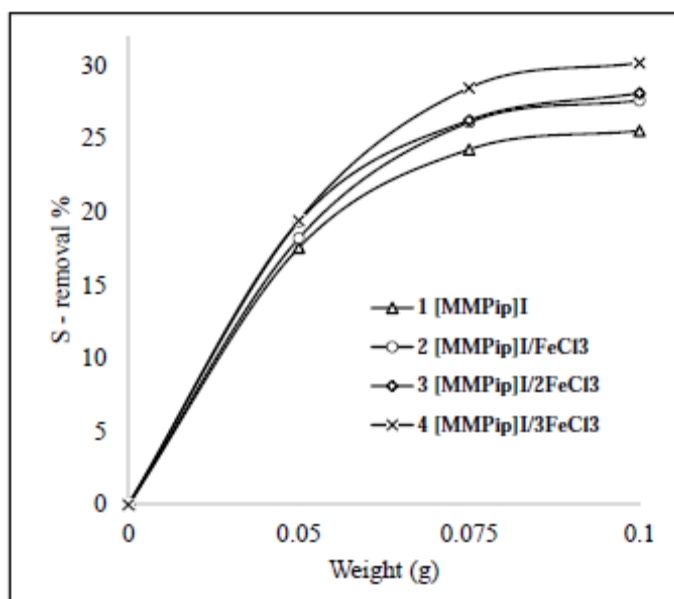


Figure S10: Effect of extractant weight: 60 min, 30 °C.

Data Set: 250 - RawData

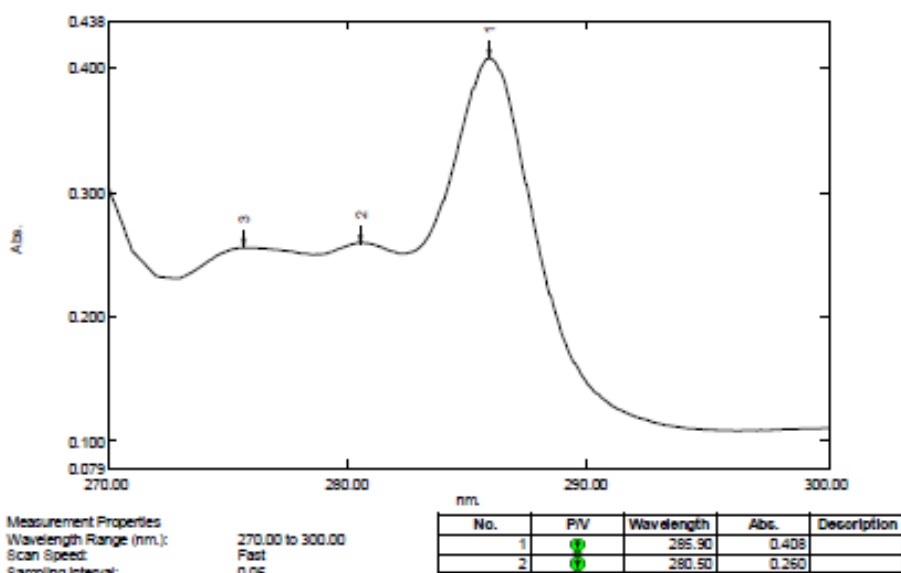


Figure S11: UV- Spectrum peak pick report of 250 ppm of DBT stranded solution.

Data Set 500 - RawData

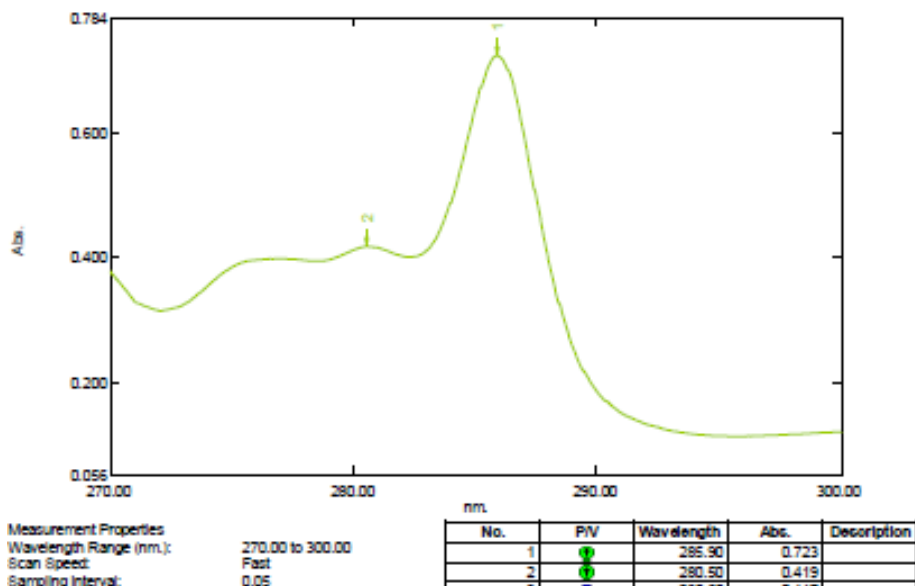


Figure S12: UV- Spectrum peak pick report of 500 ppm of DBT stranded solution.

Data Set 750 - RawData

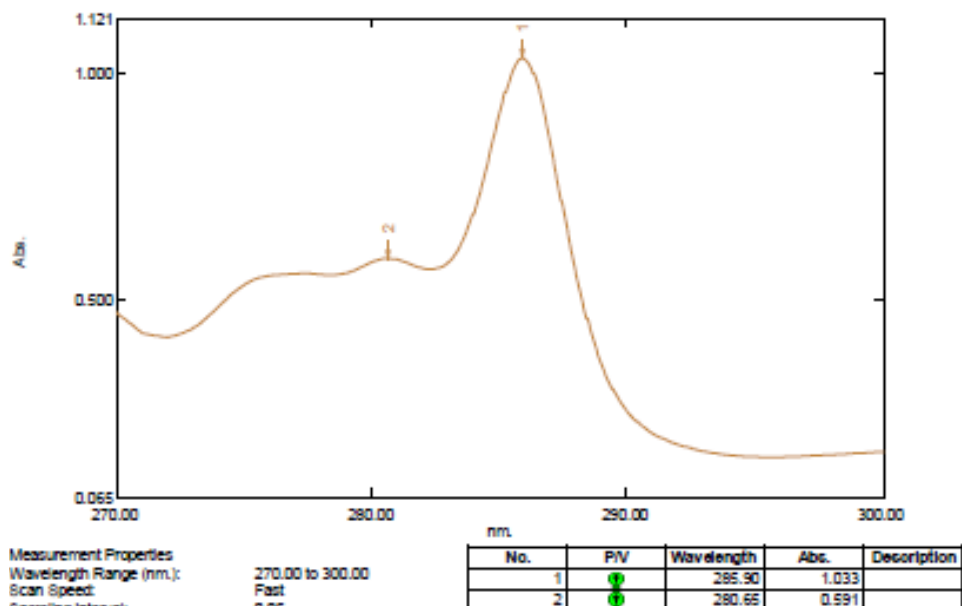


Figure S13: UV- Spectrum peak pick report of 750 ppm of DBT stranded solution.

Data Set: 1000 - RawData

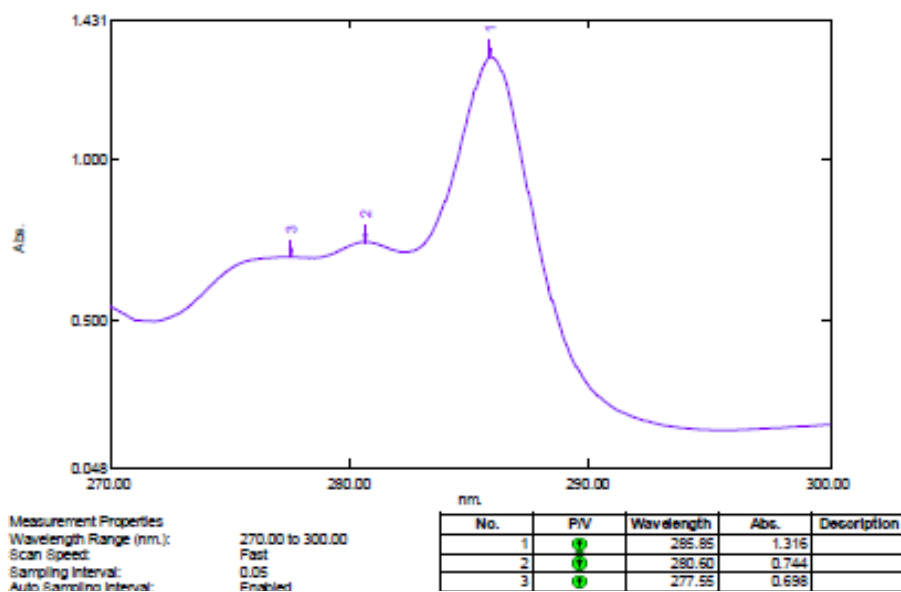


Figure S14: UV- Spectrum peak pick report of 1000 ppm of DBT stranded solution.

Data Set: 001- 1- 15c- 0.05g- 30 min - RawData

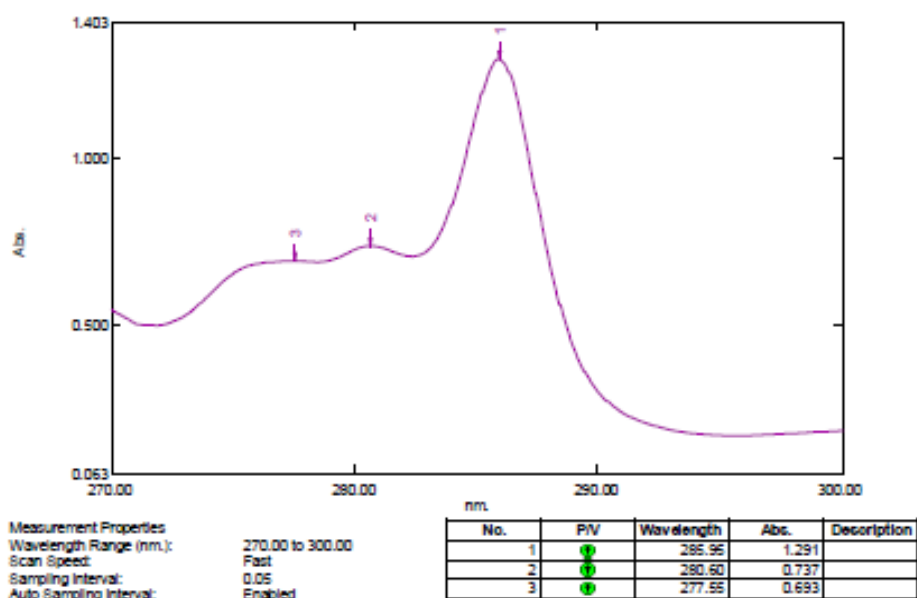


Figure S15: UV- Spectrum peak pick report of extractive desulfurization condition: extractant (1), at 15 °C, weight of extractant 0.05 g, time = 30 min.

Data Set 002- 1- 30c- 0.05g- 30 min - RawData

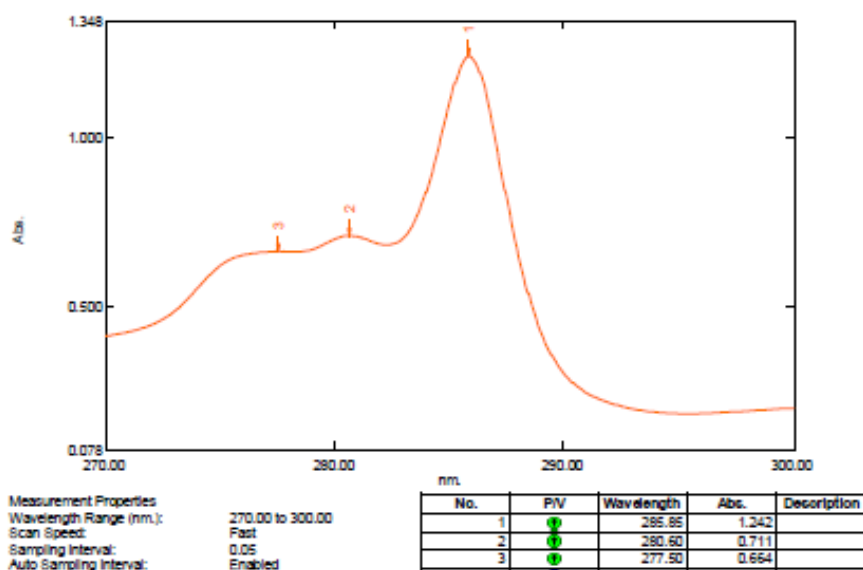


Figure S16: UV- Spectrum peak pick report of extractive desulfurization condition: extractant (1), at 30 °C, weight of extractant 0.05 g, time = 30 min.

Data Set 003- 1- 45c- 0.05g- 30 min - RawData

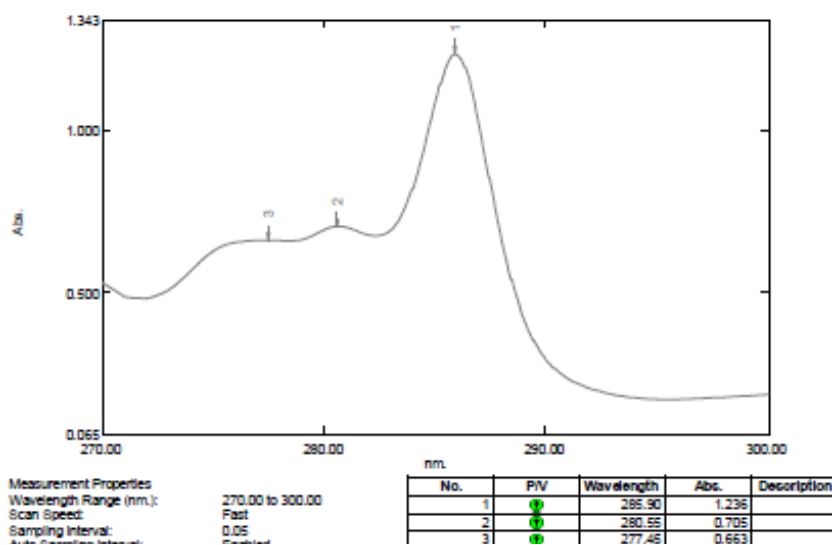


Figure S17: UV- Spectrum peak pick report of extractive desulfurization condition: extractant (1), at 45 °C, weight of extractant 0.05 g, time = 30 min.

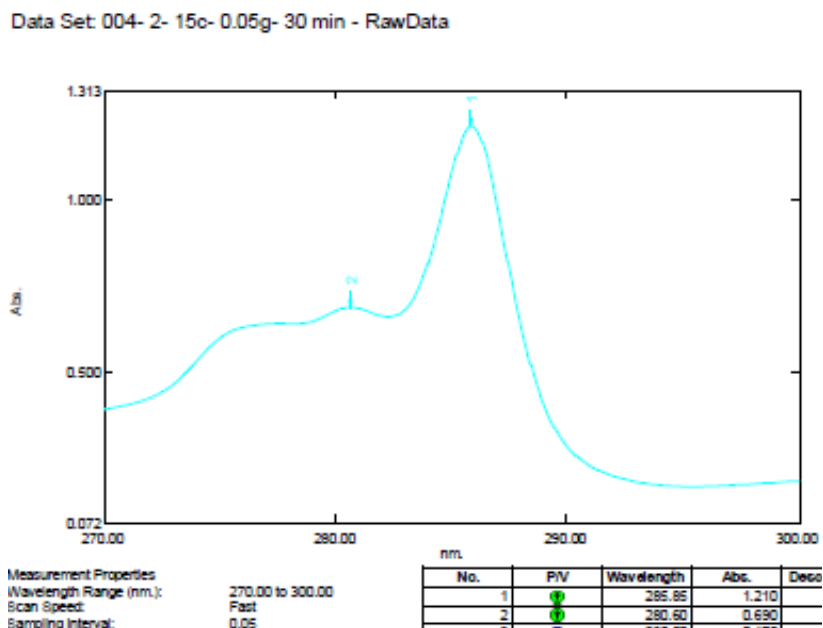


Figure S18: UV- Spectrum peak pick report of extractive desulfurization condition: extractant (2), at 15 °C, weight of extractant 0.05 g, time = 30 min.

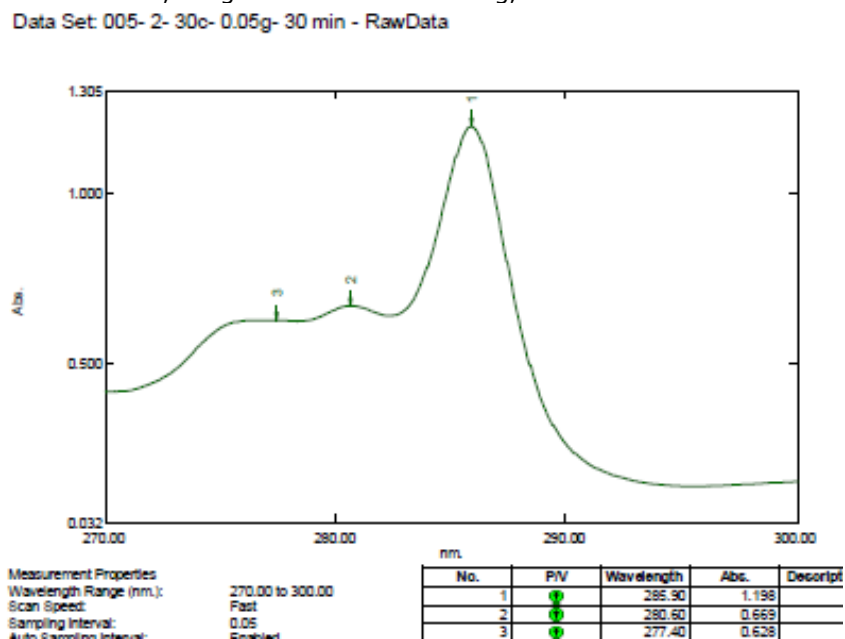


Figure S19: UV- Spectrum peak pick report of extractive desulfurization condition: extractant (2), at 30 °C, weight of extractant 0.05 g, time = 30 min.

Data Set 006- 2- 45c- 0.05g- 30 min - RawData

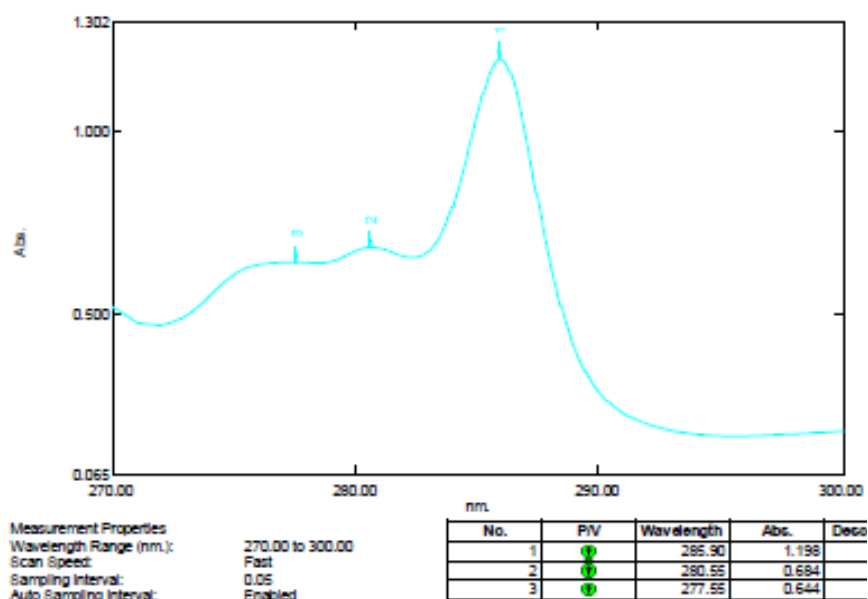


Figure S20: UV- Spectrum peak pick report of extractive desulfurization condition: extractant (2), at 45 °C, weight of extractant 0.05 g, time = 30 min.

Data Set 007- 3- 15c- 0.05g- 30 min - RawData

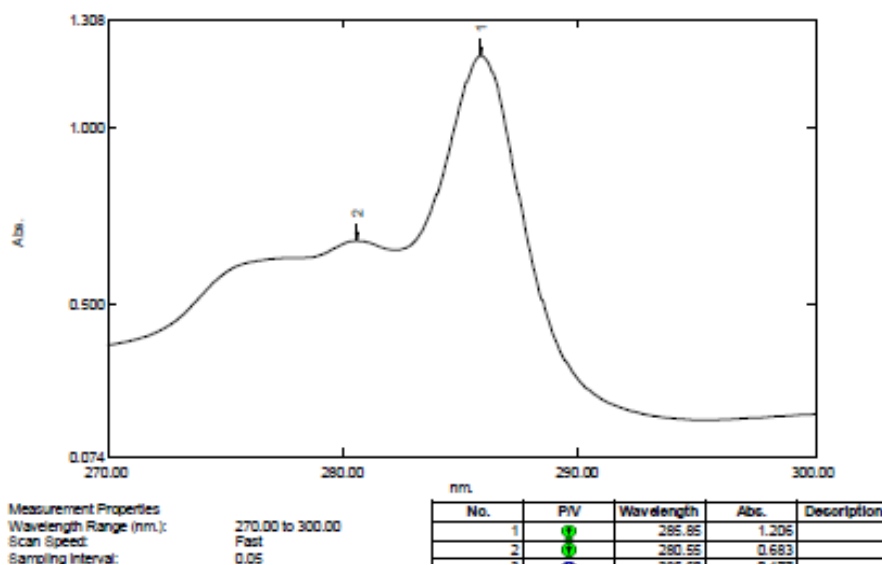


Figure S21: UV- Spectrum peak pick report of extractive desulfurization condition: extractant (3), at 15 °C, weight of extractant 0.05 g, time = 30 min.

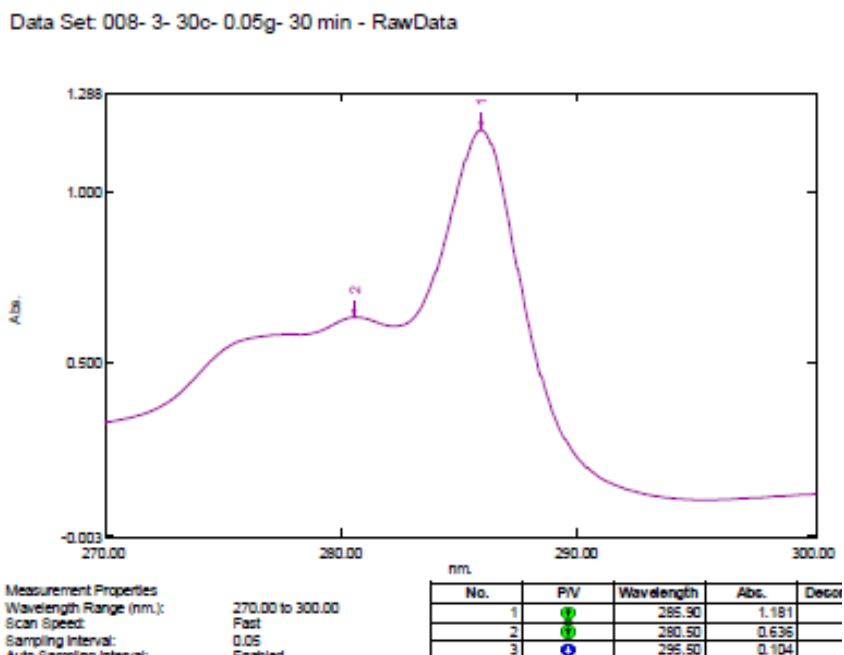


Figure S22: UV- Spectrum peak pick report of extractive desulfurization condition: Extractant (3), at 30 °C, weight of extractant 0.05 g, time = 30 min.

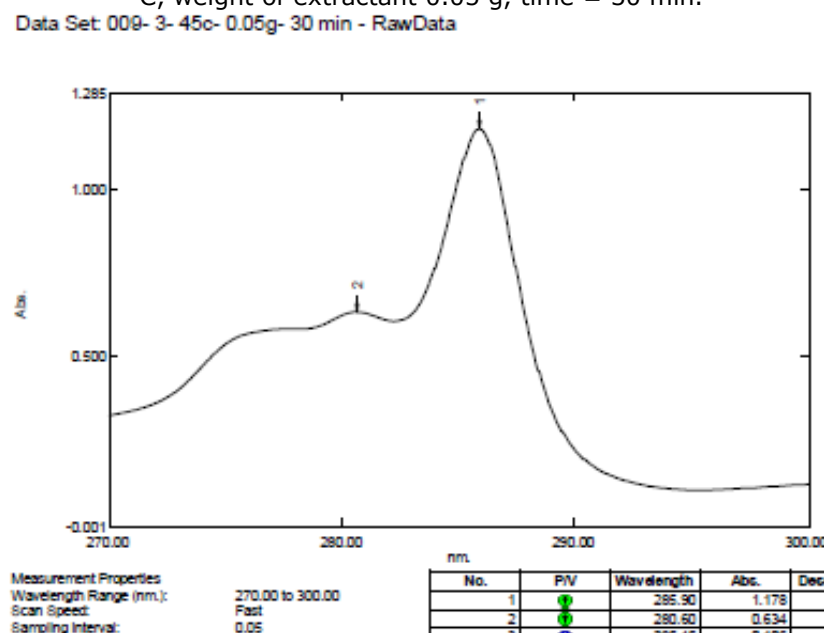


Figure S23: UV- Spectrum peak pick report of extractive desulfurization condition: extractant (3), at 45 °C, weight of extractant 0.05 g, time = 30 min.

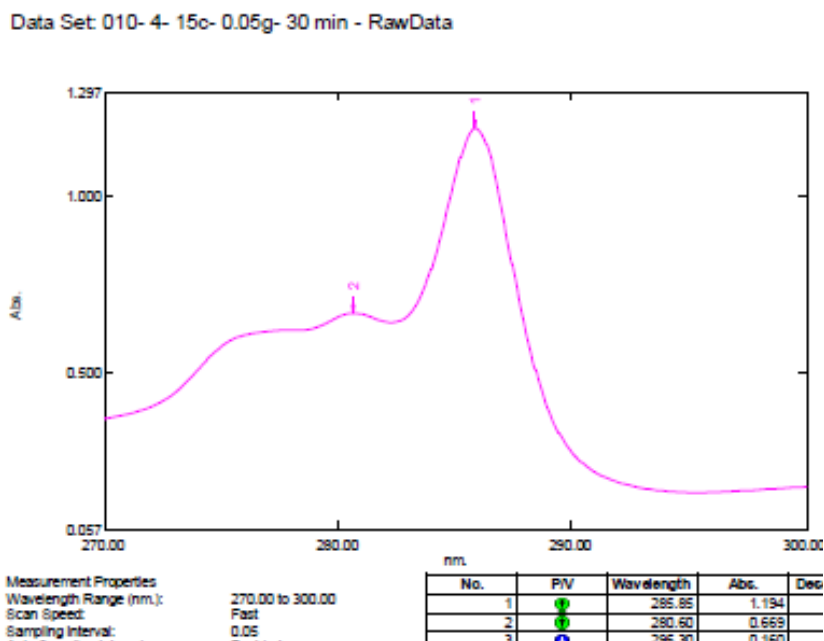


Figure S24: UV- Spectrum peak pick report of extractive desulfurization condition: extractant (4), at 15 °C, weight of extractant 0.05 g, time = 30 min.

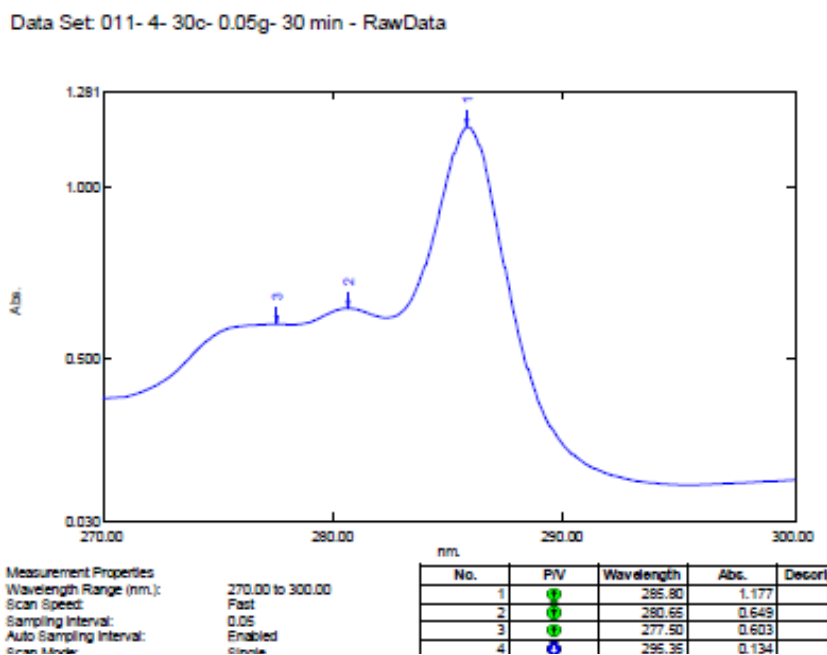


Figure S25: UV- Spectrum peak pick report of extractive desulfurization condition: extractant (4), at 30 °C, weight of extractant 0.05 g, time = 30 min.

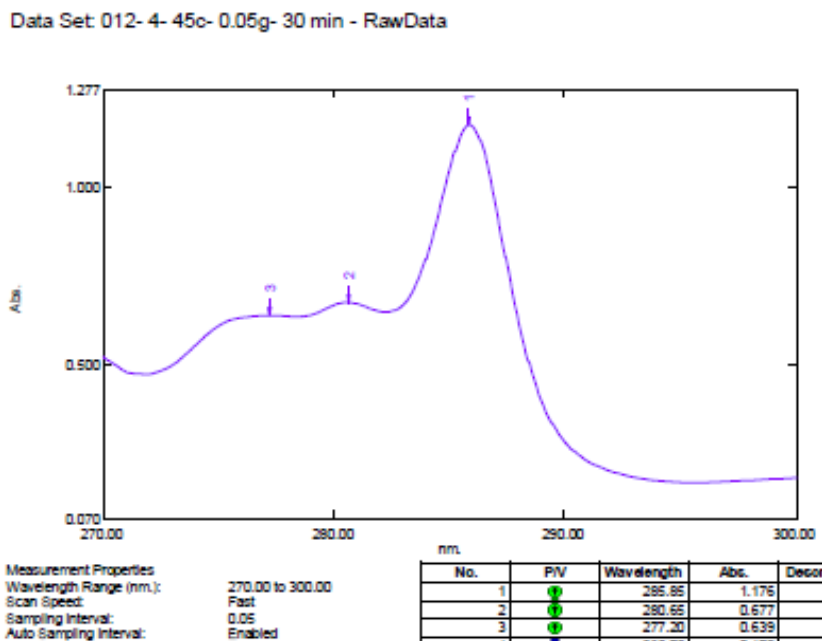


Figure S26: UV- Spectrum peak pick report of extractive desulfurization condition: extractant (4), at 45 °C, weight of extractant 0.05 g, time = 30 min.

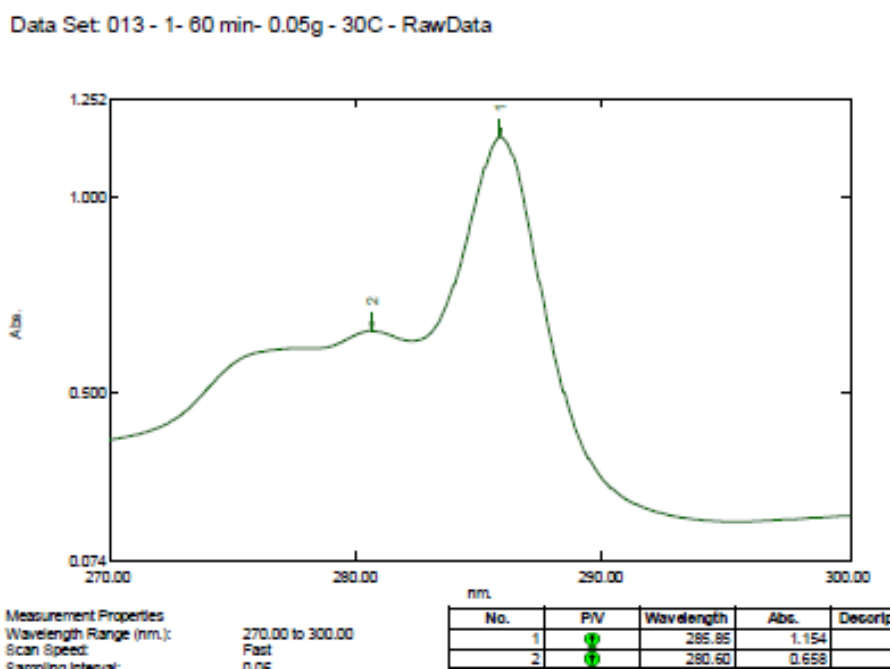


Figure S27: UV- Spectrum peak pick report of extractive desulfurization condition: extractant (1), at 30 °C, weight of extractant 0.05 g, time = 60 min.

Data Set: 014 - 1- 90 min- 0.05g - 30C - RawData

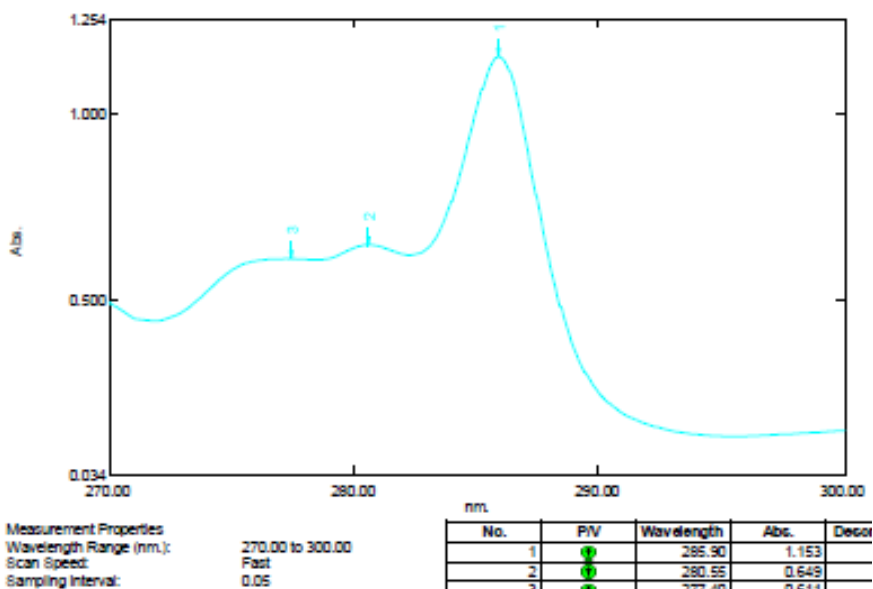


Figure S28: UV- Spectrum peak pick report of extractive desulfurization condition: extractant (1), at 30 °C, weight of extractant 0.05 g, time = 90 min.

Data Set: 015 - 2- 60 min- 0.05g - 30C - RawData

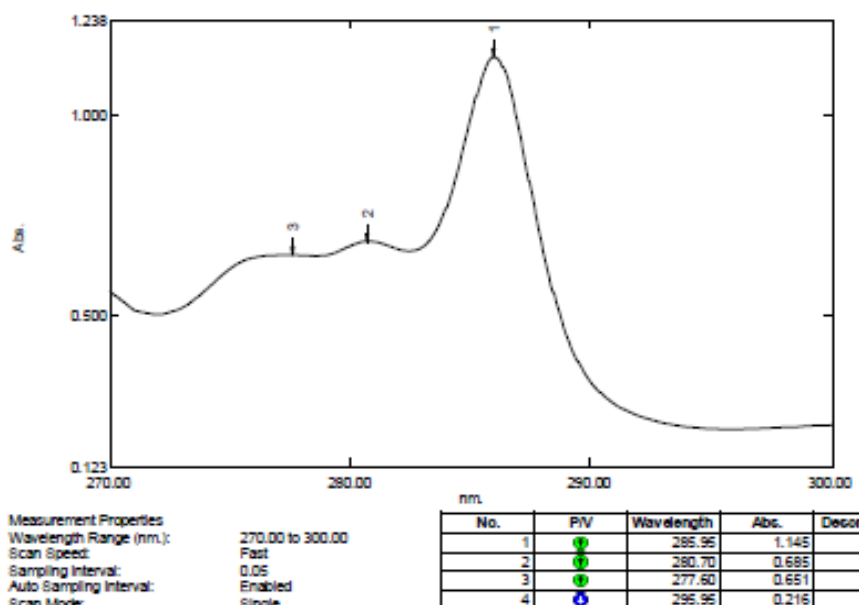


Figure S29: UV- Spectrum peak pick report of extractive desulfurization condition: extractant (2), at 30 °C, weight of extractant 0.05 g, time = 60 min.

Data Set 016 - 2- 90 min- 0.05g - 30C - RawData

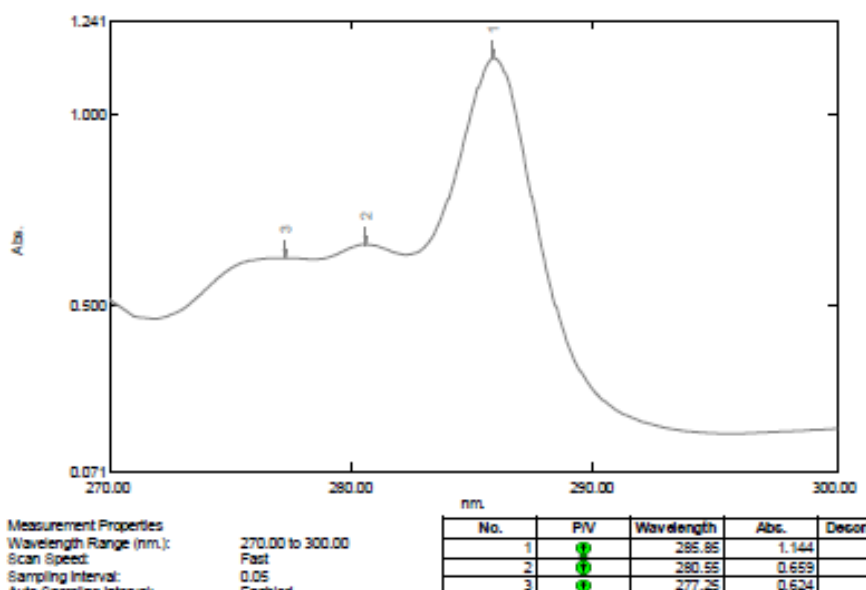


Figure S30: UV- Spectrum peak pick report of extractive desulfurization condition: extractant (2), at 30 °C, weight of extractant 0.05 g, time = 90 min.

Data Set 017 - 3- 60 min- 0.05g - 30C - RawData

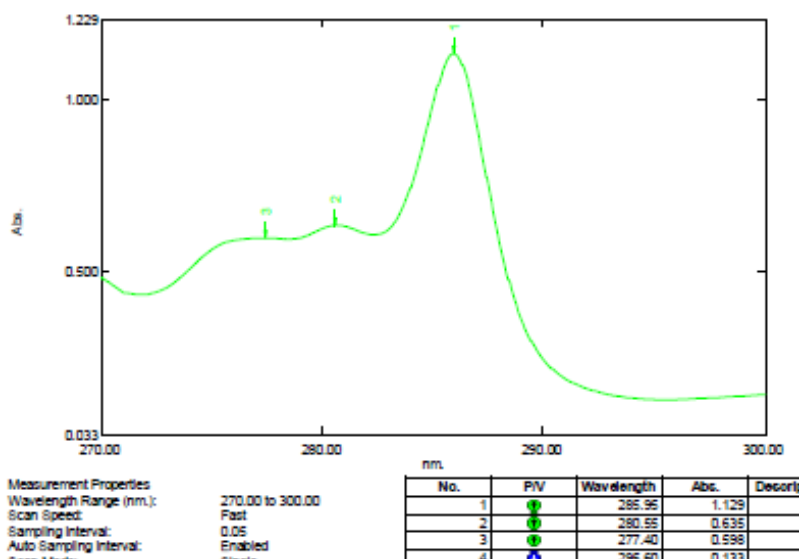


Figure S31: UV- Spectrum peak pick report of extractive desulfurization condition: extractant (3), at 30 °C, weight of extractant 0.05 g, time = 60 min.

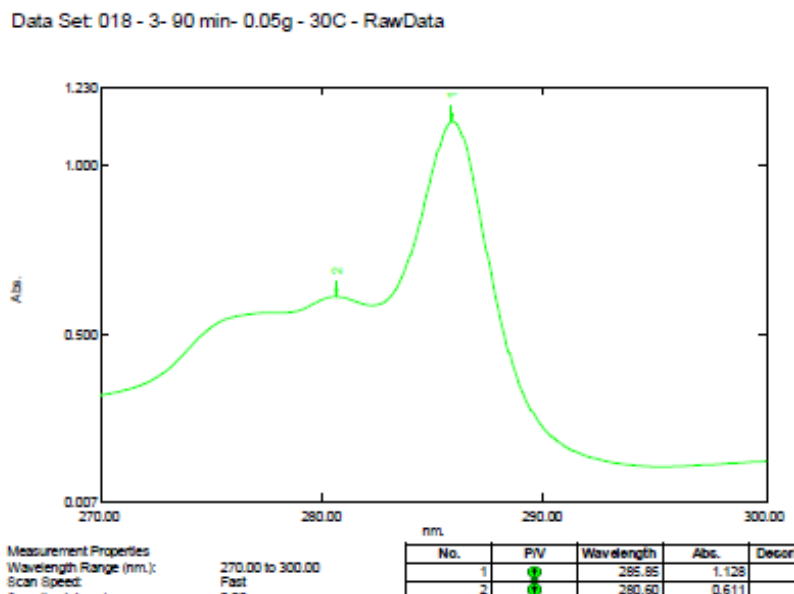


Figure S32: UV- Spectrum peak pick report of extractive desulfurization condition: extractant (3), at 30 °C, weight of extractant 0.05 g, time = 90 min.

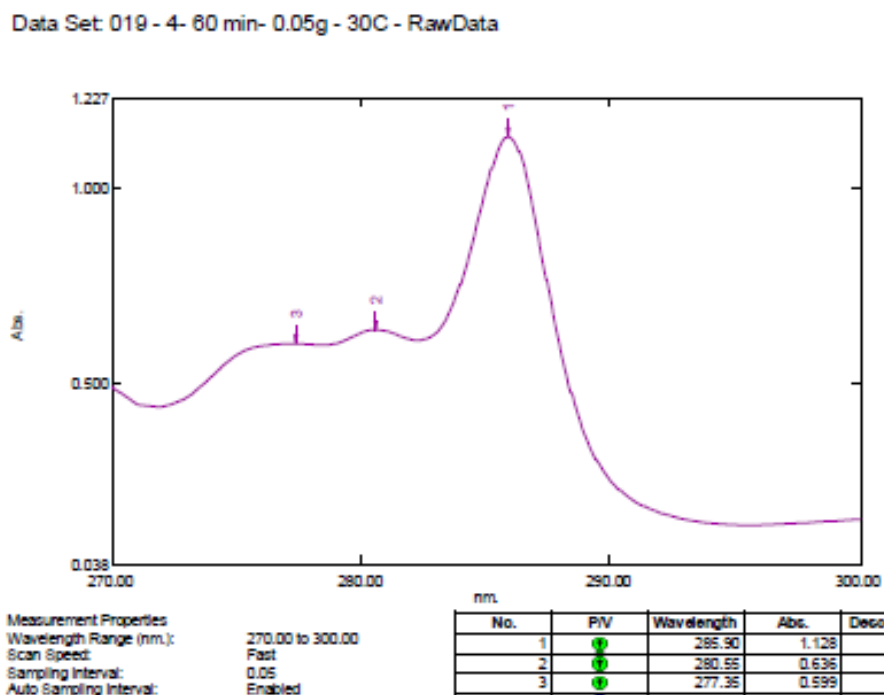


Figure S33: UV- Spectrum peak pick report of extractive desulfurization condition: extractant (4), at 30 °C, weight of extractant 0.05 g, time = 60 min.

Data Set 020 - 4- 90 min- 0.05g - 30C - RawData

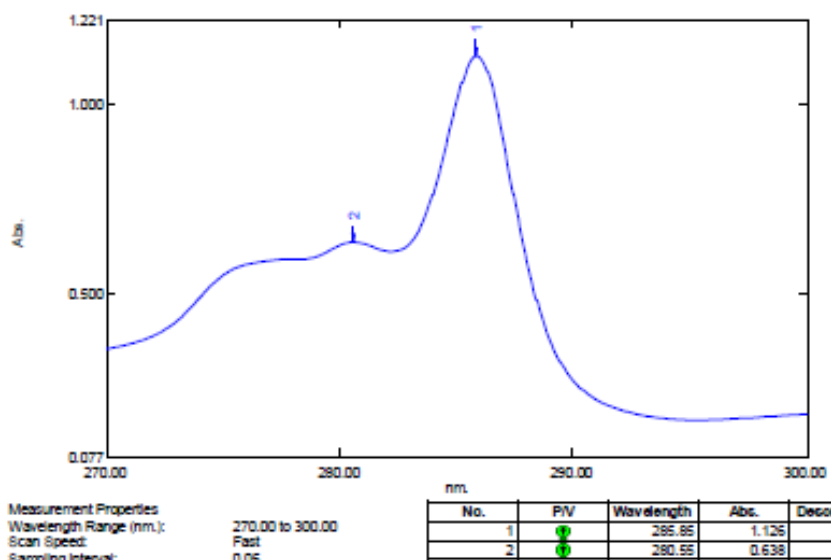


Figure S34: UV- Spectrum peak pick report of extractive desulfurization condition: extractant (4), at 30 °C, weight of extractant 0.05 g, time = 90 min.

Data Set 021 - 1- 0.075g - 60 min - RawData

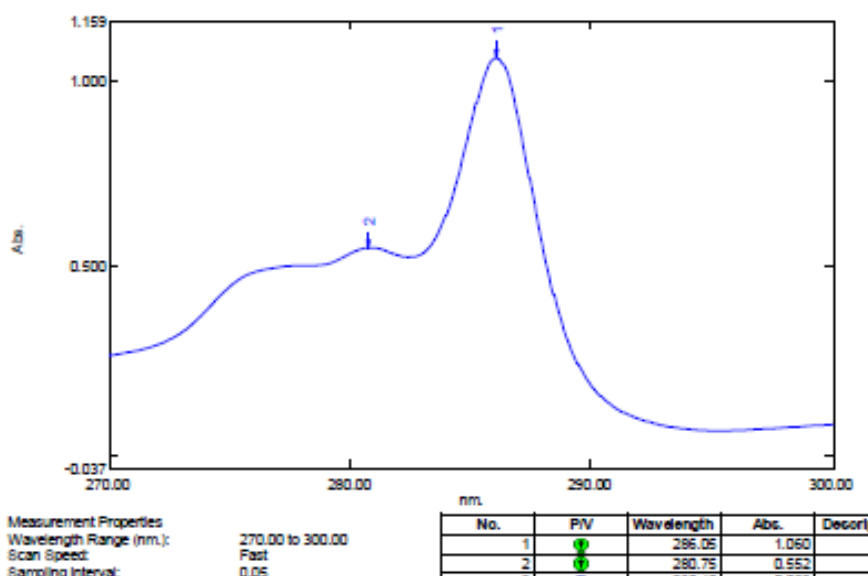


Figure S35: UV- Spectrum peak pick report of extractive desulfurization condition: extractant (1), at 30 °C, weight of extractant 0.075 g, time = 60 min.

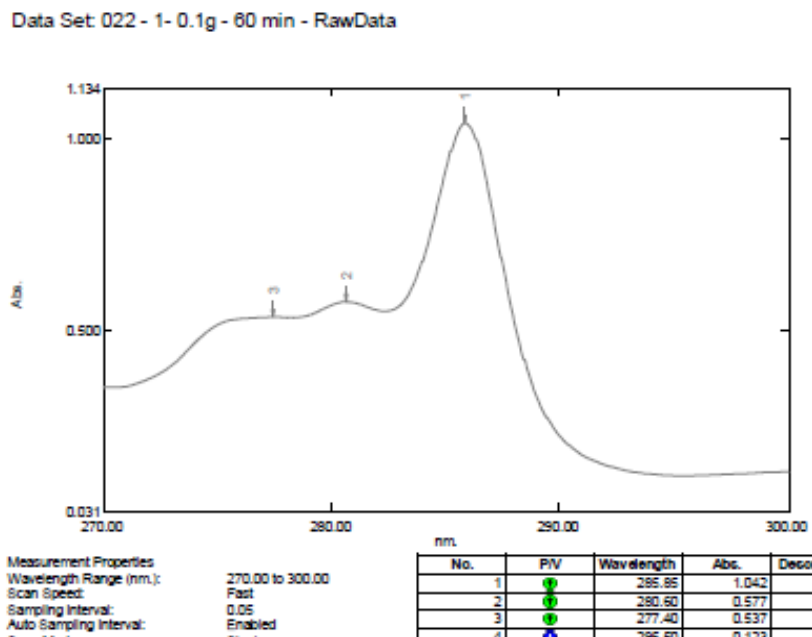


Figure S36: UV- Spectrum peak pick report of extractive desulfurization condition: extractant (1), at 30 °C, weight of extractant 0.1 g, time = 60 min.

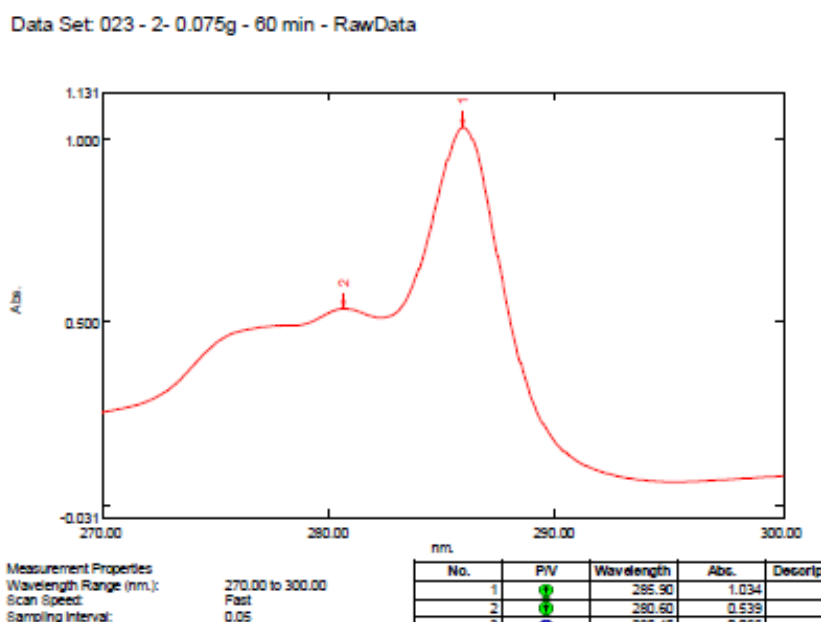


Figure S37: UV- Spectrum peak pick report of extractive desulfurization condition: extractant (2), at 30 °C, weight of extractant 0.075 g, time = 60 min.

Data Set 024 -2- 0.1g - 60 min - RawData

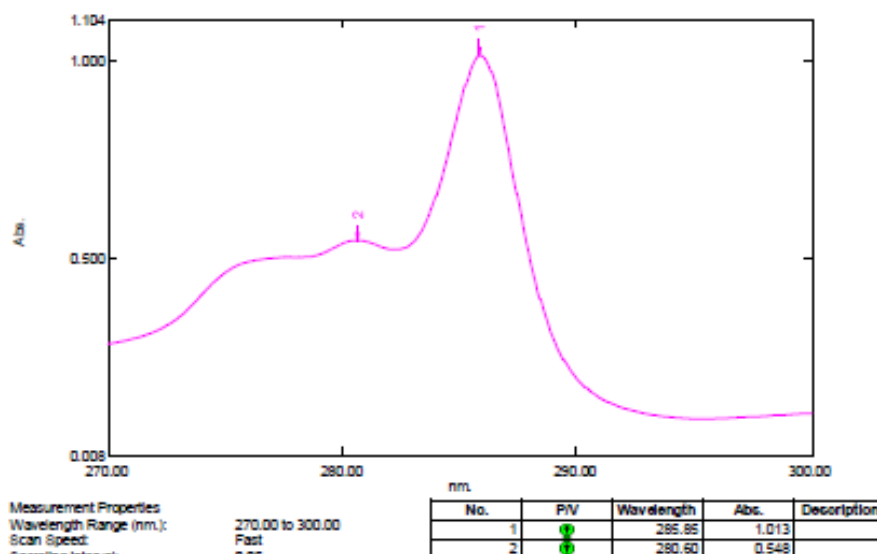


Figure S38: UV- Spectrum peak pick report of extractive desulfurization condition: extractant (2), at 30 °C, weight of extractant 0.1 g, time = 60 min.

Data Set 025 -3- 0.075g - 60 min - RawData

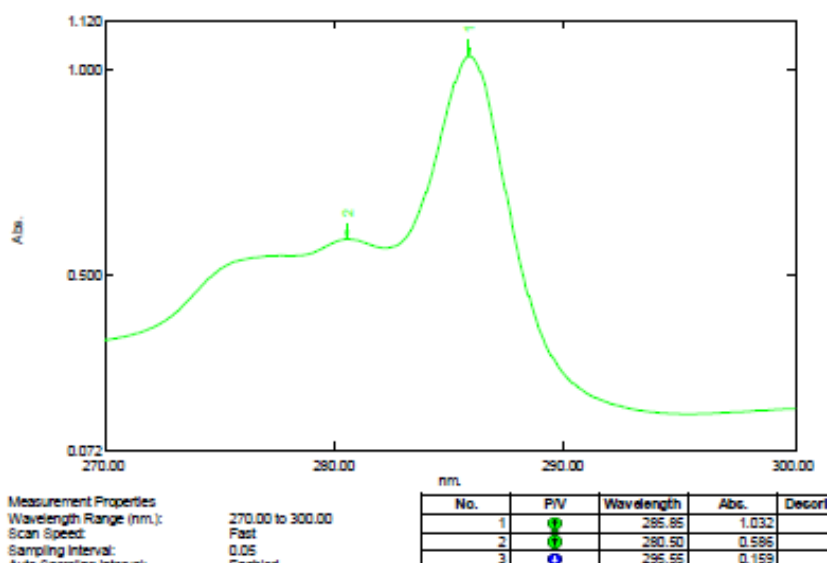


Figure S39: UV- Spectrum peak pick report of extractive desulfurization condition: extractant (3), at 30 °C, weight of extractant 0.075 g, time = 60 min.

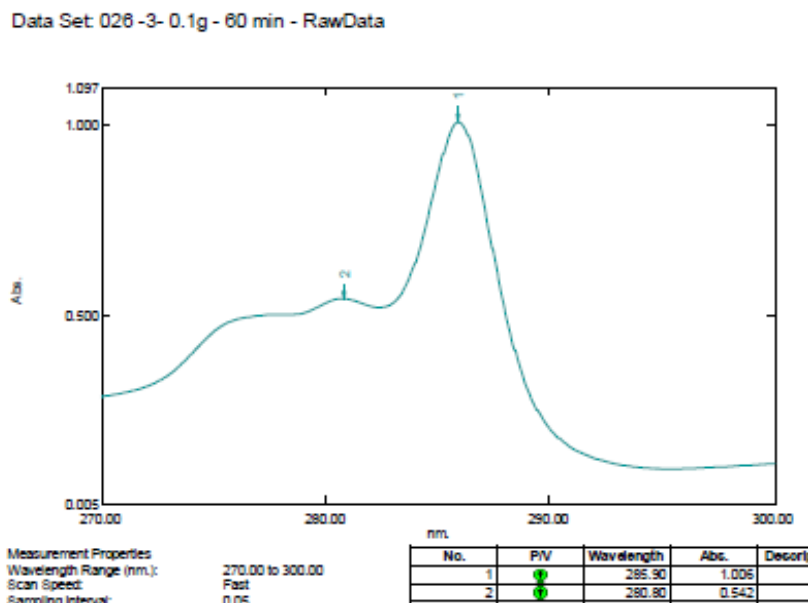


Figure S40: UV- Spectrum peak pick report of extractive desulfurization condition: extractant (3), at 30 °C, weight of extractant 0.1 g, time = 60 min.

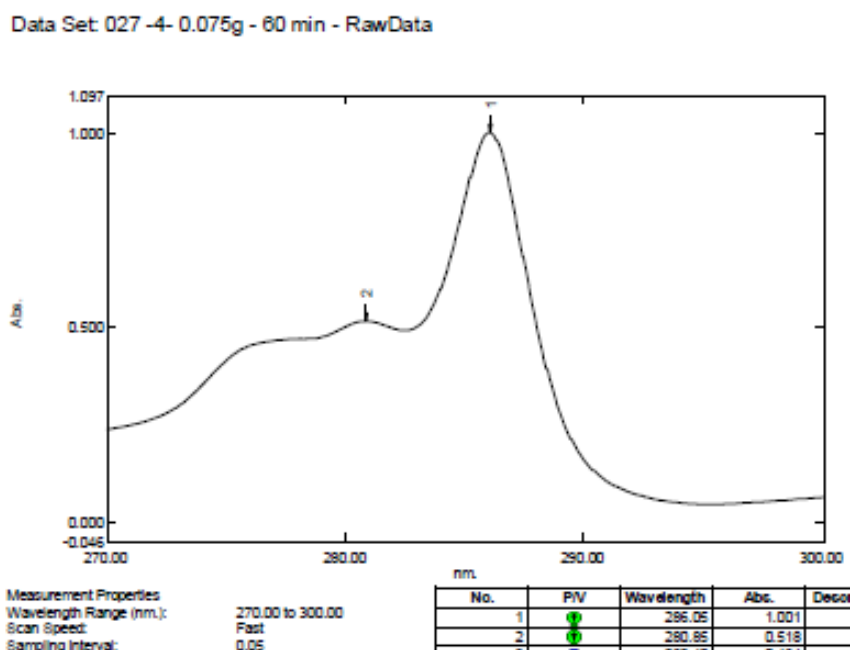


Figure S41: UV- Spectrum peak pick report of extractive desulfurization condition: extractant (4), at 30 °C, weight of extractant 0.075 g, time = 60 min.

Data Set: 028 -4- 0.1g - 60 min - RawData

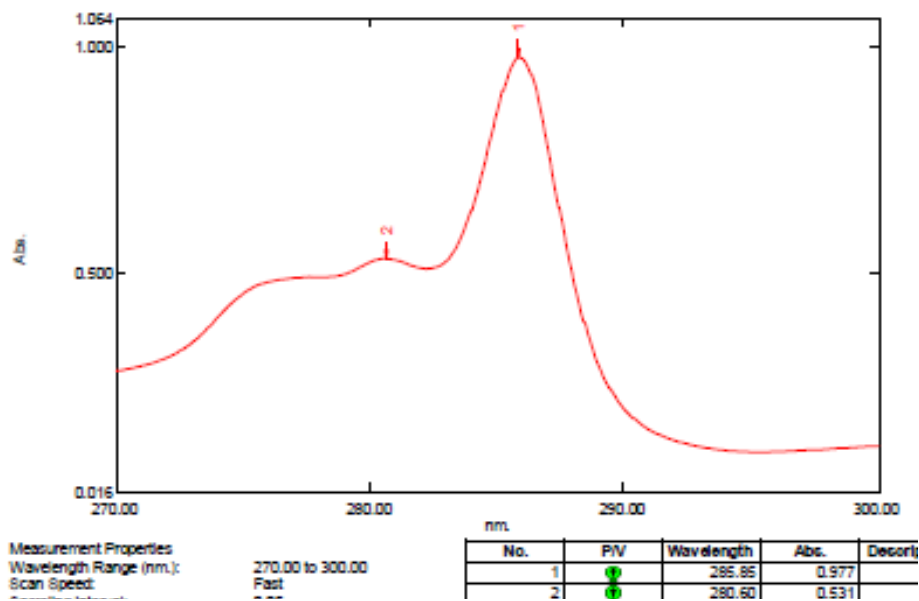


Figure S42: UV- Spectrum peak pick report of extractive desulfurization condition: extractant (4), at 30 °C, weight of extractant 0.1 g, time = 60 min.



Synthesis of Isatin and its Derivatives Containing Heterocyclic Compounds

Pratibha Mishra , Arunesh K. Mishra , Anil. K. Bahe , Atish Roy ,
and Ratnesh Das*  

Department of Chemistry, Dr. Harisingh Gour Central University, Sagar- 470003 (M.P.), INDIA

Abstract: Isatin or 1H-indole-2,3-dione or 2,3-dioxindole is an indole derivative. Isatin and its analogs are synthetically useful substances where they may be utilized for the production of a broad range of heterocyclic molecules, which are depicting a wide reach of biological and pharmacological activities, as well as anticancer, anti-inflammatory, antiviral, anticonvulsant, anti-TB, antidiabetic, anti-microbial, antitumor, antimalarial, anti-HIV, antibacterial, anti-analgesic, and antiplasmodial activities. Isatin is a precursor for many synthesized therapeutic molecules that are amenable to pharmacological action and have excellent biological potential. Isatin has a magnificent scaffold for both the natural and synthetic construction of molecules. These molecules are being used in drug therapy such as anticancer, antibiotic, and antidepressant drugs and have many more clinical applications. Due to its privileged scaffolding, the synthetic versatility of isatin has produced many structurally diverse derivatives, including the substitution of mono-, di- and tri-substitution of the aryl rings A and those derived by derivation of isatin nitrogen and C2 and C3 carbon moieties. As a result, improving and expediting access to isatin-related molecules is a challenging study in synthetic organic chemistry.

Keywords: Isatin, 1H-indole-2,3-dione, heterocyclic compounds, anticancer, anti-inflammatory, antimalaria, anti-HIV, drug therapy.

Submitted: July 04, 2021. **Accepted:** September 22, 2021.

Cite this: Mishra P, Mishra A, Bahe A, Roy A, Das R. Synthesis of Isatin and its Derivatives Containing Heterocyclic Compounds. JOTCSA. 2021;8(4):1089-98.

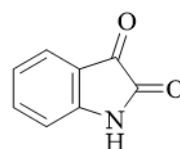
DOI: <https://doi.org/10.18596/jotcsa.962260>.

***Corresponding author. E-mail:** ratneshdas1@gmail.com.

INTRODUCTION

Isatin derivatives (1H-indole-2,3-dione) are among the most important heterocyclic compounds currently occupying an essential place in pharmaceuticals and chemicals (1,2). Isatin, also known as indole quinone and indenedione, is a biologically active compound with a wide range of properties. Isatin has two cyclic rings in its structure, one of which is six-membered (aromatic property) and the other is five-membered (anti-aromatic character). Both rings lie in the same plane, a five-membered ring contains a nitrogen atom and two carbonyl groups. Isatin was first synthesized in 1840 by Erdmann and Laurent as an oxidation product of the indigo dye by nitric acid and chromic acid, which resulted in isatin's bright

orange-colored monoclinic crystals product (3). Kekulé established isatin's present form, and the chemistry of isatins was initially studied by Sumpter and then revised by Popp and Silva et al.



Isatin

Figure 1: Chemical structure of Isatin.

Typically, isatin is found in the plant of the *Isatis* genus (4) in *Calanthe stain* LINDL.(5) and *Couroupita guianensis* Aubl. (6) and discharges

from the parotid organ of the bufo frog (7,8) and in people as it is a metabolic subsidiary of adrenaline (9). Different substituted isatin have likewise been distinguished in plants, for example, methoxy phenylmethyl isatin acquired from *Melochia tomentosa* (10,11), hydroxylated isatins

disengaged from *Streptomyces* (fungi)(12), and marine mollusks (13), where they are proposed to assume a guarded part against pathogenic creatures. Isatin is additionally discovered to be a part of coal tar (14).

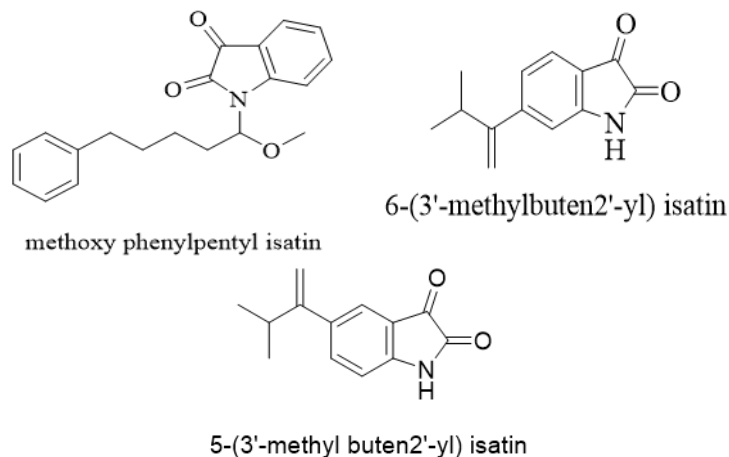


Figure 2: Structures of methoxyphenylpentyl isatin, 6-(3'-methylbuten 2'-yl) isatin and 5-(3'-methylbuten 2'-yl) isatin.

A thorough investigation of the manufacture and response of isatin, a compound with an indole motif, a ketone, and a - lactam moiety, revealed many intriguing chemical reactions and processes. Isatins' unique capacity to act as both an electrophile and a nucleophile and their wide distribution has made them important building blocks in organic synthesis. Syntheses of several heterocyclic structures of biological importance, such as indoles, β -lactams, pyrrolidine, quinolones and 2-oxindoles, etc. Literature survey revealed that isatin derivatives such as hydrazine, mannich bases, Schiff bases, and spiroindolinones possesses an extensive range of biological activities such as antimicrobial (15), antitumor (16), antimalarial (17), anti-HIV (18), analgesic,

antibacterial (19), anti-inflammatory (20), antiglycation (21), neuroprotective (22), antioxidant (23), anti-tubercular (24), antifungal (25), anticonvulsant (26), antidepressant (27), anticancer (28,29), antiplasmodial activity (30), anti-corrosive (31), antiepileptic (32), antidiabetic (7) and antiviral (33) anti-anxiety (34), and antiasthma (35). In 1965, an isatin-2,3-dione-based compound Metisazone was developed, it is an antiviral agent used against viral infections as a prophylactic agent (36). Food and Drug Administration, USA (FDA) approved an isatin derivative Sunitinib maleate to treat different malignancies such as advanced renal-cell carcinoma, pancreatic neuroendocrine tumors and gastrointestinal stromal tumors (37,38).

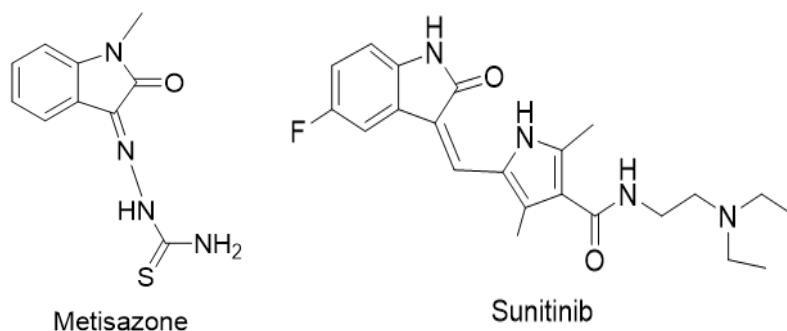


Figure 3: Structure of Metisazone and Sunitinib.

GENERAL METHODS FOR SYNTHESIS OF ISATINS

Metalation of Anilide Isatin Compound

A new strategy for creating isatin includes ortho-metalation (DoM) of N-pivaloyl- and N-(t-butoxycarbonyl)-anilines is presented. The dianions are treated with diethyl oxalate after deprotection and cyclization of the middle of the

road α -ketoesters, and isatins are created (Scheme 1). This technique for orchestrating 4-subbed isatins from meta-subbed anilines has the advantage of being regioselective (39).

Martinet's Isatin Synthesis

Isatin was made by responding a fragrant amino atom with an oxomalonate ester or its hydrate within sight of a corrosive to frame a 3-(3-hydroxy-2-oxindole) carboxylic corrosive subsidiary, which was then oxidatively decarboxylated to yield isatin (Scheme 2)(40).

Stolle's Isatin Synthesis

The Stolle isatin synthesis involves reacting anilines by oxalyl chloride to generate a chlorooxalylanilide intermediate, which is

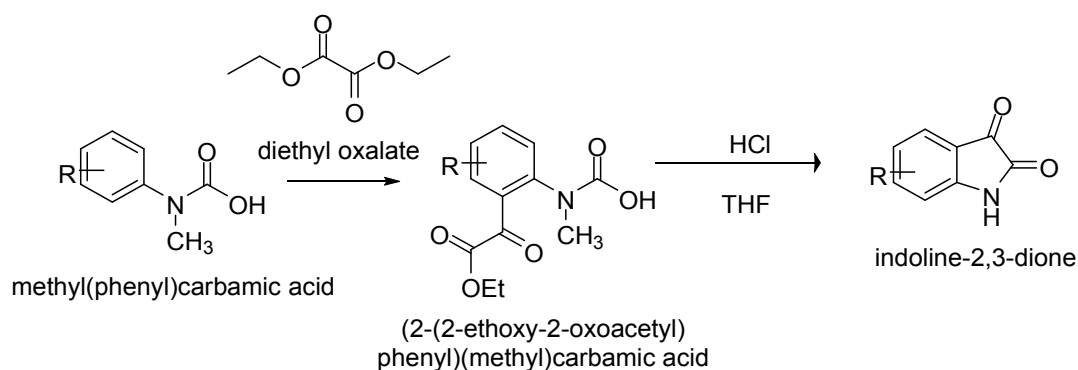
subsequently cyclized in a Lewis acid, commonly BF_3 , Et_2O , or aluminum chloride. However, TiCl_4 has been used as well (41).

Sandmeyer's Isatin Synthesis

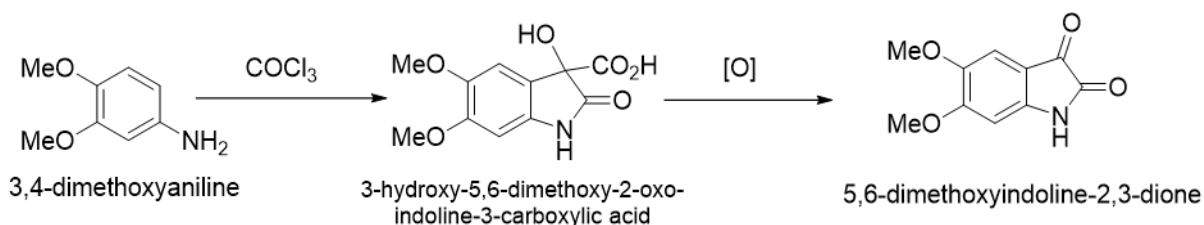
Isatin was made by combining aniline with chloral hydrate and hydroxylamine hydrochloride in aqueous sodium sulfate to generate an isonitrosoacetanilide, which was then separated following treatment with concentrated sulfuric acid to obtain >75 percent isatin (42).

Gassman's Isatin Synthesis

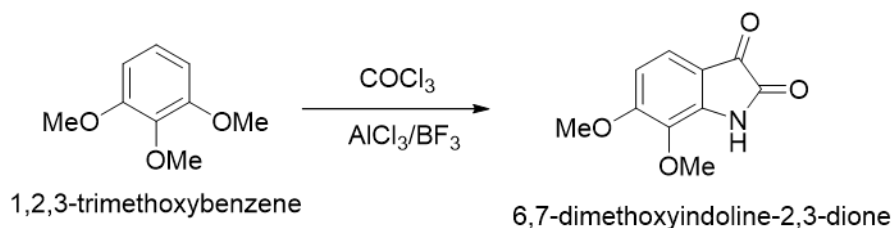
This procedure starts with creating an intermediate 3-methylthio-2-oxindole, which is then oxidized to produce substituted isatin (40-81 percent yield) (41).



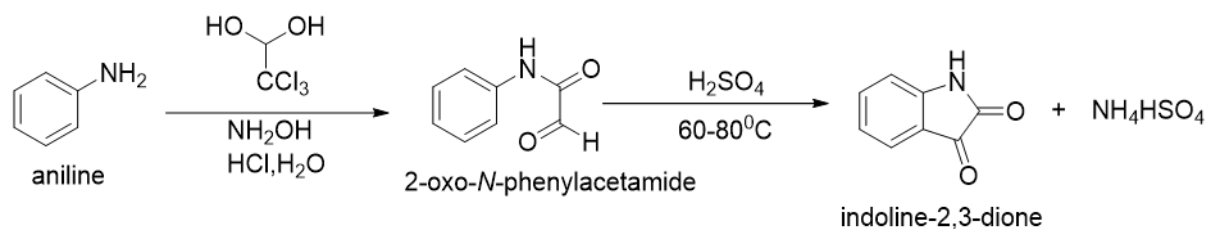
Scheme 1: Metalation of anilide isatin synthesis. Adapted from (39).



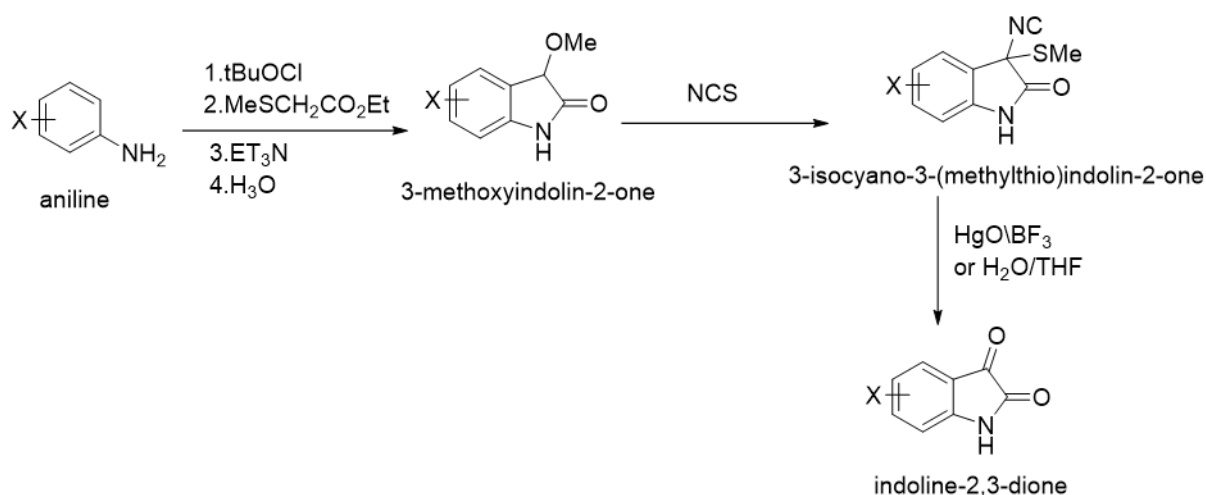
Scheme 2: Martinet's isatin synthesis. Adapted from (40).



Scheme 3: Stolle's isatin synthesis. Adapted from (41).



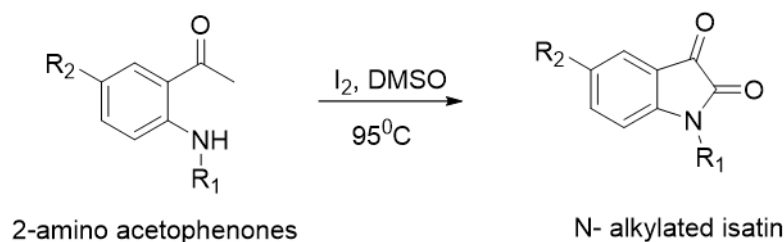
Scheme 4: Sandmeyer's isatin synthesis. Adapted from (42).



Scheme 5: Gassman's isatin synthesis. Adapted from (41).

To complete the synthesis of N-substituted isatins, several new synthetic methods have been devised. One such endeavor uses I₂-DMSO as a catalyst in a metal-free synthesis Scheme 6. The technique

involves activating the C-H bond and then internal cyclizing 2- amino acetophenones to make N-alkylated and N-arylated isatins (43).



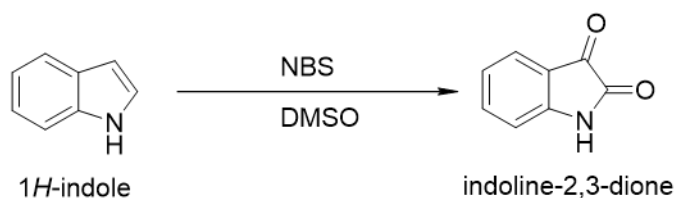
R₁ = H, Me, allyl, Et, Bn, 4-MeOBn, 4-ClBn, 4-FBn

R₂ = H, Cl, Me

Scheme 6: Combination of N-alkylated isatin subsidiaries from 2-amino acetophenones. Adapted from (43).

Indole, NBS, and anhyd. DMSO mixture were taken in a 3-necked R.B. flask that was clean and dry. The flask was heated to 60 °C for 6 hours under decreased pressure and 80 °C for 16 hours. After the reaction was finished, the mixture was placed

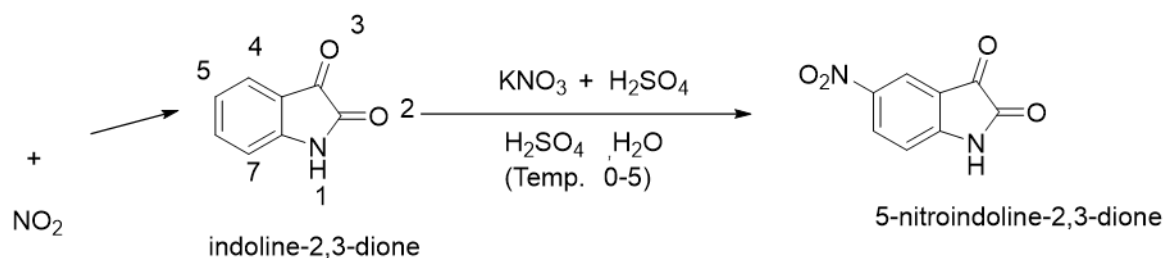
in water, and the extracts were extracted with dichloromethane. The sections were then dried over MgSO₄ and purified using silica gel chromatography with DCM as the eluent M.P.202 °C (Scheme 7)(44).



Scheme 7: Blend of isatin. Adapted from (44).

The reaction was carried out by dropping a solution of isatin, con. H₂SO₄, into a solution of at 0 to 5 °C for 1 hour, yielding 5- nitroisatin. 249-250 °C M.P.

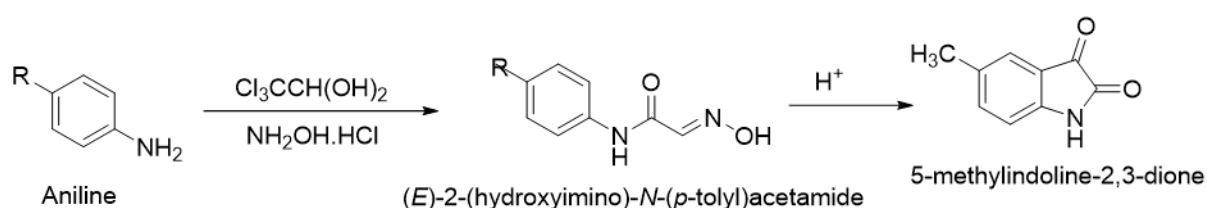
Isatin is nitrated at C-5 with KNO₃, in the presence of H₂SO₄. (Scheme 8)(44).



Scheme 8: Synthesis of 5-nitro-1H-indole-2,3-dione. Adapted from (44).

On reaction with chloral hydrate and hydroxylamine hydrochloride, isonitrosoacetanilides were produced from substituted anilines.

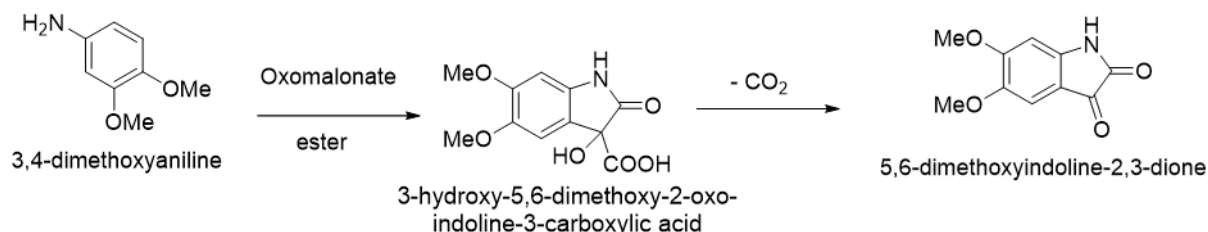
isonitrosoacetanilides gave equivalent indolin-2, 3-diones after reaction with sulfuric acid (Scheme 9) (45).



Scheme 9: Isonitrosoacetanilides have been synthesized from substituted anilines on reaction with chloral hydrate and hydroxylamine hydrochloride (45).

Isatins are made by responding a sweet-smelling amino atom with an oxomalonate ester or its hydrate within sight of a corrosive to create a 3-(3-hydroxy-2-oxindole) carboxylic corrosive

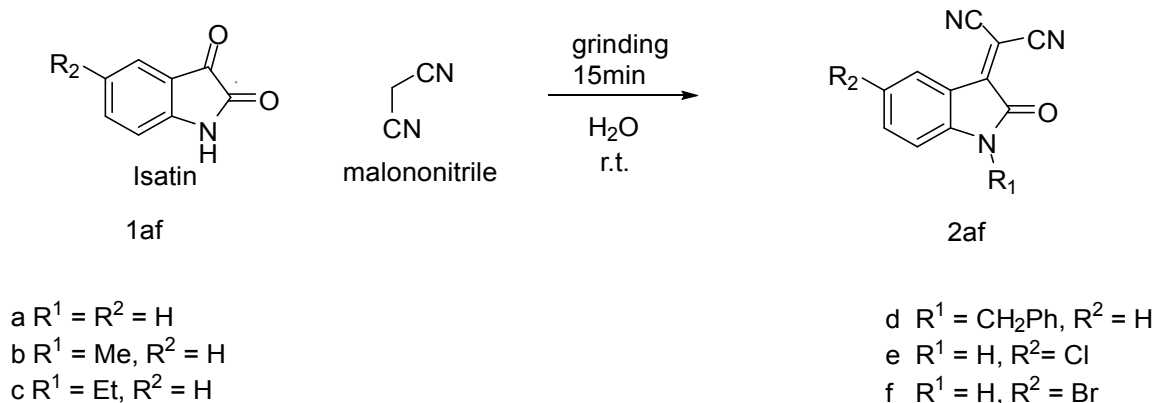
subsidiary, which is along these lines oxidatively decarboxylated to give the ideal isatin (Scheme 10)(46).



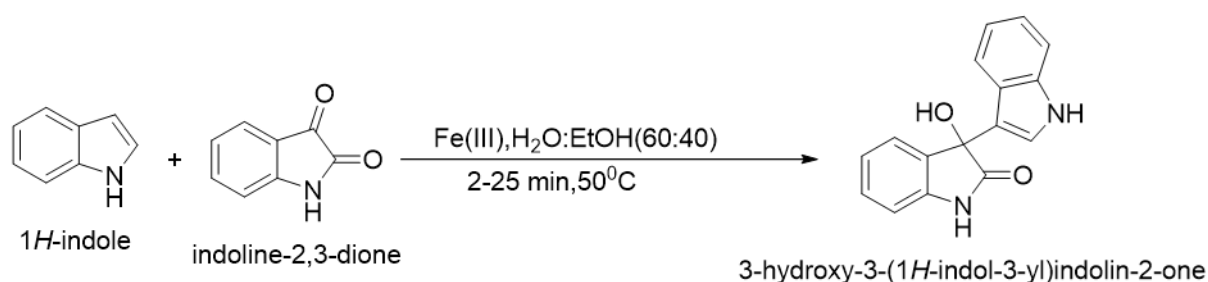
Scheme 10: Isatins are created when one aromatic amino molecule reacts with another aromatic amino molecule. Adapted from (46).

The related (2-oxo-1,2-dihydro-3H-indol-3-ylidene)malononitriles, the Knoevenagel condensation products, are obtained by grinding isatins with malononitrile for 15 minutes at room temperature in the presence of 1-5 equivalent of water (Scheme 11)(47).

Under ultrasonic irradiation, 3-(indol-3-yl)-3-hydroxyindolin-2-ones were synthesized from isatins and indoles using Fe(III) as a recyclable homogeneous catalyst (Scheme 12). It was discovered that the circumstances used resulted in 85-95 percent yields (48).



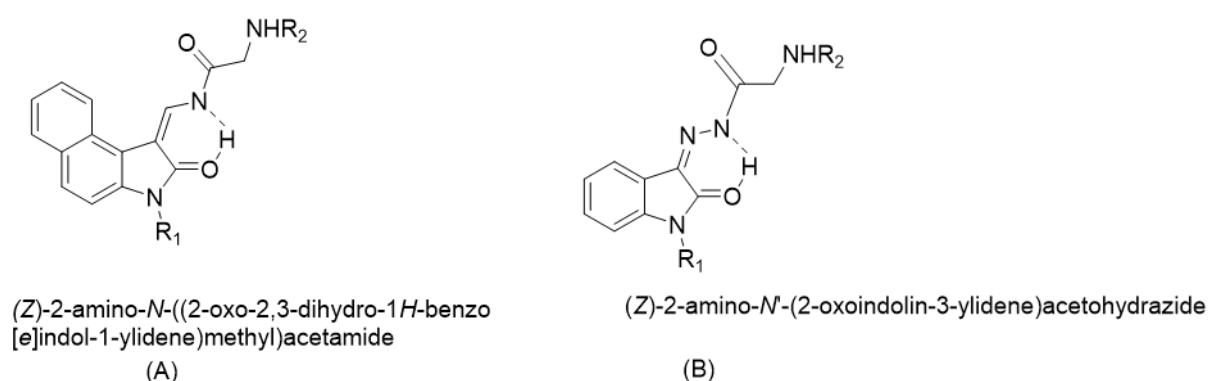
Scheme 11: Synthesis of isatines with malononitrile via Knoevenagel condensation. Adapted from (47).



Scheme 12: Ultrasound-advanced, Fe(III)-catalyzed 3-indolylolation of isatins. Adapted from (48).

The electrocatalytic change of isatins and barbituric acids in ethanol in a unified cell within sight of sodium produces subbed 5,5'- (2-oxo-2,3-dihydro-1H-indole-3,3-diyl) bis (pyrimidine-2,4,6(- 1H, 3H 5H)- triones (B) with 89–95 percent substance yields and 89–95 percent current yields (Scheme

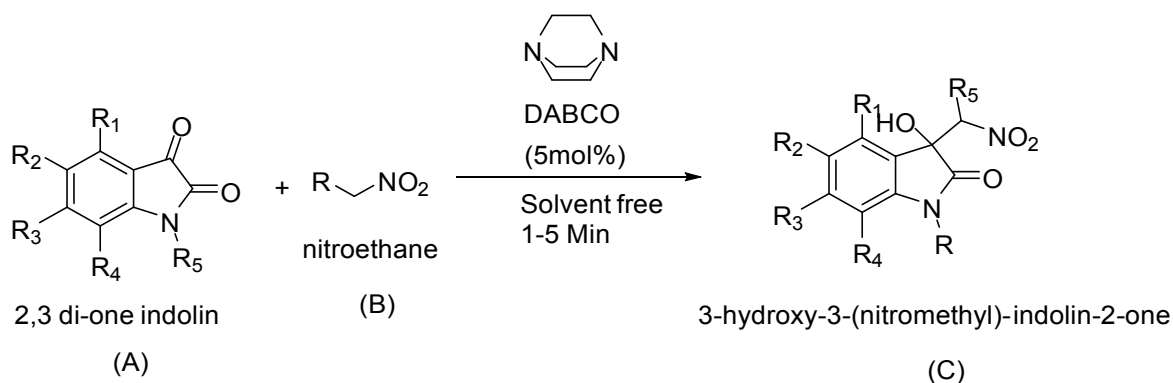
13). This novel and effective synergist strategy is fundamental because of its variety situated massive scope activities. It is an illustration of an electrocatalytic double response that is simple and biologically amicable (49).



Scheme 13: Isatin and barbituric acids are used to make a functionalized (2-oxo-2,3-dihydro-1H-indole-3,3-diyl) bis (pyrimidine) system. Adapted from (49).

The response of isatins to nitromethane/nitroethane in the presence of 1,4-diazabicyclo[2.2.2]octane (DABCO)(50) has been described as an efficient and universal technique

for the production of 3-hydroxy-3-(nitromethyl)-indolin-2-one (C). The reaction is catalytic and swift; yields are incredibly high, and no solvents are used.

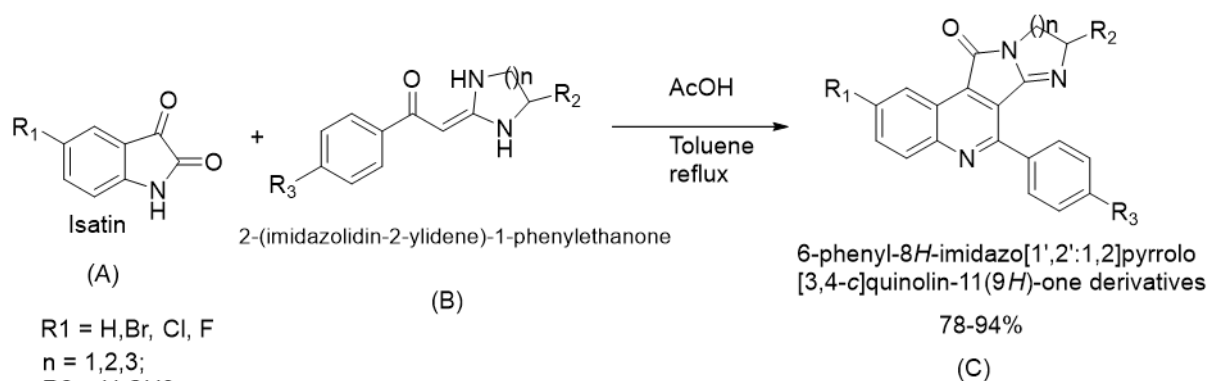


R = H, CH₃, Bn
 R₁= R₂= R₃ =R₄= H, 5-CH₃, 5-Cl, 5-Br, 5-I, 5-NO₂, 5-OCF₃
 R₅= H, CH₃
 1,4 diazabicyclo[2,2,2]octane(DABCO)

Scheme 14: 3-Formation of hydroxy-(nitromethyl) indolin-2-one derivatives utilizing DABCO as a catalyst. Adapted from (50).

By basically refluxing a response mixture of several types of isatins and heterocyclic ketene aminals (HKAs) with acetic acid, a straightforward and practical approach for synthesizing highly

substituted imidazopyrroloquinoline derivatives was devised (Scheme 15). In drug discovery, this method is appropriate for both combinatorial and equal blends (51).



R₁ = H, Br, Cl, F
 n = 1, 2, 3;
 R₂ = H, CH₃
 R₃ = CH₃O, CH₃, H, Cl

Scheme 15: Imidazopyrroloquinoline compounds with extensively modified substituents were synthesized. Adapted from (51).

CONCLUSIONS

Isatin is a heterocyclic compound that is vital for the blend of natural mixtures. Schiff bases of isatin, 3,3-disubstituted oxindoles, and spirooxindoles are a portion of the remarkable frameworks that might be created utilizing isatin as an antecedent material. They can function as electrophilic partners in many of the traditional aldehyde transformations, such as the production of 1,3-dipoles, the Knoevenagel reaction, and so on. On the other side, isatins have a sensitivity that is not seen in aldehydes, including ring-opening processes. The majority of these compounds also have biological and pharmacological characteristics. In recent times,

isatin has also been extensively used to produce a variety of chemical compounds.

REFERENCES

1. Prudhomme M. Advances in Anticancer Agents in Medicinal Chemistry. [Internet]. Sharjah: Bentham Science Publishers; 2013 [cited 2021 Sep 24]. <URL>.
2. Cândido-Bacani P de M, Reis MB dos, Serpeloni JM, Calvo TR, Vilegas W, Varanda EA, et al. Mutagenicity and genotoxicity of isatin in mammalian cells in vivo. Mutation Research/Genetic Toxicology and Environmental Mutagenesis. 2011 Feb;719(1-2):47-51.

3. Silva JFM da, Garden SJ, Pinto AC. The chemistry of isatins: a review from 1975 to 1999. *J Braz Chem Soc.* 2001 Jun;12(3):273–324. [<DOI>](#).
4. Borad MA, Bhoi MN, Prajapati NP, Patel HD. Review of Synthesis of Multispiro Heterocyclic Compounds from Isatin. *Synthetic Communications.* 2014 Apr 18;44(8):1043–57. [<DOI>](#).
5. Ramakrishna Reddy K, Mahendra K. N. Synthesis of 3-[(Z)-5-Amino-1, 3, 3-trimethyl cyclohexyl methylimino]-1, 3-dihydroindol-2-one as a novel Schiff base. *Molbank.* 2006 Dec 1;2006(6):M517. [<DOI>](#).
6. Singh GS, Desta ZY. Isatins As Privileged Molecules in Design and Synthesis of Spiro-Fused Cyclic Frameworks. *Chem Rev.* 2012 Nov 14;112(11):6104–55. [<DOI>](#).
7. Varun V, Sonam S, Kakkar R. Isatin and its derivatives: a survey of recent syntheses, reactions, and applications. *Med Chem Commun.* 2019;10(3):351–68. [<DOI>](#).
8. Khan FA, Maalik A. Advances in Pharmacology of Isatin and its Derivatives: A Review. *Trop J Pharm Res.* 2015 Nov 6;14(10):1937. [<DOI>](#).
9. Chiyanzu I, Hansell E, Gut J, Rosenthal PJ, McKerrow JH, Chibale K. Synthesis and evaluation of isatins and thiosemicarbazone derivatives against cruzain, falcipain-2 and rhodesain. *Bioorganic & Medicinal Chemistry Letters.* 2003 Oct;13(20):3527–30. [<DOI>](#).
10. Ali R, Gilani A-H, Choudhary M, Aftab K, Sener B, Turkoz S. Isolation of Antihypertensive Alkaloids from the Rhizomes of *Veratrum album*. *Planta Med.* 1993 Dec;59(06):569–71. [<DOI>](#).
11. Kapadia GJ, Shukla YN, Basak SP, Sokoloski EA, Fales HM. The melosatins—a novel class of alkaloids from *melochia tomentosa*. *Tetrahedron.* 1980 Jan;36(17):2441–7. [<DOI>](#).
12. Shaaban KA, Shaaban M, Nair V, Schuhmann I, Win HY, Lei L, et al. Structure elucidation and synthesis of hydroxylated isatins from *Streptomyces*. *Zeitschrift für Naturforschung B.* 2016 Dec 1;71(12):1191–8. [<DOI>](#).
13. Benkendorff K, Bremner J, Davis A. Indole Derivatives from the Egg Masses of Muricid Molluscs. *Molecules.* 2001 Jan 16;6(12):70–8. [<DOI>](#).
14. Mamedova YV, Hasanova AE, Gasimova SZ, Huseynova RA, Mamedov IG. Some isatin based synthesis. *New Materials, Compounds and Applications.* 2020;4(1):16–9.
15. Kumar M, Ramasamy K, Mani V, Mishra RK, Majeed ABA, Clercq ED, et al. Synthesis, antimicrobial, anticancer, antiviral evaluation and QSAR studies of 4-(1-aryl-2-oxo-1,2-dihydro-indol-3-ylideneamino)-N-substituted benzene sulfonamides. *Arabian Journal of Chemistry.* 2014 Sep;7(4):396–408. [<DOI>](#).
16. Havrylyuk D, Zimenkovsky B, Vasylenko O, Gzella A, Lesyk R. Synthesis of New 4-Thiazolidinone-, Pyrazoline-, and Isatin-Based Conjugates with Promising Antitumor Activity. *J Med Chem.* 2012 Oct 25;55(20):8630–41. [<DOI>](#).
17. Raj R, Singh P, Singh P, Gut J, Rosenthal PJ, Kumar V. Azide-alkyne cycloaddition en route to 1 H -1,2,3-triazole-tethered 7-chloroquinoline-isatin chimeras: Synthesis and antimalarial evaluation. *European Journal of Medicinal Chemistry.* 2013 Apr;62:590–6. [<DOI>](#).
18. Paul BK, Ray D, Guchhait N. Unraveling the binding interaction and kinetics of a prospective anti-HIV drug with a model transport protein: results and challenges. *Phys Chem Chem Phys.* 2013;15(4):1275–87. [<DOI>](#).
19. Kiran G, Maneshwar T, Rajeshwar Y, Sarangapani M. Microwave-Assisted Synthesis, Characterization, Antimicrobial and Antioxidant Activity of Some New Isatin Derivatives. *Journal of Chemistry.* 2013;2013:1–7. [<DOI>](#).
20. Prakash CR, Raja S, Saravanan G. Design and synthesis of 4-(1-(4-chlorobenzyl)-2,3-dioxindolin-5-yl)-1-(4-substituted/unsubstituted benzylidene) semicarbazide: Novel agents with analgesic, anti-inflammatory and ulcerogenic properties. *Chinese Chemical Letters.* 2012 May;23(5):541–4. [<DOI>](#).
21. Khan KM, Karim A, Ambreen N, Saied S, Rasheed S, Perveen S, et al. Synthesis of benzoxazoles derivatives: Antiglycation activity. *Journal of Pharmacy Research.* 2012;5(1):664–5.
22. Medvedev A, Buneeva O, Gnedenko O, Fedchenko V, Medvedeva M, Ivanov Y, et al. Isatin interaction with glyceraldehyde-3-phosphate dehydrogenase, a putative target of neuroprotective drugs: partial agonism with deprenyl. In: Parvez H, Riederer P, editors. *Oxidative Stress and Neuroprotection* [Internet]. Vienna: Springer Vienna; 2006 [cited 2021 Sep 24]. p. 97–103. (*Journal of Neural Transmission. Supplementa*; vol. 71). [<URL>](#).
23. Andreani A, Burnelli S, Granaiola M, Leoni A,

Locatelli A, Morigi R, et al. New isatin derivatives with antioxidant activity. *European Journal of Medicinal Chemistry*. 2010 Apr;45(4):1374–8. [<DOI>](#).

24. Kumar K, Carrère-Kremer S, Kremer L, Guérardel Y, Biot C, Kumar V. 1 H -1,2,3-Triazole-Tethered Isatin-Ferrocene and Isatin-Ferrocenylchalcone Conjugates: Synthesis and in Vitro Antitubercular Evaluation. *Organometallics*. 2013 Oct 28;32(20):5713–9. [<DOI>](#).

25. Jarrahpour A, Khalili D, De Clercq E, Salmi C, Brunel J. Synthesis, Antibacterial, Antifungal and Antiviral Activity Evaluation of Some New bis-Schiff Bases of Isatin and Their Derivatives. *Molecules*. 2007 Aug 7;12(8):1720–30. [<DOI>](#).

26. Saravanan G, Alagarsamy V, Dineshkumar P. Anticonvulsant activity of novel 1-(morpholinomethyl)-3-substituted isatin derivatives. *Bulletin of Faculty of Pharmacy, Cairo University*. 2014 Jun;52(1):115–24. [<DOI>](#).

27. Rane RA, Napahde S, Bangalore PK, Sahu NU, Shah N, Kulkarni YA, et al. Synthesis and Evaluation of Novel Marine Bromopyrrole Alkaloid-Based Derivatives as Potential Antidepressant Agents. *Chem Biol Drug Des*. 2014 Nov;84(5):593–602. [<DOI>](#).

28. Ibrahim S, Elsaman T. Cytotoxic and Anticancer Activities of Indoline-2,3-dione (Isatin) and Its Derivatives. *JPRI*. 2018 Feb 27;21(2):1–19. [<DOI>](#).

29. Lelyukh M, Havrylyuk D, Lesyk R. Synthesis and anticancer activity of isatin, oxadiazole and 4-thiazolidinone based conjugates. *Chemistry & Chemical Technology*. 2015;9(1):29–36. [<URL>](#).

30. Thakur RK, Joshi P, Upadhyaya K, Singh K, Sharma G, Shukla SK, et al. Synthesis of isatin based N1-alkylated 3-β-C-glycoconjugated-oxopropylidene oxindoles as potent antiplasmodial agents. *European Journal of Medicinal Chemistry*. 2019 Jan;162:448–54. [<DOI>](#).

31. Quraishi MA, Ahamad I, Singh AK, Shukla SK, Lal B, Singh V. N-(Piperidinomethyl)-3-[(pyridylidene)amino]isatin: A new and effective acid corrosion inhibitor for mild steel. *Materials Chemistry and Physics*. 2008 Dec;112(3):1035–9. [<DOI>](#).

32. Prakash CR, Raja S. Design, synthesis and antiepileptic properties of novel 1-(substituted benzylidene)-3-(1-(morpholino/piperidino methyl)-2,3-dioxindolin-5-yl)urea derivatives. *European Journal of Medicinal Chemistry*. 2011 Dec;46(12):6057–65. [<DOI>](#).

33. Kang I-J, Wang L-W, Hsu T-A, Yueh A, Lee C-C, Lee Y-C, et al. Isatin-β-thiosemicarbazones as potent herpes simplex virus inhibitors. *Bioorganic & Medicinal Chemistry Letters*. 2011 Apr;21(7):1948–52. [<DOI>](#).

34. Medvedev A, Igosheva N, Crumeyrolle-Arias M, Glover V. Isatin: Role in stress and anxiety: Review. *Stress*. 2005 Jan;8(3):175–83. [<DOI>](#).

35. Kandasamy R, Park SJ, Boyapalle S, Mohapatra S, Hellermann GR, Lockey RF, et al. Isatin down-regulates expression of atrial natriuretic peptide receptor A and inhibits airway inflammation in a mouse model of allergic asthma. *International Immunopharmacology*. 2010 Feb;10(2):218–25. [<DOI>](#).

36. Bogdanov AV, Zaripova IF, Voloshina AD, Sapunova AS, Kulik NV, Bukharov SV, et al. Synthesis and Biological Evaluation of New Isatin-Based QACs with High Antimicrobial Potency. *ChemistrySelect*. 2019 May 31;4(20):6162–6. [<DOI>](#).

37. Blumenthal GM, Cortazar P, Zhang JJ, Tang S, Sridhara R, Murgu A, et al. FDA Approval Summary: Sunitinib for the Treatment of Progressive Well-Differentiated Locally Advanced or Metastatic Pancreatic Neuroendocrine Tumors. *The Oncologist*. 2012 Aug;17(8):1108–13. [<DOI>](#).

38. Houk BE, Bello CL, Kang D, Amantea M. A Population Pharmacokinetic Meta-analysis of Sunitinib Malate (SU11248) and Its Primary Metabolite (SU12662) in Healthy Volunteers and Oncology Patients. *Clin Cancer Res*. 2009 Apr 1;15(7):2497–506. [<DOI>](#).

39. Ristovska N, Anastasova F, Stefova M. N"-[(3Z)-1-Acetyl-5-chloro-2-oxo-1,2-dihydro-3H-indol-3-ylidene]thiocarbonohydrazide. *Molbank*. 2013 Apr 16;2013(2):M798. [<DOI>](#).

40. Gassman P, Cue, Jr. B, Luh T-Y. A General Method for the Synthesis of Isatins. *J Org Chem*. 1977;42(8):1344–8. [<URL>](#).

41. Klein LL, Tufano MD. Synthesis of substituted isatins. *Tetrahedron Letters*. 2013 Feb;54(8):1008–11. [<URL>](#).

42. Mathur G, Nain S. Recent advancement in synthesis of isatin as anticonvulsant agents: a review. *Med Chem*. 2014;4(4):417–27.

43. Raghavender Reddy M, Nageswara Rao N, Ramakrishna K, Meshram HM. I2–DMSO promoted intramolecular oxidative cyclization of 2-(aryl or alkyl amino)-acetophenones for the synthesis of

isatins. *Tetrahedron Letters*. 2014 Aug;55(34):4758–62. [<DOI>](#).

44. Sonawane RP, Tripathi RR. The chemistry and synthesis of 1H-indole-2, 3-dione (Isatin) and its derivatives. *International Letters of Chemistry, Physics and Astronomy*. 2013;7.

45. Rewcastle GW, Sutherland HS, Weir CA, Blackburn AG, Denny WA. An improved synthesis of isonitrosoacetanilides. *Tetrahedron Letters*. 2005 Dec;46(50):8719–21. [<DOI>](#).

46. Vandana K, Marathakam A, Thushara B, Rajitha K. A Review on Isatin Derivatives With Diverse Biological Activities. *World Journal of Pharmaceutical Research*. 2017;6:318–32.

47. Demchuk DV, Elinson MN, Nikishin GI. 'On water'Knoevenagel condensation of isatins with malononitrile. *Mendeleev Communications*. 2011;4(21):224–5.

48. Khorshidi A, Tabatabaeian K. An ultrasound-promoted green approach for the synthesis of 3-

(indol-3-yl)-3-hydroxyindolin-2-ones catalyzed by Fe(III). *J Serb Chem Soc*. 2011;76(10):1347–53. [<DOI>](#).

49. Elinson MN, Merkulova VM, Ilovaisky AI, Barba F, Batanero B. Electrocatalytic tandem Knoevenagel–Michael addition of barbituric acids to isatins: Facile and efficient way to substituted 5,5'-(2-oxo-2,3-dihydro-1H-indole-3,3-diyl)bis(pyrimidine-2,4,6-(1H,3H,5H)-trione) scaffold. *Electrochimica Acta*. 2011 Oct;56(24):8219–23. [<DOI>](#).

50. Meshram HM, Ramesh P, Sanjeeva Kumar A, Swetha A. An efficient and environmentally friendly DABCO catalyzed Henry reaction of isatins. *Tetrahedron Letters*. 2011 Nov;52(44):5862–4. [<DOI>](#).

51. Yu F, Yan S, Hu L, Wang Y, Lin J. Cascade Reaction of Isatins with Heterocyclic Ketene Aminals: Synthesis of Imidazopyrroloquinoline Derivatives. *Org Lett*. 2011 Sep 16;13(18):4782–5. [<DOI>](#).



Evaluation of Corrosion Inhibition Properties of Pharmaceutically Active Compound Cefotaxime Sodium on Mild Steel Surface in Sulfuric Acid Medium

Sudhish Kumar SHUKLA* , Somya TANWER 

Department of Chemistry, Manav Rachna University, Faridabad (INDIA)

Abstract: Cefotaxime sodium is applied in various concentrations in 0.55 yds sulfuric acid for the mild steel and analyzed through weight loss, potentiodynamic polarization, and electrochemical impedance spectroscopy studies from 298 to 338 K. It gives better inhibition activity at lower temperature. Activation parameters, Gibbs free energy, enthalpy, and entropy of the reaction have been calculated. It was found that the inhibition process follows physical adsorption and the adsorption process follows Langmuir's adsorption isotherm. The inhibition behavior is supplemented by the surface study through atomic force microscopy and found that the inhibited surface has less roughness than the uninhibited surface.

Keywords: Eco-friendly inhibitors, weight loss, EIS, AFM.

Submitted: July 16, 2021. **Accepted:** September 22, 2021.

Cite this: Shukla S, Tanwer S. Evaluation of Corrosion Inhibition Properties of Pharmaceutically Active Compound Cefotaxime Sodium on Mild Steel Surface in Sulfuric Acid Medium. JOTCSA. 2021;8(4):1099-110.

DOI: <https://doi.org/10.18596/jotcsa.972325>.

***Corresponding author. E-mail:** sudhish.shukla@gmail.com.

INTRODUCTION

Corrosion is the natural phenomenon of the decadence of a material and its properties due to the synergy between the material and its active environment (1). The tendency of metal for corrosion to occur depends upon the surface structure and grain size, its chemical constituent, and the temperature of corrosive environment. Practically, the process of corrosion can be prevented rather than to eliminate completely. Corrosion plays a crucial role in environment, the mechanisms of corrosion is dependent upon the corrosive environment in which material surface is exposed. Corrosion depends upon these factors like metallic reactivity, presence of impurities in the metal, and corrosive medium, the presence of air, moisture, different corrosive gases like sulfur dioxide and carbon dioxide, and the presence of electrolytes (2). Corrosion is a critical and major industrial problem as it causes deterioration of metals and alloys in the presence of a corrosive environment generated by chemical or

electrochemical pathways. Corrosion is an associate degree irrecoverable reaction of a metal, ceramic, or chemical compound with its surroundings which ends up in its consumption or dissolution into the fabric of a part of the surroundings (3–6). It causes significant loss to the total GDP of the nation. Corrosion costs more than 2.0 lakh crores of the Indian economy per year (7–9). Corrosion costs glaring in the form untimely decadence or necessary maintenance failures, repairs, and replacement of damaged parts. Corrosion inhibition can be employed by using chemicals, however almost all chemicals/substances start corrosion in the presence of air, water and soil (10,11).

A chemical which, when added to a corrosive environment and hence reduces the rate of reaction of metal with its corrosive environment, is referred to as a corrosion inhibitor. Corrosive control of metals is aesthetically, economically, environmentally, and technically important (12). The inhibitor used is the best option to protect metals and alloys but there are some major

limitations of organic inhibitors which have leads to the development of green and sustainable inhibitor materials towards control the metal corrosion as they are less toxic, biodegradable, cost-effective, and ecologically acceptable. To replace these toxic and hazardous inhibitors with less toxic and less hazardous inhibitors, many research groups work on developing an environmentally benign sustainable non-toxic corrosion inhibitor likely to have oxygen, nitrogen, and sulfur-like heteroatoms. Numerous natural products and their applications as a corrosion inhibitor, especially in steel, are discussed. Green inhibitors (13) are a need of the time. Research on corrosion has been an interesting topic for quite a long time. Green inhibitors are an old dream in applied corrosion in industrial practice, but one of the challenges is to guarantee or to trust in the chemical stability of the compound. Most of the research groups infer that the inhibitor concentration required is on the higher side but it has its own disadvantages: The higher concentration cannot be guaranteed in real applications over a longer period of time. High concentrations of inexperienced (organic) corrosion inhibitors (14–16) may scale back the barrier properties of a coating and should be not even compatible with the organic coating etc.

In the last few decades, the drugs make their efficient role as a corrosion inhibitor which fascinates research attention. Literature review disclose that various types of drugs (antibacterial, antifungal, antibiotic, anti-malarial, analgesic, anti-depressant, anti-hypertensive, antihistamine) have been efficaciously vibrant as feasible corrosion inhibitors for decreasing effect of corrosion on mild steel and other metals and metal alloys (17–20). The imminent sections deliver comprehensive overview of the application of drugs and the literature on their corrosion inhibition studies. Most widely used metal in industry is mild steel in structural requirements. Acids are used in industrial applications for the purpose of pickling and descaling, etc. To minimize the corrosion due to these activities, corrosion inhibitors play a significant role to protect the metallic surfaces. Among various types of corrosion inhibitors, organic compounds are the most successful and profitable corrosion inhibitors for the protection of metallic surfaces (21). The inhibiting molecule may be adsorbed on the metallic surface due to physical or chemical interactions or it may be the combination of both. Generally organic and inorganic molecules act as corrosion inhibitors in practice are toxic in nature. Therefore, importance of the development of eco-friendly non-toxic corrosion inhibitors is the need of the day. In the current research, the development of corrosion inhibitors from commercially available drugs are used as corrosion inhibitors on metal surface owing to its low LD50 values (19, 22–28) in acidic media.

Cefotaxime sodium drug used in present study is a beta-lactam antibiotic classified as a third generation cephalosporin used to treat infections caused by bacteria. It is a cephalosporin organic sodium salt. Cefotaxime sodium is the commercial name of the sodium salt of [6R-[6- α ,7 β (z)]-3-[(acetyloxy)methyl]-[(2-amine-4-thiazolyl)(methoxyimino)acetyl]amino]-8-oxo-5-thia-1-azabicyclo[4,2,0]oct-2-ene-2-carboxylic acid (29, 30). In this paper, investigation of the corrosion inhibition activity of expired cefotaxime sodium drug is investigated towards surface of mild steel in 0.5 M H₂SO₄ using weight loss and electrochemical studies. Structure of the molecule is given in Figure 1 which has a molecular formula of C₁₆H₁₆N₅NaO₇S₂.

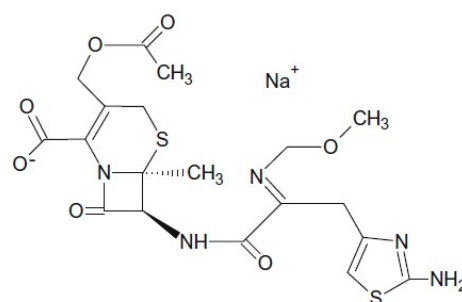


Figure 1: Chemical structure of cefotaxime sodium.

EXPERIMENTAL

Inhibitor

Cefotaxime sodium was procured from a common medicine shop and kept till the expiry date is over and the stock solution of this compound is made with water for all the experiments using dilution method for various concentrations of inhibitors (29)

Corrosion measurements

Corrosion measurements will be done on mild steel having composition (wt%) P=0.03; Mn=0.035; C=0.14; S=0.025; Si=0.17; and Fe (remains). The mild steel surface duly cleaned by emery papers and cleaned with deionized water. Acetone is used for degreasing process and the samples were further dried in hot air blower and placed in desiccator for experiments.

Weight loss technique

This study is performed on mild steel of 10 cm² area and having rectangular shape in 100 mL of acidic solution in various concentrations of inhibitors (from zero to optimum) at different temperature ranges. All the experiments were done in triplicate and the results are found to be a deviation of less than 0.1% which is due to manual error. To minimize the discrepancy, weight loss average in each condition has been taken in consideration for the calculation of different parameters. %Inhibition efficiency, corrosion rate, surface coverage, and calculation of thermodynamic and adsorption parameters were calculated as mentioned in literature (31), (32).

$$I. E. (\%) = \frac{W_0 - W_i}{W_0} \times 100 \quad (1)$$

$$\Theta = \frac{W_0 - W_i}{W_0} \quad (2)$$

W_0 = weight loss of metal in the absence cefotaxime sodium,
 W_i = Weight loss in the presence of cefotaxime sodium.

Electrochemical techniques

Polarization resistance, Tafel polarization, and EIS is conducted three electrode assembly where calomel electrode acts as reference electrode, platinum as the counter electrode, and metal sample for test as the working electrode. Working electrode area will be 1 cm². Gamry Instruments potentiostat / galvanostat with Gamry frame work system on ESA 400 for all the electrochemical studies and analysis will be done through Echem analyst version 5.50 software packages for data fitting. All the measurements will be done with the parameters reported in literature (21, 33, 34). All electrochemical studies like linear polarization, Tafel polarization and electrochemical impedance spectroscopy has been reproduces before reporting the results.

RESULTS & DISCUSSIONS

Weight loss measurements:

Weight loss measurement of the metal strip is used to calculate inhibition efficiencies (η %), corrosion rates (C_r , in mmpy), and surface coverage (θ) for varying temperatures and they are reported in Table 1. Inhibition efficiency of the cefotaxime sodium increases with the increase in the inhibitor concentration from 0 to 4.5×10^{-4} M. It was apparent from the Table 1 that while varying the temperature from 298 K to 338 K of 0.5 M H₂SO₄ solution, efficiency of inhibitor was always the highest at 4.5×10^{-4} M inhibitor percentage whereas increasing the percentage of drug in concentration makes negligible change in efficiency either in positive or negative data change. The maximum inhibitor efficiency was found at 289 K to be 95.7%, but it seems to be decreasing at various increasing temperature change in 4.5×10^{-4} M inhibitory mixture, so 4.5×10^{-4} M inhibitory percentage was found to be the best suited amount in mixture to provide 95.5% inhibitory efficiency at 298 K temperature. This inhibitory action is caused by the molecular adsorption of cefotaxime sodium on the surface of mild steel. Adsorption may be due to both π -electrons and non-bonding lone pair of electrons. These properties can also be responsible for the inhibitive action. The same has been plotted in Figures 2 and 3 report the required inhibitor efficiency at varying temperature range of mixture with respect to inhibitor efficiency and corrosion rate, respectively.

Table 1: Weight loss measurement data in absence and presence of cefotaxime sodium in towards mild steel in the aqueous solution of 0.5 M sulfuric acid.

Temperature (K)	Concentration of inhibitor (M)	Weight loss (in mg cm ⁻¹)	Inhibition efficiency (η) (%)	Corrosion rate (C _r) (mm/y)	Surface coverage (θ)
298	Blank	14.00	-	52.14	-
	0.5×10^{-4}	5.59	60.1	20.81	0.601
	1.0×10^{-4}	4.54	67.6	16.89	0.676
	1.5×10^{-4}	3.42	75.6	12.72	0.756
	2.0×10^{-4}	2.60	81.4	9.70	0.814
	2.5×10^{-4}	1.97	85.9	7.35	0.859
	3.0×10^{-4}	1.39	90.1	5.16	0.901
	3.5×10^{-4}	0.95	93.2	3.55	0.932
	4.0×10^{-4}	0.63	95.5	2.35	0.955
	4.5×10^{-4}	0.60	95.7	2.24	0.957
308	Blank	17.17	-	63.94	-
	0.5×10^{-4}	8.03	53.2	29.92	0.532
	1.0×10^{-4}	6.40	62.7	23.84	0.627
	1.5×10^{-4}	4.87	71.7	18.13	0.717
	2.0×10^{-4}	3.67	78.6	13.66	0.786
	2.5×10^{-4}	2.97	82.7	11.05	0.827
	3.0×10^{-4}	2.27	86.7	8.44	0.868
	3.5×10^{-4}	1.73	89.9	6.46	0.899
	4.0×10^{-4}	0.97	94.4	3.60	0.944
	4.5×10^{-4}	0.97	94.4	3.60	0.944
318	Blank	26.05	-	97.01	-
	0.5×10^{-4}	13.44	48.4	50.06	0.484
	1.0×10^{-4}	11.62	55.4	43.27	0.554
	1.5×10^{-4}	9.87	62.1	36.77	0.621

	2.0×10^{-4}	7.79	70.1	29.00	0.701
	2.5×10^{-4}	5.89	77.4	21.92	0.774
	3.0×10^{-4}	4.32	83.4	16.10	0.834
	3.5×10^{-4}	3.28	87.4	12.22	0.874
	4.0×10^{-4}	2.29	91.2	8.54	0.912
	4.5×10^{-4}	2.55	90.2	9.50	0.902
328	Blank	33.74	-	125.66	-
	0.5×10^{-4}	19.57	42	72.88	0.420
	1.0×10^{-4}	17.71	47.5	65.97	0.475
	1.5×10^{-4}	15.39	54.4	57.30	0.544
	2.0×10^{-4}	12.85	61.9	47.88	0.619
	2.5×10^{-4}	11.34	66.4	42.22	0.664
	3.0×10^{-4}	9.28	72.5	34.56	0.725
	3.5×10^{-4}	7.29	78.4	27.14	0.784
	4.0×10^{-4}	7.25	78.5	27.02	0.785
	4.5×10^{-4}	7.05	79.1	26.26	0.791
338	Blank	43.06	-	160.38	-
	0.5×10^{-4}	31.22	27.5	116.27	0.275
	1.0×10^{-4}	27.82	35.4	103.60	0.354
	1.5×10^{-4}	24.37	43.4	90.77	0.434
	2.0×10^{-4}	21.49	50.1	80.03	0.501
	2.5×10^{-4}	19.29	55.2	71.85	0.552
	3.0×10^{-4}	15.42	64.2	57.41	0.642
	3.5×10^{-4}	14.68	65.9	54.69	0.659
	4.0×10^{-4}	14.60	66.1	54.37	0.661
	4.5×10^{-4}	15.29	64.5	56.93	0.645

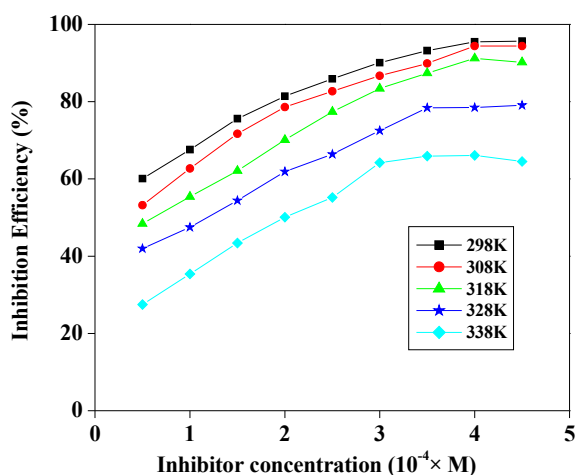


Figure 2: Inhibitor efficiency at varying temperatures on standard find concentration of the inhibitor.

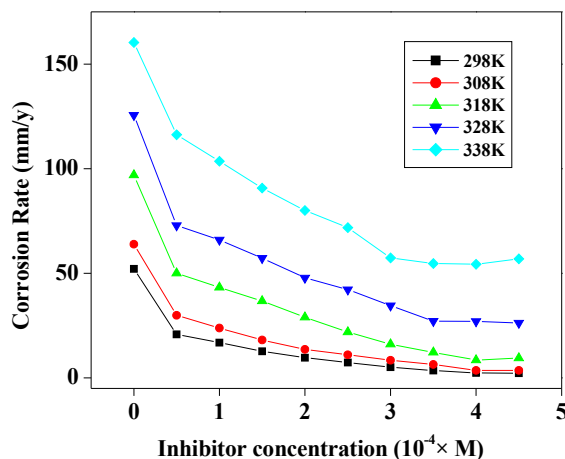


Figure 3: Corrosion rate at varying temperatures at various concentrations of cefotaxime sodium.

Effect of solution temperature on the adsorption isotherm

It is crucial to understand how organo-electrochemical reactions work through adsorption isotherms. It was tested using different isotherms by C_{inh} vs C_{inh}/θ graph (3, 35), for the experimental results presented in this trial, Langmuir adsorption isotherm was considered adequate due to most linear representation of regression coefficient (R^2). A mild steel plate, already discussed above, has been initiated for test in 0.5 M H_2SO_4 solution with 0.5×10^{-4} M inhibitor concentration in combination with the steel surface at a varying temperature range from 298 K -338 K and represented in Figure 4,

which shows the linear regression coefficient and slope of the graph. The values of R^2 listed in Table 2 range from 0.99765 to 0.98973 to extend the temperature range of the mixture from 298-338 K. Due to the presence of n-electrons, and a quaternary nitrogen atom, it has proved perfectly suited for 4.0×10^{-4} M at a temperature of 298 K at the MS surface. Desorption of inhibitor may be the reason for this phenomenon. The $-\Delta G_{ads}$ values have been calculated and reported in Table 2, and they are between $31.13 \text{ kJ mol}^{-1}$ to $38.34 \text{ kJ mol}^{-1}$, corresponding to a range of 20 to 40 kJ mol^{-1} . This suggests that the inhibitor is adsorbed on the metal surface is physically (36).

Table 2: Adsorption parameters of cefotaxime sodium on mild steel surface at different temperature ranges.

Temperature (K)	K_{ads} (Mol^{-1})	Slope	R^2	$-\Delta G_{ads}$ ($KJ \text{ mol}^{-1}$)
298	5.1×10^3	0.94	0.99765	31.13
308	6.4×10^3	0.92	0.99793	32.72
318	8.5×10^3	0.92	0.99332	34.56
328	9.9×10^3	1.04	0.99281	36.07
338	1.5×10^4	1.16	0.98973	38.34

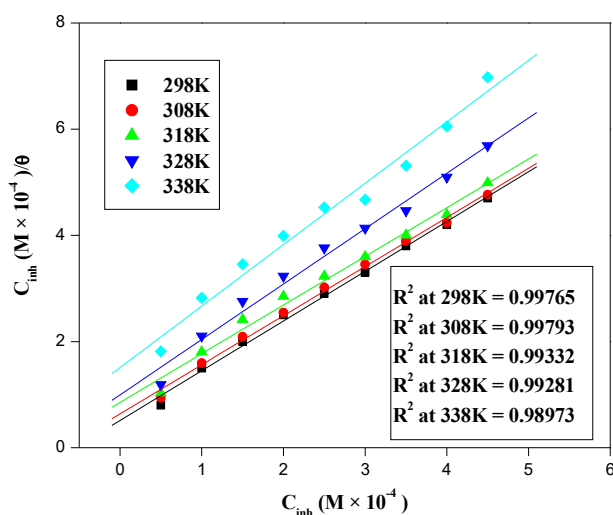


Figure 4: Langmuir's adsorption isotherm for different concentrations of cefotaxime sodium in 0.5 M sulfuric acid solution.

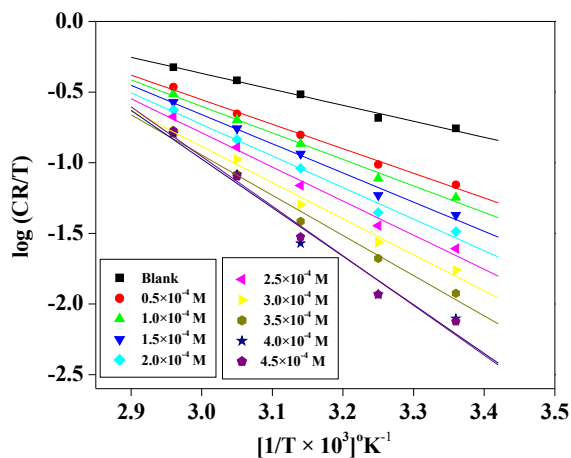


Figure 5: Transition state graph in the absence and presence of different concentrations of cefotaxime sodium for mild steel corrosion in 0.5 M sulfuric acid.

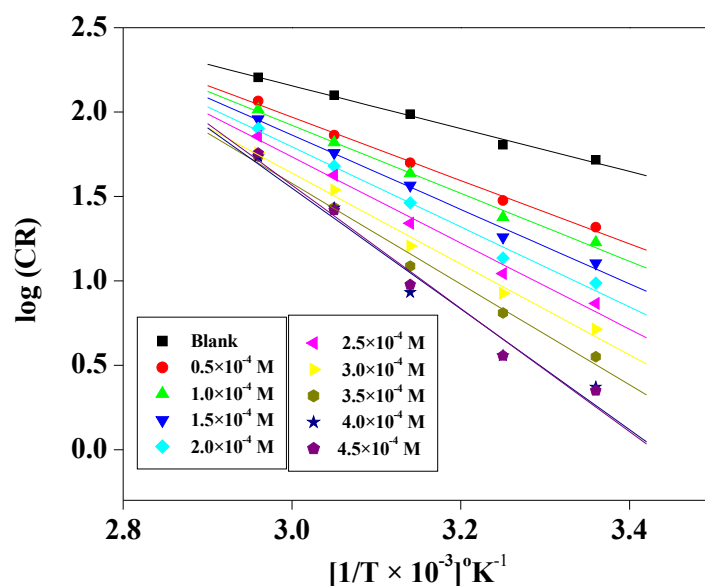


Figure 6: Arrhenius' plot of the cefotaxime sodium in 0.5 M sulfuric acid solution.

Activation parameters on the inhibition process

Temperature of the solution is key to understand the inhibitive process of corrosion. For observing the effect of temperature samples has been tested at 298 to 338 K for different concentrations of the cefotaxime sodium and inhibition efficiency and corrosion rate has been calculated and listed in Table 1. Corrosion rate at various temperatures of solution and concentration of inhibitors are correlated with the Arrhenius equation to express the relationship of corrosion rate with the temperature of acidic media (37-40).

$$\log(C_r) = \frac{-E_a}{2.303 RT} + \log \lambda \quad (\text{Eq. 3})$$

Where E_a = apparent effective activation energy,
 R = molar gas constant
 λ = Arrhenius' pre exponential factor.

A graph of CR Vs. $1/T$ has been plotted in Figure 6 which shows the regression coefficient approximately very close to unity. E_a values are calculated from the slope of the curve. The slope of the curve is equivalent to $-E_a/2.303 R$ and λ value can be calculated from the intercept which is equivalent to the $\log \lambda$. Calculated values of these two has been listed in Table 3. Value of activation energy is more than that of uninhibited sample and increasing though out the increment of the inhibitor concentration suggested that the adsorption of the inhibitor on the mild steel surface is physical adsorption. Subsequent increase in the activation energy also suggests that the inhibitor is less effective on increasing temperature towards the mild steel surface at 0.5 M sulfuric acid medium. As per observation of Arrhenius equation it is found that the corrosion rate is also influence by λ increasing the value decreases the corrosion rate (41).

Table 3: Thermodynamic parameters in absence and presence different concentration ranges of cefotaxime sodium for mild steel.

Concentration of inhibitor (M)	E_a (kJ mol ⁻¹)	λ (mg cm ⁻²)	ΔH (kJ mol ⁻¹)	ΔS (J mol ⁻¹ K ⁻¹)
Blank	24.29	9.14×10^5	21.68	-142.25
0.5×10^{-4}	35.92	3.95×10^7	33.30	-110.93
1.0×10^{-4}	38.54	9.10×10^7	35.92	-103.99
1.5×10^{-4}	42.19	2.98×10^8	39.58	-94.12
2.0×10^{-4}	45.41	8.11×10^8	42.80	-85.81
2.5×10^{-4}	48.86	2.45×10^9	46.25	-76.60
3.0×10^{-4}	51.58	5.24×10^9	48.96	-70.29
3.5×10^{-4}	57.11	3.35×10^{10}	54.50	-54.86
4.0×10^{-4}	68.49	1.90×10^{12}	65.88	-21.27
4.5×10^{-4}	69.91	3.32×10^{12}	67.30	-16.65

Value of enthalpy of activation (ΔH) and entropy of complex in transition state equation can be activation (ΔS) for the formation of the activated

calculated by alternative Arrhenius equation i.e. transition state equation (42, 43).

$$C_r = \frac{RT}{Nh} \exp\left(\frac{\Delta S}{R}\right) \exp\left(\frac{-\Delta H}{RT}\right) \quad (4)$$

Where h = Planck's constant,
N = Avogadro's number,
 ΔS = entropy of activation
 ΔH = enthalpy of activation.

A graph of $\log (CR/T)$ versus $1/T$ has been plotted as represented in Figure 5 which is a straight line. Values of enthalpy of activation (ΔH) and entropy of activation (ΔS) has been calculated from the slope and intercept of the curves and listed in Table 3. As per Table 3, in the inhibition process the value of the enthalpy is increasing with the increase in the inhibitor concentration. The positive value of enthalpy of activation reflects that the corrosion inhibition phenomenon is endothermic and dissolution of metal is difficult by increasing the inhibitor concentration (44). Higher protection efficiency is due to the presence of energy barrier for the reaction.

Entropy of activation (ΔS) is increasing with an increase in the inhibitor concentration as compared to the compared to free acid solution. Increased entropy of activation in the presence of inhibitor indicated that disorderness is increased on going from reactant to activated complex. Therefore the inhibition efficiency will increase.

Linear Polarization technique

Linear polarization data were listed in Table 4. Polarization resistance value increases with increase in inhibitor concentration results the increase in inhibition efficiency of the inhibitor used in the study. Maximum inhibition efficiency is

approximately 93%, which is in good agreement with the inhibition efficiency exhibited in the weight loss studies.

Tafel Polarization

Measurements of polarization have been measured and documented. Figure 6 shows plots demonstrating the effect of cefotaxime sodium concentrations on the anodic and cathodic polarization actions of mild stain in 0.5 M H_2SO_4 solution. Table 4 shows the electrochemical properties of plots, such as the density of corrosion current (I_{corr}), the potential for corrosion (E_{corr}), the anodic slopes (b_a and b_c), the resistance to polarization (R_p), and the inhibitor performance (IE percent) (45). As seen in Table 4, the addition of cefotaxime sodium to the 0.5 M H_2SO_4 solutions inhibit both anodic metal dissolution and cathode hydrogen evolution. Table 4 demonstrates that, when the concentration of cefotaxime sodium was increased, the inhibition of these reactions became more pronounced. Without causing major improvements in the tendency for corrosion, the inhibitor results in a lower I_{corr} corrosion current density, indicating that a mixed form inhibitor (i.e. prevents both anodic and cathodic corrosion) is adsorbed on the surface, preventing corrosion (46). Without an inhibitor, the ability of mild steel became involved and changed to 455 mV (SCE) as a more negative value due to the dissolution of an air-molded oxide film, as seen in Figure 6. With the addition of an inhibitor to the solution, the potential shifted to the positive side, and the shift became more pronounced as the inhibitor's concentration rose. The established I_{corr} density decrease was detected as cefotaxime sodium levels increased, indicating that the inhibitor's inhibitory efficacy increased as the inhibitor's concentration increased. This is the beginning of the production of protective oxide-and-cefotaxime films.

Table 4: Potentiodynamic polarization parameters for cefotaxime sodium in sulfuric acid medium on mild steel surface.

Inhibitor Conc.	Tafel data					Linear Polarization data		
	$-E_{corr}$ (mV SCE)	vs	b_a (mV dec ⁻¹)	b_c (mV dec ⁻¹)	I_{corr} ($\mu A cm^{-2}$)	IE (%)	R_p (Ωcm^2)	IE (%)
Blank	455		63	137	1275	-	55.3	-
1.0×10^{-4}	457		71	147	478	62.5	137.3	59.7
2.0×10^{-4}	460		72	151	284	77.7	255.8	78.3
3.0×10^{-4}	462		71	144	175	86.3	398.1	86.1
4.0×10^{-4}	465		74	152	88	93.7	796.4	93.0

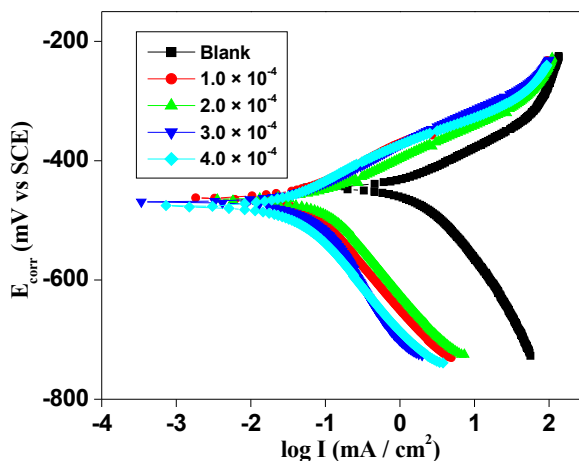


Figure 7: Tafel polarization curve with different concentrations of cefotaxime sodium on mild steel in 0.5 M sulfuric acid.

Electrochemical Impedance Spectroscopy techniques

Corrosion inhibition activity cefotaxime sodium was investigated using electrochemical impedance spectroscopy on mild steel surfaces in 0.5 M aqueous H₂SO₄ solution. Figure 7 depicts an impedance spectrum i.e. Nyquist plot mild steel corrosion where the depressed semicircles look like a depressed capacitive ring. A high frequency single semicircle, which can be transmitted via the loading phase of corrosion and the surface heterogeneity, is due to these factors which can be exacerbated by surface ruggedness, dislocations at the active site or adsorption by the inhibitor molecules represented in Figure 7. The impedance electrochemical data would be compared to F. Mansfeld's multiple theoretical circuits. The analogous circuit was applied at a

constant phase angle to demonstrate the impedance data applicable to the iron/acid interface model (47). For electrochemical impedance, the corresponding circuit parameters (R_s , R_t , Y_0 , and n) have been obtained and reported in Table 5.

The inhibitor's adsorption effect is similar to the impedance distribution on the metal surface. Adsorption of drug inhibitor molecules causes polarization resistance R_p , which increases with the number of adsorbed molecules. Furthermore, the adsorbed inhibitor film reduces capacitance at the metal-solution interface as a result of a reduction in the dielectric constant between metal and electrolyte and/or an improvement in thickness of metal (48–50).

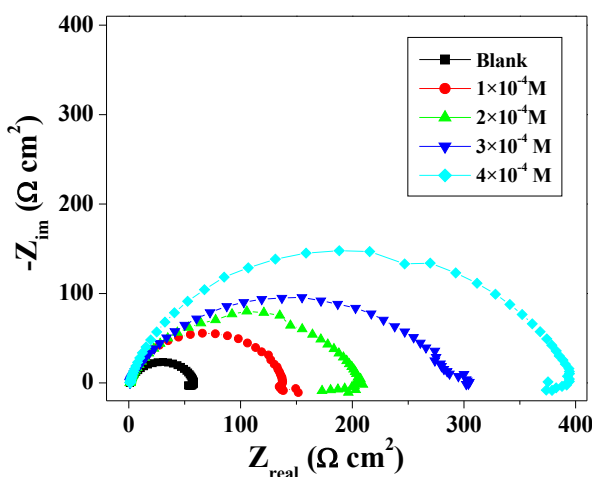


Figure 8: Nyquist plot of the electrochemical impedance spectroscopy curve of different concentrations of cefotaxime sodium on mild steel surface in 0.5 M sulfuric acid.

Table 5: Electrochemical impedance parameters values of cefotaxime sodium in 0.5M sulfuric acid

Inhibitor concentration (ppm)	R_s ($\Omega \text{ cm}^{-2}$)	R_p ($\Omega \text{ cm}^{-2}$)	Y_o ($\mu\text{F cm}^{-2}$)	N	C_{dl} ($\mu\text{F cm}^{-2}$)	IE (%)
Blank	1.13	53.3	1181.5	0.858	55	-
1.0×10^{-4}	1.07	141.8	205.7	0.836	48	62.4
2.0×10^{-4}	1.09	214.3	112.3	0.831	42	75.1
3.0×10^{-4}	0.96	309.9	87.5	0.825	38	82.8
4.0×10^{-4}	0.99	401.4	74.3	0.822	35	86.7

Surface Study (AFM)

Atomic force microscopic technique is used to know morphology of the surface of mild steel unexposed in corrosive environment, exposed in corrosive environment without inhibitor and with optimum concentration of cefotaxime sodium inhibitor and

the surface morphology is represented in Figure 8a-c. Surface roughness of untreated, uninhibited, and inhibited surface of mild steel are 51 nm, 590 nm, and 154 nm, respectively. Decrease in surface roughness shows the effectiveness of the cefotaxime sodium.

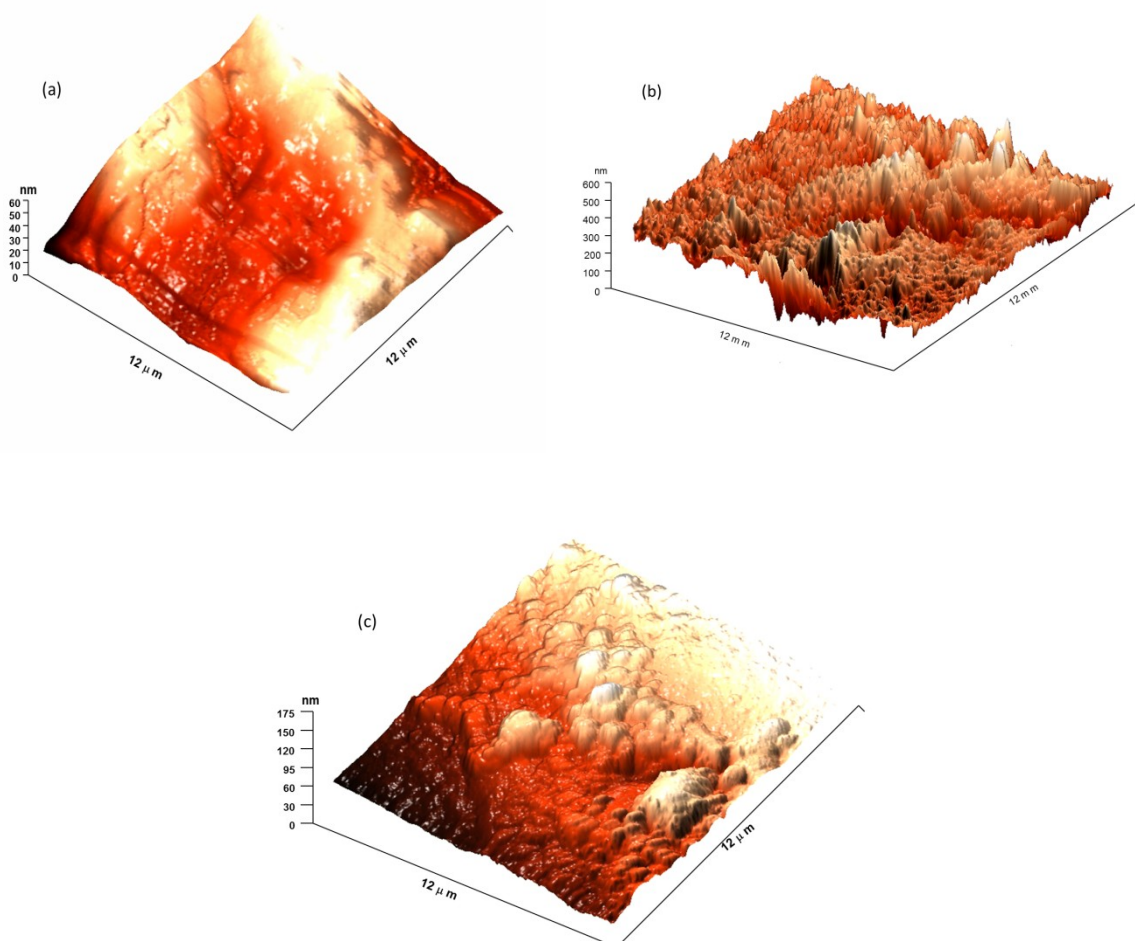


Figure 9: AFM studies of mild steel surface (a) polished surface, (b) surface exposed in corrosive medium without inhibitor, (c) surface exposed in corrosive medium with optimum concentration of cefotaxime sodium inhibitor.

CONCLUSION

- It is evident from all studies that cefotaxime sodium is good inhibitor for the surface of mild steel in 0.5M sulfuric acid medium.

- Increase in the temperature of the test solution results the decrease in the inhibitor efficiency suggest that it is a good inhibitor at lower temperature range.

- Electrochemical studies suggested that it is a mixed type of inhibitor and adsorbed on the surface in monolayer.
- Adsorption of cefotaxime sodium follows Langmuir adsorption isotherm.
- All the thermodynamic and adsorption parameters suggested that the interaction of the inhibitor on mild steel surface is of the physical adsorption type.

REFERENCES

1. Adejoro IA, Ojo FK, Obafemi SK. Corrosion inhibition potentials of ampicillin for mild steel in hydrochloric acid solution. *Journal of Taibah University for Science*. 2015 Apr;9(2):196-202. [<DOI>](#).
2. Sastri V. Types of corrosion inhibitor for managing corrosion in underground pipelines. Woodhead Publishing Limited; 2014.
3. Kuznetsov Y. Organic Inhibitors of corrosion of Metals. Thomas J, editor. Springer Science+ Business Media, LLC; 1996.
4. Roberge P. Handbook of Corrosion Engineering. 2nd Edition. McGraw-Hill Companies; 2012.
5. Kruger J. Cost of Metallic Corrosion. In: Revie RW, editor. Uhlig's Corrosion Handbook [Internet]. Hoboken, NJ, USA: John Wiley & Sons, Inc.; 2011 [cited 2021 Sep 25]. p. 15-20. ISBN: 978-0-470-08032-0. [<URL>](#).
6. Singh AK, Singh S, Ebenso EE. Cefacetriple as corrosion inhibitors for mild steel in acidic media. *International Journal of Electrochemical Science*. 2011;6:5689-700.
7. Anonymous. The Annual Cost of Corrosion to Ohio [Internet]. 2007. Available from: http://www.brown.senate.gov/imo/media/doc/Ohio_Corrosion.pdf
8. Bhaskaran, R, Palaniswamy, N, Rengaswamy, NS. COST OF CORROSION AND CORROSION AUDITING IN INDIAN INDUSTRIES. *Corrosion Reviews*. 2009 Dec;27(Supplement):1-35.
9. NACE International. NACE-international Cost of corrosion study unveiled. *Mater Perform*. 2002; (July):20.
10. Ebenso EE, Khaled K, Shukla SK, Singh AK, Eddy N, Saracoglu M, et al. Quantum chemical investigations on quinoline derivatives as effective corrosion inhibitors for mild steel in acidic medium. *Int J Electrochem Sci*. 2012.
11. Raja PB, Ismail M, Ghoreishiamiri S, Mirza J, Ismail MC, Kakooei S, et al. Reviews on Corrosion Inhibitors: A Short View. *Chemical Engineering Communications*. 2016 Sep 1;203(9):1145-56. [<DOI>](#).
12. Dwivedi A, Bharti PK, Shukla SK. An overview of the polymeric material that can be used to prevent Metal corrosion: A Review. *Journal of Turkish Chemical Society Section A: Chemistry*, 2021; 8(3):863-72. [<DOI>](#).
13. Palou R, Olivares-Xomelt O, Likhanova N. Environmentally Friendly Corrosion Inhibitors. In: *Green Corrosion Inhibitors* [Internet]. Hoboken, NJ, USA: John Wiley & Sons, Inc.; 2011 [cited 2021 Sep 25]. p. 257-303. [<URL>](#).
14. Abdullah Dar M. A review: plant extracts and oils as corrosion inhibitors in aggressive media. *Ind Lubrication and Tribology*. 2011 Jun 21;63(4):227-33. [<DOI>](#).
15. Umoren SA. Polymers as Corrosion Inhibitors for Metals in Different Media - A Review. *TOCORR J*. 2009 Jun 25;2(1):175-88. [<DOI>](#).
16. Chigondo M, Chigondo F. Recent Natural Corrosion Inhibitors for Mild Steel: An Overview. *Journal of Chemistry*. 2016;2016:1-7. [<DOI>](#).
17. Shukla SK. Corrosion inhibitive effect of N-(6-methoxyquinolin-8-yl)-pentane-1, 4-diamine on mild steel/sulphuric acid solution interface. *J Mater Environ Sci*. 2015;6:1779-86.
18. Ji G, Shukla SK, Dwivedi P, Sundaram S, Ebenso EE, Prakash R. Parthenium hysterophorus plant extract as an efficient green corrosion inhibitor for mild steel in acidic environment. *International Journal of Electrochemical Science*. 2012;7(10):9933-45.
19. Gece G. Drugs: A review of promising novel corrosion inhibitors. *Corrosion Science*. 2011 Dec;53(12):3873-98. [<DOI>](#).
20. Singh AK, Shukla SK, Quraishi MA. Corrosion behavior of mild steel in sulphuric acid solution in presence of ceftazidime. *Int. J. Electrochem. Sci*. 2011; 6(11): 5802-14.
21. Dwivedi A, Bharti P, Shukla S. Surface assimilation and corrosion inhibition characteristic of water soluble Polyvinyl Alcohol on mild steel surface in 0.5M HCl solution. *Journal of the Turkish Chemical Society Section A: Chemistry*. 2021 Jan 11;219-30. [<DOI>](#).
22. Reza I, Saleemi A, Naveed S. Corrosion inhibition of mild steel in HCl solution by Tinidazole. *Polish Journal of Chemical Technology*. 2011 Jan 1;13(1):67-71. [<DOI>](#).

23. Singh AK, Shukla SK, Singh M, Quraishi MA. Inhibitive effect of ceftazidime on corrosion of mild steel in hydrochloric acid solution. *Materials Chemistry and Physics*. 2011 Sep;129(1-2):68-76. [<DOI>](#).
24. Shukla SK, Quraishi MA. Ceftriaxone: a novel corrosion inhibitor for mild steel in hydrochloric acid. *J Appl Electrochem*. 2009 Sep;39(9):1517-23. [<DOI>](#).
25. Shukla SK, Quraishi MA. Cefalexin drug: A new and efficient corrosion inhibitor for mild steel in hydrochloric acid solution. *Materials Chemistry and Physics*. 2010 Mar;120(1):142-7. [<DOI>](#).
26. Prasanna BM, Praveen BM, Hebbar N, Venkatesha TV, Tandon HC, Abd Hamid SB. Electrochemical study on inhibitory effect of Aspirin on mild steel in 1 M hydrochloric acid. *Journal of the Association of Arab Universities for Basic and Applied Sciences*. 2017 Feb;22(1):62-9. [<DOI>](#).
27. Shukla SK, Quraishi MA. The effects of pharmaceutically active compound doxycycline on the corrosion of mild steel in hydrochloric acid solution. *Corrosion Science*. 2010 Feb;52(2):314-21. [<DOI>](#).
28. Aronson JK, editor. Polystyrene sulfonates. In: *Meyler's side effects of drugs: the international encyclopedia of adverse drug reactions and interactions*. 16. ed. Amsterdam Boston Heidelberg: Elsevier; 20. ISBN: 978-0-444-53717-1.
29. Shukla SK, Quraishi MA. Cefotaxime sodium: A new and efficient corrosion inhibitor for mild steel in hydrochloric acid solution. *Corrosion Science*. 2009 May;51(5):1007-11. [<DOI>](#).
30. Salem H, Samir E. Determination of cefotaxime, cefoperazone, ceftazidime and cefadroxil using surface plasmon resonance band of silver nanoparticles. *Braz J Pharm Sci [Internet]*. 2018 Nov 29 [cited 2021 Sep 25];54(3). [<DOI>](#).
31. SANKAR SA, Kumar AS, RAMESHKUMAR S. Corrosion Inhibition Of Mild Steel In 0.5 M H₂SO₄ By 1-(2-Methyl-4-(2-Methylphenyldiazenyl) Phenyl) Azonaphthalen-2-Ol. *Am. J. Eng. Res*. 2013; 2(9):17-22.
32. Shukla SK, Quraishi MA. Effect of some substituted anilines-formaldehyde polymers on mild steel corrosion in hydrochloric acid medium. *J Appl Polym Sci*. 2011;5130-7. [<DOI>](#).
33. Tang L. A study of the polarisation techniques for corrosion rate measurement in a steel-concrete system. *9DBMC*. 2002;158:1-10.
34. Harabor I, Nechifor G, Branzoi V, Branzoi F. Investigation of some organic polymers as corrosion inhibitors on carbon steel in cooling water systems. *Univ Politeh Buchar Sci Bull Series B-Chem Mater Sci*. 2016;78(3):145-60.
35. Ji G, Shukla SK, Ebenso EE, Prakash R. Argimone maxicana leaf extract for inhibition of mild steel corrosion in sulfuric acid solution. *Int. J. Electrochem. Sci*. 2013;8(8):10878-89.
36. Shukla S, Ebenso E. Corrosion inhibition, adsorption behaviour and thermodynamic properties of streptomycin on mild steel in hydrochloric acid medium. *International Journal of Electrochemical Science*. 2011;6:3277-91.
37. Khedr MGA, Lashien AMS. The role of metal cations in the corrosion and corrosion inhibition of aluminium in aqueous solutions. *Corrosion Science*. 1992 Jan;33(1):137-51. [<DOI>](#).
38. Schorr M, Yahalom J. The significance of the energy of activation for the dissolution reaction of metal in acids. *Corros Sci*. 1972;867-8.
39. Umoren SA, Solomon MM, Udosoro II, Udoh AP. Synergistic and antagonistic effects between halide ions and carboxymethyl cellulose for the corrosion inhibition of mild steel in sulphuric acid solution. *Cellulose*. 2010 Jun;17(3):635-48. [<DOI>](#).
40. Solomon MM, Umoren SA, Udosoro II, Udoh AP. Inhibitive and adsorption behaviour of carboxymethyl cellulose on mild steel corrosion in sulphuric acid solution. *Corrosion Science*. 2010 Apr;52(4):1317-25. [<DOI>](#).
41. Szauer T, Brandt A. On the role of fatty acid in adsorption and corrosion inhibition of iron by amine -fatty acid salts in acidic solution. *Electrochimica Acta*. 1981 Sep;26(9):1257-60. [<DOI>](#).
42. Abd El Rehim SS, Hassan HH, Amin MA. Corrosion inhibition of aluminum by 1,1(lauryl amido)propyl ammonium chloride in HCl solution. *Materials Chemistry and Physics*. 2001 Apr;70(1):64-72. [<DOI>](#).
43. Ebenso EE. Synergistic effect of halide ions on the corrosion inhibition of aluminium in H₂SO₄ using 2-acetylphenothiazine. *Materials Chemistry and Physics*. 2003 Mar;79(1):58-70. [<DOI>](#).
44. Ebenso EE, Obot IB. Inhibitive properties, thermodynamic characterization and quantum chemical studies of secnidazole on mild steel corrosion in acidic medium. *Int J Electrochem Sci*. 2010;5(12):2012-35.
45. Hermas A-EA, Elnady AM, Ali RM. Corrosion inhibition of stainless steel in sulfuric acid solution

containing sulfide ions. ACMM. 2019 May 7;66(3):360-8. [<DOI>](#).

46. Madkour LH, Elshamy IH. Experimental and computational studies on the inhibition performances of benzimidazole and its derivatives for the corrosion of copper in nitric acid. Int J Ind Chem. 2016 Jun;7(2):195-221. [<DOI>](#).

47. Murulana LC, Singh AK, Shukla SK, Kabanda MM, Ebenso EE. Experimental and Quantum Chemical Studies of Some Bis(trifluoromethylsulfonyl) Imide Imidazolium-Based Ionic Liquids as Corrosion Inhibitors for Mild Steel in Hydrochloric Acid Solution. Ind Eng Chem Res. 2012 Oct 10;51(40):13282-99. [<DOI>](#).

48. Abd-El-Khalek DE, Hassan HHAM, Ramadan SR. Water-soluble sulfonated polyaniline as multifunctional scaling inhibitor for crystallization control in industrial applications. Chemical Engineering Research and Design. 2021 May;169:135-41. [<DOI>](#).

49. Rahmani H, Meletis EI. Corrosion Inhibition of Brazing Cu-Ag Alloy with 1,2,3-Benzotriazole and 2,5-Dimercapto-1,3,4-Thiadiazole. Corrosion. 2021 Jan 1;77(1):29-39. [<DOI>](#).

50. Tsoeunyane MG, Makhatha ME, Arotiba OA. Corrosion Inhibition of Mild Steel by Poly(butylene succinate)-L-histidine Extended with 1,6-diisocynatohexane Polymer Composite in 1 M HCl. International Journal of Corrosion. 2019 Mar 3;2019:1-12. [<DOI>](#).



Extraction and Characterization of Pectin from Lemon Waste for Commercial Applications

Ketema Beyecha Hundie*¹  , Desalegn Abdissa Akuma² 

School of Chemical Engineering, Jimma Institute of Technology, Jimma University, Jimma, Ethiopia

Abstract: The objective of this paper was preliminary to extract and characterization of purified pectin from lemon wastes. Dry lemon waste was extracted applying citric acid solvent or water at various concentrations under a similar condition (85 °C for 4 h). It was found that the highest yield of pectin (20.8% dry basis) was achieved using hot water extraction with an esterification degree of 47.8%. It contained $63.2 \pm 0.74\%$ galacturonic acid, followed by $17.4 \pm 0.76\%$ total sugar. The monosaccharides found in pectin were arabinose ($2.7 \pm 0.20\%$), galactose ($2.3 \pm 0.01\%$), glucose ($1.4 \pm 0.09\%$), mannose ($0.4 \pm 0.01\%$), fructose ($0.4 \pm 0.05\%$), and xylose ($0.1 \pm 0.01\%$). The found pectin had a high atomic weight of 2060 kDa with a wide polydispersity index of 4.41, decided by high-Performance Size Exclusion Chromatography (HPSEC). The extricated lemon waste pectin was grouped into low methoxyl pectin, depends on the methoxyl content and degree of esterification affirmed by Fourier transform infrared spectroscopy (FT-IR) and rheological properties. In conclusion, the discoveries of the study show that lemon waste can be investigated as a promising elective for the commercial manufacturing of pectin.

Keywords: Lemon waste, pectin, composition, molecular weight

Submitted: March 23, 2021. **Accepted:** October 21, 2021.

Cite this: Beyecha Hundie K, Abdissa Akuma D. Extraction and Characterization of Pectin from Lemon Waste for Commercial Applications. JOTCSA. 2011;8(4):1111-20.

DOI: <https://doi.org/10.18596/jotcsa.901973>.

***Corresponding author. E-mail:** ketema.hundie@ju.edu.et, Tel: +251913557447

INTRODUCTION

Pectin is a complex polysaccharide substance found in the cell walls of plants, including a backbone of α -1,4-galacturonic acids that are partly esterified at the carboxylic acid groups and wall and other materials to create a cellulosic network for the firmness of plant tissue (1). It can be commercially extracted from citrus peels and apple pomace with an acidic solution. Several pectin sources have been found in other fruits and vegetables, including okras papayas, cocoa pod husks, and cabbages (2,3). Pectin is widely applied to form a gel and maximize viscosity and constancy in several cosmetic and food industries. It is utilized to prepare jams, jellies, marmalades, and other products to ameliorate the texture. Pectin is also a good dietary fiber, protecting diseases like diabetes and colon cancer in

the human body, and letting down cholesterol and serum glucose (4).

The galacturonic acid component units are the primary chain of pectin that is partly linked to neutral sugar side chains. The common carbohydrates found on the ramification chain are galactose, arabinose, and glucose, and to a lesser degree, xylose, mannose, and rhamnose (5). In common, pectin can be divided into two kinds depending on the degree of esterification (DE) high methoxyl pectin (HMP, $DE \geq 50\%$) and low methoxyl pectin (LMP, $DE \leq 50\%$) (6). The gelling formation gotten from HMP at a lower pH value (~ 3) within the existence of a large amount of sugar is generally utilized in high sugar jam and jelly-such as a nutrient. In contrast, the gel got from LMP in a higher pH interval (2 - 6) with or without a little

amount of sugar requires calcium ions for polymer interaction and is utilized in low calorie and non-sugar added to nutrient (7).

The amount and properties of pectin vary based on plant sources, extraction mechanism, and extraction stages in the processes. Hot water or acid extractions commonly involved in both the yield and the final quality of the extracted product (8, 9). It was detected that the best and optimum extraction parameters to get the most noteworthy pectin from natural citrus products were warm water at 90 - 110 °C for 1-5 h (10). Additionally, it was studied that natural acids such as citric acid in the pH range of 2.0 - 2.5 at higher temperature were excellent solvents for pectin extraction in other natural products (2).

Citrus fruit is the most abundant crop plant in global. Concurring to the Food and Agricultural Organization, a lot of 1.17×10^8 tons of citrus fruits (in which lemon leads 0.14×10^8 Tons) were manufactured per year (11, 12). The quantity of residual obtained from citrus fruits describes 50% of the whole fruit's original amount. It has been approximated that, on average, a juice producer forces up to 10.0×10^4 tons of fresh citrus fruits every year and represents the manufacture of the citrus residues as a waste by-product quantity 5.5×10^4 tons per year (14, 15). Thus, significant quantities of citrus wastes are available as a by-product. The peels, if addressed as waste materials, may bring environmental problems, especially water pollution. This problem could have become an asset; if possible marketable by-products like pectin could be extracted from these wastes. Previous studies

have been investigated the pectin-like and the gel formation ability with calcium cation of the pulp of lemon wastes. Some chemicals and characteristics were also separately studied (16). However, the properties and constitution of purified pectin in its waste have been less delineated.

Therefore, this research directed to a preliminary analysis of pectin extraction from lemon waste and investigated the extracted pectin components and its properties. The data obtained might be advantageous for the practical application of pectin to other items separated from food.

MATERIALS AND METHODS

Materials

The lemon wastes were collected from a juice producer in Ethiopia. Galacturonic acid, citrus pectin, and simple sugar (monosaccharide), Bovine serum albumin standard were chemical product suppliers in Addis Ababa, Ethiopia. The citrus pectin with the DE 55 - 70% and 85% as fixed by the provider were applied. Other analytical grade chemicals used in this experiment are not specified. Pectin extraction and characterization were carried out at Addis Ababa University and Jimma institute of technology.

Methodology

Preparation of lemon wastes

Lemon wastes were collected as sun-dried, washed, and electric oven-dried. The dry lemon waste (10% moisture) was scraped, powdered, and passed through a 60 mesh sieve and then stored in a sealed plastic bag at 4 °C for the subsequent analysis.

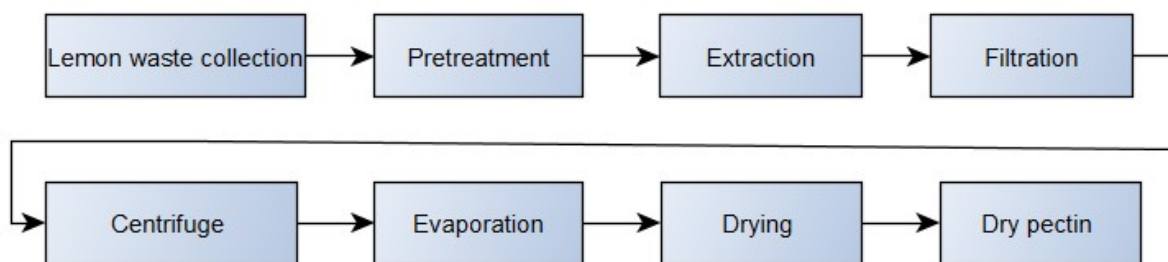


Figure 1. Lemon waste pectin extraction process flow chart.

Pectin extraction

Pectin in dry lemon waste was extracted utilizing unadulterated refined water or an arrangement of citric acid at distinctive concentrations of 6, 8, and 10% (w/v) at 85 °C for 3h (dry lemon waste to water 1:10 w/v). The extricated samples were then centrifuged for 15 min at 4,500 rpm, and the obtained supernatant was dialyzed against refined water for a day, utilizing a dialysis tube with the atomic weight cut off 12,400 Da (Sigma-Aldrich) (17). The dialyzed samples were centrifuged (4,500 rpm), the supernatants were accumulated and

accelerated with 4 mL of ethanol (96% purity, 1:3 v/v) and cooled overnight at 25 °C. After centrifugation, the supernatant was disposed of, and the coagulated accelerates were accumulated and cleaned with ethanol (96% purity) and, after that, centrifuged once more. Finally, the accelerates were hot air-dried at 60 °C, grounded, and passed through a 60 mesh analysis to get pectin powder. The amount of the extracted pectin was determined according to Eq. (1).

$$(1)$$

$$\text{Amount of pectin} = \frac{\text{Mass of pectin (g)}}{\text{Mass of dry lemon waste (g)}} \times 100\% \quad (1)$$

Determination of Moisture and Ash contents

Moisture and ash contents were decided to agree to the strategy of AOAC (18). Moisture content: 1 g of the sample was weighed and dried by employing an electric oven at 105 °C for 12 h to a constant weight. The weight loss was taken and calculated as a percentage of moisture (%).

Ash content: 2 g of the sample was weighed and burned in a furnace at 600 °C for 5 h and the remaining was weighed, and the percentage of ash content (%) was calculated.

Determination of the Degree of Esterification (DE)

Titration procedure: The titration strategy was employed to decide the DE of pectin according to USP 30-NF 23 (19). The pectin powder of 60 mg was dissolved using 30 mL of carbon dioxide-free deionized water for 20 min at 50 °C and after that cleared out to cool. After 3 drops of phenolphthalein were added, the solution was titrated with 0.2 N KOH concentrations (A). Additionally, 20 mL of 0.2N KOH was added and blended at room temperature for 25 min. Subsequently, 30 mL of 0.15 N HCl solutions were added and blended until the pink was blurred. The extra 3 drops of phenolphthalein were added and, after that titrated with 0.2 N KOH until the endpoint was indicated (B). The percentage (%) degree of esterification (DE) was calculated using Eq (2).

$$\text{Degree of esterification (DE)} = \frac{B}{(B+A)} \times 100\% \quad (2)$$

Fourier Transform Infrared Spectroscopy (FT-IR)

The powder of pectins and citrus pectin were dried for a day and blended with spectroscopic-grade KBr. The sample pectin was then put into the KBr-crucible. The infrared spectra were measured on a Bruker-Tensor 30 FT-IR spectrometer, utilizing MIR-ATR mode. The 64 filters at 4 cm⁻¹ resolution were taken from 4000 - 400 cm⁻¹. The top zone's proportion at 1725 cm⁻¹ over the entirety of the 2 top zones at 1725 and 1600 cm⁻¹ (relegated to the retention of esterified and non-esterified carboxyl bunches, separately) was determined to % degree of esterification utilizing OPUS software program version 8.3 (20).

Determination of protein content

Protein substance was analyzed, agreeing with the Bradford's strategy (21). The sample was arranged and diluted using refined water to get a concentration of 4.50 mg/mL. The Bradford buffer solution was added (counting bovine serum egg whites standard solution) and blended well before

measuring the absorbance at a wavelength of 595 nm.

Determination of galacturonic acid content

The galacturonic amount was decided to agree to Blumenkrantz and Asboe-Hansen's (2) strategy, employing a UV-Visible spectrophotometer (PG Instrument, T60, Britain) at the wavelength of 520 nm. The sample concentration of 4.50 mg/mL was developed in refined water and agitated at 50 °C for 2h and diluted to fit the galacturonic acid standard interval. The diluted sample and standard solutions were blended with 10.5 mM tetraborate in concentrated sulfuric acid and, after that, cooled quickly with an ice bath. All solutions were heated for 3 min at 90 °C and left out in an ice bath to cool. The 0.2% m-hydroxy diphenyl reagent was included, and the absorbance was studied after color improvement for 15 min.

Determination of total sugar content

The phenol-H₂SO₄ was utilized to decide the whole sugar substance as depicted by Lim et al. (22). A sample of 20 mg was weighed and hydrolyzed with 1.5 mL of 75% H₂SO₄ for 25 min at 25 °C. After diluting with 10 mL of refined water, 3 mL of the diluted sample was pipetted into a test tube and blended with 60 µL of 85% phenol. The concentrated sulfuric acid was added quickly and leftover for 20 min before reading the absorbance at 490 nm, employing a UV-Visible spectrophotometer. The glucose standard bent was plotted to compare the whole sugar as glucose equivalence.

Determination of mineral content

The mineral substance was decided by inductively coupled plasma optical emission spectrometer (ICP-OES) (Perkin Elmer, Optima 8000, and Italy) and CHNS/O analyzer (Thermo Logical, Streak 2000, and the UK).

Determination of monosaccharides

The pectin sample was hydrolyzed with 1.5 M sulfuric acid solution for 3 h at 90 °C and diluted with refined water. The monosaccharide hydrolysates were sifted through a 0.4 µm film, and the volume of 20 µL was infused onto a high-performance anion-exchange chromatography (HPAEC) apparatus (Dionex, ICS-2500, USA) isolated by CarboPac PA20 (160 mm × 4 mm) column with an electrochemical indicator (20). The 260 mM KOH and deionized water proportion was 2/23 to 0/100 to angle elute at the stream rate of 0.3 mL/min for 1 hour. Monosaccharides' types and concentrations were recognized by comparison with a blend of monosaccharides (glucose, galactose, arabinose, mannose, xylose, and fructose).

Determination of molecular weight distribution

The sample was arranged by dissolving in deionized water to the concentration of 5.5 mg/mL at 60 °C

for 4 h (22) and added with potassium chloride (KCl) and ammonium acetate ($\text{NH}_4\text{CH}_3\text{CO}_2$) to obtain 100 mM of each. A filter paper was used to filter a solution and the atomic weight was measured by high-performance size exclusion chromatography (HPSEC, Water 3754, Divisions module, Waters enterprise, Italy) utilizing multi-point laser light scrambling and refractive index (RI, Waters 4241, Waters organization, Italy) detectors. The 30 μL of the volume was infused onto Ultra hydrogel 300 columns (Waters Enterprise, USA). A blend of 90 mM KCl and 90 mM $\text{NH}_4\text{CH}_3\text{CO}_2$ was utilized as a versatile stage with a stream rate of 0.5 mL/min, and all information was utilized for atomic weight calculation.

Determination of rheological measurement

The samples were decided on a modular Compact Rheometer: MCR63 (Anton Paar, France), utilizing RheoPlus Rheometer program version 4.52. A cone and plate geometry with a distance across 40 mm was utilized for oscillatory estimations. The estimations were kept up at room temperature and subjected to the recurrence of 1.0 Hz using a strain of 3.0%. The samples of 5% (w/v) were arranged by dissolving in refined water for 15 min at 60 °C (23). After cooling, 0.3 M CaCl_2 was included and blended altogether. All samples (with and without 0.3 M CaCl_2) were stored at 25 °C for a half a day before the measurement.

Statistical analysis

All the experiments were carried out in triplicate at the time (60, 120, and 180 min), temperature (70, 90, and 110 °C) and Citric acid (6, 8, 10 v/v%), and the analyses of Variance (ANOVA) were carried on by Duncan's and Tukey's methods applying SPSS (Statistical Package for the Social Sciences) version

25. Duncan's and Tukey's tests were accomplished to examine the substantial changes between the mean values for treatments ($P < 5\%$) and standard deviation (24). The result was indicated in supplementary materials for citric acid extraction (Tables 1-5).

RESULTS AND DISCUSSION

Water and acid-extracted pectin

The impression of water and acid-extracted pectin from lemon waste and its DE are indicated in Table 1. The values showed that the maximum yield of pectin (20.8%) and DE (47.8%) of extracted pectin were found by water extraction than those of citric acid extractions. It was discovered that acid extractions (6, 8, and 10%) significantly diminished the degree of esterification values to 45.6, 33.6, and 25.4%, respectively. It was described that the higher pectin substance was found from fruits and leaves using acid treatment at higher temperature since this condition probable release pectin substance from the cell wall of the plant (25), while other authors found that acidic solvents at high temperature degraded pectin (26). In this study, the result was in correspondence with the previous finding. The *Statistical data analysis* using Duncan's and Tukey's methods applying SPSS version 25 was also indicated in supplementary materials (Table 1-6).

A diminishment in methoxyl group and pectin yield was detected. As a result of the depolymerization of acid, de-esterification could be due to higher temperature and long-time technique (27). Therefore, the extract found from water extraction was further examined concerning the maximum yield.

Table 1: Effect of water and acid extraction on yield and DE of lemon waste pectin.

Solution (at 90 °C)	Yield of pectin (%, dry basis)	DE (%)
10% Citric Acid	10.0 \pm 0.38 ^w	24.3 \pm 1.11 ^w
8% Citric Acid	16.5 \pm 0.07 ^x	31.4 \pm 1.86 ^x
6% Citric Acid	12.5 \pm 0.33 ^y	44.7 \pm 0.89 ^y
Purified water	20.7 \pm 0.23 ^z	48.3 \pm 0.29 ^z

The different letters w x, y, and z in the same column are significantly different ($P < 5\%$)

Characterization of extracted pectin

The extracted pectin was analyzed for composition as indicated in Table 2. It was determined that the pectin extracted in dry lemon waste contained 5.7% of moisture content, 3.6% of ash content, and 2.4% of protein content. It consisted of the higher value of galacturonic acid 61.2% and 19.3% of low sugar contents. The total sugar amount was similar to the pectin of citrus fruits, around 14.6 to 20.50% described by Liew et al. (2). The other components, including mannose, fructose, galactose, glucose,

arabinoses, and xylose, also existed with a few minerals. The observation results explicated that polyose in the extract was highly galacturonic acid and small amounts of neutral sugar, commonly found in pectin structure. Depend on the DE value (48.3%) and composition, the extracted pectin in this research shown that it could be grouped as low methoxyl pectin since its DE is below 50% (6). The low DE result was not coherent with the finding of 64% DE as reported by Yeoh et al. (4). Although the DE of pectin is based on the origin (source) and

extraction methods and conditions, it generally diminishes with the rise of adulthood level (10).

The FT-IR spectrum has illustrated pectin's characteristics extracted from lemon wastes by comparison to other citrus pectins. Figure 1 indicates that the wavenumber interval of 1680 - 1760 and 1540 - 1680 cm^{-1} was the extending of the ester carbonyl group ($\text{C}=\text{O}$) and carboxyl ion groups (COO^-), respectively, when equated with the information described (4, 13). It was shown that the citrus pectin addressed under the area the spectrum of $\text{C}=\text{O}$ and COO^- . The peak reign of $\text{C}=\text{O}$ diminished, in conformity with a diminish of a DE, while the peak reign of COO^- raised (10). The spectrum of lemon waste pectin was similar to that of 55 - 70% degree of esterification of citrus pectin, proposing that the extracted pectin might have a similar percentage of a DE. Nevertheless, when decided by the FT-IR method, the intensity of the peak reign of $\text{C}=\text{O}$ was estimated and determined as 46.8% of the degree of esterification, roughly close to 47.5% degree of esterification detected by the titrimetric procedure (Table 2), which affirmed that pectin in lemon wastes should be LMP.

Table 2: Chemical composition of extracted pectin.

Chemical composition	Content (% dry basis)
Moisture	5.5 ± 0.43
Ash	3.7 ± 0.03
Protein	2.8 ± 0.12
Galacturonic acid	63.2 ± 0.74
Total sugar	17.4 ± 0.76
Monosaccharides	
Arabinose	2.7 ± 0.20
Galactose	2.3 ± 0.01
Glucose	1.4 ± 0.09
Mannose	0.4 ± 0.01
Fructose	0.4 ± 0.05
Xylose	0.1 ± 0.01
Minerals	
K	1.23 ± 0.01
N	0.85 ± 0.02
Ca	0.75 ± 0.03
Si	0.075 ± 0.02
P	0.01 ± 0.02
Mn	0.011 ± 0.00
S	< 0.01

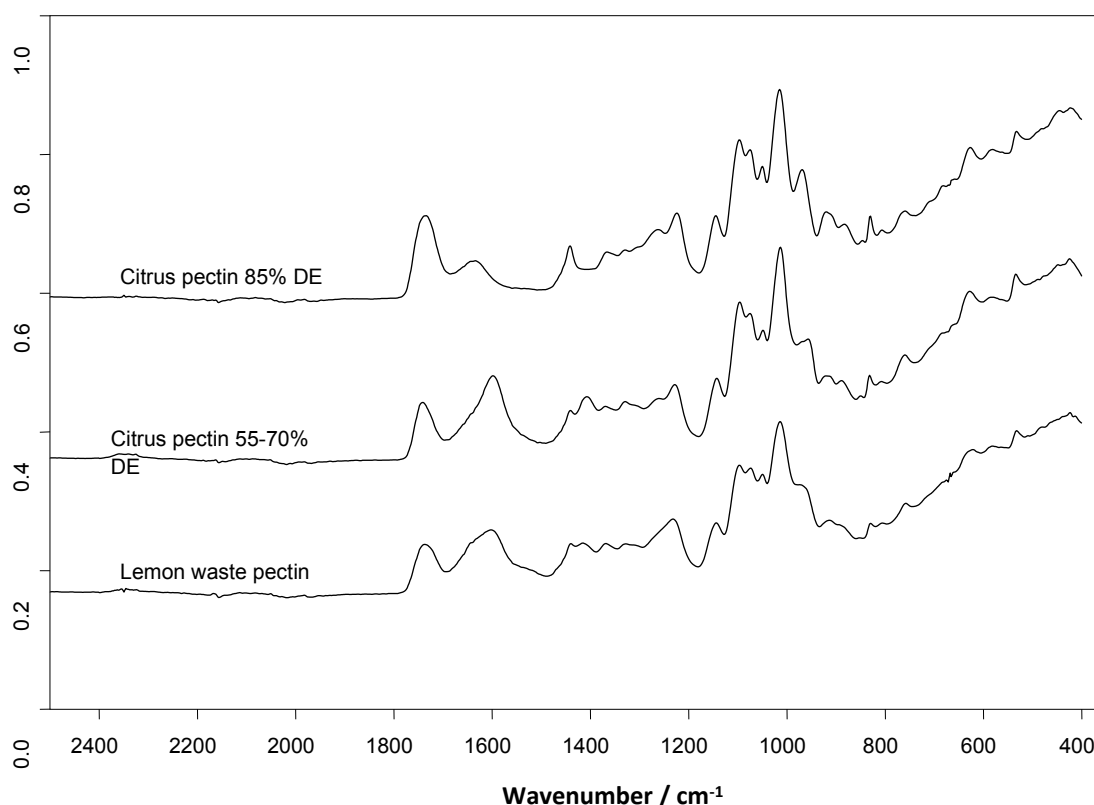


Figure 1. FT-IR Spectrum of lemon waste pectin and citrus pec. The y axis is absorbance.

Molecular weight distribution

The molecular weight dispersion chromatogram of lemon waste pectin run by HPSEC with double detectors is indicated in Figure 2. The light dispersion (LD) indicated only one large dispersion part as a function of time, while the refractive index

(RI) indicated two parts of unlike molecular size. This is due to a common argument that the LD signal is low sensitive to minor molecular dispersion. The large intensity signal observed by LD was a potential dominant large molar weight constituent galacturonic units of pectin polysaccharides in

concurrency with a high peak by RI at a retention time of roughly 20 min. The littler elution peak indicated by RI around 30 min may be led to a little number of protein atoms that are ordinarily combined in polysaccharides. It was taken note that the mean atomic weight (Aw) of lemon wastes pectin was 2060 kDa, much higher than that of the LM of citrus pectin extending from 110 - 290 kDa, and the polydispersity record (Mw/Mn) was 4.31,

too more prominent than 1.74 - 2.60 in that report measured by HPSEC chromatography methods (15, 20). The molecular (atomic) weight was higher than already detailed in LMP extricated from okra fruits which extending from 700 - 1700 kDa (28). The wide atomic mass with Aw/Mn of 4.41 of extricated lemon wastes pectin was likely due to the natural development and the impact of extraction conditions.

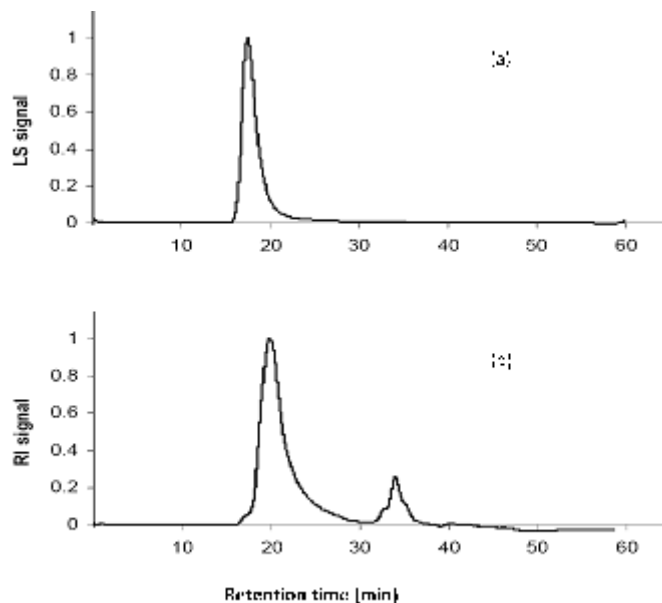


Figure 2: HPSEC chromatogram of lemon waste pectin from 2 detectors: (a) Light scattering (LS) and (b) refractive index (RI).

Rheological properties

The rheological properties of lemon waste pectin (4.5% w/v) with and without the addition of calcium chloride have appeared in Figure 3. In Figure 3(a), the fast diminishment in complex viscosity was detected with expanding frequency, clarified strong shear diminishment stream characteristics. A better complex viscosity of lemon waste pectin with

calcium chloride was recorded as a function of particular recurrence than that without calcium chloride, which shown that the existence of calcium ion affected intermolecular systems of pectin substances. When assist expanded in recurrence, the significantly diminished in complex thickness to about zero value was found likely due to shear misshapen within the consistent period.

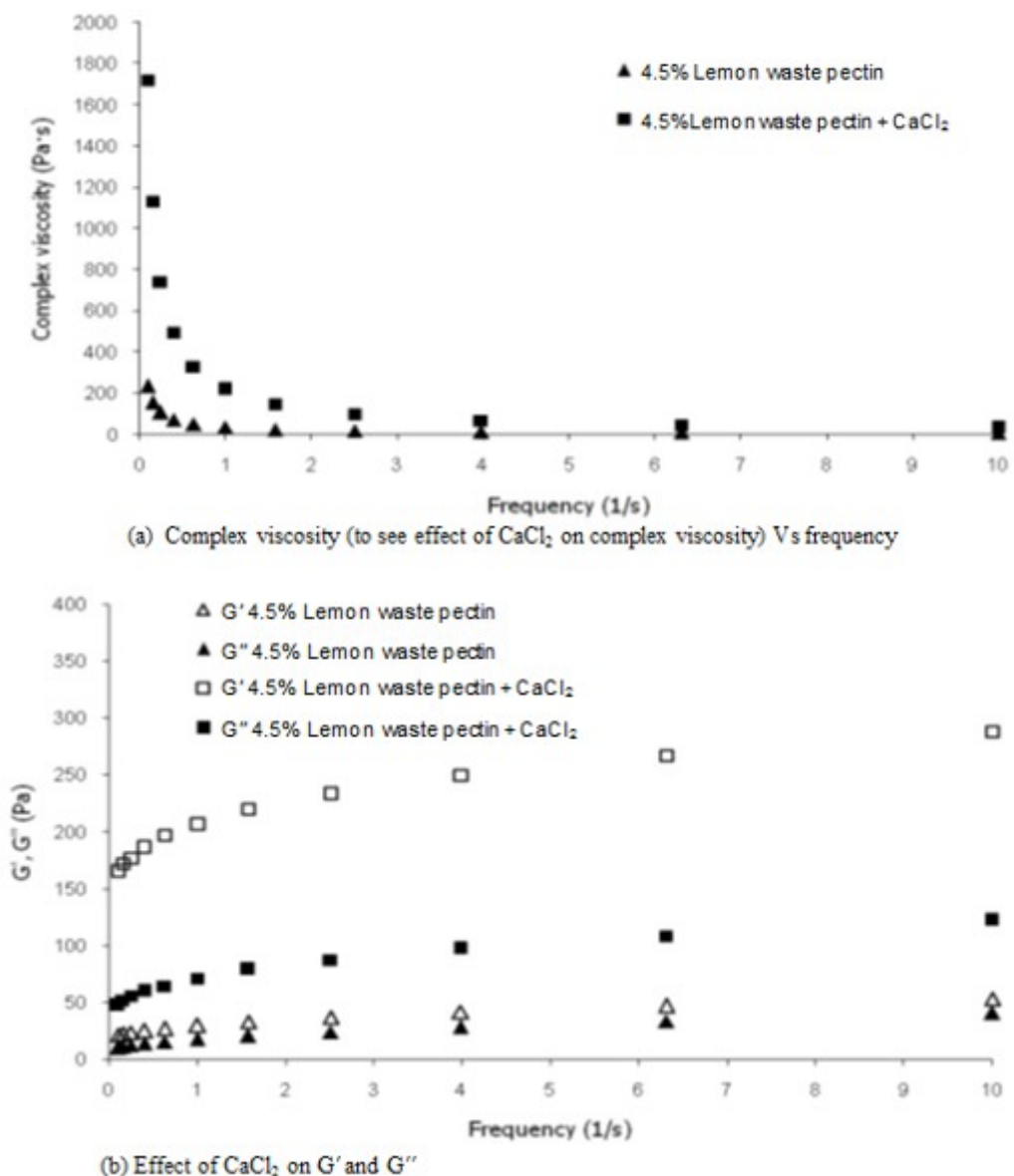


Figure 3. Rheological properties of lemon waste pectin.

Figure 3(b) outlines the capacity (G') and loss (G'') moduli in lemon waste pectin with and without the inclusion of calcium chloride. The clear recurrence tests appeared a higher G' than G'' without hybrid, within the energetic run between 0 and 10 Hz (1/s), supporting the marvel of gel-like behavior at minimum frequencies. It was detected that lemon waste pectins (with and without calcium chloride ions) were gathered to be weak-gels about G' cross all over G'' and subordinate on the powerless recurrence within the experiment (21, 29). The intelligence between carboxyl bunches on the most chain of LMP and divalent cations (Ca^{2+}) are critical for cross-bridge gelation through the component called "egg-box" due to the affiliation of intermolecular intersection zones between the smooth homogalacturonan area of diverse chains

(20). The rheological outcome confirmed that the extractable pectin in lemon waste was LMP, in which pectin polymers ionically cross-linked through free carboxyl chain and divalent cations.

CONCLUSIONS

In this work, the composition and characteristics of water-extractable pectin obtain from lemon wastes were studied. The hot water extraction gave better results than a hot acidic extraction using citric acid, since it produces the highest pectin yield. The extracted pectin was mainly composed of galacturonic acid and considered as low methoxyl pectin, based on a low degree of esterification values as it was detected by FT-IR fingerprint. The HPSEC analysis clarified those pectin

polysaccharides had high molecular weight, which enabled interaction with calcium ions as detected by rheological analysis. These results propose that lemon waste is a good source of gelling pectin that could be employed in food and non-food products.

The yield of water extracted pectin is higher than acid extracted pectin

ACKNOWLEDGEMENTS

The author expresses his gratitude to Jimma University, Jimma Institute of Technology, Addis Ababa institute of technology for supporting this research. Thanks are extended to the School of Chemical Engineering staff members and technicians and the department of chemistry for their support.

CONFLICT OF INTEREST

The author announces that there is no conflict of interest.

FINDING

This research was supported by the School of chemical engineering, Jimma Institute of Technology (JiT), and Addis Ababa Institute of Technology.

REFERENCES

- Hosseini SS, Khodaiyan F, Kazemi M, Najari Z. Optimization and characterization of pectin extracted from sour orange peel by ultrasound assisted method. *International Journal of Biological Macromolecules*. 2019 Mar;125:621–9. [<DOI>](#).
- Liew SQ, Chin NL, Yusof YA. Extraction and Characterization of Pectin from Passion Fruit Peels. *Agriculture and Agricultural Science Procedia*. 2014;2:231–6. [<DOI>](#).
- Kpodo FM, Agbenorhevi JK, Alba K, Bingham RJ, Oduro IN, Morris GA, et al. Pectin isolation and characterization from six okra genotypes. *Food Hydrocolloids*. 2017 Nov;72:323–30. [<DOI>](#).
- Yeoh S, Shi J, Langrish TAG. Comparisons between different techniques for water-based extraction of pectin from orange peels. *Desalination*. 2008 Jan;218(1–3):229–37. [<DOI>](#).
- Grassino AN, Barba FJ, Brnčić M, Lorenzo JM, Lucini L, Brnčić SR. Analytical tools used for the identification and quantification of pectin extracted from plant food matrices, wastes and by-products: A review. *Food Chemistry*. 2018 Nov;266:47–55. [<DOI>](#).
- Hosseini SS, Khodaiyan F, Yarmand MS. Aqueous extraction of pectin from sour orange peel and its preliminary physicochemical properties. *International Journal of Biological Macromolecules*. 2016 Jan;82:920–6. [<DOI>](#).
- Kazemi M, Khodaiyan F, Hosseini SS. Utilization of food processing wastes of eggplant as a high potential pectin source and characterization of extracted pectin. *Food Chemistry*. 2019 Oct;294:339–46. [<DOI>](#).
- Lu J, Li J, Jin R, Li S, Yi J, Huang J. Extraction and characterization of pectin from *Premna microphylla* Turcz leaves. *International Journal of Biological Macromolecules*. 2019 Jun;131:323–8. [<DOI>](#).
- Kurita O, Fujiwara T, Yamazaki E. Characterization of the pectin extracted from citrus peel in the presence of citric acid. *Carbohydrate Polymers*. 2008 Nov;74(3):725–30. [<DOI>](#).
- Happi Emaga T, Ronkart SN, Robert C, Wathelet B, Paquot M. Characterisation of pectins extracted from banana peels (*Musa AAA*) under different conditions using an experimental design. *Food Chemistry*. 2008 May;108(2):463–71. [<DOI>](#).
- Yapo BM. Pectin quantity, composition and physicochemical behaviour as influenced by the purification process. *Food Research International*. 2009 Oct;42(8):1197–202. [<DOI>](#).
- Xue Z, Zhang X, Zhang Z, Liu J, Wang Y, Chen D, et al. Optimization of pectin extraction from citrus peel by response surface methodology. *Food Science*. 2011;18:128–32.
- Vriesmann LC, de Mello Castanho Amboni RD, de Oliveira Petkowicz CL. Cacao pod husks (*Theobroma cacao* L.): Composition and hot-water-soluble pectins. *Industrial Crops and Products*. 2011 Jul;34(1):1173–81. [<DOI>](#).
- Alba K, Laws AP, Kontogiorgos V. Isolation and characterization of acetylated LM-pectins extracted from okra pods. *Food Hydrocolloids*. 2015 Jan;43:726–35. [<DOI>](#).
- Bagde PP, Dhenge S, Bhivgade S. Extraction of pectin from orange peel and lemon peel. *International Journal of Engineering Technology Science and Research*. 2017;4(3):1–7.
- Kulkarni SG, Vijayanand P. Effect of extraction conditions on the quality characteristics of pectin from passion fruit peel (*Passiflora edulis* f. *flavicarpa* L.). *LWT - Food Science and Technology*. 2010 Sep;43(7):1026–31. [<DOI>](#).
- Forni E, Penci M, Polesello A. A preliminary characterization of some pectins from quince fruit (*Cydonia oblonga* Mill.) and prickly pear (*Opuntia*

- ficus indica) peel. Carbohydrate Polymers. 1994 Jan;23(4):231-4. [<DOI>](#).
18. Shafie MH, Yusof R, Gan C-Y. Deep eutectic solvents (DES) mediated extraction of pectin from Averrhoa bilimbi: Optimization and characterization studies. Carbohydrate Polymers. 2019 Jul;216:303-11. [<DOI>](#).
19. Yapo BM, Lerouge P, Thibault J-F, Ralet M-C. Pectins from citrus peel cell walls contain homogalacturonans homogenous with respect to molar mass, rhamnogalacturonan I and rhamnogalacturonan II. Carbohydrate Polymers. 2007 Jun;69(3):426-35. [<DOI>](#).
20. Alba K, MacNaughtan W, Laws AP, Foster TJ, Campbell GM, Kontogiorgos V. Fractionation and characterisation of dietary fibre from blackcurrant pomace. Food Hydrocolloids. 2018 Aug;81:398-408. [<DOI>](#).
21. Rahmani Z, Khodaiyan F, Kazemi M, Sharifan A. Optimization of microwave-assisted extraction and structural characterization of pectin from sweet lemon peel. International Journal of Biological Macromolecules. 2020 Mar;147:1107-15. [<DOI>](#).
22. Lim J, Yoo J, Ko S, Lee S. Extraction and characterization of pectin from Yuza (Citrus junos) pomace: A comparison of conventional-chemical and combined physical-enzymatic extractions. Food Hydrocolloids. 2012 Oct;29(1):160-5. [<DOI>](#).
23. Liu Y, Shi J, Langrish T. Water-based extraction of pectin from flavedo and albedo of orange peels. Chemical Engineering Journal. 2006 Jul 15;120(3):203-9. [<DOI>](#).
24. Ros JM, Schols HA, Voragen AGJ. Extraction, characterisation, and enzymatic degradation of lemon peel pectins. Carbohydrate Research. 1996 Feb;282(2):271-84. [<DOI>](#).
25. Adetunji LR, Adekunle A, Orsat V, Raghavan V. Advances in the pectin production process using novel extraction techniques: A review. Food Hydrocolloids. 2017 Jan;62:239-50. [<DOI>](#).
26. Liew SQ, Ngoh GC, Yusoff R, Teoh WH. Sequential ultrasound-microwave assisted acid extraction (UMAE) of pectin from pomelo peels. International Journal of Biological Macromolecules. 2016 Dec;93:426-35. [<DOI>](#).
27. Muthusamy S, Manickam LP, Murugesan V, Muthukumaran C, Pugazhendhi A. Pectin extraction from Helianthus annuus (sunflower) heads using RSM and ANN modelling by a genetic algorithm approach. International Journal of Biological Macromolecules. 2019 Mar;124:750-8. [<DOI>](#).
28. Yuliarti O, Goh KKT, Matia-Merino L, Mawson J, Brennan C. Extraction and characterisation of pomace pectin from gold kiwifruit (Actinidia chinensis). Food Chemistry. 2015 Nov;187:290-6. [<DOI>](#).
29. Colodel C, Vriesmann LC, Lucia de Oliveira Petkowicz C. Rheological characterization of a pectin extracted from ponkan (Citrus reticulata blanco cv. ponkan) peel. Food Hydrocolloids. 2019 Sep;94:326-32. [<DOI>](#).



Progress and expansions of chitosan-graphene oxide hybrid networks utilizing as adsorbents and their organic dye removal performances: A short review

Thi Sinh Vo*  

School of Mechanical Engineering, Sungkyunkwan University, Suwon 16419, Korea.

Abstract: Increasing concentration of pollutants has significantly affected the quality of water, especially for organic dyes-contained water/wastewater. This is probably reduced effectively through adsorbing the pollutants onto potential materials-based adsorbents. Chitosan/graphene oxide (CTS/GO) hybrid networks utilizing as adsorbents are attracting considerable interest owing to the available functional groups, which can remove plenty of the organic dyes from water/wastewater. In this review, the progress and expansions of CTS/GO hybrid networks-based adsorbents are summarized and discussed in detail. Following the general introduction and properties of each material system (i.e., CTS, GO and CTS/GO hybrid networks), the CTS/GO hybrid networks-based emerging adsorbents with coupling numerous other support materials (i.e., reduced GO, magnetic iron oxide, polymeric materials, metal-organic frameworks, etc.) are compared and discussed in short, at same time that some common organic dyes used in adsorption studies are also introduced. Besides, adsorption technique and mechanisms (i.e., adsorption kinetics and isotherms) focus on the CTS/GO hybrid networks' role are discussed as well. Although there are still some challenges from the reviewed researches, the CTS/GO hybrid networks-based emerging materials can be considered promising and potential adsorbents. Moreover, this review can provide a clear overview of CTS/GO hybrid networks-based adsorbents in organic dye removal applications to readers.

Keywords: Chitosan, graphene oxide, adsorbent, organic dyes, adsorption.

Submitted: May 27, 2021. **Accepted:** September 23, 2021.

Cite this: Vo TS. Progress and expansions of chitosan-graphene oxide hybrid networks utilizing as adsorbents and their organic dye removal performances: A short review. JOTCSA. 2021;8(4):1121-36.

DOI: <https://doi.org/10.18596/jotcsa.943623>.

* **Corresponding author. E-mail:** ytsinh92@skku.edu.

INTRODUCTION

So far, organic dyes have been employed plenty in the dyeing, textiles, leather, paper, plastics, and food industries, etc.; thus, these colored matters significantly affect currently environmental problems. Various organic dye types (i.e., reactive, anionic, and cationic dyes, etc.) employed in these industries are toxic and disadvantage to the water source (1-6) (Table 1). Specifically, anionic dyes contain negative charges instead of cationic dyes with positive

charges in an aqueous solution that is due to the presence of carboxyl and/or sulfonate groups (2, 5, 6). Among them, the anionic dyes are intensely colored, water-soluble, and manifest acidic features inducing to the most challenging (7, 8).

Additionally, the organic molecular structures of these complex aromatic dyes display more stability inducing to being difficult to biodegrade, which leads to removing the organic dyes from water/wastewater with an economical way is

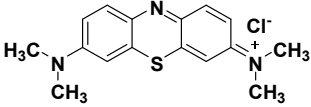
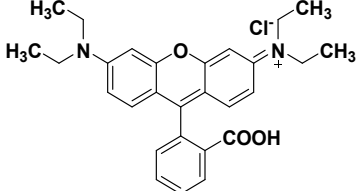
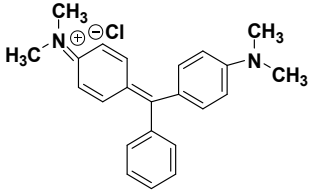
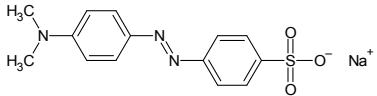
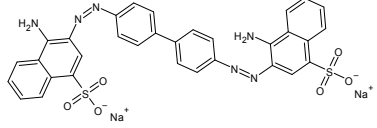
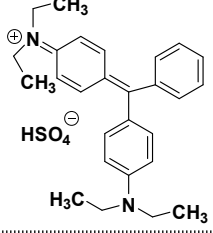
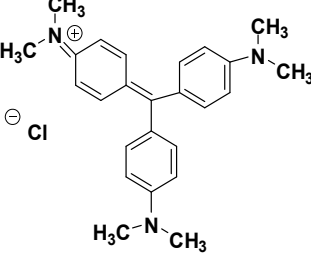
considered to be an important challenge for scientists. In fact, primary methods regarding dye-contaminated water/wastewater treatment (i.e., flotation and sedimentation) cannot be adequate to remove the colored features without general chemical manners. The treatment methods of coagulation, separation, and ion exchange are utilized for removing the color from the dye-contaminated water/wastewater as well; however, the cost is one of the main disadvantages of these methods. Whereas, adsorption is a well-known and effective technique in dye-contaminated water/wastewater treatment applications to remove the color from the dye-containing wastewater (4, 8, 9) that is mainly owing to low cost, flexibility, simple design, and easy operation (4).

So far, material system was extensively applied in different research fields and practical applications (4, 6, 10-12), at same time that remarkable factors of a material-based adsorbent almost regard to possible physical, chemical and interface properties. So, it is necessary to conduct considerably synthetic methods that can obtain better desired results corresponding to multiple researches. Concomitantly, the emerging materials-based adsorbents are found and utilized increasingly more to investigate the color removal from dye-contaminated water/wastewater (13-17), which can be novel, readily available, economical and highly effective adsorbents. Especially, chitosan (CTS) - a biopolymer is attracting interest as a matrix for the development of emerging material-based adsorbent that can be mainly owing to potentially active adsorption sites in a high density of available primary amine ($-NH_2$) and hydroxyl ($-OH$) groups; thus, the CTS is considered an efficient adsorbent (4, 6, 18). Actually, the CTS molecule is not available that is produced through N-deacetylation of chitin (19-22) basing on the replacement of acetamide group at position 2 to distinguish the structure and solubility of CTS and chitin molecules (Figure 1) (i.e., CTS is soluble in weak acids, chitin is inert and insoluble) (19-22). At the same time, graphene oxide (GO) contains plenty of functional surface groups [i.e., carbonyl ($>C=O$), epoxide ($C-O-C$), hydroxyl ($-OH$) and carboxylic ($-COOH$) groups] (Figure 2a) that can facilitate to couple with positively charged molecules through electrostatic interactions, and

which attracts significantly in combing with polymer matrices for enhancement of organic dye removal, mainly based on its high surface area and water solubility (4, 6, 23). Indeed, plenty of studies have shown the GO's excellent ability to adsorb various organic dyes through electrostatic interaction, π -stacking and hydrogen bonding (24-28). However, the organic dye adsorption performance of GO alone is lower than that of modified GO-based adsorbents (24, 25, 28).

Furthermore, the stability of GO nanosheets in colloidal solutions can lead to coupling easily with the CTS molecules (i.e., the CTS is often dissolved in acetic acid) to reach CTS/GO hybrid networks with a homogeneous mixture (Figure 2b). The CTS is known as a positively charged biopolymer that is mainly owing to protonation of the amino ($-NH_2$) groups leading to attracting the negatively charged GO nanosheets (Figure 2b). These electrostatic interactions coupling with both hydrogen bonding and π -stacking have facilitated the formation of the CTS/GO hybrid networks (Figure 2b) to reach the more stable hybrid networks-based materials with outstandingly mechanical and thermal features (6, 29). Indeed, the measurement of Fourier-transform infrared spectroscopy (FTIR) (30) has been successfully employed to demonstrate the possible reaction between the amino ($-NH_2$) groups of the CTS chains and the carboxylic ($-COOH$) groups of GO basing on the formation of amide ($-NHCO-$) linkages (Figure 2b). So far, the CTS/GO hybrid networks can be easily attained through various methods (i.e., the supplement of NaOH, violent shaking, sonication, freeze-drying, etc.) (6, 31-33), and which can also be well combined with other support material sources to develop and expand these CTS/GO hybrid networks that are applied in organic dye removal applications, especially for becoming cost-effective, eco-friendly and recyclable adsorbents. In this review article, the adsorption technique regarding the general adsorption theory and the adsorption kinetics/isotherms are introduced in detail. Significantly, the recent progress and expansions of emerging CTS/GO hybrid networks-based adsorbents for various organic dye removal applications are summarized and compared to favor the reader with a clear overview.

Table 1: Information of some organic dyes.

Organic dyes	Structures	Dye class	λ_{\max} (nm)	M.W. (g·mol ⁻¹)	Contamination sources
Methylene Blue		+	665	319.85	Textile, Leather, Dyestuff, Paper and Plastic industries; Pharmaceutical uses; Laundry activity
Rhodamine B		+	558	479.02	Natural sources; Textile, Dyestuff, Food, Leather and Plastic industries; Laundry activity
Malachite green		+	617	364.91	Textile, Leather and Dyestuff industries; Lab activities; Laundry activity
Methyl Orange		-	464	327.33	Textile, Foodstuffs, Paper and Leather industries; Lab activities; Laundry activity
Congo Red		-	498	696.67	Textile, Leather and Dyestuff industries
Brilliant green		+	625	475.60	Pigments, Dyestuff and Chemical industries; Pharmaceutical uses
Crystal violet		+	590	407.98	Textile, Leather and Dyestuff industries; Laundry activity

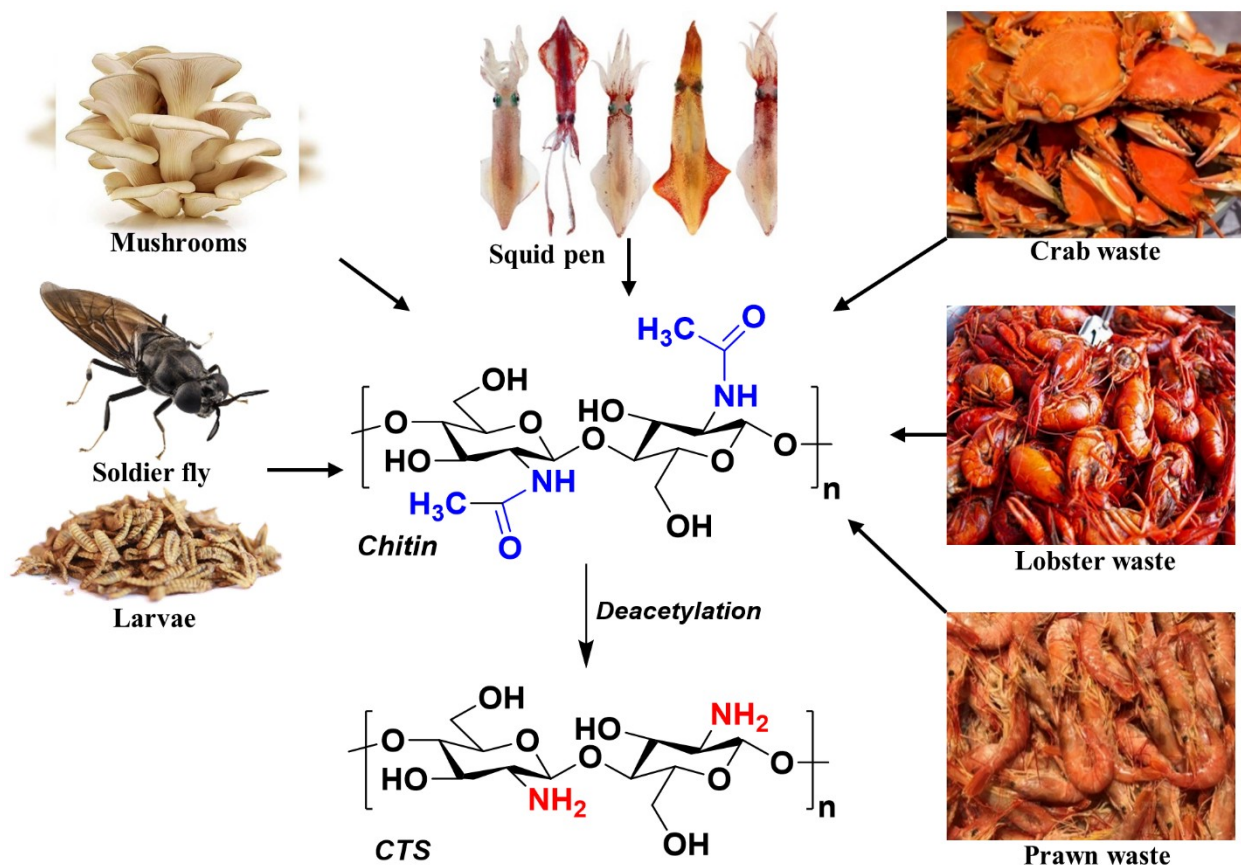


Figure 1: Preparation of chitin and CTS molecules from the waste supply sources.

ADSORPTION TECHNIQUE

Adsorption is known as a surface phenomenon, which is occurred at the surface or interface positions. In another word, it mentions a procedure in which a material is gathered at a solid surface by its gaseous or liquid surroundings. In 1881, the term "adsorption" was firstly introduced by Heinrich Kayser – a German physicist (1853–1940) in order to distinguish surface accumulation from intermolecular penetration, as well as which assumes surface accumulation of a material to be a fundamental feature of an adsorption process (4). Theoretically, two adsorption types count physisorption and chemisorption. If the attractive forces between the adsorbed molecules and the solid surface relate to van der Waals forces, which are usually weak forces inducing reversible adsorption to be named physisorption. In comparison, chemisorption involves chemical bonds between the adsorbed molecules and the solid surface, which is higher strength, leading to hard removal of the chemisorbed molecules from the solid surface (4).

Besides, adsorption techniques are extensively employed to remove plenty of pollutants from water/wastewater, especially for organic dyes that are not readily biodegradable. The general mechanism of dye adsorption consists of three steps during the process of color removal following as (34): (i) diffusion of organic dye molecules – adsorbates presented available in the bulk solution can be onto the material-based adsorbent surface; (ii) the organic dye adsorption on the material-based adsorbent surface can base on molecular interactions (i.e., "film diffusion"); and (iii) diffusion of organic dye molecules can be moved from the surface to the inside of the materials-based adsorbents (i.e., "surface diffusion" or "pore diffusion"). The processes of diffusion and surface reaction occurring on the materials-based adsorbents are described in Figure 3. Overall, agitation and concentration of the organic dye molecules in the solution probably impact to the first step. The nature of the organic dye molecules directly influences to the second step, for example, cationic and anionic features. At the same time, the third step regards to the rate-confirming stage in this process that surely impacts to the adsorption of organic dye molecules on the

substrates. In particular, external diffusion occurring in the adsorption processes is the most efficacy, while intraparticle diffusion will attain a longer contact time in non-flow systems. Moreover, these are influenced by

physicochemical factors, examples for interactions of organic dyes and adsorbents, particle sizes, surface areas of adsorbents, pH values, temperatures, and contact times.

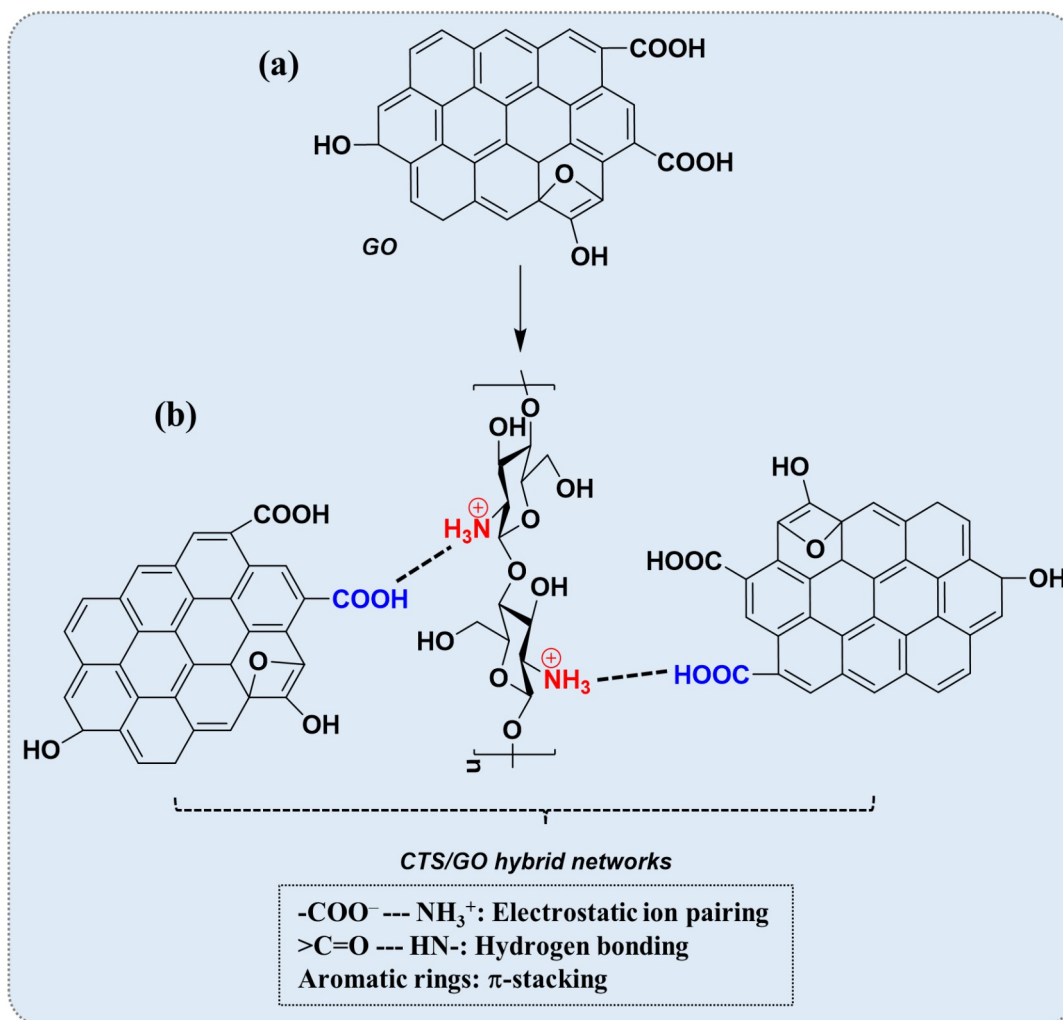


Figure 2: Schematic of chemical structure of GO (a) and possible interactions in CTS/GO hybrid networks (b).

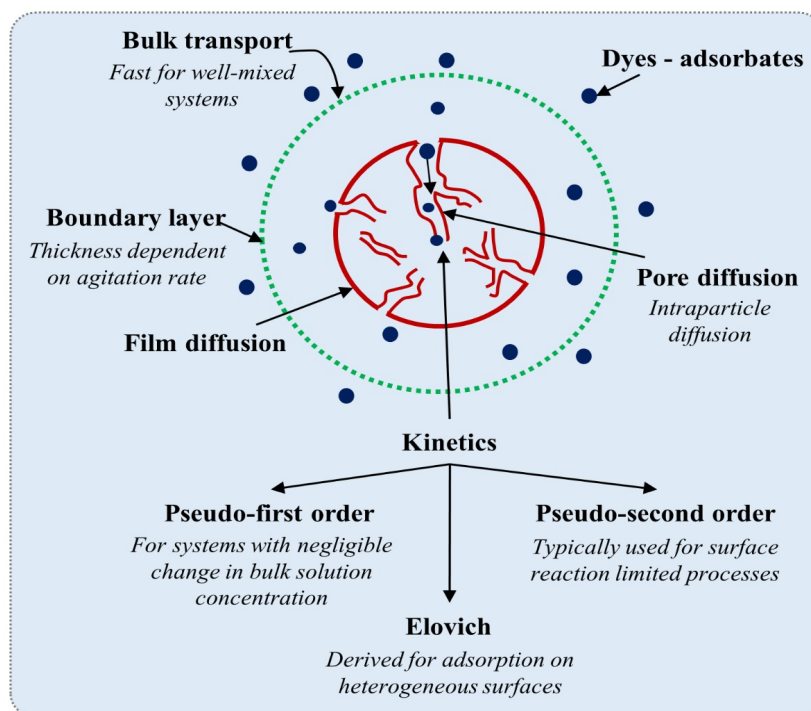


Figure 3: The processes of diffusion and surface reaction occurring on the materials-based adsorbents.

In addition, adsorption isotherms and kinetics are suitable models to evaluate the adsorption process (35). Specifically, adsorption isotherms can reach through a change in the initial concentrations of organic dye solutions, and the other corresponding parameters are constants (i.e., contact times, temperatures, pH values, and stirring speeds). Basically, the removal efficiency will attain high values through increases of the organic dye concentrations until no further uptake, which is named saturation or equilibrium state. The common adsorption isotherm models are listed in Table 2, which are on basic of the original and linearized forms. Concomitantly, many other models can also be employed to elucidate the mechanism of organic

dye adsorption on a material-based adsorbent, e.g., common adsorption kinetic models (Table 2 and Figure 3). In fact, the adsorption kinetics are usually defined by establishing plots of the adsorbed quantity vs. a time function to manifest the possible nature of the adsorption process and the kinetics. Overall, in order to more easily understand, this review has been summarized on basic of various adsorbent types studied from the progress and expansions of CTS/GO hybrid networks-based adsorbents coupled with numerous other support materials (i.e., reduced GO, magnetic iron oxide, polymeric materials, metal-organic frameworks, etc.), as well as organic dye removal efficiency and adsorption mechanisms onto these emerging adsorbents.

Table 2: Common adsorption isotherm and kinetic models.

Adsorption isotherms	Original form	Linearized form	Plot	Constants attained from the plot
Langmuir	$q_e = \frac{q_m K_L C_e}{1 + K_L C_e}$	$\frac{C_e}{q_e} = \frac{1}{q_m K_L} + \frac{C_e}{q_m}$	$\frac{C_e}{q_e}$ vs C_e	q_m and K_L
Freundlich	$q_e = K_F \frac{C_e^{1/n}}{n}$	$\log q_e = \log K_F + \frac{1}{n} \log C_e$	$\log q_e$ vs $\log C_e$	K_F and n
BET	$q_e = \frac{K_B C_e q_m}{(C_s - C_e)[1 + (K_B - 1)(\frac{C_e}{C_s})]}$	$\frac{C_e}{q_e(C_s - C_e)} = (\frac{1}{K_B q_m}) + (\frac{K_B - 1}{K_B q_m})(\frac{C_e}{C_s})$	$\frac{C_e}{q_e(C_s - C_e)}$ vs $(\frac{C_e}{C_s})$	K_B and q_m
Temkin	$q_e = \frac{R \cdot T}{b} \ln(A_T C_e)$	$q_e = \frac{R \cdot T}{b} \ln A_T + \frac{R \cdot T}{b} \ln C_e$	$\ln C_e$ vs q_e	A_T and b
Dubinin-Radushkevich	$q_e = q_s e^{-K_{D.R.} \epsilon^2}$	$\ln q_e = \ln q_s - K_{D.R.} \epsilon^2$ $\epsilon = RT \ln(1 + \frac{1}{C_e})$	$\ln q_e$ vs ϵ^2	$K_{D.R.}$ and q_s
Toth	$q_e = \frac{K_T C_e}{\sqrt[t]{a_T + C_e^t}}$	$\log q_e = 2 \log K_T - \frac{1}{t} \log a_T + (2 - \frac{1}{t}) \log C_e$	$\log q_e$ vs $\log C_e$	K_T and a_T
Redlich-Peterson	$q_e = \frac{A \times C_e}{1 + BC_e^\beta}$	$\ln \frac{C_e}{q_e} = \beta \ln C_e - \ln A$	$\ln \frac{C_e}{q_e}$ vs $\ln C_e$	A and β
Adsorption kinetics	Linearized form	Plot	Constants attained from the plot	
Pseudo-first-order	$\ln(q_e - q_t) = \ln q_e - k_1 t$	$\ln(q_e - q_t)$ vs t	k_1	
Pseudo-second-order	$\frac{t}{q_t} = \frac{1}{k_2 q_e^2} + \frac{t}{q_e}$	$\frac{t}{q_t}$ vs $\frac{t}{q_e}$	k_2	
Elovich	$q_t = \frac{1}{\beta} \ln \alpha \beta + \frac{1}{\beta} \ln t$	q_t vs $\ln t$	α and β	
Intraparticle diffusion	$q_t = k_t t^{0.5} + l$	q_t vs $t^{0.5}$	k_t and l	

VARIOUS CTS/GO HYBRID NETWORKS-BASED ADSORBENTS AND ORGANIC DYE ADSORPTION PERFORMANCES

As known, CTS is often dissolved in acetic acid, and GO is well stable in colloidal solutions, which can easily couple together to attain CTS/GO hybrid networks with a homogeneous mixture through electrostatic interactions, hydrogen bonding, and π -stacking resulting in outstandingly mechanical and thermal features (6, 29). Concomitantly, the CTS/GO hybrid networks-based materials can be prepared from various methods such as supplement of NaOH, violent shaking, sonication, freeze-drying, etc. (6, 31-33). As a result, the CTS/GO hybrid networks-based materials have been formed with various shapes such as membranes, beads, sponges, and columns (6, 36-39), and which are all utilized successfully as effective adsorbents for organic dye removal from water/wastewater (40).

Notably, other components – support materials have been supplemented to enhance the organic dye adsorption performance of the CTS/GO hybrid networks-based materials in recent years; in particular, two-dimensional GO has also been developed to reduced GO (rGO) or three-dimensional GO-based aerogels. Typically, the GO is formed through oxidizing graphite (i.e., Hummers method) (41), while the rGO is synthesized by reducing the GO (i.e., various thermal methods, reducing agents, electrochemical reduction) (42-45). Actually, the oxygen-containing functional groups on the GO are difficult to reduce, which still contained some on the rGO. Besides, the rGO can combine with various metals or metal oxide particles (46), facilitating their incorporation within the CTS molecule. For instance, CTS/rGO hybrid network has been coupled with iron oxide (Fe_3O_4) to attain magnetic CTS/rGO hybrid network-based adsorbents that are effectively applied for the cefixime adsorption (47) (Table 3). Concomitantly, a comparison of dye removal performance of CTS/GO and CTS/rGO hybrid networks utilizing as adsorbents indicated that the CTS/GO hybrid network has adsorbed efficiently more (48) (Table 3), which can involve to the presence of more numerous available functional groups offering a combination of electrostatic interactions, hydrogen bonding and π -stacking with the organic dye molecules (4, 6, 28). As a result, the pseudo-second-order model studied in this research was the best model, indicated that the organic dye adsorption could be induced on the chemical rate-limiting step (i.e., electron share or covalent forces).

So far, magnetic CTS-based adsorbent has emerged as a potential material for removing pollutants from water/wastewater. There has

recently been a considerable interest in the magnetic CTS/GO hybrid network-based material as well (49, 50) (Table 3); notably, these magnetic materials have shown a fast removal performance. Obviously, the magnetism approach can facilitate well for separating the adsorbents from water/wastewater based on a simple magnetic procedure (51). In fact, separation of CTS/GO hybrid network-based materials using conventional sedimentation and filtration techniques is an important challenge due to blocked and lost filters inducing secondary contaminations. Hence, the choice of Fe_3O_4 is the most efficacy, owing to its low toxicity, good compatibility and high magnetic features (52). For preparation methods of the magnetic CTS/GO hybrid network-based materials, it can be easily created via in- or ex-situ approach, or a combination of both these approaches (49, 53), or alterations of these two methods (50, 54) (i.e., CTS/ Fe_3O_4 hybrid network can be first created before being coupled with GO, or opposite). Nonetheless, the shape and size of the Fe_3O_4 nanoparticles are also important characteristics to couple with the CTS/GO hybrid network-based materials for organic dye removal performances. Although the Fe_3O_4 nanoparticles can be easily clustered that is mainly due to their magnetic nature, several studies have also been conducted to control the suitable shape and size with the research aims (54-56). For example, Fe_3O_4 particles could be attained with the spherical shapes and ~45 nm of size by Shafaati et al. (55), but their particle size has increased with incorporating the CTS, suggesting that the CTS chains could probably induce linking together for the neighboring Fe_3O_4 particles. Silica is employed to coat the Fe_3O_4 particles resulting from the significantly reduced agglomeration (56). Thereby, the use of silica is a promising approach to coat and protect magnetic iron-containing particles in the CTS/GO hybrid networks, as well as stability of these materials need to be investigated more to not leach the GO flakes or the magnetic iron oxide particles.

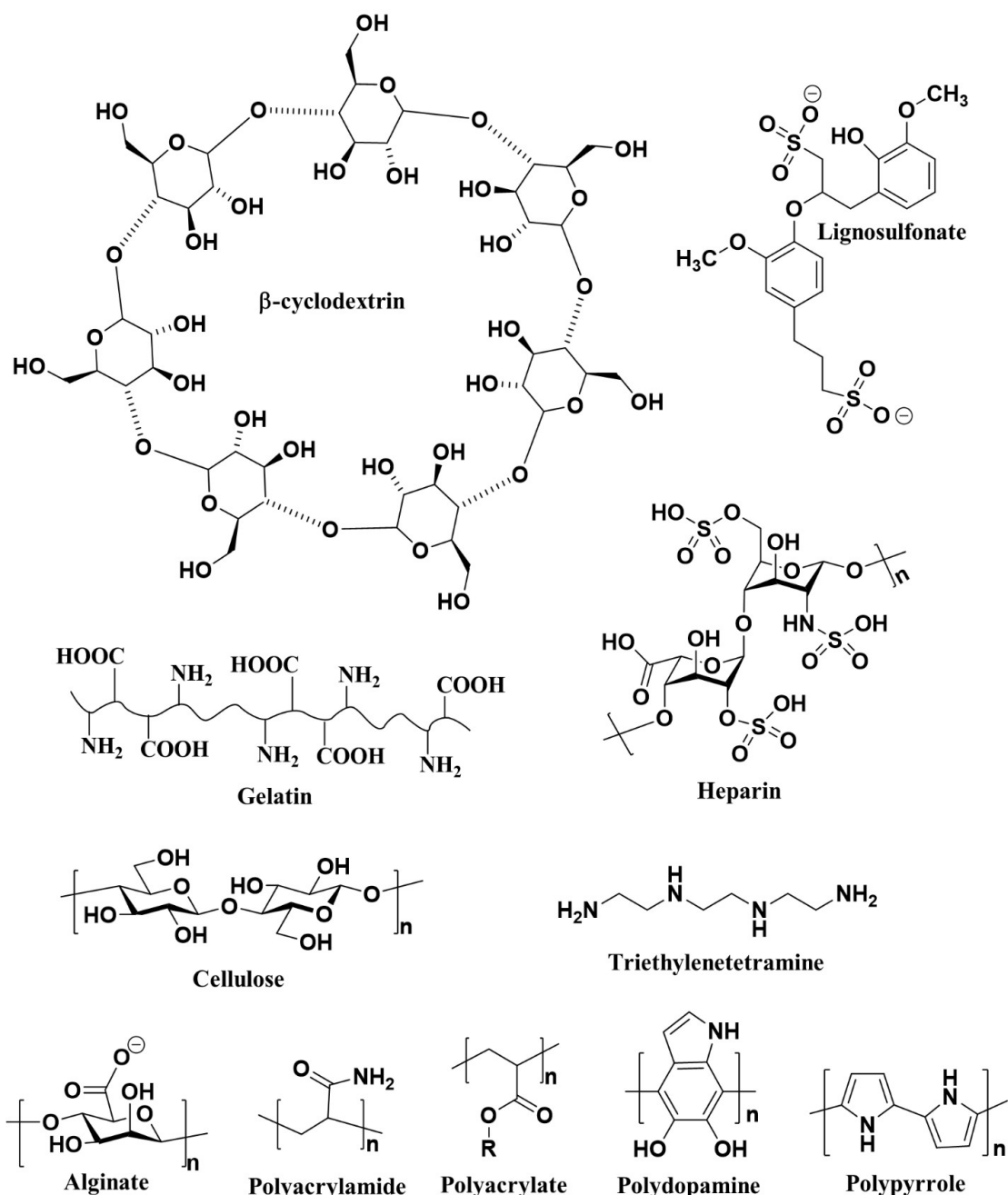
In addition, the CTS/GO (or CTS/rGO) hybrid networks-based materials with three-dimensional porous structures acting as scaffolds (i.e., aerogel, foam, sponge, column) can be fabricated through the available wrinkling and blending of GO nanosheets. These scaffolds are effectively applied in the organic dye removal applications owing to high surface areas, low mass densities (porous structure) and good mechanical strength (57, 58); besides, these scaffolds-based adsorbents are also easily regained from the aqueous solution after completing the adsorption procedure. Indeed, the GO or rGO alone with three-dimensional structures reach relatively poor stability in water, but this stability can be improved significantly through a combination of the three-dimensional GO or rGO

network and the CTS molecules. For instance, the three-dimensional CTS/GO hybrid network-based columns have been successfully applied in five adsorption-regeneration cycles reaching >90%-adsorption performances (6, 32), and the layered CTS/GO hybrid network-based sponges have also been attained good stability and effective recyclability resulting in >80%-adsorption performances over five adsorption-regeneration cycles (59). Besides, plenty of studies on CTS/GO hybrid network-based aerogel have been successfully fabricated to remove effectively azo dyes, anionic and cationic dyes (60, 61) from water.

Furthermore, other additives – support materials have been coupled with the CTS/GO hybrid network to become potential and outstanding materials-based adsorbents in environmental applications. For example, β -cyclodextrin (Figure 4) has been combined with the CTS/GO hybrid network to enhance the adsorption performance of methylene blue following GO < CTS/GO < CTS/GO/ β -cyclodextrin networks (62), similarly for a study on the adsorption performance of hydroquinone and dye molecules (63) (Table 3). Besides, polypyrrole (Figure 4) has also been used to couple with the CTS/GO hybrid network basing on polymerization of the pyrrole monomer in the above-mentioned hybrid network, resulting in the ternary CTS/GO/polypyrrole hybrid network-based material that could become efficient adsorbents in the organic dye removal applications (64, 65) (Table 3). Interestingly, these hybrid networks-based adsorbents could incorporate magnetic nanoparticles to improve the separation of these adsorbents from water/wastewater after completing the organic dye adsorption process (66) (Table 3). Concomitantly, other polymers with high molecular weights (i.e., polydopamine, polyacrylamide, and polyacrylate are shown in Figure 4) have also been employed to combine with the CTS/GO hybrid network (67-69) that could significantly enhance the swelling and adsorption performances of these hybrid networks-based adsorbents (Table 3). In another word, these support materials have offered different binding sites to enhance the adsorption

performances, and which are considered promising materials-based adsorbents.

More notably, metal-organic frameworks (MOFs) have recently attracted much interest in environmental applications that is mainly due to their high surface areas and porosities and controlled pore structures. Thus, they have been used to add into the CTS/GO hybrid network that enhances adsorption performance (70, 71). Unfortunately, the MOFs are powdered materials that are hard to separate from water, which is its main limitation in environmental applications. Thereby, the CTS/GO hybrid network can be contributed like a matrix to encapsulate these powdered materials that can couple with magnetic iron to result in a necessary magnetic separation. Besides, plenty of other support materials has also been combined with the CTS/GO hybrid network; for examples, the use of hydroxyapatite [$\text{Ca}_{10}(\text{PO}_4)_6(\text{OH})_2$] has increased strength and organic pollutant adsorption performance (72), the use of silica (numerous silanol groups, Si-OH) has favored a good dispersion of GO nanosheets within CTS to reach effective adsorbents (73, 74), the use of triethylenetetramine and lignosulfonate (Figure 4) have supplied amine groups and different binding sites to enhance adsorption performance, respectively (75-77) (Table 3). In general, these studies manifested that these materials could become cost-effective, eco-friendly, and recyclable adsorbents for organic dye removal applications. Additionally, other biopolymers (i.e., gelatin, alginate, heparin, and cellulose are shown in Figure 4) have been blended with the CTS to create polymeric mixtures, which are then coupled with the GO nanosheets to attain outstanding performing adsorbents (78-81). Overall, the pseudo-second-order model studied in these researches were the best model; nonetheless, the kinetic studies need to investigate more, and the chemical/physical characterizations of the CTS can be focused more on the degree of deacetylation levels, molecular weight, etc., similarly, for the GO. Also, it is needed to develop further suitable recovery systems, as well as preparation process of the adsorbents should be employed green solvents and material sources.

**Figure 4:** Chemical structures of various additives.**Table 3.** Adsorption data of various CTS/GO hybrid networks-based adsorbents.

Adsorbents	Organic dyes	Adsorption performance (% or mg·g ⁻¹)	Adsorption isotherm models	Adsorption kinetic models
CTS/GO_1/15 (6)	Methylene blue, Rhodamine B, Congo Red, Methyl orange	~95.0%, >90.0%, ~70.0%, ~80.0%	--	--
CTS/GO (48)	Reactive Red	32.2 mg·g ⁻¹	Langmuir	Pseudo-second order
Magnetic CTS/rGO (47)	Cefixime	30.6 mg·g ⁻¹	Freundlich	--
Magnetic CTS/GO (49)	Methylene blue	74.93 mg·g ⁻¹	Freundlich	Pseudo-second order
CTS/GO/β-	Methylene blue	1134.0 mg·g ⁻¹	Freundlich	Pseudo-second order

cyclodextrin (62)				
Magnetic CTS/GO/ β -cyclodextrin (63)	Methylene blue	84.3 mg·g ⁻¹	Langmuir	Pseudo-second order
Polypyrrole/CTS/GO (64)				
Magnetic Polypyrrole/CTS/GO (66)	Ponceau 4R	5.4 mg·g ⁻¹	Langmuir	Pseudo-second order
CTS/Polycrylamide/GO (67)				
CTS/polyacrylate/GO (68)	Methylene blue, Food yellow 3	296.5 mg·g ⁻¹ , 280.3 mg·g ⁻¹	--	Pseudo-first order, Pseudo-second order
CTS/GO/Hydroxyapatite (72)	Congo Red, Acid Red 1, Reactive Red 2	43.1 mg·g ⁻¹ , 41.3 mg·g ⁻¹ , 40.0 mg·g ⁻¹	Freundlich	Pseudo-second order
CTS/lignosulfonate/GO (75)				
Magnetic CTS/lignosulfonate/GO (76)	Methylene blue	1023.9 mg·g ⁻¹	Langmuir	Pseudo-second order

CONCLUSIONS AND FUTURE RESEARCH OUTLOOKS

With a large number of publications, the CTS/GO hybrid networks-based materials are employed as potential and interesting adsorbents for various organic dye removal applications. In summary, the CTS/GO hybrid networks easily couple with numerous other components or additives – support materials (i.e., rGO, magnetic iron oxide, polymeric materials, MOFs, etc.) that is attracting considerable attention, as well as the CTS/GO hybrid networks-based materials have attained not only magnificent adsorption capacity with organic dyes but also heavy metal ions. Nonetheless, several challenges still exist for removing a variety of pollutants directly implicating in terms of costs, which regards the regeneration of the CTS/GO hybrid networks-based adsorbents. These adsorbents should be effectively regenerated to can be employed multiple times in the adsorption process, which relates to washing-solvents and natures of polysaccharide/carbon-based materials (CTS/GO); thus, the adsorption capacity can reduce with each cycle of adsorption-regeneration (i.e., the polysaccharide hydrolysis on the CTS). These require an offer of more longer-lasting and cost-effective CTS/GO hybrid networks-based adsorbents.

In addition to the effective performances of these adsorbents, they also need to be removed from the aqueous solution after completing the adsorption purposes, especially for the magnetic CTS/GO hybrid networks. Concomitantly, there are also concerns about the environmental influences

of other CTS/GO hybrid networks-based adsorbents, which can adversely impact to the water environment if these materials-based adsorbents are leached. Consequently, the emerging CTS/GO hybrid networks-based adsorbents have to be stable and not leach regarding other support materials (i.e., magnetic iron oxide particles, GO flakes, and MOFs, etc.), which is considered as one of the importantly environmental perspectives. The other studies on intraparticle diffusion and adsorption kinetics also need to be investigated further, although most studied kinetic models regarded to pseudo-second-order models. These emerging materials-based adsorbents are attractive and potential materials that is probably due to the abundance supply source from chitin (seafood waste sources), and expansion of these materials in the various preparation methods and high-performance studies. Besides, the recent development has attended to new two-dimensional materials (i.e., MoS₂, MXenes, and MoSe₂), which are potential support materials utilized as emerging adsorbents and can easily couple with the CTS or CTS/GO hybrid networks to generate novel materials-based adsorbents with outstanding performances.

REFERENCES

1. Ceylan H, Pekdemir AD, Önal M, Sarikaya Y. The Effect of the Hydrothermal and Thermal Deactivations on the Adsorptive Properties and Liquid Permeability of a Silica Gel. *Journal of the Turkish Chemical Society Section A: Chemistry* [Internet]. 2021 Mar 14; 8(2): 477-82. <DOI>.

2. İlbay Z, Yildirim E. Vermicompost as a potential adsorbent for the adsorption of methylene blue dye from aqueous solutions. *Journal of the Turkish Chemical Society Section A: Chemistry*. 2020 Oct 23;893-902. [<DOI>](#).
3. Lalikoğlu M. Mg-Al Layered Double Hydroxide (LDH) as an Adsorbent for Removal of Itaconic Acid from Aqueous Solutions: Equilibrium and Kinetic Study. *Journal of the Turkish Chemical Society Section A: Chemistry*. 2020 Dec 5;103-16. [<DOI>](#).
4. Vo TS, Hossain MM, Jeong HM, Kim K. Heavy metal removal applications using adsorptive membranes. *Nano Convergence*. 2020 Dec;7(1):36. [<DOI>](#).
5. Yildirim A, Acay H, Baran A. Synthesis and characterization of molecularly imprinted composite as a novel adsorbent and competition with non-imprinting composite for removal of dye. *Journal of the Turkish Chemical Society Section A: Chemistry*. 2021 May 4;609-22. [<DOI>](#).
6. Vo TS, Vo TTBC, Suk JW, Kim K. Recycling performance of graphene oxide-chitosan hybrid hydrogels for removal of cationic and anionic dyes. *Nano Convergence*. 2020 Dec;7(1):4. [<DOI>](#).
7. Aksu Z, Tezer S. Biosorption of reactive dyes on the green alga *Chlorella vulgaris*. *Process Biochemistry*. 2005 Mar;40(3-4):1347-61. [<DOI>](#).
8. Salleh MAM, Mahmoud DK, Karim WAWA, Idris A. Cationic and anionic dye adsorption by agricultural solid wastes: A comprehensive review. *Desalination*. 2011 Oct;280(1-3):1-13. [<DOI>](#).
9. Sanghi R, Bhattacharya B. Review on decolorisation of aqueous dye solutions by low cost adsorbents. *Coloration Technol*. 2002 Sep;118(5):256-69. [<DOI>](#).
10. Vo TS, Vo TTBC. Preparation and Characterization of Bis-Propargyl-Succinate, and its Application in Preliminary Healing Ability of Crosslinked Polyurethane using "Azide-Alkyne" Click. *Journal of Engineering Science & Technology Review*. 2020;13(4): 110-6.
11. Vo TS, Vo TTBC, Tien TT, SiNh NT. Enhancement of mechanical property of modified polyurethane with bis-butyl succinate. *Journal of the Turkish Chemical Society Section A: Chemistry*. 2021 Mar 30;519-26. [<DOI>](#).
12. Vo TS, Vo TTBC. A Self-Healing Material Based on Microcapsules of Poly(Urea-Formaldehyde)/Bis-Propargyl-Succinate Containing in Polyurethane Matrix. *Journal of the Turkish Chemical Society Section A: Chemistry*. 2021 Jul 26;787-802. [<DOI>](#).
13. Crini G. Non-conventional low-cost adsorbents for dye removal: A review. *Bioresource Technology*. 2006 Jun;97(9):1061-85. [<DOI>](#).
14. Gupta VK, Carrott PJM, Ribeiro Carrott MML, Suhas. Low-Cost Adsorbents: Growing Approach to Wastewater Treatment - a Review. *Critical Reviews in Environmental Science and Technology*. 2009 Oct 9;39(10):783-842. [<DOI>](#).
15. Gurbanova M, LoboıChenko V, Leonova N, Strelets V. Effect Of Inorganic Components Of Fire Foaming Agents On The Aquatic Environment. *Journal of the Turkish Chemical Society Section A: Chemistry*. 2020 Oct 27;833-44. [<DOI>](#).
16. Nworie F, Ebunoha J. Hydrothermal Synthesis of Fluorescent Schiff Base Functionalized Carbon Dot Composite for The Removal Of Cd(II) Ions From Aqueous Solution: Equilibrium and Kinetic Studies. *Journal of the Turkish Chemical Society Section A: Chemistry*. 2020 Aug 2;137-56. [<DOI>](#).
17. Yakişik H, Özveren U. Synthesis of Polyaniline / Biochar composite material and modeling with nonlinear model for removal of copper(II) heavy metal ions. *Journal of the Turkish Chemical Society Section A: Chemistry*. 2021 Feb 28;8(1):291-304. [<DOI>](#).
18. Ceylan S, Alatepeli B. Evaluation of PVA/Chitosan Cryogels as Potential Tissue Engineering Scaffolds; Synthesis, cytotoxicity and genotoxicity investigations. *Journal of the Turkish Chemical Society Section A: Chemistry*. 2020 Nov 20;69-78. [<DOI>](#).
19. Islam S, Bhuiyan MAR, Islam MN. Chitin and Chitosan: Structure, Properties and Applications in Biomedical Engineering. *J Polym Environ*. 2017 Sep;25(3):854-66. [<DOI>](#).
20. Rinaudo M. Chitin and chitosan: Properties and applications. *Progress in Polymer Science*. 2006 Jul;31(7):603-32. [<DOI>](#).
21. Dutta PK, Dutta J, Tripathi V. Chitin and chitosan: Chemistry, properties and applications. 2004; *Journal of Scientific & Industrial Research*. 2004;63: 20-31.
22. Vo TS, Vo TTBC, Nguyen TS, Pham ND. Incorporation of hydroxyapatite in crosslinked gelatin/chitosan/poly(vinyl alcohol) hybrids utilizing as reinforced composite sponges, and their water absorption ability. *Progress in Natural Science: Materials International*. 2021 Sep;S1002007121001349. [<DOI>](#).
23. Tamer Y, Özeren MD, Berber H. High Adsorption Performance of Graphene Oxide Doped Double Network Hydrogels for Removal of Azo Dyes from Water and Their Kinetics. *J Polym Environ [Internet]*. 2021 May 12 [cited 2021 Sep 30]; [<URL>](#).
24. Li Y, Du Q, Liu T, Sun J, Wang Y, Wu S, et al. Methylene blue adsorption on graphene oxide/calcium alginate composites. *Carbohydrate Polymers*. 2013 Jun;95(1):501-7. [<DOI>](#).
25. Wu Z, Zhong H, Yuan X, Wang H, Wang L, Chen X, et al. Adsorptive removal of methylene blue by rhamnolipid-functionalized graphene oxide from wastewater. *Water Research*. 2014 Dec;67:330-44. [<DOI>](#).
26. Sitko R, Musielak M, Zawisza B, Talik E, Gagor A. Graphene oxide/cellulose membranes in adsorption of divalent metal ions. *RSC Adv*. 2016;6(99):96595-605. [<DOI>](#).
27. Musielak M, Gagor A, Zawisza B, Talik E, Sitko R. Graphene Oxide/Carbon Nanotube Membranes for Highly

- Efficient Removal of Metal Ions from Water. ACS Appl Mater Interfaces. 2019 Aug 7;11(31):28582-90. <DOI>.
28. Ramesha GK, Vijaya Kumara A, Muralidhara HB, Sampath S. Graphene and graphene oxide as effective adsorbents toward anionic and cationic dyes. Journal of Colloid and Interface Science. 2011 Sep;361(1):270-7. <DOI>.
29. Yang X, Tu Y, Li L, Shang S, Tao X. Well-Dispersed Chitosan/Graphene Oxide Nanocomposites. ACS Appl Mater Interfaces. 2010 Jun 23;2(6):1707-13. <DOI>.
30. Fan L, Luo C, Li X, Lu F, Qiu H, Sun M. Fabrication of novel magnetic chitosan grafted with graphene oxide to enhance adsorption properties for methyl blue. Journal of Hazardous Materials. 2012 May;215-216:272-9. <DOI>.
31. Javadi E, Baghdadi M, Taghavi L, Ahmad Panahi H. Removal of 4-nonylphenol from Surface Water and Municipal Wastewater Effluent Using Three-Dimensional Graphene Oxide-Chitosan Aerogel Beads. Int J Environ Res. 2020 Oct;14(5):513-26. <DOI>.
32. Lai KC, Lee LY, Hiew BYZ, Yang TC-K, Pan G-T, Thangalazhy-Gopakumar S, et al. Utilisation of eco-friendly and low cost 3D graphene-based composite for treatment of aqueous Reactive Black 5 dye: Characterisation, adsorption mechanism and recyclability studies. Journal of the Taiwan Institute of Chemical Engineers. 2020 Sep;114:57-66. <DOI>.
33. Zhang M, Ma G, Zhang L, Chen H, Zhu L, Wang C, et al. Chitosan-reduced graphene oxide composites with 3D structures as effective reverse dispersed solid phase extraction adsorbents for pesticides analysis. Analyst. 2019;144(17):5164-71. <DOI>.
34. Khraisheh MAM, Al-Ghouti MA, Allen SJ, Ahmad MN. Effect of OH and silanol groups in the removal of dyes from aqueous solution using diatomite. Water Research. 2005 Mar;39(5):922-32. <DOI>.
35. Allen SJ, McKay G, Porter JF. Adsorption isotherm models for basic dye adsorption by peat in single and binary component systems. Journal of Colloid and Interface Science. 2004 Dec;280(2):322-33. <DOI>.
36. Qi C, Zhao L, Lin Y, Wu D. Graphene oxide/chitosan sponge as a novel filtering material for the removal of dye from water. Journal of Colloid and Interface Science. 2018 May;517:18-27. <DOI>.
37. Croitoru A-M, Fikai A, Fikai D, Trusca R, Dolete G, Andronescu E, et al. Chitosan/Graphene Oxide Nanocomposite Membranes as Adsorbents with Applications in Water Purification. Materials. 2020 Apr 4;13(7):1687. <DOI>.
38. Kamal MA, Bibi S, Bokhari SW, Siddique AH, Yasin T. Synthesis and adsorptive characteristics of novel chitosan/graphene oxide nanocomposite for dye uptake. Reactive and Functional Polymers. 2017 Jan;110:21-9. <DOI>.
39. Li K, Zhao B, Yu Q, Xu J, Li X, Wei D, et al. Porous graphene oxide/chitosan beads with honeycomb-biomimetic microchannels as hydrophilic adsorbent for the selective capture of glycopeptides. Microchim Acta. 2020 Jun;187(6):324. <DOI>.
40. Aili Y. Preparation and Adsorption Properties of Composite Adsorbent Graphene Oxide-Chitosan. Rare metal materials and engineering. 2018;47(5):1583-8.
41. Eda G, Chhowalla M. Chemically Derived Graphene Oxide: Towards Large-Area Thin-Film Electronics and Optoelectronics. Adv Mater. 2010 Jun 2;22(22):2392-415. <DOI>.
42. Pei S, Cheng H-M. The reduction of graphene oxide. Carbon. 2012 Aug;50(9):3210-28. <DOI>.
43. Zhang J, Yang H, Shen G, Cheng P, Zhang J, Guo S. Reduction of graphene oxide via l-ascorbic acid. Chem Commun. 2010;46(7):1112-4. <DOI>.
44. Wang Z, Zhou X, Zhang J, Boey F, Zhang H. Direct Electrochemical Reduction of Single-Layer Graphene Oxide and Subsequent Functionalization with Glucose Oxidase. J Phys Chem C. 2009 Aug 13;113(32):14071-5. <DOI>.
45. Shao Y, Wang J, Engelhard M, Wang C, Lin Y. Facile and controllable electrochemical reduction of graphene oxide and its applications. J Mater Chem. 2010;20(4):743-8. <DOI>.
46. Sreepasad TS, Maliyekkal SM, Lisha KP, Pradeep T. Reduced graphene oxide-metal/metal oxide composites: Facile synthesis and application in water purification. Journal of Hazardous Materials. 2011 Feb;186(1):921-31. <DOI>.
47. Ciğeroğlu Z, Küçükyıldız G, Erim B, Alp E. Easy preparation of magnetic nanoparticles-rGO-chitosan composite beads: Optimization study on cefixime removal based on RSM and ANN by using Genetic Algorithm Approach. Journal of Molecular Structure. 2021 Jan;1224:129182. <DOI>.
48. Guo X, Qu L, Tian M, Zhu S, Zhang X, Tang X, et al. Chitosan/Graphene Oxide Composite as an Effective Adsorbent for Reactive Red Dye Removal. water environ res. 2016 Jul 1;88(7):579-88. <DOI>.
49. Singh N, Riyajuddin S, Ghosh K, Mehta SK, Dan A. Chitosan-Graphene Oxide Hydrogels with Embedded Magnetic Iron Oxide Nanoparticles for Dye Removal. ACS Appl Nano Mater. 2019 Nov 22;2(11):7379-92. <DOI>.
50. Rebekah A, Bharath G, Naushad Mu, Viswanathan C, Ponpandian N. Magnetic graphene/chitosan nanocomposite: A promising nano-adsorbent for the removal of 2-naphthol from aqueous solution and their kinetic studies. International Journal of Biological Macromolecules. 2020 Sep;159:530-8. <DOI>.
51. Kharisova OV, Dias HVR, Kharisov BI. Magnetic adsorbents based on micro- and nano-structured materials. RSC Adv. 2015;5(9):6695-719. <DOI>.
52. Shan H, Peng S, Zhao C, Zhan H, Zeng C. Highly efficient removal of As(III) from aqueous solutions using goethite/graphene oxide/chitosan nanocomposite. International Journal of Biological Macromolecules. 2020 Dec;164:13-26. <DOI>.

53. Xu L, Suo H, Wang J, Cheng F, Liu H, Qiu H. Magnetic graphene oxide decorated with chitosan and Au nanoparticles: synthesis, characterization and application for detection of trace rhodamine B. *Anal Methods*. 2019;11(30):3837–43. [<DOI>](#).
54. Tasmia, Shah J, Jan MR. Microextraction of Selected Endocrine Disrupting Phenolic Compounds using Magnetic Chitosan Biopolymer Graphene Oxide Nanocomposite. *J Polym Environ*. 2020 Jun;28(6):1673–83. [<DOI>](#).
55. Shafaati M, Miralinaghi M, Shirazi RHSM, Moniri E. The use of chitosan/Fe₃O₄ grafted graphene oxide for effective adsorption of rifampicin from water samples. *Res Chem Intermed*. 2020 Dec;46(12):5231–54. [<DOI>](#).
56. Jiang X, Pan W, Chen M, Yuan Y, Zhao L. The fabrication of a thiol-modified chitosan magnetic graphene oxide nanocomposite and its adsorption performance towards the illegal drug clenbuterol in pork samples. *Dalton Trans*. 2020;49(18):6097–107. [<DOI>](#).
57. Ma Y, Chen Y. Three-dimensional graphene networks: synthesis, properties and applications. *National Science Review*. 2015 Mar 1;2(1):40–53. [<DOI>](#).
58. Sun Z, Fang S, Hu YH. 3D Graphene Materials: From Understanding to Design and Synthesis Control. *Chem Rev*. 2020 Sep 23;120(18):10336–453. [<DOI>](#).
59. Zhang D, Li N, Cao S, Liu X, Qiao M, Zhang P, et al. A Layered Chitosan/Graphene Oxide Sponge as Reusable Adsorbent for Removal of Heavy Metal Ions. *Chem Res Chin Univ*. 2019 Jun;35(3):463–70. [<DOI>](#).
60. Wang Y, Xia G, Wu C, Sun J, Song R, Huang W. Porous chitosan doped with graphene oxide as highly effective adsorbent for methyl orange and amido black 10B. *Carbohydrate Polymers*. 2015 Jan;115:686–93. [<DOI>](#).
61. Salzano de Luna M, Ascione C, Santillo C, Verdolotti L, Lavorgna M, Buonocore GG, et al. Optimization of dye adsorption capacity and mechanical strength of chitosan aerogels through crosslinking strategy and graphene oxide addition. *Carbohydrate Polymers*. 2019 May;211:195–203. [<DOI>](#).
62. Liu Y, Huang S, Zhao X, Zhang Y. Fabrication of three-dimensional porous β -cyclodextrin/chitosan functionalized graphene oxide hydrogel for methylene blue removal from aqueous solution. *Colloids and Surfaces A: Physicochemical and Engineering Aspects*. 2018 Feb;539:1–10. [<DOI>](#).
63. Fan L, Luo C, Sun M, Qiu H, Li X. Synthesis of magnetic β -cyclodextrin–chitosan/graphene oxide as nanoadsorbent and its application in dye adsorption and removal. *Colloids and Surfaces B: Biointerfaces*. 2013 Mar;103:601–7. [<DOI>](#).
64. Salahuddin NehalA, EL-Daly HosnyA, El Sharkawy RehabG, Nasr BeshoyT. Synthesis and efficacy of PPy/CS/GO nanocomposites for adsorption of ponceau 4R dye. *Polymer*. 2018 Jun;146:291–303. [<DOI>](#).
65. Kamal S, Khan F, Kausar H, Khan MS, Ahmad A, Ishraque Ahmad S, et al. Synthesis, characterization, morphology, and adsorption studies of ternary nanocomposite comprising graphene oxide, chitosan, and polypyrrole. *Polymer Composites*. 2020 Sep;41(9):3758–67. [<DOI>](#).
66. Salahuddin NA, El-Daly HA, El Sharkawy RG, Nasr BT. Nano-hybrid based on polypyrrole/chitosan/grapheneoxide magnetite decoration for dual function in water remediation and its application to form fashionable colored product. *Advanced Powder Technology*. 2020 Apr;31(4):1587–96. [<DOI>](#).
67. Wang Z, Zhang G, Li Y. Preparation of Chitosan/Polyacrylamide/Graphene Oxide Composite Membranes and Study of Their Methylene Blue Adsorption Properties. *Materials*. 2020 Oct 2;13(19):4407. [<DOI>](#).
68. Chang Z, Chen Y, Tang S, Yang J, Chen Y, Chen S, et al. Construction of chitosan/polyacrylate/graphene oxide composite physical hydrogel by semi-dissolution/acidification/sol-gel transition method and its simultaneous cationic and anionic dye adsorption properties. *Carbohydrate Polymers*. 2020 Feb;229:115431. [<DOI>](#).
69. Fu J, Xin Q, Wu X, Chen Z, Yan Y, Liu S, et al. Selective adsorption and separation of organic dyes from aqueous solution on polydopamine microspheres. *Journal of Colloid and Interface Science*. 2016 Jan;461:292–304. [<DOI>](#).
70. Guo X, Yang H, Liu Q, Liu J, Chen R, Zhang H, et al. A chitosan-graphene oxide/ZIF foam with anti-biofouling ability for uranium recovery from seawater. *Chemical Engineering Journal*. 2020 Feb;382:122850. [<DOI>](#).
71. Li J, Wang X, Zhao G, Chen C, Chai Z, Alsaedi A, et al. Metal-organic framework-based materials: superior adsorbents for the capture of toxic and radioactive metal ions. *Chem Soc Rev*. 2018;47(7):2322–56. [<DOI>](#).
72. Sirajudheen P, Karthikeyan P, Ramkumar K, Meenakshi S. Effective removal of organic pollutants by adsorption onto chitosan supported graphene oxide-hydroxyapatite composite: A novel reusable adsorbent. *Journal of Molecular Liquids*. 2020 Nov;318:114200. [<DOI>](#).
73. Azizkhani S, Mahmoudi E, Abdullah N, Ismail MHS, Mohammad AW, Hussain SA. Synthesis and Characterisation of Graphene Oxide-Silica-Chitosan for Eliminating the Pb(II) from Aqueous Solution. *Polymers*. 2020 Aug 26;12(9):1922. [<DOI>](#).
74. Chen J, Ma Y, Wang L, Han W, Chai Y, Wang T, et al. Preparation of chitosan/SiO₂-loaded graphene composite beads for efficient removal of bilirubin. *Carbon*. 2019 Mar;143:352–61. [<DOI>](#).
75. Yan M, Huang W, Li Z. Chitosan cross-linked graphene oxide/lignosulfonate composite aerogel for enhanced adsorption of methylene blue in water. *International Journal of Biological Macromolecules*. 2019 Sep;136:927–35. [<DOI>](#).
76. Zeng W, Liu Y, Hu X, Liu S, Zeng G, Zheng B, et al. Decontamination of methylene blue from aqueous solution by magnetic chitosan lignosulfonate grafted with

graphene oxide: effects of environmental conditions and surfactant. RSC Adv. 2016;6(23):19298–307. [<DOI>](#).

77. Ge H, Ma Z. Microwave preparation of triethylenetetramine modified graphene oxide/chitosan composite for adsorption of [<DOI>](#).

78. Kovtun A, Campodoni E, Favaretto L, Zambianchi M, Salatino A, Amalfitano S, et al. Multifunctional graphene oxide/biopolymer composite aerogels for microcontaminants removal from drinking water. Chemosphere. 2020 Nov;259:127501. [<DOI>](#).

79. Wu Z, Deng W, Zhou W, Luo J. Novel magnetic polysaccharide/graphene oxide @Fe₃O₄ gel beads for adsorbing heavy metal ions. Carbohydrate Polymers. 2019 Jul;216:119–28. [<DOI>](#).

80. Wei H, Han L, Tang Y, Ren J, Zhao Z, Jia L. Highly flexible heparin-modified chitosan/graphene oxide hybrid hydrogel as a super bilirubin adsorbent with excellent hemocompatibility. J Mater Chem B. 2015;3(8):1646–54. [<DOI>](#).

81. Huang T, Shao Y, Zhang Q, Deng Y, Liang Z, Guo F, et al. Chitosan-Cross-Linked Graphene Oxide/Carboxymethyl Cellulose Aerogel Globules with High Structure Stability in Liquid and Extremely High Adsorption Ability. ACS Sustainable Chem Eng. 2019 May 6;7(9):8775–88. [<DOI>](#).



Swelling, Thermal and Mechanical Characterizations of High-Density Polyethylene/ Recycled Biochar Composites

Sameer A. Awad*  

Department of Chemistry, University of Anbar, Ministry of Higher Educations and Scientific Resaerch, Anbar, Ramadi 31001, Iraq.

Abstract: The application of recycled natural materials waste as biochar fillers in polymer composites can be observed as a sustainable approach. This article aims to study recycled biochar (R-BCH) improvements on the high-density polyethylene (HDPE) matrix properties. A series of composites was developed with a different loading varying from 0 to 10 wt.% of R-BCH, using a twin-screw extruder followed by compression molding. The results showed that the addition of 3-10% of R-BCH in pure HDPE led to an increase in the tensile strength, modulus of elasticity, and a decrease of elongation at break. Furthermore, the differential scanning calorimetry analysis (DSC) results showed that incorporating R-BCH into pure HDPE improved thermal properties because interfaces between R-BCH and pure HDPE caused decreased brittle behavior and enhanced the high crosslinking of pure HDPE.

Keywords: HDPE, Recycled Biochar, Tensile Strength, Thermal Properties.

Submitted: August 19, 2021. **Accepted:** October 03, 2021.

Cite this: Awad SA. Swelling, Thermal and Mechanical Characterizations of High-Density Polyethylene/ Recycled Biochar Composites. JOTCSA. 2011;8(4):1137-44.

DOI: <https://doi.org/10.18596/jotcsa.984583>.

***Corresponding author. E-mail:** sameer.msc1981@gmail.com.

INTRODUCTION

A composite involves combining two or more materials and that are blended in each other without a solubilizing material. At least one type of natural filler is incorporated in the dispersed phase in the polymeric material to form a composite. The performance of natural filler in composite materials can be enhanced to achieve appropriate materials regarding durability, thus being more economical than synthetic fillers composites. In addition, these natural fillers provide composites' stiffness and strength and enhance superior chemical and mechanical properties (1-4). High-density polyethylene, medium density polyethylene, low-density polyethylene polymers are commonly utilized to produce flexible films and laminates for bags, rigid containers, pipe extrusion, and injection molding of various objects (5). The advantages of

HDPE are characterized by high shrinkage, simple molding, and excellent melt strength (6-11). Biochar can be considered neutral carbon or a negative material that may play an essential role in industrial and construction applications. Biochar is the solid product found from biomass pyrolyses such as wood, agricultural wastes, and municipal wastes. It has consisted of stacked graphene sheets inside crystallites of turbostratic carbon with an amorphous compound (12). Through the thermal decomposition of biomass, biocarbon is a porous solid obtained. It is chemically stable under ambient conditions. The properties of biochar are based principally on the raw material and the pyrolysis temperature utilized in the production procedure. The thermal stability of the biochar obtained from the high pyrolysis temperature typically exceeds 350 °C. Besides, it can have functional groups on its surfaces, facilitating its

connection with the polymer matrix (13). In recent decades, natural fillers reinforced polymer composites companies and research institutions made no effort to modify alternative bio natural fillers based on the raw material limitation. However, in recent years, there is a scope for the biochar's effective application in thermoplastic composites as a result of its porous structure, large surface area, high carbon loading, which could facilitate the physical bonding with the polymer matrix (14). For example, the impact strength of the polyester reinforced 2.5% w/w of biochar increased by 77.50%, while the constant dielectric rise by 7% compared with the virgin polyester (15). Another study showed that the electrical conductivity of polyvinyl alcohol (PVA) reinforced with 2 and 10% w/w of biochar exhibited values similar to carbon nanotube and graphene-filled PVA composites. On the other hand, the thermal stability, tensile, and storage moduli for PVA/biochar composites were enhanced with the addition of BC (16).

Previous studies exhibited that utilizing crop residues or natural wastes such as rice straw, sugar cane, flax, hemp, jute, wood chips, or tea residues to replace wood fibers enhanced notably mechanical and thermal properties of wood-plastic composites (WPCs) (17-19). For example, Wu et al. (20) prepared cotton stalk bark (CSB) reinforced polypropylene (PP), and their mechanical, thermal, and morphology properties were investigated. They observed that the flexural properties and tensile modulus of CSB reinforced PP composites were improved with the increasing loading of CSB. In contrast, the tensile strengths showed a negative correlation with the loading of CSB, which achieved 32.9 MPa when the CSB incorporated was 30%. Another study by Cholake et al. (21) investigated the waste macadamia sell impact on improving the mechanical

characterizations of WPC panel. It was displayed that incorporating macadamia shell increased the comprehensive modulus 548 MPa for 75% compared to the PP matrix.

This paper applied the extrusion fabrication method to prepare bio composites HDPE with (RBCH) obtained by recycled wood chips pyrolysis. The thermal characterizations of RBCH/HDPE composites were studied to investigate the crystallization performance. In addition, the mechanical properties of RBCH/HDPE composites were presented and discussed to provide a theoretical basis for the application. In this regard, this study attempts to utilize local resources of wood chips converted to R-BCH to reinforce thermoplastic polymers. The R-BCH could have a promising future as a new reinforcement in polymer composites as a result of their low cost, low density, environmental friendliness, and great mechanical characterizations.

MATERIALS AND METHODS

Materials

R-BCH was collected from waste wood chips, cleaned, and dried. HDPE matrix with a density of 0.955 g/mL was used as a matrix and provided by Indian Chemical and Petrochemical Manufacture (CPMA).

Preparation of R-BCH

The wood waste was dried and then operated through a chipper that turns it into woodchips (20-40 mm). The woodchips were then converted through slow pyrolysis at a temperature range (450-550 °C), and the heating rate range was 0.1-1 °C/s into syngas to produce biochar. Figure 1 shows a schematic diagram for R-BCH preparation.



Figure 1: Schematic illustration of the Preparation of R-BCH.

Fabrication of HDPE Composite

Initially, the required amounts of HDPE and R-BCH were mixed thoroughly, utilizing a mixer to obtain a homogenous composite (the mixture speed was

50 rpm at mixing time six minutes). The mixture was then passed through a twin-screw extruder at a temperature of 180 °C and a screw speed of 10 rpm. Next, the extruded composites were taken

out from the extruder and compressed in a Carver press at 140 °C for 30 min to obtain a sheet (15 x 15 cm²) having a thickness of 1 mm. The amount

of R-BCH powder added to the matrix varied from 0, 3, 7, and 10 wt%, respectively. Figure 2 exhibited the proposed scheme for R-BCH/HDPE composite.

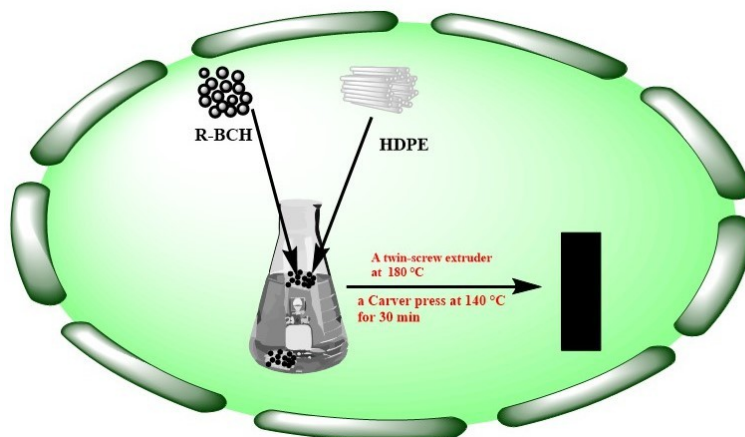


Figure 2: A scheme of HDPE/R-BCH composites preparation.

Swelling Ratio Test

To measure the swelling ratio (SR), dry HDPE composites (0.2±0.5 g) were immersed in 800 mL of distilled water solutions for 4 h at room temperature to achieve equilibrium. The swollen product was filtered through a 100-mesh screen to remove excess moisture and then weighed. Each specimen was significantly tested, and the average value was used. The capacity of water-absorbent was calculated utilizing the following Equation (1):

$$SR \% = \frac{(m_1 - m_0)}{m_0} \quad (1)$$

Where m_0 and m_1 are the mass of dried and swollen products, respectively.

Differential Scanning Calorimetry

The blends' characteristics of melting and crystallization were measured utilizing a machine type, a Mettler 820 DSC. The weight of samples was in a range of 5-10 mg. The first heating and second heating were done from 25 °C to 200 °C at 10 °C/min in a nitrogen atmosphere. The DSC thermograms provide details on the melting

temperature (T_m), crystallization temperature (T_c), melting enthalpy heat (ΔH_m), and crystallization enthalpy heat (ΔH_c). In addition, the crystallinity degrees (X_c) of the specimens were calculated using Equation 2.

$$\chi_c (\%) = \frac{\Delta H_m}{\Delta H_m^0} \quad (2)$$

Where ΔH_m^0 is the enthalpy heat of fusion of the fully crystalline HDPE, taken as 290 J/g (22-24). The ΔH_m , ΔH_c , and X_c values of HDPE and HDPE composites were normalized and accounted for based on the actual HDPE composites, as listed in Table 1.

Tensile Tests

Composite samples were tested utilizing an Instron tensile machine model type (Testometric, M500-50AT), UK, based on the standard of ASTM D 638. The crosshead speed was about 20 mm/min. Furthermore, three tests were replicated for each composite sample.

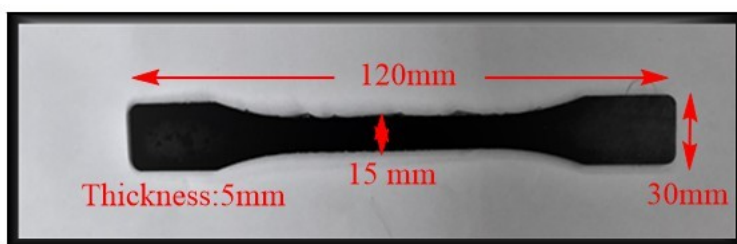


Figure 3: Tensile test simple with dimensions.

RESULTS and DISCUSSIONS

Swelling Analysis of HDPE Composites

The swelling ratio measurements against the loading of R-BCH composites are illustrated in Figure 4. The introduction of R-BCH into HDPE composites has shown a significant effect on the extrudate swelling ratio. It can be seen from Figure 1 that the swelling ratio of HDPE/R-BCH composites decreased with an increase in the R-BCH loading. The swelling ratio of 10% R-BCH/HDPE composite was reduced by 64%, while the incorporation of 3% and 7% R-BCH in HDPE

composites was decreased by 44% and 50%, respectively. The hypothesis produced concerns the ability of R-BCH in permitting further interactions of polymer molecules. An ease in the interaction of the molecules enhances the entanglement level and elastic property of HDPE melt, therefore affecting the deformation rate (in this case, referring to the extrudate swelling). Incorporating the highest loading (10% R-BCH) in the HDPE matrix showed a sharp decrease compared to other loadings of R-BCH (3% and 7%).

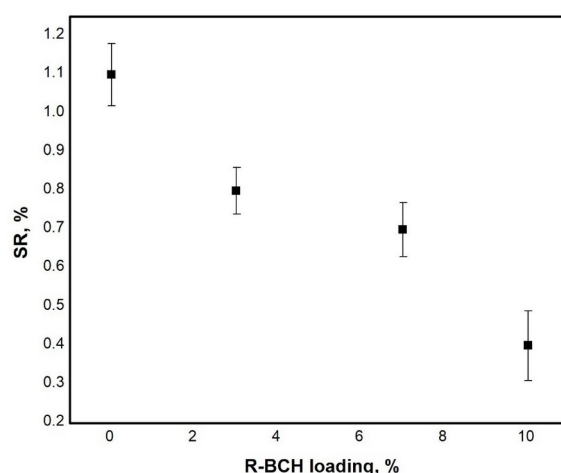


Figure 4: Effects of R-BCH loading on swelling ratio of HDPE composites.

Thermal Analysis (DSC) of HDPE Composites

The DSC curves (heating and cooling processes) at 10 °C/min of the HDPE and HDPE/R-BCH composites are illustrated in Figures 5 and 6. The relative factors, for example, crystallization temperature (T_c), melting temperature (T_m), crystallization enthalpy (ΔH_c), and melting enthalpy (ΔH_m) for HDPE/R-BCH composites, are summarized in Table 1. The DSC thermograms showed single peaks for the composites' heating and cooling scans (Figures 5 and 6). The T_m value of pure HDPE was 135 °C, while the T_m value of the R-BCH/HDPE composites increased with increasing the loading of R-BCH. The HDPE/10 wt. % R-BCH had the highest T_m , which was 141 °C

(Table 1). Incorporating R-BCH in HDPE seemed to restrict the polymer chain's mobility, resulting in higher T_m . The addition of R-BCH to the HDPE matrix increased the melting peak temperature. Hence the crystallinity increases progressively with loadings of the R-BCH. As a result, they displayed a higher melting peak temperature and crystallinity. The reason may be that further lower cooling rates take place with the addition of R-BCH, which causes longer crystallization time, thus further ideal crystals. The ΔH_m is an important parameter since its magnitude is directly proportional to the polymer's overall level of crystallinity (X). The HDPE composite with higher R-BCH loading also showed a higher ΔH_m value

when compared with those with lower R-BCH content. For the composite systems, it was observed that generally, the ΔH_m values of the composites increased with increasing R-BCH content. The ΔH_m of pure HDPE was 179.5 J/g and increased to 185 J/g at the highest loading of R-BCH. The results are listed in Table 1, which showed that the X values of these composites were slightly increased relative to that of pure HDPE (61%). Furthermore, the addition of 10% R-BCH in

the HDPE matrix increased the X value up to 66%, as shown in Figure 7. Karagoz and Tuna (25) studied the impact of (various melt temperatures) on the thermal characterizations of the HDPE composite applied at different nozzle temperatures. They reported that the HDPE composite with the greatest nozzle temperature (200 °C) achieved a significant improvement in crystallinity compared to others (180 and 190 °C).

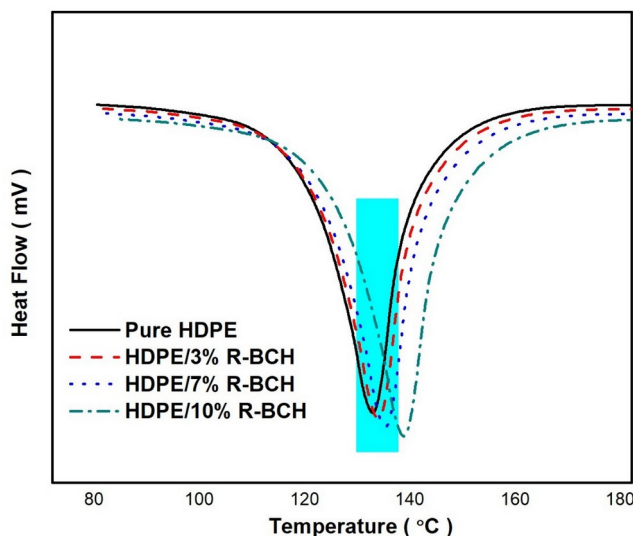


Figure 5: DSC thermograms (heating curves) of HDPE and HDPE/R-BCH composites.

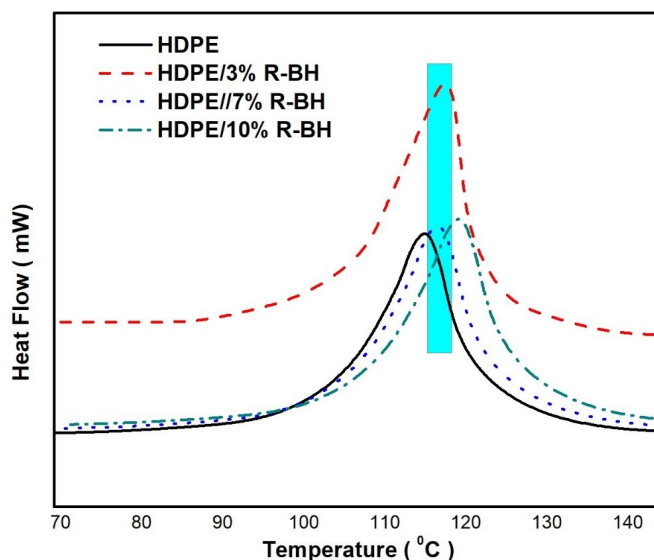
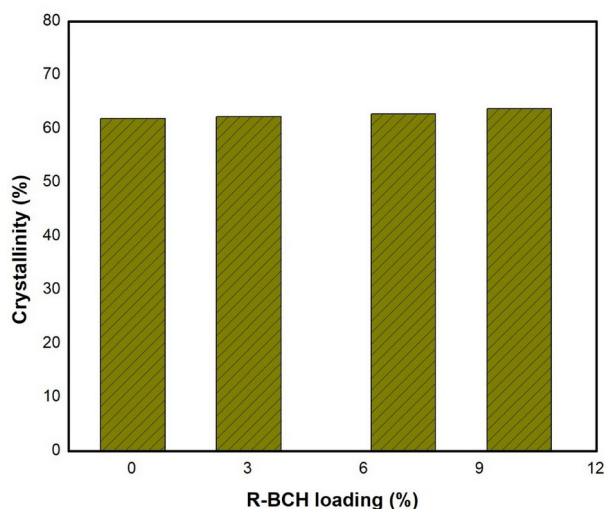


Figure 6: DSC thermograms (cooling curves) of HDPE and HDPE/R-BCH composites.

Table 1: DSC results of non-isothermal crystallization and melting of pure HDPE and HDPE composites.

Composites	T _c (°C)	T _m (°C)	ΔH _c (J/g)	ΔH _m (J/g)
Pure HDPE	115	135	184	179.5
HDPE/3% R-BCH	117	136	185	180.7
HDPE/7% R-BCH	118	138	188	182
HDPE/10% R-BCH	121	141	192	185

**Figure 7:** Crystallinity values of HDPE and HDPE/R-BCH composites.

Mechanical Properties

The results of the tensile tests are determined from tensile stress-strain curves, as shown in Figure 8. The HDPE/R-BCH composites displayed higher tensile strength and modulus when compared to the pure high-density polyethylene (HDPE). It is evident from Table 2 that tensile strength increased with increasing the loading of R-BCH from 3 to 10 wt.% in comparison to pure HDPE. The tensile strength of significant loading of 10% R-BCH was 42.5 ± 4.8 MPa compared with pure HDPE, which was 26 ± 2.5 MPa. The results of Young's modulus exhibited a significant increase with 10% R-BCH loading, which was 296 ± 25 MPa by comparing to lower loadings (3 and 7% R-BCH), and HDPE which were (284 ± 18 MPa and 289 ± 22 MPa), and 280 ± 15 MPa, respectively, as shown in Table 2. The addition of different loadings for R-BCH composites exhibited significant changes in the elongation at break, %. It decreased with increasing the loading of R-BCH in the HDPE matrix. Elongation at a break of 10% R-BCH in the HDPE matrix decreased to $7.4 \pm 0.6\%$, while pure

HDPE matrix was $14.7 \pm 1.4\%$, as shown in Table 2. This may be attributed to the high loading of R-BCH in the HDPE matrix, which displayed better interfacial interaction and improved the blend's plasticity by incorporating the compatibilizer (26). Previous work was studied by Idress (27), who found that the highest tensile strength for HDPE composite with a mold surface temperature of 50 °C. By comparing with this work, Yu et al. (28) reported in their findings regarding the mechanical characterizations for particleboard dust (PB dust) and basalt fibers (BFs)/Recycled (R-HDPE), they found that the tensile strength was increased with the loading of (1BP dust:1BFs) in HDPE composite. They reported that the tensile strength of 1PB:1BFs/RHDPE composite was 28.3 MPa while the virgin RHDPE matrix was 19.4 MPa. Poulouse et al. (14) studied the properties of date palm waste extracted as biochar (BC) and utilized as biofilters for polypropylene (PP) matrix. They observed that the mechanical characterizations of BC/PP composites improved tensile strength and modulus with increased loading of BC.

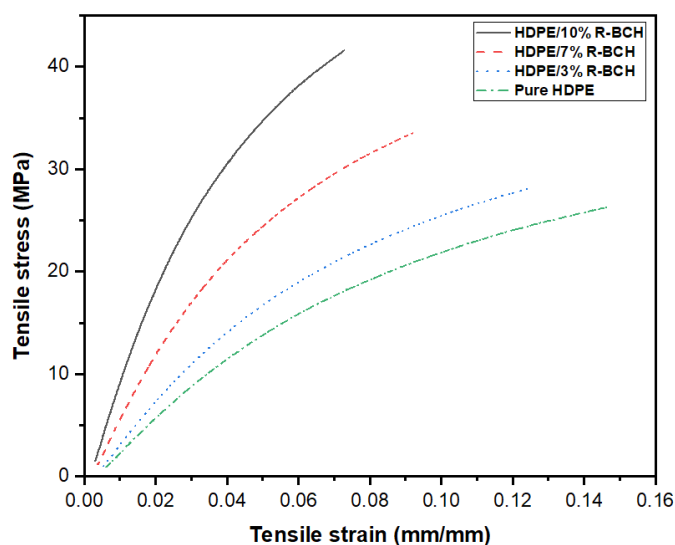


Figure 8: Tensile stress-strain curves of HDPE composites.

Table 2: Mechanical properties of pure HDPE and HDPE composites.

Composites	Tensile strength (MPa)	Young's modulus (MPa)	Elongation at break %
Pure HDPE	26.5±2.5	312.5±25	14.7±1.4
HDPE/3% R-BCH	28.2±3.5	400.7±60	12.5±1.1
HDPE/7% R-BCH	33.7±3.2	650.4±50	9.2±0.9
HDPE/10% R-BCH	42.5±4.8	1020.2±75	7.4±0.6

CONCLUSIONS

This study demonstrated that R-BCH could be used as an efficient filler for the HDPE matrix. R-BCH was reinforced into HDPE by increasing the weight fractions from 3 wt.% to 10 wt.%. The swelling ratio was reduced with increasing the loading of R-BCH in the HDPE matrix. The tensile strength and modulus of R-BCH/HDPE composites were found to be improved when compared to the virgin HDPE matrix, while the elongation at break was reduced with increasing the loading of R-BCH. The thermal studies revealed that the crystallinity of R-BCH/HDPE composites was increased compared to the virgin HDPE matrix. Further investigation could be addressed towards improving the BC/PP composites characterizations by improving the biochar properties such as porosity, surface functionalization, and purity. It can be concluded that this type of bio filler (R-BCH) enhances the interaction between the HDPE matrix and R-BCH filler and hence superior composite characterizations.

CONFLICTS OF INTEREST

The authors declared no conflict of interest.

REFERENCES

- Awad S, Khalaf E. Evaluation of thermal and mechanical properties of Low-Density Poly Ethylene (LDPE)-Corn Flour (CF) composites. *Int J Chemtech Res.* 2017;10(13):230-5.
- Awad SA, Khalaf EM. Characterisation and performance of low-density poly ethylene-corn flour composites. *Aksaray University Journal of Science and Engineering.* 2018;2(2):171-9. [<DOI>](#).
- Awad SA, Khalaf EM. Investigation of improvement of properties of polypropylene modified by nano silica composites. *Composites Communications.* 2019 Apr;12:59-63. [<DOI>](#).
- Awad S, Khalaf E. Modified performance of mechanical, thermal, and physical properties of high-density polyethylene-corn flour composites. *Usak University Journal of Engineering Sciences.* 2018;1(1):38-46.
- Trigui A, Karkri M, Peña L, Boudaya C, Candau Y, Bouffi S, et al. Thermal and mechanical properties of maize fibres-high density polyethylene biocomposites. *Journal of Composite Materials.* 2013 May;47(11):1387-97. [<DOI>](#).
- Zhang Q, Li Y, Cai H, Lin X, Yi W, Zhang J. Properties comparison of high density polyethylene composites filled with three kinds of shell fibers. *Results in Physics.* 2019 Mar;12:1542-6. [<DOI>](#).

7. Awad S, Khalaf E. An investigation of the improvements of mechanical and thermal properties of high-density polyethylene/nano clay composites. *European Mechanical Science*. 2019 Jun 20;3(2):41-4.
8. Awad S. Investigation of Chemical Modification and Enzymatic Degradation of Poly(vinyl alcohol)/Hemoprotein Particle Composites. *Journal of the Turkish Chemical Society Section A: Chemistry*. 2021 May 31;8(2):651-8. <DOI>.
9. Awad SA. Enhancing the Thermal and Mechanical Characteristics of Polyvinyl Alcohol (PVA)-Hemp Protein Particles (HPP) Composites. *International Polymer Processing*. 2021 May 26;36(2):137-43. <DOI>.
10. Wollerdorfer M, Bader H. Influence of natural fibres on the mechanical properties of biodegradable polymers. *Industrial Crops and Products*. 1998 May;8(2):105-12. <DOI>.
11. Awad SA, Khalaf EM. Characterization and modifications of low-density poly ethylene-nano cellulose crystalline composites. *Suranaree Journal of Science & Technology*. 2020;27(1).
12. Natalio F, Corrales TP, Feldman Y, Lew B, Graber ER. Sustainable Lightweight Biochar-Based Composites with Electromagnetic Shielding Properties. *ACS Omega*. 2020 Dec 22;5(50):32490-7. <DOI>.
13. Matykiewicz D. Biochar as an Effective Filler of Carbon Fiber Reinforced Bio-Epoxy Composites. *Processes*. 2020 Jun 22;8(6):724. <DOI>.
14. Poulouse AM, Elnour AY, Anis A, Shaikh H, Al-Zahrani SM, George J, et al. Date palm biochar-polymer composites: An investigation of electrical, mechanical, thermal and rheological characteristics. *Science of The Total Environment*. 2018 Apr;619-620:311-8. <DOI>.
15. Richard S, Rajadurai JS, Manikandan V. Influence of particle size and particle loading on mechanical and dielectric properties of biochar particulate-reinforced polymer nanocomposites. *International Journal of Polymer Analysis and Characterization*. 2016 Aug 17;21(6):462-77. <DOI>.
16. Nan N, DeVallance DB, Xie X, Wang J. The effect of bio-carbon addition on the electrical, mechanical, and thermal properties of polyvinyl alcohol/biochar composites. *Journal of Composite Materials*. 2016 Apr;50(9):1161-8. <DOI>.
17. He S, Zhou L, He H. Preparation and properties of wood plastic composites based on tea residue. *Polym Compos*. 2015 Dec;36(12):2265-74. <DOI>.
18. Väisänen T, Heikkinen J, Tomppo L, Lappalainen R. Softwood Distillate as a Bio-Based Additive in Wood-Plastic Composites. *Journal of Wood Chemistry and Technology*. 2016 Jul 3;36(4):278-87. <DOI>.
19. Das O, Sarmah AK, Bhattacharyya D. A sustainable and resilient approach through biochar addition in wood polymer composites. *Science of The Total Environment*. 2015 Apr;512-513:326-36. <DOI>.
20. Wu H, Liang X, Huang L, Xie Y, Tan S, Cai X. The utilization of cotton stalk bark to reinforce the mechanical and thermal properties of bio-flour plastic composites. *Construction and Building Materials*. 2016 Aug;118:337-43. <DOI>.
21. Cholake ST, Rajarao R, Henderson P, Rajagopal RR, Sahajwalla V. Composite panels obtained from automotive waste plastics and agricultural macadamia shell waste. *Journal of Cleaner Production*. 2017 May;151:163-71. <DOI>.
22. Awad SA, Khalaf EM. Investigation of Photodegradation Preventing of Polyvinyl Alcohol/Nanoclay Composites. *J Polym Environ*. 2019 Sep;27(9):1908-17. <DOI>.
23. Awad SA, Khalaf EM. Evaluation of the photostabilizing efficiency of polyvinyl alcohol-zinc chloride composites. *Journal of Thermoplastic Composite Materials*. 2020 Jan;33(1):69-84. <DOI>.
24. Awad SA. Mechanical and thermal characterisations of low-density polyethylene/nanoclay composites. *Polymers and Polymer Composites*. 2020 Oct 30;096739112096844. <DOI>.
25. Karagöz İ, Tuna Ö. Effect of melt temperature on product properties of injection-molded high-density polyethylene. *Polym Bull*. 2021 Oct;78(10):6073-91. <DOI>.
26. Awad SA, Khalaf EM. Improvement of the chemical, thermal, mechanical and morphological properties of polyethylene terephthalate-graphene particle composites. *Bull Mater Sci*. 2018 Jun;41(3):67. <DOI>.
27. Karagöz İ. An effect of mold surface temperature on final product properties in the injection molding of high-density polyethylene materials. *Polymer Bulletin*. 2021;78:2627-44. <DOI>.
28. Yu M, Mao H, Huang R, Ge Z, Tian P, Sun L, et al. Mechanical and Thermal Properties of R-High Density Polyethylene Composites Reinforced with Wheat Straw Particleboard Dust and Basalt Fiber. *International Journal of Polymer Science*. 2018;2018:1-10. <DOI>.



Comparison of the Cytotoxic Effects of Bulk and Nano-sized CeO₂ on Lymphocyte Cells

Giray Buğra AKBABA¹  

¹Kafkas University, Department of Bioengineering, Kars, 36100, Turkey

*Corresponding author's e-mail: gbugraakbaba@hotmail.com, Telephone Number: 04742251150

Abstract: Cerium(IV) oxide (CeO₂) is widely used in industrial fields such as biomedical, glass, electronics, automotive, and pharmacology. In this study, the cytotoxic effects on human peripheral blood cultures of two forms of cerium(IV) oxide with different particle sizes (Bulk-sized Cerium(IV) oxide: BC and Nano-sized Cerium(IV) oxide: NC) in concentrations range of 0.001-200 ppm were investigated. 3-(4,5-Dimethylthiazol-2-yl)-2,5-diphenyltetrazolium bromide (MTT) assay were used to determine the cytotoxicity of these forms. According to the test results, it was determined that both forms caused severe cytotoxicity at all concentrations studied. It was observed that cytotoxicity increased with increasing concentration. NCs are more toxic at all concentrations except 100 and 200 ppm concentrations.

Keywords: Cerium(IV) oxide, biomaterial, cytotoxicity, MTT assay, lymphocyte, nanoparticle.

Submitted: July 26, 2021. **Accepted:** October 08, 2021.

Cite this: Akababa G. Comparison of the Cytotoxic Effects of Bulk and Nano-sized CeO₂ on Lymphocyte Cells. JOTCSA. 2021;8(4):1145-52.

DOI: <https://doi.org/10.18596/jotcsa.974814>.

***Corresponding author. E-mail:** gbugraakbaba@hotmail.com. **Telephone:** 04742251150.

INTRODUCTION

Cerium(IV) oxide is one of the significant rare earth oxides used in many applications such as catalyst, hydrogen generation, optical displays and UV absorber due to its unique properties (1). The reason why CeO₂ is used in many industrial and biomedical applications is its redox capability (2). Due to the increasing use of cerium compounds, it is important to determine their possible toxic effects on living things and the environment. Because organic compounds can be converted into non-toxic compounds in nature, inorganic compounds often decompose into components that can cause toxicity (3).

Nanotechnology is a research area that brings innovation to technological processes with a different perspective. Today, nanomaterials are used in almost every application. In this early adopted and rapidly advancing technology, the effects of exposure to the nanoparticles used are

not yet fully known. The amount, transition, degradation, change and accumulation in nature of nanomaterials released into the environment are not known exactly. Nanoparticles that enter the body through the skin, mouth, or lungs can cause direct or indirect harm to genetic material (4,5). It is known that nano-sized cerium(IV) oxide is used in different applications such as catalyst, conductor, electrode, ultraviolet absorber, luminescence devices and glass polisher (6). In addition to these physical applications, CeO₂ nanoparticles are also used in many biological applications due to their antibacterial, antioxidant and anti-inflammatory properties (2,7-10). Without a doubt, the application of nanocerium as a biomaterial will remain a highlight of biology, biomedical and materials research in the next years. However, the Organization for Economic Cooperation and Development (OECD) has classified this nanoparticle as a hazardous chemical. The OECD advises that the toxicity profile of CeO₂ nanoparticles be studied further through *in vitro* and *in vivo* research (11).

Particle-related parameters such as size, shape, surface charge, crystal structure, concentration, pH, and exposure time are factors that affect the toxicity of the nanoparticle. Among these parameters, the most intensively investigated parameters are usually particle size and concentration. In toxicity studies on many cell lines using different methods, it has been determined that CeO₂ in nanoparticle size is generally toxic (1,12–14). There are many studies showing that CeO₂ with nanoparticle size is more toxic than that in the bulk size (15–18). Lymphocytes are critical components of the immune system as they are able to elicit a response to bacteria, viruses and existing cells that enter the human body that develop into a cancerous cell type. They are widely used in *in vitro* drug development studies because they play an active role in the synthesis of lymphocyte cells, immunoglobulins, and a wide variety of other proteins in peripheral blood. In addition, researchers and clinicians use lymphocytes in fields related to immunology, infectious disease, hematological malignancies, vaccine development, transplant therapy, personalized medicine, and toxicology. In general, *in vitro* lymphocyte studies contribute to research on cell function, biomarker identification and disease modeling (19,20). In this context, it is necessary to know the toxic properties of cerium(IV) oxide, which is widely used in many industrial areas, in terms of the sustainability of its use as a biomaterial. For this purpose, in this study, we determined and compared that cytotoxic properties of BC and NC on lymphocyte cells using MTT test.

EXPERIMENTAL SECTION

Chemicals and Instruments

Primary Peripheral Blood Mononuclear cells (ATCC PCS-800-011™) (containing a minimum of 25x10⁶ viable cells), Phosphate Buffered Saline (PBS), Fetal Bovine Serum (FBS), Penicillin-Streptomycin Solution, Dulbecco's Modified Eagle's Medium (DMEM) (Sigma), Dimethylsulfoxide (DMSO), Cerium(IV) oxide nanoparticles and Cerium(IV) oxide bulk sized particles (Sigma-Aldrich) and 3-(4,5-dimethylthiazol-2-yl)-2,5-diphenyltetrazolium bromide (Acros) were purchased commercially. In this study, NICHIRYO Nichipet Single Channel (10-100-1000 µL) automatic pipettes, Nüve BM 101 Water bath, ISOLAB vortex mixer, Panasonic MCO 170AICUVH-PE CO₂ Incubator, Hed Lab X BIO MSC CLASS II biosafety cabine, Thermoscientific-Countess II cell counter and Thermoscientific-Multiskan Sky Microplate Spectrophotometer were used. Powder X-Ray Analysis were performed Philips X'Pert Pro diffractometer with Cu, K α radiations, 40 kV of voltage and a current of 35 mA. The patterns of the samples were recorded from 5 ° to 70 ° (2 °θ) with 0.2 °/ min and a step size of 0.02 °.

Determination of particle sizes

The particle sizes of BC and NC were calculated with Scherrer's equation (1) from obtained data by powder X-ray diffraction method.

$$d = \frac{K \lambda}{\beta \cos \theta} \quad (1)$$

where d is the mean particle size, K is the grain shape-dependent constant 0.89, λ is the wavelength of the incident beam in nanometer, θ is the Bragg reflection angle and β is the line broadening at half the maximum intensity in radians (21,22).

Preparation of Cell culture and MTT assay

MTT method, which is a colorimetric method, was used to determine the cytotoxicity of bulk and nano-sized CeO₂ (23,24). Human peripheral blood mononuclear cell (PBMC) stock (1 mL) maintained at -80 °C were thawed by using a water bath. 1 mL of cell stock was diluted by adding 9 mL of culture medium that contains 89 % DMEM, 10 % FBS and 1 % penicillin- streptomycin. The number of cells in the cell suspension was calculated using a cell counter. 100 µL aliquots of the prepared cell suspension were added to the 96-well plate at approximately 25000 cells per well. After cells were seeded, 100 µL of culture medium was added to each well and incubated for 24 h at 37 °C in a 5% CO₂ and 95% humidity in a CO₂ incubator. After the incubation, 100-µL aliquots from solutions with different concentrations of BC and NC were added to the test wells. At this stage, 100 mL of culture medium was added to the cell control group wells. The incubation was continued for another 24 h. After the incubation was completed, 10 µL of MTT solution prepared in PBS with a concentration of 5 mg/mL was added to each well. Incubation was continued for 4 h and then 200 µL of DMSO used as formazan crystal solvent was added to each well. Incubation was continued for another 18 h. After the end of the incubation, absorbance values at a wavelength of 570 nm were recorded with the help of a spectrophotometer. Experiments were carried out in triplicate.

Statistical analysis

Two-way ANOVA (Tukey) test included in the IBM SPSS statistics for Windows (version 22.0, IBM Corp., Armonk, NY, USA) package program was used for the statistical calculations of the absorbance values obtained. Statistically significance level is accepted at 95% ($p < 0.05$).

RESULTS AND DISCUSSION

Characterization of particles

The average particle size of BC and NC was calculated as 231.61 nm and 27.15 nm, respectively. Powder X-ray patterns of BC and NC were given in Figure 1.

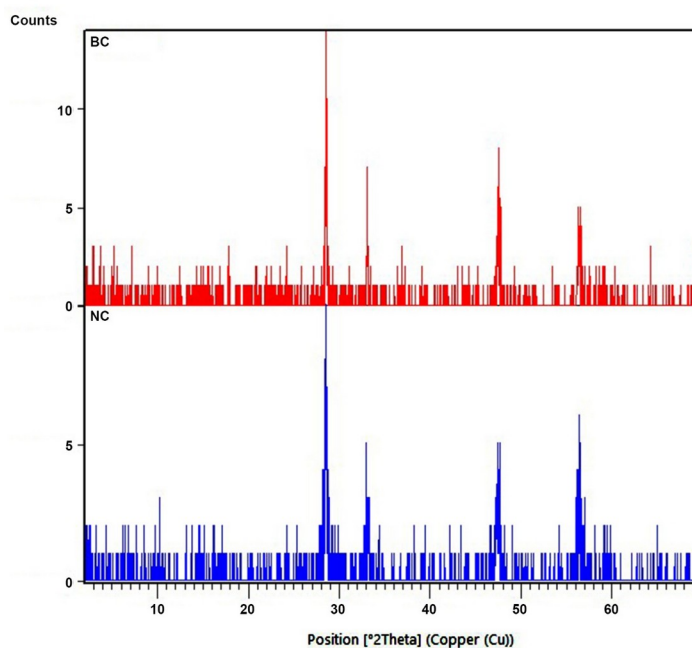


Figure 1: Powder X-ray patterns of BC and NC.

MTT assay

When Figures 2 and 3 are examined, it is seen that all application concentrations of BC and NC cause statistically significant cytotoxicity compared to the cell control group. Especially at 100 and 200 ppm

concentrations, the highest cytotoxic effect was determined and cell viability decreased below 25%. Remarkably, it is observed that BC and NC reduce cell viability to more than 50% at all concentrations.

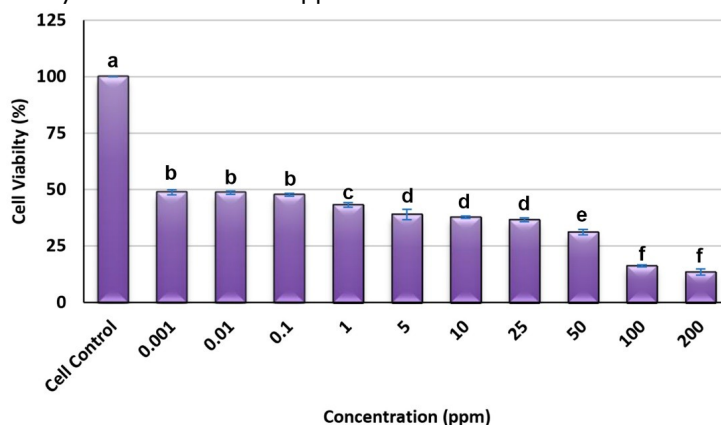


Figure 2: Effect of BC on cell viability at different concentrations.

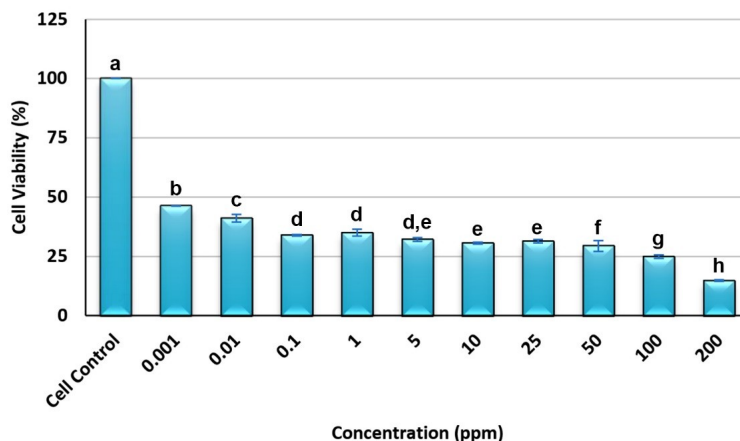


Figure 3: Effect of NC on cell viability at different concentrations.

In this study, the effects of BC and NC on human lymphocyte cell viability were also compared. It was determined that NC was more toxic than BC at all concentrations except at 100 and 200 ppm. BC was found to have a stronger toxic effect than NC at only 100 and 200 ppm concentrations. According to the

International Standard 10993-5 (25), chemicals that reduce cell viability by more than 50% are considered moderately cytotoxic. The results of this study reveal that both forms of cerium(IV) oxide are moderately cytotoxic (Figure 4).

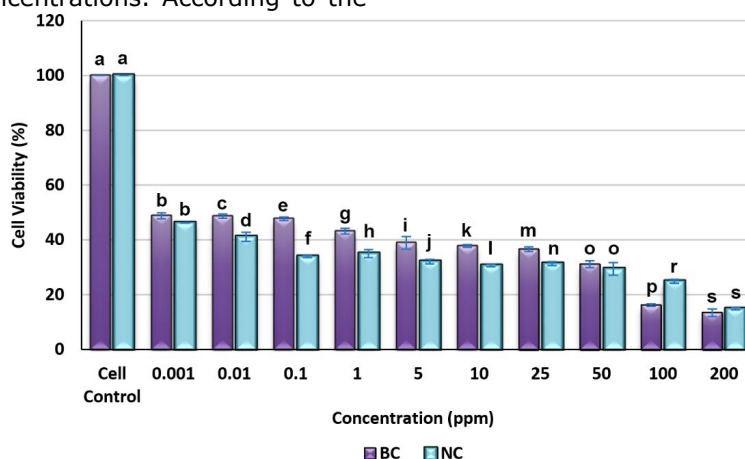


Figure 4: Comparison of cytotoxic effects of BC and NC.

There are many studies in the literature investigating the cytotoxicity of CeO₂. When the literature is examined, the toxic effects of the cerium(IV) oxide compound on cancer cell lines have been studied more. However, this compound is widely used especially in dental treatment. Therefore, it is important to know the effects of this compound on normal cells. In many of these studies, the cytotoxicity of the nanoparticle sized form of the cerium(IV) oxide compound was investigated. There are very few studies investigating the cytotoxicity of cerium(IV) oxide in bulk form. There are two different studies investigating the cytotoxicity of cerium(IV) oxide nanoparticles with a particle size of 25-30 nm. In these studies, the effects of this compound on lymphocyte cells were investigated using the MTT method. In one of these two studies, it was stated that the nanoparticle did not cause any toxicity in the concentration range of 2.5-20 ppm (11), while in the other study, it was shown that the

nanoparticle caused cytotoxicity at high concentrations (50, 100 and 200 ppm). In the same study, it was claimed that nanoparticles were not cytotoxic at 1 and 10 ppm concentrations (12). Although the method and cell type used are the same, the data obtained of our study and these two studies partially overlap. The reason for this inconsistency is thought to be due to the difference in particle size and experimental conditions. The cytotoxicity of cerium(IV) oxide on different cancer cells other than lymphocyte cells has been extensively investigated. For example, Abid *et al.* determined that nano CeO₂ caused cytotoxicity in the concentration range of 0.93-120 ppm on RD rhabdomyosarcoma and L20B cell lines by using MTT method (1). Using the same method, CeO₂ with a particle size of 2-6 nm has been reported to be cytotoxic on bone marrow mesenchymal stem cells (13). Cerium(IV) oxide with a particle size of 15-20 nm was determined by the WST-1 method to be cytotoxic on the MCF-7 cell line in the concentration

range of 1-1000 ppm (14). Rasouli *et al.* determined that CeO₂ with a particle size of 11-17 nm was more cytotoxic on HFFF2 cancer cells than on HT29 normal cells and cytotoxicity increased with increasing concentration and exposure time (26). According to the results of a similar study, 100-nm size CeO₂ caused cytotoxicity on PC-3 cancer cells, but not on L929 normal cells (27). Similarly, Kargar *et al.* found that nano-CeO₂ at 8x10⁵ ppm concentration did not cause toxicity on L929 cells (28). Contrary to these results, 11-33 nm-sized cerium(IV) oxide in the 125-1000 ppm concentration range (29) and 21-32 nm cerium(IV) oxide in the 1-500 ppm concentration range (30) was found to be non-cytotoxic on PC12 and A549 cancer cells, respectively. De Marzi *et al.* (2013) investigated the cytotoxic properties of 40 nm CeO₂ on A549, CaCo2 and HepG2 cell lines in the concentration range of 5x10²-5x10⁶ ppm. While it did not cause cytotoxic effects on cell lines exposed to nanoparticles for 24 hours, they determined that the nanoparticle caused cytotoxicity after ten days of exposure (31). In two different studies comparing the toxicity of nano and bulk sized cerium(IV) oxide, it was determined that CeO₂ with nano size was more toxic than bulk size (17,18). This result is consistent with the data obtained in our study. In a study using the MTT method, it was determined that cerium(IV) oxide with a particle size of 13.04 nm did not cause any cytotoxicity on A549, Calu-3 and 3T3 cells at 10, 100 and 500 ppm concentrations (32). Cerium(IV) oxide with a size of 4-13 nm exhibited a cytotoxic effect as the concentration increased on A549 cells in the concentration range of 1.95-500 ppm. However, it has little effect on the viability of these cells (33). It was found that cerium(IV) oxide nanoparticles (14 nm) obtained by green synthesis at a concentration of 0.01 ppm on A549 cells were mildly cytotoxic according to the WST-1 method and not cytotoxic according to the MTT method (34).

CONCLUSION

In this study, the cytotoxic properties of bulk and nano-sized cerium(IV) oxide on human peripheral blood cultures in the concentration range of 0.001-200 ppm were investigated. The particle sizes of bulk and nano-sized cerium(IV) oxide are 231.61 nm and 27.15 nm, respectively. Both forms of the compound caused cytotoxicity on lymphocyte cells at all applied concentrations. The nano form is more cytotoxic at 0.001-50 ppm concentrations and the bulk form is more cytotoxic at 100 and 200 ppm concentrations. It was determined that cell viability decreased with increasing concentration, that is, cytotoxicity increased. It has been reported in many studies, including our study, that this compound, which is widely used as a biomaterial, causes cytotoxicity on both normal and cancer cells. In this context, it is recommended to limit the use of the

compound as a biomaterial and to examine the toxicity profile in more detail with *in vivo* studies.

CONFLICT OF INTEREST

The author declared no potential conflicts of interest with respect to the research, authorship and/or publication of this article.

ACKNOWLEDGMENTS

The author thanks Füreya Elif Öztürkkan and Mustafa Sertçelik for their technical supports.

REFERENCES

1. Abid SA, Taha AA, Ismail RA, Mohsin MH. Antibacterial and cytotoxic activities of cerium oxide nanoparticles prepared by laser ablation in liquid. *Environmental Science and Pollution Research*. 2020 Aug;27(24):30479–89. <DOI>.
2. Heckert EG, Karakoti AS, Seal S, Self WT. The role of cerium redox state in the SOD mimetic activity of nanoceria. *Biomaterials*. 2008 Jun;29(18):2705–9. <DOI>.
3. Dadook M, Mehrabian S, Salehi M, Irian S. Morphological, Biochemical and Molecular Characterization of Twelve Nitrogen-Fixing Bacteria and Their Response to Various Zinc Concentration. *Jundishapur Journal of Microbiology*. 2014 Apr;7(4):e9415. <DOI>.
4. Li S, He P, Dong J, Guo Z, Dai L. DNA-Directed Self-Assembling of Carbon Nanotubes. *Journal of the American Chemical Society*. 2005 Jan;127(1):14–5. <DOI>.
5. Oberdörster G, Oberdörster E, Oberdörster J. Nanotoxicology: An Emerging Discipline Evolving from Studies of Ultrafine Particles. *Environmental Health Perspectives*. 2005 Jul;113(7):823–39. <DOI>.
6. He L, Su Y, Lanhong J, Shi S. Recent advances of cerium oxide nanoparticles in synthesis, luminescence and biomedical studies: a review. *Journal of Rare Earths*. 2015 Aug;33(8):791–9. <DOI>.
7. Pirmohamed T, Dowding JM, Singh S, Wasserman B, Heckert E, Karakoti AS, et al. Nanoceria exhibit redox state-dependent catalase mimetic activity. *Chemical Communications*. 2010;46(16):2736. <DOI>.
8. Varini E, Sánchez-Salcedo S, Malavasi G, Lusvardi G, Vallet-Regí M, Salinas AJ. Cerium (III) and (IV) containing mesoporous glasses/alginate beads for bone regeneration: Bioactivity, biocompatibility and reactive oxygen species

- activity. *Materials Science and Engineering: C*. 2019 Dec;105:109971. [<DOI>](#).
9. Walkey C, Das S, Seal S, Erlichman J, Heckman K, Ghibelli L, et al. Catalytic properties and biomedical applications of cerium oxide nanoparticles. *Environmental Science: Nano*. 2015;2(1):33–53. [<DOI>](#).
 10. Zhang M, Zhang C, Zhai X, Luo F, Du Y, Yan C. Antibacterial mechanism and activity of cerium oxide nanoparticles. *Science China Materials*. 2019 Nov;62(11):1727–39. [<DOI>](#).
 11. Naz S, Kazmi STB, Zia M. CeO₂ nanoparticles synthesized through green chemistry are biocompatible: In vitro and in vivo assessment. *Journal of Biochemical and Molecular Toxicology*. 2019 May;33(5):e22291. [<DOI>](#).
 12. Eskandari N, Nejadi Babadaei MM, Nikpur S, Ghasrahmad G, Attar F, Heshmati M, et al. Biophysical, docking, and cellular studies on the effects of cerium oxide nanoparticles on blood components: in vitro. *International Journal of Nanomedicine*. 2018 Aug;13:4575–89. [<DOI>](#).
 13. Sangsefidi FS, Nejati M, Verdi J, Salavati-Niasari M. Green synthesis and characterization of cerium oxide nanostructures in the presence carbohydrate sugars as a capping agent and investigation of their cytotoxicity on the mesenchymal stem cell. *Journal of Cleaner Production*. 2017 Jul;156:741–9. [<DOI>](#).
 14. Hamidian K, Saberian MR, Miri A, Sharifi F, Sarani M. Doped and un-doped cerium oxide nanoparticles: Biosynthesis, characterization, and cytotoxic study. *Ceramics International*. 2021 May;47(10):13895–902. [<DOI>](#).
 15. Könen-Adıgüzel S, Ergene S. In vitro evaluation of the genotoxicity of CeO₂ nanoparticles in human peripheral blood lymphocytes using cytokinesis-block micronucleus test, comet assay, and gamma H2AX. *Toxicology and Industrial Health*. 2018 May;34(5):293–300. [<DOI>](#).
 16. Arslan K, Akbaba GB. In vitro genotoxicity assessment and comparison of cerium(IV) oxide micro- and nanoparticles. *Toxicology and Industrial Health*. 2020 Feb;36(2):76–83. [<DOI>](#).
 17. Arnold MC, Badireddy AR, Wiesner MR, Di Giulio RT, Meyer JN. Cerium Oxide Nanoparticles are More Toxic than Equimolar Bulk Cerium Oxide in *Caenorhabditis elegans*. *Archives of Environmental Contamination and Toxicology*. 2013 Aug;65(2):224–33. [<DOI>](#).
 18. Rosenkranz P, Fernández-Cruz ML, Conde E, Ramírez-Fernández MB, Flores JC, Fernández M, et al. Effects of cerium oxide nanoparticles to fish and mammalian cell lines: An assessment of cytotoxicity and methodology. *Toxicology in Vitro*. 2012 Sep;26(6):888–96. [<DOI>](#).
 19. Smith JL, Forbes IJ. Use of Human Lymphocytes in Studies of Drug Action. *Nature*. 1967 Jul;215(5100):538–9. [<DOI>](#).
 20. Kammula US, Lee K-H, Riker AI, Wang E, Ohnmacht GA, Rosenberg SA, et al. Functional Analysis of Antigen-Specific T Lymphocytes by Serial Measurement of Gene Expression in Peripheral Blood Mononuclear Cells and Tumor Specimens. *The Journal of Immunology*. 1999 Dec 15;163(12):6867–75.
 21. Farrukh MA, Tan P, Adnan R. Influence of reaction parameters on the synthesis of surfactant-assisted tin oxide nanoparticles. *Turkish Journal of Chemistry*. 2012;36(2):303–14. [<DOI>](#).
 22. Alexander L, Klug HP. Determination of Crystallite Size with the X-Ray Spectrometer. *Journal of Applied Physics*. 1950 Feb;21(2):137–42. [<DOI>](#).
 23. Mosmann T. Rapid colorimetric assay for cellular growth and survival: Application to proliferation and cytotoxicity assays. *Journal of Immunological Methods*. 1983 Dec;65(1–2):55–63. [<DOI>](#).
 24. Akbaba GB. Determination of Cytotoxicity of Zinc 2-Bromobenzoate with Nicotinamide and N,N'-Diethylnicotinamide Complexes. *Caucasian Journal of Science*. 2020 Dec;7(2):130–9. [<DOI>](#).
 25. ISO 10993-5:2009(en), Biological evaluation of medical devices — Part 5: Tests for in vitro cytotoxicity.
 26. Rasouli Z, Yousefi M, Torbati MB, Samadi S, Kalateh K. Synthesis and characterization of nanocerium-based composites and in vitro evaluation of their cytotoxicity against colon cancer. *Polyhedron*. 2020 Jan;176:114297. [<DOI>](#).
 27. Renu G, Rani VVD, Nair SV, Subramanian KRV, Lakshmanan V-K. Development of Cerium Oxide Nanoparticles and Its Cytotoxicity in Prostate Cancer Cells. *Advanced Science Letters*. 2012 Mar;6(1):17–25. [<DOI>](#).
 28. Kargar H, Ghasemi F, Darroudi M. Bioorganic polymer-based synthesis of cerium oxide nanoparticles and their cell viability assays. *Ceramics International*. 2015 Jan;41(1):1589–94. [<DOI>](#).
 29. Sabouri Z, Sabouri M, Amiri MS, Khatami M, Darroudi M. Plant-based synthesis of cerium oxide nanoparticles using *Rheum turkestanicum* extract

and evaluation of their cytotoxicity and photocatalytic properties. *Materials Technology*. 2020 Dec;1–14. [<DOI>](#).

30. Elahi B, Mirzaee M, Darroudi M, Sadri K, Kazemi Oskuee R. Bio-based synthesis of Nano-Ceria and evaluation of its bio-distribution and biological properties. *Colloids and Surfaces B: Biointerfaces*. 2019 Sep;181:830–6. [<DOI>](#).

31. De Marzi L, Monaco A, De Lapuente J, Ramos D, Borrás M, Di Gioacchino M, et al. Cytotoxicity and Genotoxicity of Ceria Nanoparticles on Different Cell Lines in Vitro. *International Journal of Molecular Sciences*. 2013 Feb;14(2):3065–77. [<DOI>](#).

32. García-Salvador A, Katsumiti A, Rojas E, Aristimuño C, Betanzos M, Martínez-Moro M, et al. A

Complete In Vitro Toxicological Assessment of the Biological Effects of Cerium Oxide Nanoparticles: From Acute Toxicity to Multi-Dose Subchronic Cytotoxicity Study. *Nanomaterials*. 2021 Jun;11(6):1577. [<DOI>](#).

33. Miri A, Beiki H, Najafidoust A, Khatami M, Sarani M. Cerium oxide nanoparticles: green synthesis using Banana peel, cytotoxic effect, UV protection and their photocatalytic activity. *Bioprocess and Biosystems Engineering*. 2021 Sep;44(9):1891–9. [<DOI>](#).

34. Rosário F, Bessa MJ, Brandão F, Costa C, Lopes CB, Estrada AC, et al. Unravelling the Potential Cytotoxic Effects of Metal Oxide Nanoparticles and Metal(Loid) Mixtures on A549 Human Cell Line. *Nanomaterials*. 2020 Mar;10(3):447. [<DOI>](#).



Surface Acidities of Bentonite, Sepiolite, and Synthetic Silica-Aluminas

Mehmet Kadir Yurdakoç , Hasibe Bölük , Aylin Altınışik Tağaç 

Dokuz Eylul University, Faculty of Science, Department of Chemistry, Izmir, Turkey

Abstract: The surface acidities of Bentonite, Sepiolite, and Silica-Aluminas were determined by Hammett indicators, amine titrations, and of pyridine adsorption-IR spectroscopy. The quantitative estimation of surface acidities of silica-aluminas and their natures as Brønsted and Lewis acid sites were evaluated. Lewis and total surface acidity values of sepiolite were higher than bentonite, 0.53 and 2.22 mmole g⁻¹, respectively. Surface acidity values of sepiolite and bentonite were much lower than Siral compounds. Among the Siral compounds, Siral 30 was found to be more effective in terms of acidity. All samples have both Lewis and Brønsted acid centers in which the Lewis sites predominated. IR spectroscopy with pyridine as a probe molecule was still very useful for the estimation of the surface acidities of the silica-alumina and also aluminosilicate structures such as clays and clay minerals.

Keywords: Surface acidity, Hammett indicators, amine titration, pyridine adsorption, FTIR spectroscopy

Submitted: April 02, 2021. **Accepted:** October 11, 2021.

Cite this: Yurdakoç MK, Bölük H, Altınışik Tağaç A. Surface Acidities of Bentonite, Sepiolite, and Synthetic Silica-Aluminas. JOTCSA. 2021;8(4):1153–66.

DOI: <https://doi.org/10.18596/jotcsa.962665>.

***Corresponding author. E-mail:** k.yurdakoc@deu.edu.tr.

INTRODUCTION

Clays and clay minerals are used as catalytic carriers and direct catalysts because they contain silica and alumina. The catalytic properties of clays have also been the subject of many studies. Their catalytic activity results from the surface acidity, that is, from the Brønsted and Lewis acid centers they contain. Silica and alumina are also used as catalysts in chemical reactions (1-3). The surface acidities and catalytic activities of metal oxides, clay and clay minerals has been recently reported in a review article. (4).

In the determination of the surface acidity of the catalysts, Hammett indicators (5-8), amine titration (9), calorimetric method (10-12) and investigation of the gas phase adsorption of bases such as pyridine by FTIR method (13-18) were studied. Thermal desorption methods can also be used for the determination of the types of acid sites and their amounts in the catalysts (5, 12, 19-22). Gas phase adsorption of pyridine onto metal oxides examined by IR spectroscopy used for the estimation of the surface acidities (23-27).

However, the results on the acidity of catalysts were not comparable as both the catalysts and acidity measurement methods in liquid phase or in gas phase. This is due to the fact that origins of the sites, the preparation methods and conditions (i.e. pretreatment, calcinations etc.) were arbitrarily different. The basic properties of silica and alumina and their mixtures, and especially the source of their acidic properties, were examined on a basic chemical content and published as a review article (28).

Clay minerals have Brønsted and Lewis acid sites because of their structures. The acidity and Brønsted to Lewis sites ratio related with the water content and SiO₂/Al₂O₃ (Si⁴⁺, Al³⁺ and Fe³⁺ ions) of the mineral. The acidity of bentonite results from the removal of exchangeable cations from the structure and the removal of water. Anhydrous interlayer cations also function as Lewis acids (29-33). Pyridine adsorption were also analyzed by density functional theory (DFT) simulations (34).

In recent years, silica-alumina as catalyst carriers and their effects on catalytic activity in terms of

acidities in various catalytic reactions has been investigated (35). Also, 2,4,6-tri-tert-butylpyridine (TTBP) was used as a new probe molecule for the determination of the acidities of zeolites as well as to silica and alumina (36). Nuclear magnetic resonance (NMR) relaxation time measurements and temperature-programmed desorption (TPD) techniques have also been developed as alternatives to IR spectroscopy, especially for zeolites (37).

The subject of this article, the surface acidity of synthetic Si-Al compounds, natural bentonite and sepiolite will be examined in terms of the amount of silica and their ratios they contain. The surface acid centers and amounts will also be studied. For this purpose, Hammett indicators, amine titration and FTIR spectroscopy investigation of in situ gas phase pyridine adsorption methods will be carried out.

EXPERIMENTAL SECTION

Materials

The chemical compositions of bentonite and sepiolite taken from Edirne and Eskişehir were given in a previous study (38). $\text{SiO}_2/\text{Al}_2\text{O}_3$ ratios in bentonite and sepiolite samples were calculated as 3 and 96, respectively. The physicochemical properties of SIRAL samples are given in our previous study. SIRAL consists of synthetic silicon and aluminum oxide. It is given as an abbreviation for silica and alumina. $\text{SiO}_2/\text{Al}_2\text{O}_3$ ratios in these compounds are given by the manufacturer as 20% SiO_2 and 80% Al_2O_3 in SIRAL 20 sample. Other chemicals used in our study were purchased from various companies as commercial and pure products and used as they are without any processing.

Acid Strength Measurements

Details about the experiment were given in a previous study (39). Therefore, it is briefly mentioned here. Dried powder samples were treated with three drops of all indicators in benzene. By looking at the color of the solution, it was decided whether the samples are basic to all indicators or the H_0 , which was between the pK_a of two consecutive indicators.

Quantitative determination of acid sites

In this method, the sample was first dispersed in benzene and then titrated with n-butyl amine in the presence of an indicator which was determined in acid strength measurement experiments. Dry benzene (sodium wire drawn) was chosen as a liquid that does not wet the surface and does not interact with the surface of the samples. If the liquid (or solvent) contains water or humidity from air, the acidity of the surface changes.

Fourier Transform Infrared (FTIR) Spectroscopic Analysis

At first, dry pure sample is tableted. The sample to be examined is taken into the IR cell and pre-treated by heating at 110 °C under vacuum. The IR cell for gas phase used in the study is made of quartz, contains NaCl windows and has a heating system. Pyridine adsorption experiments were carried out in situ on pure tablets in the form of a gas phase in a special gas manipulation line setup. In our previous studies (39), a different FTIR device was used. IR spectra after each pyridine adsorption applied at certain time intervals and temperatures are recorded in Perkin-Elmer BX-II spectrometer. After the adsorption experiments, the desorption process is carried out by applying vacuum for 10 minutes at certain temperatures and recording the spectra at each stage. In the IR spectra recorded during the adsorption and desorption experiments, the area values below the relevant absorption bands are calculated. These area values were used in surface acidity calculations.

RESULTS AND DISCUSSION

Acid Strength Measurements

In the study conducted with Hammett indicators, it was determined that the samples were sensitive to which indicators in terms of surface acidity. Acidity strength measurement experiments were carried out on seven samples and eight indicators. The indicators used in the study and their pK_a values were neutral red, $\text{pK}_a = +6.8$; methyl red, $\text{pK}_a = +4.8$; 4-nitroaniline, $\text{pK}_a = +1.1$; crystal violet, $\text{pK}_a = +0.8$; 2-nitroaniline, $\text{pK}_a = -0.2$; 4-chloro-2-nitroaniline, $\text{pK}_a = -0.9$; 2,4-dinitroaniline, $\text{pK}_a = -4.4$; anthraquinone, $\text{pK}_a = -8.2$, respectively. All samples showed positive color change only with neutral red and methyl red indicators. The studied substances give color conversion with the indicators of pK_a values greater than +1.1. As the pK_a values increase, the acidity strength decreases. After the indicators were determined, butyl amine titration was performed for the estimation of quantitatively the acid strength and sites. Titrations were carried out with neutral red and methyl red indicators in benzene.

n-butyl Amine Titration Results

The titration results were presented in Table 1. The total acidity of Siral samples was about 0.8 mmole/g. It increased with SiO_2 content. In the case of clays, Bentonite was more acidic than Sepiolite, as 1.76 and 1.14 mmole g^{-1} . This result may be due to SiO_2 content.

Table 1: The acidities from the n-butyl amine titration (mmole g⁻¹)

Indicator	Siral 5	Siral 20	Siral 30	Siral 40	Siral 80	Sepiolite	Bentonite
Neutral red (pKa= +6.8)	0.17	0.20	0.24	0.28	0.45	0.57	0.26
Methyl red (pKa= +4.8)	0.30	0.40	0.47	0.55	0.36	0.57	1.50
Total	0.47	0.60	0.71	0.83	0.81	1.14	1.76

It was published that the binary oxides such as SiO₂-Al₂O₃ were more strongly acidic than the oxides alone when heating under vacuum. It was found that the acidity strength increased proportionally with increasing SiO₂ amounts (1). This may be due to the water content of these samples and also the method of preparation. In another study, it was determined that grinding and steam heating changed the acidity strength (18).

Fourier Transform Infrared (FTIR) Spectroscopic Experiments in Acidity

Today, as a standard method in surface acidity, the concentrations of Brønsted and Lewis acid sites are

calculated according to equation 1 as moles per dry sample weight (40).

$$q_H = \frac{A \pi R^2}{w \epsilon} \quad (1)$$

Where A is the absorbance of the band from FTIR spectrum, R is disk formed sample radius as cm, and w is the sample weight as g before the experiment. ϵ , for the Brønsted and Lewis acid sites, the absorption bands at 1490 cm⁻¹ and 1450 cm⁻¹; 1.67 and 2.22 cm²μmol⁻¹ were taken as reference, respectively (23). The acid sites were calculated from the equation (1) and given in Table 2.

Table 2: The acid sites as mmole g⁻¹ from the adsorption of pyridine.

Sample	q _H ^L	q _H ^B + q _H ^L
Siral 5	1.23	2.55
Siral 20	1.32	4.08
Siral 30	3.16	4.86
Siral 40	2.88	4.90
Siral 80	3.09	4.24
Sepiolite	0.53	2.22
Bentonite	0.20	0.58

The IR spectra of pyridine adsorbed on the samples were presented in Figures 1-7. Figure 1-3 were organized in a Supplementary File as S1. On the other hand, Siral 40, Siral 80, Sepiolite and Bentonite were given in Figures 4-7, respectively. The pyridine bands used in the evaluation of the data in the FTIR spectroscopic examination of pyridine adsorption from the gas phase on solid samples are given in Table 3 (14,15). All spectra (Figures 1-7) were evaluated according to this chart.

Table 3: The pyridine bands used in the evaluation of the data.

Type	PY cm ⁻¹	HPY cm ⁻¹	BPY cm ⁻¹	LPY cm ⁻¹
Mode 8a	1582	1614	1639	1617
8b	-	1593	1613	-
19a	1483	1490	1489	1495
19b	1440	1438	1539	1451

Therefore, the observed bands at 1634, 1576 and 1394 cm⁻¹ were defined to pyridinium ion as Brønsted species. For Lewis species, the bands at 1621, 1576 and 1456 cm⁻¹ were attributed. The band at 1490 cm⁻¹ was related with BPY and LPY as stated in Table 3. This band was observed as common in all spectra (Figure 1-7). The band at 1456 cm⁻¹ is also located in all spectra and can be taken close to the band at 1451 cm⁻¹, which is the closest for LPY, and shows Lewis acid locations. Pyridine is physically adsorbed by surface hydroxyl groups in the studied oxide structures. Absorption bands in the wavenumber range of 1590-1620 cm⁻¹ appear as an indicator of this interaction. While 1595 cm⁻¹ of these bands which was due to HPY species as in Table 3 observed especially in Siral compounds, it was not observed in sepiolite and bentonite. On the other hand, characteristic PY mode 8a was observed at 1588 cm⁻¹ in bentonite and sepiolite samples as in Figures 6 and 7,

respectively. Especially in the desorption experiments carried out at increasing temperatures, it was seen that a water molecule consisting of two hydroxyl groups leaving from the structures is strongly adsorbed on the surfaces, and it did not completely move away from the surface even in desorption at 573 K.

In the mutual evaluation of the spectra (Figures 1-7), synthetic silica-alumina compounds (Sirals) and natural clays (bentonite, sepiolite) were selected according to their SiO₂ and Al₂O₃ contents. In this respect, the spectra of Siral 40, Siral 80, sepiolite and bentonite (Figures 4-7) were clearly evaluated because of the SiO₂ content.

Bands were observed at 1593, 1490 and 1456 cm⁻¹ for Siral 40 in Figure 4. The band at 1490 cm⁻¹ can be explained as pyridinium ion and pyridine bound to Lewis site. This band did not disappear in the

desorption experiment (Spectrum f in Figure 4) conducted at 373 K, and the desorptions carried out up to 573 K were also permanent. This was observed as an increase in band intensity in Siral 80 (Figure 5a-f). On the other hand, this band was relatively absent in sepiolite (Figure 6). In bentonite (Figure 7), band intensity was initially observed as very weak (spectrum b), then the band intensity increases and eventually becomes permanent. This was observed as an increase in band intensity in Siral 80 (Figure 5a-f). The band at 1490 cm^{-1} was relatively absent in sepiolite (Figure 6). In bentonite (Figure 7), band intensity was initially observed as very weak (spectrum b), increased gradually and the eventually becomes permanent. This behavior of the band at 1490 cm^{-1} can be interpreted as that pyridine interacts strongly with the Brønsted and Lewis acid centers on the surface and is also chemically adsorbed.

The bands observed at 1490 and 1456 cm^{-1} in Siral 40 (Fig. 4) were preserved, although the intensities decreased partially in desorption carried out with increasing temperature (Figure 4f). In Siral 80 (Figure 5), HPY (Mode 8b, Table 3) at 1595 cm^{-1} and $1454\text{-}1444\text{ cm}^{-1}$ (LPY) were observed. The bands at 1435 , 1456 , 1574 and 1588 cm^{-1} were observed for sepiolite (Figure 6).

There was an interesting situation here. All bands disappeared at 298 K during the desorption process. It can be interpreted that pyridine was poorly and physically adsorbed to the acid centers on the

surface. If we look at the situation with bentonite, the band at 1490 cm^{-1} was gradually narrowed and its intensity decreased after desorption at 298 K, but still observed the last desorption at 573K (Figure 7e is not given here). Although common bands are observed at 1588 , 1490 and 1456 cm^{-1} in the adsorption spectra of pyridine on sepiolite and bentonite, differences are observed especially in desorption spectra.

CONCLUSION

Surface acidity of silica-alumina compounds and the amount of acid centers vary depending on many factors such as $\text{SiO}_2/\text{Al}_2\text{O}_3$ ratio, SiO_2 percentage, preparation conditions, water content heat treatment. In situ adsorption/desorption experiments carried out in the gas phase where pyridine is used as the base and the monitoring of the processes with the IR method are quite fruitful. The method can be used as a standard in a wide range. While the order of total acidity values calculated according to the amine titration method in the samples was determined as Bentonite> Sepiolite>Siral 40> Siral 80> Siral 30> Siral 20> Siral 5, the order according to FTIR data was quite different from the amine titration method as Siral 40> Siral 30> Siral 80> Siral 20> Siral 5> Sepiolite> Bentonite. All of the samples showed surface acidity and can be used as solid acid catalysts in a variety of reactions.

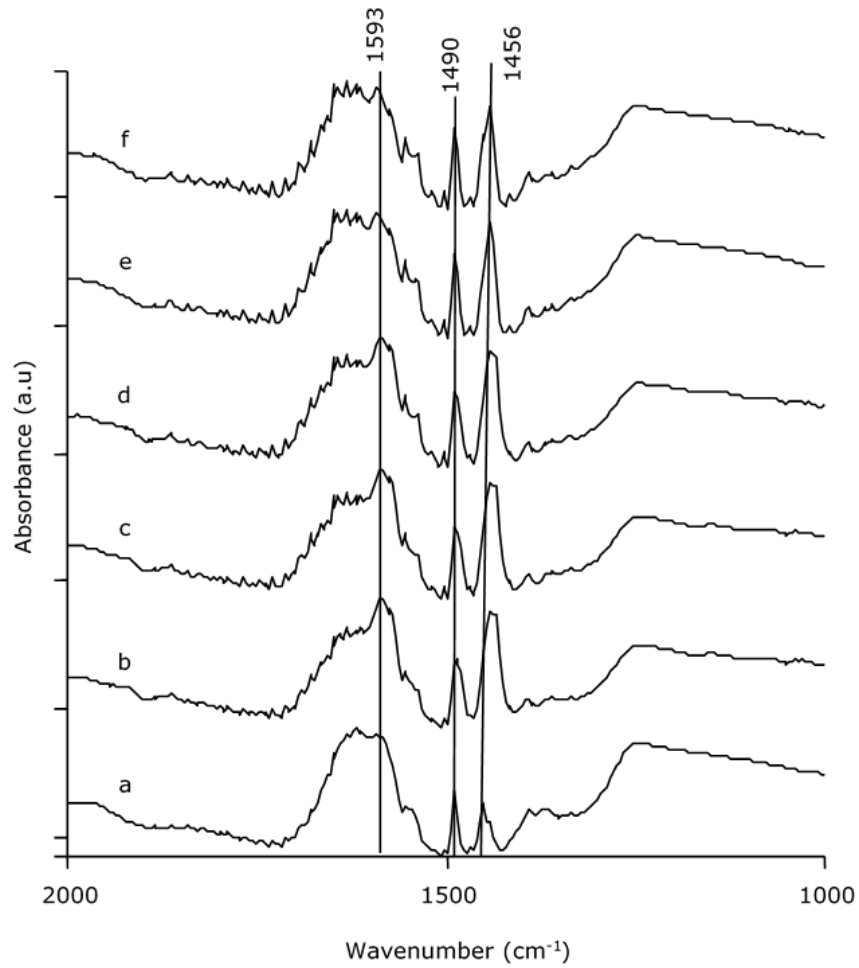


Figure 4: FTIR spectra of pyridine adsorbed on Siral 40 a) reference b) initial ads. c) 15 min. ads d) 373 K, 30 min. ads. e) 298 K, 5 min. des. f) 373 K, 10 min. des.

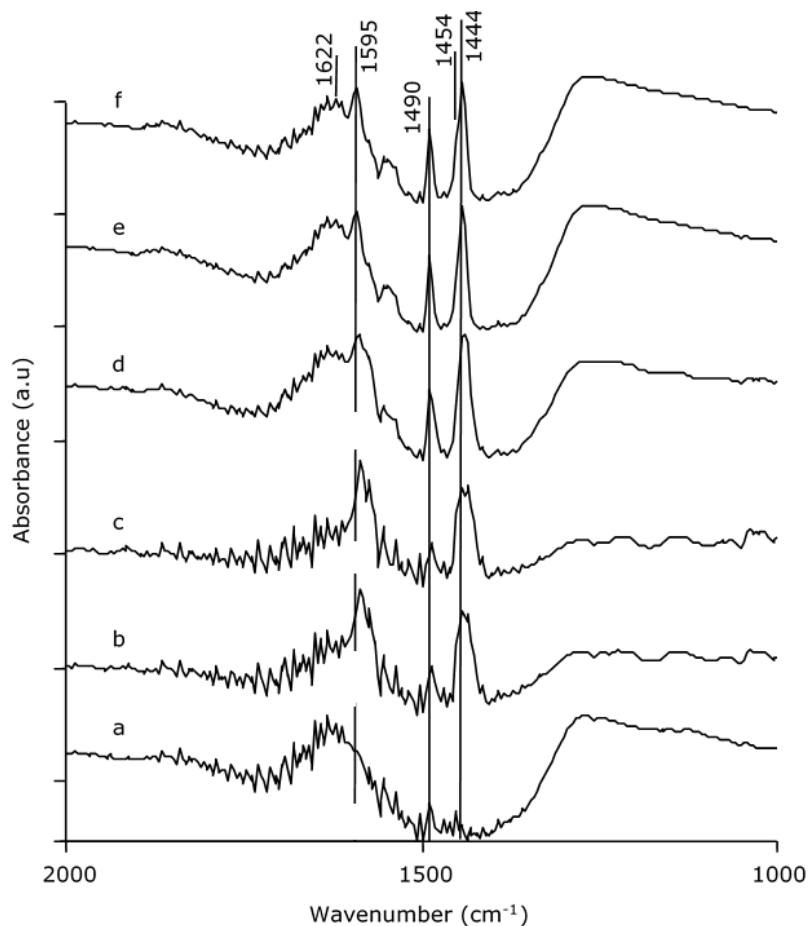


Figure 5: FTIR spectra of pyridine adsorbed/desorbed on Siral 80 a) reference b) initial ads. c) 15 min. ads. d) 373 K, 30 min. ads. e) 298 K, 5 min. des. f) 373 K, 10 min. des.

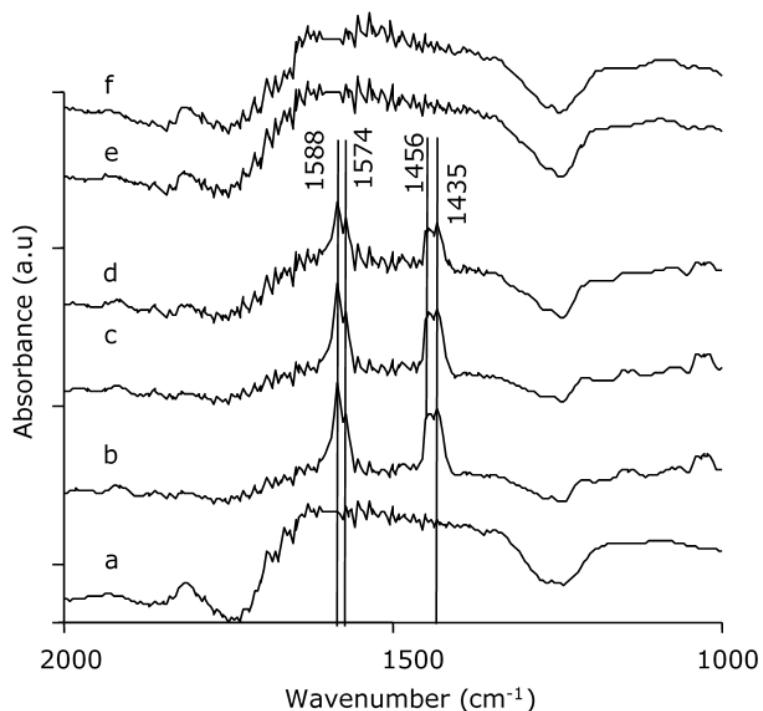


Figure 6: FTIR spectra of pyridine adsorbed / desorbed on Sepiolite a) reference b) initial ads. c) 15 min. ads. d) 373 K, 30 min. ads. e) 298 K, 5 min. des. f) 373 K, 10 min. des.

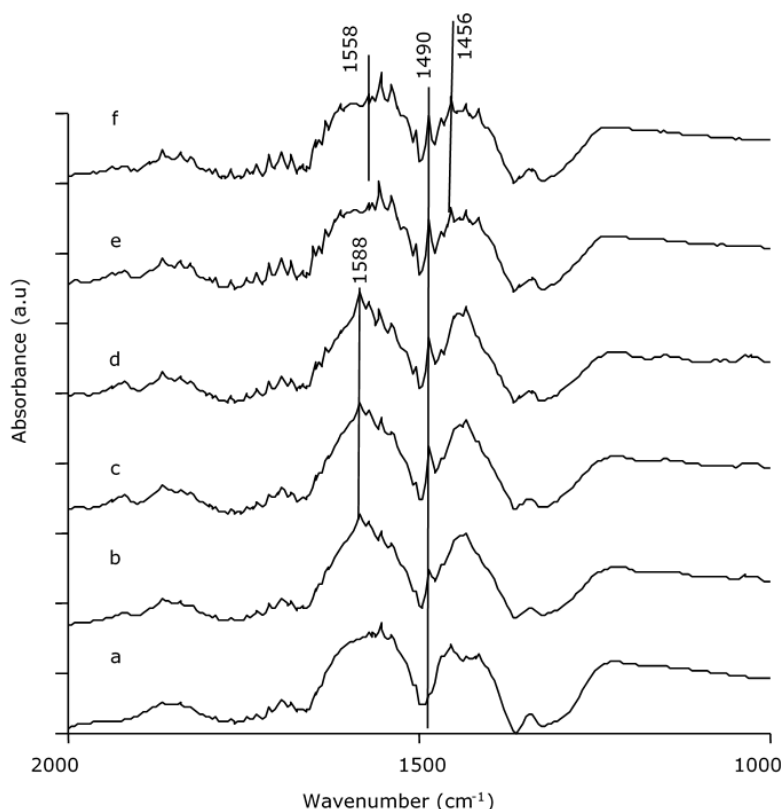


Figure 7: FTIR spectra of pyridine adsorbed / desorbed on Bentonite a) reference b) initial ads. c) 15 min. ads. d) 373 K, 30 min. ads. e) 298 K, 5 min. des. f) 373 K, 10 min. des.

CONFLICT OF INTEREST

There is no conflict of interest with any institution or person.

SUPPLEMENTARY INFORMATION

FTIR spectrum results related to the adsorption of pyridine from the gas phase on Silica-alumina compounds (Siral 5, 20 and 30) are presented as supplementary file (S1) so that it does not take up too much space.

REFERENCES

1. Tanabe K, Misono M, Ono Y, Hattori H. 2 Determination of Acidic and Basic Properties on Solid Surfaces. In: *Studies in Surface Science and Catalysis* [Internet]. Elsevier; 1989 [cited 2021 Oct 16]. p. 5–25. <URL>
2. Kijeński J, Baiker A. Acidic sites on catalyst surfaces and their determination. *Catalysis Today*. 1989 Mar;5(1):1–120. <DOI>
3. Selli E, Forni L. Comparison between the surface acidity of solid catalysts determined by TPD and FTIR analysis of pre-adsorbed pyridine. *Microporous and Mesoporous Materials*. 1999 Oct;31(1–2):129–40. <DOI>
4. Busca G, Gervasini A. Solid acids, surface acidity and heterogeneous acid catalysis. In: *Advances in Catalysis* [Internet]. Elsevier; 2020 [cited 2021 Oct 16]. p. 1–90. <URL>
5. Liu D, Yuan P, Liu H, Cai J, Qin Z, Tan D, et al. Influence of heating on the solid acidity of montmorillonite: A combined study by DRIFT and Hammett indicators. *Applied Clay Science*. 2011 Jun;52(4):358–63. <DOI>
6. Topaloğlu Yazıcı D, Bilgiç C. Determining the surface acidic properties of solid catalysts by amine titration using Hammett indicators and FTIR-pyridine adsorption methods: Determining the surface acidic properties of solid catalysts. *Surf Interface Anal*. 2010 Jun;42(6–7):959–62. <DOI>
7. Benesi HA. Acidity of Catalyst Surfaces. II. Amine Titration Using Hammett Indicators. *J Phys Chem*. 1957 Jul;61(7):970–3. <DOI>
8. Hart MP, Brown DR. Surface acidities and catalytic activities of acid-activated clays. *Journal of Molecular Catalysis A: Chemical*. 2004 Apr;212(1–2):315–21. <DOI>
9. Brown DR, Rhodes CN. Brønsted and Lewis acid catalysis with ion-exchanged clays. *Catalysis Letters*. 1997;45(1/2):35–40. <DOI>

10. Breen C, Deane AT, Flynn JJ. The acidity of trivalent cation-exchanged montmorillonite. Temperature-Programmed desorption and infrared studies of pyridine and n -butylamine. *Clay miner.* 1987 Jun;22(2):169-78. <DOI>.
11. Jankovic L. Metal cation-exchanged montmorillonite catalyzed protection of aromatic aldehydes with Ac₂O. *Journal of Catalysis.* 2003 Aug 15;218(1):227-33. <DOI>.
12. Breen C. Thermogravimetric study of the desorption of cyclohexylamine and pyridine from an acid-treated Wyoming bentonite. *Clay miner.* 1991 Dec;26(4):473-86. <DOI>.
13. Richardson RL, Benson SW. A Study of the Surface Acidity of Cracking Catalyst. *J Phys Chem.* 1957 Apr;61(4):405-11. <DOI>.
14. Basila MR, Kantner TR, Rhee KH. The Nature of the Acidic Sites on a Silica-Alumina. Characterization by Infrared Spectroscopic Studies of Trimethylamine and Pyridine Chemisorption 1. *J Phys Chem.* 1964 Nov;68(11):3197-207. <DOI>.
15. Bourne KH, Cannings FR, Pitkethly RC. Structure and properties of acid sites in a mixed-oxide system. I. Synthesis and infrared characterization. *J Phys Chem.* 1970 May;74(10):2197-205. <DOI>.
16. Cannings FR. Acidic sites on mordenite: an infrared study of adsorbed pyridine. *J Phys Chem.* 1968 Dec;72(13):4691-3. <DOI>.
17. Parry E. An infrared study of pyridine adsorbed on acidic solids. Characterization of surface acidity. *Journal of Catalysis.* 1963 Oct;2(5):371-9. <DOI>.
18. Tanabe K. Solid acids and bases: their catalytic properties. Tokyo, New York: Kodansha; Academic Press; 1970. 175 p. ISBN: 978-0-12-683250-1.
19. Liu D, Yuan P, Liu H, Cai J, Tan D, He H, et al. Quantitative characterization of the solid acidity of montmorillonite using combined FTIR and TPD based on the NH₃ adsorption system. *Applied Clay Science.* 2013 Aug;80-81:407-12. <DOI>.
20. Bilgiç C, Topaloglu Yazıcı D, Vural N. Characterizing the surface acidity of bentonite by various methods: The surface acidity of bentonite. *Surf Interface Anal.* 2010 Jun;42(6-7):1000-4. <DOI>.
21. Benaliouche F, Boucheffa Y, Ayrault P, Mignard S, Magnoux P. NH₃-TPD and FTIR spectroscopy of pyridine adsorption studies for characterization of Ag- and Cu-exchanged X zeolites. *Microporous and Mesoporous Materials.* 2008 Apr;111(1-3):80-8. <DOI>.
22. Hughes TR, White HM. A study of the surface structure of decationized Y zeolite by quantitative infrared spectroscopy. *J Phys Chem.* 1967 Jun;71(7):2192-201. <DOI>.
23. Emeis CA. Determination of Integrated Molar Extinction Coefficients for Infrared Absorption Bands of Pyridine Adsorbed on Solid Acid Catalysts. *Journal of Catalysis.* 1993 Jun;141(2):347-54. <DOI>.
24. Makarova MA, Karim K, Dwyer J. Limitation in the application of pyridine for quantitative studies of brönsted acidity in relatively aluminous zeolites. *Microporous Materials.* 1995 Jun;4(2-3):243-6. <DOI>.
25. Khabtou S, Chevreau T, Lavalley JC. Quantitative infrared study of the distinct acidic hydroxyl groups contained in modified Y zeolites. *Microporous Materials.* 1994 Sep;3(1-2):133-48. <DOI>.
26. Datka J. Acidic properties of supported niobium oxide catalysts: An infrared spectroscopy investigation. *Journal of Catalysis.* 1992 May;135(1):186-99. <DOI>.
27. Turek AM, Wachs IE, DeCanio E. Acidic properties of alumina-supported metal oxide catalysts: an infrared spectroscopy study. *J Phys Chem.* 1992 Jun;96(12):5000-7. <DOI>.
28. Busca G. Catalytic materials based on silica and alumina: Structural features and generation of surface acidity. *Progress in Materials Science.* 2019 Jul;104:215-49. <DOI>.
29. Akçay M. FT-IR spectroscopic investigation of the adsorption pyridine on the raw sepiolite and Fe-pillared sepiolite from anatolia. *Journal of Molecular Structure.* 2004 Jun;694(1-3):21-6. <DOI>.
30. Akçay M. The surface acidity and characterization of Fe-montmorillonite probed by in situ FT-IR spectroscopy of adsorbed pyridine. *Applied Catalysis A: General.* 2005 Oct;294(2):156-60. <DOI>.
31. Madejová J. FTIR techniques in clay mineral studies. *Vibrational Spectroscopy.* 2003 Jan;31(1):1-10. <DOI>.
32. Yariv S, Michaelian K. Structure and surface acidity of clay minerals. In: Yariv S, Cross H, editors. *Organo-clay complexes and interactions.* New York: Marcel Dekker; 2002. p. 1-38. ISBN: 978-0-8247-0586-2.
33. Heller-Kallai L. Clay catalysis in reactions of organic matter. In: *Organo-Clay Complexes and Interactions.* New York: Marcel Dekker; 2002. p. 567-614. ISBN: 978-0-8247-0586-2.

34. Jystad A, Leblanc H, Caricato M. Surface Acidity Characterization of Metal-Doped Amorphous Silicates via Py-FTIR and ^{15}N NMR Simulations. *J Phys Chem C*. 2020 Jul 16;124(28):15231–40. [<DOI>](#).
35. Saito M, Aihara T, Miura H, Shishido T. Brønsted acid property of alumina-based mixed-oxides-supported tungsten oxide. *Catalysis Today*. 2021 Sep;375:64–9. [<DOI>](#).
36. Beutel TW, Willard AM, Lee C, Martinez MS, Dugan R. Probing External Brønsted Acid Sites in Large Pore Zeolites with Infrared Spectroscopy of Adsorbed 2,4,6-Tri-tert-butylpyridine. *J Phys Chem C*. 2021 Apr 29;125(16):8518–32. [<DOI>](#).
37. Robinson N, Bräuer P, York APE, D'Agostino C. Nuclear spin relaxation as a probe of zeolite acidity: a combined NMR and TPD investigation of pyridine in HZSM-5. *Phys Chem Chem Phys*. 2021;23(33):17752–60. [<DOI>](#).
38. Cengiz S, Çavaş L, Yurdakoç K. Bentonite and sepiolite as supporting media: Immobilization of catalase. *Applied Clay Science*. 2012 Sep;65–66:114–20. [<DOI>](#).
39. Yurdakoç M, Akçay M, Tonbul Y, Yurdakoç K. Acidity of silica-alumina catalysts by amine titration using Hammett indicators and FT-IR study of pyridine adsorption. *Turk J Chem*. 1999;23(3):319–218. [<URL>](#).
40. Barzetti T, Selli E, Moscotti D, Forni L. Pyridine and ammonia as probes for FTIR analysis of solid acid catalysts. *Faraday Trans*. 1996;92(8):1401. [<DOI>](#).

Surface Acidities of Bentonite, Sepiolite, and Synthetic Silica-Aluminas

Mehmet Kadir Yurdakoç , Hasibe Bölük , Aylin Altınışik Tağaç 

Supplementary File (S1)

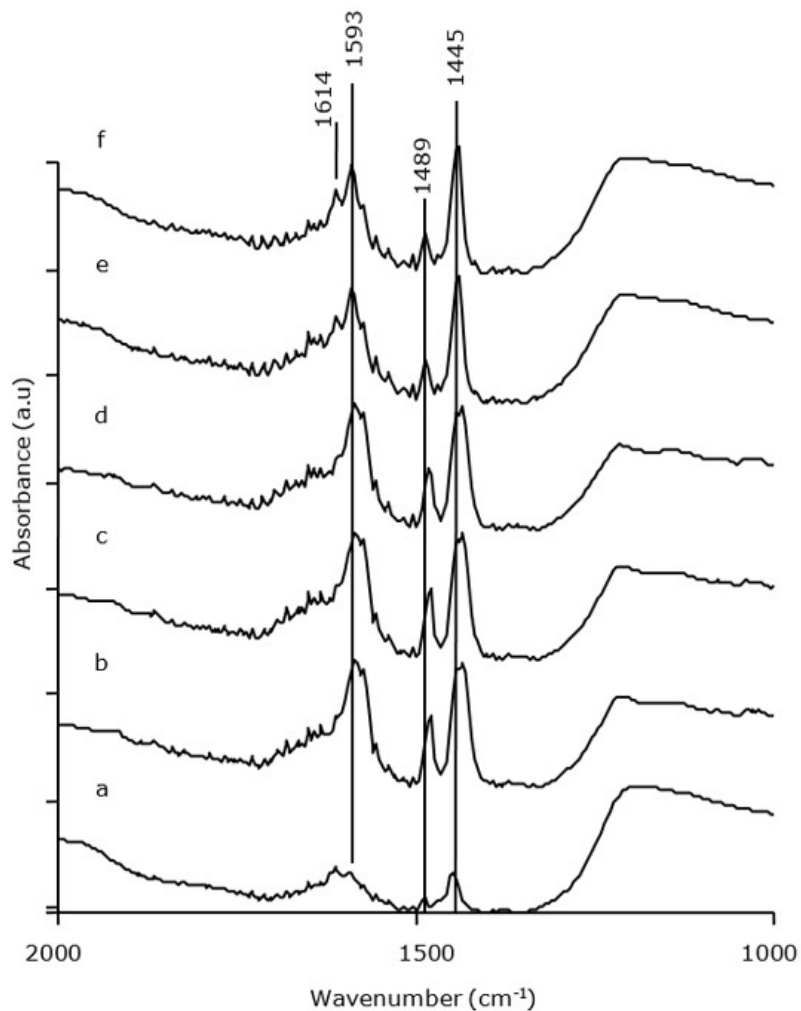


Figure S1: FTIR spectra of pyridine adsorbed/desorbed on Siral 5 a) reference b) initial ads. c) 15 min. ads. d) 373 K, 30 min. ads. e) 298 K, 5 min. des. f) 373 K, 10 min. des.

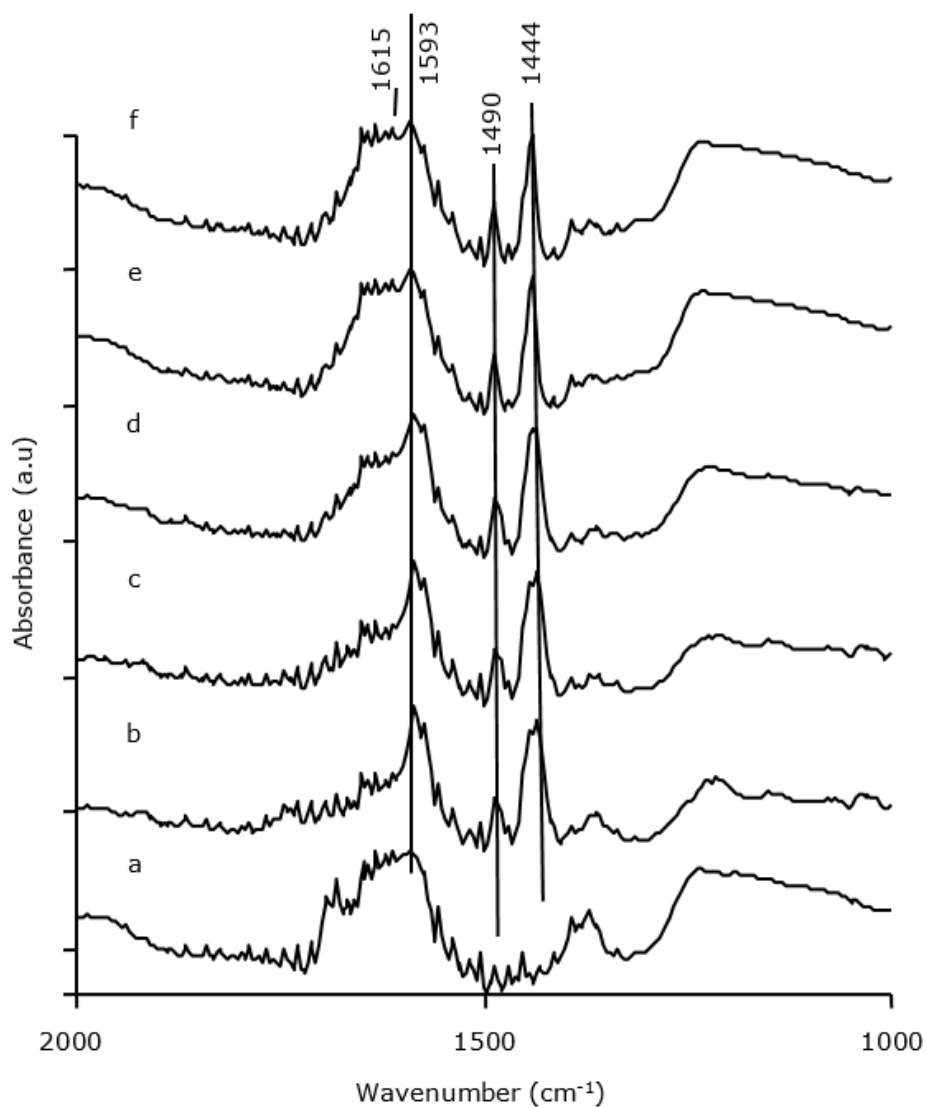


Figure S2: FTIR spectra of pyridine adsorbed/desorbed on Siral 20 a) reference b) initial ads. c) 15 min. ads. d) 373 K, 30 min. ads. e) 298 K, 5 min. des. f) 373 K, 10 min. des.

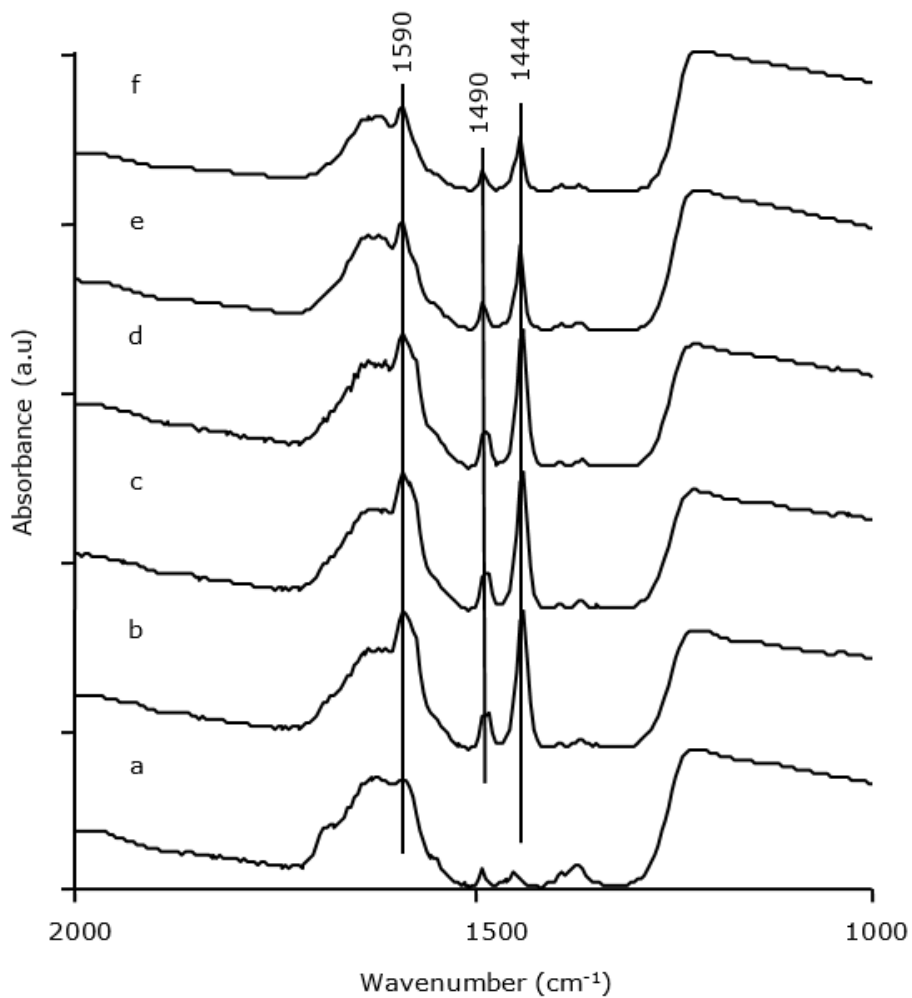





Figure S3: FTIR spectra of pyridine adsorbed/desorbed on Siral 30 a) reference b) initial ads. c) 15 min. ads. d) 373 K, 30 min. ads. e) 298 K, 5 min. des. f) 373 K, 10 min. des.



Reduction of the Structural Iron in Montmorillonite by Electron Transfer from Catechol and its Derivatives

Jasim Hamadi Hassen^{1*}  , Jack Silver² 

¹University of Anbar, College of Pharmacy, Department of Pharmaceutical Chemistry, Ramadi, Iraq.

²University of Brunel, Wolfson Centre for Material Processing, London, UK.

Abstract: The structural Fe(III) in montmorillonite (MMT) clay has been reduced using catechol and its derivatives. It was found that the reduction process is pH-dependent and also depends on the ring substituents. If the catecholic ring has electron-donating substituents, reduction happens at high pH; if the catecholic ring has electron-withdrawing substituents, no reduction occurs. The process involves electron transfer from the hydroxy groups on the compounds to the active site at the iron atoms within the MMT lattice. This site acts as an electron acceptor (Lewis acid). Heat treatment of the reduced sample at 100-300 °C showed an enhancement of the Fe²⁺/Fe³⁺ ratio, which is attributed to an increase in the proportion of radicalic formation induced by dehydration. The MMT sample was added to the solutions of the catecholic compound and the slurries were stirred for 24 hours in order to reach equilibrium, then filtered, washed, and air-dried. The reactions were monitored using Mössbauer spectroscopy, x-ray powder diffraction, differential thermal analysis, electron spin resonance, infrared, and total surface area determination.

Keywords: Catechol, montmorillonite, reduction, electron transfer.

Submitted: April 02, 2021. **Accepted:** October 11, 2021.

Cite this: Hassen JH, Silver J. Reduction of the Structural Iron in Montmorillonite by Electron Transfer from Catechol and its Derivatives. JOTCSA. 2021;8(4):1167-78.

DOI: <https://doi.org/10.18596/jotcsa.908713>.

***Corresponding author.** E-mail: ph.jasimhu@uoanbar.edu.iq, Tel: (009647805845839).

INTRODUCTION

MMT belongs to the sizeable specific surface area clay minerals with a 2:1 layer structure. An octahedral sheet of alumina surrounded by two layers of tetrahedral silica sheets. There is an access net negative charge that can be balanced by cations like Na⁺, Ca²⁺, and Mg²⁺ (1). The process of reducing structural iron of MMT and other clays has received significant interest from many researchers due to the wide application of this process in different fields. The iron existence in the clay mineral structure adds to its unique importance. The reason for this is the fact that the oxidation state can be changed and controlled by the influence of external factors. This in turn, leads to changes in the clay properties. The Fe oxidation state in the crystal lattice of MMT clay has an essential role in determining the surface and colloidal chemistry. It also plays an essential role

in the physical behavior of the clay. The valence states of clay's structural iron affect the physicochemical properties such as cation exchange capacity and surface area (2-4). Bacterial reduction of Fe-bearing clay has the ability to change the structure of the clay and causes a decrease in the surface area and an increase in the cation exchange capacity. The process is mainly reversible (5-7). A reduced nontronite clay has shown a noticeable antibacterial activity at pH 6 toward *E. coli* (8). It was found that *D. vulgaris* is able to reduce structural Fe(III) in four types of clay minerals (9). Humic acid can effectively stimulate the bioreduction rate of structural Fe(III) in clays (10). The Fe(II) in MMT was found to reduce 2-nitrophenol after adsorption (11). The reactivity of structural and surface-bonded Fe(II) in chemically reduced and oxidized nontronite and reduced MMT was investigated using two acetyl nitrobenzene

isomers as a probe (12). An experiment was conducted to investigate the mechanism of Se sorption on MMT clay in deep geological environments under reducing conditions. The Se element was dissolved as selenide (Se(-II)) anions. It was shown by X-ray absorption that the Se-sorbed oxidation state was (0), which implies that Se was oxidized on MMT (13). Mössbauer spectroscopy study showed that Fe(II) reduces a large amount of Fe(III) in a low-Fe MMT. The reduction rate extends from 12 to 78% through a pH range of 4.0-7.5. It was suggested that extensive reduction occurs by electron transfer through the basal plane (14). The oxidant production that was produced after oxygenation of reduced nontronite was studied in the presence of four different compounds. The compounds were phosphate, tripolyphosphate, nitrilotriacetic acid, and diaminetetraacetic acid. All the compounds increase the oxidant yields, but the mechanisms vary, depending on the compound type (15). Electron transfer mechanism was suggested in a study concerning Fe(II)-goethite systems (16,17). On the other hand, Fe-bearing clay minerals were used for the reduction of hexavalent chromium. The process is affected by different environmental factors (18-21). Several studies have demonstrated the adsorption of phenol, substituted phenols catechol, and its derivatives on clay minerals (22-26). The structural Fe(II) of MMT can be reduced to Fe(III) at high pH if the phenolic ring has an electron donating substituent. The adsorption process includes transferring an electron from the hydroxyl group to the Fe atoms inside the lattice (27). The aim of the current research is to understand how catechols attack and reduce MMT's structural iron, using different analytical tool. The information collected from different analytical tools may help in understanding how the reduction process occurs and how the oxidation state of iron changes.

MATERIALS AND METHODS

The MMT sample was obtained from Podmore and Sons Ltd. All the chemicals used in this research were of analytical grade obtained from Sigma-Aldrich Company. Mössbauer spectra were recorded at 77 °K on a Canberra Multichannel Analyzer using ^{57}Co as a source. The source used was 25 mCi cobalt-57 in a rhodium matrix obtained from the Radiochemical Centre, Amersham. X-ray diffraction patterns were recorded on a Philips diffractometer using CuK α radiation. The differential thermal analysis curves were recorded on a DUPONT 900 Differential Thermal Analyzer. The ESR spectra were recorded on a Varian EI04A X-band spectrometer. The infra-red spectra were recorded on a Perkin Elmer 1330 infra-red spectrophotometer. The surface area of the samples was measured by the methods described by other researchers (28). The pH was monitored using a Philips (PW-91109) digital pH meter.

MMT- Catecholic Compounds Reaction

The catecholic compound (100 mg) was added to 1 g of the MMT clay sample dispersed in 50 mL distilled water. The pH was adjusted to 1, 7, and 10.5 and monitored periodically in the first few hours using 0.1 N NaOH and 0.1 N HCl. The mixtures were stirred for 24 hours to reach equilibrium, then filtered, washed, and air-dried.

RESULTS AND DISCUSSION

When catecholic molecules or their derivatives are brought together with the MMT clay in solution at a pH high enough to dissociate one or both protons, electron transfer occurs from the catecholic compound to the active sites of the MMT clay. These sites are aluminum exposed at the edges and/or transition metal cations in a high valency state at the planar surface. Our concern is the latter site. Both sites act as electron acceptors, and any initial reduction occurs at the surface; it can propagate into the planar sites by electron diffusion or hopping (29). The organic molecules may approach the pyramidal edges of the MMT, and electron diffusion takes place within the octahedral layers since the organic compounds are expected to be negatively charged at high pH (Figure 1). When the reduction process is done, there will be a charge imbalance, which may be maintained by the protonation of the adjacent OH group (30).

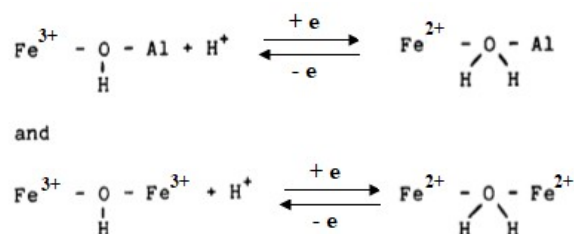


Figure 1: The electron transfer process.

The protons in the equations are derived from molecules of water dissociated in the interlayer space. These protons penetrate the structure by proton tunneling. The resulting OH⁻ ions in the spaces can pick up H⁺ from the solution outside the proton pump process. At high pH, small amounts of iron, and some other ions, are expected to be extracted from the MMT structure and present in the solution as hydroxides. These hydroxides interact with the catecholic molecules to form iron-catechol complexes:

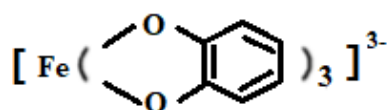


Figure 2: Structure of the iron-catechol complex.

The mechanism of the MMT structural iron reduction by the catecholic compounds can be described as in Figure 3.

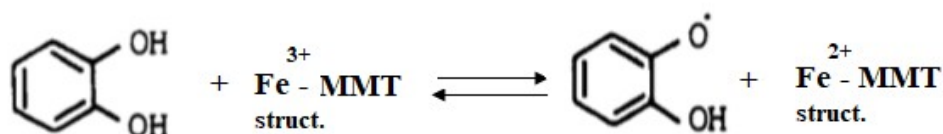


Figure 3: Mechanism of the MMT structural iron reduction by the catecholic compounds.

The radical produced in the last equation undergoes further oxidation to a quinone. For o-substituted compounds like catechol, the expected compound is o-benzoquinone (31).

Mössbauer Spectroscopy

Mössbauer spectra of MMT-catechol

The Mössbauer spectra of the MMT sample reacted with catechol at pH 1 and 7 showed the same behavior as that of the original sample at the same pH; no effect was seen in the presence of catechol;

in fact, some of the iron(II) was oxidized to iron(III), presumably indirectly by oxygen contamination in the solution. The sample reacted with catechol at pH 10.5 shows a considerable enhancement of iron(II) at the expense of the iron(III) content. The $\text{Fe}^{2+}/\text{Fe}^{3+}$ ratio derived from the Mössbauer spectrum was 2.4[5]. The parameter is presented in Table 1, and Figure 4 shows the spectra at 77 K of MMT sample reacted with catechol at pH 1, 7, and 10.5.

Table 1: The ^{57}Fe Mössbauer parameters at 77 °K of the original MMT sample and the sample reacted with catechol at different pH's in an aqueous solution. Data were collected on the dried solids.

Sample	pH	$\delta \text{ mms}^{-1}$	$\Delta \text{ mms}^{-1}$	$\Gamma \text{ mms}^{-1}$	Absorption area %	$\text{Fe}^{2+}/\text{Fe}^{3+}$ ratio
Original MMT	-	0.43[2]	0.65[2]	0.30[2]	51[4]	1[2]
		1.25[1]	3.03[1]	0.14[1]	49[3]	
MMT-catechol	1	0.43[1]	0.64[1]	0.31[1]	100	-
	7	0.39[1]	0.79[1]	0.40[2]	78[3]	0.3[1]
=	10.5	1.48[2]	2.56[4]	0.24[3]	22[4]	2.4[5]
		0.49[2]	0.73[4]	0.26[3]	30[5]	
		1.27[1]	3.04[1]	0.12[1]	70[4]	

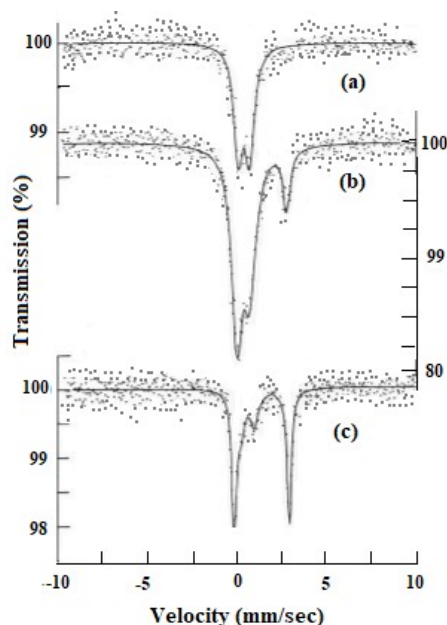


Figure 4: The ^{57}Fe Mössbauer spectra at 77 °K of MMT reacted with catechol at (a) pH 1, (b) pH 7, (c) pH 10.5.

Mössbauer spectra of MMT-substituted catechol

Two substituted catechol compounds with electron-donating substituents, 4-tert-butylcatechol and 4-

methcatechol, and two compounds with electron-withdrawing substituents, 4-nitrocatechol and tetrabromocatechol were reacted with the MMT

sample at pH 10.5. The Mössbauer parameters are listed in Table 2, and the spectra of these samples are shown in Figure 5.

Table 2: The ^{57}Fe Mössbauer parameters at 77 °K of the MMT samples reacted with different substituted catechol at pH 10.5 in an aqueous solution. Data were collected on the dried solids.

Samples	δ mms $^{-1}$	Δ mms $^{-1}$	Γ mms $^{-1}$	Absorption area %	$\text{Fe}^{2+}/\text{Fe}^{3+}$ ratio
MMT-4-tert-butylcatechol	0.42[2]	0.74[2]	0.30[2]	30[3]	2.4[3]
	1.26[1]	3.04[1]	0.20[1]	70[2]	
MMT-4-methylcatechol	0.44[3]	0.76[3]	0.30[3]	29[4]	2.4[3]
	1.23[1]	3.02[1]	0.14[1]	71[3]	
MMT-4-nitrocatechol	0.44[1]	0.67[2]	0.28[2]	46[3]	1.2[2]
	1.26[1]	3.04[1]	0.16[1]	54[3]	
MMT-tetrabromocatechol	0.31[1]	0.82[3]	0.41[2]	78[6]	0.3[1]
	1.47[1]	2.60[2]	0.17[2]	22[3]	

The samples reacted with 4-tert-butylcatechol and 4-methylcatechol showed a clear reduction. While little or no reduction is observed in the sample reacted with 4-nitrocatechol and tetrabromocatechol compounds. The 4-nitro and tetrabromo are withdrawing substituents and tend to withdraw electron density from the catecholic

ring. The electron can be considered to reside on the substituent, leaving the molecule unable to transfer an electron to active sites on MMT. Electron-donating substituents, such as 4-tert-butyl and 4-methyl, facilitate electron transfer from the ring to the clay.

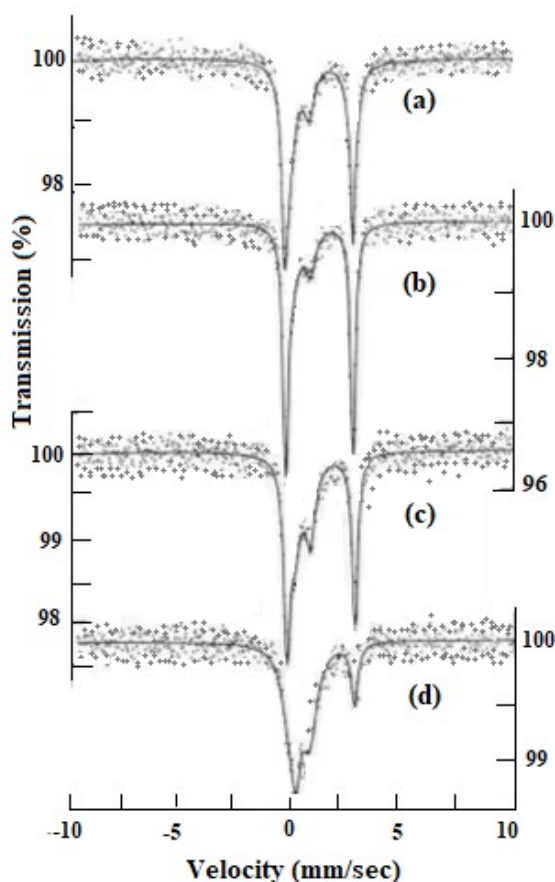


Figure 5: The ^{57}Fe Mössbauer spectra at 77 °K of MMT reacted at pH 10.5 with (a) 4-tert-butylcatechol, (b) 4-methylcatechol, (c) 4-nitrocatechol, (d) tetrabromocatechol.

Mössbauer spectra of the fired MMT-catechol sample

In order to investigate the effect of firing on the powdered catechol-reduced MMT, the sample was subjected to a firing treatment ranging from 100 to

800 °C for a period of 10 minutes under air (Figure 6). As the firing temperature increased, the quadrupole splitting of the Fe^{3+} doublet shows a very small increase which indicates a mild distortion of the lattice. The linewidth of the Fe^{2+} peak became very narrow ($\Gamma = 0.15 \text{ mms}^{-1}$), which indicates a unique type of coordination. Oxidation of the Fe^{2+} ions by firing occurred at higher temperatures than the original MMT sample. The Fe^{2+} doublet disappeared at 300 °C in the original sample, while its appearance continued to 600 °C in the MMT-catechol sample. The amount of Fe^{2+}

increased with increasing the firing temperature from 100-300 °C and then decreasing with firing to a higher temperature as shown in the $\text{Fe}^{2+}/\text{Fe}^{3+}$ ratio in Table 3. Other researchers noticed the reduction enhancement upon firing during the reaction between phenol and MMT (32). They attributed this to an enhancement of radical species induced by dehydration. The transferring of the electrons from the organic compounds to the active site of the Fe^{3+} may be facilitated by firing (Table 3).

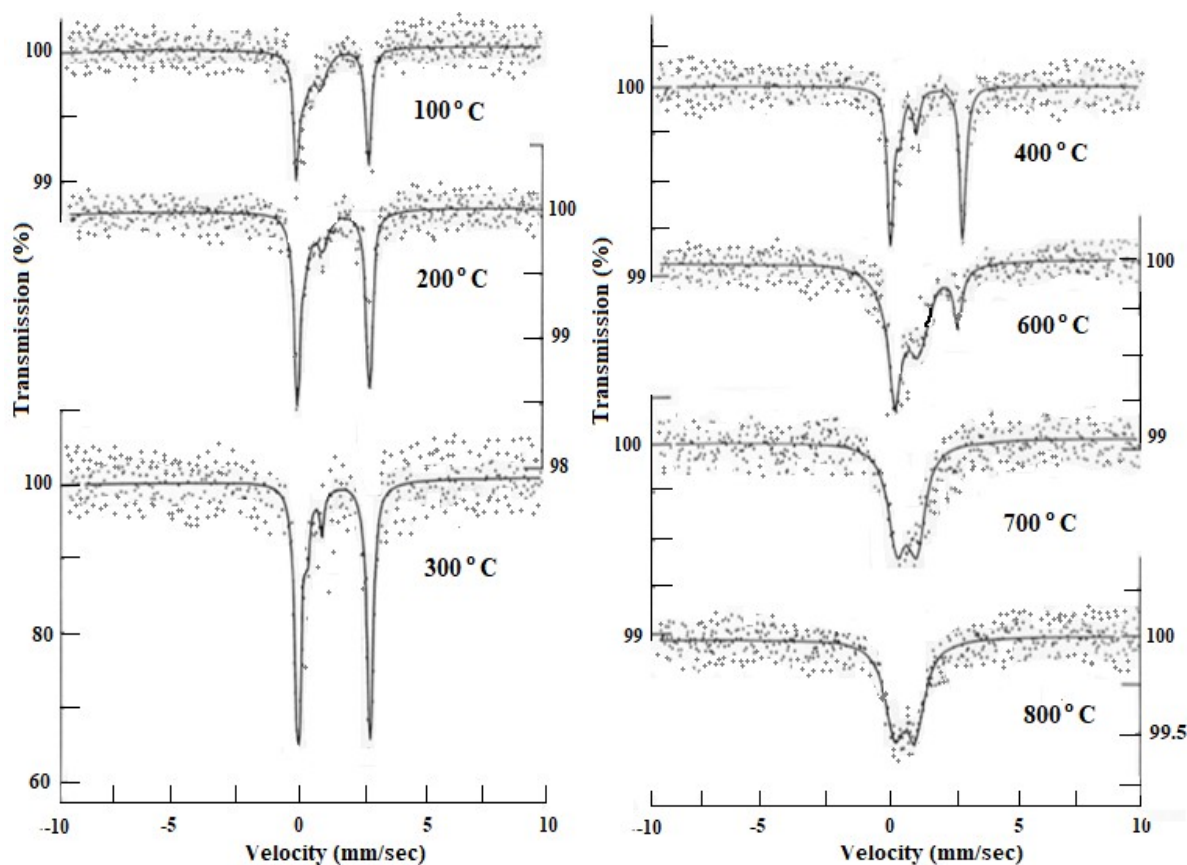


Figure 6: The ^{57}Fe Mössbauer at 77 K of MMT-catechol samples reacted at pH 10.5 and fired in the air at various temperatures for 10 minutes. The temperature of firing is indicated.

Table 3: The ^{57}Fe Mössbauer parameters at 77 K of the fired MMT-catecholic sample.

Temp.	$\delta \text{ mms}^{-1}$	$\Delta \text{ mms}^{-1}$	$\Gamma \text{ mms}^{-1}$	Absorption Area %	$\text{Fe}^{2+}/\text{Fe}^{3+}$ ratio
100 °C	0.43[4] 1.26[1]	0.65[5] 3.06[1]	0.31[5] 0.14[1]	39[8] 61[5]	1.6[4]
200 °C	0.44[3] 1.26[1]	0.73[5] 3.03[1]	0.27[4] 0.16[1]	24[5] 76[4]	3.3[9]
300 °C	0.46[4] 1.27[1]	0.57[6] 3.03[1]	0.12[5] 0.16[1]	11[7] 89[8]	14.3[9]
400 °C	0.48[1] 1.25[1]	0.67[5] 3.02[1]	0.15[4] 0.15[1]	22[8] 78[8]	4.2[1]
600 °C	0.41[3] 1.21[2]	0.96[5] 2.64[4]	0.53[5] 0.20[3]	21[7] 79[9]	4.3[1]
700 °C	0.36[2]	0.80[4]	0.44[4]	100	-
800 °C	0.31[2]	0.47[4]	0.47[4]	100	-

X-Ray Powder Diffraction (XRD)

The basal spacing of the air-dried MMT sample is 13 Å increasing to 17 Å on ethylene glycol treatment. When this sample heated at 120 °C for two hours, it showed partial collapse with a basal spacing of 12.62 Å. The collapse was completed on heating at 375 °C for 1 hour (Figure 7). MMT gives a basal spacing of 9.6 Å when no molecules are between the unit layers. The MMT sample that reacted with the catecholic compounds at pH 10.5 did not show the 13 Å basal spacing of the original sample, possibly due to the presence of sodium ions from the NaOH used to adjust the pH. The sample containing the organics did not show the 17 Å basal spacing on treatment with ethylene glycol again, which suggests that the ligands are present on the MMT crystal edges. These then cause blocking of some of the layers and prevent the complete swelling of ethylene glycol. In addition to this, the XRD pattern peaks obtained are slightly asymmetrical in the air-dried samples, which suggests a mixed-layer sequence (Table 4).

From the results listed in Table 4, there is no evidence for the intercalation of the catecholic compounds into the MMT interlayer. Therefore, an experiment was carried out to open the MMT lattice by dispersing 1 g of the MMT in a 50 mL solution of NaCl in water, as the sodium ions are able to open the interlayer to about 20 Å in water. The sample was allowed to stir for 1 hour, and then 100 mg of catechol was added, and the mixture was stirred for a further 24 hours. Upon examination, the sample showed no indications of

intercalation. The sample gave basal spacing of 12.3, 16.67, 12.45, and 11.78 Å for the air-dried, ethylene glycol treated, 120 °C heated, and 300 °C heated samples, respectively. At low pH, where no sodium ions are present, the basal spacing of the catechol-MMT sample was 13 Å, but the ethylene glycol treated sample did not swell to 17 Å, which provides further evidence for these compounds affecting the interlayer swelling. Figure 8 shows the XRD patterns of the air-dried MMT-catechol samples reacted at pH 1, 7, and 10.5.

Differential Thermal Analysis, DTA

DTA analysis showed that the curves of the original MMT sample subjected to pH's of 1, 7, and 10.5 are similar to the curve of the original sample. The change in pH does not affect the curve. When the MMT was reacted with the organic compounds, only the curves of the sample reacted at pH 10.5 were extensively modified (Figure 9). Catechol has two endothermic peaks at 100 and 200 °C (33), which do not appear on the curve of an MMT sample reacted with catechol, probably due to complexation with MMT. The main alteration in the curves of the sample reacted at pH 10.5 may be due to the formation of metal-ligand complexes adsorbed onto the clay surface since some cations such as iron are solubilized by catechol and expected to be found in the solution at high pH. Such complexes are associated with water molecules, which can be driven off as endothermic peaks before the first endothermic reaction of the MMT occurs.

Table 4: The basal spacing of some MMT-compounds.

Samples	----- d spacing in Å -----			
	Air-dried	EG	Heated at 120 °C 2 h.	Heated at 375 °C 1 h.
MMT	13	17	12.62	9.6
MMT-catechol pH 10.5	12.8	16.67	12.27	10.04
MMT-4-tert-butylcatechol pH 10.5	12.45	16.67	13.3	10.28
MMT-4-methylcatechol pH 10.5	12.27	16.67	12.81	9.71
MMT-4-nitrocatechol pH 10.5	12.27	16.67	13	9.71
MMT-tetrabromocatechol pH 10.5	11.94	16.67	13	9.71

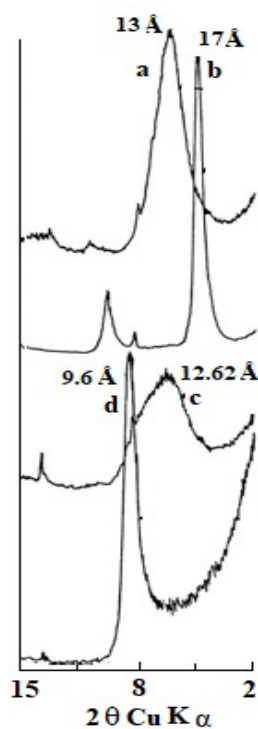


Figure 7: X-ray powder diffraction patterns of MMT (a) untreated sample, (b) treated with EG, (c) heated at 120 °C, (d) 375 °C.

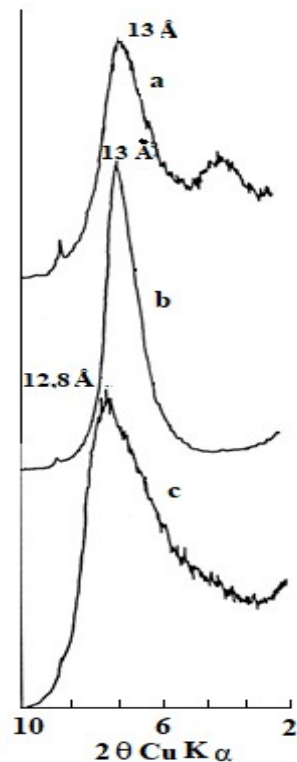


Figure 8: X-ray powder diffraction patterns of MMT-catechol sample reacted at (a) pH 1, (b) pH 7, (c) pH 10.5.

Electron Spin Resonance (ESR)

Silicon, aluminum, magnesium and alkali, and alkaline earth metals are the most abundant ions usually found in clays that are diamagnetic. Paramagnetic ions such as Fe^{3+} may be found substituted for silicon, aluminum, or magnesium. The spectrum of the original sample is characterized by features with g -values of 2.0, 2.2, 3.7, 4.3, and 9.6, similar to the result reported by other workers (34). The ESR features with g -values of 3.7, 4.3, and 9.6 have been assigned to Fe^{3+} in a site of near rhombic symmetry, while the other features arise from Fe^{3+} in a different type of environment (Figure 10).

The sample of catechol-reduced MMT exhibits substantial changes in the main features of the spectra. The 2.2 and 9.6 g -value signals are broader than those found in the untreated sample. The 3.7 g -value signals disappeared from the spectra, and that with a g -value of 4.3 was narrower and less intense than in the untreated sample. The reduction of MMT with catechol caused a reduction in the intensities of the signals, which can be assigned to the structural Fe^{3+} . This result

is in good agreement with the Mössbauer data, which revealed an incomplete reduction of the structural Fe^{3+} . An enhancement in the $g = 2.0$ signal was observed due to the formation of a radical. This signal is similar to those reported by other workers (35) obtained from the reaction of some aromatic molecules with clays. The reaction of the hydroxybenzene compounds with the MMT involves a radical formation in the first stage, which oxidized to a quinone at a later stage. From the ESR results, it appears that part of these compounds remains in the radical (semiquinone) form on the MMT surface. These radicals are responsible for the signal at $g = 2.0$.

Similar behavior in the ESR spectra was observed for the MMT samples reduced by 4-methyl and 4-tert-butylcatechol, which have electron-donating ability (Figure 10). The $g = 2.0$ signal was greatly enhanced in the sample reduced with 4-tert-butylcatechol. However, there were some remnants of the signal at $g = 3.7$. Reaction with the 4-nitro and tetrabromo substituents also showed an enhancement of the signal $g = 2.0$, and the $g = 2.2$ signal became broader.

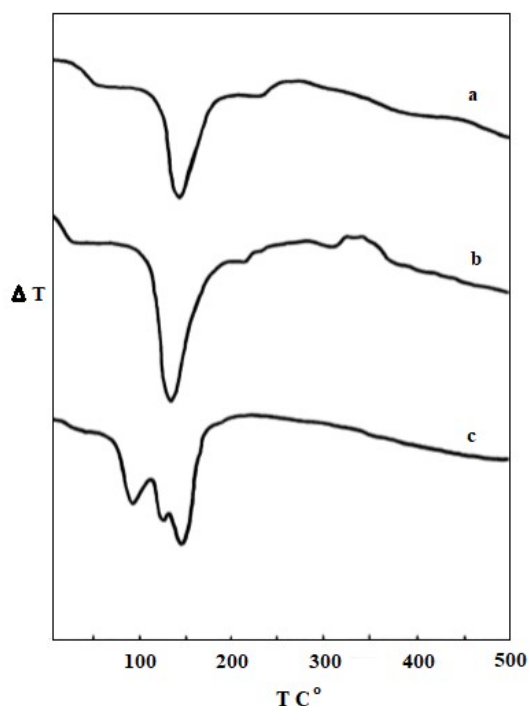


Figure 9: DTA curves of MMT reacted with catechol at (a) pH 1, (b) pH 7, (c) pH 10.5.

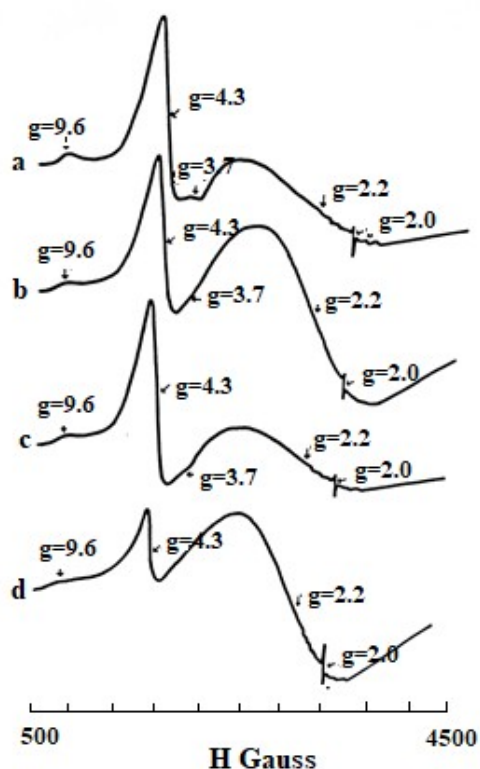


Figure 10: ESR spectra at room temperature of (a) MMT, MMT reacted with catechol at (b) pH 1, (c) pH 7, (d) pH 10.5.

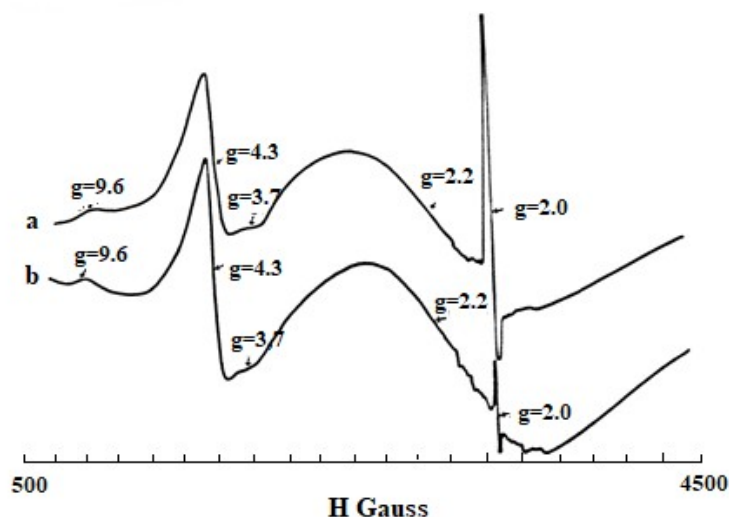


Figure 10: ESR spectra at room temperature of MMT reacted at pH 10.5 with (a) 4-tert-butylcatechol, (b) 4-methylcatechol.

Infra-Red Spectra (IR)

The MMT's main features in the IR region are the Si-O stretching and OH bending. The position of these bands are at 800, 850, 880, 917, and 1040 cm^{-1} and are assigned to $\text{Fe}^{3+}\text{-OH-Fe}^{3+}$, Al-OH-Mg , $\text{Fe}^{3+}\text{-OH-Al}$, Al-OH-Al , and Si-O , respectively (36,37) (Table 5). The IR spectrum also exhibits bands due to the adsorbed compounds on the MMT, but we will discuss only the effect of these compounds on the prominent montmorillonite

bands. The sharpness and position of OH bending modes of the sample reacted with different compounds varies from one compound to another.

The Si-O stretching band at 1040 cm^{-1} and the $\text{Fe}^{3+}\text{-OH-Al}$ band at 880 cm^{-1} disappeared in most of the samples. The disappearance of the latter band is noticeable in the reduced samples. This band disappeared in MMT and nontronite samples reduced with hydrazine and dithionite, and its

disappearance was attributed to the protonation of the adjacent OH group (30). The band at 800 cm^{-1} in the catechol reduced MMT sample, which is assigned to $\text{Fe}^{3+}\text{-OH-Fe}^{3+}$ bending, is shifted to 790 cm^{-1} . This shift has also been found in some other samples. The band at 850 cm^{-1} , which is assigned to Al-OH-Mg bending, is shifted to 838 cm^{-1} . Both bands are enhanced upon reduction with catechol. The 880 cm^{-1} band disappeared from the catechol reduced sample and also from the substituted catechol reduced samples, 4-methyl and 4-tert-butyl catechol.

Total Surface Area Determination

The total surface area is a fundamental property of clays. It can be determined by the retention of ethylene glycol (EG). MMT clay can take two layers of EG molecules between the interlayer spacing. The resultant areas were calculated using Dyal and Hendricks (38) value of $810\text{ m}^2/\text{g}$ for the total surface area of MMT. The original MMT sample gave a value of $839\text{ m}^2/\text{g}$ (Table 6). This value was decreased by about $100\text{ m}^2/\text{g}$ in the sample reacted with the compounds at pH 10.5, which is attributed to the presence of these compounds on the crystal edges of MMT causes blocking of some

layers, preventing complete swelling. No apparent decrease in the values was found in the sample reacted at pH 1 and 7. The possibility of the presence of the organic compounds on the crystal edges at pH 10.5 seems greater than at pH 1 and 7. This may be due to the formation of complexes of these compounds and cations that are liberated at high pH. These complexes increase the possibility of blocking the layers.

CONCLUSIONS

Catecholic compounds containing electron-donating substituents have the ability to reduce the structural iron of MMT at high pH. The process depends on the pH, ring substituents and conjugation. No reduction occurs if the catecholic ring has electron-withdrawing substituents. The process involves electron transfer from the hydroxy groups on the compounds to the active site at the iron atoms within the MMT lattice. The reduction process can be enhanced by heating the powdered sample up to $300\text{ }^\circ\text{C}$. The $\text{Fe}^{2+}/\text{Fe}^{3+}$ ratio increases due to the increase in the proportion of radical formation induced by dehydration.

Table 5: Selected features of the infra-red spectra (cm^{-1}) of the MMT sample reacted with the catecholic compounds.

Sample	pH	Si-O	Al-OH-Al	$\text{Fe}^{3+}\text{-OH-Al}$	Al-OH-Mg	$\text{Fe}^{3+}\text{-OH-Fe}^{3+}$
MMT	-	1050 sh	917 w	880 w	850 m	800 s
MMT-catechol	10.5	-	915 sh	-	838 s	790 s
MMT-4-nitrocatechol	=	-	915 w	890 sh	848 m	800 m
MMT-tetrabromocatechol	=	1015 sh	918 w	885 sh	835 m	795 s
MMT-4-methylcatechol	=	-	915 m	-	845 m	800 m
MMT-4-tert-butylcatechol	=	-	913 s	-	840 m	795 s

Table 6: The total surface areas of the samples.

Samples	pH	Total surface area in m^2/g
MMT	-	839
MMT-catechol	10.5	710
MMT-4-methylcatechol	10.5	629
MMT-4-tert-butylcatechol	10.5	634
MMT-4-nitrocatechol	10.5	641
MMT-tetrabromocatechol	10.5	622

REFERENCES

1. Ziemiański P, Kałahurska K, Samojedan B. Selective catalytic reduction of NO with NH_3 on mixed alumina-iron (III) oxide pillared

montmorillonite "Cheto" Arizona, modified with hexamminecobalt (III) chloride. Adsorption Science & Technology. 2017 Dec;35(9-10):825-33. [<DOI>](#).

2. Pentráková L, Su K, Pentrák M, Stucki JW. A review of microbial redox interactions with structural Fe in clay minerals. *Clay miner.* 2013 Jun;48(3):543–60. [<DOI>](#).
3. Luan F, Liu Y, Griffin AM, Gorski CA, Burgos WD. Iron(III)-Bearing Clay Minerals Enhance Bioreduction of Nitrobenzene by *Shewanella putrefaciens* CN32. *Environ Sci Technol.* 2015 Feb 3;49(3):1418–26. [<DOI>](#).
4. Lee K, Kostka JE, Stucki JW. Comparisons of structural Fe reduction in smectites by bacteria and dithionite: an infrared spectroscopic study. *Clays Clay Miner.* 2006 Apr 1;54(2):195–208. [<DOI>](#).
5. Perdrial JN, Warr LN, Perdrial N, Lett M-C, Elsass F. Interaction between smectite and bacteria: Implications for bentonite as backfill material in the disposal of nuclear waste. *Chemical Geology.* 2009 Jun;264(1–4):281–94. [<DOI>](#).
6. Stucki JW, Kostka JE. Microbial reduction of iron in smectite. *Comptes Rendus Geoscience.* 2006 Jun;338(6–7):468–75. [<DOI>](#).
7. Pentráková L, Su K, Pentrák M, Stucki JW. A review of microbial redox interactions with structural Fe in clay minerals. *Clay miner.* 2013 Jun;48(3):543–60. [<DOI>](#).
8. Wang X, Dong H, Zeng Q, Xia Q, Zhang L, Zhou Z. Reduced Iron-Containing Clay Minerals as Antibacterial Agents. *Environ Sci Technol.* 2017 Jul 5;51(13):7639–47. [<DOI>](#).
9. Liu D, Dong H, Bishop ME, Zhang J, Wang H, Xie S, et al. Microbial reduction of structural iron in interstratified illite-smectite minerals by a sulfate-reducing bacterium: Bioreduction of structural iron in clay minerals by a SRB. *Geobiology.* 2012 Mar;10(2):150–62. [<DOI>](#).
10. Liu G, Qiu S, Liu B, Pu Y, Gao Z, Wang J, et al. Microbial reduction of Fe(III)-bearing clay minerals in the presence of humic acids. *Sci Rep.* 2017 Jun;7(1):45354. [<DOI>](#).
11. Wu H, Song Z, Lv M, Zhao D, He G. Iron-Pillared Montmorillonite As An Inexpensive Catalyst For 2-Nitrophenol Reduction. *Clays Clay Miner.* 2018 Oct;66(5):415–25. [<DOI>](#).
12. Hofstetter TB, Neumann A, Schwarzenbach RP. Reduction of Nitroaromatic Compounds by Fe(II) Species Associated with Iron-Rich Smectites. *Environ Sci Technol.* 2006 Jan 1;40(1):235–42. [<DOI>](#).
13. Sugiura Y, Tomura T, Ishidera T, Doi R, Francisco PCM, Shiwaku H, et al. Sorption behavior of selenide on montmorillonite. *J Radioanal Nucl Chem.* 2020 May;324(2):615–22. [<DOI>](#).
14. Latta DE, Neumann A, Premaratne WAPJ, Scherer MM. Fe(II)–Fe(III) Electron Transfer in a Clay Mineral with Low Fe Content. *ACS Earth Space Chem.* 2017 Jun 15;1(4):197–208. [<DOI>](#).
15. Zeng Q, Dong H, Wang X. Effect of ligands on the production of oxidants from oxygenation of reduced Fe-bearing clay mineral nontronite. *Geochimica et Cosmochimica Acta.* 2019 Apr;251:136–56. [<DOI>](#).
16. Notini L, Latta DE, Neumann A, Pearce CI, Sassi M, N'Diaye AT, et al. A Closer Look at Fe(II) Passivation of Goethite. *ACS Earth Space Chem.* 2019 Dec 19;3(12):2717–25. [<DOI>](#).
17. Notini L, Latta DE, Neumann A, Pearce CI, Sassi M, N'Diaye AT, et al. The Role of Defects in Fe(II)–Goethite Electron Transfer. *Environ Sci Technol.* 2018 Mar 6;52(5):2751–9. [<DOI>](#).
18. Joe-Wong C, Brown GE, Maher K. Kinetics and Products of Chromium(VI) Reduction by Iron(II/III)-Bearing Clay Minerals. *Environ Sci Technol.* 2017 Sep 5;51(17):9817–25. [<DOI>](#).
19. Liu X, Dong H, Zeng Q, Yang X, Zhang D. Synergistic Effects of Reduced Nontronite and Organic Ligands on Cr(VI) Reduction. *Environ Sci Technol.* 2019 Dec 3;53(23):13732–41. [<DOI>](#).
20. Liao W, Ye Z, Yuan S, Cai Q, Tong M, Qian A, et al. Effect of Coexisting Fe(III) (oxyhydr)oxides on Cr(VI) Reduction by Fe(II)-Bearing Clay Minerals. *Environ Sci Technol.* 2019 Dec 3;53(23):13767–75. [<DOI>](#).
21. Joe-Wong C, Weaver KL, Brown ST, Maher K. Chromium isotope fractionation during reduction of Chromium(VI) by Iron(II/III)-bearing clay minerals. *Geochimica et Cosmochimica Acta.* 2021 Jan;292:235–53. [<DOI>](#).
22. Carriazo J, Guérou E, Barrault J, Tatibouët JM, Molina R, Moreno S. Catalytic wet peroxide oxidation of phenol by pillared clays containing Al–Ce–Fe. *Water Research.* 2005 Oct;39(16):3891–9. [<DOI>](#).
23. Cheng J, Ming Yu S, Zuo P. Horseradish peroxidase immobilized on aluminum-pillared interlayered clay for the catalytic oxidation of phenolic wastewater. *Water Research.* 2006 Jan;40(2):283–90. [<DOI>](#).
24. Ko CH, Fan C, Chiang PN, Wang MK, Lin KC. p-Nitrophenol, phenol and aniline sorption by organo-clays. *Journal of Hazardous Materials.* 2007 Oct;149(2):275–82. [<DOI>](#).

25. Shakir K, Ghoneimy HF, Elkafrawy AF, Beheir ShG, Refaat M. Removal of catechol from aqueous solutions by adsorption onto organophilic-bentonite. *Journal of Hazardous Materials*. 2008 Feb;150(3):765–73. [<DOI>](#).
26. Liu Y, Gao M, Gu Z, Luo Z, Ye Y, Lu L. Comparison between the removal of phenol and catechol by modified montmorillonite with two novel hydroxyl-containing Gemini surfactants. *Journal of Hazardous Materials*. 2014 Feb;267:71–80. [<DOI>](#).
27. Hassen JH. Montmorillonite Nanoclay Interaction with 2-Aminophenol and 2-Nitrophenol. *Rese Jour of Pharm and Technol*. 2019;12(6):2828. [<DOI>](#).
28. Eltantawy IM, Arnold PW. Reappraisal Of Ethylene Glycol Mono-Ethyl Ether (Egme) Method For Surface Area Estimations Of Clays. *Journal of Soil Science*. 1973 Jun;24(2):232–8. [<DOI>](#).
29. Solomon DH, Loft BC, Swift JD. Reactions catalysed by minerals. IV. The mechanism of the benzidine blue reaction on silicate minerals. *Clay miner*. 1968 Dec;7(4):389–97.
30. Rozenson I. Reduction and Oxidation of Fe³⁺ in Dioctahedral Smectites—1: Reduction with Hydrazine and Dithionite. *Clays and Clay Minerals*. 1976;24(6):271–82. [<DOI>](#).
31. Sofen SR, Ware DC, Cooper SR, Raymond KN. Structural, electrochemical, and magnetic properties of a four-membered redox series ([Cr(L3)]_n-, n = 0-3) in catechol-benzoquinone complexes of chromium. *Inorg Chem*. 1979 Feb 1;18(2):234–9. [<DOI>](#).
32. Isaacson PJ, Sawhney BL. Sorption and transformation of phenols on clay surfaces: effect of exchangeable cations. *Clay miner*. 1983 Sep;18(3):253–65. [<DOI>](#).
33. Greene-Kelly R. The Montmorillonite Minerals (Smectites). In: Mackenzie R, editor. *The Differential Thermal Investigation of Clay*. London: Mineralogical Society; 1957. p. 140–64.
34. Goodman BA. An investigation by Mössbauer and EPR spectroscopy of the possible presence of iron-rich impurity phases in some montmorillonites. *Clay miner*. 1978 Sep;13(3):351–6. [<DOI>](#).
35. Pinnavaia TJ, Hall PL, Cady SS, Mortland MM. Aromatic radical cation formation on the intracrystal surfaces of transition metal layer lattice silicates. *J Phys Chem*. 1974 May;78(10):994–9. [<DOI>](#).
36. Rozenson I. Reduction and Oxidation of Fe³⁺ in Dioctahedral Smectites—III.* Oxidation of Octahedral Iron in Montmorillonite. *Clays and Clay Minerals*. 1978;26(2):88–92. [<DOI>](#).
37. Holtzer M, Bobrowski A, Grabowska B. Montmorillonite: a comparison of methods for its determination in foundry bentonites. *Metalurgija*. 2011;50(2):119–22.
38. Dyal RS, Hendricks SB. Total surface of clays in polar liquids as a characteristic index: soil science. 1950 Jun;69(6):503–9. [<DOI>](#).



Experimental and DFT Computational Insights on the Adsorption of Selected Pharmaceuticals of Emerging Concern from Water Systems onto Magnetically Modified Biochar

Umar Yunusa^{1*}  , Umaru Umar¹ , Sulaiman Adamu Idris² , Abdulrahman Ibrahim Kubo³ 
and Tahir Abdullahi⁴ 

¹ Department of Pure and Industrial Chemistry, Bayero University, Kano-Nigeria

² Department of Science Laboratory Technology, Federal Polytechnic Offa, Kwara-Nigeria

³ Department of Pure and Applied Chemistry, Adamawa State University, Mubi-Nigeria

⁴ Department of Physics, Yobe State University, Damaturu-Nigeria

Abstract: This work aimed to fabricate a magnetically modified biochar (MBC) through a one-step pyrolysis of *Vitex doniana* nut at 500 °C and investigate its feasibility for the removal of two pharmaceuticals, namely, amoxicillin (AMX) and trimethoprim (TMT) from aqueous environment. The textural characteristics, chemical composition and magnetic properties of the MBC were analyzed using Brunauer-Emmett-Teller (BET) analysis, scanning electron microscopy (SEM), Fourier Transform Infrared (FTIR) spectroscopy, X-ray diffraction (XRD) and vibrating sample magnetometer (VSM). The results demonstrated the successful incorporation of the magnetic particles in the biochar matrix. The specific surface area and average pore volume of the MBC were obtained as 108.90 m²/g and 2.98 cm³/g, respectively. The adsorption process was observed to be strongly pH-dependent, and equilibrium was attained within 1 h. The kinetic data favors pseudo-second-order model ($R^2 > 0.999$), implying that the most plausible mechanism for the adsorption was chemisorption. The isothermal data was best fitted by the Langmuir model ($R^2 > 0.985$), signifying that the process was mainly monolayer adsorption on homogeneous surface. The maximum adsorption capacity achieved for AMX and TMT was 41.87 and 55.83 mg/g at 303 K, respectively. The thermodynamic examination highlighted that the adsorption was feasible and accompanied with absorption of heat and increase of entropy for both the adsorbates. Furthermore, the MBC exhibited a good recycling capability such that the adsorption capacity decreases by ~ 25% after reuse for six cycles. Besides, the theoretical results based on density functional theory (DFT) calculations demonstrated that the TMT molecules ($\Delta E = 3.762$ eV) are more reactive compared to the AMX molecules ($\Delta E = 3.855$ eV) which correlates with the experimental observations.

Keywords: Adsorption, pharmaceuticals, *Vitex doniana*, magnetic biochar, DFT calculations.

Submitted: March 20, 2021. **Accepted:** October 25, 2021.

Cite this: Yunusa U, Umar U, Idris S, Kubo A, Abdullahi T. Experimental and DFT Computational Insights on the Adsorption of Selected Pharmaceuticals of Emerging Concern from Water Systems onto Magnetically Modified Biochar. JOTCSA. 2021;8(4):1179–96.

DOI: <https://doi.org/10.18596/jotcsa.900197>.

***Corresponding author. E-mail:** umaryunusa93@gmail.com.

INTRODUCTION

Over the last few decades, many classes of micro-pollutants including pharmaceuticals, steroid hormones, pesticides, endocrine disrupting compounds, and personal care products have been detected in various freshwater resources worldwide. Among them, pharmaceuticals have emerged as one of the major concerns of public health authorities (1,2). The drug industries, hospitals, and households are the main sources of pharmaceutical contaminants in water systems (3). Most compounds of pharmaceutical origins are persistent, non-biodegradable and often not appreciably eliminated due to their ability to pass through the treatment processes largely undisturbed (4). Therefore, their residues are rampant in surface water, partially treated water and groundwater, typically at trace quantities from ng/L to µg/L. Long-term exposure to pharmaceuticals may pose a deleterious risk to humans and has been established to have significant disruptive impacts in aquatic ecosystems (5). To date, the treatment of pharmaceuticals has been a daunting task due to their complex physicochemical properties.

Numerous decontamination technologies have been employed to eliminate pharmaceutically active compounds from aqueous medium including coagulation, biological treatment, adsorption, filtration, and advanced oxidation processes. However, the efficiencies of these traditional processes such as filtration, coagulation and biodegradation were insufficient. In contrast, advanced oxidation processes are also not easily applicable in industrial scale owing to expensiveness of energy and the generation of undesired byproducts. In this regard, adsorption appears to be favorite alternative due to its effectiveness, low-cost of operation and complete elimination of the pharmaceutical without causing any secondary pollution (6).

The use of carbon-based materials is the most prominent method for removal of organic contaminants from water streams. Biochar is a carbon-rich material produced mainly from the carbonization of biomass feedstock in an oxygen-depleted medium. The preparation of biochar does not require the activation process and uses less energy (7). Although biochar in their ordinary forms have been employed as solid adsorbents, they suffer from limitations such as small particle size, poor adsorption performance, and ability of separation from bulk solution (8). Therefore, it is imperative to modify biochars in order to enhance their adsorption efficiency towards pollutants. Recently, magnetic modification has seen tremendous interest as a remedy to overcome these shortcomings. Magnetic

response is attained through functionalization of biochar surface with magnetic particles such as magnetite and maghemite (9). High adsorption performance, easy to separate from water, reuse potential, and natural abundance of precursors are the main attributes which promote magnetic biochar as a promising adsorbent for the removal of various pollutants.

Vitex doniana (VD), also known as black plum, is one of the most abundant trees present in tropical Africa. The plant has emerged as a priority species because of the multiplicity of its uses. For instance, the plant is extensively used for food, source of timber and for medical purposes (10). The *Vitex doniana* nut is the major waste generated from processing of this plant and most are discarded on the fields. Few studies have reported the use of this plant's leaves and nut as adsorbents for the elimination of toxic metals (11,12). Nevertheless, to the best of our knowledge, no work has been reported so far on the preparation of biochar from *Vitex doniana* nut and its application for the removal of medicinal drugs from water.

In this regard, two pharmaceuticals, amoxicillin (AMX) and trimethoprim (TMT) were chosen as the model pollutants for this study. The selection of these two antibiotics was based on the frequency of occurrence in freshwater resources. Moreover, information on their removal from aquatic environment is relatively scarce. TMT is among the most prominent antibiotics employed in veterinary and human medicine worldwide acting as an inhibitor in the chemotherapy treatment (13). AMX belongs to a class of drugs that are majorly excreted in a non-metabolized form, and some reports have highlighted that AMX might pose an acute risk to the aquatic ecosystem (14,15).

With this background, the overall objective of this research is to investigate the adsorption of amoxicillin and trimethoprim molecules on the surface of magnetically modified biochar derived from *Vitex doniana* nut wastes. To achieve this objective, the influence of experimental factors such as pH, ionic strength, temperature, initial concentration, and contact time on the adsorption capacity of the adsorbent was studied. Additionally, the removal process was assessed isothermally, thermodynamically, and kinetically in order to gain insight about the mechanism and spontaneity of adsorption. Finally, density functional theory (DFT) computations were performed to obtain qualitative insights on the chemical reactivity of amoxicillin and trimethoprim molecules.

EXPERIMENT AND COMPUTATION

Chemicals and Materials

Amoxicillin and Trimethoprim were obtained from Sigma-Aldrich (USA). Their physicochemical properties are depicted in Table 1. Ferric chloride ($\text{FeCl}_3 \cdot 6\text{H}_2\text{O}$), sodium nitrate (NaNO_3) and other chemicals used were AnalaR grade sourced from Fisher Chemicals (USA). *Vitex doniana* nut was acquired from Kano State, Nigeria. Demineralized water was employed during the entire adsorption tests.

Preparation of Magnetically Modified Biochar

Vitex doniana nuts were cut into small pieces, washed, and then subsequently dried at 110 °C for 48 h. The dried nut was pulverized and sieved into desirable particle sizes (≤ 1 mm) and subsequently heated in a muffle furnace from room temperature to 500 °C for 3 h. The process of pyrolysis was performed at a heating rate of 10 °C/min and under an oxygen-depleted condition. After pyrolysis, the resulting biochar was collected from the furnace after being cooled to room temperature. Then 10 g of the obtained biochar was immersed into a mixed solution containing 4 g of $\text{FeCl}_2 \cdot 2\text{H}_2\text{O}$ and 8 g $\text{FeCl}_3 \cdot 6\text{H}_2\text{O}$ in 50 mL of demineralized water. The obtained mixture was homogenized by vigorous stirring for 10 h at 90 °C. The precipitation of iron oxide particles on the biochar was achieved by the addition of drops of 10 mL NH_4OH solution into the mixture with the aid of rapid stirring for 30 min at 90 °C. After that, the stable suspension was cooled to room temperature. Finally, the produced magnetically modified biochar (MBC) was retrieved from the mixture using external magnet. The MBC was washed repeatedly with demineralized water to attain pH 7.0, and then dried in oven at 50 °C for 24 h.

Determination of Characteristics of the Magnetic Biochar

Surface functional group characteristics of the MBC was elucidated using FTIR spectrometer (Cary 630; Agilent Technologies) in the 4000-650 cm^{-1} wave number range under a resolution of 8 cm^{-1} , while the crystallographic structure was analyzed using XRD (Rigaku Ultima IV) with a Cu K α radiation in the 2θ range of 5-85°. The surface texture of the MBC was examined by means of electron microscopy utilizing a scanning electron microscope (JEOL-JSM6480). The BET surface area was measured using a specific surface area and pore size analyzer (BET, Builder, SSA-4300). Magnetic properties of MBC was assessed at 298 K using a vibrating sample magnetometer (VSM, EV9) with a maximum applied magnetic field of 15 kOe. The influence of varying pHs over the surface charge was probed via determination of the point of zero charge, pH_{pzc} . The pH_{pzc} is the pH value in which

MBC surface presents a net electrical neutrality. A pH_{pzc} of 6.9 was obtained following a salt addition method described in the literature (16). More precisely, 0.2 g of MBC sample was added to 40 mL of 0.1 M NaNO_3 solution in a centrifuge tube. The medium pH was adjusted to a value between 2 and 11 by addition of dilute HCl or NaOH solutions. All solutions were stirred continuously for 24 h and the final pH was recorded. A graph between the changes in pH (ΔpH) was plotted against the initial pH and the intersection point was taken as pH_{pzc} .

Experimental Protocol of Pharmaceuticals' Adsorption

A known mass of MBC (0.1 g) was mixed with 100 mL of aqueous pharmaceutical solution of known concentrations in series of 250 mL Erlenmeyer flasks placed on thermostatically controlled incubator shaker. The mixture was agitated at 150 rpm for pre-decided residence times. 0.1 M NaOH or 0.1 M HCl solutions were used as pH adjusters to desired value. After the adsorption process, the spent adsorbent was retrieved by an external magnet, and about 3 mL of the solution was transferred to the cuvette and analyzed by the procedure highlighted in subsequent section. Each experiment was run at least in triplicate and the mean values were adopted in the report. Relative standard deviation is not reported as it is negligible (<2%).

The effect of pH on the AMX and TMT uptake was evaluated with initial solution pH varying from 2 to 10. The tests for effect of ionic strength were implemented at varying NaCl concentrations (0.05 to 0.15 mol/L). The influence of contact time (kinetic study) was assessed from 5 min up to 120 min. Equilibrium experiments (isotherm study) were carried out at initial concentrations ranging from 20 to 100 mg/L. The impact of temperature (thermodynamic study) on the adsorption process was evaluated from 303 to 333 K.

Regeneration and Reuse

The MBC was cleaned after adsorption of AMX and TMT using demineralized water and acetone. Briefly, 0.1 g of MBC was placed into 50 mL of acetone. The mixture was agitated in an incubator shaker maintained at 150 rpm under room temperature (30 ± 1 °C) for 12 h. Afterward, the regenerated adsorbent was washed with demineralized water and dried at 90 °C. The adsorbent was used to assess the adsorption capacities up to six cycles.

Quantification of Amoxicillin and Trimethoprim in Aqueous Solution

The quantitative determination of AMX and TMT was accomplished by UV-visible spectrophotometry. The absorbance of the pharmaceutical solutions was

recorded by UV-visible spectrophotometer (Lambda 35; Perkin Elmer) at a characteristic wavelength of 228 nm for AMX and 275 nm for TMT. Calibration curves were established using solutions of each pharmaceutical in demineralized water in a range of 1-10 mg/L. The calibration curves for both the adsorbates exhibited an excellent linearity ($R^2 > 0.99$).

The adsorption performance of the MBC was assessed through the parameter q , (mg of pharmaceuticals adsorbed per gram of MBC), as expressed in Equation 1:

$$q = \frac{C_0 - C_f}{m} \times V \quad (1)$$

where C_0 stands for initial pharmaceutical concentration (mg/L), C_f represent the pharmaceutical concentration at any time given (mg/L), V reflects the volume of the experimental solution in liters, and m denotes the weight of the MBC used in grams.

Adsorption Modelling

The kinetics of the adsorption of the pharmaceuticals onto the MBC was assessed by conducting the time-dependent studies. Many kinetics models, viz., pseudo-first-order (PFO), pseudo-second-order (PSO) and intraparticle diffusion (IPD) models were employed to interpret the experimental data. The PFO, PSO and IPD models in their linear form are represented by Eqs. 2, 3, and 4, respectively:

$$\log(q_e - q_t) = \log q_e - k_1 t \quad (2)$$

$$t/q_t = 1/(k_2 q_e^2) + t/q_e \quad (3)$$

$$q_t = k_{id} t^{(1/2)} + C \quad (4)$$

where q_e and q_t represent the adsorption capacity of the MBC at the equilibrium state and at time of t , respectively; k_1 (min^{-1}), k_2 (g/mg min) and k_{id} denote the moduli of PFO, PSO and IPD adsorption, respectively.

The equilibrium data were adjusted to the Langmuir and Freundlich models. The linear expressions of these models are illustrated by Equations 5 and 6, respectively:

$$C_e/q_e = 1/(K_L q_{max}) + C_e/q_{max} \quad (5)$$

$$\ln q_e = \ln [K_F] + \ln(1)/n \ln C_e \quad (6)$$

where C_e (mg/L) is the equilibrium concentration of pharmaceuticals, q_e (mg/g) is the amount of

pharmaceuticals adsorbed per gram of MBC under equilibrium, q_{max} (mg/g) is the theoretical monolayer adsorption capacity of MBC for pharmaceuticals, and K_L (L/mg) is a constant pointing the affinity in the Langmuir adsorption process; K_F is the Freundlich empirical constant representing the relative adsorption capacity of the MBC, and n (dimensionless) is a constant illustrative of the intensity of the Freundlich adsorption.

Validity of Models

The capability of the studied kinetic models in fitting the experimental data and the suitability of the investigated isotherms in describing the behavior of the adsorptive system was validated through coefficient of determination (R^2), chi square (χ^2) and sum squares of errors (SSE, %). These error functions can be represented by Eqs. 7-9, respectively (17):

$$R^2 = 1 - \frac{(\sum (q_{(e,exp)} - q_{(e,model)})^2)}{(\sum (q_{(e,exp)} - q_{(e,mean)})^2)} \quad (7)$$

$$\chi^2 = \sum \frac{(q_{(e,exp)} - q_{(e,model)})^2}{q_{(e,model)}} \quad (8)$$

$$SSE (\%) = \frac{\sqrt{(\sum (q_{(e,exp)} - q_{(e,model)})^2)}}{N} \quad (9)$$

where $q_{e,model}$ and $q_{e,exp}$ (mg/g) represent the model predicted and experimental uptake capacity, respectively; $q_{e,mean}$ denotes the mean of the $q_{e,exp}$ values; and N is the number of data points. The best fitting model exhibits the highest value of R^2 , but the lowest value of SSE and χ^2 .

Computational Methods

The molecular structures of the pharmaceuticals were designed using ChemDraw Ultra 7.0 software. Then the structures were imported for DFT calculations using the Materials Studio 8.0 software package (BIOVIA, Accelrys). The optimization of the full molecular geometry of AMX and TMT was implemented using DMol³ module at the level B3LYP/DND. No symmetry constraints were imposed during the geometrical optimization of the tested molecules. The quantum chemical parameters were estimated from energies associated with frontier molecular orbitals [the highest occupied molecular orbital (HOMO; E_H), lowest unoccupied molecular orbital (LUMO; E_L), and an energy gap ($\Delta E = E_H - E_L$), electron affinity ($A = -E_L$), and ionization potential ($I = -E_H$)]. The global reactivity indexes namely, chemical potential (μ), chemical hardness (η), chemical softness (σ) electronegativity (χ) and global electrophilicity power (ω), were approximated

in terms of Frontier orbital energies as expressed by Equations 10-14, respectively (18):

$$\mu = \frac{(E_H + E_L)}{2} \quad (10)$$

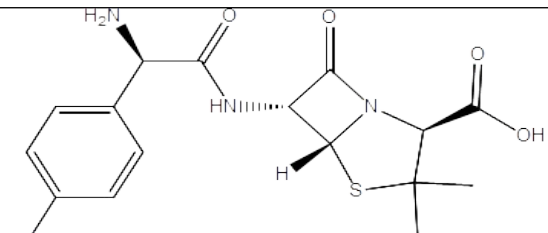
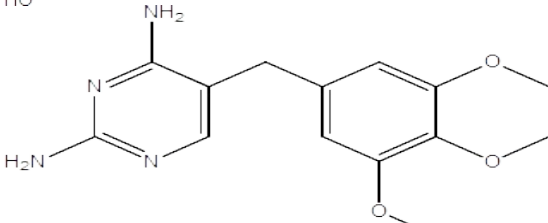
$$\eta = \frac{(E_L - E_H)}{2} \quad (11)$$

$$\sigma = \frac{1}{\dot{\eta}} \quad (12)$$

$$\chi = \frac{(I + A)}{2} \quad (13)$$

$$\omega = \frac{\mu^2}{2\dot{\eta}} \quad (14)$$

Table 1: Target pharmaceuticals and their characteristics.

Pharmaceutical	Molecular Structure	MW (g/mol)	pKa
Amoxicillin		365.4	3.2 (carboxyl) 11.7 (amine)
Trimethoprim		290.3	7.1

RESULTS AND DISCUSSION

Characterizations

SEM micrographs clearly depicting the morphological characteristics of the native and modified biochar are presented in Figure 1. As can be seen in Figure 1a, the micrograph revealed the rough and heterogeneous nature of the biochar surface. After magnetic modification, the SEM micrograph depicts a relatively porous flower-like structure on the surface, demonstrating that the surface structure of MBC is different from those of native biochar, presumably due to the presence of Fe particles (Figure 1b). This indicates that the modification of the biochar enhances the porosity of the material, and thus can facilitate the penetration and binding of the pharmaceuticals.

The Brunauer–Emmett–Teller (BET) analysis was performed to determine the specific surface area and pore size of the adsorbent. The results showed that the magnetic modification of the biochar led to an increase in specific surface area from 96.31 m²/g for the native biochar to 108.90 m²/g for the MBC. This signifies that the MBC has a remarkable potential to adsorb the target adsorbates. Meanwhile, the average

pore volume (VP), and pore diameter were found to be 0.55 cm³/g and 1.17 nm, respectively, for biochar and 2.98 cm³/g and 0.76 nm, respectively, for MBC. The change in the textural properties may be ascribed to the decoration of biochar with magnetic particles.

The XRD profile of MBC (Figure 2) revealed the diffraction peaks at 2θ = 30.7° (220), 35.6° (311), 43.5° (400), 57.3° (511) and 62.9° (440), which was associated with the standard XRD data of γ-Fe₂O₃ and Fe₃O₄ spinel structure (19,20). The sharp diffraction peaks suggest that the as-synthesized iron oxides were incorporated into the biochar matrix (21). The difference between the two magnetic iron oxides is not feasible by XRD since their diffraction peaks are very similar. But, it is safe to state that γ-Fe₂O₃ and Fe₃O₄ are the major crystalline components present in MBC.

The surface functional groups of MBC that might participate in pharmaceuticals adsorption are elucidated by FTIR analysis (Figure 3). An obvious band centered at around 3409 cm⁻¹ was ascribed to the O–H and –NH₂ stretching vibration (22). The peak at around 1628 cm⁻¹ was attributed to C=C stretching vibrations of aromatic ring. The bands observed in the

range of 1000-1200 cm^{-1} may be assigned to stretching vibration of C-O- (ether or alcohol) and -N-H, signifying the presence of diverse functional groups (23). Lastly, a weak peak at 579 cm^{-1} can be assigned to Fe-O bonds vibrations compatible with the presence of $\gamma\text{-Fe}_2\text{O}_3$ and Fe_3O_4 (20). The aforementioned result further affirmed that iron oxide was successfully incorporated into the biochar matrix. Characteristics of infrared spectra of blank MBC and adsorbate-loaded MBC are also contrasted in Figure 3. Some slight changes in peak positions were observed after adsorption which signify the interactions between the pharmaceuticals and MBC's surface functional groups.

The magnetic properties of the adsorbent was recorded at the magnetic fields of $-15000 \leq H \leq 15000$ Oe at 298K. As presented in Figure 4, the MBC displayed appreciable saturation magnetization (M_s) value of 7.70 emu/g. This was attributed to the presence of iron oxides particles on the biochar surface. The $\text{Fe}_3\text{O}_4/\gamma\text{-Fe}_2\text{O}_3$ particles loaded on the adsorbent surface exhibit magnetic properties, which in turn render the biochar magnetically active (24). Moreover, the magnetization curve suggested that the adsorbent was ferromagnetic, attesting the potential for easy retrievability and reusability through magnetic recovery.

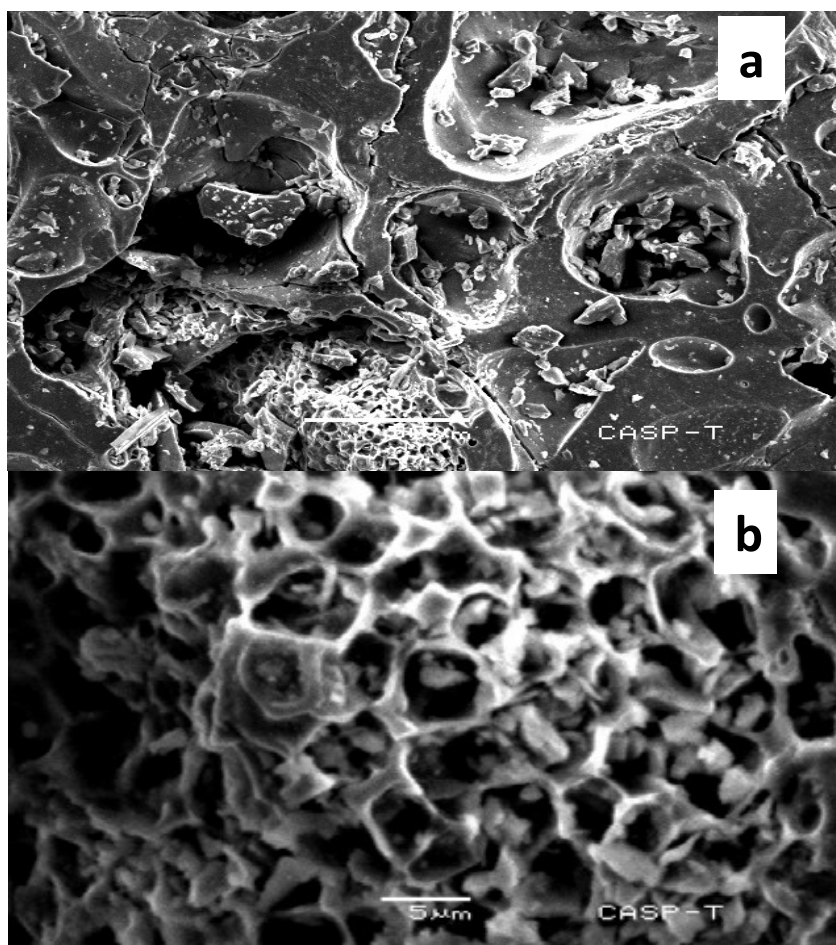


Figure 1: SEM images of (a) biochar (b) MBC.

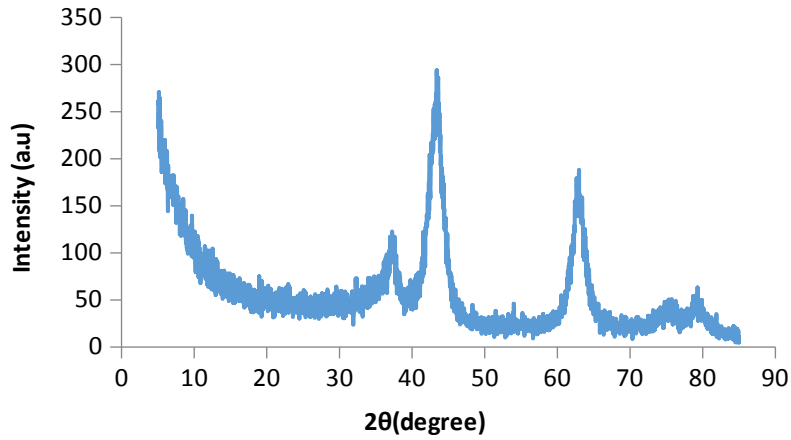


Figure 2: XRD pattern of MBC.

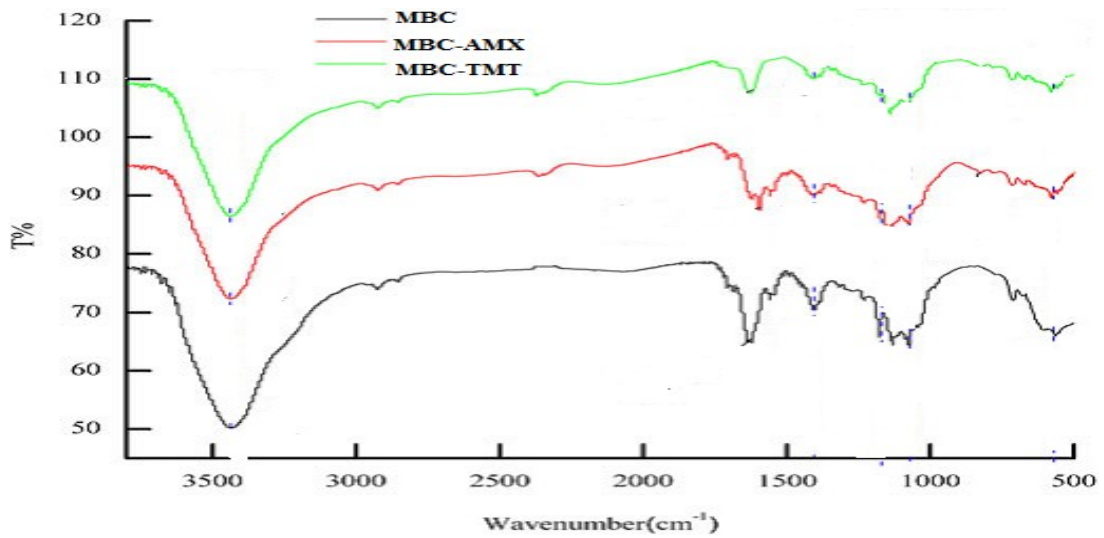


Figure 3: FTIR spectra of the MBC before and after adsorption of AMX and TMT.

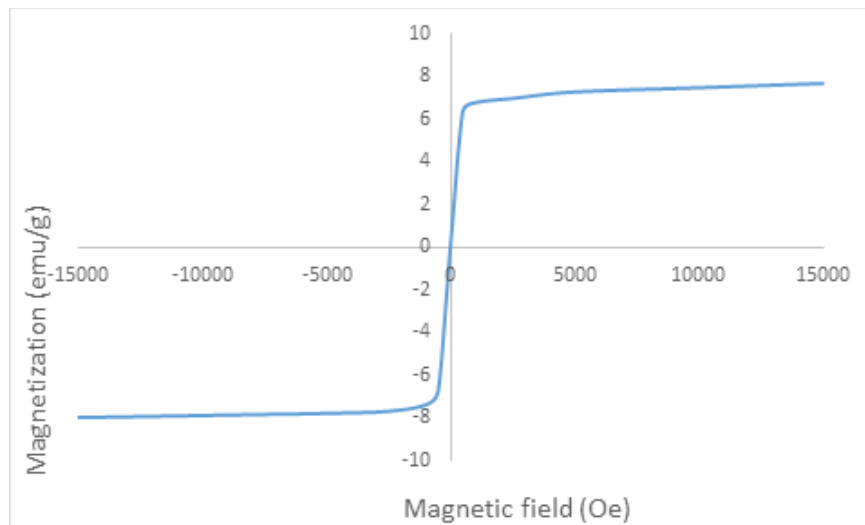


Figure 4: Magnetic hysteresis curve of MBC.

Study of the Effects of pH and Ionic Strength

Due to discrepancy in the values of acid dissociation constants (pK_a) of the examined pharmaceuticals, it is anticipated that both AMX and TMT could yield different charges under varying experimental conditions. As can be observed in Figure 5, the adsorption potential of AMX appreciably increases with a decrease in the pH, and maximum uptake was observed at $pH = 3$. However, TMT exhibited a different behavior from the AMX as the decrease in pH resulted in a lower adsorption yield and the optimum condition was presented at $pH = 8$. The distinct behavior of the adsorption of the pharmaceuticals can be explained by considering the electrostatic interactions between the examined adsorbates and target adsorbent. For $pH < p_{H_{pzc}}$, the surface of the MBC is positively charged, while for $pH > p_{H_{pzc}}$, the adsorbent bears a negative charge at its surface. The solution pH also determines the appearances of charges in the examined pharmaceuticals, therefore, both attractive and repulsive interactions could be induced. The high adsorption of AMX in acidic

environment may be explained by considering the ionization of the carboxyl group ($pK_a = 3.2$). It is obvious that the pK_a value of the aliphatic carboxylic acid functionality of AMX is close to pH 3. Therefore, this group is not completely protonated carrying partial negative charges that could enhance electrostatic attraction between the AMX and MBC (25). By contrast, TMT performs better in basic medium, having a similar pK_a (7.1) to the pH_{pzc} (6.9) which induces greater repulsion in low pHs (26).

Since there are many types of ions in different wastewaters, it seems imperative to investigate ionic strength's influence on the adsorption process. To achieve this, sodium chloride (NaCl) salt was used for adjusting the ionic strength of the adsorbates' solution. As shown in Figures 6 and 7, the adsorption capacity of MBC for both AMX and TMT decreases slightly with increasing ionic strength of the solution. This indicates that the salt concentration has an insignificant influence on the adsorption of AMX and TMT onto the MBC.

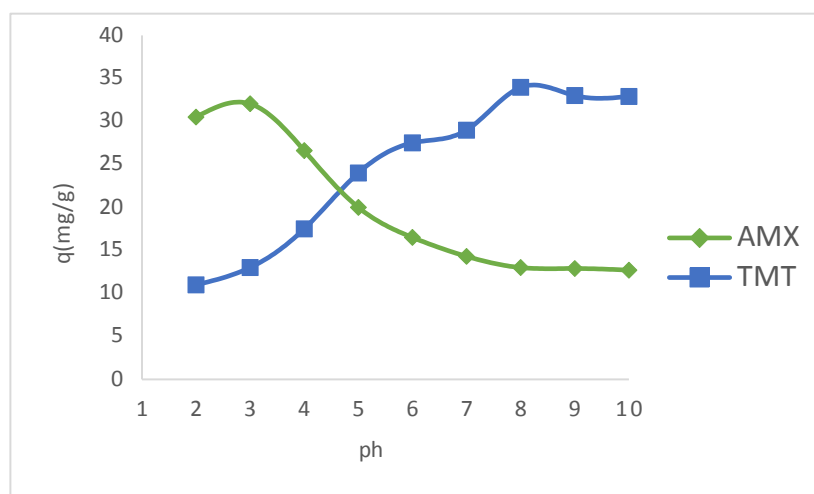


Figure 5: Effect of pH on the adsorption of AMX and TMT onto MBC (Conditions: $pH = 2-10$; contact time = 60 min; adsorbent weight = 0.1 g; $C_0 = 60$ mg/L, solution volume = 100 mL and temperature = 303 K).

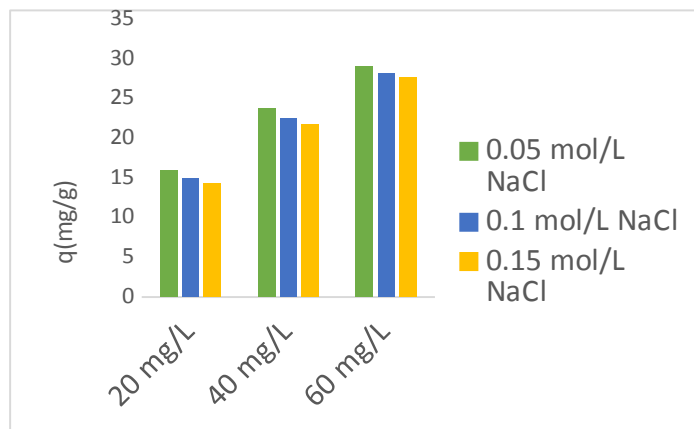


Figure 6: Effect of ionic strength on AMX adsorption by MBC at different initial concentration (Conditions: salt concentration = 0.05-0.15 mol/L; pH = 3; contact time = 60 min; adsorbent weight = 0.1 g; C_o = 20-60 mg/L, solution volume = 100 mL and temperature = 303 K).

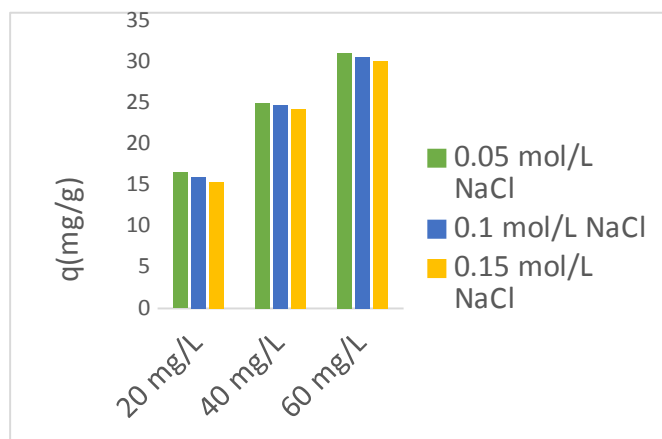


Figure 7: Effect of ionic strength on TMT adsorption by MBC at different initial concentration (Conditions: salt concentration = 0.05-0.15 mol/L; pH = 8; contact time = 60 min; adsorbent weight = 0.1 g; C_o = 20-60 mg/L, solution volume = 100 mL and temperature = 303 K).

Adsorption Kinetics

The impact of contact time on the adsorption process of AMX and TMT onto MBC was presented in Figure 8. It can be seen that the adsorption process attained a relatively fast equilibrium at around 60 min of residence time, suggesting that the MBC surface had a high affinity towards the pharmaceutical molecules in solution.

The values of kinetic parameters for the adsorption of pharmaceuticals onto the MBC as evaluated from the curve-fitting graphs (Figures 9 and 10) are presented in Table 2. An excellent agreement between the theoretical adsorption capacities computed from the PSO kinetic model with the experimental adsorption capacity for both the adsorbates together with higher R^2 values illustrated that the kinetics of the adsorption process is compatible with this model. The implication of this outcome is that the adsorption rate is influenced by the concentration of both the adsorbate

and adsorbent. According to the PSO rate constant, AMX is the fastest adsorbing compound compared to TMT. The PSO kinetic model hints that the rate-controlling step was chemisorption between the adsorbates and the adsorbent (27). A similar trend of PSO kinetics has also been reported in the previous studies for the adsorption of pharmaceuticals onto different adsorbents (26,28).

The IPD model was explored to further elucidate the mechanism of adsorption of AMX and TMT onto the MBC. The values of the parameters linked with this model are presented in Table 2. It was observed that the regression of q_t versus $t^{1/2}$ (Figure 11) is non-linear and does not pass through the origin. This deviation signifies that the intraparticle diffusion is not the sole rate-controlling step. Furthermore, the plot indicates the multi-linearity represented by two linear segments, which indicates that the adsorption of both the pharmaceuticals was accompanied by two steps.

The first sharper segment depicts the instantaneous external surface adsorption while the second segment is ascribed to the gradual adsorption stage of intraparticle diffusion and the attainment of equilibrium (27).

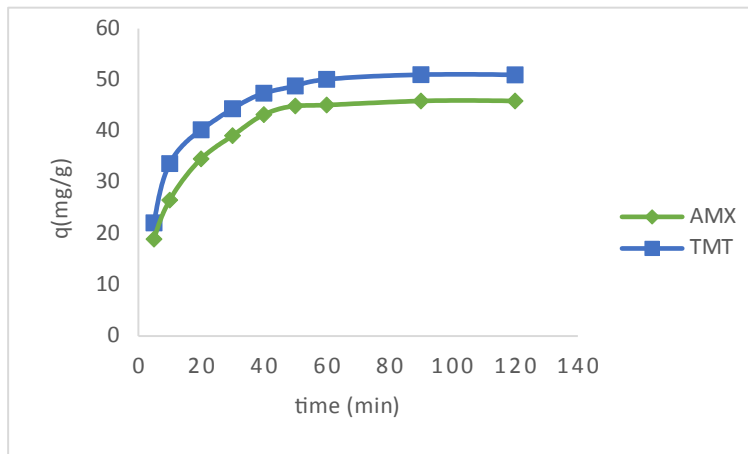


Figure 8: Effect of contact time on the adsorption capacity of MBC towards AMX and TMT (Conditions: contact time = 5-120 min; $C_0 = 60$ mg/L; solution volume = 100 mL; adsorbent weight = 0.1 g; temperature = 303 K).

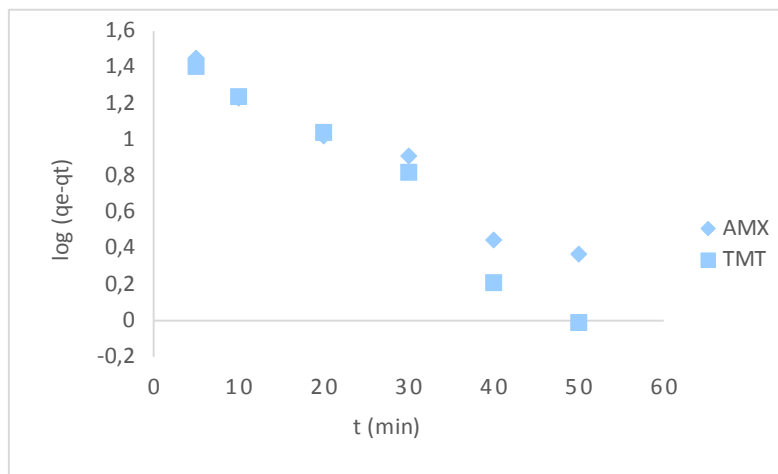


Figure 9: Kinetic data of AMT and TMT adsorption onto MBC adjusted to PFO model (Conditions: contact time = 5-120 min; $C_0 = 60$ mg/L; solution volume = 100 mL; adsorbent weight = 0.1 g; temperature = 303 K).

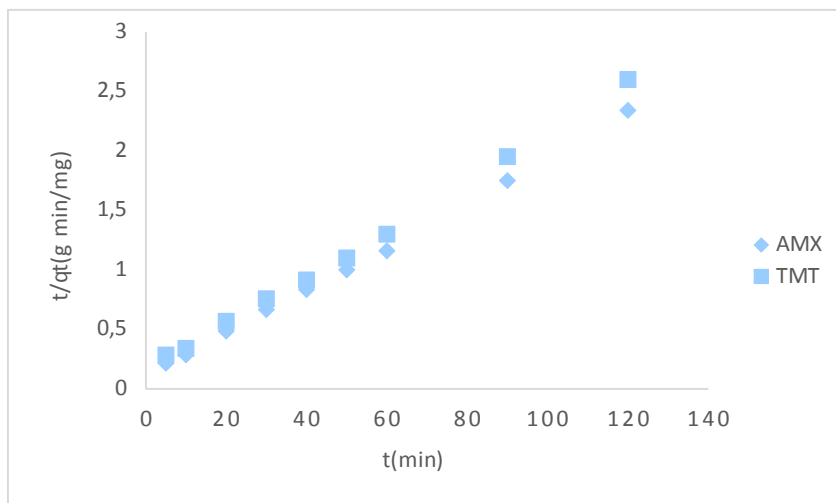


Figure 10: Kinetic data of AMT and TMT adsorption onto MBC adjusted to PSO model (Conditions: contact time = 5-120 min; $C_0 = 60$ mg/L; solution volume = 100 mL; adsorbent weight = 0.1 g; temperature = 303 K).

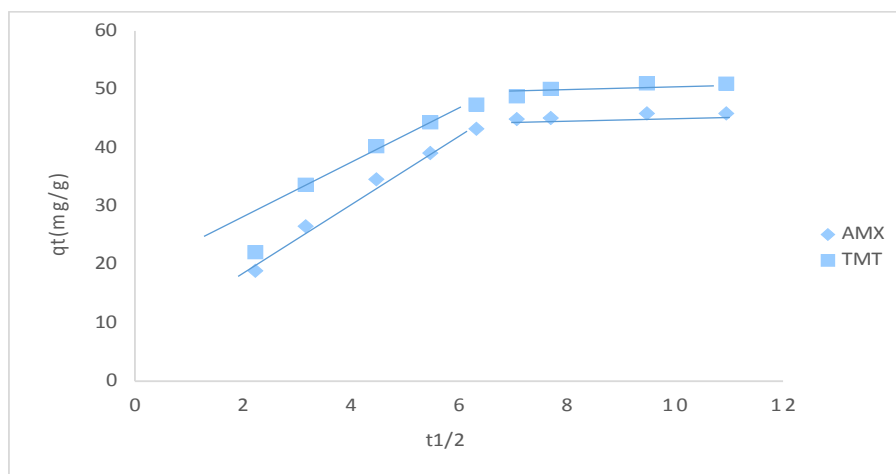


Figure 11: Kinetic data of AMT and TMT adsorption onto MBC adjusted to IPD model (Conditions: contact time = 5-120 min; $C_0 = 60$ mg/L; adsorbent weight = 0.1 g; solution volume = 100 mL; temperature = 303 K).

Adsorption Isotherm

The study of adsorption isotherms is essential to describe how examined adsorbates interact with the target adsorbent surface. Two commonly used models, viz., Langmuir and Freundlich models have been employed to interpret the isotherm data and outcomes so generated are shown in Table 3. The equilibrium data for both adsorbates exhibit appreciable fit to the Langmuir model, attested by highest R^2 and lowest value of SSE and χ^2 . This implies that the adsorption occurred in a homogeneous surface (sites of equal energy and accessibility) leading to the formation of a monolayer of pharmaceuticals on the surface of the MBC that saturates the pores and hampers the transmigration

(25). Furthermore, the value of R_L lies in the range of 0–1, intimating a high degree of favorability of the adsorption process. The maximum adsorption capacities of AMX and TMT calculated from the Langmuir isotherm model are 41.87 and 55.83 mg/g, respectively. This demonstrates the potential of MBC for adsorption of this pharmaceuticals under the employed conditions. On the other hand, the Freundlich model exhibit higher values of SSE and χ^2 for both the adsorbates indicating its unsuitability for inferring adsorption of pharmaceuticals onto the MBC. It is worth mentioning that the affinity for the Langmuir model has been observed in previous studies dealing with AMX and TMT adsorption (26,29).

Table 2: Relevant kinetic fitting parameters for AMX and TMT adsorption onto MBC.

Kinetic model	Parameters	AMX	TMT
Pseudo-first-order	$q_{e,exp}$ (mg/g)	45.10	50.10
	$q_{e,model}$ (mg/g)	33.55	40.98
	k_1 (1/min)	0.06	0.07
	R^2	0.964	0.967
	χ^2	3.98	2.03
Pseudo-second-order	SSE (%)	4.72	3.72
	$q_{e,model}$	44.34	49.75
	$k_2 \times 10^{-3}$ (g/mg min)	4.90	2.88
	R^2	0.999	0.999
	χ^2	0.01	0.007
Intraparticle diffusion	SSE (%)	0.25	0.11
	K_{id}	3.03	3.02
	C	19.10	24.11
	R^2	0.785	0.771

Table 3: Parameters of the fitting to Langmuir and Freundlich models for AMX and TMT.

Isotherm model	Parameters	AMX	TMT
Langmuir	q_{max} (mg/g)	41.87	55.83
	K_L (L/mg)	0.21	0.23
	R_L	0.20	0.68
	R^2	0.994	0.986
	χ^2	0.12	0.14
Freundlich	SSE (%)	0.97	1.04
	K_F (L/mg)	14.53	10.68
	n	2.28	2.50
	R^2	0.969	0.979
	χ^2	2.65	3.96
	SSE (%)	17.20	18.93

Thermodynamic Behavior

In order to examine the nature of the adsorption of pharmaceuticals onto the MBC, the thermodynamic factors, such as the changes in enthalpy ΔH (J/mol), Gibbs free energy ΔG (J/mol), and entropy ΔS (J/mol K) associated with the adsorption process were computed by using Eqs. 15-17:

$$K_d = \frac{q_e}{C_e} \quad (15)$$

$$\Delta G = -RT \ln K_d \quad (16)$$

$$\ln K_d = \frac{-\Delta H}{RT} + \frac{\Delta S}{R} \quad (18)$$

where R denotes the universal gas constant (8.314 J/mol K); T represent the absolute temperature of the

system (K), and the parameter K_d is dimensionless since the unit of R, T and ΔG , are J/mol K, K, and J/mol, respectively. Furthermore, the system's ΔS and ΔH values were estimated from the intercept and gradient of Van't Hoff plot ($\ln K_d$ versus $1/T$), respectively.

Values of ΔG at varying temperatures (303–333 K) evaluated from Eq. (16) and other thermodynamic quantities such as ΔH and ΔS as obtained from Van't Hoff plot (Figure 12) are presented in Table 4. This table revealed that the thermodynamic behavior of both AMX and TMT towards MBC is the same. The negative ΔG values specify that the adsorption phenomenon is thermodynamically feasible under the employed laboratory conditions. The positive values of ΔH and ΔS for both the adsorbates signify that the process is endothermic in nature and accompanied with the increase in the degree of randomness at the adsorbate/adsorbent interface during adsorption (30).

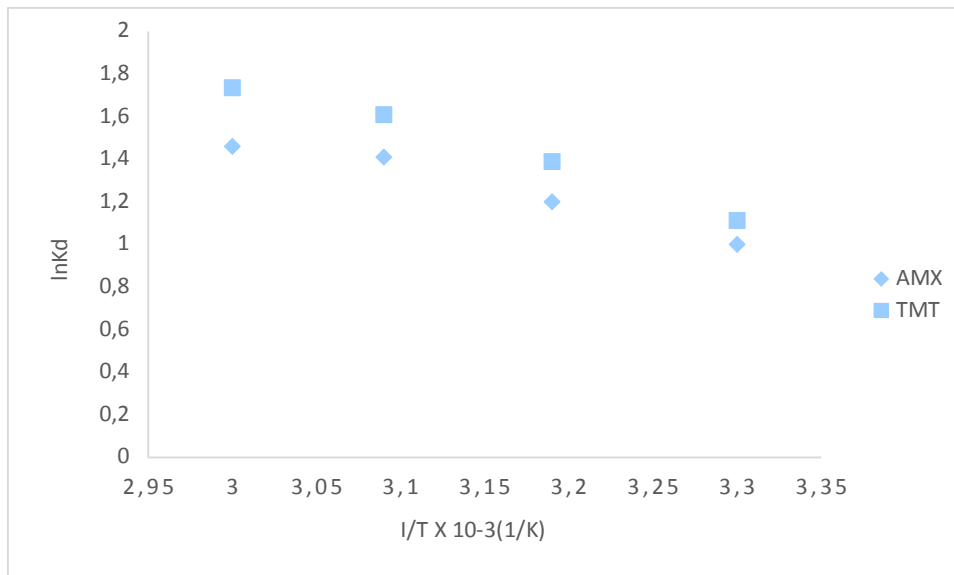


Figure 12: Van't Hoff plot for estimating the ΔH and ΔS of the adsorption system.

Table 4: The thermodynamic parameters for pharmaceuticals adsorption onto MBC.

Adsorbate	ΔH (J/mol)	ΔS (J/molK)	ΔG (J/mol)			
			303K	313K	323K	333K
AMX	13.32	52.42	-2519	-3123	-3786	-4042
TMT	17.47	67.09	-2801	-3615	-4321	-4805

Regeneration and Reuse Analysis

The reusability of adsorbent material is a crucial factor that needs to be taken into cognizance in order to lower the treatment cost as well as mitigate the hazard that might be occasioned by the disposal of pollutant-laden adsorbents. Although there are diverse regeneration strategies, we opted for the chemical method because of its low-cost nature and

zero adsorbent loss. Figure 13 displayed the results in six adsorption cycles. It was apparent that the adsorption amounts were maintained high and relatively stable. The MBC adsorbent retained about 75% of its original adsorption capacity after six reuse cycles. This result verified that the MBC has high economic viability since it could be recycled and reused efficiently.

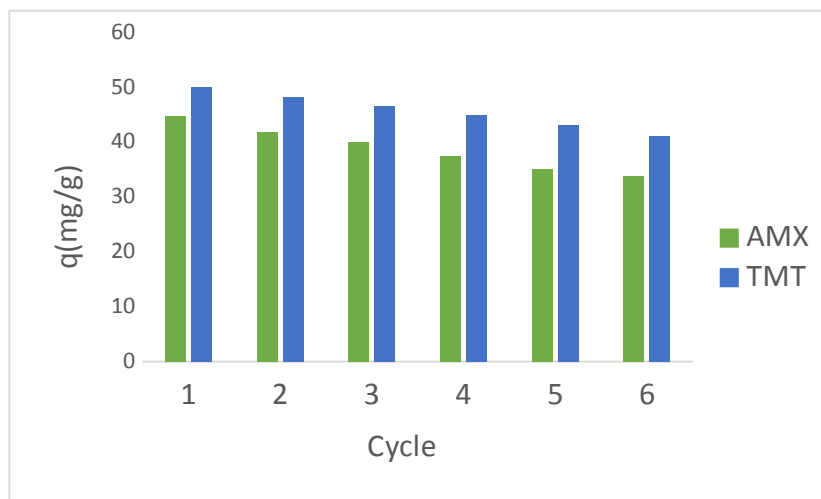


Figure 13: Reuse experiments results.

Density Functional Theory (DFT) Studies

Frontier molecular orbitals (FMOs) analysis

The frontier molecular orbitals are essential descriptors for diagnosing the most reactive site in π -electron systems (31). The values of the computed quantum chemical parameters such as the E_H , E_L , ΔE , A , and I are displayed in Table 5 and the plots generated from the computations are displayed in Figure 14. The value of HOMO energy (E_H) depicts the ability of electron to be donated. When the value of E_H is high, it signifies the ease of donating electron to the vacant orbital of the receptor molecule. When the value of LUMO energy (E_L) is small, this implies that a molecule has a slight resistance to accept electrons. The energy gap (ΔE) is directly linked to the molecular chemical stability. The pharmaceutical AMX exhibited highest energy band gap ($\Delta E = 3.855$ eV) which illustrates its less reactivity and higher stability. The TMT presented the lowest energy gap ($\Delta E =$

3.762 eV) signifying its high reactivity and lowest stability. The determination of parameters like electron affinity and ionization potential is crucial as they are linked to the orbital energies of the LUMO and HOMO, respectively. The higher the value of A , the more the molecule will be a better electron acceptor. The lower the value of I , the more the molecule will be a better electron donor (32).

From Figure 14, it is obvious that the spread of isodensities of LUMOs and HOMOs is different in both the pharmaceuticals. As we can see, for AMX molecule, the HOMO is dispersed over the phenyl ring including its attached oxygen atom and a small part of the side chain attached to the ring. However, the LUMO shows no distribution over the phenyl ring. For TMT, the HOMO density was not spread over the benzene rings while the LUMO was distributed throughout the molecule ring excluding the terminal oxygen atoms attached to the benzene ring.

Table 5: Molecular orbital energies and other properties of studied compounds.

Compounds	E_H (eV)	E_L (eV)	ΔE (eV)	I (eV)	A (eV)
AMX	-5.372	-1.517	3.855	5.372	1.517
TMT	-4.620	-0.858	3.762	4.620	0.858

Global reactivity descriptors

The values of the important global reactivity parameters of the pharmaceuticals under investigation are presented in Table 6. These descriptors are imperative to gain insights about the reactivity and stability of studied molecules. From Table 6, it is obvious that among the two pharmaceuticals, AMX is the chemically hardest having the highest value of η (3.855 eV), whereas TMT has the highest value of σ (0.266 eV) and therefore chemically softer and more reactive. The chemical potential (μ) value gives a clue about the charge transfer within any compound in its lowest energy state. It is clear that AMX has the highest chemical potential value (-3.445 eV). ω is a thermodynamic parameter that plays a vital role in explaining the reactivity of a chemical system. It quantifies the energy changes when a chemical

system becomes saturated by electrons addition. The results indicate that TMT has the lowest ω value (0.997 eV) and is nucleophilic in nature, whereas AMX has the highest value i.e., of 1.539 eV and is electrophilic in nature (32). χ describes the capability of a molecule to draw electrons towards itself in a covalent bond. Thus, AMX possesses higher electronegativity value (3.445 eV) than TMT (2.739 eV); hence it is the best electron acceptor.

According to the results obtained from DFT-based descriptors, TMT molecules are chemically softer (easiness to adsorb) and more reactive in comparison with molecules of AMX. These findings affirm the experimental observations related to the high adsorption capacity of MBC for TMT in comparison with AMX.

Table 6: Global reactivity indices of studied pharmaceuticals.

Property	AMX	TMT
μ (eV)	-3.445	-2.739
η (eV)	3.855	3.762
σ (eV ⁻¹)	0.259	0.266
χ (eV)	3.445	2.739
ω (eV)	1.539	0.997

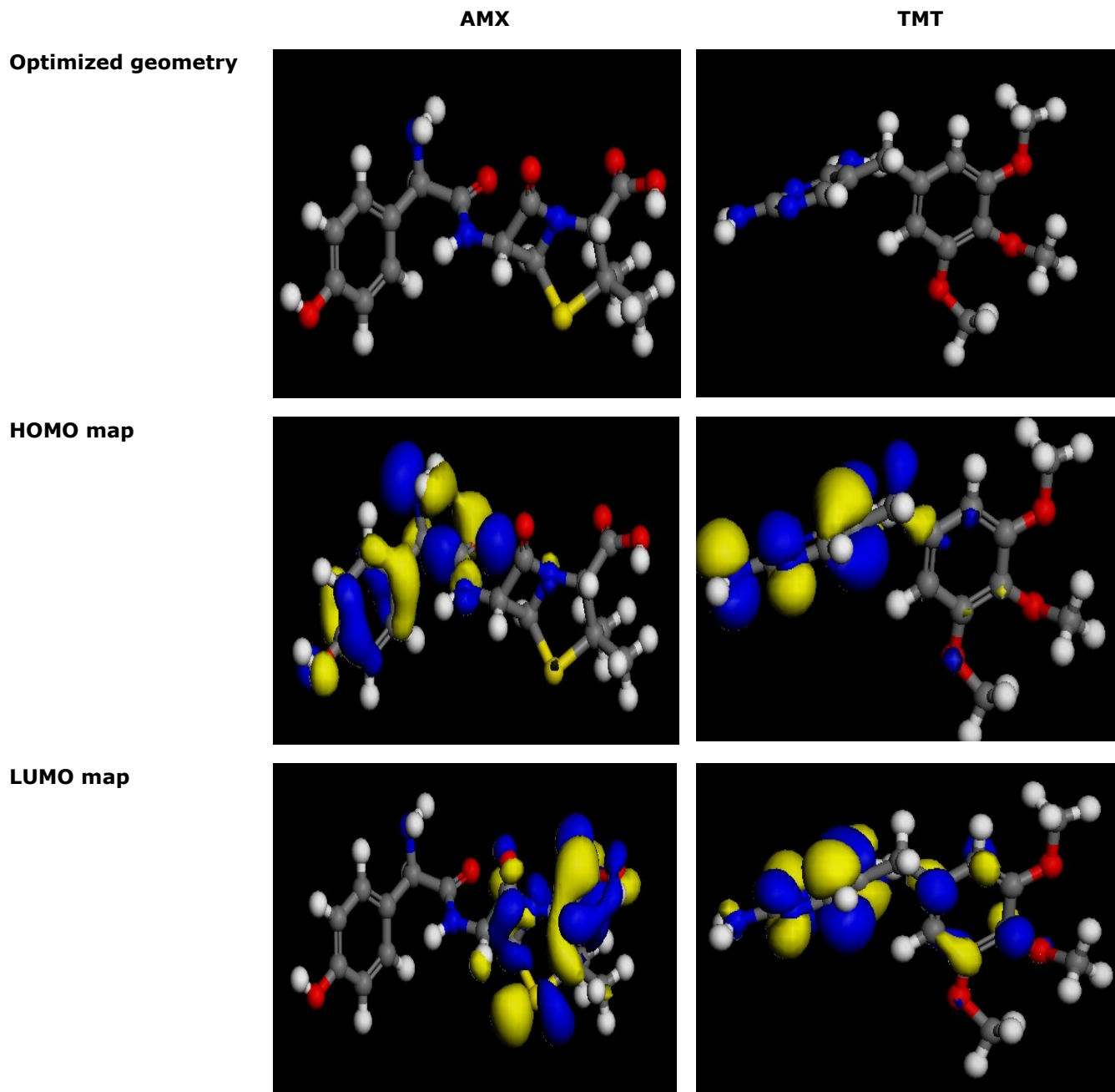


Figure 14: Structural and electronic properties of AMX and TMT.

CONCLUSION

Magnetic biochar derived from *Vitex doniana* nut was fabricated and successfully applied for the effective adsorption of pharmaceuticals from aqueous media. The adsorption behavior of AMX and TMT on MBC adsorbent was investigated. The amount of TMT adsorbed on MBC was higher than that of AMX. Compared to ionic strength, the influence of pH on the adsorption of the adsorbates was significant. The

adsorption kinetics was compatible with the pseudo-second-order model. The adsorption isotherms of AMX and TMT on the magnetic biochar were consistent with the Langmuir model. Thermodynamic investigation showed that the adsorption process was endothermic and spontaneous under studied conditions. The TMT molecules are chemically softer and more reactive in comparison with molecules of AMX. The experimental results of AMX and TMT adsorption onto surface of MBC are in conformity with

the DFT investigation of molecular reactivity of the examined pharmaceuticals. The results showed that the MBC would be a promising material for environmental protection.

REFERENCES

- Ebele AJ, Abou-Elwafa Abdallah M, Harrad S. Pharmaceuticals and personal care products (PPCPs) in the freshwater aquatic environment. *Emerging Contaminants*. 2017 Mar;3(1):1–16. [<DOI>](#).
- Daughton CG. Pharmaceuticals and the Environment (PiE): Evolution and impact of the published literature revealed by bibliometric analysis. *Science of The Total Environment*. 2016 Aug;562:391–426. [<DOI>](#).
- Nazari G, Abolghasemi H, Esmaili M. Batch adsorption of cephalixin antibiotic from aqueous solution by walnut shell-based activated carbon. *Journal of the Taiwan Institute of Chemical Engineers*. 2016 Jan;58:357–65. [<DOI>](#).
- Domínguez JR, González T, Palo P, Cuerda-Correa EM. Removal of common pharmaceuticals present in surface waters by Amberlite XAD-7 acrylic-ester-resin: Influence of pH and presence of other drugs. *Desalination*. 2011 Mar;269(1–3):231–8. [<DOI>](#).
- Sophia A. C, Lima EC. Removal of emerging contaminants from the environment by adsorption. *Ecotoxicology and Environmental Safety*. 2018 Apr;150:1–17. [<DOI>](#).
- Danalioğlu ST, Bayazit ŞS, Kerkez Kuyumcu Ö, Salam MA. Efficient removal of antibiotics by a novel magnetic adsorbent: Magnetic activated carbon/chitosan (MACC) nanocomposite. *Journal of Molecular Liquids*. 2017 Aug;240:589–96. [<DOI>](#).
- Dai Y, Zhang N, Xing C, Cui Q, Sun Q. The adsorption, regeneration and engineering applications of biochar for removal organic pollutants: A review. *Chemosphere*. 2019 May;223:12–27. [<DOI>](#).
- Zhang A, Li X, Xing J, Xu G. Adsorption of potentially toxic elements in water by modified biochar: A review. *Journal of Environmental Chemical Engineering*. 2020 Aug;8(4):104196. [<DOI>](#).
- Hao Z, Wang C, Yan Z, Jiang H, Xu H. Magnetic particles modification of coconut shell-derived activated carbon and biochar for effective removal of phenol from water. *Chemosphere*. 2018 Nov;211:962–9. [<DOI>](#).
- Dadjo C, Assogbadjo AE, Fandohan B, Glèlè Kakaï R, Chakeredza S, Houehanou TD, et al. Uses and management of black plum (*Vitex doniana* Sweet) in Southern Benin. *Fruits*. 2012 Jul;67(4):239–48. [<DOI>](#).
- Ameh PO, Odoh R, Oluwaseye A. Equilibrium study on the adsorption of Zn (II) and Pb (II) ions from aqueous solution onto *Vitex doniana* nut. *Int J Modern Chem*. 2012;3(2):82–97.
- Atolaiye BO, Babalola JO, Adebayo MA, Aremu MO. Equilibrium modeling and pH-dependence of the adsorption capacity of *Vitex doniana* leaf for metal ions in aqueous solutions. *African Journal of Biotechnology*. 2009;8(3). [<URL>](#).
- Florey K. *Analytical profile of drug substances*. Academic Press; 1978.
- Kerkez-Kuyumcu Ö, Bayazit ŞS, Salam MA. Antibiotic amoxicillin removal from aqueous solution using magnetically modified graphene nanoplatelets. *Journal of Industrial and Engineering Chemistry*. 2016 Apr;36:198–205. [<DOI>](#).
- Kakavandi B, Rezaei KR, Jonidi JA, Esrafiy A, Gholizadeh A, Azari A. Efficiency of powder activated carbon magnetized by Fe₃O₄ nanoparticles for amoxicillin removal from aqueous solutions: Equilibrium and kinetic studies of adsorption process. 2014; 7(1): 21–34. [<URL>](#).
- Bakatula EN, Richard D, Neculita CM, Zagury GJ. Determination of point of zero charge of natural organic materials. *Environ Sci Pollut Res*. 2018 Mar;25(8):7823–33. [<DOI>](#).
- Tran HN, You S-J, Hosseini-Bandegharai A, Chao H-P. Mistakes and inconsistencies regarding adsorption of contaminants from aqueous solutions: A critical review. *Water Research*. 2017 Sep;120:88–116. [<DOI>](#).
- Ouasfi N, Zbair M, Bouzikri S, Anfar Z, Bensitel M, Ait Ahsaine H, et al. Selected pharmaceuticals removal using algae derived porous carbon: experimental, modeling and DFT theoretical insights. *RSC Adv*. 2019;9(17):9792–808. [<DOI>](#).
- Chen Y, Shi J, Du Q, Zhang H, Cui Y. Antibiotic removal by agricultural waste biochars with different forms of iron oxide. *RSC Adv*. 2019;9(25):14143–53. [<DOI>](#).
- Cornell RM, Schwertmann U. *The iron oxides: structure, properties, reactions, occurrences, and uses*. 2nd, completely rev. and extended ed ed.

Weinheim: Wiley-VCH; 2003. 664 p. ISBN: 978-3-527-30274-1.

21. Liu P, Li H, Liu X, Wan Y, Han X, Zou W. Preparation of magnetic biochar obtained from one-step pyrolysis of *salix mongolica* and investigation into adsorption behavior of sulfadimidine sodium and norfloxacin in aqueous solution. *Journal of Dispersion Science and Technology*. 2020 Jan 28;41(2):214–26. [<DOI>](#).

22. Yunusa U, Bishir U, Bashir IM. Experimental and quantum chemical investigation for the single and competitive adsorption of cationic dyes onto activated carbon. *Alg J Eng Technol*. 2021 Feb 4;4:7–21. [<DOI>](#).

23. Devi P, Saroha AK. Simultaneous adsorption and dechlorination of pentachlorophenol from effluent by Ni-ZVI magnetic biochar composites synthesized from paper mill sludge. *Chemical Engineering Journal*. 2015 Jul;271:195–203. [<DOI>](#).

24. Santhosh C, Daneshvar E, Tripathi KM, Baltrėnas P, Kim T, Baltrėnaitė E, et al. Synthesis and characterization of magnetic biochar adsorbents for the removal of Cr(VI) and Acid orange 7 dye from aqueous solution. *Environ Sci Pollut Res*. 2020 Sep;27(26):32874–87. [<DOI>](#).

25. Alnajrani MN, Alsager OA. Removal of Antibiotics from Water by Polymer of Intrinsic Microporosity: Isotherms, Kinetics, Thermodynamics, and Adsorption Mechanism. *Sci Rep*. 2020 Dec;10(1):794. [<DOI>](#).

26. Berges J, Moles S, Ormad MP, Mosteo R, Gómez J. Antibiotics removal from aquatic environments: adsorption of enrofloxacin, trimethoprim, sulfadiazine, and amoxicillin on vegetal powdered activated carbon. *Environ Sci Pollut Res*. 2021 Feb;28(7):8442–52. [<DOI>](#).

27. Ahmed M, Mashkoo F, Nasar A. Development, characterization, and utilization of magnetized orange peel waste as a novel adsorbent for the confiscation of crystal violet dye from aqueous solution. *Groundwater for Sustainable Development*. 2020 Apr;10:100322. [<DOI>](#).

28. Mokhati A, Benturki O, Bernardo M, Kecira Z, Matos I, Lapa N, et al. Nanoporous carbons prepared from argan nutshells as potential removal agents of diclofenac and paroxetine. *Journal of Molecular Liquids*. 2021 Mar;326:115368. [<DOI>](#).

29. Liu H, Hu Z, Liu H, Xie H, Lu S, Wang Q, et al. Adsorption of amoxicillin by Mn-impregnated activated carbons: performance and mechanisms. *RSC Adv*. 2016;6(14):11454–60. [<DOI>](#).

30. Yunusa U, Usman B, Ibrahim M. Modeling and Regeneration Studies for the Removal of Crystal Violet Using *Balanites aegyptiaca* Seed Shell Activated Carbon. *Journal of the Turkish Chemical Society Section A: Chemistry*. 2020 Dec 29;197–210. [<DOI>](#).

31. Umar Y, Abu-Thabit N, Jerabek P, Ramasami P. Experimental FTIR and theoretical investigation of the molecular structure and vibrational spectra of acetanilide using DFT and dispersion correction to DFT. *J Theor Comput Chem*. 2019 Mar;18(02):1950009. [<DOI>](#).

32. Khan SA, Rizwan K, Shahid S, Noamaan MA, Rasheed T, Amjad H. Synthesis, DFT, computational exploration of chemical reactivity, molecular docking studies of novel formazan metal complexes and their biological applications. *Appl Organometal Chem [Internet]*. 2020 Mar [cited 2021 Oct 29];34(3).5444, 1-24. [<DOI>](#).



A Survey on Various Methods of Extraction and Recovery of Thorium

Sugyani Dash¹ , Pallabi K. Hial¹ , Sagarkanya Senapati¹ , and
Biswajit Dalai^{2*}  

¹PG Scholar, Department of Physics, School of Sciences, GIET University, Gunupur, Odisha 765022, India

²Department of Physics, School of Sciences, GIET University, Gunupur, Odisha 765022, India

Abstract: In this survey, some methods of extraction of thorium such as selective extraction of thorium using phosphorodiamidate, selective cloud point extraction of thorium, extraction of thorium from sulfuric acid baking and leaching of monazite, extraction of thorium from chloride solution using Schiff base were discussed. The decomposition of monazite was manifested by sulfuric acid baking and leaching at an elated temperature. The recovery of thorium (Th) from various sources of rare earth and some selective extraction of thorium by using phosphorodiamidate as an extractant was also reported. Using a special synthesized surface-active ionic liquid extractant (SAIL), the cloud point extraction of thorium was analyzed. A synthesized Schiff base was applied for the extraction of thorium in the strategic solvent extraction method. Thorium, using α -amino phosphate extractant from bastnaesite, recovery by using Cyanex 572 and N1923, recovery of Th from industrial residues and recovery of Th from radioactive waste by using IREPO and monazite leached solution were discussed. In this study, the recovery of thorium from the industrial residue as well as from radioactive residue was also discussed.

Keywords: Extraction, Thorium, Monazite, SAIL, Cyanex[®] 572

Submitted: June 23, 2021. **Accepted:** October 27, 2021.

Cite this: Sugyani D, Pallabi KH, Sagarkanya S, Biswajit D. A Survey on Various Methods of Extraction and Recovery of Thorium. JOTCSA. 2021;8(4):1197-210.

DOI: <https://doi.org/10.18596/jotcsa.955211>.

***Corresponding author. Email:** biswajit@giet.edu.

INTRODUCTION

The history of human development is often told by the various form of energy. At first, it was muscle, and later when humans learned to control fire, it was heat energy. Eventually using coal and oil, the world was industrialized. With a growing population, the consumption of energy has been increased. This growing energy demand is met when a human entered into this atomic era. The energy harvested from the splitting of a nucleus has made humans the most advanced species on earth. When the demand for nuclear energy increased, the demand for nuclear fuel like thorium (Th) and uranium (U) is also increased. Even though thorium is not fissile, it is referred to nuclear energy since it is three to four times more

abundant on the surface of the earth than uranium and it also provides the most promising options for nuclear power generation in terms of fuel efficiency and economy (1). Lots of researches had been conducted to find a source of energy that would substitute the place of earth's energy resources that has been depleting rapidly day-by-day. The very promising and environment-friendly approach for meeting the ever-growing energy demand is nuclear energy with the least amount of nuclear waste. One of the greenest energy productions is the thorium reactor (2, 3). The possibility of thorium being the nuclear fuel, has given more importance to the production of thorium worldwide and Thorium is a naturally occurring radioactive material (4, 5).

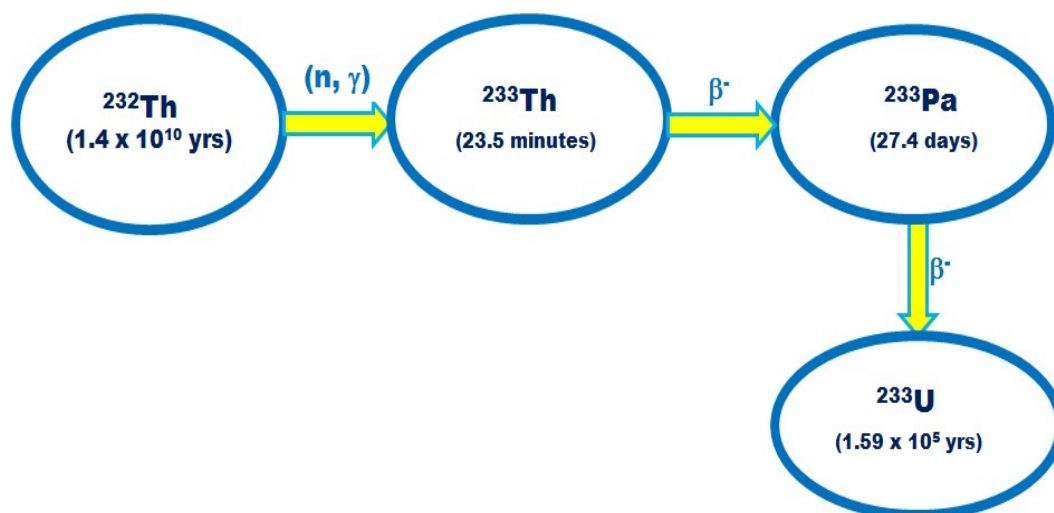


Figure 1: Production of uranium from Thorium (1).

Normally thorium isotopes exist as thorium-232 (^{232}Th) and its half-cycle is around 14 billion years. ^{232}Th is a fertile material that doesn't undergo fission reaction by itself. But a fissile material, i.e., uranium, is produced from its two-beta decay reaction of thorium with a neutron (Figure 1). Out of all nuclear fuels, thorium(IV) oxide (ThO_2) has more advantages compared to uranium because of its lower thermal expansion than uranium(VI) oxide (UO_2) and despite having a similar isometric structure, it is relatively inert (3, 4). The high thermal conductivity of ThO_2 makes it better fuel for nuclear reactors and the thorium fuel is considered an efficient fuel because of its lower hazard nuclear reaction accidents as well as its lower nuclear by-products. In the reactor, there will be no need for fuel reprocessing. The increasing awareness of fuel resources is changing its attitude towards the use of thorium as a fuel resource (5-7). The role of thorium in futuristic green energy production, gives rise to the demand for thorium extraction. There are various methods

for production of Thorium like extraction of thorium by using phosphorodiamidate as extractant, selective cloud point extraction of Th, selective extraction of Th by sulfuric acid baking and leaching of monazite, extraction of Th using a Schiff base etc. (8-12). The extraction behaviors of U(VI) and Th(IV) were investigated by Tan et al. (13) using di(1-methyl-heptyl) methyl phosphonate (DMHMP) as an extractant and kerosene as a diluent. Some novel extractants were synthesized for the separation of thorium and rare earth (RE) by Dong et al. (14). Among the synthesized neutral organophosphorus extractants, n-octyl phosphate diphenyl (ODP) revealed excellent extraction efficiencies and selectivities for Th(IV). The extraction mechanisms of uranium and thorium were studied by Nasab (12). Taguchi's method (12) was used to determine the optimum conditions for the separation of uranium and thorium using neutral extractants. In solvent extraction method, this method has been proposed as powerful method of experimental design (12)

$$(S/N)_i = -10 \left(\frac{1}{n} \sum_i \left(\frac{1}{y_i^2} \right) \right) \quad (1)$$

Where the signal to noise (S/N) ratio is used to determine the best experimental conditions, y_i is the experimental value and n is the number of tests in the experiment. In recent years, the extraction and recovery of thorium ions and their separations from various geological rare earth minerals have gained vital significance due to their wide applications in industries. The different extraction processes of thorium in a single review paper were not found in literatures and thus we have attempted to analyze the processes herewith.

METHODS OF EXTRACTION

Selective Extractions from Rare Earth by Using Phosphorodiamidate as an Extractant

In this method of extraction, an extractant named phosphorodiamidate was synthesized. To separate thorium from rare earth, the medium for the extraction chosen was nitrate medium. The molecular structure for this extractant is given in Figure 2.

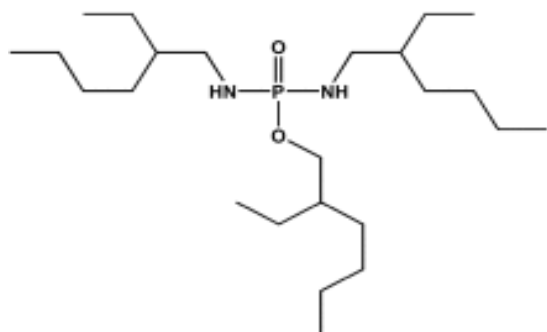


Figure 2: Molecular structure of phosphorodiamidate ligand, designated as **L** (8).

The molecular formula for this extractant is 2-Ethylhexyl-N, N'-di(2-ethylhexyl) phosphorodiamidate. The above extractant was added with a required concentration in n-heptane. The standard solution with concentrated nitric acid was prepared by dissolving corresponding oxides. The prepared solution was diluted with distilled water. The experiment was carried out in a temperature-controlled shaker bath at 298 K. For higher efficiency, nitrate medium with acidity ranging from 0.01 mol/L to 7 mol/L was taken in the extraction process. The extraction of thorium in a different acidic medium generally decreases by the increase in hydration energy of their ions and decrease in hydrophobicity of the extracted complex. The maximum loading capacity of Th in this method was about 48.56 g Th per liter of working solution with 0.69 mol/L of phosphorodiamidate at a 2.1 mol/L concentrated

nitrate medium. The extraction of Th(IV) and U(VI) from dilute nitric acid solution by several neutral phosphorus-based extractants has been studied as a function of temperature in the range of 0–50 °C by Kalina et al. (15). The order of extraction capacity of Th from the different medium: $\text{H}_2\text{SO}_4 < \text{HCl} < \text{HNO}_3$ (16-18). (16-18). In case of phosphoric acid, when the concentration is increased from 1 mol/L to 6.5 mol/L, the thorium stripping becomes 40 % to 70 %. When the concentration of the extractant (L) is increased, the extraction efficiency of thorium has been found more than REs. To reach higher extraction efficiency, the thorium extraction was studied with the acid concentration ranging from 0.01 mol/L to 7 mol/L in different acid medium (8, 16). The stripping of thorium by nitric acid confirmed that the loaded thorium can not be stripped even at high nitric acid concentration. There are maximum value for the stripping efficiency at about 1.5 mol/L for H_2SO_4 and 2.4 mol/L for HCl (8, 16). (8, 16). The higher acid concentration is more helpful for separation of REs. In this method, thorium is extracted in ionic form, Th(IV). The extraction is spontaneous and exothermic.

Cloud Point Extraction (CPE)

It is an eco-friendly method of extraction (9, 19-26). This method of extraction is considered noble because it is inexpensive, fast, selective, precise, and accurate. The procedure is considered green extraction as this method consumes a minimum amount of toxic organic solvents. Figure 3 shows how the cloud point extraction of metal can be done.

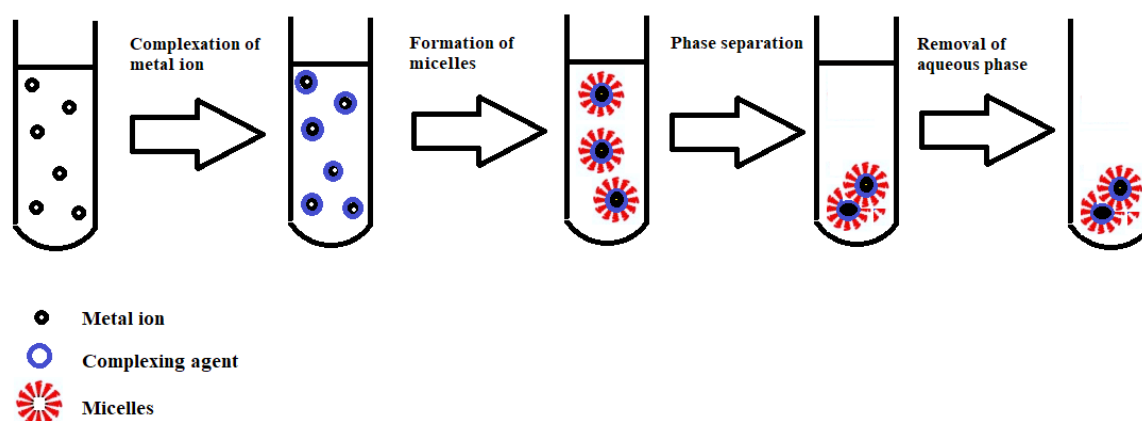


Figure 3: Cloud point extraction method (19).

In the experiment, a known amount of thorium was mixed with an Arsenazo III solution of 0.001 mol/L concentration in a 10 mL centrifuge tube. Then in the Th-Arsenazo III complex, the solutions: 1.0 mL of Triton X-100, 0.5 mL of KI (0.01 mol/L), and 2.5 mL of newly synthesized tetra-cationic surface-active ionic liquid (SAIL)

based on tetraazonia-tricyclodecane derivative (0.001 mol/L) were added respectively with an adjusted pH of 5.0. After taking the solution with deionized water to the mark, it was left in a thermostatic bath (353.15 K) for 30 min to an induced separation. Since the surfactant is denser than water, the solution gets separated into two

phases and the surfactant-rich phase settled through the aqueous phase. Then the tube was cooled down in an ice bath and centrifuged at 6000 rpm for 10 min. Then the aqueous phase was decanted leaving the surfactant-rich phase at the bottom of the tube. The surfactant-rich phase is then diluted with methanol to decrease the viscosity. After that, the extracted sample is moved to the quartz cell for a spectrophotometric determination as shown in Figure 4.

As per the work of Z F Akl and M. A. Hegazy (26), the highest extraction efficiency was achieved at

pH 5.0 with 2.5×10^{-3} mol/L SAIL and 1.0% (v/v) Triton X - 100. At the optimized conditions, the developed method exhibited a linear working range from 10 to 100 ng/mL with a detection limit of 0.77 ng/mL. The temperature also plays a vital role. For efficient extraction, the optimum temperature is 80°C. When the sample is spiked with pre-concentrated Th(IV) by a factor 20, then the extraction percentage of thorium increases more than 98%. This work reported the development of a green, sensitive, selective, and inexpensive method for extraction Th(IV).

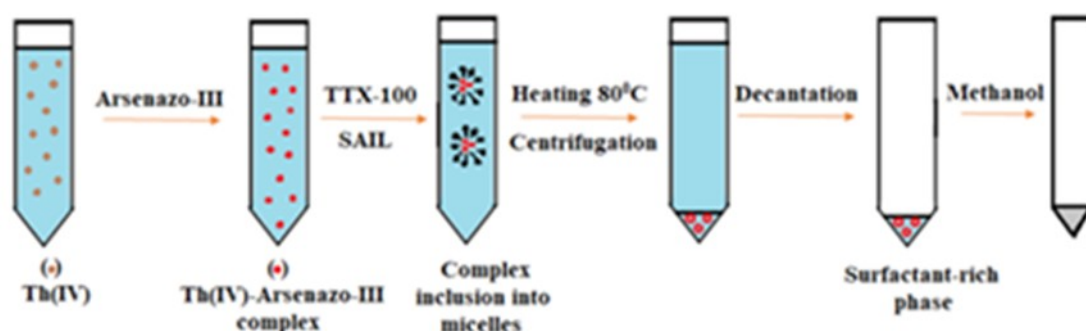


Figure 4: Spectrophotometric determination after cloud point extraction of Th (25).

Selective Extraction of Th by Sulfuric Acid Baking and Leaching of Monazite

Monazite is one of the major sources of thorium and many rare earth elements (REE). In sulfuric acid baking, the rare earth elements were converted into sulfates and those sulfates get dissolved in water leaching process. Monazite was either processed by sulfuric acid baking or alkaline digestion (10). In this process of extraction, at first monazite-sulfuric acid mixture was digested in the stirred reactor at 200 °C to 246 °C. Then the baking was carried out at various temperatures between 200 °C and 800 °C (27). After the baking, the heated sample was removed from the heated furnace and cooled. The cooled sample was ground to a fine powder before it was leached at 40:1 liquid to solid ratio at 20 °C to 29 °C in 0.9 M sulfuric acid for two hours. Then the separation of solid and liquid was done by vacuum filtration. The monazite bearing different concentrates have different bake temperatures. Individual rare earth is not easy to separate from each other because of their similar chemical and physical properties. Before the advancement in industrial solvent extraction, ion exchange techniques were prominent. In environmental and high-tech applications, rare earths are non-replaceable and indispensable because of their unique electro-chemical, luminescent and magnetic properties. To satisfy the diverse application of rare earth, it is mined, screened, and leached for separating it into proper feed materials (28). In this method, one of the influencing factor is precipitation pH. It

is ranging from 2.5 to 5.5 for thorium. But now-a-days solvent extraction is accepted as the most appropriate technique for separating rare earth commercially (29, 30). In this method of extraction, the behaviors of rare earth play a vital role. The separation of uranium and thorium in pure products can be achieved by this method using sulfuric acid liquor and one of the important variables to be considered in the process is the dosage of acid and dilution (31-33). In sulfuric acid baking of rare earth, uranium and thorium get converted into soluble sulfate (34). In the HCl leaching system, the issue of acid consumption is more pronounced. For mineral decomposition in industry, sulfuric acid baking is one of the major processes. This process is responsible for 81% of the world's rare-earth production. There are numerous techniques to investigate the extraction of rare earth metals, but only a few of them are found to be effective and successful. Sulfuric acid baking and leaching are one of them (27, 35-37). The flow chart of sulfuric acid decomposition of monazite is displayed in Figure 5. Various conditions for the baking of minerals, e.g. monazite, have been presented by numerous researchers (27,35-57). This extraction method is exothermic process. The baking of monazite with sulfuric acid gives an enthalpy of -171 kJ/ mol. J. Demol et al. (27) found that the sulfation reaction of monazite with acid resulting in more than 90% solubilization of rare earth elements phosphate and thorium. Their result shows the virtual complete dissolution of rare earth, phosphate, and thorium

during leaching after 250 °C bake. A thorium phosphate type precipitate was formed during leaching after baking at 300 °C and it leads to sharp decrease in extraction of phosphate and

thorium. This method requires high temperature and excessive acids for digestion which involves a number of risk factors while handling the steps.

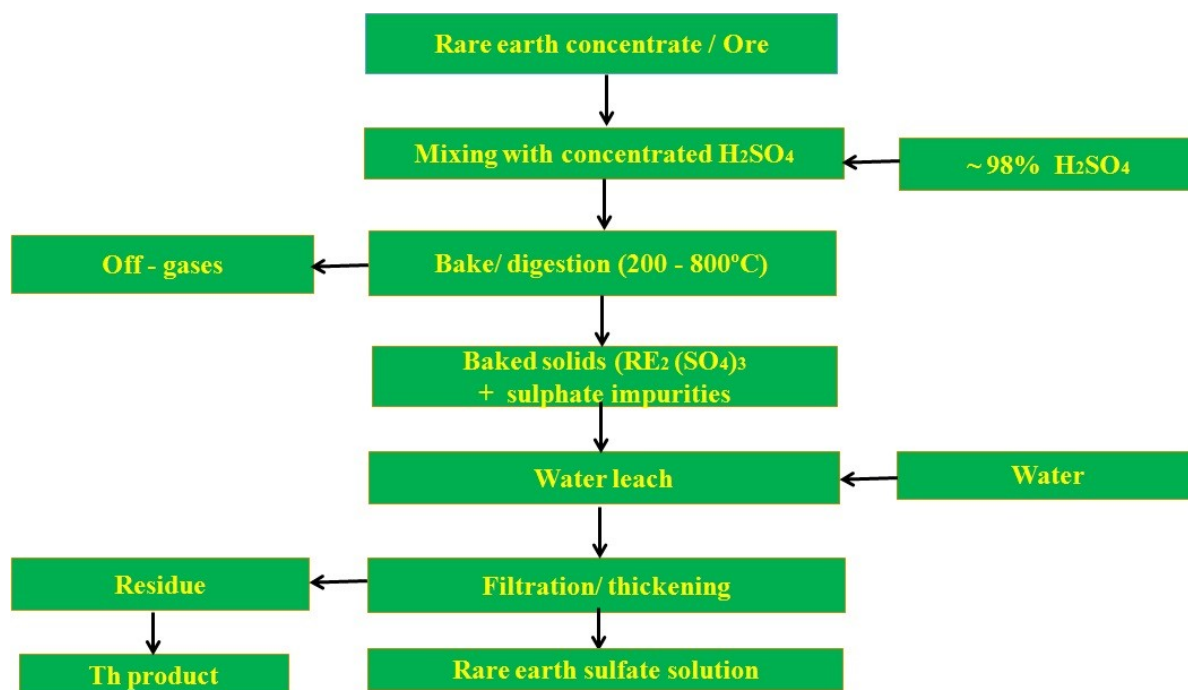


Figure 5: Sulfuric acid treatment of a rare earth mineral concentrate (37).

Extraction of Thorium (IV) from Chloride Solution using Schiff Base

In this strategic method of solvent extraction for thorium selective group extractants such as neutral phosphate (12), amines (12, 58), oximes (59), phosphoric acid (60, 61) and, Schiff base (11, 62, 63) were employed. In this process of extraction,

initially, a synthesized Schiff base (AcPh) was applied for the extraction of thorium from standard solution (1000 mg/L of Th IV) which was prepared by dissolving 2.535 g of thorium nitrate in acidified distilled with 10 mL of concentrated HCl. The preparation of the Schiff base is shown in Figure 6.

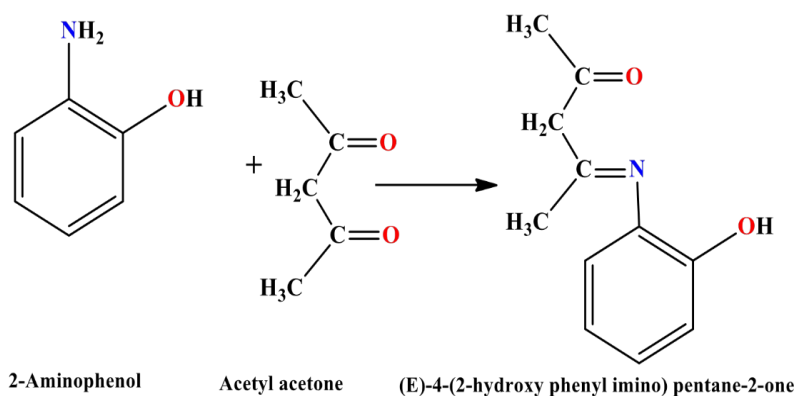


Figure 6: Preparation of the Schiff base (AcPh) (11).

After adding AcPh, then the sample mixture was dissolved in a mixture of diethyl ether and chloroform at the ratio of 2:3. After that sodium malonate was added to the sample containing Th(IV) in chloride form. A dilute solution of HCl/NaOH was added to obtain the desired pH. Then the sample was equilibrated by shaking it for about 7 minutes in a glass with an appropriate

volume of the organic phase. After equilibration, Th in ionic form was separated from its aqueous phase (63, 64). The pH value (≈ 6.5) and concentration of Schiff base are influencing factors for extraction. When the concentration of Schiff base is increased from 0.001 M to 0.002 M, the extraction efficiency of Th(IV) increases from 44% to 96.2% provided the organic phase to aqueous

phase is to be 1:3. M. F. Cheria et al. (11) reported that the maximum extraction efficiency of thorium was obtained at 0.02 M AcPh/chloroform and diethyl ether mixture, 3:1 aqueous to the organic ratio for 5 min contact time at room temperature. The extraction process using Schiff base in chloride medium gives an increased sensitivity of analysis of thorium ions in rock samples. Using this method thorium can be extracted about 330 mg/kg approximately. When phosphorodiamidate extractant used for the extraction, the extraction capacity was found to be 48.55 g per liter of the sample solution. sample solution. The efficiency of stripping decreases gradually with the increase in temperature above room temperature. For efficient extraction the room temperature is considered optimum. This extractant is considered noble as it makes selective extraction of Th from rare earth possible.

RECOVERY OF THORIUM USING DIFFERENT TECHNIQUES, EXTRACTANTS, AND FROM RADIOACTIVE WASTE

Recovery of Thorium(IV) by α -amino phosphate Extractant in Sulfate Medium and from Leach Solution with Cextrant 230

In this process of recovery, α -aminophosphate extractant and Cextrant 230 were used to recovery Th(IV) in sulfate medium and by using leach solution respectively. Here the use of the amine group in phosphate increases the extraction of Th(IV). Bastnasite leaching can be used, in which purities of Th were increased by 98%. Due to the increasing global demand of energy, the recovery

of Th, and U from various sources have drawn great attention at present time (64, 65). Bastnasite ((RE)(CO₃) F), monazite((RE(PO₄), xenotime (YPO₄), and RE-bearing clay have been used as rare earth minerals (65,66). Recently, aminophosphate compounds have drawn the attraction of researchers, and have been extensively used as extractants, herbicides, anticancer agents, etc. It also shows marvelous extractive properties (67-71). Here metals were analyzed using an inductively coupled plasma optical emission spectrometer (72, 73). To determine the pH of an aqueous solution, PHS-3C digital meter was used. The molecular structure of Cextrant 230 is shown in Figure 7.

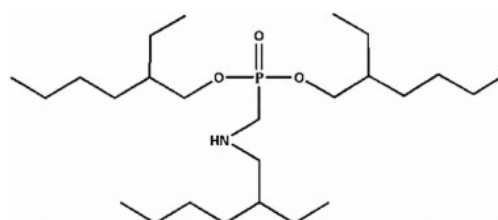


Figure 7: Molecular structure of Cextrant 230 (73).

Cextrant 230 is the most important extractant for the recovery of radioactive elements Th and U from an aqueous solution. It contains aluminium and iron in a sulfate medium. The extraction process of Th and U with cextrant 230 is exothermic (72-74). The flow chart of separating cerium (IV) and thorium (IV) from bastnaesite leaching is shown in Figure 8.

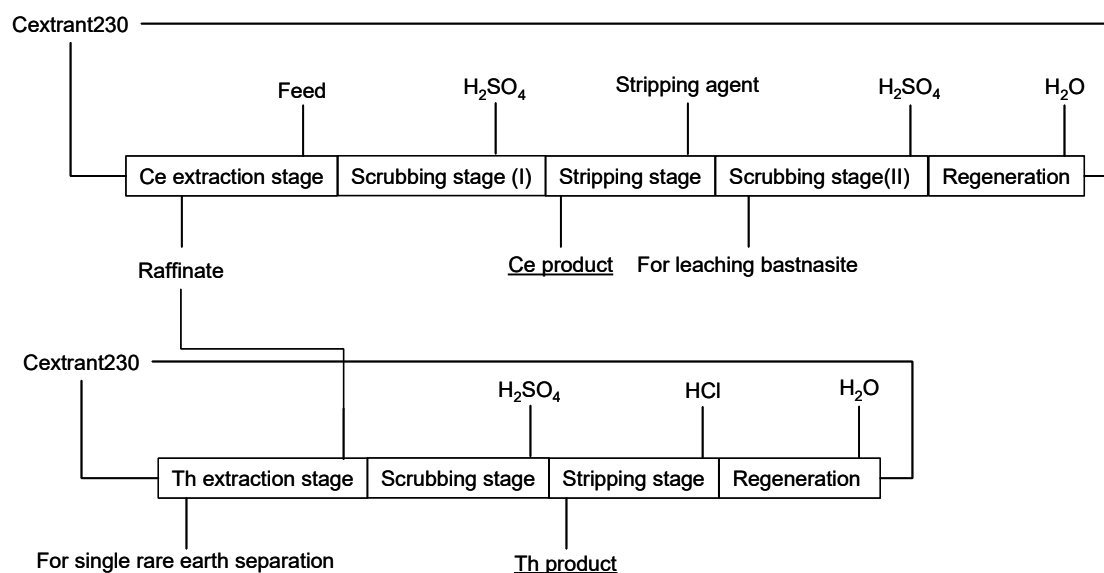


Figure 8: Flow chart of separating cerium(IV) and thorium(IV) from bastnaesite leaching (74).

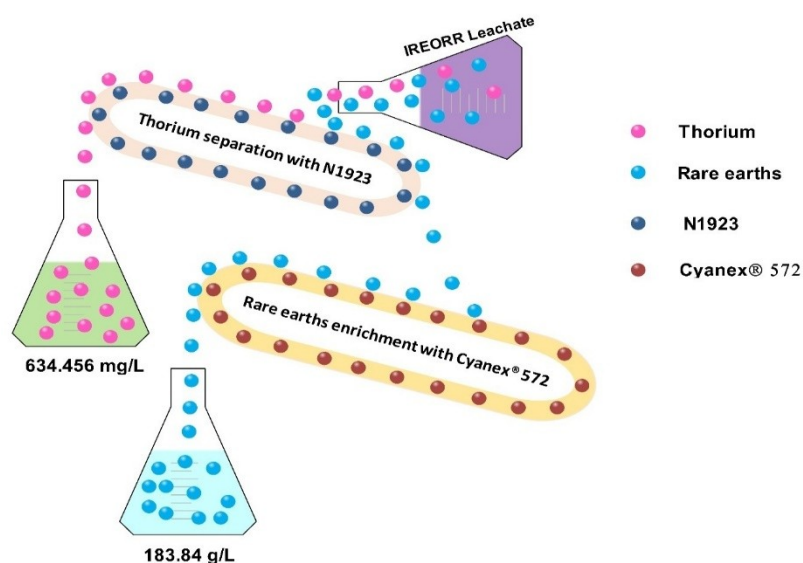


Figure 9: Th separation with N1923 and REE enrichment with Cyanex®572 (75).

Th separation with N1923 and REE enrichment with Cyanex®572 is shown in Figure 9. N1923 and Cyanex®572 can be used for the recovery of thorium using HCl leachate (75). In the method of formulating a high concentration rare earth (RE) feed for individual RE separation, hydrochloric acid is used to dissolve the RE concentrate to reduce the leaching of impurities, about 5% of REEs remains in the dissolved residues (76, 77).

Recovery of Th from Industrial Residues and Monazite Leach Solution

The main chemical used for this process was sulfuric acid digestion followed by water leaching. The lanthanides group as well as the scandium and yttrium group come under a rare-earth group, as the chemical structure of Th and U are similar to REE. They are found in the residues generated in REE processing. In monazite minerals, Th is found in high quantity as compared to U (78, 79). Here the acid digestion is performed with concentrated sulfuric acid and then adds directly to the solid. Sulfuric acid digestion followed by water leaching was found to be the best method to solubilize the metal (80). To recover thorium from monazite, solvent extraction, i.e. liquid-liquid extraction process (80, 81). It is one of the strategic methods and utmost reliable technique to reach out on target metal recovery with enrichment factor. Korean monazite is managed using hydrometallurgical techniques such as water leaching, sulfation, double salt precipitation by using Na_2SO_4 and acidic leaching by HCl (81, 82).

The flowchart for synthesis of thorium-rich residue associated with minor quantities of rare earth elements is shown in Figure 10.

Recovery of Th from Radioactive Waste

There is also removal of thorium using IREPO from radioactive waste (83). In this method, the recovery of Th by using IREOPR was analyzed. In this process, the convenient and effective chemical treatment of IREORR was to dissolve them with a mineral acid before recovering the valuable elements. A process for separating Th and REEs from IREORR leachate using POAA has been designed and illustrated. Here the chemical composition of residues was first analyzed and then the leaching factors such as acid type and acid concentration were noted down. A cost-effective process for recovering thorium and rare earths from radioactive residues is shown in Figure 11.

EXTRACTION AND SEPARATION RESULT WITH THE OPTIMAL CONDITIONAL ANALYSIS

The extraction process follows different steps with response to various diluents, concentration of extractants, pH value, temperature, contact time, acids (HNO_3 , HCl, H_2SO_4) etc. In this study, we have highlighted some important works of different researchers on extraction and separation of thorium from other metals. The parameters studied in the above said processes are calculated by using the following relations (65, 73, 83).

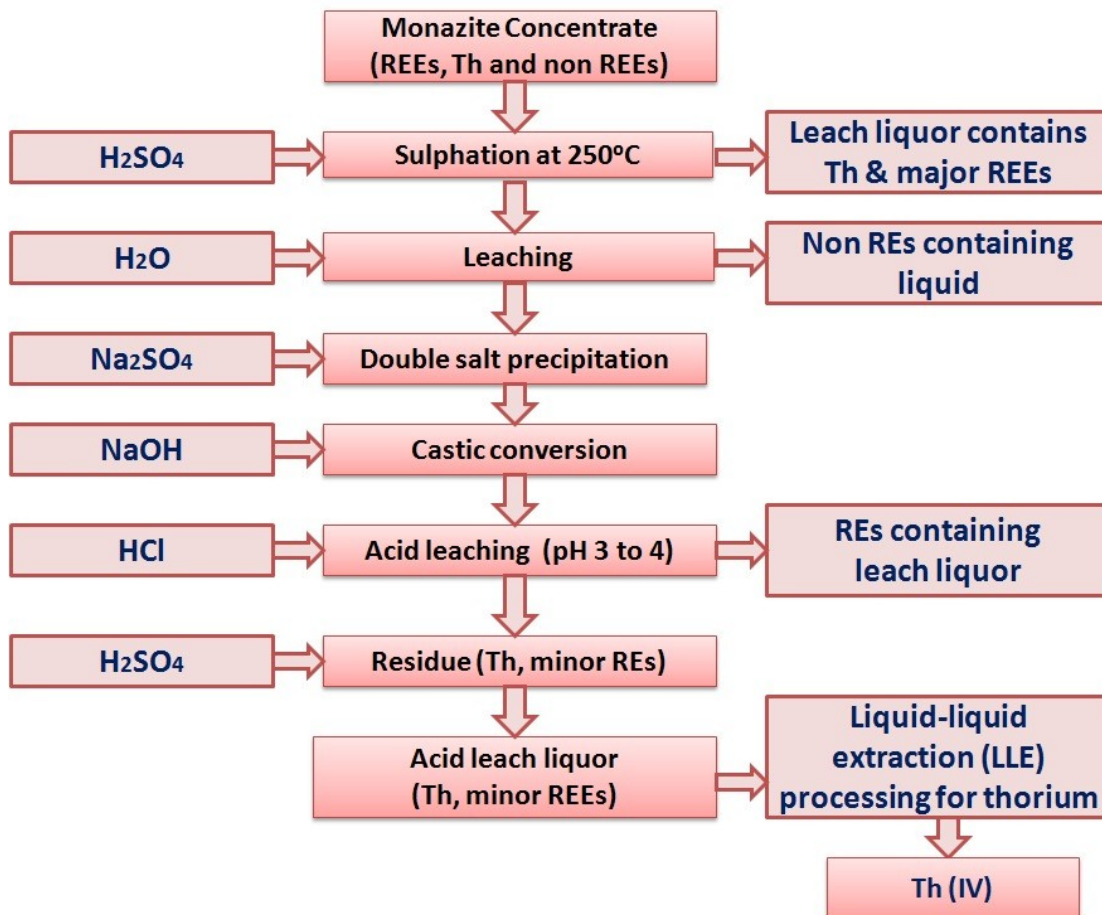


Figure 10: Flowchart for the synthesis of thorium-rich residue associated with minor quantities of rare earth elements (REE) (36).

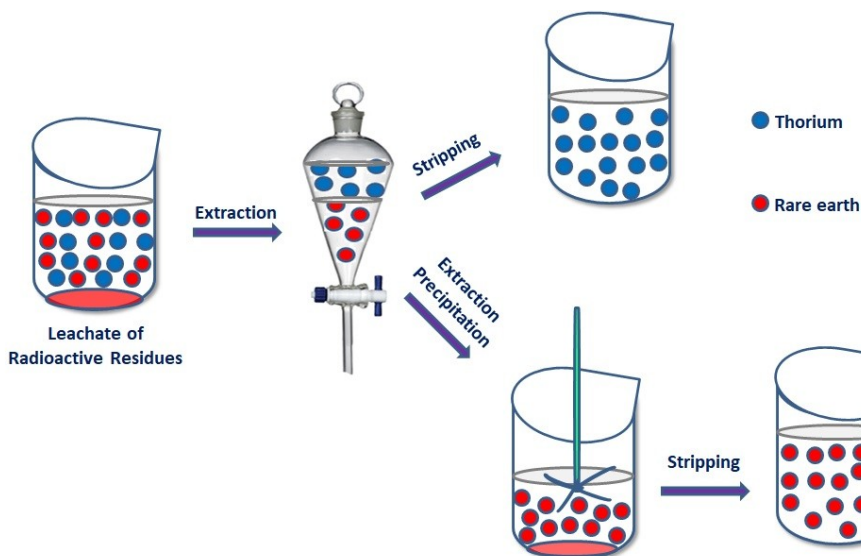


Figure 11: A cost-effective process for recovering thorium and rare earths from radioactive residues.

$$\text{Distribution ratio } (D) = \frac{(M)_O}{(M)_a} \quad (2)$$

$$\text{Stripping percentage (St\%)} = \frac{(M)_a}{(M)_{O,i}} \times 100 \quad (4)$$

$$\text{Separation Factor } (\beta) = \frac{D_1}{D_2} \quad (3)$$

$$\text{Extraction percentage (E\%)} = \frac{(M)_O}{(M)_{a,i}} \times 100 \quad (5)$$

Where $(M)_a$ and $(M)_o$ represent the metal concentrations in the aqueous and organic phases at equilibrium, respectively. $(M)_{a,i}$ and $(M)_{o,i}$ denotes the initial metal ions concentration in the aqueous phase and loaded organic phase respectively.

$$\text{Extraction efficiency} = \frac{C_{M(o)}}{C_{M(o)} \times C_{M(a)}} \times 100\% \quad (6)$$

$$\text{Recovery efficiency} = \frac{C_{M(a)} \times V_{(a)}}{C_{M(a),i} \times V_{(a),i}} \times 100\% \quad (7)$$

$$\text{Stripping efficiency} = \frac{C_{M(a)} \times V_{(a)}}{C_{M(o),i} \times V_{(o)}} \times 100\% \quad (8)$$

Where $C_{M(o)}$, $C_{M(a)}$ are the concentration metal ions in the organic and aqueous phases respectively; $V_{(o)}$ and $V_{(a)}$ are the volume of organic and aqueous phases, respectively; $V_{(a),i}$ is the initial volume of aqueous phase; $C_{M(o),i}$ and $C_{M(a),i}$ are the initial concentration of a metal in organic phase and aqueous phases, respectively.

Y. Lu et al. (74) reported the separation factors between Ce(IV) and Th(IV) at different acidity concentration and their work has shown a recovery of thorium 98% by using a -aminophosphate in acid concentration of H_2SO_4 . X. Yang et al. (73) found the separation factors between Th(IV) and other metal ions (RE, Fe and Al) at different acidity concentrations. The values of separation factor are higher than 160 at 1.0 mol/L of H^+ ion. So, Cextrant 230 can be used as a good extractant for the removal of thorium from a mixed solution of REs and other metals (Fe, Al etc.). The extraction capacity of 5% (v/v) cextrant 230 for Th(IV) was found 4.08 g/L. Again, J. Su et al. (74) reported a fractional extraction experiment for separating thorium and enriching of rare earth elements. They found the yield of Th is higher than 99.9% and the concentration of rare earth elements was 183.89 g/L. Chung et al. (36) reported that 2.5 mol/L acidic conditions was suitable for their work. HCl and H_2SO_4 were tested for recovery of the thorium and HCl showed better results than H_2SO_4 . Higher molar HCl (5 mol/L, 250 °C) appears to be suitable for thorium. As reported by S M Ghag and S D Pawar (84), the separation of Th(IV) and U(VI) from multicomponent mixtures with cyanex®-923 in toluene with specific concentrations with acid, Th(IV) was found to be 99.3% in a 20 µg sample. U (VI) and Th(IV) were extracted in the acid concentration range 5×10^{-5} to 1×10^{-4} M and 5×10^{-5} to 5×10^{-3} M respectively.. J C Amaral et al. (78) proposed a process to recover Thorium, Uranium and REs from an industrial residue. Under the optimized condition, the metal dissolution of 81% (using H_2SO_4) for thorium was obtained. S M

Ibrahim et al. (85), HDEHDGA provides useful selectivity for Th(IV) over light Ln(III) ions, giving new processes for actinides-lanthanides extraction/separation and REs production in the industry. Sulfuric acid digestion followed by water action was found to be the simplest technique to solubilize the metals.

CONCLUSIONS

The different methods of extraction of thorium such as selective extraction of thorium using phosphorodiamidate, selective cloud point extraction of thorium, extraction of thorium from sulfuric acid baking and leaching of monazite, extraction of thorium from chloride solution using Schiff base were discussed. Out of all the discussed methods of extraction, cloud point extraction is considered the best of all as it is more precise, accurate, and cheap as compared with other methods. The method is environmentally friendly as it gives very few toxic by-products. HCl and H_2SO_4 were taken for recovery of the metallic element and the former one is showing better results over latter one. Later on, high molar HCl (5 mol/L) seems to be appropriate for metallic element recovery. The primary aims of all these methods of extractions and recoveries of thorium are for getting an efficient amount of thorium and procedure to get high efficiency of thorium.

CONFLICT OF INTEREST

The authors declared no conflict of interest.

ACKNOWLEDGMENTS

The authors are thankful to Prof. Bipin B. Swain, former Professor of Khallikote University, Berhampur, India; Prof. Sarat Kumar Dash, Department of Physics, Regional Institute of Education, Bhubaneswar, India; Dr. Wael I. Mortada, Clinical Chemistry Laboratory, Urology and Nephrology Center, Mansoura University, Egypt; Dr. Zeinab Farouk Hassan AKL, Nuclear Safeguards and Physical Protection Department, Egyptian Atomic Energy Authority (EAEA), Egypt; Dr. Liao Wuping, State Key Laboratory of Rare Earth Resource Utilization, Changchun Institute of Applied Chemistry, Chinese Academy of Sciences, Changchun, China and Dr. Mohammed Farid Cheira, Research Sector, Nuclear Materials Authority, Cairo, Egypt for their valuable inputs in preparing our review article.

REFERENCES

1. Aziman ES, Ismail AF, Muttalib NA, Hanifah MS. Investigation of thorium separation from rare-earth extraction residue via electrosorption with carbon based electrode toward reducing waste volume. Nuclear Engineering and Technology. 2021 Sep;53(9):2926–36. <DOI>.

2. Kademani B, Vijai K, Anil S, Anil K, Lalit M, Surwase G. Scientometric dimensions of thorium research in India. *DESIDOC Bull Inf Technol.* 2006;26(3):9–25.
3. Balakrishna P. ThO₂ and (U,Th)O₂ processing—A review. *NS.* 2012;04(11):943–9. [<DOI>](#).
4. Humphrey UE, Khandaker MU. Viability of thorium-based nuclear fuel cycle for the next generation nuclear reactor: Issues and prospects. *Renewable and Sustainable Energy Reviews.* 2018 Dec;97:259–75. [<DOI>](#).
5. Badash L. The discovery of thorium's radioactivity. *J Chem Educ.* 1966 Apr;43(4):219. [<DOI>](#).
6. Ünak T. What is the potential use of thorium in the future energy production technology? *Progress in Nuclear Energy.* 2000 Jan;37(1–4):137–44. [<DOI>](#).
7. Wilson D. The use of thorium as an alternative nuclear fuel [Internet]. Australian Atomic Energy Commission; 1982 [cited 2021 Nov 1]. [<URL>](#).
8. Lu Y, Wei H, Zhang Z, Li Y, Wu G, Liao W. Selective extraction and separation of thorium from rare earths by a phosphorodiamidate extractant. *Hydrometallurgy.* 2016 Aug;163:192–7. [<DOI>](#).
9. Tani H, Kamidate T, Watanabe H. Micelle-mediated extraction. *Journal of Chromatography A.* 1997 Sep;780(1–2):229–41. [<DOI>](#).
10. Gupta CK, Krishnamurthy N. Extractive metallurgy of rare earths. *International Materials Reviews.* 1992 Jan;37(1):197–248. [<DOI>](#).
11. Cheira MF, Orabi AS, Hassanin MA, Hassan SM. Solvent extraction of thorium (IV) from chloride solution using Schiff base and its application for spectrophotometric determination. *Chemical Data Collections.* 2018 Mar;13–14:84–103. [<DOI>](#).
12. Eskandari Nasab M. Solvent extraction separation of uranium(VI) and thorium(IV) with neutral organophosphorus and amine ligands. *Fuel.* 2014 Jan;116:595–600. [<DOI>](#).
13. Tan M, Huang C, Ding S, Li F, Li Q, Zhang L, et al. Highly efficient extraction separation of uranium(VI) and thorium(IV) from nitric acid solution with di(1-methyl-heptyl) methyl phosphonate. *Separation and Purification Technology.* 2015 May;146:192–8. [<DOI>](#).
14. Dong Y, Li S, Su X, Wang Y, Shen Y, Sun X. Separation of thorium from rare earths with high-performance diphenyl phosphate extractant. *Hydrometallurgy.* 2017 Aug;171:387–93. [<DOI>](#).
15. Kalina DG, Mason GW, Philip Horwitz E. The thermodynamics of extraction of U(VI) and Th(IV) from nitric acid by neutral phosphorus-based organic compounds. *Journal of Inorganic and Nuclear Chemistry.* 1981 Jan;43(1):159–63. [<DOI>](#).
16. Lu Y, Bi Y, Bai Y, Liao W. Extraction and separation of thorium and rare earths from nitrate medium with *p*-phosphorylated calixarene: Extraction and separation of thorium and rare earths with calixarene derivative. *J Chem Technol Biotechnol.* 2013 Oct;88(10):1836–40. [<DOI>](#).
17. Sun X, Dong Y, Wang Y, Chai Y. The synergistic extraction of heavy rare earth elements using EHEHP-type and BTMPP-type functional ionic liquids. *RSC Adv.* 2015;5(61):49500–7. [<DOI>](#).
18. Prabhu DR, Sengupta A, Murali MS, Pathak PN. Role of diluents in the comparative extraction of Th(IV), U(VI) and other relevant metal ions by DHOA and TBP from nitric acid media and simulated wastes: Reprocessing of U–Th based fuel in perspective. *Hydrometallurgy.* 2015 Dec;158:132–8. [<DOI>](#).
19. Bezerra MA, Ferreira da Mata Cerqueira UM, Ferreira SLC, Novaes CG, Novais FC, Valasques GS, et al. Recent developments in the application of cloud point extraction as procedure for speciation of trace elements. *Applied Spectroscopy Reviews.* 2021 May 12;1–15. [<DOI>](#).
20. Bezerra M de A, Arruda MAZ, Ferreira SLC. Cloud Point Extraction as a Procedure of Separation and Pre-Concentration for Metal Determination Using Spectroanalytical Techniques: A Review. *Applied Spectroscopy Reviews.* 2005 Nov;40(4):269–99. [<DOI>](#).
21. Liu J, Liu R, Yin Y, Jiang G. Triton X-114 based cloud point extraction: a thermoreversible approach for separation/concentration and dispersion of nanomaterials in the aqueous phase. *Chem Commun.* 2009;(12):1514. [<DOI>](#).
22. Mortada WI. Recent developments and applications of cloud point extraction: A critical review. *Microchemical Journal.* 2020 Sep 1;157:105055. [<DOI>](#).
23. Khalifa ME, Kenawy IMM, Hassanien MM, Elnagar MM. Mixed Micelle-mediated Extraction and Separation of Scandium from Yttrium and Some Lanthanide Ions. *Anal Sci.* 2016;32(4):395–400. [<DOI>](#).
24. Stalikas CD. Micelle-mediated extraction as a tool for separation and preconcentration in metal

- analysis. *TrAC Trends in Analytical Chemistry*. 2002 May;21(5):343–55. [<DOI>](#).
25. Ravi Kumar K, Shyamala P. Catanionic mixed micellar cloud point extraction of metal ions in coal fly ash samples and their determination by CS-ETAAS. *Journal of Environmental Chemical Engineering*. 2019 Jun;7(3):103119. [<DOI>](#).
26. Akl ZF, Hegazy MA. Selective cloud point extraction of thorium (IV) using tetraazonium based ionic liquid. *Journal of Environmental Chemical Engineering*. 2020 Oct;8(5):104185. [<DOI>](#).
27. Demol J, Ho E, Senanayake G. Sulfuric acid baking and leaching of rare earth elements, thorium and phosphate from a monazite concentrate: Effect of bake temperature from 200 to 800 °C. *Hydrometallurgy*. 2018 Aug;179:254–67. [<DOI>](#).
28. Xie F, Zhang TA, Dreisinger D, Doyle F. A critical review on solvent extraction of rare earths from aqueous solutions. *Minerals Engineering*. 2014 Feb;56:10–28. [<DOI>](#).
29. Zhu Z, Pranolo Y, Cheng CY. Separation of uranium and thorium from rare earths for rare earth production – A review. *Minerals Engineering*. 2015 Jun;77:185–96. [<DOI>](#).
30. Zhang Z, Jia Q, Liao W. Progress in the Separation Processes for Rare Earth Resources. In: *Handbook on the Physics and Chemistry of Rare Earths* [Internet]. Elsevier; 2015 [cited 2021 Nov 1]. p. 287–376. [<URL>](#).
31. Teixeira LAV, Silva RG, Majuste D, Ciminelli V. Selective Extraction of Rare Earth Elements from Complex Monazite Ores. In: Davis BR, Moats MS, Wang S, Gregurek D, Kapusta J, Battle TP, et al., editors. *Extraction 2018* [Internet]. Cham: Springer International Publishing; 2018. p. 2381–90. (The Minerals, Metals & Materials Series). Available from: [<URL>](#).
32. Moustafa MI, Abdelfattah NA. Physical and Chemical Beneficiation of the Egyptian Beach Monazite: Beneficiation of monazite. *Resource Geology*. 2010 Aug 24;60(3):288–99. [<DOI>](#).
33. Lim H, Ibana D, Eksteen J. Leaching of rare earths from fine-grained zirconosilicate ore. *Journal of Rare Earths*. 2016 Sep;34(9):908–16.
34. Berry L, Agarwal V, Galvin J, Safarzadeh MS. Decomposition of monazite concentrate in sulphuric acid. *Canadian Metallurgical Quarterly*. 2018 Oct 2;57(4):422–33. [<DOI>](#).
35. Kumari A, Jha MK, Yoo K, Panda R, Lee JY, Kumar JR, et al. Advanced process to dephosphorize monazite for effective leaching of rare earth metals (REMs). *Hydrometallurgy*. 2019 Aug;187:203–11. [<DOI>](#).
36. Chung KW, Yoon H-S, Kim C-J, Lee J-Y, Jyothi RK. Solvent extraction, separation and recovery of thorium from Korean monazite leach liquors for nuclear industry applications. *Journal of Industrial and Engineering Chemistry*. 2020 Mar;83:72–80. [<DOI>](#).
37. Demol J, Ho E, Soldenhoff K, Senanayake G. The sulfuric acid bake and leach route for processing of rare earth ores and concentrates: A review. *Hydrometallurgy*. 2019 Sep;188:123–39. [<DOI>](#).
38. Mccoy H. Method of manufacturing thorium nitrate. US 1,366,128.
39. Pilkington ES, Wylie AW. Production of rare earth and thorium compounds from monazite. Part I. *J Chem Technol Biotechnol*. 1947 Nov;66(11):387–94. [<DOI>](#).
40. Urie RW. Pilot plant production of rare earth hydroxides and thorium oxalate from monazite. *J Chem Technol Biotechnol*. 1947 Dec;66(12):437–9. [<DOI>](#).
41. Shaw K. A process for separating thorium compounds from monazite sands [PhD Thesis]. Iowa State University; 1953.
42. Barghusen J, Smutz M. Processing of Monazite Sands. *Ind Eng Chem*. 1958 Dec;50(12):1754–5. [<DOI>](#).
43. Borrowman S, Rosenbaum J. Recovery of thorium from a Wyoming ore. US Department of the Interior, Bureau of Mines; 1962.
44. Tobia SK. Separation of the light lanthanons from Egyptian monazite. *J Appl Chem*. 2007 May 4;13(4):189–92. [<DOI>](#).
45. Kawamura K, Takeuchi T, Ando T. Direct recovery of thorium and rare earths as sulphate precipitates from digestion mass. *Trans Nat Res Inst Met (Japan)*. 1966;8(1).
46. Shamsuddin M. *Hydrometallurgy*. In: *Physical Chemistry of Metallurgical Processes, Second Edition* [Internet]. Cham: Springer International Publishing; 2021. p. 429–529. (The Minerals, Metals & Materials Series). [<URL>](#).
47. Teriele W. A process for the recovery of mixed rare-earth oxides from monazite. National Inst. for Metallurgy; 1982.
48. Al-Fulaij O, Abdel-Aziz I. Extraction of lanthanons from Egyptian monazite. *Ihd J Chem*. 1996;35(2):168–9. [<URL>](#).

49. Chen Y, Wei Y, He L, Tang F. Separation of thorium and uranium in nitric acid solution using silica based anion exchange resin. *Journal of Chromatography A*. 2016 Sep;1466:37-41. [<DOI>](#).
50. Papangelakis V, Moldoveanu G. Recovery of rare earth elements from clay minerals. In *Milos*; 2014. p. 191-202.
51. Ahmed S, Helaly O, Abd El-Ghany M. Evaluation of rare earth double sulphate precipitation from monazite leach solutions. *Int J Inorg Bioinorg Chem*. 2015;5(1):1-8.
52. Singh H, Gupta CK. Solvent Extraction in Production and Processing of Uranium and Thorium. *Mineral Processing and Extractive Metallurgy Review*. 2000 Sep;21(1-5):307-49. [<DOI>](#).
53. Bunzli J, Pecharsky V. *Handbook on the Physics and Chemistry of Rare Earths: Including Actinides*. Elsevier; 2016.
54. Sadri F, Rashchi F, Amini A. Hydrometallurgical digestion and leaching of Iranian monazite concentrate containing rare earth elements Th, Ce, La and Nd. *International Journal of Mineral Processing*. 2017 Feb;159:7-15. [<DOI>](#).
55. Soltani F, Abdollahy M, Petersen J, Ram R, Becker M, Javad Koleini SM, et al. Leaching and recovery of phosphate and rare earth elements from an iron-rich fluorapatite concentrate: Part I: Direct baking of the concentrate. *Hydrometallurgy*. 2018 May;177:66-78. [<DOI>](#).
56. da Silva RG, de Morais CA, Teixeira LV, de Oliveira ÉD. Selective removal of impurities from rare earth sulphuric liquor using different reagents. *Minerals Engineering*. 2018 Oct;127:238-46. [<DOI>](#).
57. Patkar S, Burungale A, Patil R. Separation and liquid-liquid extraction of thorium (IV) as sulphate complex with synergistic mixture of Nn-octylaniline and trioctylamine as an extractant. *Rasayan J Chem*. 2009;2:4825-32.
58. Sehati N, Shiri-Yekta Z, Zamani AA, Yaftian MR, Noshiranzadeh N. Solvent Extraction of Th(IV) and Eu(III) Ions by 3,5-di-*tert*-butyl-2-Hydroxy-Benzaldehyde Oxime from Aqueous Chloride Media. *Separation Science and Technology*. 2012 Mar;47(5):670-6. [<DOI>](#).
59. Curtui M, Haiduc I, Haiduc I. Solvent extraction of thorium (IV) with dialkyldithiophosphoric acids. *Journal of Radioanalytical and Nuclear Chemistry Letters*. 1992 May;165(2):95-105. [<DOI>](#).
60. Bayyari MA, Nazal MK, Khalili FI. The effect of ionic strength on the extraction of thorium(IV) from perchlorate solution by didodecylphosphoric acid (HDDPA). *Arabian Journal of Chemistry*. 2010 Apr;3(2):115-9. [<DOI>](#).
61. Panda CR, Chakravorty V, Dash KC. A quadridentate Schiff base as an extractant for thorium/IV/, uranium/VI/ and zirconium/IV/. *Journal of Radioanalytical and Nuclear Chemistry Letters*. 1987 Jan;108(2):65-75. [<DOI>](#).
62. Pawar RR, Suryavanshi VJ, Salunkhe ST, Patil SS, Mulik GN. Liquid-liquid extraction of thorium(IV) with N-n-heptylaniline from acid media. *J Radioanal Nucl Chem*. 2017 Jan;311(1):419-26. [<DOI>](#).
63. Binnemans K, Jones PT, Blanpain B, Van Gerven T, Pontikes Y. Towards zero-waste valorisation of rare-earth-containing industrial process residues: a critical review. *Journal of Cleaner Production*. 2015 Jul;99:17-38. [<DOI>](#).
64. Sinha S, Abhilash, Meshram P, Pandey BD. Metallurgical processes for the recovery and recycling of lanthanum from various resources—A review. *Hydrometallurgy*. 2016 Mar;160:47-59. [<DOI>](#).
65. Su J, Xu R, Ni S, Li F, Sun X. A cost-effective process for recovering thorium and rare earths from radioactive residues. *Journal of Cleaner Production*. 2020 May;254:119931. [<DOI>](#).
66. Lapidus GT, Doyle FM. Selective thorium and uranium extraction from monazite: I. Single-stage oxalate leaching. *Hydrometallurgy*. 2015 Apr;154:102-10. [<DOI>](#).
67. Matveeva E, Sharova E, Turanov A, Karandashev V, Odinets I. Extraction properties of β -aminophosphine oxides towards lanthanides and alkaline earth metals. *Open Chemistry*. 2012 Dec 1;10(6):1933-41. [<DOI>](#).
68. Garifzyanov AR, Zakharov SV, Kryukov SV, Galkin VI, Cherkasov RA. Liquid Extraction of Noble Metal Ions with an α -Amino Phosphonate. *Russ J Gen Chem*. 2005 Aug;75(8):1208-11. [<DOI>](#).
69. Cherkasov RA, Garifzyanov AR, Bazanova EB, Davletshin RR, Leont'eva SV. Liquid extraction of some rare earth elements with aminomethylphosphine oxides. *Russ J Gen Chem*. 2012 Jan;82(1):33-42. [<DOI>](#).
70. Jagodić V, Herak MJ, Šipalo B, Radošević J. Solvent extraction study of lanthanum and europium by acidic esters of aminophosphonic acids. *Journal of Inorganic and Nuclear Chemistry*. 1971 Aug;33(8):2651-9. [<DOI>](#).

71. Hung NT, Thuan LB, Thanh TC, Watanabe M, Khoai DV, Thuy NT, et al. Separation of thorium and uranium from xenotime leach solutions by solvent extraction using primary and tertiary amines. *Hydrometallurgy*. 2020 Dec;198:105506. [<DOI>](#).
72. Chen S, Zhang Z, Kuang S, Li Y, Huang X, Liao W. Separation of zirconium from hafnium in sulfate medium using solvent extraction with a new reagent BEAP. *Hydrometallurgy*. 2017 May;169:607–11. [<DOI>](#).
73. Yang X, Zhang Z, Kuang S, Wei H, Li Y, Wu G, et al. Removal of thorium and uranium from leach solutions of ion-adsorption rare earth ores by solvent extraction with Cextrant 230. *Hydrometallurgy*. 2020 Jun;194:105343. [<DOI>](#).
74. Lu Y, Zhang Z, Li Y, Liao W. Extraction and recovery of cerium(IV) and thorium(IV) from sulphate medium by an α -aminophosphonate extractant. *Journal of Rare Earths*. 2017 Jan;35(1):34–40. [<DOI>](#).
75. Su J, Guo X, Gao Y, Wu S, Xu R, Sun X. Recovery of thorium and rare earths from leachate of ion-absorbed rare earth radioactive residues with N1923 and Cyanex® 572. *Journal of Rare Earths*. 2021 Oct;39(10):1273–81. [<DOI>](#).
76. Sun P, Huang K, Wang X, Song W, Zheng H, Liu H. Separation of V from alkaline solution containing Cr using acidified primary amine N1923 with the addition of trisodium citrate. *Separation and Purification Technology*. 2017 May;179:504–12. [<DOI>](#).
77. Abreu RD, Morais CA. Purification of rare earth elements from monazite sulphuric acid leach liquor and the production of high-purity ceric oxide. *Minerals Engineering*. 2010 May;23(6):536–40. [<DOI>](#).
78. Amaral JCBS, Morais CA. Thorium and uranium extraction from rare earth elements in monazite sulfuric acid liquor through solvent extraction. *Minerals Engineering*. 2010 May;23(6):498–503. [<DOI>](#).
79. Amaral JCBS, Sá MLCG, Morais CA. Recovery of uranium, thorium and rare earth from industrial residues. *Hydrometallurgy*. 2018 Nov;181:148–55. [<DOI>](#).
80. Park KH, Kim HI, Parhi PK, Mishra D, Nam CW, Park JT, et al. Extraction of metals from Mo-Ni/Al₂O₃ spent catalyst using H₂SO₄ baking-leaching-solvent extraction technique. *Journal of Industrial and Engineering Chemistry*. 2012 Nov;18(6):2036–45. [<DOI>](#).
81. Kiegiel K, Abramowska A, Biełuszka P, Zakrzewska-Kołtuniewicz G, Wołkowicz S. Solvent extraction of uranium from leach solutions obtained in processing of Polish low-grade ores. *J Radioanal Nucl Chem*. 2017 Jan;311(1):589–98. [<DOI>](#).
82. Zalupski PR, Klaehn JR, Peterman DR. Complete Recovery of Actinides from UREX-like Raffinates Using a Combination of Hard and Soft Donor Ligands. II. Soft Donor Structure Variation. Solvent Extraction and Ion Exchange. 2015 Sep 19;33(6):523–39. [<DOI>](#).
83. Su J, Gao Y, Ni S, Xu R, Sun X. A safer and cleaner process for recovering thorium and rare earth elements from radioactive waste residue. *Journal of Hazardous Materials*. 2021 Mar;406:124654. [<DOI>](#).
84. Ghag S, Pawar S. Extraction and separation of U(VI) and Th(IV) from hydrobromic acid media using Cyanex-923 extractant. *J Serb Chem Soc*. 2010;75(11):1549–57. [<DOI>](#).
85. Ibrahim SM, Zhang Y, Xue Y, Yang S, Ma F, Tian G. Extraction of Lanthanides(III) along with Thorium(IV) from Chloride Solutions by *N,N*-di(2-Ethylhexyl)-Diglycolamic Acid. *Solvent Extraction and Ion Exchange*. 2020 Jun 6;38(4):417–29. [<DOI>](#).



Comparative Determination of Melittin by Capillary Electrophoretic Methods

Melda Akay¹ , Zeynep Kalaycıoğlu¹ , Sevgi Kolaylı² , F. Bedia Erım¹  

¹Istanbul Technical University, Department of Chemistry, Istanbul, Turkey

²Karadeniz Technical University, Department of Chemistry, Trabzon, Turkey

Abstract: Bee venom from honey bees (*Apis Mellifera* L.) is known to have many pharmacological and biological properties. Melittin, a peptide consisting of 26 amino acids, is known as the main component of bee venom. The study aims to develop a rapid capillary electrophoresis method for separating and quantifying melittin in honeybee venom. Since melittin is a basic peptide, it will adhere to the capillary wall during separation. Two different methods were developed in this study for the capillary electrophoretic separation of melittin. As a first approach, a low pH buffer system was used. For the second approach, the capillary column was coated with a positively charged polymer (PEI). With both methods developed, the migration of melittin in the capillary was achieved by preventing wall adsorption. Melittin migrated in 6 min when the low-pH buffer system was applied, whereas its migration time is longer than 10 min in the PEI-coated capillary column. Thus, a low-pH buffer system was preferred for the analysis of the actual bee-venom sample. 100 mmol L⁻¹ phosphoric acid/sodium dihydrogen phosphate system at pH 1.55 was chosen as separation buffer. As a conclusion, a fast and reliable method was developed for the determination of melittin in honeybee venom. The method was applied to an Anatolian bee venom sample to highlight the melittin amount. The melittin amount was found as 24.5 ± 3.4 g 100 g⁻¹ in the bee venom sample.

Keywords: Apitherapy, Apitoxin, Melittin, Capillary electrophoresis, Bee venom.

Submitted: June 08, 2021. **Accepted:** November 05, 2021.

Cite this: Akay M, Kalaycıoğlu Z, Kolaylı S, Erım FB. Comparative Determination of Melittin by Capillary Electrophoretic Methods. JOTCSA. 2021;8(4):1211-6.

DOI: <https://doi.org/10.18596/jotcsa.949188>.

***Corresponding author. E-mail:** erim@itu.edu.tr.

INTRODUCTION

Honey bees (*Apis mellifera* L.) are one of the most important insects that associated with a number of anthropogenic activities (1). The most well-known examples are honey production, pollen, resins, wax, royal jelly, and bee venom which is also known as apitoxin (2). Extensive studies have been conducted on the substances produced by bees due to their numerous therapeutic applications (3-6).

Bee venom (BV) is one of the most important ones among the substances produced by bees (7). It is synthesized by the glands located in the abdomen of female worker bees (7). The medicinal application of bee venom, also known as bee venom therapy, has

been used as an alternative medicine since ancient times (8). The application could be either indirectly by extracting bee venom with an electrical stimulus or directly via bee stings (7).

BV is a colorless liquid whose pH changes between 4.5-5.5. It consists of 88% water, while the remaining 12% contains peptides (such as melittin, adolapin, apamin, mast cell degranulating peptide), enzymes (such as phospholipase A2 and hyaluronidase), amino acids, and volatile compounds. The biological activities, including anti-cancer, anti-bacterial, anti-viral, anti-HIV, and anti-inflammation of these components, have been reported (9, 10). Moreover, there are many studies on BV components that have potential treating

effects on central nervous system diseases such as Alzheimer's disease (AD), Parkinson's disease (PD), and amyotrophic lateral sclerosis (ALS) (11).

One of the main components of bee venom is melittin. It is a toxic, water-soluble, and small peptide consisting of 26 amino acid residues (12).

The chemical structure of melittin was given in Figure 1. Various pharmacological, toxicological, and biological properties such as antifungal, antibacterial, and antiviral activities of melittin have been reported (13, 14). The inhibitory effect of melittin on the proliferation of different cancer cells and gastrointestinal cells (15).

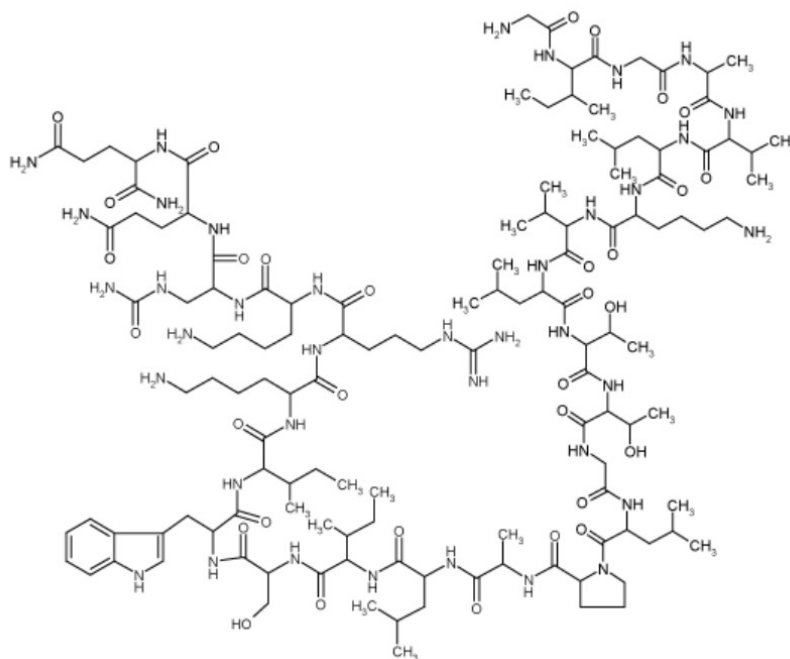


Figure 1: Structure of melittin.

During the last two decades, some investigations have been carried out in order to separate, identify, and quantify the major bee venom constituents. The majority of these studies are on liquid chromatography (16-21). A capillary electrophoresis technique was also applied to find the amounts of peptides, including melittin in bee venom samples (22). Among these studies, we could find only one study on Anatolian bee venom (21) by HPLC.

Many methods in order to characterize bee venom have been described. These either determine individual components or measure the biological effects of bee venom and its bioactive components.

It is known that the honeybee venom has a complex nature. Thus its content and the amount of the ingredients may depend on many factors such as the bee strain, the collection year and season, and the sample collection area. Only one CE method has been reported so far for the analysis of melittin (22). The highest melittin amount was determined in Polish bee venom samples with 70.1% in the literature (20). The samples from Iran (66.4%) (16) and Romania (64.2%) (18) followed the Polish bee venom (20). Whereas the lowest melittin amount found was in another Polish sample with 9.16% (19). The published results obtained from these studies were given in Table 1.

Table 1: The content of melittin in bee venom samples.

Area of Sample Collection	Melittin (g 100 g ⁻¹)	Method	Ref.
Iran	21.9-66.4	HPLC-PDA	(16)
China	33.9-46.2	UPLC-QqTOF-MS	(17)
Romania	27.7-64.2	HPLC-PDA	(18)
Poland	9.16-19.3	LC-DAD	(19)
Poland	61.1-70.1	HPLC-DAD	(20)
Anatolia	36.9-46.8	HPLC-UV	(21)
Georgia and Poland	25.4-60.3	CE-DAD	(22)

Anatolia has a great beekeeping potential due to its very rich flora and suitable ecology. Determination of the active compounds in apicultural products is

critical for diagnosing the quality of the products. In this study, a capillary electrophoretic technique has been developed for melittin. The developed

technique has been applied for the determination of melittin in Anatolian honey bee venom.

EXPERIMENTAL SECTION

Chemicals

Standard melittin was from Sigma-Aldrich (Steinheim, Germany). Polyethyleneimine (PEI), orthophosphoric acid, acetic acid, hydrochloric acid, and sodium hydroxide were purchased from Merck (Darmstadt, Germany). All solutions were prepared with water purified by an Elga Purelab Option-7-15 model system (Elga, UK).

Dried bee venom sample were obtained from Düzce University, Beekeeping Research Development and Application Centre (DAGEM).

Preparation of Standard Solution and Bee Venom Samples

Standard solution of melittin was prepared at 1.0 mmol L⁻¹ level using distilled water and stored at deep freeze until the analysis. The calibration solutions were prepared by diluting the stock standard melittin solution (23). The calibration ranges were between 70-350 µg mL⁻¹ for low pH buffer system and 35-350 µg mL⁻¹ for PEI-coated capillary column system.

One mg of crude bee venom sample was weighed. The extraction of melittin from bee venom was performed by deionized water. The mixture was vortexed for 5 min at 2500 rpm and sonicated for 30 min. The supernatant was filtered through a microfilter.

Instrumentation and Conditions of Analysis

A capillary electrophoresis/UV-DAD detector system (Agilent 1600, Waldbronn, Germany) was utilized for melittin analysis. The Agilent ChemStation software was used for the data processing. The separations were performed in a bare fused silica capillary and PEI coated fused silica capillary column. Both columns were 50 µm i.d. (Polymicro Technology, Phoenix, AZ, USA). The length of the capillary column was 65 cm in total and the effective length was 57 cm. In the bare fused silica column, the separation was performed at 25 kV. In the PEI-coated column, the separation was performed at -25 kV. The temperature was set at 25 °C, and injections were made at 50 mbar for 6 s in both approaches.

Before first use, the capillary was conditioned by rinsing with 1 mol L⁻¹ NaOH for 30 min followed by deionized water for 10 min. At the beginning of each working day, the capillary was flushed with 1 mol L⁻¹

NaOH for 15 min, deionized water for 10 min, and working buffer for 10 min, respectively. Between runs, the capillary was flushed for 2 min with 1 mol L⁻¹ NaOH, 2 min with deionized water, 5 min with buffer, respectively. For PEI coated column studies, the capillary was flushed by running buffer for 15 min at the beginning of every working day and running buffer for 2 min between runs.

In this study, we focused on two different approaches in order to prevent capillary wall's adsorption. The first approach is based on the low pH buffer system to suppress the negative wall charge significantly (24). The second approach is to coat the capillary inner wall with a suitable positively charged polymer such as PEI (25). Thus, the capillary inner wall is positively charged. In this case, injection is performed from the cathodic side.

Dynamic Coating Process for Capillary Column

The capillary coating process was performed as described in the literature (22). The fused silica capillary was flushed with 1 mol L⁻¹ NaOH solution for 30 min and then deionized water for 15 min. Then the capillary was flushed with 10% (v/v) PEI solution in water at 1000 mbar for 10 min. The solution of PEI was left in the capillary for one hour. After 1 h, the PEI polymer solution was pressed out of the capillary with air at 1000 mbar. Finally, the capillary was rinsed with water for 15 min and running buffer for 15 min.

RESULTS AND DISCUSSION

In the capillary electrophoretic separation of basic peptides such as melittin, the major difficulty is the possibility of capillary wall's adsorption. Efficiency of separation is decreased due to the capillary wall's adsorption. It occurs due to the electrostatic attraction which becomes between positively charged species and negatively charged silanol groups of the capillary wall.

Figure 2 was given for the comparison of the electropherograms of melittin which was performed at low pH (Figure 2A) and in PEI-coated silica column (Figure 2B). In the separation and identification of melittin which is performed at low pH, 100 mmol L⁻¹ orthophosphoric acid/sodium dihydrogen phosphate buffer system at pH 1.55 was chosen as the separation buffer (Fig. 2A). Whereas 50 mmol L⁻¹ acetic acid/acetate buffer solution (pH 5.50) was performed in PEI-coated silica capillary column (Fig. 2B). The optimal concentrations of both buffer systems were found according to the peak symmetry and peak height of melittin.

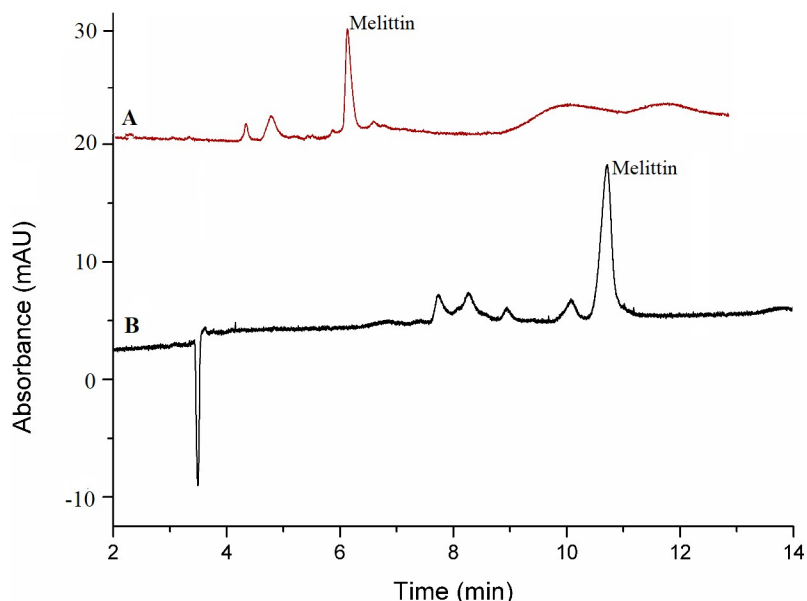


Figure 2: Electropherogram of 175 µg mL⁻¹ standard melittin solution. Conditions of analysis: (A): Bare fused silica column, Buffer: 100 mmol L⁻¹ orthophosphoric acid at pH 1.55; Voltage: 25 kV; (B): PEI-coated silica column, Buffer: 50 mmol L⁻¹ acetic acid pH 5.50; Voltage: -25 kV (Temperature: 25 °C; Injection: 50 mbar, 6 s; Detection: UV-DAD detector, λ: 200 nm)

Validation studies were performed for both two approaches, and the data was given in Table 2. Calibration curves were constructed by plotting corrected peak areas versus analyte concentrations. The precision of the method was tested by intra- and inter-day precisions. For the intra-day precision of the methods, standard melittin was injected five times in one day, and for the inter-day precision, it was injected 15 times in three days. The LOD and the LOQ values were calculated as three times and ten times of the average noise taken from three different baseline areas, respectively.

The RSD% values of both methods are below the values accepted for CE analysis. The LOD value

appears slightly lower in the PEI coated column than the uncoated column in the separation. However, considering the amount of melittin in bee venom, this difference does not become significant. Both methods seem suitable for analyzing melittin in bee venom. On the other hand, melittin's arrival time in low pH buffer in uncoated capillaries is significantly shorter than the time to arrival in capillaries coated with PEI (see Figure 2). Considering the time for coating procedure and the long arrival time of melittin peak for the separation in PEI coated capillary, it was decided that the uncoated capillary-low pH method is more advantageous in applying to actual bee venom samples.

Table 2: Method validation data for melittin.

Analytical Parameter	Low-pH buffer	PEI-coated capillary
Intra-day precision (n=5)		
Corrected peak area (RSD, %)	2.54	1.25
Migration time (RSD, %)	3.12	2.13
Inter-day precision (n=15)		
Corrected peak area (RSD, %)	3.42	2.57
Migration time (RSD, %)	4.84	3.16
Linearity		
Linear range (µmol L ⁻¹)	70-350	35-350
Regression equation	y=0.0004x-0.0158	y=0.0004x-0.0052
Correlation coefficient	0.983	0.996
LOD, µmol L⁻¹	19.3	10.0
LOQ, µmol L⁻¹	64.9	33.3

Due to the advantage of a short analysis period, the method using low pH buffer was preferred for analyzing actual bee venom sample. The preparation of the sample solution was given above. The sample was analyzed in triplicate, and the

standard deviation was calculated. One representative electropherogram of the bee venom sample is given in Figure 3. Melittin concentration of the bee venom sample was found as 24.5 ± 3.4 g 100 g⁻¹.

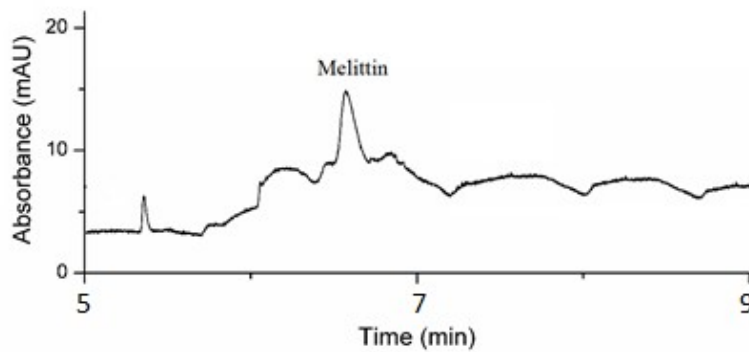


Figure 3: Bee venom sample extract. Analytic conditions: Bare fused silica column (50 μm x 57 cm), Buffer: 100 mM orthophosphoric acid at pH 1.55; Voltage: 25 kV; Temperature: 25 $^{\circ}\text{C}$; Injection: 50 mbar, 6 s; Detection: UV-DAD detector, λ : 200 nm.

The amount of melittin detected in bee venom in this study is consistent with the values reported in different countries in the literature (16, 18-19, 22). There is only one CE method reported for melittin analysis (22). However, in this literature study, the separation of melittin could be achieved in more than 20 minutes (22). Our method is much more rapid than the reported CE study for melittin. Moreover, melittin of an Anatolian honey bee venom was firstly highlighted using a CE method.

CONCLUSION

In this study, separation and quantification of melittin in an Anatolian honey bee venom sample was determined by capillary electrophoresis. In order to eliminate the capillary wall adsorption of positively charged melittin, two different methodologies were examined. Based on the rapid analysis, low-pH buffer system was selected for the analysis of the actual sample. By applying this methodology, melittin of Anatolian honey bee venom was highlighted. The method is presented as a fast and reliable method for screening and quantifying honeybee venom's melittin.

CONFLICT OF INTEREST

The authors have declared no conflict of interest.

ACKNOWLEDGMENTS

The authors would like to thank Assoc. Prof. Dr. Sibel Döşler for donating standard melittin. The Research Foundation of Istanbul Technical University was financially supported this study.

REFERENCES

1. Gupta RK, Stangaciu S. Apitherapy: Holistic Healing Through the Honeybee and Bee Products in Countries with Poor Healthcare System. In: Gupta RK, Reybroeck W, van Veen JW, Gupta A, editors. *Beekeeping for Poverty Alleviation and Livelihood Security* [Internet]. Dordrecht: Springer Netherlands; 2014 [cited 2021 Nov 6]. p. 413-46. ISBN: 978-94-017-9199-1. [<URL>](#).
2. Luo X, Dong Y, Gu C, Zhang X, Ma H. Processing Technologies for Bee Products: An Overview of Recent Developments and Perspectives. *Front Nutr*. 2021 Nov 3;8:727181. [<DOI>](#).
3. Kalaycıoğlu Z, Kaygusuz H, Döker S, Kolaylı S, Erım FB. Characterization of Turkish honeybee pollens by principal component analysis based on their individual organic acids, sugars, minerals, and antioxidant activities. *LWT*. 2017 Oct;84:402-8. [<DOI>](#).
4. Kaygusuz H, Tezcan F, Erım FB, Yıldız O, Sahin H, Can Z, et al. Characterization of Anatolian honeys based on minerals, bioactive components and principal component analysis. *LWT-Food Science and Technology*. 2016 May;68:273-9. [<DOI>](#).
5. Kaygusuz H. Analysis of a Rare Honey Sample From Tuzluca/Iğdır Region. *Journal of the Institute of Science and Technology*. 2020 Jun 1;1139-45. [<DOI>](#).
6. Sarıkaya AO, Ulusoy E, Öztürk N, Tunçel M, Kolaylı S. Antioxidant Activity And Phenolic Acid Constituents Of Chestnut (*Castanea Sativa* Mill.) Honey And Propolis. *Journal of Food Biochemistry*. 2009 Aug;33(4):470-81. [<DOI>](#).
7. Ali M. Studies on Bee Venom and Its Medical Uses. 2012;1:1-15.

8. Bellik Y. Bee Venom: Its Potential Use in Alternative Medicine. AIA. 2015 May 20;13(1):3-16. [<DOI>](#).
9. Wehbe R, Frangieh J, Rima M, El Obeid D, Sabatier J-M, Fajloun Z. Bee Venom: Overview of Main Compounds and Bioactivities for Therapeutic Interests. Molecules. 2019 Aug 19;24(16):2997. [<DOI>](#).
10. Uzuner SÇ, Birinci E, Tetikoğlu S, Birinci C, Kolaylı S. Distinct Epigenetic Reprogramming, Mitochondrial Patterns, Cellular Morphology, and Cytotoxicity after Bee Venom Treatment. PRA. 2021 Aug;16(3):377-92. [<DOI>](#).
11. Silva J, Monge-Fuentes V, Gomes F, Lopes K, Anjos L, Campos G, et al. Pharmacological Alternatives for the Treatment of Neurodegenerative Disorders: Wasp and Bee Venoms and Their Components as New Neuroactive Tools. Toxins. 2015 Aug 18;7(8):3179-209. [<DOI>](#).
12. Kim W. Bee Venom and Its Sub-Components: Characterization, Pharmacology, and Therapeutics. Toxins. 2021 Mar 7;13(3):191. [<DOI>](#).
13. Alia O, Laila M, Antonious A. Antimicrobial Effect of Melittin Isolated From Syrian Honeybee (*Apis Mellifera*) Venom and Its Wound Healing Potential. Int J Pharm Sci Rev Res. 2013;21:318-24.
14. Raghuraman H, Chattopadhyay A. Melittin: a Membrane-active Peptide with Diverse Functions. Bioscience Reports. 2007 Aug 6;27(4-5):189-223. [<DOI>](#).
15. Rady I, Siddiqui IA, Rady M, Mukhtar H. Melittin, a major peptide component of bee venom, and its conjugates in cancer therapy. Cancer Letters. 2017 Aug;402:16-31. [<DOI>](#).
16. Haghi G, Hatami A, Mehran M. Qualitative and quantitative evaluation of melittin in honeybee venom and drug products containing honeybee venom. Journal of Apicultural Science. 2013 Dec 1;57(2):37-44. [<DOI>](#).
17. Huang S, Wang J, Guo Z, Wang Y, Liu C. Quantitative Measurement of Melittin in Asian Honeybee Venom Using a New Method Including UPLC-QqTOF-MS. Toxins. 2020 Jul 4;12(7):437. [<DOI>](#).
18. Ionete R, Dinca O, Tamaian R, Geana E. Exploring *Apis Mellifera* Venom Compounds Using Highly Efficient Methods. Progress of Cryogenics and Isotopes Separation. 2013;16:89-100.
19. Kokot ZJ, Matysiak J. Simultaneous Determination of Major Constituents of Honeybee Venom by LC-DAD. Chroma. 2009 Jun;69(11-12):1401-5. [<DOI>](#).
20. Rybak-Chmielewska H, Szczêsna T. HPLC Study of Chemical Composition of Honeybee (*Apis Mellifera* L.) Venom. J Apic Sci. 2004;48:103-9.
21. Samanci T, Kekeçoğlu M. Comparison of Commercial and Anatolian Bee Venom in Terms of Chemical Composition. Uludağ Arıcılık Dergisi. 2019 May 29;61-8. [<DOI>](#).
22. Kokot ZJ, Matysiak J, Urbaniak B, Dereziński P. New CZE-DAD method for honeybee venom analysis and standardization of the product. Anal Bioanal Chem. 2011 Mar;399(7):2487-94. [<DOI>](#).
23. Barwick V, editor. Eurachem/CITAC Guide: Guide to Quality in Analytical Chemistry: An Aid to Accreditation [Internet]. Available from: www.eurachem.org. ISBN: 978-0-948926-32-7.
24. Chen F-TA, Evangelista RA. Protein analysis by capillary electrophoresis. In: Shintani H, Polonský J, editors. Handbook of Capillary Electrophoresis Applications [Internet]. Dordrecht: Springer Netherlands; 1997 [cited 2021 Nov 6]. p. 173-97. ISBN: 978-94-009-1561-9. [<URL>](#).
25. Erim FB, Cifuentes A, Poppe H, Kraak JC. Performance of a physically adsorbed high-molecular-mass polyethyleneimine layer as coating for the separation of basic proteins and peptides by capillary electrophoresis. Journal of Chromatography A. 1995 Aug;708(2):356-61. [<DOI>](#).



On the Biological Importance, Preparation, and Uses of Imidazo[1,2-*b*]pyridazine-Based Compounds

Barbaros AKKURT  

Istanbul Technical University, Faculty of Science & Letters, Department of Chemistry, 34469 Maslak, Istanbul, Turkey

Abstract: While studying several pyridazine compounds, the author discovered imidazo[1,2-*b*]pyridazine (IMP), which is a very versatile compound class. It has been an inhibitor for many enzymes and also it is used as a brominating reagent in organic syntheses. Owing to its high biological activity, researchers have always considered including this molecule in their final structures. This humble attempt just aims to introduce this very powerful molecule to the readers, primarily of chemical origin, and should not be considered as a full treatise of, especially, the medicinal chemistry of the molecule. This work discusses the inhibitory effects, organic chemistry, applications in material chemistry, and theoretical studies of IMP and related molecules. The readers are hereby encouraged to work with medicinal chemists with the newly prepared molecules including this and similar molecules, in the struggle with many diseases like cancer, Alzheimer's, and others.

Keywords: Imidazo[1,2-*b*]pyridazine, synthesis, inhibitors, applications, reactions.

Submitted: September 25, 2021. **Accepted:** November 06, 2021.

Cite this: Akkurt B. On the Biological Importance, Preparation, and Uses of Imidazo[1,2-*b*]pyridazine-Based Compounds. JOTCSA. 2021;8(4):1217-50.

DOI: <https://doi.org/10.18596/jotcsa.1000771>.

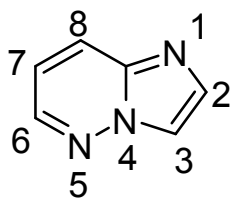
***Corresponding author. E-mail:** akkurtb@itu.edu.tr.

INTRODUCTION

This review article discusses the importance of imidazo[1,2-*b*]pyridazine (IMP) nucleus, which was first synthesized in 1967 by Stanovnik (1). IMP (compound **1**, see Figure 1 below) has a structure and numbering scheme depicted in Figure 1. IMP is reported to be an inhibitor including, but not limited to, for the following enzymes: Break point cluster-Abelson (BCL-ABL) kinase (2), vascular endothelial growth factor (VEGF) Receptor 2 kinase (3), tumor necrosis factor alpha (4), Bruton's tyrosine kinase (BTK) (5), ATP-competitive mTOR (mammalian target of rapamycin) (6), PDE 10A (7), activin receptor-like kinase 2 (8), Pim kinase (9), death-associated protein kinase (DAPK) (10), glycogen synthase kinase-3 (11), fibroblast growth factor receptor 1 (FGFR1) (12), dengue fever (13), tyrosine kinase 2 (2), and calcium-dependent protein kinase 1 (14). It has also been reported as an ingredient of anticancer drugs (15), antiparasitic (16), and antiproliferative agents (17), and used as

radioligands for tropomyosin receptor kinase family (18). The review article also sheds light on the synthetic works, such as arene C-H functionalization (19), addition of osmium carbynes to conjugated systems (20), C-H silylation of IMP (21), photoelectrochemical C-H alkylation (22), photoinduced oxidative activation (23), ceric ammonium nitrate (CAN) oxidation (24), also bromination agents originating from IMP (25). IMP is an n-type unit and was used in the red phosphorescent organic light-emitting devices (26). Photochromic IMP-based iodoargentate hybrid materials were also reported (27). There are a handful of theoretical studies conducted with IMP and its derivatives (28). These all will be discussed adequately in the article.

The imidazo[1,2-*b*]pyridazine (IMP) (compound **1**) has a structure and numbering scheme depicted in Figure 1.



(1)

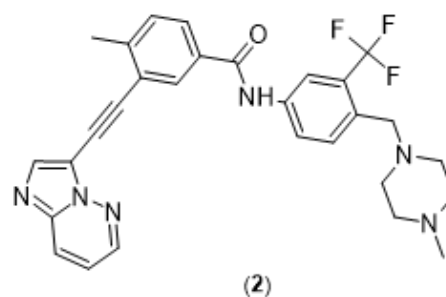
Figure 1: The IMP nucleus, along with its numbering scheme.

INHIBITORY PROPERTIES OF IMP ON MANY ENZYMES

Inhibition of Bcr-Abl Kinase of Substituted Imidazopyridazine Scaffold as a Trusted Structure

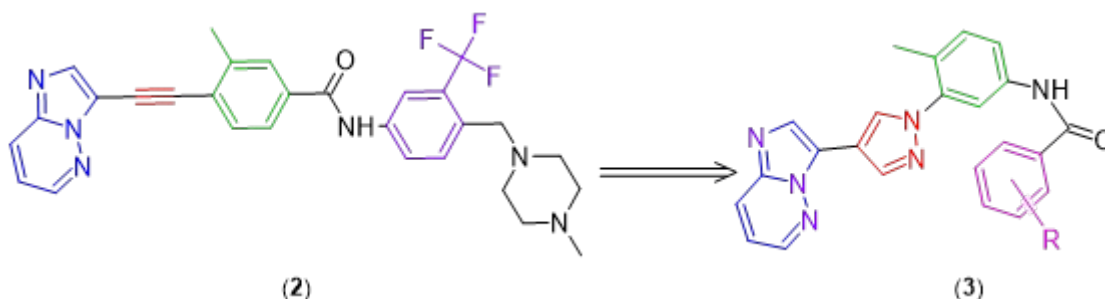
Liu and colleagues reported, in a review article, that BCR gene and the C-ABL protooncogene are fused to create the BCR-ABL (break point cluster-Abelson) gene, which is considered to be the main cause of chronic myelogenous leukemia (CML) production. To treat CML, selective BCR-ABL kinase inhibitors are employed, but there is a problem, namely, a gatekeeper mutant called as T315I disrupts the interaction between the enzyme and the inhibitor. Some molecules prepared are in the preclinical stage, where many others are employed in the clinical research. Ponatinib is an IMP-containing drug used in these researches (see Figure 2, compound **2**) (2). Another review article states that Ponatinib is approved as an auxiliary treatment molecule for chronic myelogenous leukemia (CML) and Philadelphia chromosome-positive acute lymphoblastic leukemia (ALL). The drug, ponatinib, is a multikinase inhibitor and is active against BCR-AblT315I, BCR-Abl, Flt3, FGFR1, Kit, RET, Src, and VEGFR2 and BCR-Abl is the prime target for treating CML and ALL (29). Pyrazole-containing IMP-phenylbenzamide derivatives were reported to possess BCR-ABL kinase inhibition. Combinational strategies of scaffold hopping and conformational constraint were employed. The new compounds were screened for BCR-ABL1 kinase

inhibitory activity, and most of them showed good inhibitory activity against BCR-ABL1 kinase (30) (See Scheme 2). Ponatinib was reported to be five to seven fold more potent at inhibiting ABL than the mutant, referred to as the ABLT315I, although there are only minimal variations in the binding modes. There are five hydrogen bonds in the binding of ponatinib to ABL and ABLT315I. The conformation is called as "DFG-out". The IMP moiety produces van der Waals interactions with the both lobes of the kinase binding site. The ethynyl link is very important to bind to native and mutant ABL kinase. It forms favorable interactions in the binding. The rigid nature of ethynyl group enables the adoption of correct orientation and correct conformation in the binding site, and important entropic advantage is gained. When binding to the mutant site, the inhibitor conformation is somewhat perturbed and favorable interactions are allowed and steric clash is alleviated. This adjustment is accounted for the loss of potency with the mutant site (31). Ponatinib was also reported to possess an alkyne linker between the IMP and diarylamide (a 2,3-diarylethyne motif) and a slim alkyne moiety was found to be crucial to activity by avoiding steric hindrance (32). Ponatinib (see Figure 2) is used as an antileukemic agent, and is also considered for other anticancer therapies. It is toxic and researchers look for other derivatives of it for improved kinase selectivity as Ponatinib itself is not considered for MNK1 or 2 inhibition, but recent derivatives in which a nitrogen is introduced into the molecule report that the new compounds are potent inhibitors of MNKs (see Figure 3, (33)).



(2)

Figure 2: The chemical structure of Ponatinib.



(2)

(3)

Figure 3: Pyrazole-containing IMP-phenylbenzamide derivatives (3) as inspired from ponatinib (2) Color coding: Blue = head; red = linker; green = middle; violet = tail.

VEGF Receptor 2 Kinase Inhibitor

Miyamoto and colleagues reported the design, synthesis, and biological evaluation of 2-acylamino-6-phenoxy-IMP derivatives. Hybridization and

optimization yielded the discovery of N-[5-({2-[(cyclopropylcarbonyl)amino]IMP-6-yl}oxy)-2-methylphenyl]-1,3-dimethyl-1H-pyrazole-5-carboxamide (TAK-593) as a highly potent VEGF

receptor 2 kinase inhibitor. TAK-593 applied a strong suppression to the proliferation of VEGF-stimulated human umbilical vein endothelial cells. Kinase selectivity profiling showed an inhibition of

platelet-derived growth factor receptor kinases as well as VEGF receptor kinases (34) (see Figure 5, Scheme 1, Scheme 2, Figure 6).

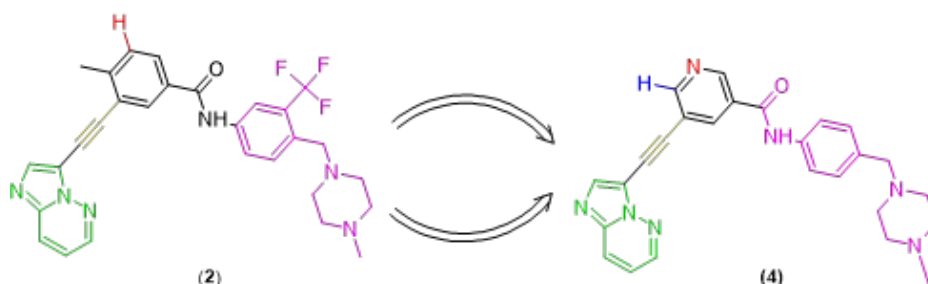
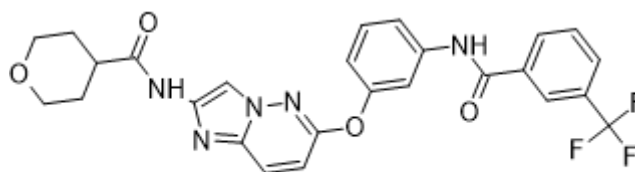
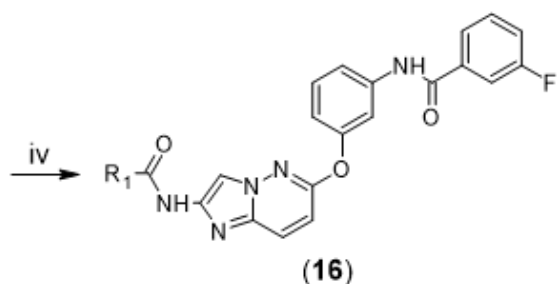
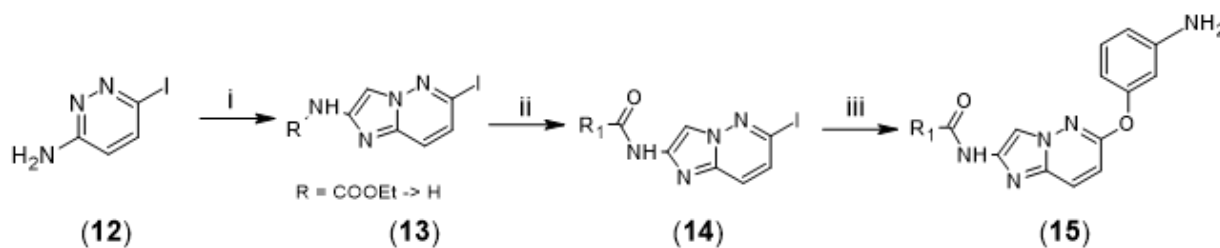


Figure 4: Modifications were made to Ponatinib and some new compounds emerged, with better performance.



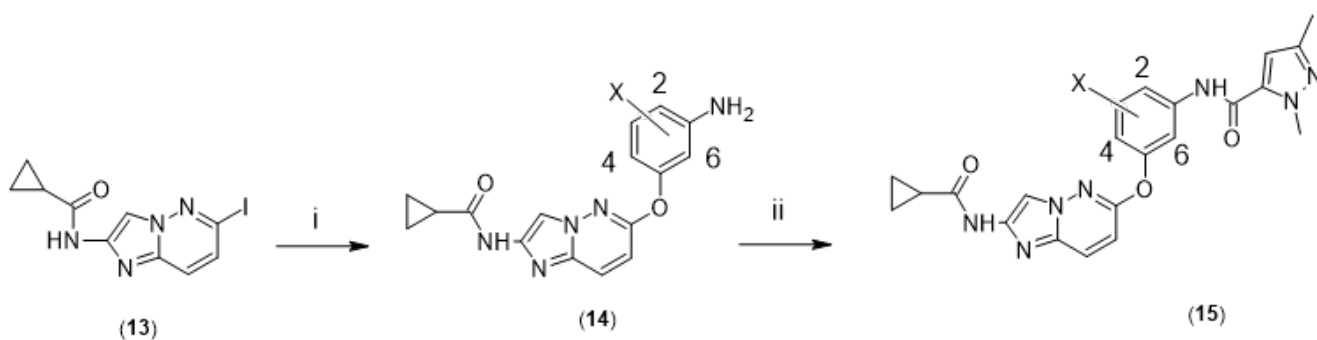
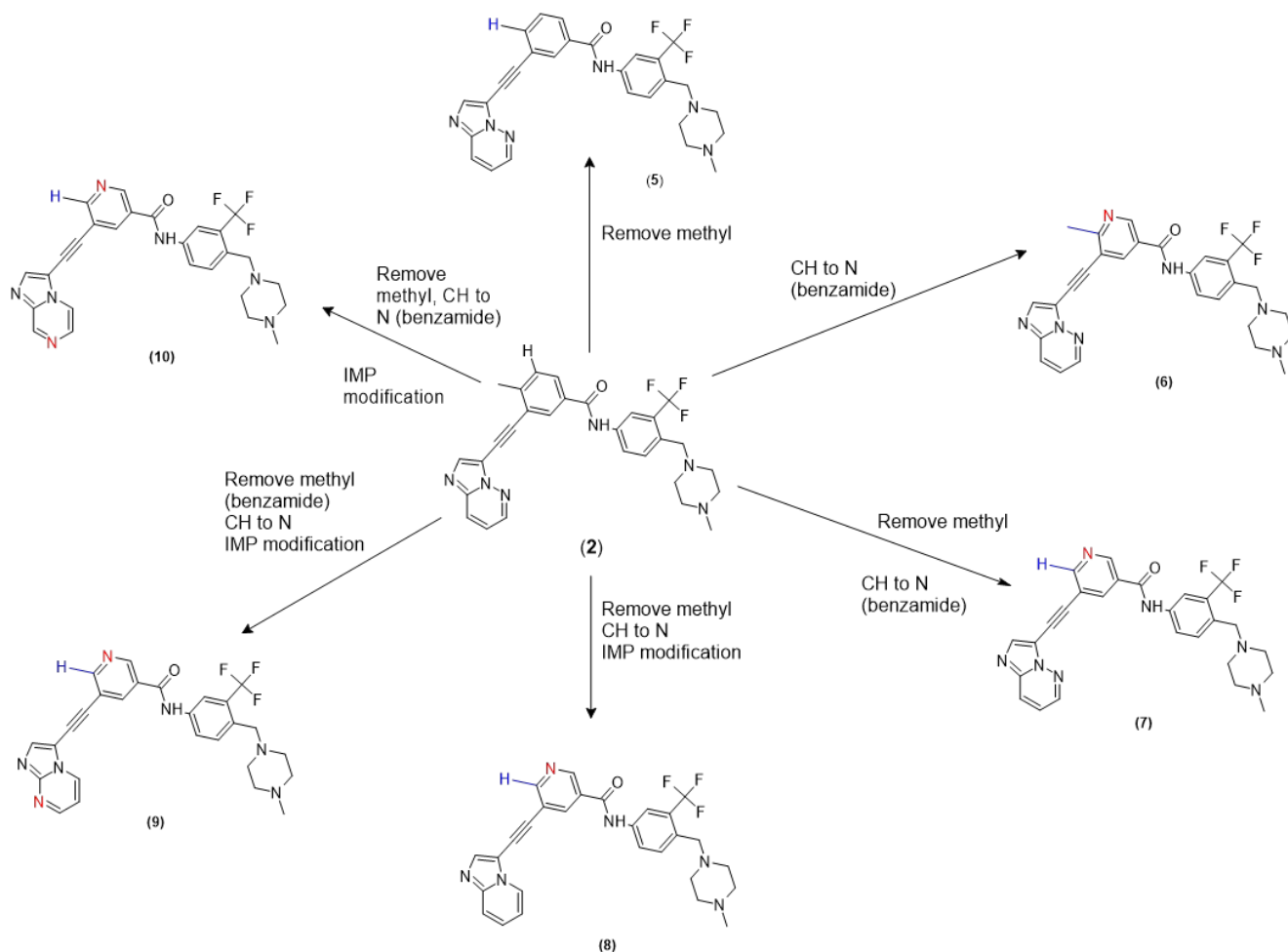
(11)

Figure 5: Chemical structure of a hybrid compound developed.



(16)

Scheme 1: Synthesis of compound (16). Reaction conditions: i) ethyl (chloroacetyl)carbamate, Na₂HPO₄, DMA; ii) Ba(OH)₂, NMP/H₂O; iii) R₁COCl, DMA; iv) 3-aminophenol, K₂CO₃, DMF; v) 3-fluorobenzoyl chloride, DMA.



Inhibitors of TNF- α Production

Tumor necrosis factor- α (TNF- α) is an important pro-inflammatory cytokine responsible for a diverse range of inflammatory diseases including rheumatoid arthritis. In their manuscript, Pandit *et al.* summarized the medicinal chemistry efforts on the design, synthesis and TNF- α evaluation of a series of 3, 6-disubstituted imidazo[1,2-b]pyridazine (4) (see Figure 7, Figure 8, Scheme 4, Scheme 5).

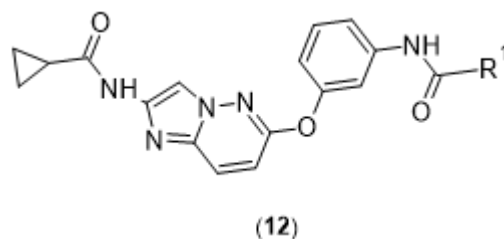


Figure 6: A series of compounds containing the IMP nucleus, having VEGFR2 binding ability. R^1 = cyclopropyl, *tert*-butyl, pyridin-4-yl, 1,2-oxazol-5-yl, 3-methyl-1,2-oxazol-5-yl, 1-methyl-1,2,3-triazol-5-

yl, 2,3-dimethylpyrazol-5-yl, 3,5-dimethyl-1,2-oxazol-4-yl, 1,3-dimethylpyrazol-5-yl, 1-phenyl-3-

methylpyrazol-5-yl, trifluoromethylpyrazol-5-yl.

1-methyl-3-

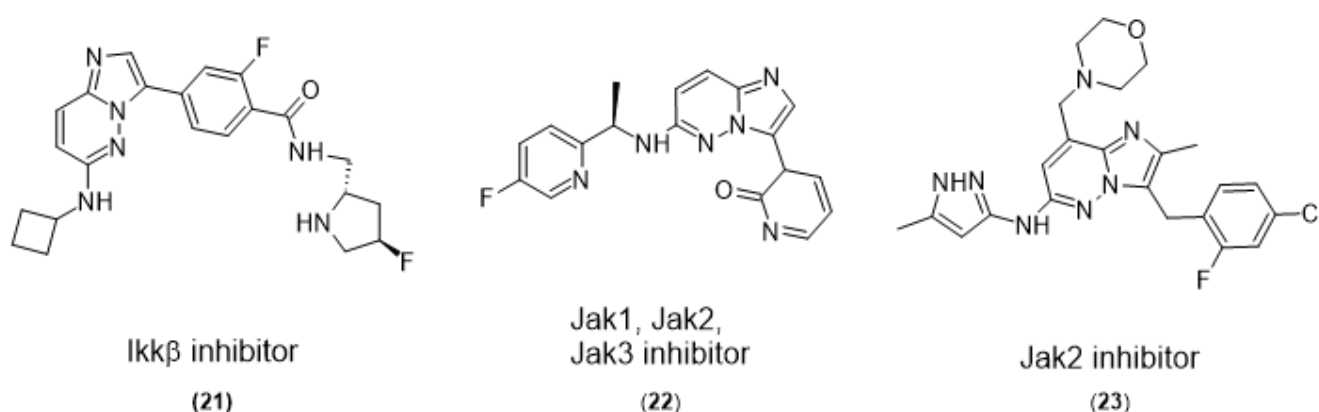


Figure 7: Some example molecules and their inhibitory activities.

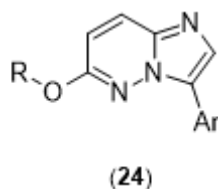
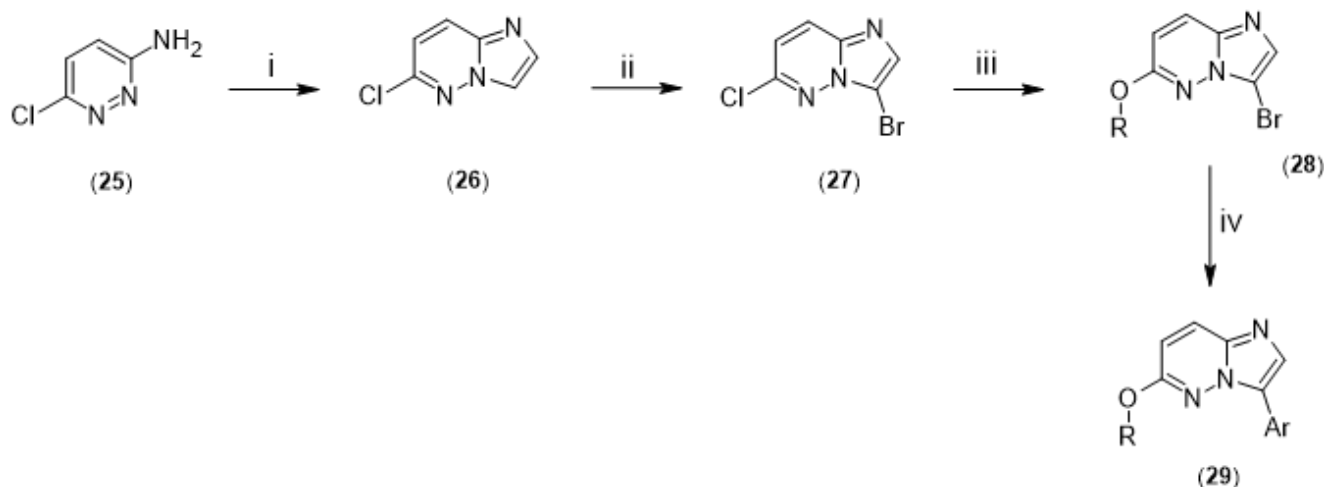
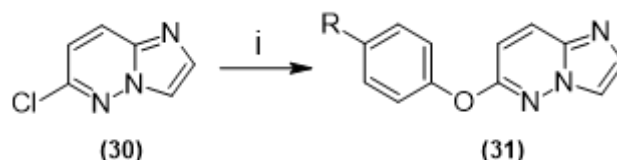


Figure 8: Designed modifications on IMP scaffold. R is alkyl or aryl.



Scheme 4: Synthetic procedure for some inhibitors, starting from a pyridazine derivative. Reagents and conditions: i) Chloroacetaldehyde dimethyl acetal, sodium acetate, concentrated HCl, 60% aqueous ethanol, reflux, overnight. ii) NBS, CHCl₃, 25-30 °C, 15 min. iii) cyclopentylmethanol or cyclohexanol, NaH, THF, 0 °C to room temp, overnight. iv) ArB(OH)₂ / ArB(pin), Pd(PPh₃)₂Cl₂, K₂CO₃, DMF-H₂O, microwave, 140 °C, 0.5-1 h.



Scheme 5: Part of the synthetic scheme, starting from chloro-IMP. Reaction conditions: CuI, Cs₂CO₃ DMF, 140 °C. MW, 40-120 min.

BTK Inhibitors for Autoimmune Diseases

As potential inhibitors for BTK, two imidazopyrazine derivatives were synthesized. The imidazopyrazine

core was changed with an IMP moiety and it was reported that the replacement led to a better outcome (5) (see Figure 9) .

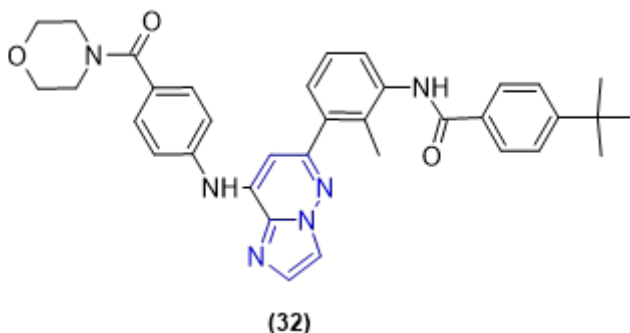


Figure 9: Heterocyclic replacement of the imidazo[1,2-*a*]pyrazine core with IMP.

Pyridazine Nucleus as an Active Ingredient of Anticancer Drugs

To have a more active and less toxic anticancer drug at hand is a mostly wanted asset. There are numerous pyridazine-containing anticancer drugs on the market, and the review by Zhang-Xu He and their colleagues shed light on their properties. It is reported that TAK-593 (compound **33**) is in the first phase, targeted on VEGF and PDGF and clinically used on solid tumors (15) (See Figure 10).

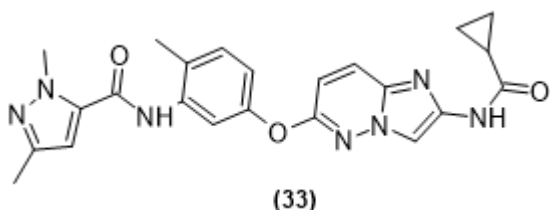


Figure 10: Chemical structure of TAK 593.

mTOR Inhibition by IMP Derivatives

ATP-competitive mTOR (mammalian target of rapamycin) inhibitors have been studied as potential

antitumor agents. A new class of IMP analogues were reported as potential mTOR inhibitors, in which structural modifications were focused on positions 3, 6, 8 of IMP skeleton. The promising compound **34** (see Figure 12) had a strong antitumor activity toward A549 cells, and bind to mTOR kinases. Guided by the principle of scaffold hopping, Chen and co-authors developed a novel class of IMP derivatives simplified as **35** as potent IRAK4 (interleukin-1 receptor associated kinase 4) inhibitors (see Figure 12). Above results confirmed that pyridazine-based **35** could be a potent IRAK4 inhibitor and worthy of further exploration for the treatment of mutant MYD88 DLBCL (15). A series of IMP derivatives were prepared as competitive inhibitors of ATP mTOR. Compound **34** and its isomer **35** in which the pyridine nitrogen is placed at the 4 position below were reviewed among other compounds (6). A promising compound, **36**, is considered to be a potent compound. Scaffold hopping of **37** to **38** produces a good substance (15).

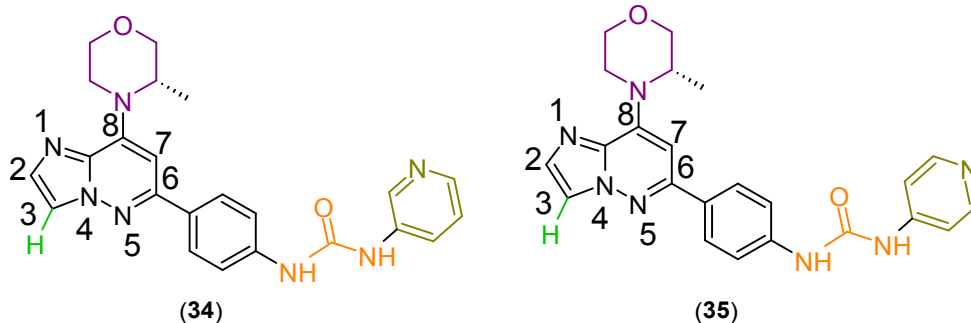


Figure 11: Regions of activity for an IMP molecule under design. For substitution of IMP at position 8 (magenta), (S)-3-methylmorpholine > morpholine > 8-oxa-3-azabicyclo[3.2.1]octane. For the hydrogen at position 3 (green), H > Me > Et. The uredo group provides improved activity. As for the olive-colored area on the right, pyridyl is greater than phenyl. Also, the pyridine nitrogen's position was tested.

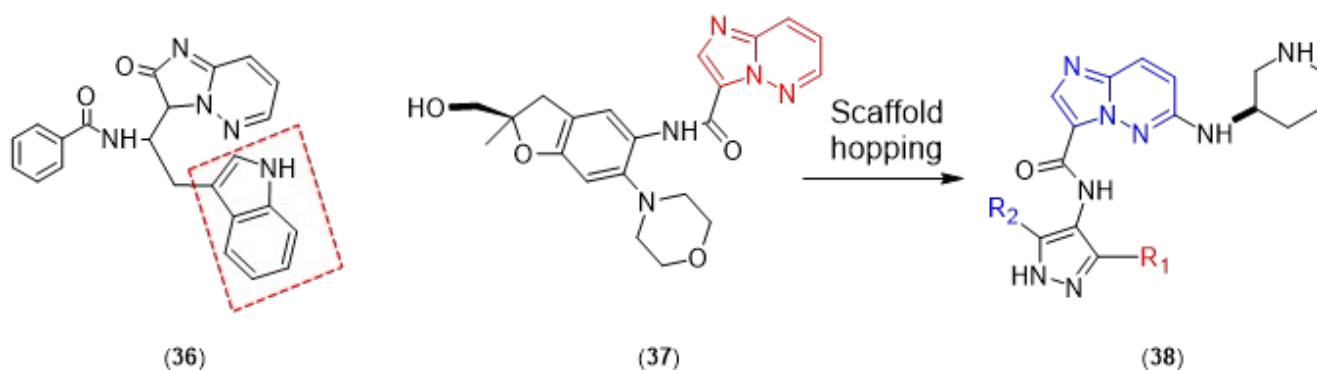
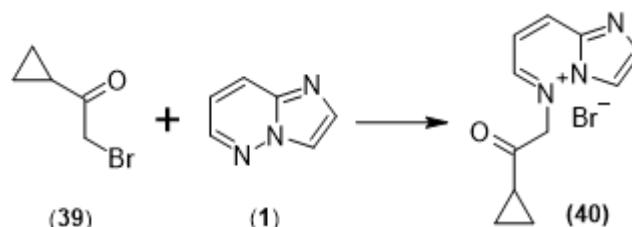


Figure 12: A promising compound **36** (left). Scaffold hopping of compound **37** in the middle, which is an IRAK inhibitor, produces the compound **38** on the right (R_1 is methyl, cyano, difluoromethyl, carbamoyl and R_2 is methyl, ethyl, isopropyl, 4-piperidyl, and 4-THP).

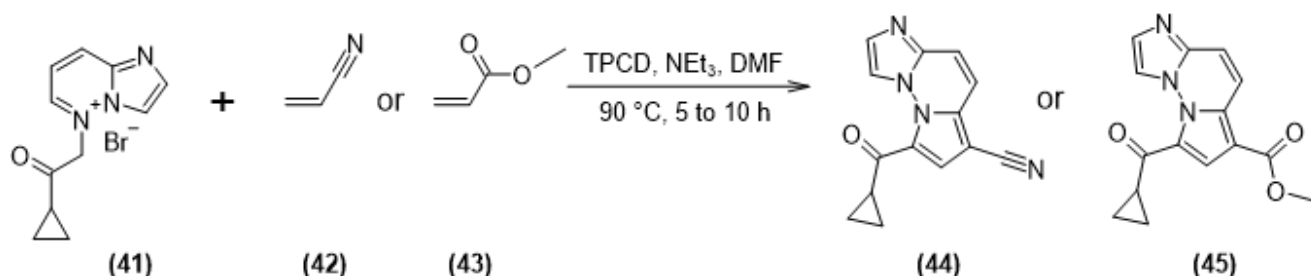
Anticancer Activity

Shen and coworkers studied about indolizine derivatives, and reported the successful anticancer activity of some of them. Some compounds contained IMP nucleus, the structures are given in Scheme 6 and Scheme 7 (35). An Indian research group prepared 1,2,4-thiazole-substituted IMP molecules for a possible anticancer activity. The cancer types investigated were breast (MCF-7, MDA MB-231), lung (A549), and prostate (DU-145) with MTT assay. Five of the compounds prepared were found to be potent against the cancer types, especially one of them was found to possess the most promising anticancer activity (Scheme 8) (36).

Tewari and coworkers have filed a patent in which IMP was present in a structure called Cefozopran (**46**, see Figure 13) (37).



Scheme 6: Alkylation of IMP from the nitrogen at position 5.



Scheme 7: Synthesis of indolizine derivatives from the cationic IMP starting material. TPCD is tetrakis(pyridine)cobalt(II) dichromate, an oxidizing material.

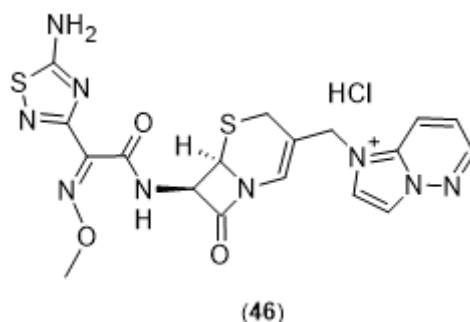
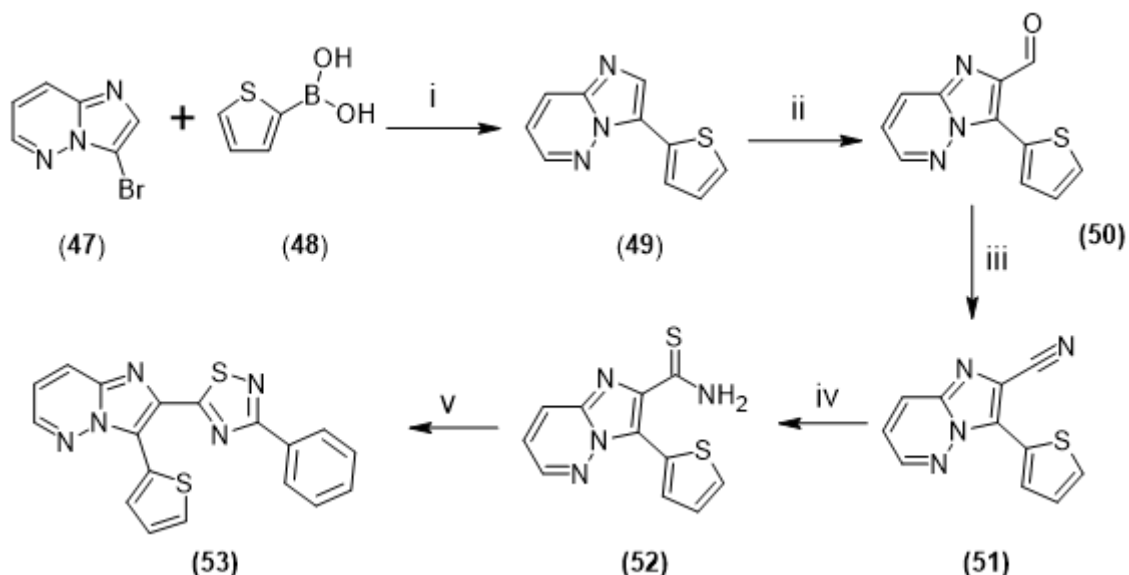


Figure 13: Chemical structure of Cefozopran.



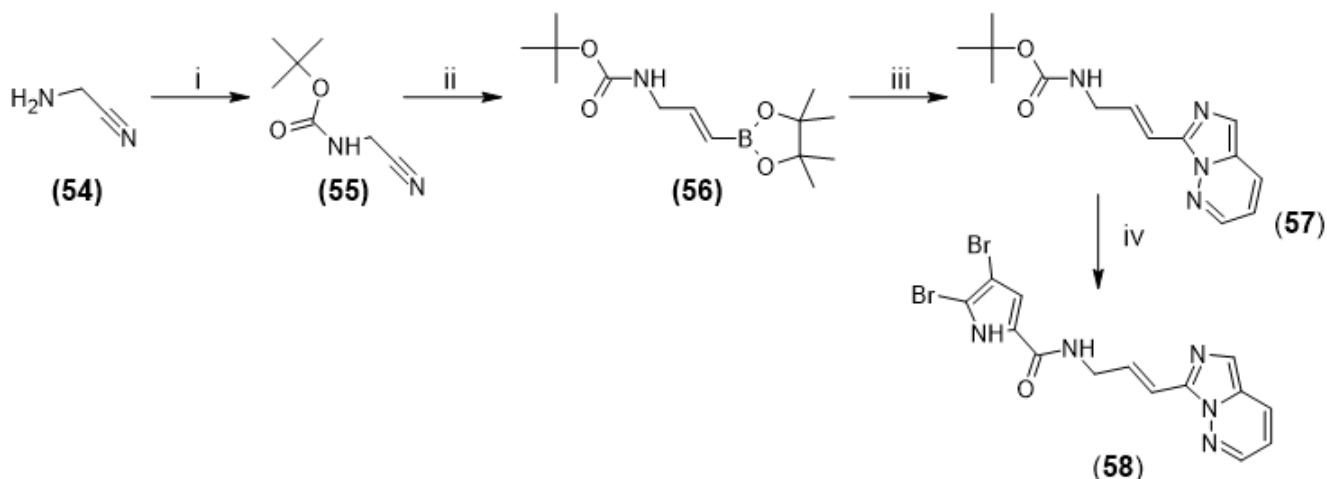
Scheme 8: Functionalization of the IMP starting compound, **47**. Reaction conditions: i) Pd(PPh₃)₄, Cs₂CO₃, DMA, 80 °C, 21 h. ii) HMTA, AcOH, H₂O, reflux, 12 h. iii) NH₂OH.HCl, DMSO, 90 °C, 2 h. iv) NaSH, MgCl₂.6H₂O, DMF, 40 °C, 90 min. v) Substituted cyanobenzenes, AlCl₃, n-BuOAc, 70 °C, 5 h. The final compound has the following substituents at the benzene ring: H, 3,4,5-trimethoxy, 3,5-dimethoxy, 4-methoxy, 4-chloro, 4-bromo, 4-nitro, 3,5-dinitro, 4-methyl, and 4-(dimethylamino).

PDE 10A Inhibition

A review article by Jankowska *et al.* in 2019 provides deep information about PDE10A and what has recently been done about the design of selective PDE10A inhibitors. Schizophrenia, Huntington's, and Parkinson's diseases are central nervous system-related disorders and treatment of them with PDE10A inhibitors are discussed (38).

Inhibition of Aurora B Kinases

Juillet and colleagues tried to vary the flexibility of the molecules and first replaced the acetylene linker with an alkene moiety. The preparation of the alkene series is depicted in Scheme 9 (39).



Scheme 9: Formation of the IMP nucleus, among other compounds, and addition of a dibromopyrrole to the side. Reagents and conditions: i) (Boc)₂O, DMAP, DCM. ii) pinacolborane, Cp₂ZrHCl 25 mol%, Et₃N, 25 mol %, 40 °C. iii) R-I, Pd(PPh₃)₄, 5 mol %, K₂CO₃ (2 M), dioxane, 80 °C. iv) 4 N HCl, then trichloroacetyl dibromopyrrole.

Activin Receptor-Like Kinase 2 (R206H) Inhibition

Classic FOP (fibrodysplasia ossificans progressiva) is caused by the R206H mutation in ALK2/ACVR1. There are many activin receptor-like kinase 2 (ALK2) inhibitors which are effective in animal models of this disease, however most of the ALK2

(R206H) inhibitors did not have an adequate oral bioavailability to be efficient. In the study, there were 12 ALK2 (R206H) inhibitors selected for the best performance, in which an IMP derivative was found to work efficiently (see Figure 14) (8).

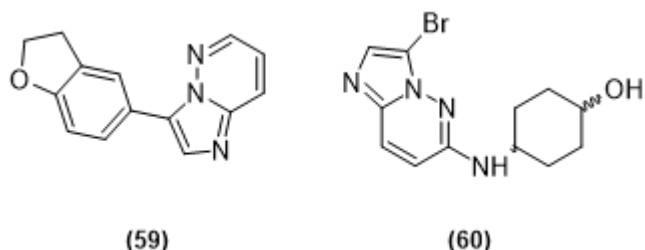


Figure 14: Two ALK2 (R206H) inhibitors based on IMP skeleton.

PIM Kinase Inhibitors

IMP was considered as a new PIM-1/2 inhibitor. Preliminary SAR studies at C3 and C6 positions of the heterocycle yielded three inhibitors. Further SAR studies of IMP were reported in the Supergen patent and the structure of SGI-1776 was disclosed (see Figure 15). SGI-1776 was the first clinically evaluated PIM inhibitor in patients with relapsed and/or refractory leukemias. It was unfortunate that the clinical assessment of this molecule was terminated, since its affinity to inhibit the ether-a-go-go-related gene (hERG) channel resulted in cardiac toxicity. Nevertheless, efforts are continuing with identification of potent and selective PIM -1 inhibitor TP-3654 without hERG or cytochrome P450 inhibition. In current, TP-3654 is under clinical assessment in patients having advanced solid tumors (See Figure 15) (9). Shannan and co-

workers reported about SGI-1776, which has previously been investigated in patients. SGI-1776 is reported to inhibit all three PIM kinases. When this pan-PIM kinase inhibitor was treated with AML xenografts, concentration-dependent tumor regressions were previously shown; therefore, they investigated the different preclinical models of melanoma of this drug. AlamarBlue assay, when combined with adherent melanoma cultures, let the researchers observe that SGI 1776 possessed inhibitory effects similar to SM200, melanoma cell lines were mostly inhibited, but not normal fibroblasts. At 10 μ M concentration, SGI-1776 increased cell death significantly in the melanoma cell lines when compared to normal fibroblasts. They used propidium iodide staining (40). Moloney leukemia virus (PIM) kinases are serine/threonine kinases and they are present in many important cancer cell signaling pathways. The research group evaluated PIM expression in low- and high-grade urothelial carcinoma cases and assessed the role of PIM in the progression of disease and their potential to serve as molecular therapeutic targets. A total of 137 cases were investigated. All three PIM family members were highly expressed in non-invasive and invasive urothelial carcinoma cases. A bladder cancer case was subjected to a in vivo xenograft study and it was found that PIM kinase inhibition led to a reduction in tumor growth; therefore PIM kinase inhibitors may be active players in human urothelial carcinomas (41).

Substitutions at 5 and 8 are not tolerated.

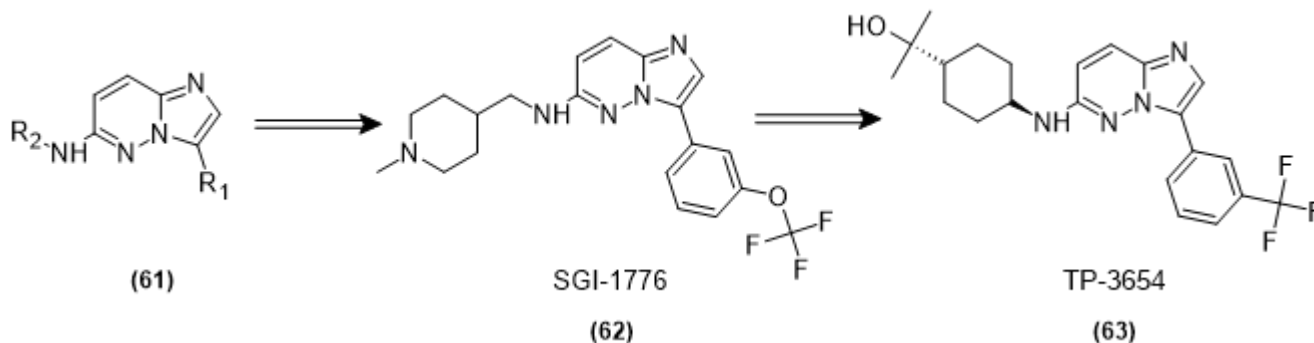


Figure 15: Development of SGI-1776 and TP-3654.

Death-Associated Protein Kinase (DAPK) Inhibitors

Many compounds have been reported as DAPK inhibitors, including aminopyridazine and IMP (See Figure 16) (10).

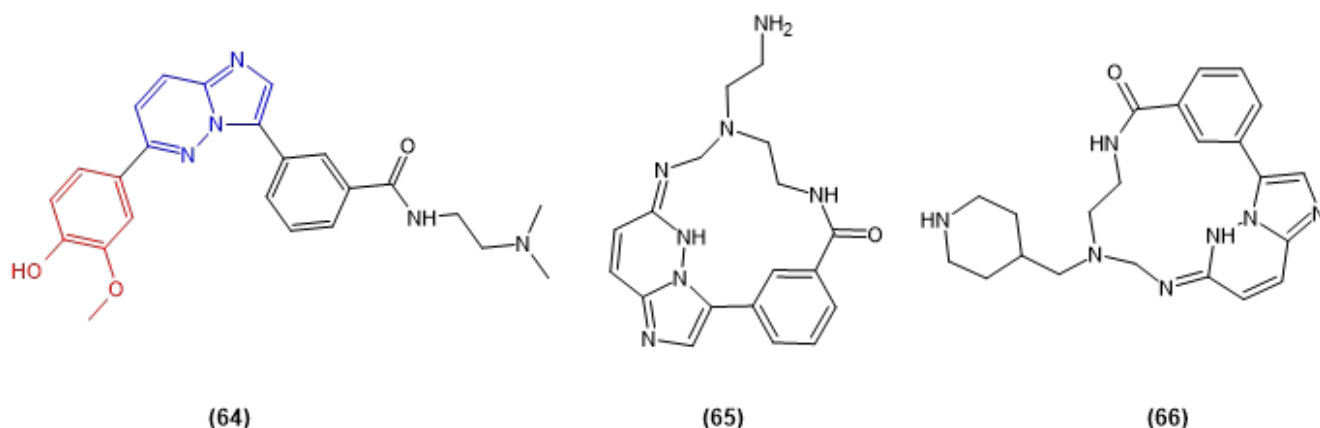


Figure 16: As DAPK1 inhibitors, three IMP derivatives were prepared. Molecule **64** shows that red color is the hydrophobic pocket-binding core, and blue color depicts the hinge-binding core.

Glycogen Synthase Kinase-3 Inhibition

IMP substitution at the R2 position in **43** gave the lowest IC₅₀ values for the series of other compounds (see Figure 17) (11).

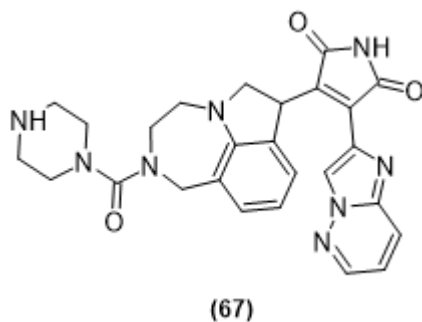


Figure 17: An IMP-containing molecule, having advantageous properties.

Radioligands for Tropomyosin Receptor Kinase Family

Tropomyosin receptor kinases family (TrkA, TrkB, and TrkC) represent adult life and aging, and when they downregulate, diseases like Alzheimer's emerge. In addition, overexpressed or abnormally expressed TrkA/B/C proteins point to neurogenic or non-neurogenic human cancers and they are under intensive clinical research. Small molecule kinase catalytic domain binding inhibitors were selected for ¹¹C and ¹⁸F positron electron tomography (PET, see Figure 18, Figure 19) (18).

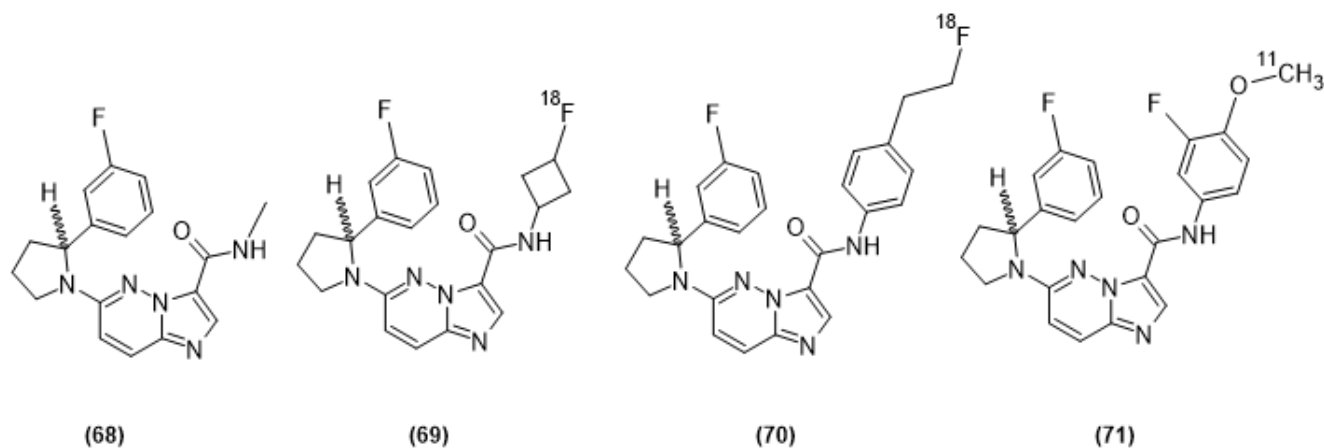


Figure 18: Chemical structures of precilical IMP-based Trk-targeted PET radioligands.

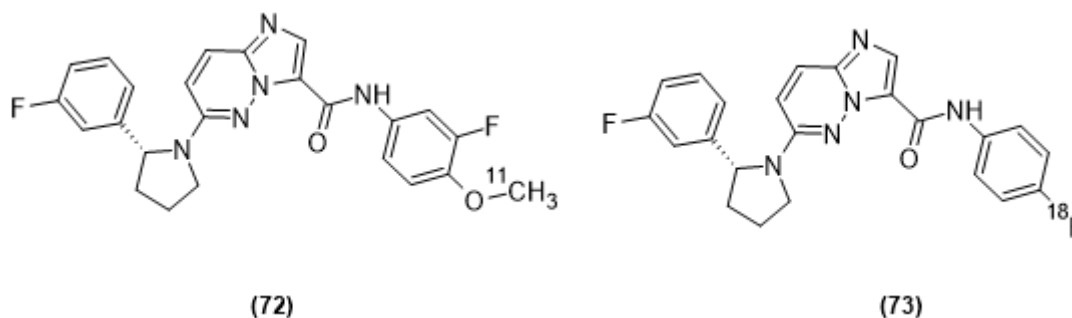


Figure 19: Chemical structures of clinical IMP-based Trk-targeted PET radioligands.

Using IMP's FGFR1 Activity in Another Class of Heterocyclic Compound

A research group in China wanted to synthesize a new class of pyrrolo[2,3-*b*]pyrazine, and to use the π - π stacking interaction of an IMP derivative with residue Phe489 of the protein, they decided to preserve this interaction and, they also simplified the synthetic procedure. They used the IMP skeleton to see the Fibroblast Growth Factor Receptor 1 (FGFR1) enzymatic activity. IMP was sulfonated and chlorinated to make it ready to couple to the pyrazine structure (see Figure 20) (12).

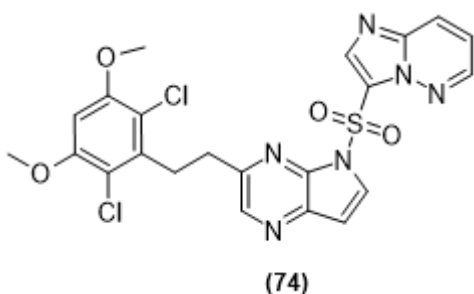


Figure 20: An IMP-based compound tested for FGFR1 activity.

Inhibitors for Dengue Fever

Dengue virus (DENV) is an arboviral human pathogen transmitted through mosquito bite that

infects, annually, an estimated circa 400 million humans (about 5 percent of the global population). No therapeutic agents have currently been developed for prevention or treatment of the infections owing to this pathogen. IMP is an inhibitor of AAK1 and GAK pathways that inhibit DENV replication (13).

Inhibitors for Tyrosine Kinase 2

An IMP derivative underwent modifications to yield a molecule, which showed good functional potency and its kinase selectivity was excellent, yet its metabolic stability was poor, pharmacokinetic properties (in mouse) were modest, and phosphodiesterase 4 (PDE4) activity was in a medium state (42). As a member of the Janus (JAK) family of non-receptor tyrosine kinases, TYK2 mediates the signaling of pro-inflammatory cytokines including IL-12, IL-23 and type 1 interferon (IFN), and therefore represents an attractive potential target for treating the various immuno-inflammatory diseases in which these cytokines have been shown to play a role. IMP was identified as a promising hit compound. Iterative modification was exercised for each of the substituents of the IMP scaffold, and the cellular potency was improved, selectivity was maintained over the JH1 domain (see Figure 21, Scheme 10, Scheme 11) (43).

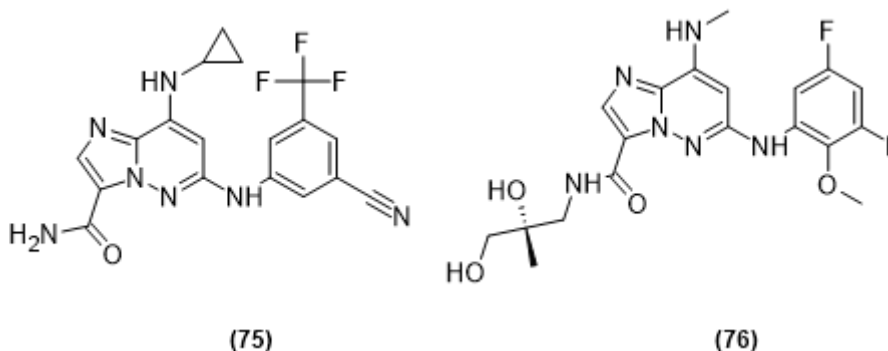
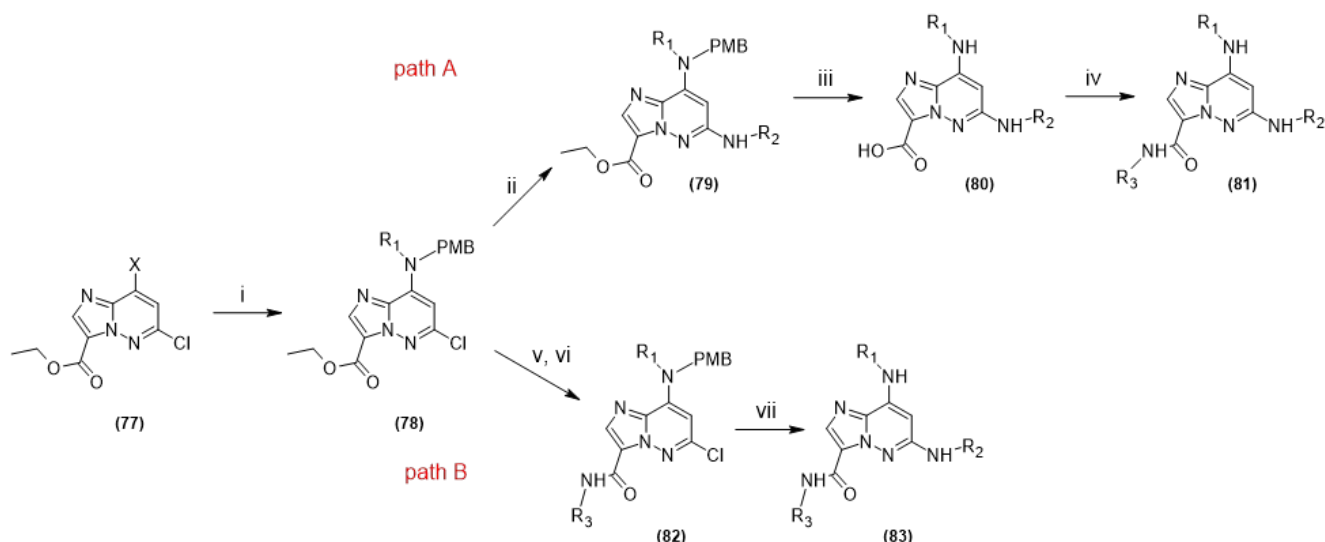
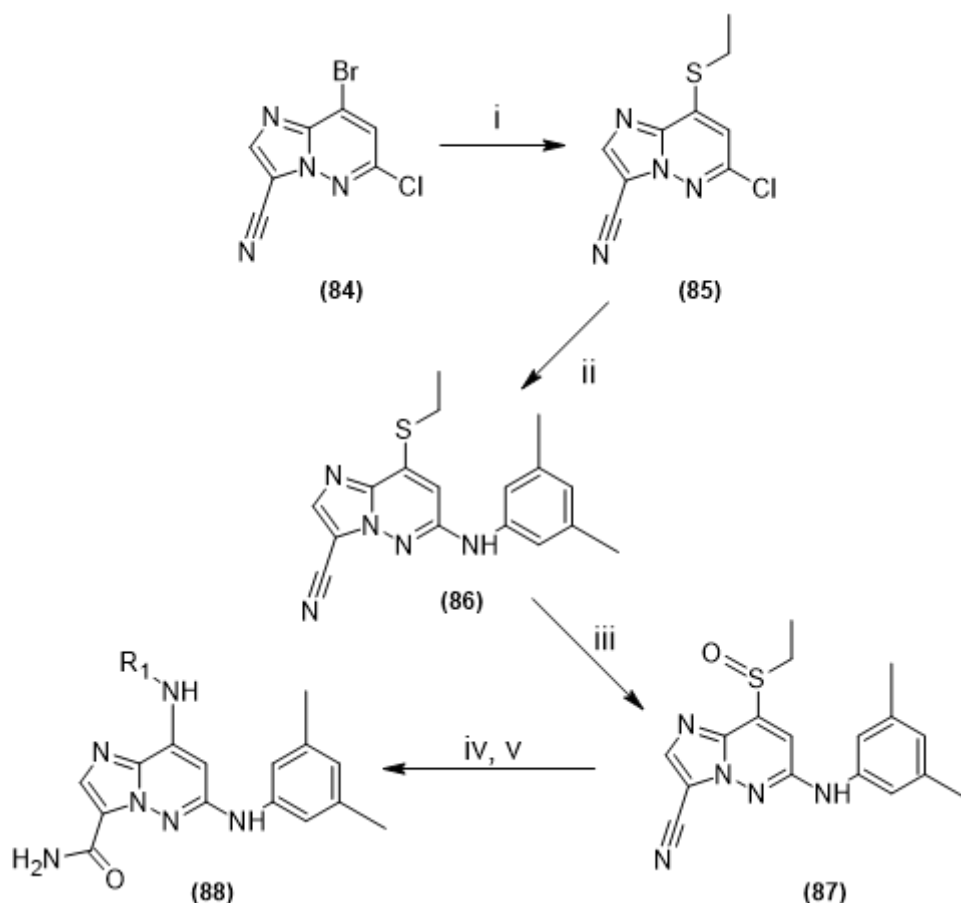


Figure 21: Previously reported TYK2 JH2 ligands.



Scheme 10: Synthesis of TYK2 JH2 ligands with two different paths. Reaction conditions: i) R^1 -NH-PNB, NEt_3 , 1,4-dioxane, 90 °C, ii) H_2NR_2 , Pd_2dba_3 , Xantphos, Cs_2CO_3 , DMA, 100 °C, iii) a-HCl, dioxane, RT, b-NaOH, MeOH, H_2O , iv) HATU; H_2NR_3 , DMF, *N*-methylmorpholine, RT, v) LiOH, MeOH, THF, H_2O , RT, vi) NH_2R_3 , BOP, iPr_2NEt , DMF, vii) a- H_2NR_2 , Pd_2dba_3 , Xantphos, Cs_2CO_3 , DMA, 125 °C, b-HCl (4 M, in dioxane), DCM, RT.



Scheme 11: The synthesis for allowing late stage examination of the C8 group, utilizing a thiol group to block this position.

Calcium-Dependent Protein Kinase 1 of *Toxoplasma gondii*

For toxoplasmosis, the currently available tools are drugs that are non-specific to the parasite and cause serious side effects. There is an urgent need

of development of anti-Toxoplasma compounds that have higher efficiency and that are more specific to it. IMP derivatives were designed to inhibit the *Toxoplasma gondii*'s calcium-dependent protein kinase 1 (TgCDPK1) and they were effective against

tachzoite growth *in vitro*. The authors stress that IMP salts are strongly efficient, *in vivo*, on acute toxoplasmosis and that a mouse congenital toxoplasmosis model should be set up for further testing (14).

Steroyl-CoA Desaturase (SCD)

A number of patents about small molecule inhibitors of SCD-1 have been published. As an example,

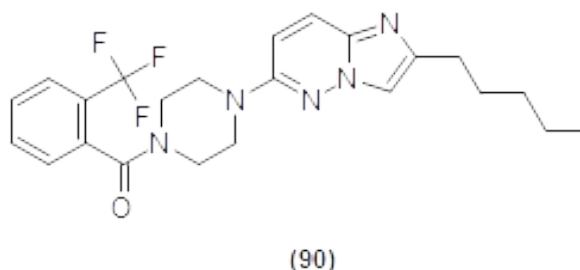
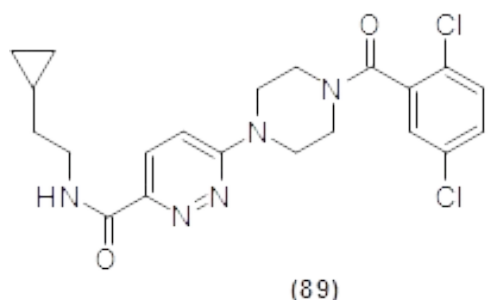


Figure 22: A small molecule SCD inhibitor (**89**) and its IMP derivative (**90**).

Antimicrobial and Antimalarial Activity

A series of 1-oxacephem analog compounds were prepared and their antibacterial properties against five Gram-positive and Gram-negative bacterial strains were evaluated *in vitro*. Ceftazidime was selected as the control. Some compounds contained IMP nucleus, and their structures are given below (see Figure 23) (45).

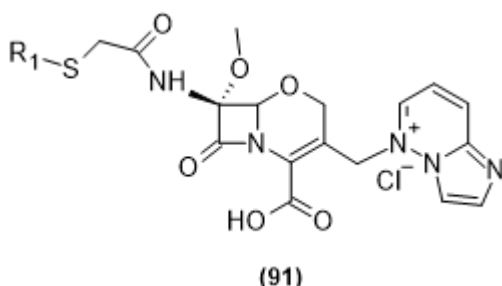


Figure 23: 1-Oxacephem derivative, having an IMP skeleton on side. R₁ is difluoromethyl, 2-chlorophenyl, or 2,5-dichlorophenyl.

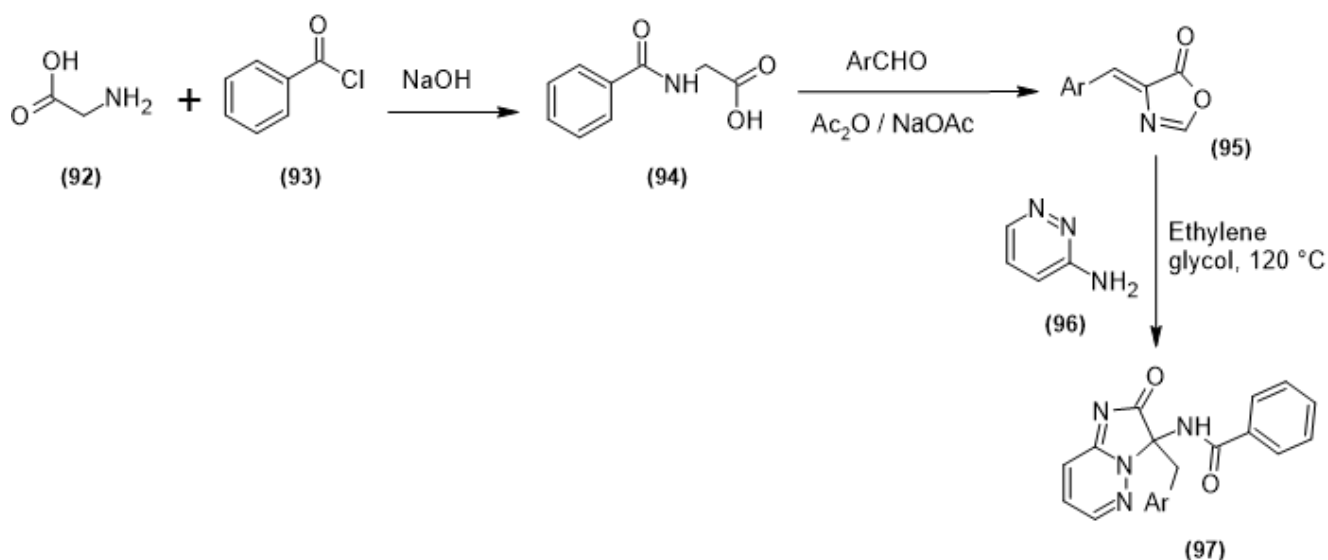
many patents describe related piperazine-based inhibitors of SCD-1 (like Figure 22, **90**). As an interesting note, the diazine-amide portion of compound **89** (Figure 22) can be mimicked by IMP in compound **90**. Presently, work in this field is known to be at the pre-clinical stage (see Figure 22) (44).

Antiparasitic Activity

Despite being a small molecule, 3-nitro-6-oxopropyl-IMP was considered for clinical trials (16).

Antiproliferative Agents

Sruthi and co-workers devised a synthetic method in which they obtained the IMP-2-one derivatives with a simple synthetic method. Then, they studied the *in silico* and *in vitro* activity against human cancer cell lines A375 and Colo-205, using MTT assay. Two of the synthesized compounds showed high antiproliferative activity and some of the other compounds displayed significant activity. All tested compounds were reported to be druggable and were free from toxicity and teratogenicity (see Scheme 12) (17).



Scheme 12: Synthesis of benzamido-substituted IMP-2-one derivatives. R is benzene, chlorophenyl, bromophenyl, 4-hydroxyphenyl, 3-hydroxyphenyl, 4-methylphenyl, 4-methoxyphenyl, 4-aminophenyl, 1-naphthyl, 1H-pyrrol-2-yl, pyridin-2-yl, furan-2-yl, 1H-benzimidazol-3-yl, and 5-bromo-1H-benzimidazol-3-yl.

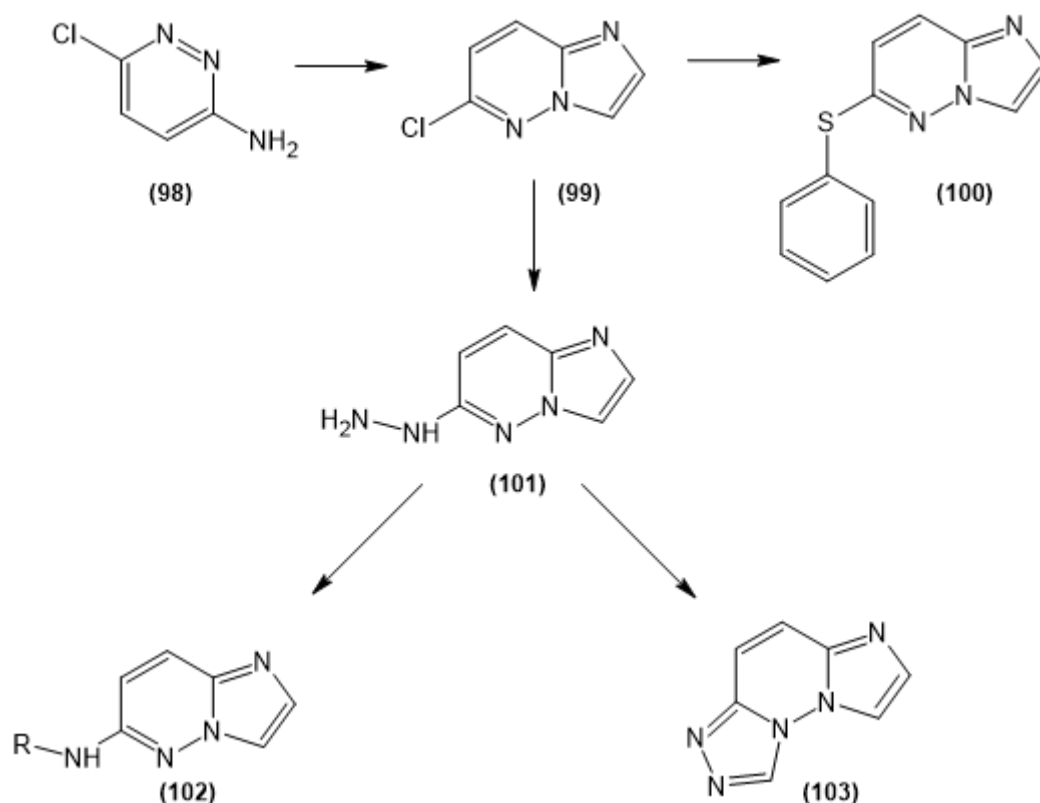
REVIEWS ABOUT SIMILAR MOLECULES

The synthesis and properties of organic compounds with anticonvulsant properties have been reviewed by Özbek and Gürdere (46). The same authors published in Phosphorus, Sulfur and Silicon and Related Elements in 2021 about 2-aminothiazole derivatives for their anticancer properties. They state in their article that medicinal chemists and drug discovery researchers widely prefer 2-aminothiazole moiety to adjust pharmacokinetic and pharmacodynamic properties of different molecules (47).

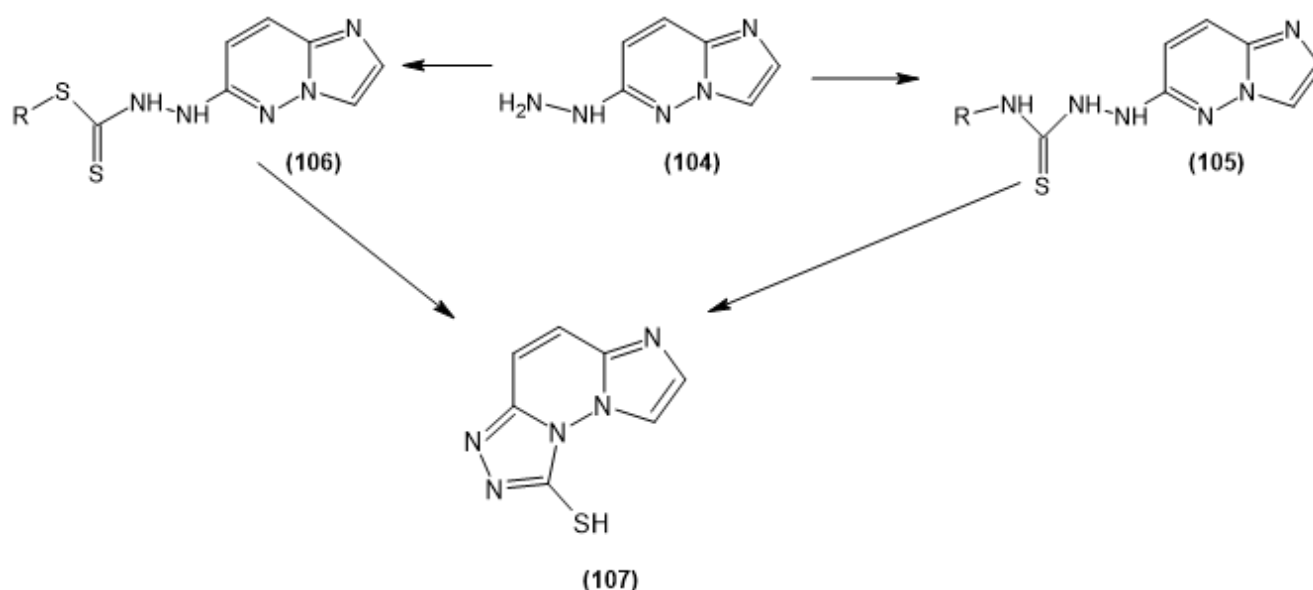
SYNTHETIC WORKS

The Historical Synthesis of IMP Derivatives

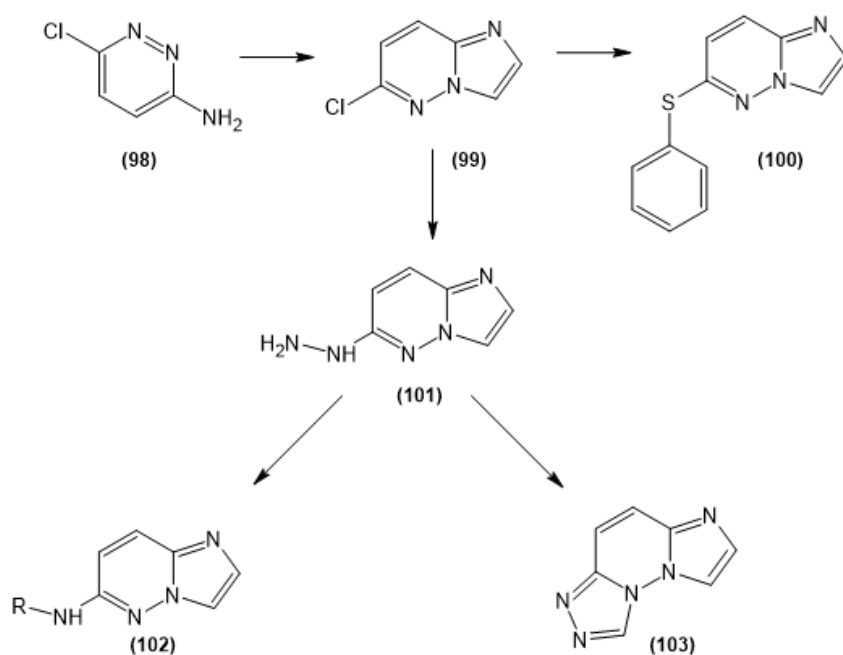
Branko Stanovnik and his colleagues reported the first instance of IMP chemistry in Tetrahedron in 1967. A year later, the same group published, in Tetrahedron again, about further synthetic modifications of the IMP nucleus (see Scheme 13, Scheme 14, Scheme 15, Scheme 16) (1,48). Many research groups still rely on these historical documents about the synthesis of IMP derivatives. Austrian and Yugoslavian groups joined forces about synthesizing new pyridazine-containing heterocycles and a series of IMP derivatives were also prepared (see Scheme 17, Scheme 18, Figure 24) (49).



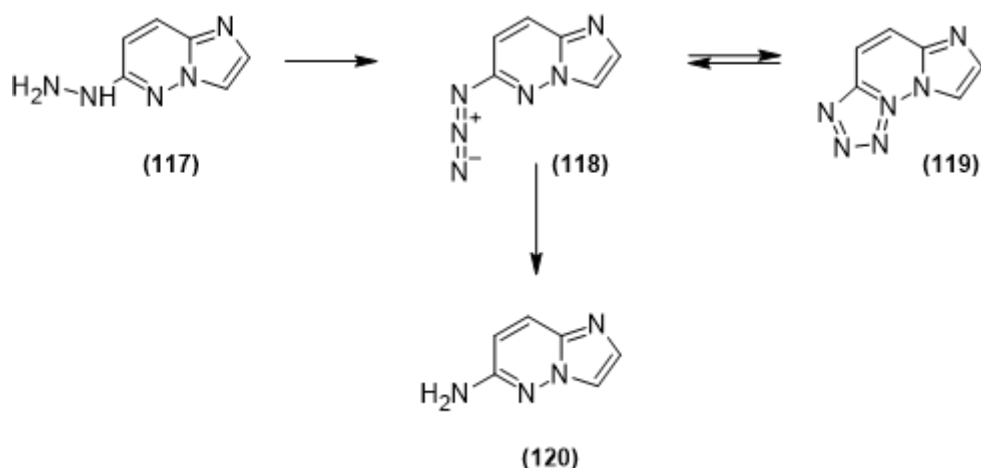
Scheme 13: Formation of 6-chloro-IMP from 3-amino-6-chloropyridazine, and synthesis of 6-phenylsulfanyl-IMP and 6-hydrazinyl-IMP molecules. The latter can be reacted to give Schiff's bases or cyclized to give another heterocycle.



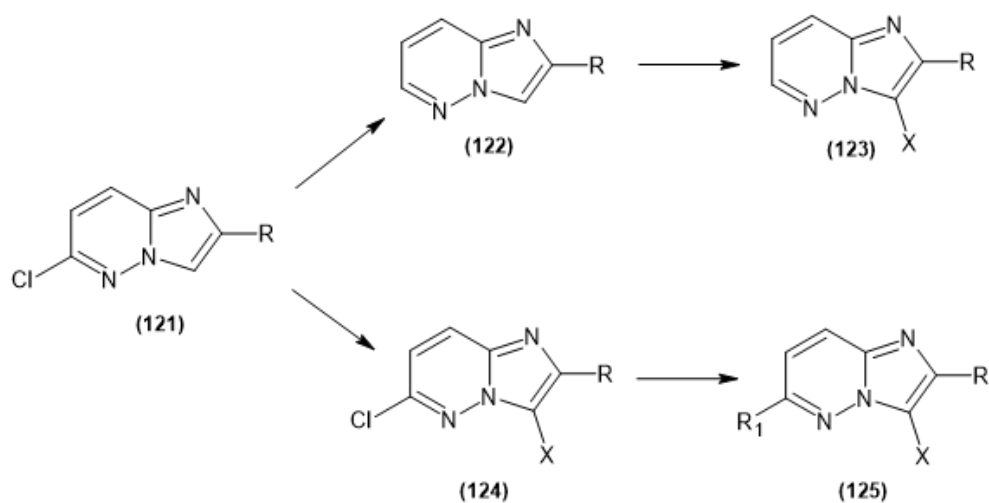
Scheme 14: Reactions of hydrazino-substituted IMP skeleton; thiosemicarbazide, dithiocarbamate, and by ring closure, thio-substituted heterocycle can be obtained.



Scheme 15: Functional group conversions and cyclizations of IMP nucleus.



Scheme 16: Reactions of the hydrazide derivative. Formation of triazido, amino, and tetrazolo-IMP derivatives are depicted.



Scheme 17: Starting from 6-chloro-IMP (a), dehalogenation was effected (122, R = H). Also, the molecule is easily brominated (123, 125; X = Br). The chloro group could be substituted for hydrazine (125).

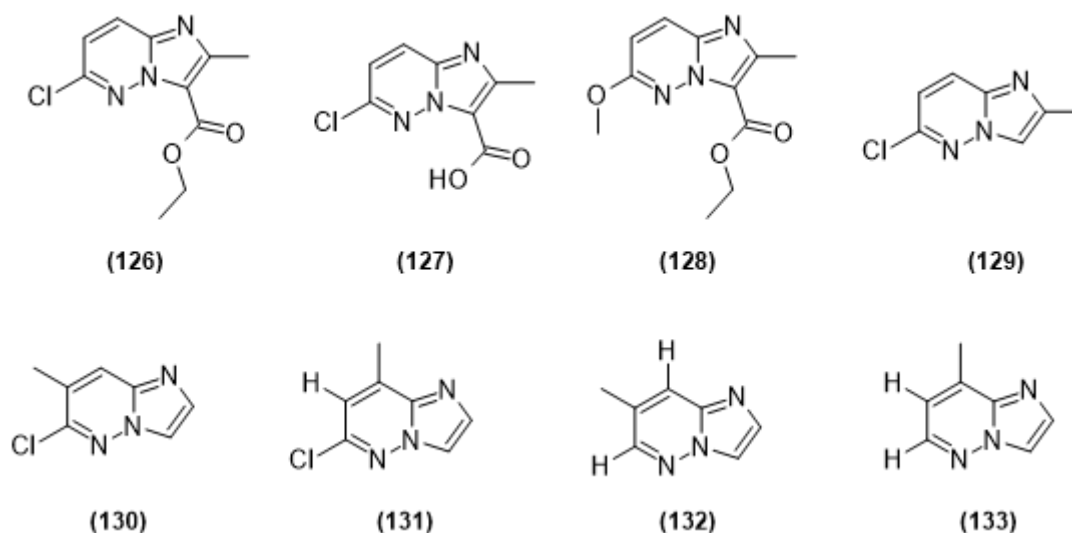
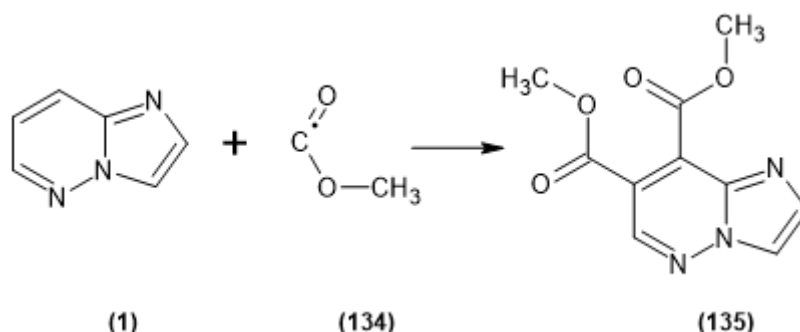


Figure 24: Synthesized IMP derivatives.

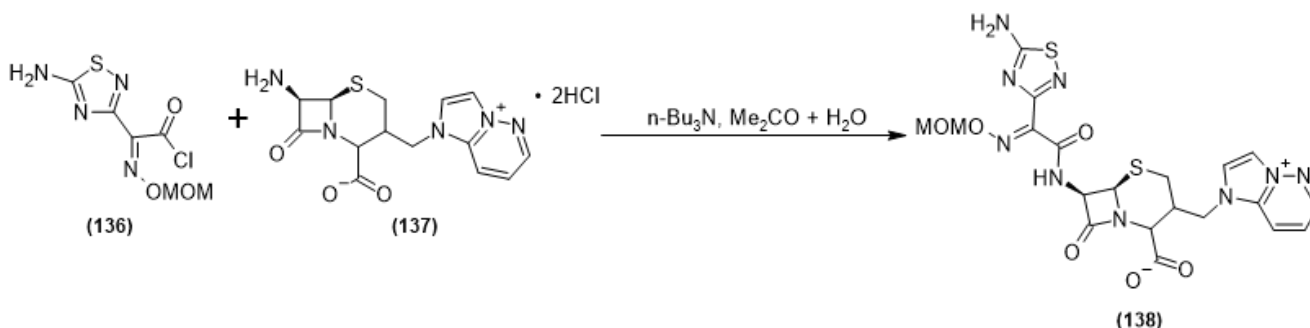


Scheme 18: Attack of methyl ester of carboxy radical to form 7,8-bis(carboxymethyl ester)-substituted IMP derivative.

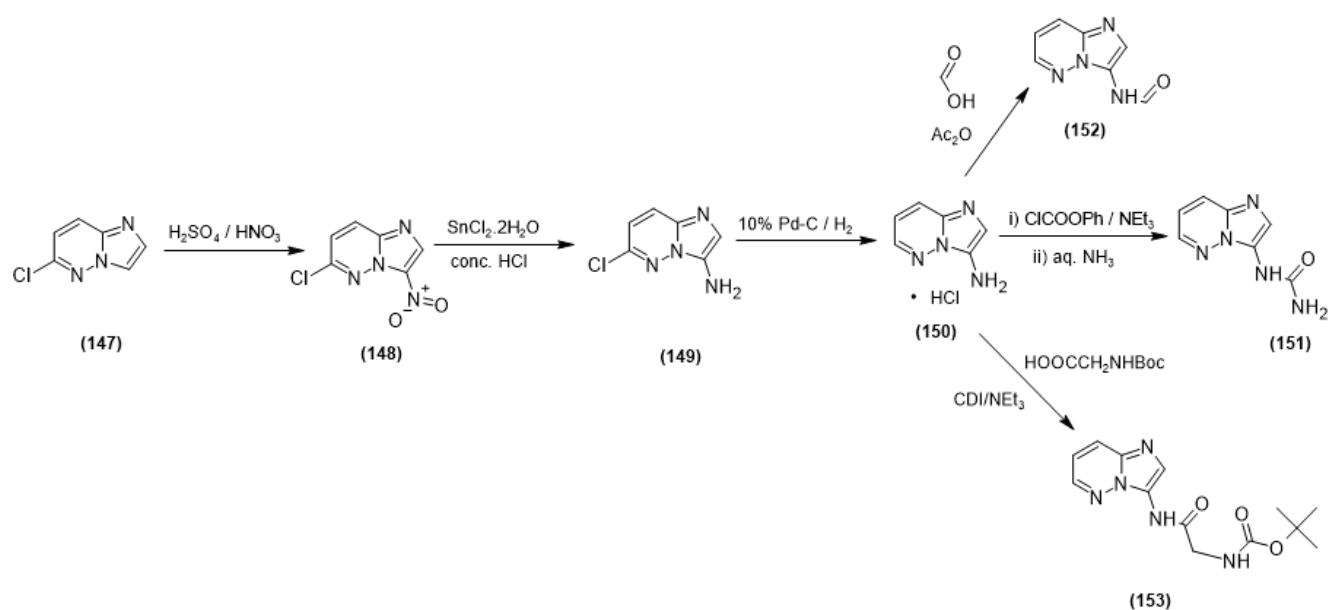
Multistep Synthesis of IMP Derivatives

Methicillin-resistant *Staphylococcus aureus* (MRSA) required a modification in the related molecule, to be 2-(5-amino-1,2,4-thiadiazol-3-yl)-2(2)-hydroxyimino acetyl group at the C-7 position and a 3- or 6-substituted IMP-ium or 5-substituted imidazo[1,2-a]pyridinium group at the C-3' position. Among the novel derivatives, 3-(6-amino-IMP-ium-1-yl)methyl-7β-[2-(5-amino-1,2,4-thiadiazol-3-yl)-2(Z)-hydroxyiminoacetamido]-3-cephem-4-carboxylate showed an excellent balance of activity

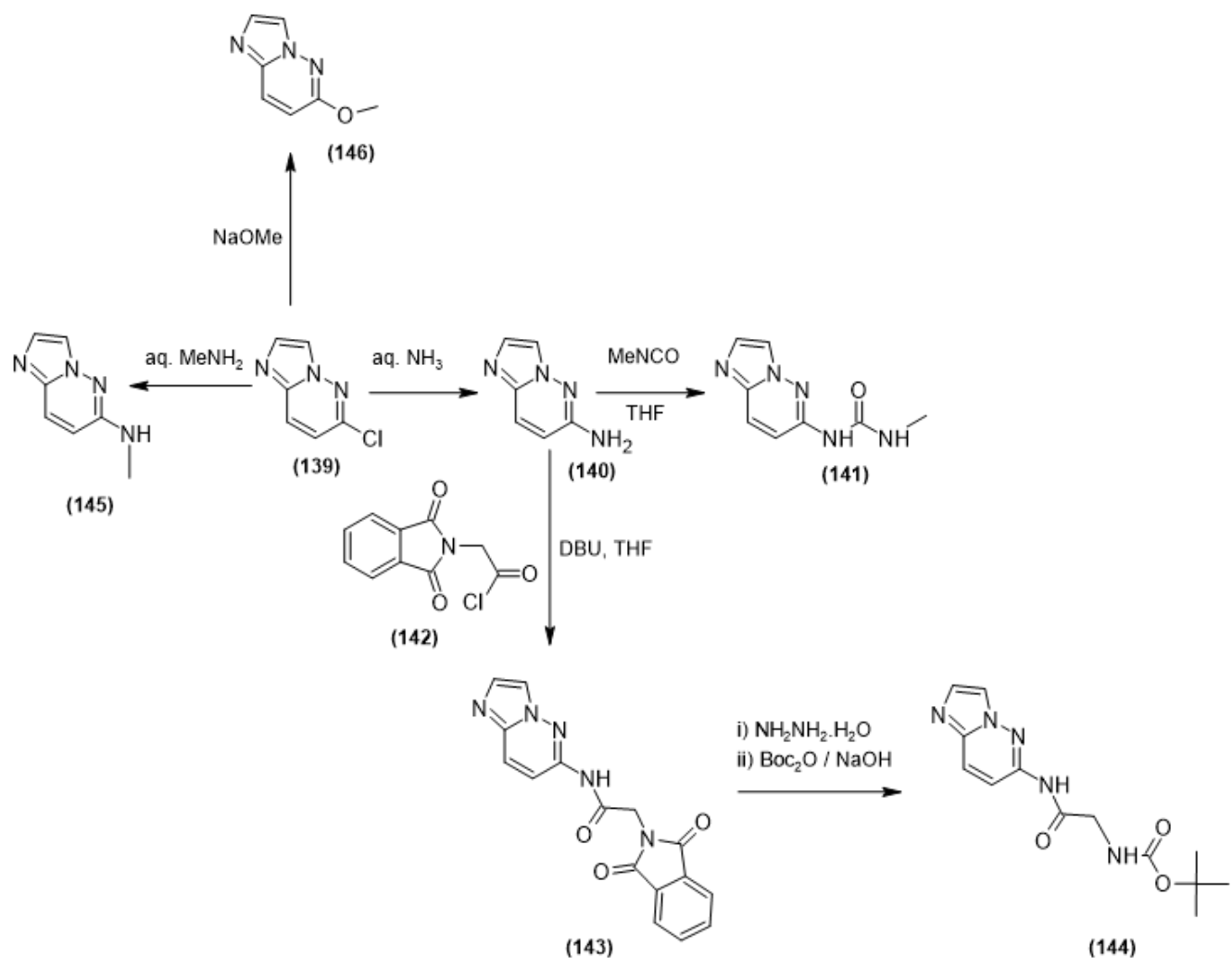
against MRSA and Gram-negative bacteria (see Scheme 19, Scheme 21, Scheme 20, Scheme 22) (50). Possible antitumor efficacy for various human cancers led to the synthesis of compounds as inhibitors for c-mesenchymal epithelial transition factor (c-Met) and vascular endothelial growth factor receptor 2 (VEGFR2) kinases. Para-substituted inhibitors were prepared, by using known inhibitors with co-crystal structural information from c-Met and VEGFR2 in the complex structure (see Figure 25) (51).



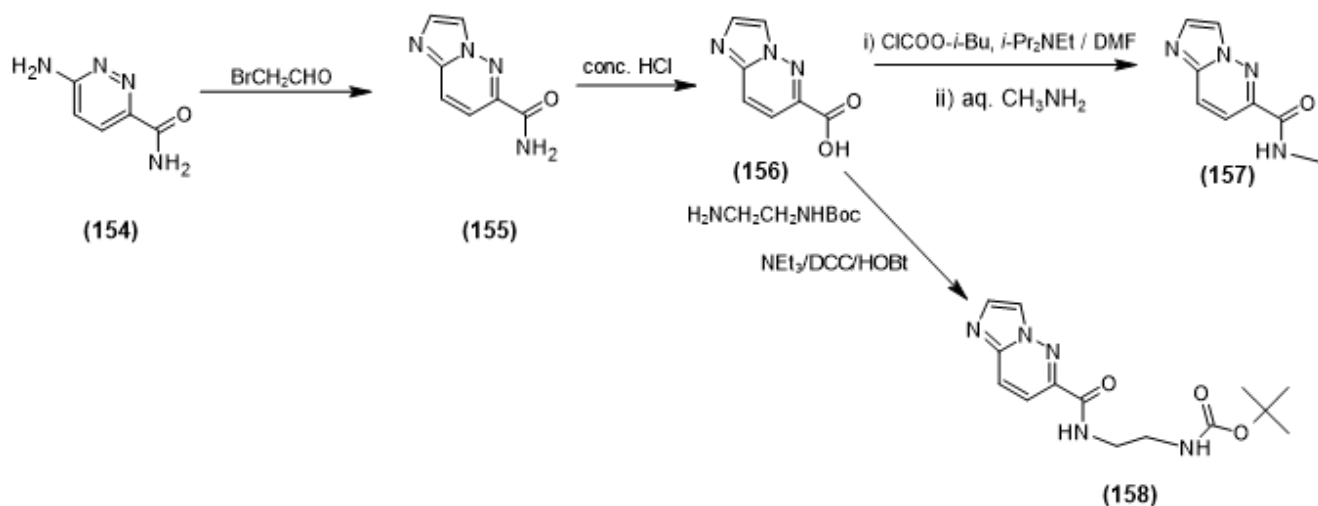
Scheme 19: Reaction of a protected thiadiazole and an IMP molecule.



Scheme 20: Starting from 6-chloro-IMP, 3-amino-IMP was obtained and many other substances were prepared from the latter.



Scheme 21: Several reactions of the IMP skeleton with amines and phthalimides.



Scheme 22: Formation of IMP heterocyclic system and synthesis of two different compounds (**157** and **158**) from the carboxy-terminated IMP molecule.

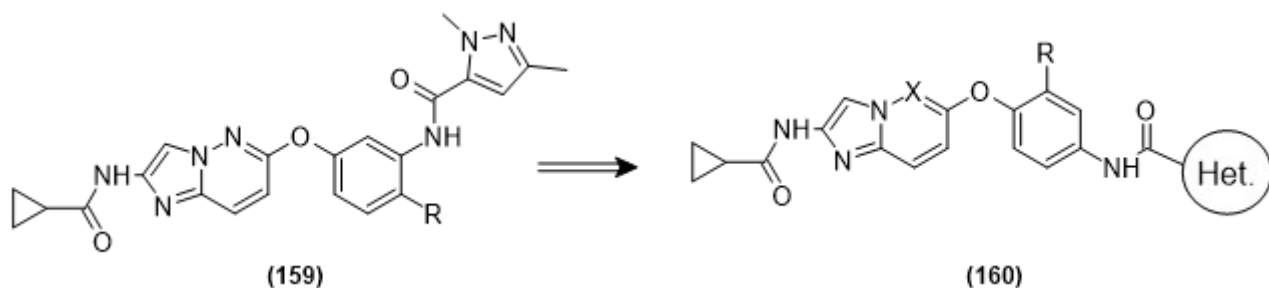
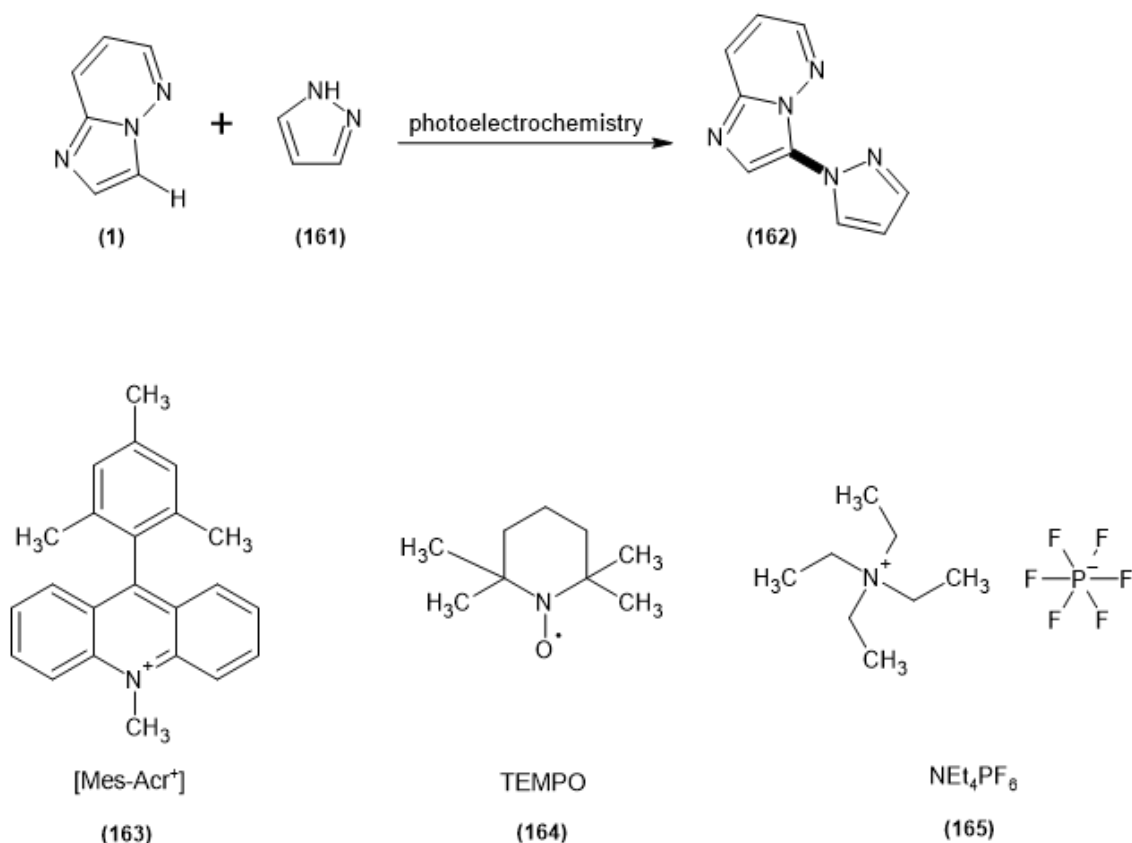


Figure 25: Design of a new compound (**160**) which has dual c-Met and VEGFR2 inhibition properties.

Arene C-H Functionalization

One equivalent of arene and two equivalents of substituted pyrazole were reacted to obtain the pyrazole-substituted IMP compound in 49% yield, in

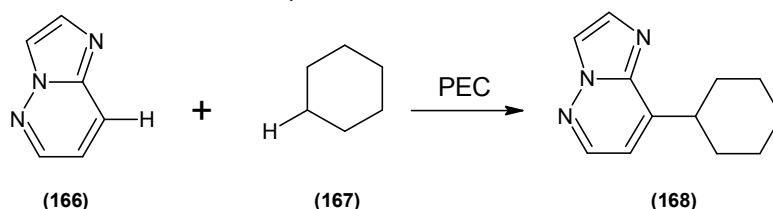
which a C-H functionalization was effected with a combination of photochemistry and electrochemistry (see Scheme 23) (52).



Scheme 23: Using photoelectrochemical conditions led to a C-H functionalization of IMP and pyrrole. Reaction conditions: Arene, 1 equivalent, pyrrole, 2 equivalent; [Mes-Acr⁺], 5 mol%, TEMPO, (20 mol%), Et₄NBF₄ (0,1 equivalent), dichloroethane, blue LED, 2 mA, 16 h.

In another study, new and functionalized heteroarenes were prepared via dehydrogenative cross-coupling. One of the studied compounds

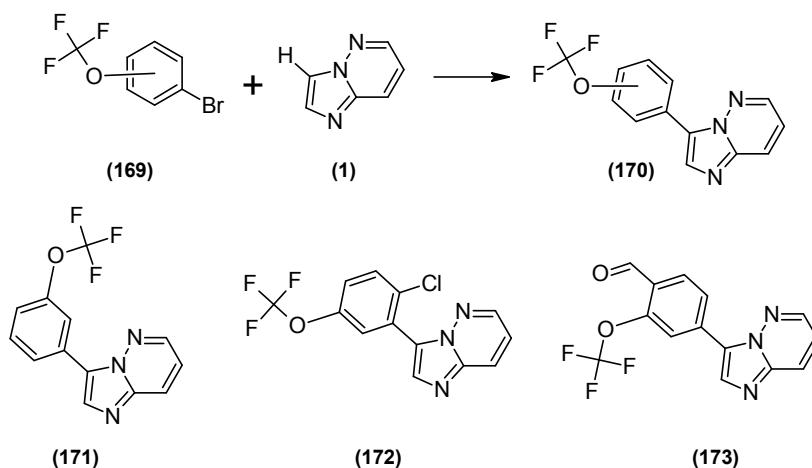
contained IMP skeleton and it was successfully alkylated (see Scheme 24) (53).



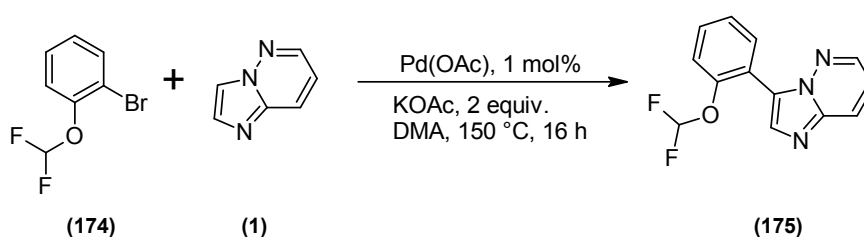
Scheme 24: Photoelectrochemistry of the IMP-cyclohexane system yields the 8-cyclohexyl-IMP molecule. Reaction conditions: 0.3 equivalent Et₄NCl, 6 equivalents of HCl, acetonitrile, 392 nm, 10 W LED, 2 mA. RVC anode, Pt cathode, 0.3 mmol heteroarene, 1 mL of cyclohexane, 6 mL of acetonitrile, 34-42 °C internal temperature.

Huang and co-workers reported another instance of C-H activation, in which (trifluoromethoxy)IMP derivative was successfully synthesized from a bromobenzene derivative, the heterocycle, and a catalytic amount of palladium acetate. The trifluoromethoxy substituent was changed to *m*-trifluoromethoxyphenyl, and it was successful, too. The research group tried another starting compound having difluoromethoxyphenyl group, and the IMP-

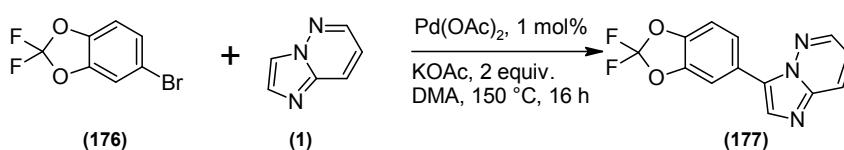
containing new heterocycle was also obtained nicely. 5-bromo-2,2-difluorobenzo[d][1,3]dioxole led to a substituted IMP in 86% yield. Lastly, they reacted 1-bromo-4-(1,1,2,2-tetrafluoroethoxy)benzene with IMP and obtained, with 87% yield, the substituted compound (see Scheme 25, Scheme 26, Scheme 27, Scheme 28) (54).



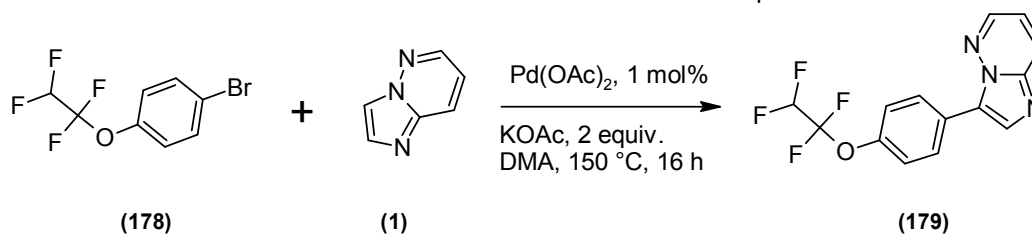
Scheme 25: Three C-H functionalization examples for IMP; reaction conditions, IMP, 1.5 equivalents; Pd(OAc)₂, 1 mol%; KOAc, 2 equivalents; DMA, 150 °C, 16 hours.



Scheme 26: 3-(2-difluoromethyl)phenyl-containing IMP molecule, IMP was used in 1.5 equivalents to the bromo compound.



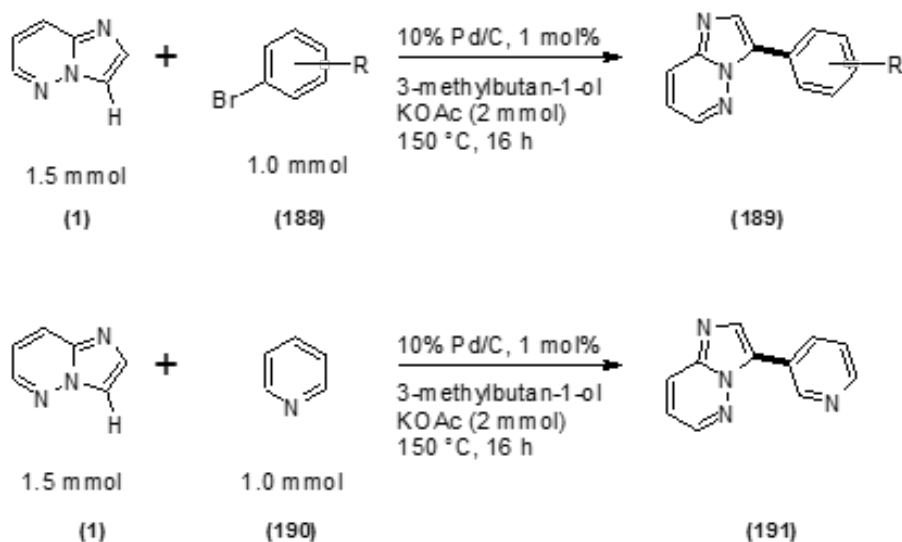
Scheme 27: Another C-H functionalization example for IMP.



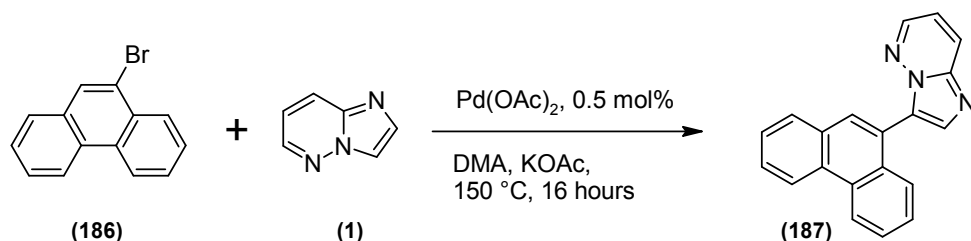
Scheme 28: The preparation scheme for tetrafluoroethoxyphenyl-containing IMP molecule. IMP was taken 1.5 equivalents with respect to the bromo compound.

Mao *et al.* published another of their publications about C-H activation of IMP with Pd/C in green solvents (see Scheme 29) (55). Bouzayani and co-workers investigated the reactivity of positions C9 and C10 of 9- or 10-bromophenanthrenes and for

catalyst, they used 0.5-0.1 mol% of phosphine-free Pd(OAc)₂. They also successfully reacted imidazopyridazines introduced at phenanthrene C9-position (see Scheme 30) (56).



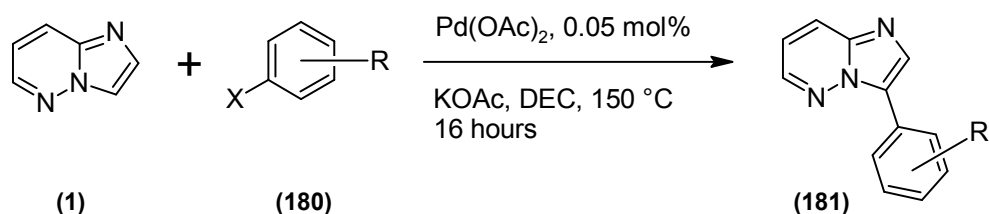
Scheme 29: Addition of a bromobenzene derivative or pyridine to IMP to yield 3-substituted IMP; R groups are 4-cyano, 4-nitro, 4-chloro, 4-methoxy, and 2-cyano.



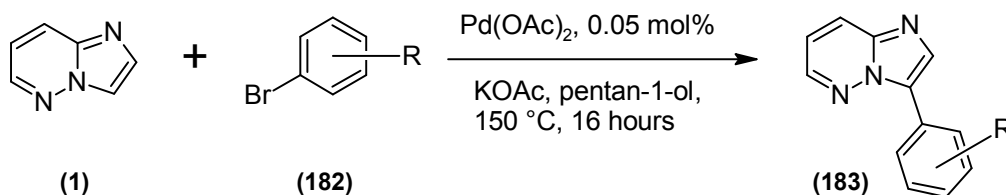
Scheme 30: 1.3 equivalents of IMP was used to obtain the phenanthrene-substituted molecule in good yield.

In another publication, green solvents associated to Pd/C were investigated in the C-H arylation in which metal residues cause contamination in the environment. The research team found that only 1 mol% of Pd/C allows, very efficiently, for the direct arylations of most heteroaromatic compounds. With this catalyst and potassium acetate as the base, the direct arylation of many compounds, including IMP derivatives, were

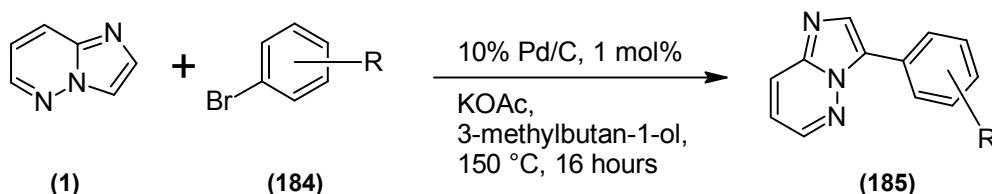
effected, using aryl bromides as coupling partners, in a high regioselectively and in moderate to very high yields. Electron-deficient and electron-rich aryl bromides were tolerated; what is more, for the most reactive heteroarenes, Pd/C catalyst tolerated green solvents such as diethyl carbonate, 3-methylbutan-1-ol and pentan-1-ol, provided a low impact to the environment (see Scheme 31, Scheme 32, Scheme 33) (57).



Scheme 31: IMP is coupled to haloarenes in diethylcarbonate with Pd(OAc). X=Br, R = 4-OMe; X = Br, R = 4-NO₂; X = Br, R = 4-COMe; X = Cl, R = 4-CN(*); X = Cl, R = 4-CF₃(*); X = Cl, R = 4-CO₂Me(*); X = Cl, R = 3-CN(*). For X and R pairs, asterisk indicates that Pd(OAc)₂ was taken in 0.1 mol%.



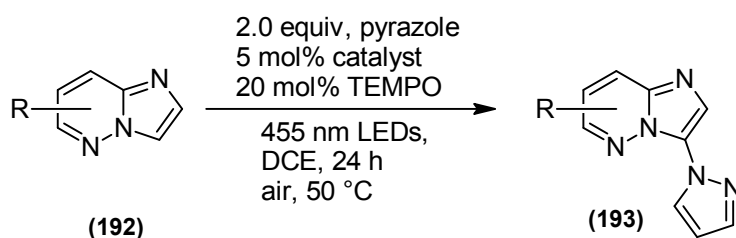
Scheme 32: Several examples concerning the C-H activation of IMP, having 3-substituted phenyl group. R is 4-cyano, 4-nitro, 4-formyl, 4-acetyl, 4-fluoro, 4-methoxy, 3-carboxymethyl, and 2-cyano.



Scheme 33: Instead of palladium(II) acetate, 10% Pd/C was used in 1 mol% proportion. R is 4-cyano (in DEC, a reduced yield was observed), 4-nitro (in DEC, a reduced yield was observed), 4-chloro, 4-methoxy, and 2-cyano.

According to computational predictions, many bridging-nitrogen polyaromatic compounds, such as IMP derivatives, should be susceptible to oxidation by the photocatalyst. This hypothesis was verified in experimental manner, and in most cases, only a single regioisomer was obtained. Whatever the substituents are, derivatives of IMP yielded 3-substituted functionalization products. When two halogen substituents are present in the IMP

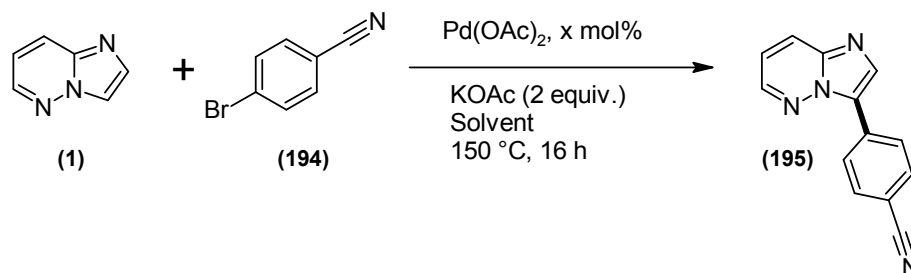
derivative, and although it is more electron-deficient, this IMP derivative was obtained with a dramatic loss of reaction yield and it is important to stress that substitution still occurred at the 3-position. For IMP derivatives and imidazo[1,2-*a*]pyrimidines, there is an enamine character in the ring. Similarly to *N*-methylpyrazoles, these nitrogen-bridged heterocycles react at the electrophilic carbon of the iminium radical (see Scheme 34) (19).



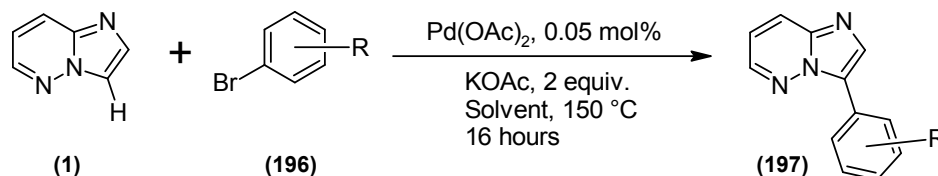
Scheme 34: Addition of pyrazole nucleus to IMP at position 3. When no substituent is present, the reaction yield is 70%. When a Cl is bound to position 6, the yield is 50%. Finally, when 2-phenyl- and 6-chloro- are present, the yield is 73%.

Chikhi and co-workers reported on the Pd-catalyzed direct arylation of IMP. Phosphine-free Pd(OAc)₂ was found to be a very efficient catalyst in the direct arylation of IMP at C3 position, with employing a very low catalyst loading. The reaction requires only 0.1-0.05 mol% catalyst loading, works with a wide range of aryl bromides, and yields very high TOF

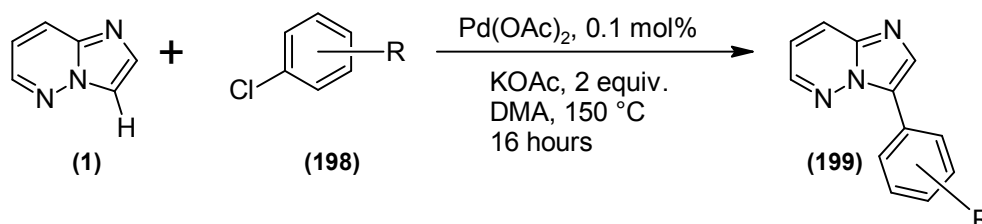
and TON numbers. Some electron-deficient aryl chlorides were also observed to work well as substrates. Green, safe, and renewable solvents like pentan-1-ol were used in the synthesis of 31 examples, and the efficiency did not go down (see Scheme 35, Scheme 36, Scheme 37, Scheme 38, Scheme 39) (58).



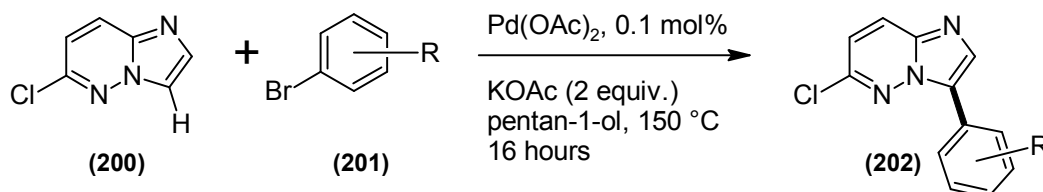
Scheme 35: Optimization of the catalyst in preparing 3-(4-cyanophenyl)IMP. The solvents with highest yields based on the product were DMA, pentan-1-ol, and CPME. Catalyst percentage was 0.05 mol% in the mentioned green solvents and in the subsequent experiments, this percentage was used.



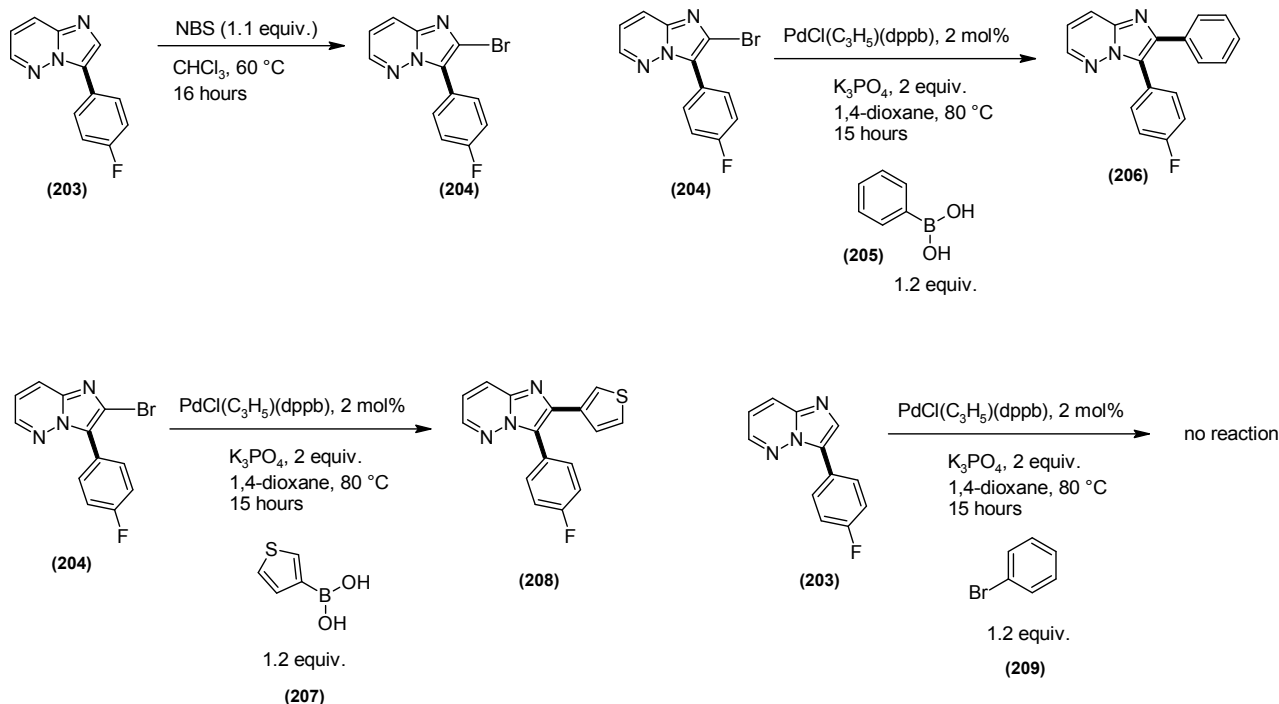
Scheme 36: C-H functionalization of IMP with several bromobenzenes. R is 4-OMe, 4-NO₂, 4-CHO, 4-COMe, 4-COOEt, 4-Cl, 4-F, 4-Me, 4-NH₂, 3-COOMe, 3-COMe, 3-Br, 3-NH₂, 3,5-bis(CF₃), 2-CN, 2-CHO, 2-CF₃, 1-naphthyl (instead of benzene), 1-pyrenyl (instead of benzene), 3-quinoliny (instead of benzene), 3-pyridyl (instead of benzene), and 5-pyrimidinyl (instead of benzene). Some reactions were conducted in diethylcarbonate, pentan-1-ol, or CPME instead of DMA.



Scheme 37: Using chlorobenzene derivatives instead of bromobenzenes: Reaction conditions and products. IMP was taken in 1.1 equivalents. R is 4-CN, 4-NO₂, 4-CF₃, 4-COOMe, 3-CN, 3-NO₂, 2-NO₂, and 4-NO₂-2-CN.



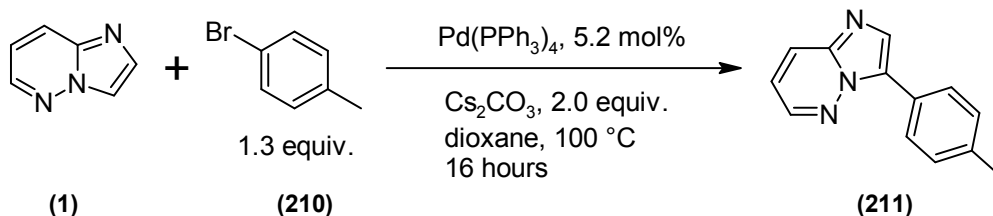
Scheme 38: 6-Chloro-IMP was treated with bromobenzene derivatives to afford a series of 3-(substituted phenyl) IMP compounds. R is 4-NO₂, 4-CHO, 4-Br, 2-COOMe, 1-naphthyl, 3-quinoliny, and 3-pyridyl.



Scheme 39: Bromination of 3-(4-fluorophenyl)substituted IMP and further substitutions at 2 position.

A wide spectrum of biological and therapeutic properties is known for imidazo[1,2-b]pyridazine derivatives, but there is only one method in the literature for the synthesis of a 3-arylimidazo-IMP derivative via palladium-catalyzed regioselective

arylation of IMP. Treatment of IMP with 4-bromotoluene in 1,4-dioxane at 100 °C, where Cs_2CO_3 was used as a base along with a catalytic amount of $\text{Pd}(\text{PPh}_3)_4$ gives 3-(4-tolyl)IMP in 92% yield (see Scheme 40) (59).

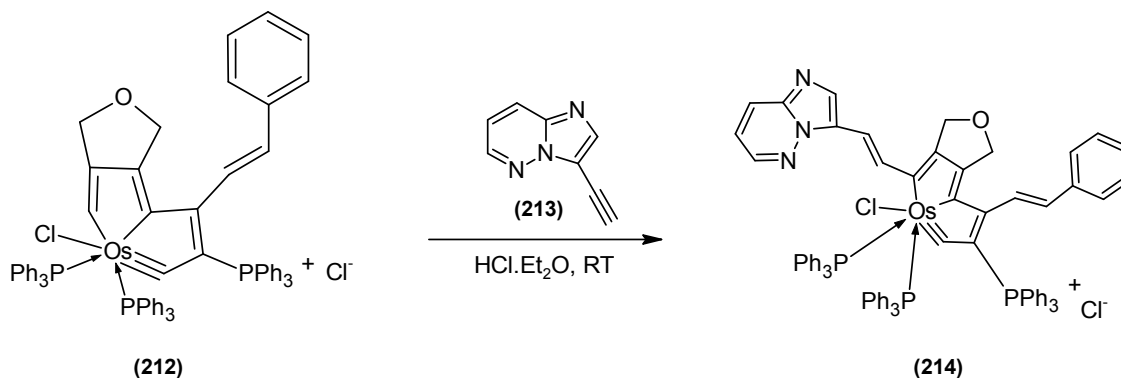


Scheme 40: Another C-H functionalization with phosphine-containing palladium complex.

Addition of Alkynes or Osmium Carbynes to Functionalized d-n Conjugated Systems

Chen and co-workers reported a reaction of metal carbynes and alkynes yielding acyclic addition products. These reactions are newly discovered and are highly efficient, regio- and stereospecific, along

with a nice tolerance of functional groups, and even are stable under air and at room temperature. The authors reported that the synthesized materials could find use in functional materials (see Scheme 41) (20).

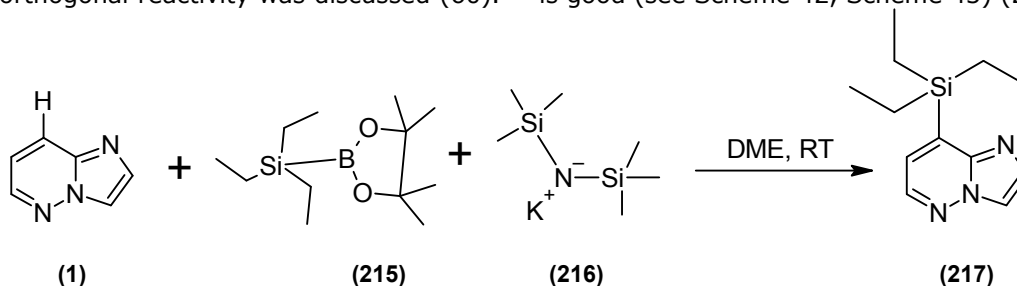


Scheme 41: Osmium carbyne reacting with an alkyne-containing IMP derivative.

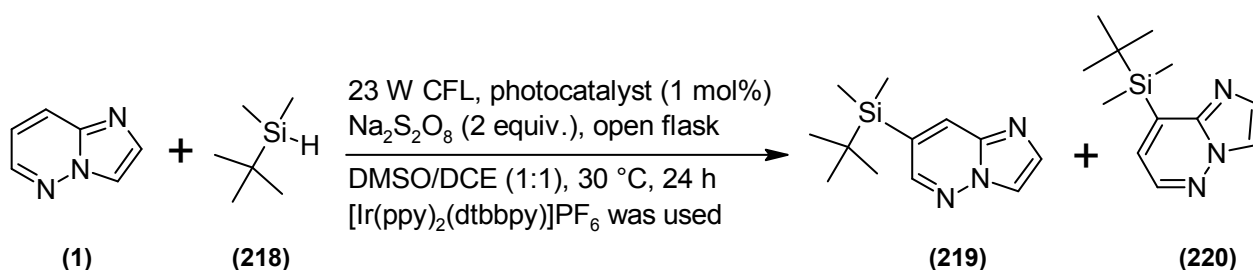
Site-Selective C-H Silylation of Azines

For the site-selective sp^2 C–H silylation of azines, Gu et al. have devised a base-mediated synthetic method. Authors report that the conditions are mild, the protocol is simple, and for a diverse set of azines, the site selectivity is excellent. With classical silylations, orthogonal reactivity was discussed (60).

Another group has reported about visible light-promoted photocatalytic C–H silylation. This method enables the direct coupling of trialkylhydrosilanes with electron-deficient and electron-rich heteroarenes and also with cyano-bearing arenes. The yields are moderate to high and regioselectivity is good (see Scheme 42, Scheme 43) (21).



Scheme 42: Silylation of IMP.

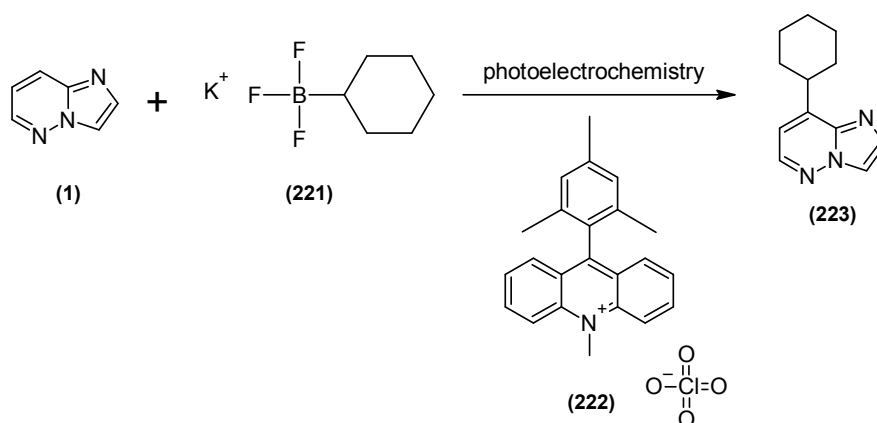


Scheme 43: C–Si bond formation of IMP and dimethyl-tert-butylsilane and C8 product is twice as much as the C7 product.

Photoelectrochemical C-H Alkylation of Heteroarenes with Organotrifluoroborates

Electrocatalysis and photoredox catalysis are joined to provide an approach which does not use chemical oxidants and organotrifluoroborates were used for

obtaining and using alkyl radicals. Using primary, secondary and tertiary alkyltrifluoroborates, a variety of heteroarenes were functionalized and the regioselectivity and chemoselectivity were found to be excellent (see Scheme 44) (22).

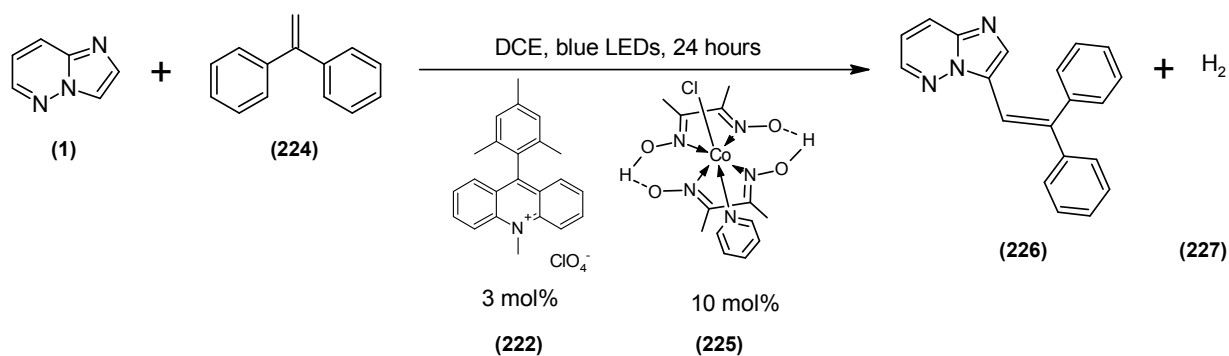


Scheme 44: Photoelectrochemistry of IMP with cyclohexyltrifluoroborate potassium salt to give 8-cyclohexyl-IMP.

Photoinduced Oxidative Activation of Electron-Rich Arenes

Hu and coworkers published a photo-induced dehydrogenative cross-coupling between electron-rich arenes and styrene derivatives using a dual catalytic system, in which an acridinium

photosensitizer and a cobaloxime proton-reducing catalyst were used. H_2 evolution was evidenced with this catalytic system, using the Csp^2 – Csp^2 bond formation. Various substituted aryl alkenes can be afforded with good to excellent yields and high β -regioselectivity (see Scheme 45) (23).

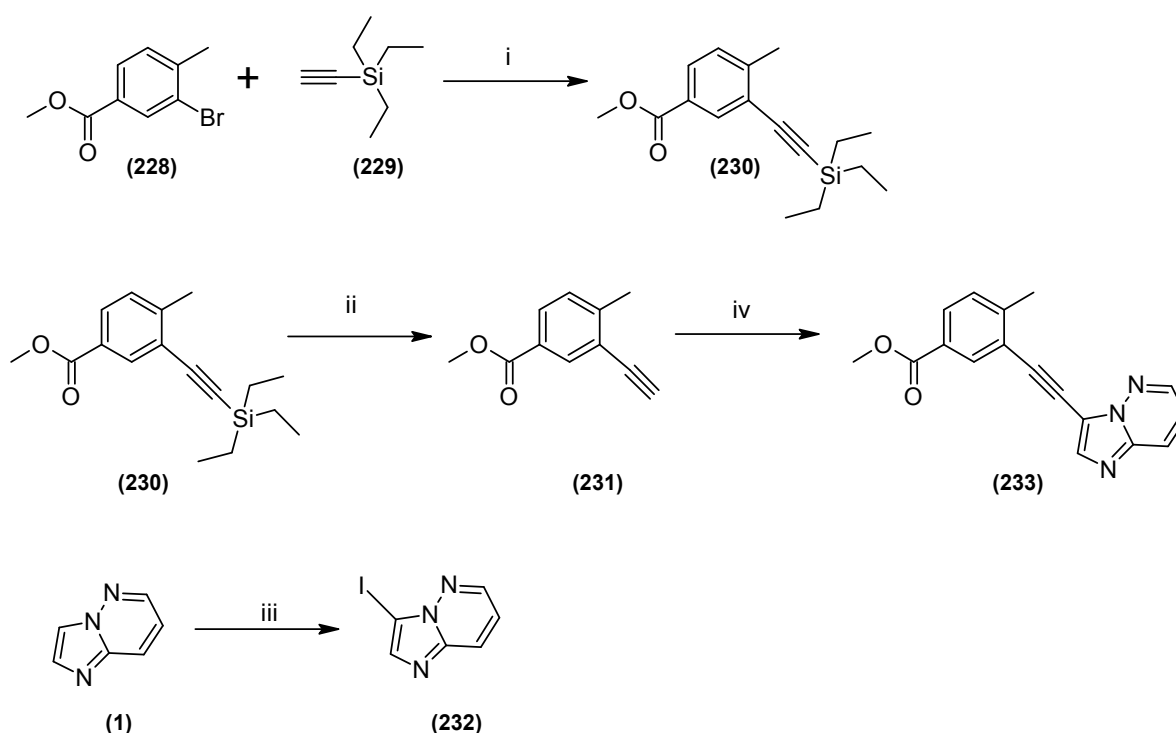


Scheme 45: Functionalization of IMP with diphenylethenyl moiety.

Use of Sonogashira Coupling for an Easier Intermediate to Ponatinib

Handa and coworkers devised an easier path in which an iron-palladium nanoparticle was used to

the intermediate of Ponatinib (see Scheme 46), also referred to as "intermediate 37" (61).



Scheme 46: An easier path to Ponatinib intermediate 37. Reaction conditions: i) 3-bromo-4-methylbenzoic acid methyl ester, 1.0 equiv.; (triethylsilyl)acetylene, 1.5 equiv.; Fe/ppm Pd NPs (contains 500 ppm Pd); Et₃N, 3.0 equiv.; 0.5 M in 2 wt% TPGS-750 M/H₂O, 50 °C, argon, 14 hours. ii) 3-(triethylsilylacetylene)-4-methylbenzoic acid methyl ester, 1.0 equiv.; K₂CO₃, 20 mol%, 0.5 M in 1:1 MeOH/THF, 45 °C, 5 hours. iii) IMP, 1.0 equiv., *N*-iodosuccinimide, 1.2 equiv., 0.53 M in DMF; 80 °C, argon, overnight. iv) 3-iodo-IMP, 1.0 equiv.; 3-(triethylsilylacetylene)-4-methylbenzoic acid methyl ester, 1.2 equiv.; Fe/ppm Pd NPs (contains 1000 ppm Pd), Et₃N, 3.0 equiv.; 0.5 M in 2 wt% TPGS-750-M/H₂O, 50 °C, argon, 43 hours.

Oxidation with CAN of Aryl and Heteroaryl Hydrazines and Hydrazides

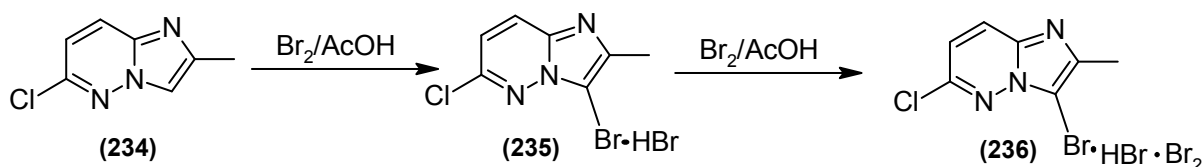
Aryl and heteroaryl hydrazines and hydrazides were oxidized with ceric ammonium nitrate (CAN) and dehydrazinated products were observed. The reaction was dependent upon the substrate and hydrocarbons and alkoxy compounds were obtained (24).

IMP Derivatives as Brominating Agents

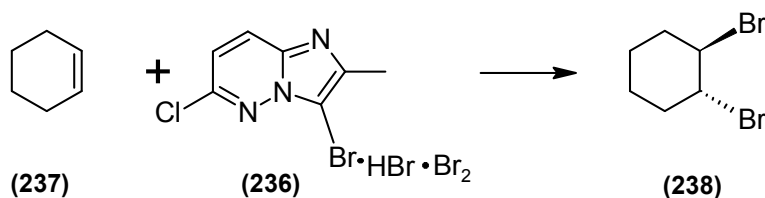
Dr. Branko Stanovnik is and has been a pioneer in the IMP chemistry. He and his colleagues devised three brominating agents from 3-bromo-6-chloro-2-methyl-IMP-bromine, 3-bromo-IMP-bromine, and 3-bromo-6-chloro-IMP-bromine. These were prepared by starting from IMP or 6-chloro-IMP by applying bromine in acetic acid. Using 3-bromo-6-chloro-2-methyl-IMP-bromine, they described a method about how to brominate α -ergocryptine and similar ergot alkaloids, to obtain the corresponding 2-

bromo derivatives in pure form, with reaction yields up to 81%. When comparing this brominating agent with the others already known in the literature, this new brominating agent was found to be advantageous. Alkenes, ketones, 3-oxoalkanoic acid esters, monocyclic N-heterocycles, and polycyclic N-heterocycles were successfully brominated with 3-bromo-IMP-bromine and 3-bromo-6-chloro-IMP-bromine. 1,2-Trans-dibromocyclohexane was synthesized from cyclohexene. Alkynyl ketones and

3-oxoalkanoic acid esters were obtained as α -bromo derivatives. At position 5, 2-aminopyridine and 2-aminopyrimidine were successfully brominated. It is however different when these two compounds were reacted with the IMP derivative, bromination occurred at position 3. At room temperature, or on gentle heating, the brominations with these reagents were completed smoothly (see Scheme 47, Scheme 48) (25,62).



Scheme 47: Stanovnik and his colleagues performed this bromination and obtained a powerful brominating agent. 6-Cl may be 6-H, and 2-CH₃ may be 2-H.



Scheme 48: Application of the IMP-brominating agent with cyclohexene to obtain the 1,2-dibromo compound.

IMP-CONTAINING MOLECULES IN MATERIAL SCIENCE

Red Phosphorescent Organic Light-Emitting Devices

IMP was, for the first time, considered as a host material in OLEDs. The heterocycle possesses an excellent ability of electron-transportation, and an extreme thermal stability. As the p-type unit, carbazole was chosen, while IMP was the n-type unit. The most promising compounds were 6-substituted and 6,8-substituted in terms of the best electroluminescent performance (see Figure 26) (26).

Photochromic Iodoargentate Hybrid Materials

Three iodoargentate hybrids with the respective closed formulas [MIPDz]₂[Ag₂I₄], [AIPDz][Ag₂I₃], and [MIPDz]₂[Ag₅I₇], in which MIPDz⁺ is methylimidazopyridazinium, and AIPDz⁺ is acetonylimidazopyridazinium. They showed good photochromism and hierarchically responsive mechanism where they were optically inert and then they underwent photolysis of iodoargentates, and as secondary electron donor, Ag particles play a role in the photoinduced intermolecular electron transfer (see Scheme 49) (27).

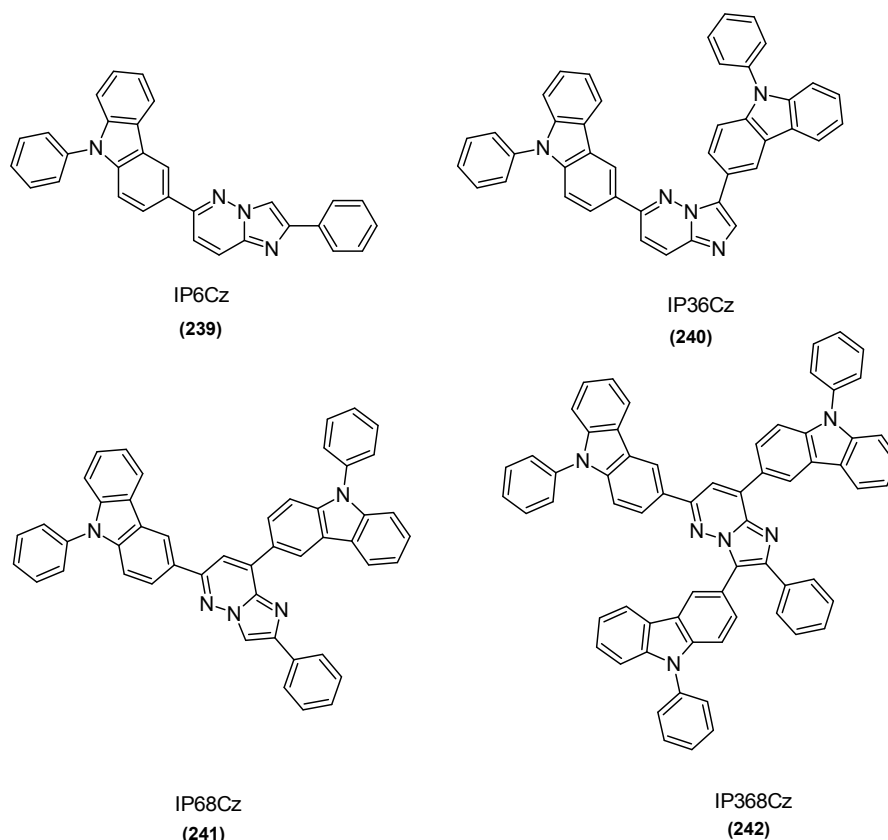
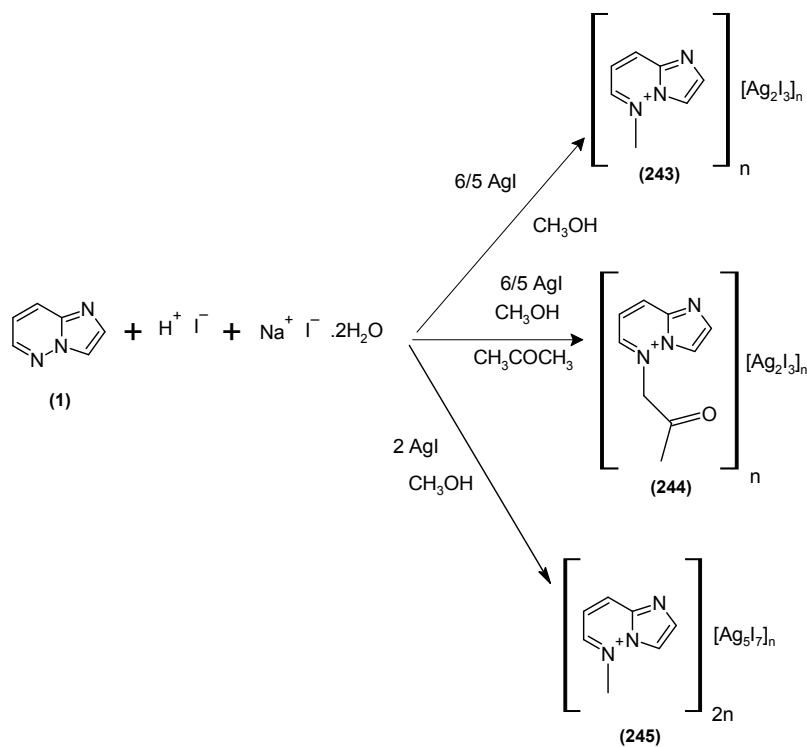


Figure 26: Carbazole-containing IMP skeletons. 3, 6, and 8 refer to the positions on the IMP skeleton on which carbazole units are bound.



Scheme 49: Under solvothermal conditions, the three iodoargentate hybrid compounds were synthesized and used for tunable and improved photochromism.

THEORETICAL-EXPERIMENTAL STUDIES

Some heterocycles could be tested for their reported C-H radical functionalization sites with the condensed Fukui function. This method is able to also predict the innate C-H sites on multi-nitrogen-containing arenes. The calculated results were validated with experiments (28). In a work by Tagore and co-workers, the unsubstituted IMP molecule was studied, both theoretically and experimentally. Experimental spectral methods included FT-IR, FT-Raman, $^1\text{H-NMR}$, $^{13}\text{C-NMR}$, and UV-Vis and comparisons with the theoretically obtained spectra yielded a high correlation with each other (63). Coulombic ion-pairing complex of the modeled compounds, as acetate ion accompanies them, was calculated in terms of the ionic interaction energy. According to the results, stability is one of the significant factors about the inhibitory potency of fibrinogen-receptor binding (64). Twenty-two azoloazine compounds were selected for carbon-13 nuclear magnetic resonance data. A stepwise linear multiple regression with nitrogen substituents in the 5- and 6-membered ring system. Pyrrolo[1,2-*a*]pyridine was decided to be the reference for chemical shift correlation. The researchers found that a highly correlated set of chemical parameters are present (65). The magnetic circular dichroism (MCD) *B* terms of the two *L* transitions in 14 azaindolizines in neutral and protonated forms have been measured by a collaboration between an American group and a Yugoslavian research group. Interpretation was based on the perimeter model and consideration of the effect of the $-\text{CH} \Rightarrow -\text{N}=\text{}$ and $-\text{CH} \Rightarrow -\text{NH}^+=$ replacements on the orbital energy double difference $-\Delta\text{HOMO}-\Delta\text{LUMO}$. The INDO/S calculations seemed to fit well to the first-order perturbation theory and these calculations along with PPP calculations were successfully used to predict the *B* terms in the MCD spectra with a good agreement (66). ^{15}N NMR chemical shift data for 14 azolopyridines were obtained as well as the results of INDO/S-SOS calculations of nitrogen shieldings. The ^{15}N data and their assignments are shown to be reliable for the indolizine's nitrogen as based on relative line widths. The pyridine nitrogens are more reliably assigned from the ^{15}N spectra when complimented with INDO/S-SOS calculations for individual molecules (67). A joint work between two Yugoslavian groups yielded the orbital correlation diagram for IMP molecule and its substituted derivatives (68).

CONCLUSION

IMP and its derivatives attract a great deal of attention owing to their biological activities. Enzyme inhibition and some biological activity (antitumoral activity, etc) could be grasped in the first look. Being recognized as a heteroarene, there are also works about IMP and its derivatives, theoretical aspects this versatile molecule. The presence of

many enzyme inhibition reports may attract the attention of researchers and a collaboration with medicinal chemists will undoubtedly lead to new and powerful molecules to be used in many diseases, including Alzheimer's, cancer, and a lot more.

CONFLICT OF INTERESTS

The author declares that there are no conflict of interests.

REFERENCES

1. Stanovnik B, Tišler M. Synthesis of pyridazine derivatives—VIII. *Tetrahedron*. 1967 Jan;23(1):387–95. [<DOI>](#).
2. Liu J, Zhang Y, Huang H, Lei X, Tang G, Cao X, et al. Recent advances in Bcr-Abl tyrosine kinase inhibitors for overriding T315I mutation. *Chem Biol Drug Des*. 2021 Mar;97(3):649–64. [<DOI>](#).
3. AbdelHaleem A, Mansour AO, AbdelKader M, Arafa RK. Selective VEGFR-2 inhibitors: Synthesis of pyridine derivatives, cytotoxicity and apoptosis induction profiling. *Bioorganic Chem*. 2020 Oct;103:104222. [<DOI>](#).
4. Pandit SS, Kulkarni MR, Ghosh U, Pandit YB, Lad NP. Synthesis and biological evaluation of imidazo[1,2-*b*]pyridazines as inhibitors of TNF- α production. *Mol Divers*. 2018 Aug;22(3):545–60. [<DOI>](#).
5. Shi Q, Tebben A, Dyckman AJ, Li H, Liu C, Lin J, et al. Purine derivatives as potent Bruton's tyrosine kinase (BTK) inhibitors for autoimmune diseases. *Bioorg Med Chem Lett*. 2014 May;24(9):2206–11. [<DOI>](#).
6. Abdel-Maksoud MS, El-Gamal MI, Benhalilou DR, Ashraf S, Mohammed SA, Oh C. Mechanistic/mammalian target of rapamycin: Recent pathological aspects and inhibitors. *Med Res Rev*. 2019 Mar;39(2):631–64. [<DOI>](#).
7. Amin HS, Parikh PK, Ghate MD. Medicinal chemistry strategies for the development of phosphodiesterase 10A (PDE10A) inhibitors - An update of recent progress. *Eur J Med Chem*. 2021 Mar;214:113155. [<DOI>](#).
8. Sato T, Sekimata K, Sakai N, Watanabe H, Mishima-Tsumagari C, Taguri T, et al. Structural Basis of Activin Receptor-Like Kinase 2 (R206H) Inhibition by Bis-heteroaryl Pyrazole-Based Inhibitors for the Treatment of Fibrodysplasia Ossificans Progressiva Identified by the Integration of Ligand-Based and Structure-Based Drug Design Approaches. *ACS Omega*. 2020 May 26;5(20):11411–23. [<DOI>](#).

9. Alnabulsi S, Al-Hurani EA. Pim kinase inhibitors in cancer: medicinal chemistry insights into their activity and selectivity. *Drug Discov Today*. 2020 Nov;25(11):2062–9. [<DOI>](#).
10. Farag AK, Roh EJ. Death-associated protein kinase (DAPK) family modulators: Current and future therapeutic outcomes. *Med Res Rev*. 2019 Jan;39(1):349–85. [<DOI>](#).
11. Pandey MK, DeGrado TR. Glycogen Synthase Kinase-3 (GSK-3)-Targeted Therapy and Imaging. *Theranostics*. 2016;6(4):571–93. [<DOI>](#).
12. Wei P, Liu B, Wang R, Gao Y, Li L, Ma Y, et al. Discovery of a series of dimethoxybenzene FGFR inhibitors with 5H-pyrrolo[2,3-b]pyrazine scaffold: structure–activity relationship, crystal structural characterization and in vivo study. *Acta Pharm Sin B*. 2019 Mar;9(2):351–68. [<DOI>](#).
13. Ahammad F, Tengku Abd Rashid TR, Mohamed M, Tanbin S, Ahmad Fuad FA. Contemporary Strategies and Current Trends in Designing Antiviral Drugs against Dengue Fever via Targeting Host-Based Approaches. *Microorganisms*. 2019 Aug 28;7(9):296. [<DOI>](#).
14. Moine E, Moiré N, Dimier-Poisson I, Brunet K, Couet W, Colas C, et al. Imidazo[1,2-b]pyridazines targeting *Toxoplasma gondii* calcium-dependent protein kinase 1 decrease the parasite burden in mice with acute toxoplasmosis. *Int J Parasitol*. 2018 Jun;48(7):561–8. [<DOI>](#).
15. He Z-X, Gong Y-P, Zhang X, Ma L-Y, Zhao W. Pyridazine as a privileged structure: An updated review on anticancer activity of pyridazine containing bioactive molecules. *Eur J Med Chem*. 2021 Jan;209:112946. [<DOI>](#).
16. Werbel LM, Worth DF. Chapter 13. Antiparasitic Agents. In: *Annual Reports in Medicinal Chemistry* [Internet]. Elsevier; 1980 [cited 2021 Jun 22]. p. 120–9. ISBN: 978-0-12-040515-2. [<URL>](#).
17. Sruthi K, Sumakanth M, Mahendra KC, Naresh K. Synthesis, in silico and in vitro anti-proliferative studies of some novel benzamido substituted imidazo[1,2-b]pyridazin-2-ones. *Ank Üniversitesi Eczacı Fakültesi Derg*. 2017;41(1):9–25. [<DOI>](#).
18. Schirmmacher R, Bailey JJ, Mossine AV, Scott PJH, Kaiser L, Bartenstein P, et al. Radioligands for Tropomyosin Receptor Kinase (Trk) Positron Emission Tomography Imaging. *Pharmaceuticals*. 2019 Jan 3;12(1):7. [<DOI>](#).
19. Margrey KA, McManus JB, Bonazzi S, Zecri F, Nicewicz DA. Predictive Model for Site-Selective Aryl and Heteroaryl C–H Functionalization via Organic Photoredox Catalysis. *J Am Chem Soc*. 2017 Aug 16;139(32):11288–99. [<DOI>](#).
20. Chen S, Liu L, Gao X, Hua Y, Peng L, Zhang Y, et al. Addition of alkynes and osmium carbynes towards functionalized dn–pn conjugated systems. *Nat Commun*. 2020 Dec;11(1):4651. [<DOI>](#).
21. Liu S, Pan P, Fan H, Li H, Wang W, Zhang Y. Photocatalytic C–H silylation of heteroarenes by using trialkylhydrosilanes. *Chem Sci*. 2019;10(13):3817–25. [<DOI>](#).
22. Yan H, Hou Z, Xu H. Photoelectrochemical C–H Alkylation of Heteroarenes with Organotrifluoroborates. *Angew Chem Int Ed*. 2019 Mar 26;58(14):4592–5. [<DOI>](#).
23. Hu X, Zhang G, Bu F, Luo X, Yi K, Zhang H, et al. Photoinduced oxidative activation of electron-rich arenes: alkenylation with H₂ evolution under external oxidant-free conditions. *Chem Sci*. 2018;9(6):1521–6. [<DOI>](#).
24. Štefane B, Polanc S. CAN-Mediated Oxidation of Electron-Deficient Aryl and Heteroaryl Hydrazines and Hydrazides. *Synlett*. 2008 May;2008(9):1279–82. [<DOI>](#).
25. Stanovnik B, Tisler M, Drnovsek I. 3-bromoimidazo (1,2-b)pyridazine-bromine and 3-bromo-6-chloroimidazo (1,2-b) pyridazine-bromine complexes; new brominating agents for organic compounds. *Synthesis*. 1981;(12):987–9. [<DOI>](#).
26. Song W, Xu Q, Zhu J, Chen Y, Mu H, Huang J, et al. Imidazo[1,2- b]pyridazine as Building Blocks for Host Materials for High-Performance Red-Phosphorescent Organic Light-Emitting Devices. *ACS Appl Mater Interfaces*. 2020 Apr 29;12(17):19701–9. [<DOI>](#).
27. Lin S, Hao P, Shen J, Fu Y. Hierarchically responsive and photochromic imidazopyridazinium iodoargentate hybrid materials. *Dyes Pigments*. 2018 Dec;159:457–63. [<DOI>](#).
28. Ma Y, Liang J, Zhao D, Chen Y-L, Shen J, Xiong B. Condensed Fukui function predicts innate C–H radical functionalization sites on multi-nitrogen containing fused arenes. *RSC Adv*. 2014;4(33):17262–4. [<DOI>](#).
29. Roskoski R. Properties of FDA-approved small molecule protein kinase inhibitors. *Pharmacol Res*. 2019 Jun;144:19–50. [<DOI>](#).
30. Hu L, Cao T, Lv Y, Ding Y, Yang L, Zhang Q, et al. Design, synthesis, and biological activity of 4-(imidazo[1,2- b]pyridazin-3-yl)-1 H -pyrazol-1-yl-phenylbenzamide derivatives as BCR–ABL kinase inhibitors. *Bioorg Med Chem Lett*. 2016 Dec;26(23):5830–5. [<DOI>](#).

31. Lambert GK, Duhme-Klair A-K, Morgan T, Ramjee MK. The background, discovery and clinical development of BCR-ABL inhibitors. *Drug Discov Today*. 2013 Oct;18(19–20):992–1000. [<DOI>](#).
32. Lee HJ, Pham PC, Hyun SY, Baek B, Kim B, Kim Y, et al. Development of a 4-aminopyrazolo[3,4-d]pyrimidine-based dual IGF1R/Src inhibitor as a novel anticancer agent with minimal toxicity. *Mol Cancer*. 2018 Dec;17(1):50. [<DOI>](#).
33. Larocque E, Chu EFY, Naganna N, Sintim HO. Nicotinamide–Ponatinib Analogues as Potent Anti-CML and Anti-AML Compounds. *ACS Omega*. 2020 Feb 18;5(6):2690–8. [<DOI>](#).
34. Miyamoto N, Sakai N, Hirayama T, Miwa K, Oguro Y, Oki H, et al. Discovery of N-[5-((2-(cyclopropylcarbonyl)amino)imidazo[1,2-b]pyridazin-6-yl)oxy)-2-methylphenyl]-1,3-dimethyl-1H-pyrazole-5-carboxamide (TAK-593), a highly potent VEGFR2 kinase inhibitor. *Bioorg Med Chem*. 2013 Apr;21(8):2333–45. [<DOI>](#).
35. Shen Y-M, Lv P-C, Chen W, Liu P-G, Zhang M-Z, Zhu H-L. Synthesis and antiproliferative activity of indolizine derivatives incorporating a cyclopropylcarbonyl group against Hep-G2 cancer cell line. *Eur J Med Chem*. 2010 Jul;45(7):3184–90. [<DOI>](#).
36. Chidella K, Seelam N, Cherukumalli PKR, Reddy N J, Sridhar G. Design and synthesis of novel 1,2,4-Thiadiazole linked imidazo[1,2-b]pyridazine as anticancer agents. *Chem Data Collect*. 2020 Dec;30:100554. [<DOI>](#).
37. Tewari N, Mohammad K, Rai B, Prakash H, Hussain M. Processes for the preparation of cefozopran, its salts and polymorphic forms thereof [Internet]. WO2010/89729. p. 57. [<URL>](#).
38. Jankowska A, Świerczek A, Wyska E, Gawalska A, Bucki A, Pawłowski M, et al. Advances in Discovery of PDE10A Inhibitors for CNS-Related Disorders. Part 1: Overview of the Chemical and Biological Research. *Curr Drug Targets*. 2018 Nov 27;20(1):122–43. [<DOI>](#).
39. Juillet C, Ermolenko L, Boyarskaya D, Baratte B, Josselin B, Nedev H, et al. From Synthetic Simplified Marine Metabolite Analogues to New Selective Allosteric Inhibitor of Aurora B Kinase. *J Med Chem*. 2021 Jan 28;64(2):1197–219. [<DOI>](#).
40. Shannan B, Watters A, Chen Q, Mollin S, Dörr M, Meggers E, et al. PIM kinases as therapeutic targets against advanced melanoma. *Oncotarget*. 2016 Aug 23;7(34):54897–912. [<DOI>](#).
41. Foulks JM, Carpenter KJ, Luo B, Xu Y, Senina A, Nix R, et al. A Small-Molecule Inhibitor of PIM Kinases as a Potential Treatment for Urothelial Carcinomas. *Neoplasia*. 2014 May;16(5):403–12. [<DOI>](#).
42. Moslin R, Zhang Y, Wroblewski ST, Lin S, Mertzman M, Spergel S, et al. Identification of *N*-Methyl Nicotinamide and *N*-Methyl Pyridazine-3-Carboxamide Pseudokinase Domain Ligands as Highly Selective Allosteric Inhibitors of Tyrosine Kinase 2 (TYK2). *J Med Chem*. 2019 Oct 24;62(20):8953–72. [<DOI>](#).
43. Moslin R, Gardner D, Santella J, Zhang Y, Duncia JV, Liu C, et al. Identification of imidazo[1,2-*b*]pyridazine TYK2 pseudokinase ligands as potent and selective allosteric inhibitors of TYK2 signalling. *MedChemComm*. 2017;8(4):700–12. [<DOI>](#).
44. Yeh V, Judd AS, Souers AJ. Chapter 11 Lipid-Metabolizing Enzymes as Targets for Dyslipidemia and Insulin Resistance. In: *Annual Reports in Medicinal Chemistry* [Internet]. Elsevier; 2007 [cited 2021 Jun 22]. p. 161–75. ISBN: 978-0-12-373912-4. [<URL>](#).
45. He Y, Wu JB, Lei F, Chen P, Hai L, Wu Y. Design, synthesis and antibacterial activity of novel 1-oxacephem analogs. *Chin Chem Lett*. 2012 Apr;23(4):407–10. [<DOI>](#).
46. Özbek O, Gürdere MB. A review on the synthesis and applications of molecules as anticonvulsant drug agent candidates. *Med Chem Res*. 2020 Sep;29(9):1553–78. [<DOI>](#).
47. Özbek O, Gürdere MB. Synthesis and anticancer properties of 2-aminothiazole derivatives. *Phosphorus Sulfur Silicon Relat Elem*. 2021 May 4;196(5):444–54. [<DOI>](#).
48. Kobe J, Stanovnik B, Tišler T. Synthesis of pyridazine derivatives—XV. *Tetrahedron*. 1968 Jan;24(1):239–45. [<DOI>](#).
49. Heinisch G, Lötsch G, Offenberger S, Stanovnik B, Tisler M. Preparation of azolopyridazinecarboxylic acids. *J Heterocycl Chem*. 1989;26(6):1751–4. [<DOI>](#).
50. Ishikawa T, Iizawa Y, Okonogi K, Miyake A. Studies on Anti-MRSA Parenteral Cephalosporins. I. Synthesis and Antibacterial Activity of 7-BETA.-[2-(5-Amino-1,2,4-thiadiazol-3-yl)-2(Z)-hydroxyiminoacetamido]-3-(substituted imidazo[1,2-*b*]pyridazinium-1-yl)methyl-3-cephem-4-carboxylates and Related Compounds. *J Antibiot (Tokyo)*. 2000;53(10):1053–70. [<DOI>](#).
51. Matsumoto S, Miyamoto N, Hirayama T, Oki H, Okada K, Tawada M, et al. Structure-based design, synthesis, and evaluation of imidazo[1,2-

- b]pyridazine and imidazo[1,2-a]pyridine derivatives as novel dual c-Met and VEGFR2 kinase inhibitors. *Bioorg Med Chem.* 2013 Dec;21(24):7686–98. [<DOI>](#).
52. Hou Z, Xu H. Electrophotocatalytic C–H Azolation of Arenes. *ChemElectroChem.* 2021 May 3;8(9):1571–3. [<DOI>](#).
53. Xu P, Chen P, Xu H. Scalable Photoelectrochemical Dehydrogenative Cross-Coupling of Heteroarenes with Aliphatic C–H Bonds. *Angew Chem.* 2020 Aug 17;132(34):14381–6. [<DOI>](#).
54. Huang H, Li H, Cordier M, Soulé J, Doucet H. Pd-Catalyzed Direct Arylations of Heteroarenes with Polyfluoroalkoxy-Substituted Bromobenzenes. *Eur J Org Chem.* 2020 Oct 15;2020(38):6094–101. [<DOI>](#).
55. Mao S, Li H, Shi X, Soulé J, Doucet H. Environmentally Benign Arylations of 5-Membered Ring Heteroarenes by Pd-Catalyzed C–H Bonds Activations. *ChemCatChem.* 2019 Jan 9;11(1):269–86. [<DOI>](#).
56. Bouzayani B, Ben Salem R, Soulé J-F, Doucet H. Synthesis of C9,C10-Diheteroarylated Phenanthrenes via Palladium-Catalyzed C-H Bond Activation: Synthesis of C9,C10-Diheteroarylated Phenanthrenes via Palladium-Catalyzed C-H Bond Activation. *Eur J Org Chem.* 2018 Dec 2;2018(44):6092–100. [<DOI>](#).
57. Mao S, Shi X, Soulé J-F, Doucet H. Exploring Green Solvents Associated to Pd/C as Heterogeneous Catalyst for Direct Arylation of Heteroaromatics with Aryl Bromides. *Adv Synth Catal.* 2018 Sep 3;360(17):3306–17. [<DOI>](#).
58. Chikhi S, Djebbar S, Soulé J-F, Doucet H. Environmentally-Safe Conditions for a Palladium-Catalyzed Direct C3-Arylation with High Turn Over Frequency of Imidazo[1,2- b]pyridazines Using Aryl Bromides and Chlorides. *Chem - Asian J.* 2016 Sep 6;11(17):2443–52. [<DOI>](#).
59. Bellina F, Rossi R. Recent advances in the synthesis of (hetero)aryl-substituted heteroarenes via transition metal-catalysed direct (hetero)arylation of heteroarene C–H bonds with aryl halides or pseudohalides, diaryliodonium salts, and potassium aryltrifluoroborates. *Tetrahedron.* 2009 Dec;65(50):10269–310. [<DOI>](#).
60. Gu Y, Shen Y, Zarate C, Martin R. A Mild and Direct Site-Selective sp^2 C–H Silylation of (Poly)Azines. *J Am Chem Soc.* 2019 Jan 9;141(1):127–32. [<DOI>](#).
61. Handa S, Jin B, Bora PP, Wang Y, Zhang X, Gallou F, et al. Sonogashira Couplings Catalyzed by Fe Nanoparticles Containing ppm Levels of Reusable Pd, under Mild Aqueous Micellar Conditions. *ACS Catal.* 2019 Mar;9(3):2423–31. [<DOI>](#).
62. Saikia I, Borah AJ, Phukan P. Use of Bromine and Bromo-Organic Compounds in Organic Synthesis. *Chem Rev.* 2016 Jun 22;116(12):6837–7042. [<DOI>](#).
63. Tagore SS, Swaminathan J, Manikandan D, Gomathi S, Nirmal Ram S, Ramalingam M, et al. Molecular, vibrational (FT-IR and FT-Raman), NMR and UV spectral analysis of imidazo[1,2-b]pyridazine using experimental and DFT calculations. *Chem Phys Lett.* 2020 Jan;739:136943. [<DOI>](#).
64. Miyashita M, Akamatsu M, Ueno H, Nakagawa Y, Nishimura K, Hayashi Y, et al. Structure-Activity Relationships of RGD Mimetics as Fibrinogen-Receptor Antagonists. *Biosci Biotechnol Biochem.* 1999 Jan;63(10):1684–90. [<DOI>](#).
65. Pugmire RJ, Smith JC, Grant DM, Stanovnik B, Tišler M, Verček B. Correlation of ring nitrogen substituents with carbon-13 nuclear magnetic resonance data in azoloazines. *J Heterocycl Chem.* 1987 May;24(3):805–9. [<DOI>](#).
66. Downing JW, Waluk JW, Stanovnik B, Michl J. Applications of magnetic circular dichroism: a Hammett-like equation for structural work. Determination of protonation sites in azaindolizines. *J Org Chem.* 1985;50(3):302–11. [<URL>](#).
67. Stefaniak L, Roberts JD, Witanowski M, Hamdi BT, Webb GA. A15N NMR investigation of some azolopyridines. *Org Magn Reson.* 1984 Apr;22(4):209–14. [<DOI>](#).
68. Kovač B, Klasinc L, Stanovnik B, Tišler M. Photoelectron spectroscopy of heterocycles. Azaindenes and azaindolizines. *J Heterocycl Chem.* 1980 Jun;17(4):689–94. [<DOI>](#).



Ultrasonic-Assisted Removal of Eriochrome Black T onto Vermicompost: Characterization, Isotherm and Kinetic Modelling

Zeynep Çiğeroğlu¹ , Eyüp Yildirim^{1*}  

¹University of Uşak, Department of Chemical Engineering, Uşak, 64000, Turkey

Abstract: Recently, utilization of biological adsorbents plays an important role in the removal of toxic dyes such as Eriochrome Black T (EBT) azo-dye as they are considered as being produced from natural renewable source, easy availability, low cost, and being environmentally friendly. In this study, vermicompost (VC) was utilized to remove Eriochrome Black T (EBT) azo-dye from aqueous solution along ultrasonic ultrasonic-assisted adsorption. The parameters such as pH, adsorbent amount, operating time, and initial EBT concentration were investigated. The highest adsorption capacity was obtained as 50.64 (mg-EBT g⁻¹-VC) at the pH of 2 after 2 minutes of ultrasonic adsorption. Pseudo first order kinetic model fitted very well with the experimental data ($R^2=0.9824$). The determination coefficient of Temkin isotherm model ($R^2=0.8659$) revealed that suggested model was compatible to experimental results. The results suggested that ultrasonic assisted adsorption of EBT onto VC could be cost- and time-efficient. Besides, the Scanning Electron Microscopy (SEM) analysis of adsorbent identified the surface structure morphology of VC. Moreover, functional groups of VC were detected after and before the ultrasonic-assisted adsorption by using Fourier Transform Infrared Spectroscopy (FTIR). Thus, interaction mechanism between VC and EBT were determined.

Keywords: Ultrasonic assisted adsorption, vermicompost, Eriochrome Black T

Submitted: September 21, 2021. **Accepted:** November 10, 2021.

Cite this: Çiğeroğlu Z, Yildirim E. Ultrasonic-Assisted Removal of Eriochrome Black T onto Vermicompost: Characterization, Isotherm and Kinetic Modelling. JOTCSA. 2021;8(4):1251-62.

DOI: <https://doi.org/10.18596/jotcsa.997521>.

***Corresponding author. E-mail:** eyup.yildirim@usak.edu.tr, Tel: +90 276 221 2121/2768.

INTRODUCTION

Treating wastewater for reusing is vital for a sustainable future as fresh water resources are depleting due to rapid growth of population, pollution of water bodies, and drought due to global warming. Especially the textile industry produces a vast amount of wastewater as around 150 L of fresh water per kg of textile product is necessary and hence, great amount of wastewater containing many hazardous and toxic substances such as dye effluents is discharged during the process (1). Dyes in textile industry are synthetic organic materials with complex structure and they are non-biodegradable (2). In addition, dyes containing -N=N- azo group (azo dyes) are considered toxic and carcinogenic and may create serious effects on organisms in the water bodies and human health

(3). There is a great variety in treatment of dye effluents in wastewater such as extraction via solvent, separation via membrane, advanced oxidation process, photodegradation, and adsorption (4-6). All these treatment processes have several advantages and disadvantages, while adsorption is a widely used technique due to its easy applicability, feasibility, and low cost.

The main drawback of adsorption process is the long residence times, however, application of ultrasound overcomes this situation and shortens the time required to reach equilibrium (7). In addition, its simplicity, low cost, satisfactory energy efficiency, and being environmentally friendly promotes its utilization (8). Ultrasound creates acoustic cavitation and the formed bubbles start to collide and create high temperature and pressure zones locally. Also,

the shock waves promote the microscopic turbulence within the interfacial films surrounding the adsorbent's surface and increase the mass transfer, yielding a rapid adsorption and shorter residence time. During the collapse of the bubbles, micro-jets of solvent are formed perpendicular to the adsorbents surface and due their high speed, corrosion and erosion of the surface occurs (7,9,10). As a result, without requiring a chemical additive and with a suitable adsorbent, ultrasound adsorption can be proper to remove dye effluents from the wastewater.

There are many studies in the literature showing that by using active carbon as adsorbent, many type of dye effluents can be cleaned (11,12). The recent efforts to enhance the ultrasound adsorption is to utilize a low cost, stable adsorbent as active carbon is too expensive for the process. Vermicompost as soil amendment has unique properties such as high surface area with high porosity, high density of negative charges, low cost and functional groups within its structure. These properties make vermicompost a good adsorbent especially during the adsorption of metals, dye effluents and organic pollutants (13–16). However, there is not any report showing its applicability for dye adsorption from the wastewater in ultrasound media. In this work, Eriochrome Black T (EBT) as an azo-dye sample was subjected to adsorption via vermicompost in ultrasound media. The influences of pH, adsorbent amount, operating time and initial EBT concentration on the adsorption capacity were examined. In addition, kinetic models (the first and second order pseudo and intraparticulate models) and isotherm models (Langmuir, Freundlich, and Temkin) were utilized to determine their applicability with the experimental data.

MATERIALS AND METHODS

Materials

All chemicals were purchased from Sigma Aldrich. Bidistilled water was used in the all ultrasonic-assisted adsorption experiments. VC was purchased from a local producer from İzmir, Turkey and it was produced from various city markets' waste and MSW. Initially, vermicompost was dried and sieved to yield a particle size of $0.125 < D_p < 0.600$ [mm] for homogenization of the sample. Vermicompost had 31.05% ash content. The details of ash content determination method were given in our previous work (5).

Ultrasonic-Assisted Adsorption

The batch experimental set-up consisted of an ultrasonic homogenizer (Sonoplus HD 2200.2),

operating at 200 W (nominal output) with a 13 mm titanium probe. 50 mL of conical centrifuge tubes were filled with 30 mL of EBT solutions comprising of different pHs. In ultrasonic-assisted adsorption experiments, 0.1 g of vermicompost was fed into a falcon tube. The amplitude of ultrasonic homogenizer was adjusted as 70%. After the ultrasonic adsorption process completed within the designated time, the solution in the tube was syringed and centrifuged at 5000 rpm for 1 minute. By using a UV-Vis spectrophotometer (Perkin Elmer, Lambda 365) at λ max (508 nm) for pH 2 the first and the final concentrations of EBT were determined. Adsorption capacity and removal percentage of EBT were calculated according to the Equations 1 and 2, respectively.

$$q_e = \frac{(C_0 - C_e) * V}{W} \quad (1)$$

$$R \% = \frac{(C_0 - C_e)}{C_0} * 100 \quad (2)$$

C_0 and C_e represent the initial and equilibrium concentration of the solution (mgL^{-1}), and W denotes the weight of VC (g).

Characterization of Vermicompost

The functionality, structural morphology and crystallinity tests of raw vermicompost were performed via Spectrum Two Fourier Transform Infrared (FTIR) Spectrometer, Scanning electron microscope with Energy Dispersive X-Ray spectroscopy (SEM-EDX) and X-Ray Diffraction (XRD) for characterization. Moreover, point of zero charged of VC was determined in our previously published paper (5).

Batch Kinetic Study

The kinetic study of ultrasonic-assisted adsorption was carried out using several kinetic models in order to define the ultrasonic-assisted adsorption rate and mechanism. The applied kinetic models used in this study were pseudo-first order (17), the pseudo-second-order (18), and intraparticulate (19) as shown in Table 1. The best suitable model was determined by the determination of coefficient (R^2) of the kinetic models.

Isotherm Models

Four different initial concentrations of EBT were used for determination of three isotherm models. These models with their equations are summarized in Table 2. All isotherm experiments conducted with pH 2 of EBT solutions with a sonication time of 2 minutes. The obtained models served to explain the relations between the adsorbate and adsorbent.

Table 1: Applied kinetic models for EBT adsorption onto vermicompost.

Model	Equation
Pseudo First Order	$\ln(q_e - q_t) = \ln q_e - k_1 t$
Pseudo Second Order	$\frac{t}{q_t} = \frac{1}{k_2 q_e^2} + \frac{t}{q_e}$
Intraparticle	$q_t = K t^{0.5} + C$

q_t =Adsorption capacity at any time (mg g^{-1}). k_1 =pseudo-first order rate constant (min^{-1}); k_2 =second-order pseudo rate constant ($\text{g mg}^{-1}\text{min}^{-1}$), K =intraparticle kinetic model constant ($\text{mg g}^{-1}\text{min}^{-0.5}$) and C = y intercept.

Table 2: Applied Isotherm Models with their equations and units.

Models	Equations	Units	Ref.
Langmuir	$\frac{C_e}{q_e} = \frac{1}{q_{max} K_L} + \frac{C_e}{q_{max}}$	q_e : adsorbed amount (mg g^{-1}) C_e : adsorbed equilibrium (mg L^{-1}) K_L : Langmuir constant related to sorption energy (L mg^{-1}) q_{max} : maximum adsorption capacity (mg g^{-1}) related to monolayer coverage	(20)
Freundlich	$\ln q_e = \ln K_F + \frac{1}{n \ln C_e}$	C_e : adsorbed equilibrium (mg L^{-1}) K_F : Freundlich constant ($\text{mg g}^{-1})(\text{L mg}^{-1})^n$ $1/n$: intensity of adsorption	(21)
Temkin	$q_e = B \ln a_T + B \ln C_e$ $B = \frac{RT}{b_T}$	C_e : adsorbed equilibrium (mg L^{-1}) a_T : equilibrium bond constant B, b_T : Temkin constants	(22)

RESULTS AND DISCUSSION

Effect of pH of EBT Solutions on Adsorption Capacity

Around 200 mg L^{-1} of initial concentrations of EBT with different pHs (2-12) were prepared in order to predict the impact of pHs of adsorbate solution on the adsorption capacity. The ultrasonic-assisted adsorption experiments were performed with 70% amplitude during one minute. Figure 1 represents the effect of pH on the adsorption capacity. The highest adsorption capacity was obtained as $50.64 \text{ (mg-EBT g}^{-1}\text{-VC)}$ at the pH of value of 2. The minimum adsorption capacity ($4.22 \text{ mg-EBT g}^{-1}\text{-VC}$) was observed at pH 12. After determining the best pH of solution as pH 2, all ultrasonic-assisted

adsorption experiments were carried out at a pH value of 2.

The positive charge of VC was found as 8.51 in our previously published paper (5). The surface charge of VC has positive at $\text{pH} < 8.51$. The electrostatic attraction was occurred between the protonation of VC and the negatively charged EBT. While the pH increasing, VC has negatively charged and the repulsion dominated the VC and EBT interaction. Khan et al. (23) and Akhouairi et al. (24) mentioned similar findings in their studies. Moreover, Sriram et al. reported that UV-Vis spectrum of EBT solution was affected by pH (25). Between the pH 6 and 10, dark blue color was gained and therefore, the wavelength of EBT's was shifted to 614 nm (25).

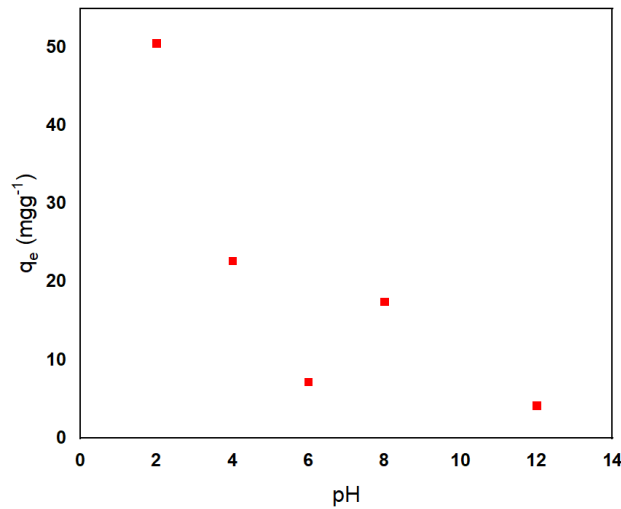


Figure 1: The effect of pH on the adsorption of EBT onto VC.

Effect of the Adsorbent Amount on the Adsorption Capacity

85 mgL⁻¹ of EBT solution was prepared at optimal pH (2) for batch adsorption. Four levels of adsorbent doses (0.1-1 g) on adsorption capacity were evaluated. Figure 2 represents the various

adsorbent doses versus adsorption uptake of EBT onto vermicompost. The value of 23.19 mg g⁻¹ for EBT uptake on vermicompost found as the maximum adsorption capacity in the adsorbent dose range studied (Figure 2). Therefore, 0.1 g of vermicompost was used for the further evaluation.

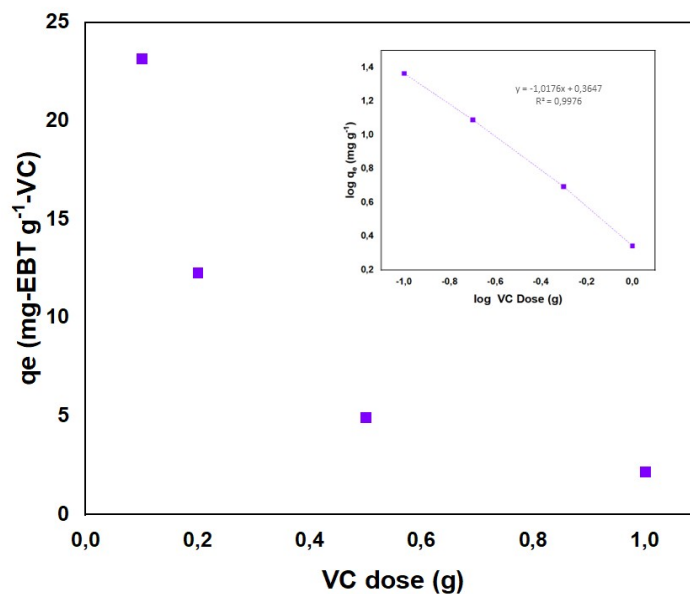


Figure 2: The effect of the amount of VC on the adsorption uptake of EBT onto VC.

Increasing adsorption dose leads to the logarithmic decrease on adsorption uptake of EBT onto adsorbent. Similar trend was observed by Bayomie et al. who investigated the methylene blue removal using fava bean peels utilizing ultrasonic-assisted method (26). They attributed the result to aggregation of adsorbent due to high amount of adsorbent and yielding a decrease in the surface area due to the overlapping of the functional vacant sites.

Effect of Operation Time

In order to investigate the effect of ultrasonication time on adsorption capacity of vermicompost, ultrasonic assisted adsorption carried out by using 0.1 g of VC and 130 mg L⁻¹ of initial EBT solution concentration at pH 2. Figure 3 represents that optimum ultrasound duration was found to be 120 seconds. The obtained maximum adsorption capacity of EBT onto VC was determined as 31.83 mg-EBT/g⁻¹ adsorbent. In addition, it can be said

that 83.3% of maximum adsorption capacity was reached within 60 sec. Isotherm studies were performed with a ultrasonication time of 120 sec according to the determined optimal conditions. A rapid adsorption was appeared owing to the ultrasonic-assisted adsorption via cavitation

phenomena. These findings have similar trends with the results of Roosta et al. (27) who studied malachite green removal by using ultrasound effect. It can be interpreted that a highly fast adsorption occurred owing to the dispersion of adsorption by the ultrasonic cavitation.

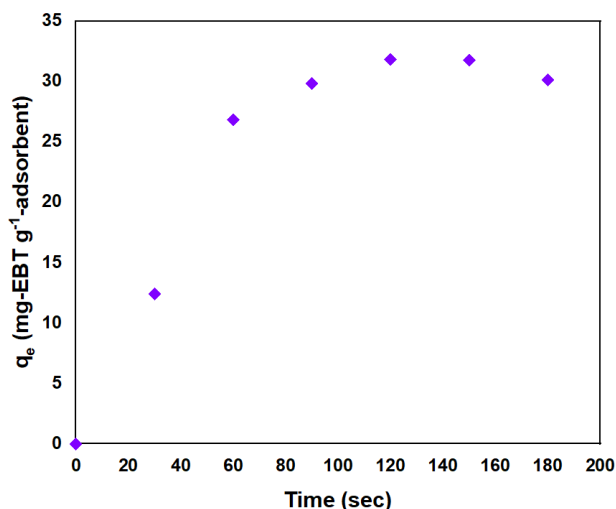


Figure 3: The effect of ultrasonic duration on the adsorption uptake of EBT onto VC.

Effect of initial EBT concentration

To assess the impact of numerous initial concentrations of EBT (122-494 mg L⁻¹) on adsorption uptake of EBT onto VC was applied. The increase of the sorption uptake onto VC was from 31 to 139 mg g⁻¹, when initial concentration of EBT were varied from 122 mgL⁻¹ to 494 mgL⁻¹ (Figure 4). An increase of the EBT concentration could be

resulted in the increase of driving force concentration and this led to a situation that mass transport occurred very fast from the solute to the surface of VC (11). Besides, it is well known that sonication helps to the improvement of mass transfer. Accordingly, the micro-jets occurred owing to the ultrasound and hence, the increase of the mass transfer was observed (27).

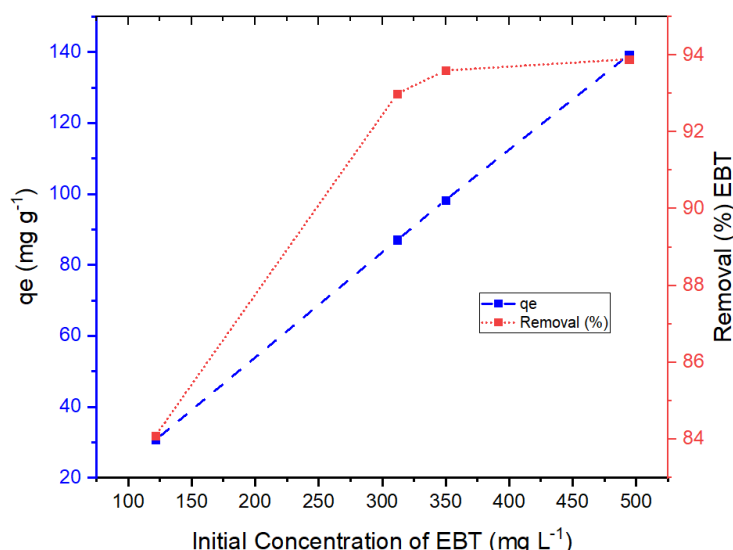


Figure 4: The effect of EBT's initial concentration on the adsorption uptake of EBT onto VC.

Kinetic Study of EBT Sorption onto VC

Table 3 presents the relevant values of sorption rate constants and determination coefficients of the applied kinetic models. The highest R² value was

found to be 0.9824 for pseudo-first order. This value indicated that a good correlation occurred between the model and the results of the experimental findings. Furthermore, R² value of 0.9580 was

obtained for intraparticle-diffusion model. According to Figure 5, there are two linear regions on the plot of intraparticular model. While the first line shows EBT dye ions transport to VC's external surface, the

second line implies that the intraparticle diffusion was occurred through the macropores (28). All of the graphs of kinetic models are represented in Figures 5 a-c.

Table 3: Applied kinetic models' parameters for EBT adsorption onto VC at 298 K.

Models	Parameters	Value
Pseudo-first order	q_e	36.02
	k_1	0.03
	R^2	0.9824
Pseudo-second order	q_e	36.90
	k_2	0.0011
	R^2	0.8304
Intraparticular Diffusion	K_d	3.11
	C	-0.759
	R^2	0.9580

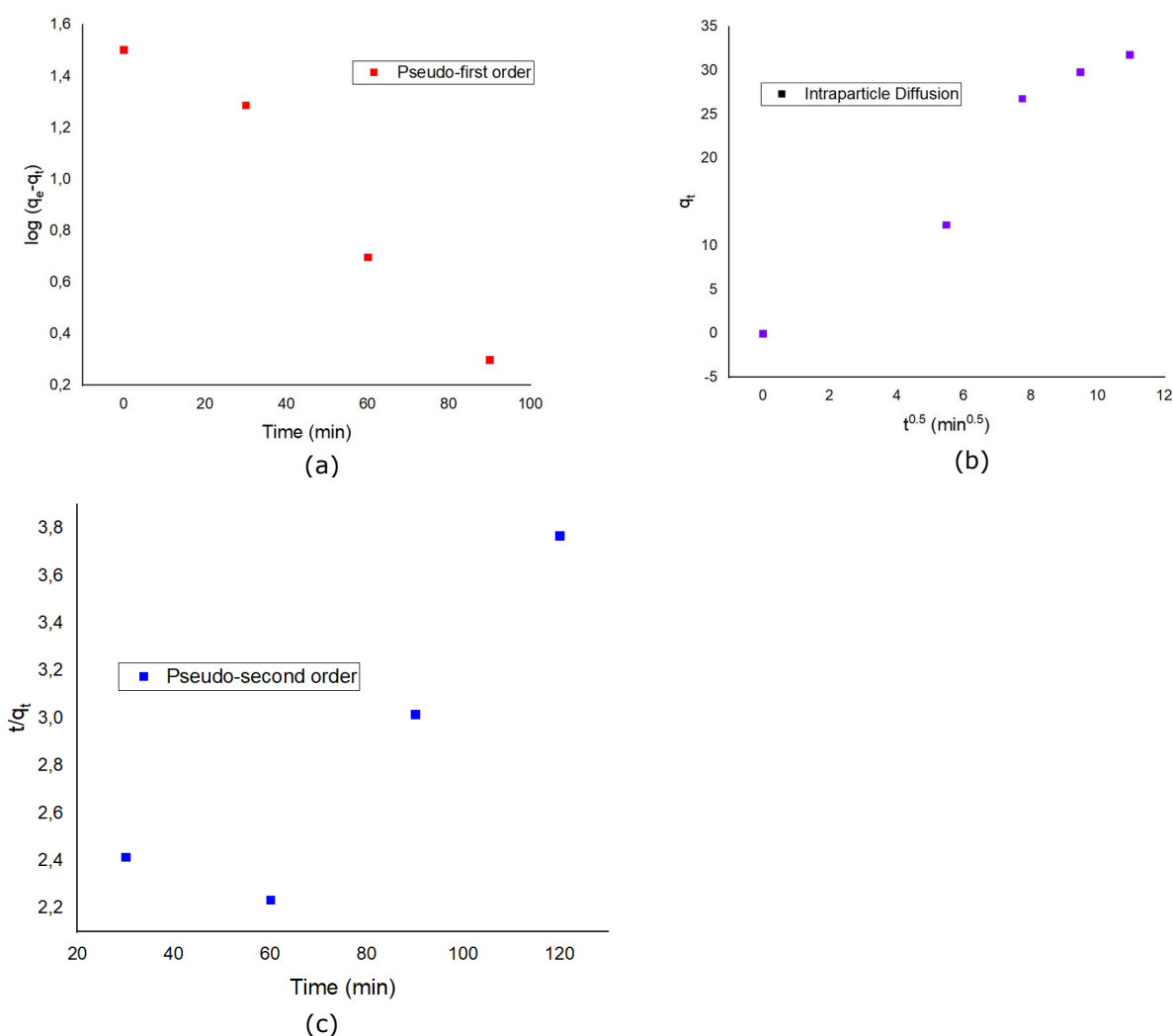


Figure 5: Modelling kinetics of EBT adsorption onto the VC a) pseudo-first-order b) pseudo- second-order, c) intraparticle diffusion.

Modelling Isotherms of EBT Sorption onto VC

The independent variables of isotherm models are shown in Table 4. The determination coefficients of both Langmuir and Temkin isotherm models were 0.87 and 0.8659, respectively. However, the

determination coefficient of Freundlich isotherm was obtained as 0.6941. The Freundlich isotherm indicates that a monolayer adsorption onto VC occurred. There was no lateral interactions between the VC and adsorbed EBT dye ions (29).

Furthermore, Temkin isotherm model's parameters determined as a positive value and the interaction suggest that the ultrasonic-assisted EBT adsorption between the adsorbent and adsorbate was onto VC was exothermic since Bt value was physisorption (30).

Table 4: Applied isotherm models' parameters for EBT adsorption onto VC at 298 K.

Models	Parameters	Value
Langmuir	$q_{e, c}$ (calculated)	36.02
	q_m (max)	-36.64
	K_L	-0.029
	R^2	0.87
Freundlich	q_e	36.90
	k_2	0.0097
	R^2	0.6941
	n	0.3493
Temkin	K_t	5.4735
	B_t	219.84
	R^2	0.8659

Characterization of VC

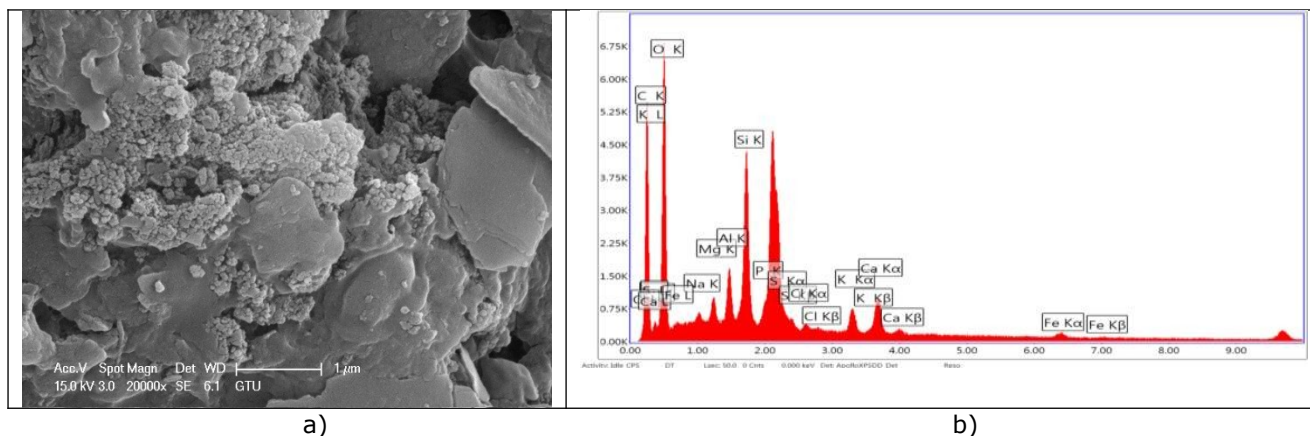


Figure 6: a) SEM image of raw VC at a scale of 1 μm, (b) EDS of raw VC.

Vermicompost has gained attention to be used as an adsorbent for disposal of organic and inorganic contaminants in the water and studies showed that due to functional groups existing naturally, made vermicompost an effective adsorbent (31). The flakes and fragments were shown in the micrograph of raw vermicompost (Figure 6a). This phenomenon may be explained owing to the organic and inorganic content of the vermicompost's structure. In fact, enzyme and numerous bacteria stick to the substrate until they get to the earthworm's gut (32,33). Hence, the degree of degradation of them was reflected by the image of SEM. EDX spectrum (Figure 6b) reveals that various metals exist in its structure.

The FTIR spectrum of raw vermicompost is shown in Figure 7. The very broad peak between the wavenumbers of 3700 and 3000 cm^{-1} represents the hydroxyl (-OH) functional group in carboxylic acids as well as alcohols and phenols. In addition, the broad peak also overlaps the C-H peak observed around 2900 cm^{-1} , which is typical for carboxylic acids (13). Vermicompost consists of organic and inorganic fractions and humic substances which are

of carboxylic acid nature, are comprising the majority of the organic constituents (34). The sharp peak at 1630 cm^{-1} indicates the existence of amides as it might belong to stretching -C=O bands (31). While the small peak at 1490 cm^{-1} can be attributed to C=C, the peak at 1420 cm^{-1} shows the CO_3^{2-} groups (14). Stretching O-C bands are observed at 1030 cm^{-1} which might represent carboxylic acids (2).

After the adsorption of EBT, the broad peak representing -OH almost flattened suggesting that hydroxyl groups on the surface of vermicompost involved in the adsorption. In addition, the magnitude of the peaks at 1630, 1420 and 1030 cm^{-1} lowered indicating that EBT dye molecules attached to the functional groups of -C=O and O-C on the surface of vermicompost (35).

XRD pattern of vermicompost was shown in Figure 8. The peaks at 21.70 and 26.64 were attributed to quartz (SiO_2). The other low intensity peak appeared at 27.91 owing to the existence of sylvite (36). The sharp two peaks emerged at 54.86 and 69.24 corresponding to kotoite (37).

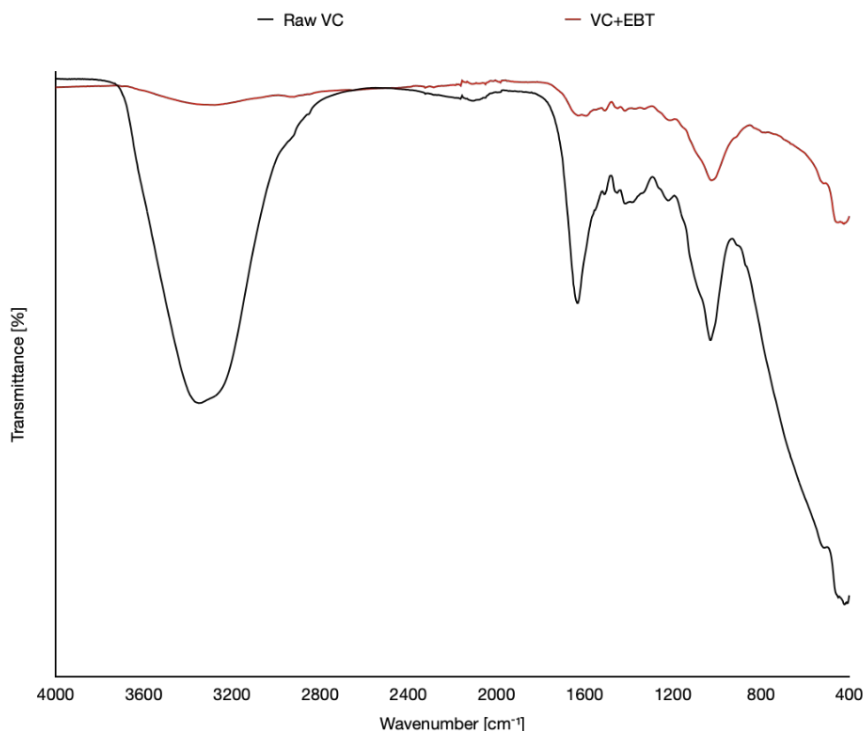


Figure 7: FTIR spectrum of raw VC and VC-adsorbed EBT.

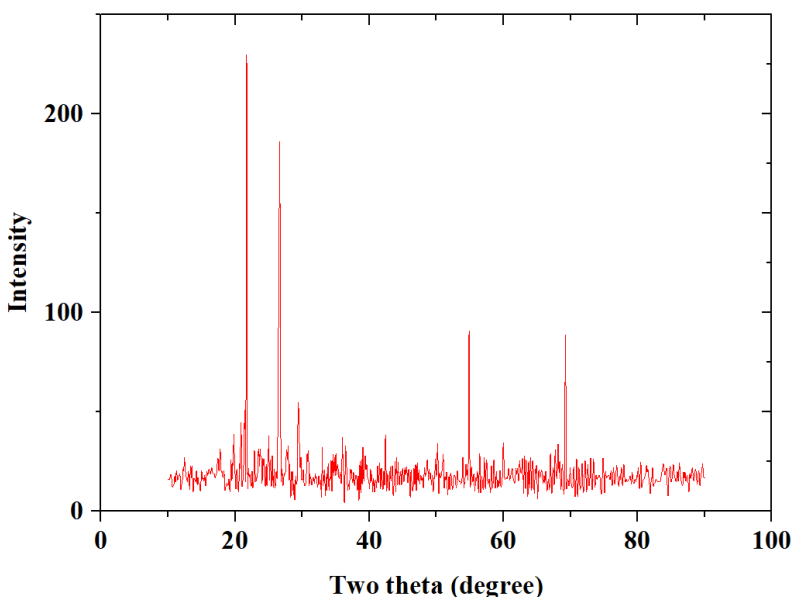


Figure 8: X-ray diffraction (XRD) pattern of raw VC.

Comparison of Different Adsorbents for the Removal of EBT

Table 5 displays the summary of literature for adsorbents for EBT removal. The adsorbents were prepared in many steps including microwave, impregnation, pyrolysis methods which are time-consuming and bring economic burden to the

adsorption process. Thus, it can be said that VC as adsorbent is cost-effective. Besides, ultrasonication-adsorption process gave better results in a short time containing less solvent. As a result, these advantages make ultrasonic assisted adsorption of EBT onto VC as a promising method.

Table 5: Comparison of adsorbents for EBT adsorption.

Adsorbents	Maximum adsorption capacity (mg g ⁻¹)	Ref.
Almond Shell with Microwave radiation	29.41	(38)
Almond Shell with cold	18.18	
Almond Shell (untreated)	6.06	
Peanut shell	40.81	(39)
Hydrophobic cross-linked polyzwitterionic acid	15.9	(40)
MoNiO ₄	6.66	(41)
Alginate/basil seed mucilage biocomposite	2.80	(42)
Alrhaji Steel slag	25.88–34.82	(43)
Arabian Steel slag	34.93 – 39.69	
HCl activated Nteje Clay	24.04	(44)
Bare ZnO	32.56	(45)
CTAB@ZnO	56.82	
BMTF@ZnO	78.34	
Raw Montmorillonite	99.0	(46)
Raw VC	50.64	This study

CONCLUSION

The current study indicated that VC could be an economical sorbent for EBT elimination from aqueous media. The ultrasonic-assisted adsorption as one of the novel enhanced adsorption methods was preferred since the removal of EBT from aqueous media was high, owing to the microjet effects. Various independent factors were selected such as pH, VC dose, initial concentration of EBT. The adsorption efficiency was highly affected with the changing pH value. The vital pH of this process was determined as 2. The determination coefficient of Temkin isotherm model ($R^2=0.8659$) revealed that suggested model was compatible to experimental results. The applied kinetic data revealed that the pseudo-first order kinetic model is well-fitted to ultrasonic-assisted data with high coefficient of determination ($R^2=0.9824$). Furthermore, ultrasonic-assisted adsorption was so rapid that this technique could reduce the time required hence, providing better results compared to batch adsorption. Besides, EDX analysis revealed that VC has numerous organic and inorganic materials, thus flakes and segments were observed. Moreover, FTIR analyses explained well the adsorption behavior between the VC and EBT. XRD analysis enlighten the crystallographic structure of VC.

REFERENCES

1. Yin H, Qiu P, Qian Y, Kong Z, Zheng X, Tang Z, et al. Textile Wastewater Treatment for Water Reuse: A Case Study. *Processes*. 2019 Jan 11;7(1):34. [<DOI>](#).

2. de Luna MDG, Flores ED, Genuino DAD, Futralan

CM, Wan M-W. Adsorption of Eriochrome Black T (EBT) dye using activated carbon prepared from waste rice hulls—Optimization, isotherm and kinetic studies. *Journal of the Taiwan Institute of Chemical Engineers*. 2013 Jul;44(4):646–53. [<DOI>](#).

3. Paixão K, Abreu E, Lamas Samanamud GR, Boscaro França A, Almeida Loures CC, Prado Baston E, et al. Normal boundary intersection applied in the scale-up for the treatment process of Eriochrome Black T through the UV/TiO₂/O₃ system. *Journal of Environmental Chemical Engineering*. 2019 Feb;7(1):102801. [<DOI>](#).

4. Khurana I, Shaw AK, Bharti, Khurana JM, Rai PK. Batch and dynamic adsorption of Eriochrome Black T from water on magnetic graphene oxide: Experimental and theoretical studies. *Journal of Environmental Chemical Engineering*. 2018 Feb;6(1):468–77. [<DOI>](#).

5. İlbay Z, Yildirim E. Vermicompost as a potential adsorbent for the adsorption of methyleneblue dye from aqueous solutions. *Journal of the Turkish Chemical Society Section A: Chemistry*. 2020 Oct 23;893–902. [<DOI>](#).

6. Crini G. Non-conventional low-cost adsorbents for dye removal: A review. *Bioresource Technology*. 2006 Jun;97(9):1061–85. [<DOI>](#).

7. Ismail BB, Yusuf HL, Pu Y, Zhao H, Guo M, Liu D. Ultrasound-assisted adsorption/desorption for the enrichment and purification of flavonoids from baobab (*Adansonia digitata*) fruit pulp. *Ultrasonics Sonochemistry*. 2020 Jul;65:104980. [<DOI>](#).

8. Ismail BB, Guo M, Pu Y, Wang W, Ye X, Liu D.

- Valorisation of baobab (*Adansonia digitata*) seeds by ultrasound assisted extraction of polyphenolics. Optimisation and comparison with conventional methods. *Ultrasonics Sonochemistry*. 2019 Apr;52:257–67. [<DOI>](#).
9. Thompson LH, Doraiswamy LK. *Sonochemistry: Science and Engineering*. *Ind Eng Chem Res*. 1999 Apr 1;38(4):1215–49. [<DOI>](#).
10. Pankaj, Sharma R, Verma SK. Equilibrium, kinetic and mechanism studies on adsorption of textile disperse dye from aqueous solution onto TiO₂ in the presence of ultrasound and rare earth ions. *Materials Today: Proceedings*. 2021;44:2158–67. [<DOI>](#).
11. Hamdaoui O, Chiha M, Naffrechoux E. Ultrasound-assisted removal of malachite green from aqueous solution by dead pine needles. *Ultrasonics Sonochemistry*. 2008 Jul;15(5):799–807. [<DOI>](#).
12. Hamdaoui O, Naffrechoux E, Tifouti L, Pétrier C. Effects of ultrasound on adsorption–desorption of p-chlorophenol on granular activated carbon. *Ultrasonics Sonochemistry*. 2003 Mar;10(2):109–14. [<DOI>](#).
13. Yang G, Wang Z, Xian Q, Shen F, Sun C, Zhang Y, et al. Effects of pyrolysis temperature on the physicochemical properties of biochar derived from vermicompost and its potential use as an environmental amendment. *RSC Adv*. 2015;5(50):40117–25. [<DOI>](#).
14. Zhou B, Wang Z, Shen D, Shen F, Wu C, Xiao R. Low cost earthworm manure-derived carbon material for the adsorption of Cu²⁺ from aqueous solution: Impact of pyrolysis temperature. *Ecological Engineering*. 2017 Jan;98:189–95. [<DOI>](#).
15. Zhu W, Du W, Shen X, Zhang H, Ding Y. Comparative adsorption of Pb²⁺ and Cd²⁺ by cow manure and its vermicompost. *Environmental Pollution*. 2017 Aug;227:89–97. [<DOI>](#).
16. Yang G, Wu L, Xian Q, Shen F, Wu J, Zhang Y. Removal of Congo Red and Methylene Blue from Aqueous Solutions by Vermicompost-Derived Biochars. *Singer AC, editor. PLoS ONE*. 2016 May 4;11(5):e0154562. [<DOI>](#).
17. Lagergren S. About the Theory of So-called Adsorption of Soluble Substances. *Kungliga Svenska Vetenskapsakademiens Handlingar*. 1898;24:1–39.
18. Ho YS, McKay G. A Comparison of Chemisorption Kinetic Models Applied to Pollutant Removal on Various Sorbents. *Process Safety and Environmental Protection*. 1998 Nov;76(4):332–40. [<DOI>](#).
19. Weber WJ, Morris JC. Kinetics of Adsorption on Carbon from Solution. *J Sanit Engrg Div*. 1963 Apr;89(2):31–59. [<DOI>](#).
20. Langmuir I. The adsorption of gases on plane surfaces of glass, mica and platinum. *J Am Chem Soc*. 1918 Sep;40(9):1361–403. [<DOI>](#).
21. Freundlich H. Über die Adsorption in Lösungen. *Zeitschrift für Physikalische Chemie*. 1907 Oct 1;57U(1):385–470. [<DOI>](#).
22. Temkin M. Kinetics of ammonia synthesis on promoted iron catalysts. *Acta physiochim URSS*. 1940;12:327–56.
23. Khan A, Wang X, Gul K, Khuda F, Aly Z, Elseman AM. Microwave-assisted spent black tea leaves as cost-effective and powerful green adsorbent for the efficient removal of Eriochrome black T from aqueous solutions. *Egyptian Journal of Basic and Applied Sciences*. 2018 Jun;5(2):171–82. [<DOI>](#).
24. Akhouairi S, Ouachtak H, Addi AA, Jada A, Douch J. Natural Sawdust as Adsorbent for the Eriochrome Black T Dye Removal from Aqueous Solution. *Water Air Soil Pollut*. 2019 Aug;230(8):181. [<DOI>](#).
25. Sriram G, Uthappa UT, Rego RM, Kigga M, Kumeria T, Jung H-Y, et al. Ceria decorated porous diatom-xerogel as an effective adsorbent for the efficient removal of Eriochrome Black T. *Chemosphere*. 2020 Jan;238:124692. [<DOI>](#).
26. Bayomie OS, Kandeel H, Shoeib T, Yang H, Youssef N, El-Sayed MMH. Novel approach for effective removal of methylene blue dye from water using fava bean peel waste. *Sci Rep*. 2020 Dec;10(1):7824. [<DOI>](#).
27. Roosta M, Ghaedi M, Shokri N, Daneshfar A, Sahraei R, Asghari A. Optimization of the combined ultrasonic assisted/adsorption method for the removal of malachite green by gold nanoparticles loaded on activated carbon: Experimental design. *Spectrochimica Acta Part A: Molecular and Biomolecular Spectroscopy*. 2014 Jan;118:55–65. [<DOI>](#).
28. Asfaram A, Ghaedi M, Hajati S, Goudarzi A. Ternary dye adsorption onto MnO₂ nanoparticle-loaded activated carbon: derivative spectrophotometry and modeling. *RSC Adv*. 2015;5(88):72300–20. [<DOI>](#).
29. Shikuku VO, Mishra T. Adsorption isotherm modeling for methylene blue removal onto magnetic kaolinite clay: a comparison of two-parameter

- isotherms. *Appl Water Sci.* 2021 Jun;11(6):103. [<DOI>](#).
30. Rahangdale D, Kumar A. Chitosan as a substrate for simultaneous surface imprinting of salicylic acid and cadmium. *Carbohydrate Polymers.* 2018 Dec;202:334–44. [<DOI>](#).
31. Pereira MG, Arruda MAZ. Vermicompost as a natural adsorbent material: characterization and potentialities for cadmium adsorption. *J Braz Chem Soc.* 2003 Jan;14(1):39–47. [<DOI>](#).
32. Hussain N, Abbasi T, Abbasi SA. Vermicomposting-mediated conversion of the toxic and allelopathic weed ipomoea into a potent fertilizer. *Process Safety and Environmental Protection.* 2016 Sep;103:97–106. [<DOI>](#).
33. Ali U, Sajid N, Khalid A, Riaz L, Rabbani MM, Syed JH, et al. A review on vermicomposting of organic wastes. *Environ Prog Sustainable Energy.* 2015 Jul 8;34(4):1050–62. [<DOI>](#).
34. Manzar MS, Zubair M, Khan NA, Husain Khan A, Baig U, Aziz MA, et al. Adsorption behaviour of green coffee residues for decolourization of hazardous congo red and eriochrome black T dyes from aqueous solutions. *International Journal of Environmental Analytical Chemistry.* 2020 Aug 26;1–17. [<DOI>](#).
35. Khalid A, Zubair M, Ihsanullah. A Comparative Study on the Adsorption of Eriochrome Black T Dye from Aqueous Solution on Graphene and Acid-Modified Graphene. *Arab J Sci Eng.* 2018 May;43(5):2167–79. [<DOI>](#).
36. Azargohar R, Nanda S, Kozinski JA, Dalai AK, Sutarto R. Effects of temperature on the physicochemical characteristics of fast pyrolysis biochars derived from Canadian waste biomass. *Fuel.* 2014 Jun;125:90–100. [<DOI>](#).
37. Zhu F, Hou J, Xue S, Wu C, Wang Q, Hartley W. Vermicompost and Gypsum Amendments Improve Aggregate Formation in Bauxite Residue. *Land Degrad Develop.* 2017 Oct;28(7):2109–20. [<DOI>](#).
38. Şahin Ö, Saka C, Kutluay S. Cold plasma and microwave radiation applications on almond shell surface and its effects on the adsorption of Eriochrome Black T. *Journal of Industrial and Engineering Chemistry.* 2013 Sep;19(5):1617–23. [<DOI>](#).
39. Boumchita S, Lahrichi A, Benjelloun Y, Lairini S, Nenov V, Zerrouq F. Application of Peanut shell as a low-cost adsorbent for the removal of anionic dye from aqueous solutions. *Journal of Materials and Environmental Science.* 2017;8(7):2353–64.
40. Saleh TA, Musa AM, Ali SA. Synthesis of hydrophobic cross-linked polyzwitterionic acid for simultaneous sorption of Eriochrome black T and chromium ions from binary hazardous waters. *J Colloid Interface Sci.* 2016 Apr 15;468:324–33. [<DOI>](#).
41. Salimi F, Valiei V, Karami C. Removal of EBT dye from aqueous solution by modified MoNiO₄ adsorbent. *Desalination Water Treat.* 2020;190:340–52. [<DOI>](#).
42. Javanbakht V, Shafiei R. Preparation and performance of alginate/basil seed mucilage biocomposite for removal of eriochrome black T dye from aqueous solution. *International Journal of Biological Macromolecules.* 2020 Jun;152:990–1001. [<DOI>](#).
43. Manzar MS, Khan G, dos Santos Lins PV, Zubair M, Khan SU, Selvasembian R, et al. RSM-CCD optimization approach for the adsorptive removal of Eriochrome Black T from aqueous system using steel slag-based adsorbent: Characterization, Isotherm, Kinetic modeling and thermodynamic analysis. *Journal of Molecular Liquids.* 2021 Oct;339:116714. [<DOI>](#).
44. Onu CE, Nwabanne JT, Ohale PE, Asadu CO. Comparative analysis of RSM, ANN and ANFIS and the mechanistic modeling in eriochrome black-T dye adsorption using modified clay. *South African Journal of Chemical Engineering.* 2021 Apr;36:24–42. [<DOI>](#).
45. Kaur Y, Jasrotia T, Kumar R, Chaudhary GR, Chaudhary S. Adsorptive removal of eriochrome black T (EBT) dye by using surface active low cost zinc oxide nanoparticles: A comparative overview. *Chemosphere.* 2021 Sep;278:130366. [<DOI>](#).
46. Rashidi R, Omidic Khaniabadi Y, Ghaderpoori M. Adsorption of Eriochrome black-T from aqueous environment by raw Montmorillonite. *International Journal of Environmental Analytical Chemistry.* 2021 Mar 8;1–15. [<DOI>](#).



Kinetic Study of the Free Radical Copolymerization of Methyl Methacrylate with 2-Perfluorooctyl Ethyl Methacrylate by Quantum Computational Approach

Ramazan Katirci¹  and Salih Ozbay^{2*}  

¹ Department of Metallurgical and Materials Engineering, Sivas University of Science and Technology, 58000, Sivas, Turkey

² Department of Chemical Engineering, Sivas University of Science and Technology, 58000, Sivas, Turkey

Abstract: Fluorinated copolymers with perfluoroalkyl side chains have widespread use in applications requiring superior technology due to their unique surfacial properties. Kinetic analysis of copolymerization of fluorinated acrylates with conventional acrylates is necessary to synthesize such copolymers efficiently. However, kinetic investigation of such reactions are limited in the literature due to the experimental difficulties. In this study, the kinetics of copolymerization of methyl methacrylate with 2-perfluorooctyl ethyl methacrylate in toluene medium using AIBN initiator was investigated using quantum chemistry postulates as an alternative to experimental methods. Reaction rate constants (k_p) for propagation were determined using transition state theory. A terminal effect models were used to examine four different addition reactions involving monomeric and dimeric radicals and monomers for both self- and cross-propagation. Reactant and product conformations were optimized with a DFT method using PBE0 function. The Evans-Polanyi relationship was used to calculate the rate of self- and cross-propagation of monomers. The results showed that the reactivity ratio of 2-perfluorooctyl ethyl methacrylate was found to be higher than that of methyl methacrylate. In addition, it was observed that the reaction conditions caused the random polymer structure due to the different rate constants in self and cross propagation.

Keywords: 2-Perfluorooctyl ethyl methacrylate, methyl methacrylate, free radical polymerization, kinetics, DFT

Submitted: May 30, 2021. **Accepted:** November 09, 2021.

Cite this: Katirci R, Ozbay S. Kinetic Study of the Free Radical Copolymerization of Methyl Methacrylate with 2-Perfluorooctyl Ethyl Methacrylate by Quantum Computational Approach. JOTCSA. 2021;8(4):1263-74.

DOI: <https://doi.org/10.18596/jotcsa.945056>.

***Corresponding author. E-mail:** salihozbay@sivas.edu.tr. Phone: +90 (346) 219 1398.

INTRODUCTION

Fluorinated polymers have widespread applications in both scientific studies and industry due to their unique surface properties such as oil/water repellency originated from low polarizability and high electronegativity of the fluorine atoms (1-6). Design of superhydrophobic (7, 8) superoleophobic (9, 10) or superamphiphobic (11-13) surfaces using fluoropolymers is a common and practical way. Perfluorinated (meth)acrylates (FMA) are an important member of fluoropolymers because of their extremely low surface free energy properties (14-17).

However, adaptation of homopolymers of FMA to many systems is limited due to the many drawbacks such as being expensive, having poor mechanical properties and solubility difficulties in organic solvents (3, 13, 18). Copolymerization of FMA with methyl methacrylate (MMA) is an efficient solution to overcome these problems, and FMA-MMA copolymer couples have been experimentally synthesized by free radical polymerization using thermal initiators many times in the literature under different reaction conditions (15, 18-28). Organic solvents such as butyl acetate (19, 20, 23), methyl ethyl ketone (MEK) (7, 21), cyclohexanone (24), toluene (29, 30) and solvent mixtures such as 1,1,2-

trichlorotrifluoroethane (R-113)/ α,α,α -trifluorotoluene (TFT) (15, 18), toluene/MEK (25) were previously used in solution copolymerizations to synthesize fluorinated acrylate copolymers. Apart from conventional organic solvents, supercritical CO₂ has been used in many studies as an alternative medium for the free radical polymerization of fluoro monomers (26-28). Although these studies were successful in understanding the reaction conditions to obtain such polymers, and to find out the bulk and surface properties of the synthesized polymer, additional studies are needed for a detailed kinetic examination.

The kinetics of free radical copolymerization are critical for controlling the polymerization process and the last product (31). In a copolymerization where two different monomers are bonded to each other covalently, there are four divergent possible combinations of monomers and radical ends, and there is no experimental method that can directly measure the individual rate constant (k_p) values for different combinations of monomers and radicals (32). In addition, the determination of the overall k_p is also difficult by experimental methods due to the reactivity differences between secondary and tertiary carbon radicals (33, 34). Whereas, quantum computational approaches which does not require experimental investigations provides convenience to determine many reaction parameters and molecular structure properties such as the rate constant (k_p), activation energy (E_a), Gibbs free energy difference, ΔG , transition state geometries, and molecular architecture.

In this study, we investigated the kinetic of copolymerization of 2-perfluorooctyl ethyl methacrylate (FOEMA) with MMA by quantum computational approaches. Copolymers of FOEMA with MMA were synthesized computationally using different monomer feed compositions by a free radical process in toluene medium. AIBN was used as a thermal initiator. The main aim of this study is to find out the propagation rate in the intermediate steps and find the step determining the reaction rate, which provide us to estimate the sequence of the polymerization. In addition, the reactivity ratios were determined for the copolymerization of MMA with FOEMA to evaluate feed/bulk composition balance. A computational methodology was used to study such acrylate polymerization reactions, which is adaptable to other fluorinated or non-fluorinated acrylate polymerization systems.

COMPUTATIONAL METHODOLOGY

Four addition reactions of monomeric and dimeric radicals to monomers in all possible different combinations were studied for MMA and FOEMA as shown in Tables 1 and 2. For all reactions, k_p were calculated individually. The ΔG for these reactions was calculated at 350 K and 1 atm pressure to acquire the

reaction rates of free radical polymerizations using the Evans-Polanyi equation (32) as shown in Equation (1),

$$k_p = \frac{k_B T}{h c^\circ} e^{-\Delta^\ddagger G^\circ / RT} \quad (1)$$

where k_B denotes Boltzmann's constant (1.3806×10^{-23} J/K); h is Planck's constant (6.6261×10^{-34} J/mol.K); c° standard state concentration (mol/L), which can be taken as 1, and $\Delta^\ddagger G^\circ$ is the free energy difference between the activated complex and the reactants (with inclusion of zero point vibration energies). G energy is associated with a chemical reaction which can be used to do a work.

The preliminary study was performed to identify the best functional and basis set compatible with the experimental study. In the preliminary study, the optimization and frequency calculations were carried out with M062X/6-31G(d,p), B3LYP/6-31G(d,p), PBE/6-31G(d,p) and PBE0/def2-TZVP functional and basis sets. The best results were acquired with PBE0/def2-TZVP method and we continued our computations with this method. The results of other method were presented in the supporting information file (Table S3). All electronic energy calculations and vibrational frequencies were calculated using Orca 4.2 (35, 36). All the reactants and product conformations were optimized using DFT method and PBE0 function with def2-TZVP basis set (37) at 350 K and 1 atm pressure. However, the conventional optimization method employed is based on the gradient in energy and can only locate local minima, and thus the optimized geometry is sensitive to the input structure. Therefore, different conformations were explored using a systematic rotor search method which is present in Avogadro software. The conformations having the lowest energy were used as the input.

Transition state (TS) structures were screened using the relaxed scan method in Orca 4.2 software. The geometry owning the lowest energy in TS mode was used as the optimized TS geometry. Transition states were confirmed to have one imaginary frequency, which corresponded to the motion along the reaction coordinate, and an intrinsic reaction coordinate (IRC) (32) was performed to verify that the correct reactants and product were obtained. The conductor-like polarizable continuum model (CPCM) was used to calculate the solution effect (36).

It is critical to have a quantum chemical calculation method/basis set which is accurate yet computationally affordable due to the size of the polymer structures which were studied in this work. In many studies, it was reported that the activation energies and k_p values obtained using the PBE0 function with the basis set of def2-TZVP was a good enough agreement with experimental data (38).

RESULTS AND DISCUSSION

The TS geometries of the fluorinated acrylate molecules are presented in Figure 1.

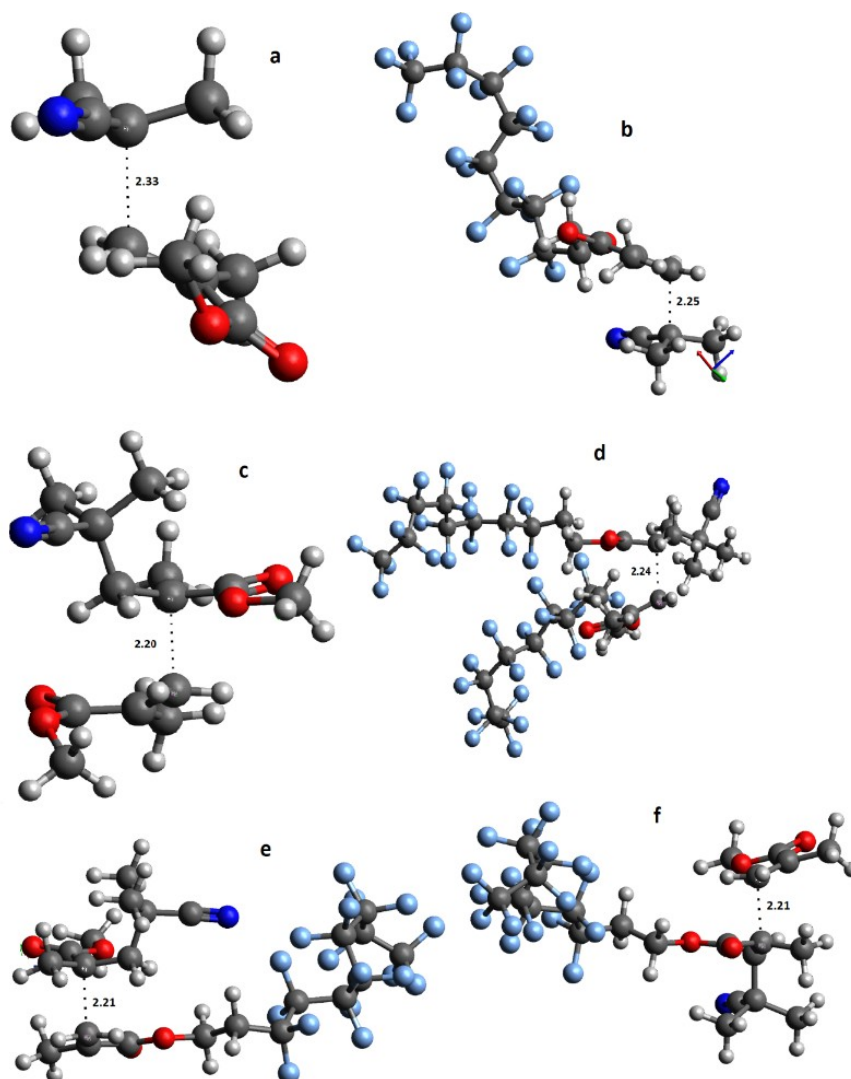


Figure 1: Transition state geometries of a) R-MMA b) R-FOEMA c) R-MMA-MMA d) R-FOEMA-FOEMA e) R-MMA-FOEMA f) R-FOEMA-MMA (PBE0/ def2-TZVP, 1 atm, 350 K, toluene medium (CPCM)).

The geometry of the transition states, which shows the minimum energy for the reaction formation, gives the significant information about combinations of fluorine atoms. The difference between the energies of the transition and the initial states determine the experimental activation energy for the reaction (39). The geometry of TS has the highest energy along the reaction coordinate and more free energy in comparison to the substrate or product; thus, it is the least stable state. Reactants, products and an estimation of the transition states are required to locate the transition state structures. Chemical structures of reactants and representative reaction of MMA, FOEMA and AIBN are given in Figure 2. The

addition of the radical center to the unsaturated C=C bond of the monomer is shown in Figure 3. The distance between the addition monomer and radical in the transition state was varied in the range of 2.20-2.33. These distances indicate that they have the partial bond at their maximum length. Because the lifetime of the transition state is too short and rapidly relaxes to the product, it is too difficult to determine the k_p values experimentally. Transition states are specified as saddle points on the potential energy surface, possessing one imaginary frequency. Once possible transition state locations were acquired, they were confirmed using intrinsic reaction coordinate (IRC) (40).

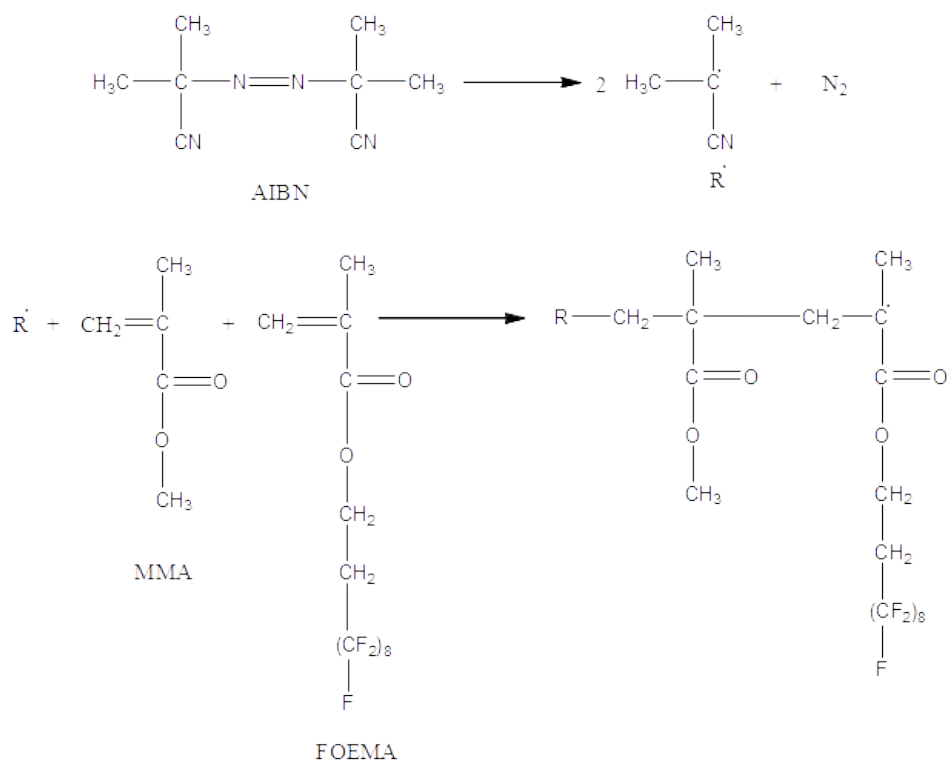


Figure 2. Representative reaction of methyl methacrylate (MMA), 2-perfluorooctyl ethyl methacrylate (FOEMA) and 2,2'-azobisisobutyronitrile (AIBN).

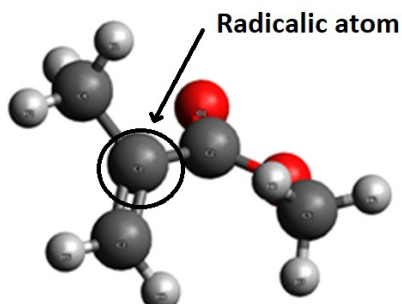


Figure 3. The geometric structure of MMA monomer (PBE0/ def2-TZVP, 1 atm, 350 K, toluene medium (CPCM)).

Table 1. Relative Gibbs free energy of monomers, radicals, and transition states (TS) of molecules (PBE0/ def2-TZVP, 1 atm, 350 K, toluene medium (CPCM)).

	Gibbs Free Energy (kcal/mol)
RA [•] (Radical) + A (Monomer)	0
RB [•] (Radical) + B (Monomer)	0
RA [•] (Radical) + B (Monomer)	0
RB [•] (Radical) + A (Monomer)	0
RA -- A (TS)	16.5
RB -- B (TS)	16.5
RA -- B (TS)	16.3
RB -- A (TS)	16.8

Table 2. Frequency factors (A), Activation energies (E_a) and rate constants for the MMA-FOEMA polymerizations (PBE0/ def2-TZVP, 1 atm, 350 K, toluene medium (CPCM)).

Polymerizations	Log ₁₀ (A)	E _a (kcal/mol)	k _p (s ⁻¹)
RA• + A → RAA•	3.32	1.20	3.688×10 ²
RA• + B → RAB•	3.23	0.90	4.681×10 ²
RB• + B → RBB•	*	*	3.877×10 ^{2*}
RB• + A → RBA•	2.57	0.28	2.497×10 ²

E_a: Activation Energy. A: The frequency or pre-exponential factor. k_p: Rate constant. "R" stands for 2,2'-azobisisobutyronitrile, "A" denotes methyl methacrylate (MMA), and "B" denotes perfluorooctyl ethyl methacrylate (FOEMA). *The Gibbs free energy of TS in this reaction was computed as -4980.71 hartree. But the k_p value in Table 2 was calculated according to the number of 4980.73 (Table S4). We searched many conformations to find the global minima, but we could not reach the global minimum conformation. The computations took too much cpu time and large memory because the structure of the molecule was too large. Because the other k_p values were compatible with the experimental studies, we decided to report by estimating the Gibbs free energy of TS of RB- B•.

Table 1 shows the Relative Gibbs free energy (G) of the reactants and TS molecules. The k_p constants and kinetic parameters (A, E_a) of the polymerizations in Table 2 were computed using the data in supporting information Table S4. Reaction rate constants (k_p) for propagation were computed using equation (1) (41). The calculations were carried out in toluene and gas phase. In the gas phase, the k_p constants were too low (k_p = ~10⁻³⁰-10⁻⁵⁰), so it can be said that the polymerization reaction was not possible in the gas phase. The results in the gas phase were presented in supporting information Table S1 and Table S2. When the toluene as the solution was included in the calculations, the k_p constants raised abruptly, which means the solution effect is very high. The CPCM model was implemented to compute the solution effect. In this model, the solvent is represented as a dielectric polarizable continuum and the solute is located in a cavity of approximately the molecular shape. The solvent reaction area is described by polarization charges on the surface of the cavity. The cavity is generated by the GEPOL algorithm using a solvent-excluding or solvent-accessible surface.

The monomer reactivity ratios of r_A and r_B were computed using the Equations (2) and (3).

$$r_A = \frac{k_{A-A}}{k_{A-B}} \quad (2)$$

$$r_B = \frac{k_{B-B}}{k_{B-A}} \quad (3)$$

According to the calculations, r_A and r_B were estimated as 0.79 and 1.55, respectively indicating that the fluorinated acrylate monomer is much more reactive than MMA monomer. Reactivity ratio differences between fluorinated acrylate and MMA can be seen in the previous experimental reports considering reactivity ratio values or feed/bulk composition balance (19, 20, 24-28). For example, van de Grampel et al. reported r_{MMA} = 0.76 and r_{fluoro methacrylate} = 1.31 for poly(MMA-co-1,1-dihydroperfluoroheptyl methacrylate) copolymer system using ¹H-NMR data and nonlinear least-squares data fitting (19). The reactivity ratios can also be used to evaluate the composition in the copolymer product as a function of monomer feed fractions based on Mayo-Lewis equations (42) as shown in Equation (4) (43),

$$F_1 = \frac{r_1 f_1^2 + f_1 f_2}{r_1 f_1^2 + 2 f_1 f_2 + r_2 f_2^2} \quad (4)$$

where F denotes a molar fraction of monomer in the copolymer, f denotes molar fraction of monomers in the feed and r denotes reactivity ratios. Using the reactivity ratio values and equation (4) simultaneously, Mayo-Lewis plot of F_{FOEMA} vs f_{FOEMA} was constructed and is shown in Figure 4. The predicted composition curve is in good accordance with the previous experimental reports associated with the perfluoro acrylate - MMA copolymerization systems, indicating that our approach is easily able to adaptable to the real copolymerization systems.

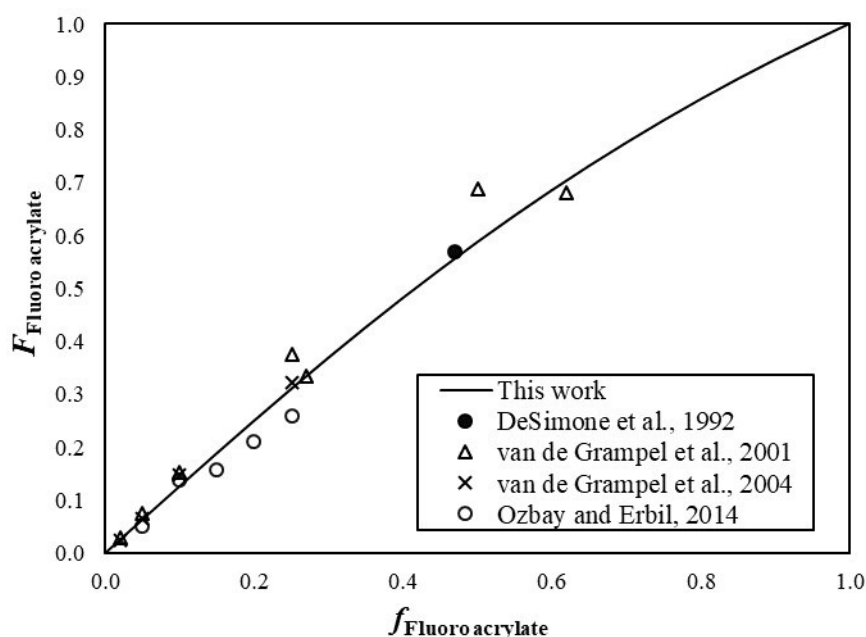


Figure 4. Mayo-Lewis plot for MMA-FOEMA copolymerization at 350 K and 1 atm. Copolymer composition data for poly(1,1-dihydroperfluorooctyl acrylate-co-MMA) copolymerization synthesized in supercritical CO₂ medium at 332.55 K (●) (26); for poly(1,1-dihydroperfluoroheptyl methacrylate-co-MMA) copolymerization synthesized in butyl acetate at 353.15 K (Δ) (19); for poly(1,1-dihydroperfluoroheptyl methacrylate-co-MMA) copolymerization synthesized in butyl acetate at 353.15 K (×) (20); poly(perfluoroalkyl ethyl methacrylate-co-MMA) synthesized in toluene/MEK solvent mixture at 348.15 K (o) (25).

On the other hand, linear copolymers can be in random, block, or alternative copolymer structure depending on the arrangement of their monomers. DSC analysis is the most practical experimental way to say that a copolymer is random. If a copolymer shows one glass transition peak, this polymer can be considered as random copolymer. In general, copolymerization of acrylates with fluorinated acrylates by using thermal initiators gives random copolymer structure. For example, Chang et al. synthesized fluoroacrylate-MMA random copolymer in MEK solvent using AIBN initiator at 70 °C (7). Similarly, Nishino et al. synthesized 2-perfluorooctylethyl methacrylate-MMA random copolymer in MEK solvent using AIBN initiator at 70 °C (21). Park et al. synthesized perfluoroalkylethyl methacrylate-MMA random copolymer in R-113/TFT solvent mixture using AIBN initiator at 70 °C (15, 18). Ye et al. synthesized 2-perfluorooctylethyl methacrylate-MMA random copolymer in cyclohexanone solvent using benzoyl peroxide (BPO) initiator at 70 °C (24). Ozbay and Erbil synthesized 2-perfluoroalkylethyl methacrylate-MMA random copolymers in toluene/MEK solvent mixture using AIBN initiator at 75°C (25). All of these results experimentally indicate that free radical copolymerization of fluorinated acrylates with conventional acrylates using thermal initiators caused random copolymer structure. However, the computational proof of this experimental result is

another case. The rate constant of a reaction can be used to estimate the molecular architecture of copolymer. For example, it is expected that the reactivity ratios (r_A and r_B) of all monomers should be equal to or close to zero for an alternating copolymer. When the k_p values are examined in Table 2, it is seen that they are quite different from each other. Therefore, it can be said that the alternating copolymer is not possible in these reactions. If we make this evaluation for a block copolymer, the reactivity ratios of both monomers should be higher than 1. In our study, the r_A value is lower than 1. This indicates that the formation of block copolymer is not possible in these reactions. However, in a random copolymer, the two monomers may react in any order. The proportion of the monomers added into the copolymer is a result of a combination of the properties of the monomers, the polymerization conditions and the conversion of the polymerization. For example, if the two monomers do not have the same reactivity exactly, the ratio in the product will not occur exactly 1-to-1. It results in a change in the copolymer composition while the reaction proceeds. At the beginning, the more reactive monomer is added more than the less reactive one. When the k_p values are examined in Table 2, the reactivity of the polymer chain is different. Thus, it can be deduced that the polymer reaction proceeds randomly. This result is compatible with the experimental studies carried out by various researchers (20, 21-28).

CONCLUSIONS

A computational methodology based on quantum postulates and transition state theory has been used to estimate the kinetic parameters of MMA and FOEMA propagation reactions. A conventional geometric optimization method was used to locate the global minimum geometry of the monomers. These monomers were added in a different order. All reactants and products were optimized. To determine the transition state, relaxed potential energy scans were carried out. The bond defining the transition state was used to estimate the Gibbs free energy in the highest energy along the reaction coordinate. IRC calculations were performed to verify the location of the transition state. The k_p constants were determined at 350 K for free radical copolymerization in toluene medium. The reactivity ratios for the free radical copolymerization of MMA and FOEMA in toluene medium were determined to be $r_{\text{MMA}}=0.79$ and $r_{\text{FOEMA}}=1.55$. It was observed that predicted reactivity ratios and feed/bulk composition balance are in good accordance with the previous experimental reports, indicating that our approach is easily able to adaptable to the various copolymerization systems.

REFERENCES

1. Ciardelli F, Aglietto M, Montagnini di Mirabello L, Passaglia E, Giancristoforo S, Castelvetro V, et al. New fluorinated acrylic polymers for improving weatherability of building stone materials. *Progress in Organic Coatings*. 1997;32(1-4):43-50. [<DOI>](#).
2. Anton D. Surface-fluorinated coatings." *Advanced Materials*. 1998;10:1197-205.
3. Imae T. Fluorinated polymers. *Current Opinion in Colloid & Interface Science*. 2003;8(3):307-14. [<DOI>](#).
4. Huang P-Y, Chao Y-C, Liao Y-T. Preparation of fluoroacrylate nanocopolymer by miniemulsion polymerization used in textile finishing. *Journal of Applied Polymer Science*. 2004;94(4):1466-72. [<DOI>](#).
5. Bruno A. Controlled Radical (Co)polymerization of Fluoromonomers. *Macromolecules*. 2010;43(24):10163-84. [<DOI>](#).
6. Lee S, Park J-S, Lee TR. The Wettability of Fluoropolymer Surfaces: Influence of Surface Dipoles. *Langmuir*. 2008;24(9):4817-26. [<DOI>](#).
7. Chang K-C, Chen H, Huang C-K, Huang S-I. Preparation of super-hydrophobic film with fluorinated-copolymer. *Journal of Applied Polymer Science*. 2007;104(3):1646-53. [<DOI>](#).
8. Ozbay S, Erbil HY. Superhydrophobic and oleophobic surfaces obtained by graft copolymerization of perfluoroalkyl ethyl acrylate onto SBR rubber. *Colloids and Surfaces A: Physicochemical and Engineering Aspects*. 2015;481:537-46. [<DOI>](#).
9. Tuteja A, Choi W, Ma M, Mabry JM, Mazzella SA, Rutledge GC, et al. Designing superoleophobic surfaces. *Science*. 2007;318(5856):1618-22. [<DOI>](#).
10. Steele A, Bayer I, Loth E. Inherently Superoleophobic Nanocomposite Coatings by Spray Atomization. *Nano Letters*. 2009;9(1):501-5. [<DOI>](#).
11. Xiong D, Liu G, Hong L, Duncan EJS. Superamphiphobic Diblock Copolymer Coatings. *Chemistry of Materials*. 2011;23(19):4357-66. [<DOI>](#).
12. Lee SG, Ham DS, Lee DY, Bong H, Cho K. Transparent Superhydrophobic/Translucent Superamphiphobic Coatings Based on Silica-Fluoropolymer Hybrid Nanoparticles. *Langmuir*. 2013;29(48):15051-7. [<DOI>](#).
13. Ozbay S, Cengiz U, Erbil HY. Solvent-Free Synthesis of a Superamphiphobic Surface by Green Chemistry. *ACS Applied Polymer Materials*. 2019;1(8):2033-43. [<DOI>](#).
14. Katano Y, Tomono H, Nakajima T. Surface Property of Polymer Films with Fluoroalkyl Side Chains. *Macromolecules*. 1994;27(8):2342-4. [<DOI>](#).
15. Park IJ, Lee S-B, Choi CK. Surface Properties of the Fluorine-Containing Graft Copolymer of Poly((perfluoroalkyl)ethyl methacrylate)-g-poly(methyl methacrylate). *Macromolecules*. 1998;31(21):7555-8. [<DOI>](#).
16. Stone M, Nevell TG, Tsibouklis J. Surface energy characteristics of poly(perfluoroacrylate) film structures. *Materials Letters*. 1998;37(1-2):102-5. [<DOI>](#).
17. Tsibouklis J, Graham P, Eaton PJ, Smith JR, Nevell TG, Smart JD, et al. Poly(perfluoroalkyl methacrylate) Film Structures: Surface Organization Phenomena, Surface Energy Determinations, and Force of Adhesion Measurements. *Macromolecules*. 2000;33(22):8460-5. [<DOI>](#).
18. Park IJ, Lee S-B, Choi CK. Synthesis of fluorine-containing graft copolymers of poly(perfluoroalkylethyl methacrylate)-g-poly(methyl

- methacrylate) by the macromonomer technique and emulsion copolymerization method. *Polymer*. 1997;38(10):2523–7. [<DOI>](#).
19. Van De Grampel RD, Van Geldrop J, Laven J, Van Der Linde R. P[CF₃(CF₂)₅CH₂MA-co-MMA] and P[CF₃(CF₂)₅CH₂MA-co-BA] copolymers: Reactivity ratios and surface properties. *Journal of Applied Polymer Science*. 2001;79(1):159–65. [<DOI>](#).
20. Van de Grampel RD, Ming W, Gildenpfennig A, Van Gennip WJH, Laven J, Niemantsverdriet JW, et al. The Outermost Atomic Layer of Thin Films of Fluorinated Polymethacrylates. *Langmuir*. 2004;20(15):6344–51. [<DOI>](#).
21. Nishino T, Urushihara Y, Meguro M, Nakamae K. Surface properties and structures of diblock and random copolymers with perfluoroalkyl side chains. *Journal of Colloid and Interface Science*. 2004;279(2):364–9. [<DOI>](#).
22. Choi D, Yeom EH, Park M, Kim JK, Kim BC. Preparation and properties of methyl methacrylate and fluoroacrylate copolymers for plastic optical fiber cladding. *Journal of Applied Polymer Science*. 2004;93(5):2082–9. [<DOI>](#).
23. Hartmann P, Collet A, Viguier M. Acrylic Copolymers with Perfluoroalkylated Biphenyl Side Groups: Correlation Structure–Surface Properties. *Macromolecules*. 2006;39(20):6975–82. [<DOI>](#).
24. Ye X, Zuo B, Deng M, Hei Y, Ni H, Lu X, et al. Surface segregation of fluorinated moieties on poly(methyl methacrylate-ran-2-perfluorooctylethyl methacrylate) films during film formation: Entropic or enthalpic influences. *Journal of Colloid and Interface Science*. 2010;349(1):205–14. [<DOI>](#).
25. Ozbay S, Erbil HY. Solution copolymerization of perfluoroalkyl ethyl methacrylate with methyl methacrylate and butyl acrylate: Synthesis and surface properties. *Colloids and Surfaces A: Physicochemical and Engineering Aspects*. 2014;452:9–17. [<DOI>](#).
26. DeSimone AJM, Guan Z, Elsbernd CS. Synthesis of Fluoropolymers in Supercritical Carbon Dioxide. *Science*. 1992;257(5072):945–7.
27. Cengiz U, Gengec NA, Ugur Kaya N, Yildirim Erbil H, Sezai Sarac A. Mechanical and thermal properties of perfluoroalkyl ethyl methacrylate–methyl methacrylate statistical copolymers synthesized in supercritical carbon dioxide. *Journal of Fluorine Chemistry*. 2011;132(5):348–55. [<DOI>](#).
28. Cengiz U, Gengec NA, Erbil HY. Surface characterization of flat and rough films of perfluoromethacrylate-methylmethacrylate statistical copolymers synthesized in CO₂-expanded monomers. *Colloid and Polymer Science*. 2013;291(3):641–52. [<DOI>](#).
29. Ding L, Olesik S V. Dispersion Polymerization of MMA in Supercritical CO₂ in the Presence of Copolymers of Perfluorooctylethylene Methacrylate and Poly(propylene glycol) Methacrylate. *Macromolecules*. 2003;36(13):4779–85. [<DOI>](#).
30. Valtola L, Hietala S, Tenhu H, Denifl P, Wilen C-E. Association behavior and properties of copolymers of perfluorooctyl ethyl methacrylate and eicosanyl methacrylate. *Polymers for Advanced Technologies*. 2009;20(3):225–34. [<DOI>](#).
31. Fukuda T, Kubo K, Ma Y-D. Kinetics of free radical copolymerization. *Progress in Polymer Science*. 1992;17(5):875–916. [<DOI>](#).
32. Yu X, Levine SE, Broadbelt LJ. Kinetic Study of the Copolymerization of Methyl Methacrylate and Methyl Acrylate Using Quantum Chemistry. *Macromolecules*. 2008;41(21):8242–51. [<DOI>](#).
33. Asua JM, Beuermann S, Buback M, Castignolles P, Charleux B, Gilbert RG, et al. Critically Evaluated Rate Coefficients for Free-Radical Polymerization, 5,. *Macromolecular Chemistry and Physics*. 2004;205(16):2151–60. [<DOI>](#).
34. Dossi M, Storti G, Moscatelli D. A quantum chemistry study of the free-radical copolymerization propagation kinetics of styrene and 2-hydroxyethyl acrylate. *Polymer Engineering & Science*. 2011;51(10):2109–14. [<DOI>](#).
35. Neese F. The ORCA program system. *WIREs Computational Molecular Science*. 2012;2(1):73–8. [<DOI>](#).
36. Neese F. Software update: the ORCA program system, version 4.0. *WIREs Computational Molecular Science*. 2018;8:e1327. [<DOI>](#).
37. Treutler O, Ahlrichs R. Efficient molecular numerical integration schemes. *The Journal of Chemical Physics*. 1995;102(1):346–54. [<DOI>](#).
38. Liu S, Srinivasan S, Tao J, Grady MC, Soroush M, Rappe AM. Modeling Spin-Forbidden Monomer Self-Initiation Reactions in Spontaneous Free-Radical Polymerization of Acrylates and Methacrylates. *The Journal of Physical Chemistry A*. 2014;118(40):9310–8. [<DOI>](#).

39. Verma P, Perera A, Bartlett RJ. Increasing the applicability of DFT I: Non-variational correlation corrections from Hartree-Fock DFT for predicting transition states. *Chemical Physics Letters*. 2012;524:10-5. [<DOI>](#).
40. Maeda S, Harabuchi Y, Ono Y, Taketsugu T, Morokuma K. Intrinsic reaction coordinate: Calculation, bifurcation, and automated search. *International Journal of Quantum Chemistry*. 2015;115(5):258-69. [<DOI>](#).
41. Wubbels GG. Use of the Bell-Evans-Polanyi Principle to predict regioselectivity of nucleophilic aromatic photosubstitution reactions. *Tetrahedron Letters*. 2014;55(36):5066-9. [<DOI>](#).
42. Mayo FR, Lewis FM. Copolymerization. I. A Basis for Comparing the Behavior of Monomers in Copolymerization; The Copolymerization of Styrene and Methyl Methacrylate. *Journal of the American Chemical Society*. 1944;66(9):1594-601. [<DOI>](#).
43. Odian G. *Principles of Polymerization* [Internet]. Hoboken, NJ, USA: John Wiley & Sons, Inc.; 2004. [<DOI>](#).

SUPPORTING INFORMATION

Kinetic Study of the Free Radical Copolymerization of Methyl Methacrylate with Perfluorooctyl Ethyl Methacrylate by Quantum Computational Approach

Ramazan Katirci^a and Salih Ozbay^{b*}^a Department of Metallurgical and Materials Engineering, Sivas University of Science and Technology, 58000, Sivas, Turkey^b Department of Chemical Engineering, Sivas University of Science and Technology, 58000, Sivas, Turkey**Table S1.** Thermodynamic parameters computed at 298 K temperature and 1 atm pressure in the gas phase (PBE0 function and def2-TZVP basis set).

	ΔG (TS-react) (cal)	k (rate) s ⁻¹
R--MMA	134795.9732	9.48348773E-87
R-MMA--MMA	191331.3701	3.40388261E-128
R-2MMA---MMA	253066.1944	1.88530918E-173
R-- FOEMA	423292.0851	0.00000000E+00
R- FOEMA -- FOEMA	803668.3095	0.00000000E+00
R-2 FOEMA -- FOEMA	1159976.621	0.00000000E+00
R- FOEMA ---MMA	483062.7089	0.00000000E+00
R-MMA--- FOEMA	483461.3283	0.00000000E+00
R- FOEMA -MMA---MMA	460561.1927	0.00000000E+00
R- FOEMA -MMA--- FOEMA	767284.4602	0.00000000E+00
R-MMA- FOEMA ---MMA	558585.622	0.00000000E+00
R-MMA- FOEMA --- FOEMA	870388.8911	0.00000000E+00

Table S2. Thermodynamic parameters computed at 350 K temperature and 1 atm pressure in the gas phase (PBE0 function and def2-TZVP basis set).

	ΔG (TS-react) (cal)	k (rate) s ⁻¹
R--MMA	136429.3997	4.62900018E-73
R-MMA--MMA	189728.7037	2.40518257E-106
R-2MMA---MMA	250298.7436	3.60065233E-144
R-- FOEMA	423853.5596	1.49590195E-252
R- FOEMA -- FOEMA	800609.6047	0.00000000E+00
R-2 FOEMA -- FOEMA	1156812.665	0.00000000E+00
R- FOEMA ---MMA	484992.2149	9.88661068E-291
R-MMA--- FOEMA	481709.1224	1.10987083E-288

R- FOEMA -MMA---MMA	556443.4876	0.00000000E+00
R- FOEMA -MMA--- FOEMA	862918.3969	0.00000000E+00
R-MMA- FOEMA ---MMA	555915.6346	0.00000000E+00
R-MMA- FOEMA --- FOEMA	867352.8704	0.00000000E+00

Table S3. The preliminary study results in the different function and basis set.

File name	Job	opt	freq
aibn_opt-freq	B3LYP 6-31G(d,p) opt freq	-530.683898777583	+
aibn_opt-freq_m062x	M062X 6-31G(d,p) opt numfreq	-530.789754769161	+
aibn_opt-freq_PBE	PBE 6-31G(d,p) opt freq	-530.342724848908	+
r-aibn_opt-freq_b3lyp	B3LYP 6-31G(d,p) opt freq	-210.605002312145	+
r-aibn_opt-freq_m062x	m062x 6-31G(d,p) opt numfreq	-210.635285657286	+
r-aibn_opt-freq_pbe	pbe 6-31G(d,p) opt freq	-210.459817022986	+
MMA_g1_opt-freq_b3lyp	B3LYP 6-31G(d,p) opt freq	-345.573917406707	+
MMA_g1_opt-freq_m062x	M062X 6-31G(d,p) opt numfreq	-345.619493292794	+
MMA_g1_opt-freq_pbe	PBE 6-31G(d,p) opt freq	-345.348240266100	-
MMA_g2_opt-freq_b3lyp	B3LYP 6-31G(d,p) opt freq	-345.588611162832	-158.92, -99.61
MMA_g2_opt-freq_m062x	M062X 6-31G(d,p) opt numfreq	-345.638040898266	+
MMA_g2_opt-freq_pbe	PBE 6-31G(d,p) opt freq	-345.366536159985	-
r-MMA_g1_opt-freq_b3lyp	B3LYP 6-31G(d,p) opt freq	-556.191975070327	-16.68
r-MMA_g1_opt-freq_b3lyp_g1	B3LYP 6-31G(d,p) opt freq	-556.191975062726	-36.59
r-MMA_g1_opt-freq_b3lyp_g2	B3LYP 6-31G(d,p) opt freq	-556.191974040997	+
r-MMA_g1_opt-freq_m062x	M062X 6-31G(d,p) opt numfreq	-556.288521310507	+
r-MMA_g1_opt-freq_pbe	PBE 6-31G(d,p) opt freq	-555.833081894961	+
r-2MMA_g1_opt-freq_b3lyp	B3LYP 6-31G(d,p) opt freq	-862.529154688673	+
r-2MMA_g1_opt-freq_m062x	M062X 6-31G(d,p) opt numfreq	-862.683756120450	+
r-2MMA_g1_opt-freq_pbe	PBE 6-31G(d,p) opt freq	-861.982881250647	+
r-3MMA_g1_opt-freq_b3lyp	B3LYP 6-31G(d,p) opt freq	-1168.839909183060	+
r-3MMA_g1_opt-freq_m062x	M062X 6-31G(d,p) opt numfreq	-1169.058152291700	+
r-3MMA_g1_opt-freq_pbe	PBE 6-31G(d,p) opt freq	-1168.109343076010	-6.27
r-4MMA_g1_opt-freq_b3lyp	B3LYP 6-31G(d,p) opt freq	-1475.142105875250	+
r-4MMA_g1_opt-freq_m062x	M062X 6-31G(d,p) opt numfreq	-1475.422366291610	+
r-4MMA_g1_opt-	PBE 6-31G(d,p) opt freq	-1474.222309328250	+

freq_pbe			
r-5MMA_g1_opt-freq_b3lyp	B3LYP 6-31G(d,p) opt freq	-1781.421693099380	+
r-5MMA_g1_opt-freq_m062x	M062X 6-31G(d,p) opt numfreq	-1781.780927190650	-62.38
r-5MMA_g1_opt-freq_pbe	PBE 6-31G(d,p) opt freq	-1780.325191210910	19.71
tm_g1_opt-freq_b3lyp	B3LYP 6-31G(d,p) opt freq	-2385.588424993400	-159.81
tm_g1_opt-freq_b3lyp_g1	B3LYP 6-31G(d,p) opt freq	-2385.590759104760	15.76
tm_g1_opt-freq_m062x	M062X 6-31G(d,p) opt numfreq	-2385.797913196300	-14.91
tm_g1_opt-freq_pbe	PBE 6-31G(d,p) opt freq	-2384.210973070660	-151.44
r-tm_g1_opt-freq_b3lyp	B3LYP 6-31G(d,p) opt freq	-2596.216012481470	+
r-tm_g1_opt-freq_m062x	M062X 6-31G(d,p) opt numfreq	-2596.470088206310	+
r-tm_g1_opt-freq_pbe	PBE 6-31G(d,p) opt freq	-2594.700783056990	-10.13
r-2tm_g1_opt-freq_b3lyp_duz	B3LYP 6-31G(d,p) opt freq	-4981.820703723510	+
r-3tm_g1_freq_b3lyp	B3LYP 6-31G(d,p) numfreq	-7367.426722815420	+
r-3tm_g1_opt-freq_m062x_devam	M062X 6-31G(d,p) opt numfreq	-7368.137540547900	Not available
r-3tm_g1_opt-freq_pbe	PBE 6-31G(d,p) opt freq	-7363.178413765410	Not available
r-3tm_g1_opt-freq_pbe_devam	PBE 6-31G(d,p) numfreq	-7363.178413561820	-56.43

Table S4. Gibbs Free Energy of monomers, radicals and transition states (TS) of molecules.

	Gibbs Free Energy (Eh)
RA (Radical)	-555.93
RB (Radical)	-2595.63
A (Monomer)	-345.43
B (Monomer)	-2385.13
RA -- A (TS)	-901.33
RB -- B (TS)	-4980.73
RA -- B (TS)	-2941.03
RB -- A (TS)	-2941.03



Dioxomolybdenum(VI) Complexes of ONN-Chelating Thiosemicarbazones: Crystallographic and Spectroscopic (UV, IR and NMR) Studies

Songül Eğlence-Bakır^{a*}  

^aDepartment of Chemistry, Faculty of Science, Istanbul University, 34134, Istanbul, Turkey

Abstract: Four new *cis*-dioxomolybdenum(VI) complexes of the closed formula [MoO₂(L)CH₃OH] have been obtained by the condensation of bis(acetylacetonato)dioxomolybdenum(VI) with S-allyl/propyl thiosemicarbazones in methanol. The compounds were identified with elemental analysis, and molecular characterization by UV-Vis, FT-IR, ¹H-NMR and ¹³C-NMR spectroscopies. Also, crystal structures of **1** and **2** were resolved by X-ray diffraction analysis. The single crystal studies indicated a distorted octahedral geometry for complexes. It was noticed that **1** crystallized in the monoclinic P2₁/c space group with Z=4, while **2** crystallized in triclinic P-1 space group with Z=2. The O=Mo=O angles of 105.68(8)° (for **1**) and 105.96(7)° (for **2**) indicated the *cis*-dioxomolybdenum structure. The spectroscopic and crystallographic studies show that the thiosemicarbazone ligands are bound to *cis*-MoO₂²⁺ moiety as ONN tridentate agent and the 6th coordinated position of the molybdenum is located by the methanol molecule.

Keywords: Thiosemicarbazone; dioxomolybdenum(VI) complex; X-ray crystallography; spectroscopic studies; structural analysis.

Submitted: September 01, 2021. **Accepted:** November 13, 2021.

Cite this: Eğlence-Bakır S. Dioxomolybdenum(VI) Complexes of ONN-Chelating Thiosemicarbazones: Crystallographic and Spectroscopic (UV, IR and NMR) Studies. JOTCSA. 2021;8(4):1275-300.

DOI: <https://doi.org/10.18596/jotcsa.989318>.

***Corresponding author. E-mail:** songul@istanbul.edu.tr.

INTRODUCTION

Thiosemicarbazones, obtained through the condensation reaction of thiosemicarbazides with an aldehyde or a ketone, are one of the main subgroups of hydrazones (1, 2). After their activities on living systems was discovered in 1950s, investigators have exhibited an increased attention in thiosemicarbazones and their metal complexes (3). Thiosemicarbazone-metal complexes are an important group of compounds with numerous biological activities (4-13). Thiosemicarbazones can behave as monodentate (14, 15), bidentate (16, 17),

tridentate (18-20), or multidentate (21, 22) ligands. Common metal complexes of thiosemicarbazones have tridentate ONS or ONN functions. In both forms, the oxygen atom of an arylidene moiety and the azomethine nitrogen coordinate to the metal ion. Also, the sulfur atom or the thioamide nitrogen coordinate to metal center for ONS- or ONN-coordinated complexes, respectively (12, 18).

Molybdenum is a special cofactor for molybdoenzymes such as sulfite oxidase and xanthine oxidase (23). These molybdoenzymes have oxo-groups and the molybdenum ion has

an oxidation state of (VI) or (IV) during the reaction cycle (24). The solvate dioxomolybdenum(VI) complexes of thiosemicarbazones can behave as catalysts. It is because the solvent molecule may be relocated with the activated enzyme molecule. Several chelates containing *cis*-MoO₂²⁺ moiety have been obtained for explain the structure of molybdoenzymes and oxygen atom transfer (OAT) reactions (25). As mentioned above, molybdenum complexes are used as models in many biological activity studies, primarily in enzyme systems. In order to study in detail how the activity changes with the structure, it becomes important to systematically synthesize and characterize compounds with different groups on both the aromatic ring, the amide or sulfur atoms and different solvents coordinated to the sixth site of the molybdenum. In early studies, the solvated mononuclear dioxomolybdenum(VI) complexes of thiosemicarbazones containing pyridine (26), acetonitrile (27), methanol (18), ethanol (25), γ -picoline (28), dimethylsulfoxide (29) as solvents have been reported.

The current study was focused on obtain and characterize the ONN-coordinated dioxomolybdenum(VI) complexes of S-allyl/propylthiosemicarbazones. For this purpose, different substitutions have been studied on the aromatic ring, amide nitrogen, and the sulfur atom (Figure 1). The characterization results of ligands and complexes were determined by elemental analysis, UV-Vis, IR, ¹H-NMR and ¹³C-NMR spectroscopies.

The structures of *cis*-dioxo-(S-allyl-N¹-2-hydroxy-4-methoxybenzylidene-thiosemicarbazonato) (O,N,N')-methanol-molybdenum(VI) (**1**) and *cis*-dioxo-(S-allyl-N¹-2-hydroxy-5-chlorobenzylidene-N⁴-ethylthiosemicarbazonato) (O,N,N')-methanol-molybdenum(VI) (**2**) were also determined by X-ray diffraction analysis. Effects of different substitutions on structures were compared using the crystallographic and spectroscopic studies.

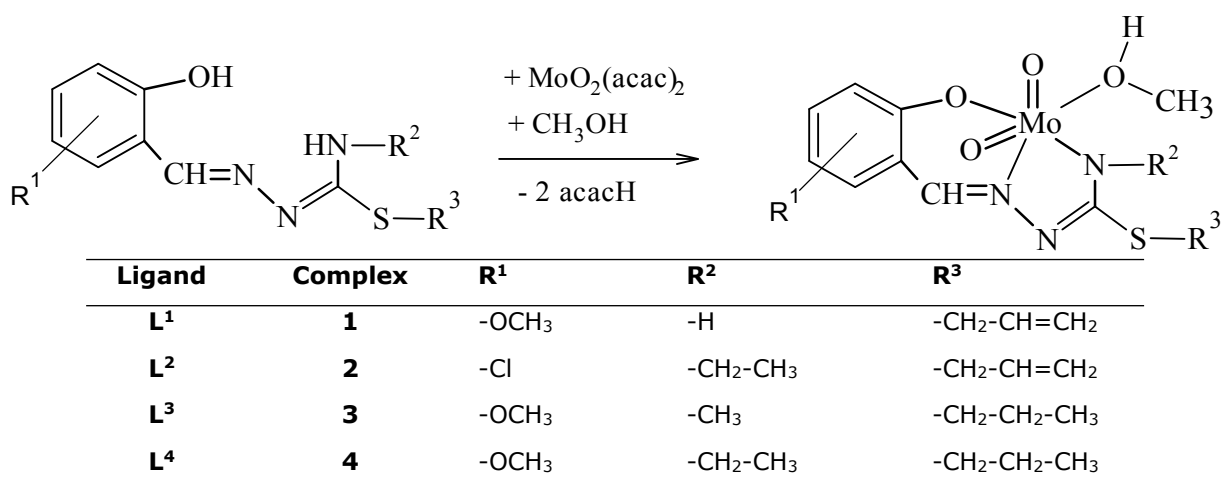


Figure 1: Formation of the complexes.

EXPERIMENTAL

Materials and Physical Measurements

Thermo-Finnigan Flash EA 1112 Series Elementary Analyzer was used for record elemental analyses. UV-Vis spectra of the thiosemicarbazones and complexes were performed in chloroform, 3x10⁻⁵ M, with a Shimadzu 2600 UV-Vis spectrophotometer. The infrared spectra of the compounds were obtained on a Bruker Alpha II compact Fourier Transform Infrared (FTIR) spectrometer in range of 4000 to 400 cm⁻¹. Varian VNMRJ 600 Nuclear Magnetic Resonance (NMR)

spectrometer was used for the measurements of ¹H-NMR and ¹³C-NMR using CDCl₃ as solvent. The X-ray intensity data were recorded on a Bruker APEX-II CCD imaging plate area detector with graphite monochromatic Mo-K α radiation ($\lambda = 0.71073 \text{ \AA}$).

Synthesis of Thiosemicarbazones

The thiosemicarbazones were obtained for the first time with very minor modifications from known procedures (18, 30). The synthesis method was explained as follows by the 2-hydroxy-4-methoxybenzylidene-S-allylthiosemicarbazone (**L¹**) as representative

example. 0.5 gram (5 millimoles) of thiosemicarbazide and 0.47 milliliter (5 millimoles) of allyl bromide were mixed up in 15 milliliters of ethanol at about 75 °C. The reaction formation was controlled by chromatography. After two hours, the four milliliters of alcoholic solution of 2-hydroxy-4-methoxybenzaldehyde (0.83 gram, 5 millimol) was added dropwise to colourless mix. An aqueous solution of sodium bicarbonate was added for neutralization of the hydrogen bromide form. The yellow-colored product precipitated from the reaction medium was filtered, washed first with a few drops of ethanol, and then water. The obtained product was recrystallized from ethanol after drying. Other thiosemicarbazones were obtained by using N-methylthiosemicarbazide (**L³**), N-ethylthiosemicarbazide (**L²**, **L⁴**), bromopropane (**L³**, **L⁴**) and 5-chlorosalicylaldehyde (**L²**) with the same procedure. The colors, melting points (°C), % yields, elemental analysis, UV-Vis, IR, ¹H-NMR and ¹³C-NMR data of the ligands are given below:

L¹: Yellow, m.p. 186.2-187.4 °C, yield 75 %. Anal. Calc. for C₁₂H₁₅N₃O₂S (265.33 g/mol): C, 54.32; H, 5.70; N, 15.84; S, 12.08. Found: C, 54.15; H, 5.52; N, 15.69; S, 12.23 %. UV-Vis (nm (log ε)): 240 (3.40); 295 (3.36); 305 (3.45); 338 (3.66) (Fig.S1). IR (cm⁻¹): ν(OH) 3350; ν_{as}(NH₂) 3414; ν_s(NH₂) 3302; ν(CH)_{aliphatic} 2960, 2834; ν(C-O) 1160; ν(C-N) 993; ν(C-S) 836; ν(C=N¹) 1627; ν(C=N²) 1602 (Fig.S5). ¹H-NMR (ppm): 11.75, 11.59 (s, i:1/1, 1H, -OH); 8.37, 8.23 (s, i:2/1, 1H, CH=N¹); 7.13 (m, 1H, d); 6.47 (m, 2H, a, c); 5.08 (s, 2H, N⁴H₂); 3.79 (s, 3H, -OCH₃); 3.71, 3.60 (d, 2H, S-C¹H₂-); 5.98 (m, 1H, -C²H=); 5.29, 5.15 (d, 2H, =C³H₂) (Fig.S13). ¹³C-NMR (ppm): 165.35 (=CN-S); 163.40 (-CH=N), 160.76, 158.05, 135.35, 114.66, 109.46, 103.75 (aromatics); 58.20 (-OCH₃); 36.01 (S-CH₂-); 136.21 (-CH=); 120.95 (=CH₂) (Fig.S21).

L²: Yellow, m.p. 101.2-102.4 °C, yield 62 %. Anal. Calc. for C₁₃H₁₆ClN₃OS (297.80 g/mol): C, 52.43; H, 5.42; N, 14.11; S, 10.77. Found: C, 52.25; H, 5.52; N, 14.26; S, 10.63 %. UV-Vis (nm (log ε)): 240 (3.83); 294 (3.80); 305 (3.89); 336 (4.10) (Fig.S2). IR (cm⁻¹): ν(OH) 3407; ν(NH) 3394; ν(CH)_{aliphatic} 2970, 2885; ν(C-O) 1186; ν(C-N) 935; ν(C-S) 861; ν(C=N¹) 1629; ν(C=N²) 1600 (Fig.S7). ¹H-NMR (ppm): 11.77, 11.41 (s, i:3/1, 1H, -OH); 8.31, 8.29 (s, i:1/3, 1H, CH=N¹); 7.17 (m, 2H, b, d); 6.90 (m, 2H, a); 5.45, 4.67 (t, i:1/2, 1H, N⁴H); 3.42, 3.32 (m, i:3/1, 2H, N⁴-CH₂); 1.21 (t, 3H, -CH₃); 3.76, 3.54 (d, 2H, S-C¹H₂-); 5.95 (m, 1H, -

C²H=); 5.36, 5.27 (d, 2H, =C³H₂) (Fig.S15). ¹³C-NMR (ppm): 164.26 (=CN-S); 159.87 (-CH=N), 156.04, 132.91, 132.95, 126.24, 122.74, 121.56 (aromatics); 36.41 (S-CH₂-); 136.75 (-CH=); 120.57 (=CH₂); 41.26 (N-CH₂-); 17.04 (-CH₃) (Fig.S23).

L³: Yellow, m.p. 185.5-186.2 °C, yield 87 %. Anal. Calc. for C₁₃H₁₉N₃O₂S (281.37 g/mol): C, 55.49; H, 6.81; N, 14.93; S, 11.40. Found: C, 55.25; H, 6.72; N, 14.79; S, 11.23 %. UV-Vis (nm (log ε)): 240 (4.03); 294 (4.02); 305 (5.08); 337 (4.33) (Fig.S3). IR (cm⁻¹): ν(OH) 3310; ν(NH) 3396; ν(CH)_{aliphatic} 2961, 2842; ν(C-O) 1163; ν(C-N) 974; ν(C-S) 859; ν(C=N¹) 1627; ν(C=N²) 1599 (Fig.S9). ¹H-NMR (ppm): 12.12, 11.64 (s, i:3/1, 1H, -OH); 8.33, 8.31 (s, i:2/1, 1H, CH=N¹); 7.11 (m, 1H, d); 6.45 (m, 2H, a, c); 5.43, 4.47 (q, i:1/2, 1H, N⁴H); 3.78 (s, 3H, -OCH₃); 2.99, 2.93 (d, i:3/1, 3H, N⁴-CH₃); 3.04, 2.79 (t, 2H, S-C¹H₂-); 1.70 (m, 2H, -C²H₂); 1.01 (t, 3H, -C³H₃) (Fig.S17). ¹³C-NMR (ppm): 164.65 (=CN-S); 163.29 (-CH=N), 158.96, 157.51, 134.48, 115.22, 108.92, 103.86 (aromatics); 58.04 (-OCH₃); 33.26 (S-CH₂-); 25.39 (-CH₂-); 16.18 (-CH₃); 35.08 (N-CH₃) (Fig.S25).

L⁴: Yellow, m.p. 174.8-175.4 °C, yield 79 %. Anal. Calc. for C₁₄H₂₁N₃O₂S (295.40 g/mol): C, 56.92; H, 7.17; N, 14.22; S, 10.85. Found: C, 56.85; H, 7.32; N, 14.16; S, 10.53 %. UV-Vis (nm (log ε)): 243 (4.16); 296 (4.23); 308 (4.25); 345 (4.27) (Fig.S4). IR (cm⁻¹): ν(OH) 3457; ν(NH) 32390; ν(CH)_{aliphatic} 2932, 2838; ν(C-O) 1187; ν(C-N) 959; ν(C-S) 854; ν(C=N¹) 1627; ν(C=N²) 1603 (Fig.S11). ¹H-NMR (ppm): 12.12, 11.69 (s, i:2/1, 1H, -OH); 8.33, 8.32 (s, i:1/2, 1H, CH=N¹); 7.12 (m, 1H, d); 6.46 (m, 2H, a, c); 5.40, 4.25 (t, i:1/2, 1H, N⁴H); 3.80 (s, 3H, -OCH₃); 3.45, 3.32 (m, i:2/1, 2H, N⁴-CH₂); 1.25, 1.21 (t, i:2/1, 3H, -CH₃); 3.05, 2.81 (t, 2H, S-C¹H₂-); 1.72 (m, 2H, -C²H₂); 1.03 (t, 3H, -C³H₃) (Fig.S19). ¹³C-NMR (ppm): 164.59 (=CN-S); 163.28 (-CH=N), 158.86, 157.39, 134.47, 115.22, 108.98, 103.94 (aromatics); 58.04 (-OCH₃); 35.18 (S-CH₂-); 25.51 (-CH₂-); 16.10 (-CH₃); 41.12 (N-CH₂-); 17.30 (-CH₃) (Fig.S27).

Synthesis of Complexes

The new complexes were prepared using literature method with small modifications (25, 26) (Figure 1). The synthesis procedure of complexes is the same as for complex **1**, which is given as an example and has the IUPAC name *cis*-dioxo-(S-allyl-N¹-2-hydroxy-4-methoxybenzylidene thiosemicarbazonato) (N,N',O)-methanol-molybdenum(VI). 0.26 gram

(1 millimole) gram of N¹-2-hydroxy-4-methoxybenzylidene thiosemicarbazone was dissolved in 3 milliliters of methanol with heating. 0.32 gram (1 millimole) of bis(acetylacetonato)dioxomolybdenum(VI) was dissolved in 2 milliliters of methanol and added dropwise to the reaction medium. The mixture was blended at about 45 °C for one and a half hours. The red product was filtered and washed with a few drops of methanol. The product was recrystallized in methanol and obtained pure for use in characterization. The colors, melting points (°C), % yields, elemental analysis, UV-Vis, IR, ¹H-NMR and ¹³C-NMR data of the complexes are given below:

1: Red, m.p. 215.8-216.4 °C, yield 47 %. Anal. Calc. for C₁₃H₁₇MoN₃O₅S (423.29 g/mol): C, 36.89; H, 4.05; N, 9.93; S, 7.58. Found: C, 36.99; H, 3.91; N, 9.77; S, 7.70 %. UV-Vis (nm (log ε)): 254 (4.35); 302 (4.35); 420 (3.84) (Fig.S1). IR (cm⁻¹): ν(OH) 3376; ν(NH) 3228; ν(CH)_{aliphatic} 2984, 2843; ν(C-O) 1187; ν(C-N) 1013; ν(C-S) 846; ν(C=N¹) 1540; ν(C=N²) 1498; ν_s, ν_{as}(MoO₂) 929, 901 (Fig.S6). ¹H-NMR (ppm): 8.73 (s, 1H, CH=N¹); 7.43 (d, 1H, d); 6.71 (dd, 1H, c); 6.65 (d, 1H, a); 6.90 (s, 1H, N⁴H); 3.86 (s, 3H, -OCH₃); 3.77 (d, 2H, S-C¹H₂-); 5.98 (m, 1H, -C²H=); 5.33, 5.20 (d, 2H, =C³H₂); 3.48 (s, 3H, O-CH₃) (Fig.S14). ¹³C-NMR (ppm): 171.35 (=CN-S); 168.90 (-CH=N), 165.44, 158.84, 135.42, 115.55, 114.42, 105.55 (aromatics); 58.52 (-OCH₃); 37.68 (S-CH₂-); 136.84 (-CH=); 121.62 (=CH₂); 56.15 (OH-CH₃) (Fig.S22).

2: Red, m.p. 115.7-116.4 °C, yield 35 %. Anal. Calc. for C₁₄H₁₈ClMoN₃O₄S (455.76 g/mol): C, 36.89; H, 3.98; N, 9.22; S, 7.04. Found: C, 36.72; H, 3.80; N, 9.37; S, 7.17 %. UV-Vis (nm (log ε)): 252 (4.34); 302 (4.34); 420 (3.84) (Fig.S2). IR (cm⁻¹): ν(OH) 3394; ν(CH)_{aliphatic} 2962, 2815; ν(C-O) 1164; ν(C-N) 1018; ν(C-S) 833; ν(C=N¹) 1597; ν(C=N²) 1566; ν_s, ν_{as}(MoO₂) 909, 882 (Fig.S8). ¹H-NMR (ppm): 8.64 (s, 1H, CH=N¹); 7.45 (m, 2H, b, d); 7.06 (m, 1H, a); 3.84 (m, 2H, N⁴-CH₂); 1.32 (t, 3H, -CH₃); 3.84 (m, 2H, S-C¹H₂-); 5.98 (m, 1H, -C²H=); 5.33, 5.20 (d, 2H, =C³H₂); 3.47 (s, 3H, O-CH₃) (Fig.S16). ¹³C-NMR (ppm): 175.24 (=CN-S); 161.37 (-CH=N), 156.26, 135.39, 133.88, 129.63, 123.28, 123.20 (aromatics); 37.51 (S-CH₂-); 137.35 (-CH=); 121.69 (=CH₂); 51.76 (N-CH₂-); 17.80 (-CH₃); 57.05 (OH-CH₃) (Fig.S24).

3: Red, m.p. 200.1-200.8 °C, yield 80 %. Anal. Calc. for C₁₄H₂₁MoN₃O₅S (439.34 g/mol): C, 38.27; H, 4.82; N, 9.56; S, 7.30. Found: C,

38.41; H, 4.91; N, 9.73; S, 7.45 %. UV-Vis (nm (log ε)): 254 (4.32); 303 (4.33); 420 (3.78) (Fig.S3). IR (cm⁻¹): ν(OH) 3325; ν(CH)_{aliphatic} 2961, 2869; ν(C-O) 1152; ν(C-N) 1022; ν(C-S) 848; ν(C=N¹) 1582; ν(C=N²) 1539; ν_s, ν_{as}(MoO₂) 930, 904 (Fig.S10). ¹H-NMR (ppm): 8.64 (s, 1H, CH=N¹); 7.37 (d, 1H, d); 6.66 (dd, 1H, c); 6.60 (d, 1H, a); 3.85 (s, 3H, -OCH₃); 3.52 (s, 3H, N⁴-CH₃); 3.11 (t, 2H, S-C¹H₂-); 1.77 (m, 2H, -C²H₂); 1.04 (t, 3H, -C³H₃); 3.48 (d, 3H, O-CH₃) (Fig.S18). ¹³C-NMR (ppm): 174.20 (=CN-S); 168.79 (-CH=N), 164.89, 157.71, 136.45, 115.48, 113.89, 105.22 (aromatics); 58.55 (-OCH₃); 36.73 (S-CH₂-); 25.19 (-CH₂-); 16.18 (-CH₃); 48.92 (N-CH₃); 53.56 (OH-CH₃) (Fig.S26).

4: Red, m.p. 150.4-151.2 °C, yield 56 %. Anal. Calc. for C₁₅H₂₃MoN₃O₅S (453.36 g/mol): C, 39.74; H, 5.11; N, 9.27 S, 7.07. Found: C, 39.59; H, 5.31; N, 8.48; S, 7.24 %. UV-Vis (nm (log ε)): 252 (4.29); 303 (4.30); 422 (3.76) (Fig.S4). IR (cm⁻¹): ν(OH) 3312; ν(CH)_{aliphatic} 2967, 2872; ν(C-O) 1175; ν(C-N) 1023; ν(C-S) 858; ν(C=N¹) 1576; ν(C=N²) 1531; ν_s, ν_{as}(MoO₂) 933, 907 (Fig.S12). ¹H-NMR (ppm): 8.64 (s, 1H, CH=N¹); 7.37 (d, 1H, d); 6.66 (dd, 1H, c); 6.62 (d, 1H, a); 3.85 (s, 3H, -OCH₃); 3.82 (q, 2H, N⁴-CH₂); 1.31 (t, 3H, -CH₃); 3.12 (t, 2H, S-C¹H₂-); 1.77 (m, 2H, -C²H₂); 1.04 (t, 3H, -C³H₃); 3.47 (d, 3H, O-CH₃) (Fig.S20). ¹³C-NMR (ppm): 173.02 (=CN-S); 168.86 (-CH=N), 164.97, 157.66, 136.40, 115.51, 113.81, 105.32 (aromatics); 58.47 (-OCH₃); 36.68 (S-CH₂-); 25.24 (-CH₂-); 16.14 (-CH₃); 53.51 (N-CH₂-); 17.57 (-CH₃); 56.66 (OH-CH₃) (Fig.S28).

X-ray Crystallography

The suitable crystals of **1** and **2** were obtained by slow evaporation of methanolic solutions. Red crystals of **1** (C₁₃H₁₇MoN₃O₅S) and **2** (C₁₄H₁₈ClMoN₃O₄S) having dimensions of 0.243×0.11×0.057 mm³ and 0.156×0.097×0.049 mm³ respectively were mounted on a glass fiber. The measurements were made on a Bruker APEX-II CCD imaging plate area detector with graphite monochromatic Mo-K α radiation (λ= 0.71073 Å). The conditions of experimental details were summed up in Table 1. The crystal structures were solved and refined with SHELXTL (31). Other atoms except hydrogen were refined anisotropically. The structures were drawn with ORTEP-III program with 50% probability displacement ellipsoids (32).

RESULTS AND DISCUSSION

Some Characteristics of the Compounds

The color of thiosemicarbazones is yellow. They can easily dissolve in common solvents like pyridine, dimethylformamide, dimethyl sulfoxide, and alcohols. The reaction of the thiosemicarbazones with bis(acetylacetonato)dioxomolybdenum(VI) in methanol gave diamagnetic $[\text{MoO}_2(\text{L})\text{CH}_3\text{OH}]$ complexes. These dioxomolybdenum(VI) complexes are dissolve in chloroform, dichloromethane, dimethyl sulfoxide and alcohols. They are stable in the air but lose their shine after a few months. They decompose and turn into black amorphous substances, when stirred for several hours at about 50-60 °C in solution.

The S-alkyl thiosemicarbazones were obtained in higher yields than dioxomolybdenum(VI) complexes. The 5-chloro derivative compounds (**L**² and **2**) were obtained with the lowest yield (62 and 35 %) and melting point (101.2 and 115.7 °C) in its group. In addition, the melting point of the complexes was higher than the corresponding ligands except **L**⁴ and **4**.

Crystallographic Studies

The crystals of **1** $[\text{MoO}_2\text{L}^1\text{CH}_3\text{OH}]$ and **2** $[\text{MoO}_2\text{L}^2\text{CH}_3\text{OH}]$ were obtained by slow evaporation of methanolic solutions. To confirm the certain structure of the dioxomolybdenum(VI) complexes, X-ray

crystallographic analysis have been carried out for **1** and **2**. The ORTEP diagrams with the atoms labeled were presented in Figures 2 and 3, while the network formation and molecular packing arrangement are given in Figures 4 and 5. The parameters of refinement and some details of crystallographic data were summed up in Table 1. The molybdenum centered bond lengths and angles were given in Table 2. Also, Table 3 shows the intermolecular H-bond interactions. Complex **1**, (0.243×0.11×0.057 mm³) crystallized in the monoclinic P2₁/c space group with Z=4, while **2** (0.156×0.097×0.049 mm³) crystallized within triclinic crystal system with P-1 space group (Z=2). The angular values of O(2)-Mo(1)-O(3) (for **1**) and O(1)-Mo-O(4) (for **2**) were 105.68 and 105.97 respectively, showing the *cis*- character of MoO_2^{2+} (33, 34). Considering the bonds and angles, it can be said that the geometric parameters of complexes are within the expected ranges when compared with similar *cis*-dioxomolybdenum centered complexes of thiosemicarbazones (18, 33). As results, the single crystal diffraction studies of dioxomolybdenum(VI) complexes revealed a distorted octahedral geometry. Accordingly, the thiosemicarbazones behaved as ONN tridentate by binding to *cis*- MoO_2^{2+} with the oxygen atom of aromatic moiety, the nitrogen atom of $\text{CH}=\text{N}^1$ and the thioamide group. Methanol molecule which reactions were carried out behaved as co-ligand and it occupied the sixth coordination site of molybdenum center (35).

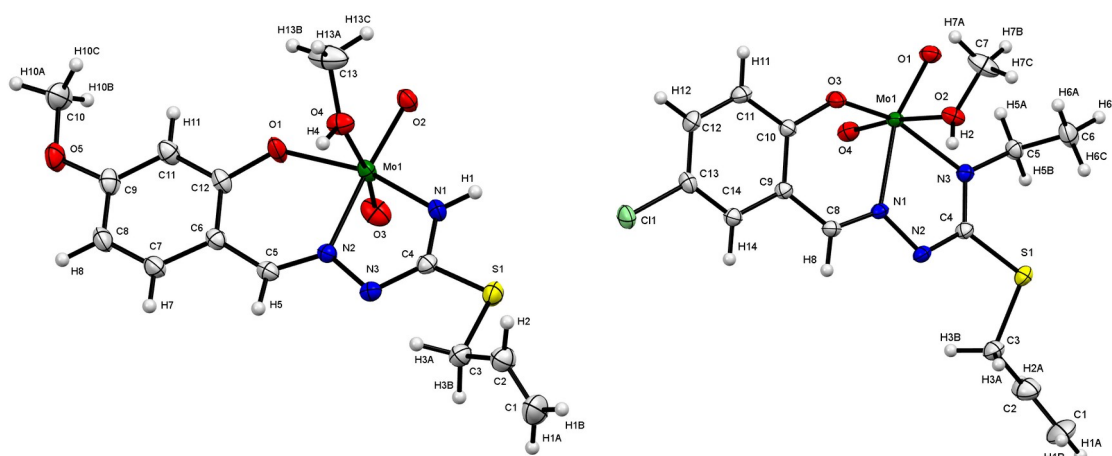


Figure 2: ORTEP view of *cis*-dioxo-(*S*-allyl- N^1 -2-hydroxy-4-methoxybenzylidene-thiosemicarbazonato) (*O,N,N'*)-methanol-molybdenum(VI) (**1**)

Figure 3: ORTEP view of *cis*-dioxo-(*S*-allyl- N^1 -2-hydroxy-5-chlorobenzylidene- N^4 -ethyl thiosemicarbazonato) (*O,N,N'*)-methanol-molybdenum(VI) (**2**)

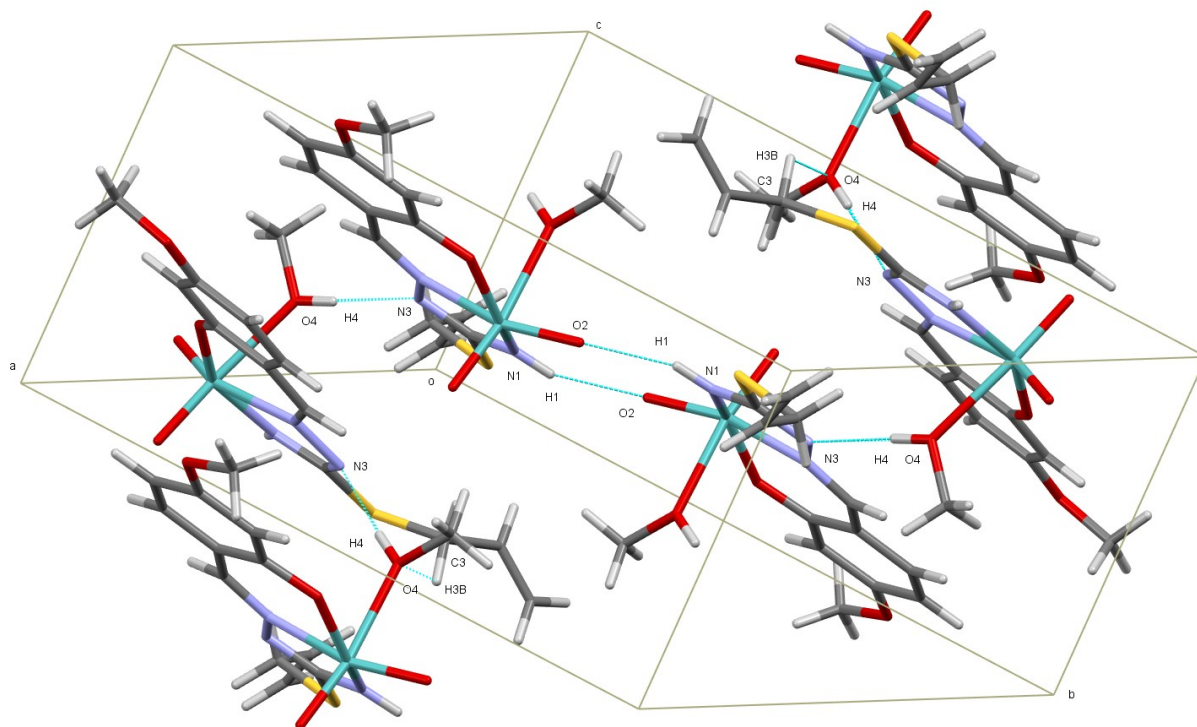


Figure 4: The packing diagram and hydrogen bonding network of complex **1**.

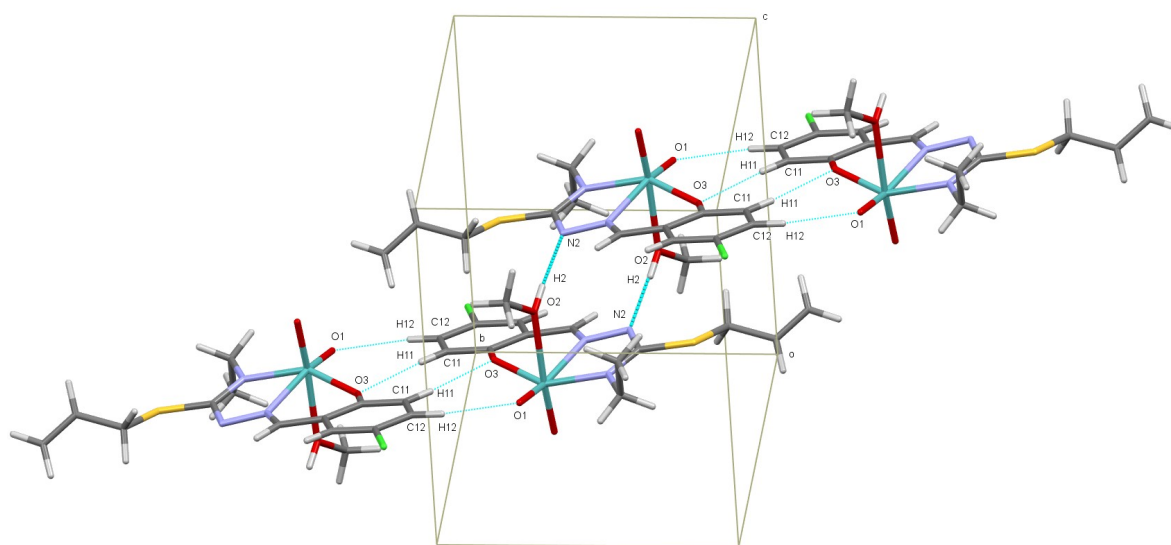


Figure 5: The packing diagram and hydrogen bonding network of complex **2**.

Table 1: The structure refinements and crystal data for **1** and **2**.

Parameters	1	2
CCDC deposition no.	2104647	2104646
Chemical formula	C ₁₃ H ₁₇ MoN ₃ O ₅ S	C ₁₄ H ₁₈ ClMoN ₃ O ₄ S
Formula weight (g.mol ⁻¹)	423.29	455.76
Temperature (K)	173.01	173.01
Wavelength (Å)	0.71073	0.71073
Crystal system	monoclinic	triclinic
Space group	P2 ₁ /c	P-1
Unit cell parameters		
a, b, c (Å)	13.577(6), 17.124(8), 7.528(3)	8.7870(7), 10.7115(9), 10.8189(9)
α, β, γ(°)	90.000, 101.738(6), 90.000	100.1090(10), 105.6400(10), 108.7600(10)
Volume (Å ³)	1713.6(13)	889.27(13)
Z	4	2
D _{calc} (g.cm ⁻³)	1.641	1.702
Absorption correction	multi-scan	multi-scan
F(000)	856.0	460.0
Crystal size (mm ³)	0.243 × 0.111 × 0.057	0.156 × 0.097 × 0.049
Diffractometer/measurement method		
Index ranges h,k,l	-17 ≤ h ≤ 17, -22 ≤ k ≤ 22, -9 ≤ l ≤ 9	-11 ≤ h ≤ 11, -13 ≤ k ≤ 13, -14 ≤ l ≤ 14
2θ Range for data collection (°)	3.064 < 2θ < 54.966	4.082 < 2θ < 54.95
Reflections collected	23095	13504
Independent reflections	3916 [R _{int} = 0.0452, R _{sigma} = 0.0311]	4072 [R _{int} = 0.0269, R _{sigma} = 0.0277]
Refinement method	Full-matrix least-squares	Full-matrix least-squares on F ²

Parameters	1	2
	on F ²	
Data/restraints/parameters	3916/0/211	4072/3/230
Goodness-of-fit on F ²	1.042	1.037
Final R indexes [I>=2σ (I)]	R ₁ = 0.0256, wR ₂ = 0.0581	R ₁ = 0.0232, wR ₂ = 0.0521
R indices (all data)	R ₁ = 0.0342, wR ₂ = 0.0617	R ₁ = 0.0282, wR ₂ = 0.0541

Table 2: The molybdenum centered bond lengths (Å) and angles (°) for complex **1** and **2**.

Complex	Atoms	Distances	Atoms	Angles
1	Mo(1)-N(1)	2.0230(19)	O(4)-Mo(1)-N(1)	81.85(7)
	Mo(1)-N(2)	2.229(2)	O(2)-Mo(1)-N(1)	93.63(8)
	Mo(1)-O(1)	1.9373(17)	O(3)-Mo(1)-N(1)	100.48(9)
	Mo(1)-O(4)	2.3513(17)	O(2)-Mo(1)-O(4)	83.61(7)
	Mo(1)-O(2)	1.7110(16)	O(3)-Mo(1)-O(4)	171.13(7)
	Mo(1)-O(3)	1.6954(18)	O(2)-Mo(1)-O(3)	105.68(8)
2	Mo(1)-N(3)	2.0695(16)	O(2)-Mo(1)-N(3)	79.64(6)
	Mo(1)-N(1)	2.2422(16)	O(1)-Mo(1)-N(3)	95.43(6)
	Mo(1)-O(3)	1.9476(13)	O(4)-Mo(1)-N(3)	99.84(7)
	Mo(1)-O(2)	2.3515(14)	O(2)-Mo(1)-O(1)	82.92(6)
	Mo(1)-O(1)	1.7076(14)	O(4)-Mo(1)-O(2)	171.09(6)
	Mo(1)-O(4)	1.6948(15)	O(1)-Mo(1)-O(4)	105.96(7)

Table 3: Intermolecular interaction parameters (\AA and $^\circ$) of complex **1** and **2**.

Complex	D—H...A	D—H	H...A	D...A	D—H...A
1	N1-H1...O2	0.88	2.158	3.003(3)	160.8
	O4-H4...N3	0.84	1.957	2.796(3)	176.7
	C3-H3B...O4	0.99	2.713	3.221(3)	112.32
2	C12-H12...O1	0.950	2.705	3.336(3)	124.6
	C11-H11...O3	0.950	2.694	3.639(3)	172.8
	O2-H2...N2	0.86(2)	1.85(2)	2.707(3)	176(2)

UV-Vis Spectra

In order to follow the formation of the complex and to determine at which wavelengths the electronic transitions are, the UV-Vis absorption bands of the compounds were recorded in chloroform solution (3×10^{-5} M) between 200 and 800 nm. In the spectra of the **L¹-L⁴** the bands recorded at 240-243 nm belong to $n \rightarrow \pi^*$ transitions of 4-methoxy and 5-chloro substituted aromatic rings (33, 35). The bands at about 295, 305 (as shoulders) and 336-345 (broad) nm can attributed as $n \rightarrow \pi^*$ transitions originating from the non-bonding electrons of thioamide and imine nitrogen atoms. In the spectra of **1-4**, the absorption bands seen at 252-254 nm and 302-303 nm were related to the transitions of $n \rightarrow \pi^*$ and $n \rightarrow \pi^*$. The ligand-metal charge transfer transitions of the **1-4** were seen in range of 420-422 nm. The forbidden transitions were not observed in the spectra of complexes since they have $4d^0$ configuration (12, 27). The UV-Vis spectra of all compounds were given in the supplementary file (Figure S1-S4).

IR Spectra

In the IR spectra of **L¹-L⁴**, the bands belonging to $\nu(\text{OH})$ were recorded at $3457\text{-}3310\text{ cm}^{-1}$. This band disappeared after complexation. Instead, bands belonging to the hydroxy group originating from methanol, which is coordinated to the metal center, were also observed at $3394\text{-}3276\text{ cm}^{-1}$. These values are lower than the $\nu(\text{OH})$ frequency value of non-coordinated of methanol molecule; 3682 cm^{-1} (36). This indicates that the methanol is coordinated. In the spectrum of **L¹**, the asymmetric and symmetric $\nu(\text{NH}_2)$ vibration bands were recorded at 3414 and 3310 cm^{-1} respectively. The fact that this band was observed as a single band at 3228 cm^{-1} in the spectrum of **1** supports deprotonation of the ligand. Also, the $\nu(\text{NH})$ vibration of other ligands (**L²-L⁴**), recorded at $3396\text{-}3228\text{ cm}^{-1}$, were disappeared by complexation. The band belonging to the $\text{C}=\text{N}^2$ group was recorded between $1602\text{-}1599\text{ cm}^{-1}$ in the spectra of thiosemicarbazones. After complexation, these bands shifted to lower

frequencies as $1566\text{-}1498\text{ cm}^{-1}$. These situations support the ONN coordination formed by the removal of a hydrogen atom from the thioamide group. In addition, for all molybdenum complexes (**1-4**), the ν_{as} and ν_{s} bands of cis-MoO_2^{2+} were recorded between $933\text{-}909$ and $907\text{-}882\text{ cm}^{-1}$ (12, 18). The IR spectra of all compounds were given in the supplementary file (Figure S5-S12).

¹H-NMR Spectra

In the ¹H-NMR spectra of **L¹-L⁴**, the expected isomeric peaks of phenolic hydrogen, azomethine ($\text{CH}=\text{N}^1$), N^4H and also N/S-alkyl protons were recorded with different isomeric ratios. The signals of phenolic hydrogen belonging to the 2-OH aldehyde appeared as two singlets between $12.12\text{-}11.41$ ppm due to cis-trans isomerism. The absence of this peak in the spectra of **1-4** clearly proves the bonding of oxygen atom of aromatic moiety to the metal center. The syn-anti isomerism of the azomethine group, seen between $8.37\text{-}8.29$ ppm, was not observed in the spectra of complexes (18). Besides, the shifting of these peaks to higher field indicates the coordination through azomethine group (35). In the spectrum of **L¹** the band of the N^4H_2 was recorded in two proton integral at 5.08 ppm. When its corresponding complex **1** spectrum was examined, it was observed that this peak shifted to a lower area at 6.90 ppm, and was in a single proton integral. In the other complexes **2-4** spectra, there were no proton signals of N^4H group. This situation supports that the thiosemicarbazones coordinate to the molybdenum center with amide nitrogen. When the spectra of all complexes (**1-4**) were examined, the $-\text{CH}_3$ group protons of the methanol, coordinated as second ligand, were observed in the range of $3.48\text{-}3.47$ ppm as singlets or doublets. The reason why the signal of the $-\text{OH}$ group of methanol is not seen can be considered as the proton becoming more acidic due to intermolecular interactions (12, 33). The ¹H-NMR spectra of all compounds were given in the supplementary file (Figures S13-S20).

¹³C-NMR Spectra

In the ¹³C-NMR spectra of **L¹-L⁴**, the signal of the =CN-S was observed in the lowest field between 164.26-165.35 ppm (37). When the spectra of complexes (**1-4**) were examined, it was observed that this signal shifted to about 10 ppm lower area. Also, the signals showed by azomethine nitrogen (-CH=N) for thiosemicarbazone ligands were recorded at the range 159.87-163.40 ppm. A slight lowfield shift in the azomethine resonance signal observed in complexes is due to the coordination of nitrogen atom. In addition, the carbon signals belonging to the N-alkyl group (N-CH₃ and N-CH₂-) were also shifted to the lower area due to the coordination of the thioamide nitrogen to the metal center. In all compounds except **L²** and **2**, the signals belonging to the methoxy group was observed at approximately 58 ppm (38). No significant change was observed with the complexation in the signals belonging to the methoxy and S-alkyl groups. The peaks appearing at 53.56-57.05 ppm in the complex spectra belong to the methanol molecule coordinated as second ligand to the dioxomolybdenum(VI) center. The ¹³C-NMR spectra of all compounds were given in the supplementary file (Figures S21-S28).

CONCLUSION

In this study, four dioxomolybdenum(VI) complexes were prepared with new thiosemicarbazone ligands having different substituents on the aromatic ring, the amide nitrogen and sulfur atoms to be used as models in future biological studies. The structural characterizations of all compounds were carried out by using elemental analysis, UV-Vis, IR, ¹H-NMR and ¹³C-NMR spectroscopies. The formation of dioxomolybdenum(VI) complexes was observed with the band recorded around 420 nm in the UV-Vis spectra, and the characteristic symmetric and asymmetric stretch bands recorded between 933-909 and 907-882 cm⁻¹ belonging to the MoO₂²⁺ group in the IR spectra. When the ¹H-NMR spectra are examined, the disappearance of the signals belonging to the protons of the phenolic oxygen and thioamide nitrogen supports the coordination from these atoms to the metal center. In addition, when both the ¹H-NMR and ¹³C-NMR spectra of the complexes were examined, the peaks of the methanol molecule were clearly observed. The crystal structure of two complexes (**1**, **2**) were confirmed by X-ray diffraction method. Crystal analysis of complexes indicated a distorted octahedral geometry. Comparison with complexes and

previous reported similar molecules revealed that the bonds and angles of complexes are within the expected ranges. The crystallographic and spectroscopic data of the compounds clearly demonstrated the formation of ONN coordinated dioxomolybdenum(VI) complexes and binding to the metal center of the methanol molecule as second ligand.

ACKNOWLEDGMENTS

CCDC-2104647 for **1** (C₁₃H₁₇MoN₃O₅S) and CCDC-2104646 for **2** (C₁₄H₁₈ClMoN₃O₄S) contain the supplementary crystallographic data for this study. These data can be obtained free of charge from The Cambridge Crystallographic Data Centre via www.ccdc.cam.ac.uk/data_request/cif

REFERENCES

1. Leovac V, Gerbeleu N, Canic V. Coordination compounds of cobalt (III), chromium (III), and vanadium (III) with salicylaldehyde S-methylthiosemicarbazone. Russ J Inorg Chem. 1982;27:514-7.
2. Nehar OK, Mahboub R, Louhibi S, Roisnel T, Aissaoui M. New thiosemicarbazone Schiff base ligands: Synthesis, characterization, catecholase study and hemolytic activity. Journal of Molecular Structure. 2020 Mar;1204:127566. <DOI>.
3. Behnisch R, Mietzsch F, Schmidt H. Chemical Studies on Thiosemicarbazones with Particular Reference to Antituberculous Activity. American review of tuberculosis. 1950;61(1):1-7.
4. Plech T, Wujec M, Siwek A, Kosikowska U, Malm A. Synthesis and antimicrobial activity of thiosemicarbazides, s-triazoles and their Mannich bases bearing 3-chlorophenyl moiety. European Journal of Medicinal Chemistry. 2011 Jan;46(1):241-8. <DOI>.
5. Kesel AJ. Broad-spectrum antiviral activity including human immunodeficiency and hepatitis C viruses mediated by a novel retinoid thiosemicarbazone derivative. European Journal of Medicinal Chemistry. 2011 May;46(5):1656-64. <DOI>.
6. Li MX, Chen CL, Zhang D, Niu JY, Ji BS. Mn(II), Co(II) and Zn(II) complexes with heterocyclic substituted thiosemicarbazones: Synthesis, characterization, X-ray crystal structures and antitumor comparison. European

- Journal of Medicinal Chemistry. 2010 Jul;45(7):3169–77. <DOI>.
7. Rodríguez-Argüelles MC, López-Silva EC, Sanmartín J, Pelagatti P, Zani F. Copper complexes of imidazole-2-, pyrrole-2- and indol-3-carbaldehyde thiosemicarbazones: Inhibitory activity against fungi and bacteria. *Journal of Inorganic Biochemistry*. 2005 Nov;99(11):2231–9. <DOI>.
8. Saswati, Dinda R, Schmiesing CS, Sinn E, Patil YP, Nethaji M, et al. Mixed-ligand nickel(II) thiosemicarbazone complexes: Synthesis, characterization and biological evaluation. *Polyhedron*. 2013 Feb;50(1):354–63. <DOI>.
9. Viñuelas-Zahínos E, Luna-Giles F, Torres-García P, Fernández-Calderón MC. Co(III), Ni(II), Zn(II) and Cd(II) complexes with 2-acetyl-2-thiazoline thiosemicarbazone: Synthesis, characterization, X-ray structures and antibacterial activity. *European Journal of Medicinal Chemistry*. 2011 Jan;46(1):150–9. <DOI>.
10. Chen J, Huang Y, Liu G, Afrasiabi Z, Sinn E, Padhye S, et al. The cytotoxicity and mechanisms of 1,2-naphthoquinone thiosemicarbazone and its metal derivatives against MCF-7 human breast cancer cells. *Toxicology and Applied Pharmacology*. 2004 May;197(1):40–8. <DOI>.
11. Afrasiabi Z. Transition metal complexes of phenanthrenequinone thiosemicarbazone as potential anticancer agents: synthesis, structure, spectroscopy, electrochemistry and in vitro anticancer activity against human breast cancer cell-line, T47D. *Journal of Inorganic Biochemistry*. 2003 Jul 1;95(4):306–14. <DOI>.
12. Eğlence-Bakır S, Sacan O, Şahin M, Yanardag R, Ülküseven B. Dioxomolybdenum(VI) complexes with 3-methoxy salicylidene-N-alkyl substituted thiosemicarbazones. Synthesis, characterization, enzyme inhibition and antioxidant activity. *Journal of Molecular Structure*. 2019 Oct;1194:35–41. <DOI>.
13. Eğlence-Bakır S. New nickel(II) complexes containing N2O2 donor thiosemicarbazones: Synthesis, characterization and antioxidant properties. *Journal of Molecular Structure*. 2021 Dec;1246:131121. <DOI>.
14. Bakkar MS, Siddiqi MY, Monshi MS. Preparation and Investigation of the Bonding Mode in the Complexes of Pt(II) with Thiosemicarbazone Ligands. *Synthesis and Reactivity in Inorganic and Metal-Organic Chemistry*. 2003 Jan 8;33(7):1157–69. <DOI>.
15. Ren P, Liu T, Qin J, Chen C. Synthesis, Crystal Structure, Spectroscopy and Calculated First-Order Molecular Hyperpolarizability of a New Square-pyramidal Complex Zn(DMABT)(acac) 2. *Journal of Coordination Chemistry*. 2003 Jan 1;56(2):125–32. <DOI>.
16. Sankaraperumal A, Karthikeyan J, Shetty AN, Lakshmisundaram R. Nickel(II) complex of p-[N,N-bis(2-chloroethyl)amino]benzaldehyde-4-methyl thiosemicarbazone: Synthesis, structural characterization and biological application. *Polyhedron*. 2013 Feb;50(1):264–9. <DOI>.
17. Małeckı JG, Maroń A, Serda M, Polański J. Ruthenium(II) carbonyl complexes with thiosemicarbazone ligands. *Polyhedron*. 2013 Jun;56:44–54. <DOI>.
18. Eğlence S, Şahin M, Özyürek M, Apak R, Ülküseven B. Dioxomolybdenum(VI) complexes of S-methyl-5-bromosalicylidene-N-alkyl substituted thiosemicarbazones: Synthesis, catalase inhibition and antioxidant activities. *Inorganica Chimica Acta*. 2018 Jan;469:495–502. <DOI>.
19. Güveli Ş. Nickel(II)-PPh₃ 3 complexes of substituted benzophenone thiosemicarbazones: Electrochemistry, structural analysis, and antioxidant properties. *Journal of Coordination Chemistry*. 2020 Jan 2;73(1):137–53. <DOI>.
20. Takjoo R, Hashemzadeh A, Rudbari HA, Nicolò F. Copper(II) and molybdenum(VI) complexes with 5-bromosalicylaldehyde S-allylthiosemicarbazone: Syntheses, characterizations and crystal structures. *Journal of Coordination Chemistry*. 2013 Jan 1;66(2):345–57. <DOI>.
21. Yampolskaya M, Shova S, Gerbeleu N, Belskii V, Simonov YA. Synthesis And Structure Of [S-Methyl-N1, N4-Bis (Salicylidene) Thiosemicarbazide] Ferrocene (III). *Zhurnal Neorganicheskoi Khimii*. 1982;27(10):2551–7.
22. Şahin M, Eğlence-Bakır S, Alpay M, Alpay S, Özmerdivenli R, Ülküseven B. Effective copper(II) and nickel(II) complexes with N3O and ON3 thiosemicarbazidato ligands.

Synthesis, structural analysis and in vitro cytotoxicity on melanoma B16F10 cells. *Inorganica Chimica Acta*. 2020 Mar;502:119347. <DOI>.

23. Hille R. The Mononuclear Molybdenum Enzymes. *Chem Rev*. 1996 Jan 1;96(7):2757-816. <DOI>.

24. Hussein MA, Guan TS, Haque RA, Ahamed MBK, Majid AMSA. Synthesis and characterization of thiosemicarbazonato molybdenum(VI) complexes: In vitro DNA binding, cleavage, and antitumor activities. *Polyhedron*. 2015 Jan;85:93-103. <DOI>.

25. Duman S, Kızılcıklı İ, Koca A, Akkurt M, Ülküseven B. ONN-complexes of dioxomolybdenum(VI) with 2-hydroxy-1-naphthaldehyde S-ethyl-4-H/phenyl-thiosemicarbazones: Crystal structure, electrochemistry and in situ spectroelectrochemistry. *Polyhedron*. 2010 Oct;29(15):2924-32. <DOI>.

26. Duman S, Kizilcikli İ, Ülküseven B. Dioxomolybdenum(VI) Complexes of 5-Bromo/3,5-Dibromo-Salicylaldehyde 4-(H/C 6 H 5)- S -Propyl-Thiosemicarbazones. Phosphorus, Sulfur, and Silicon and the Related Elements. 2015 Mar 4;190(3):342-51. <DOI>.

27. Moradi-Shoaili Z, Boghaei DM, Amini M, Bagherzadeh M, Notash B. New molybdenum(VI) complex with ONS-donor thiosemicarbazone ligand: Preparation, structural characterization, and catalytic applications in olefin epoxidation. *Inorganic Chemistry Communications*. 2013 Jan;27:26-30. <DOI>.

28. Vrdoljak V, Đilović I, Cindrić M, Matković-Čalogović D, Strukan N, Gojmerac-Ivšić A, et al. Synthesis, structure and properties of eight novel molybdenum(VI) complexes of the types: [MoO₂LD] and [MoO₂L₂] (L=thiosemicarbazonato ligand, D=N-donor molecule). *Polyhedron*. 2009 Apr;28(5):959-65. <DOI>.

29. Takjoo R, Akbari A, Ahmadi M, Amiri Rudbari H, Bruno G. Synthesis, spectroscopy, DFT and crystal structure investigations of 3-methoxy-2-hydroxybenzaldehyde S-ethylisothiosemicarbazone and its Ni(II) and Mo(VI) complexes. *Polyhedron*. 2013 May;55:225-32. <DOI>.

30. Yamazaki C. The structure of isothiosemicarbazones. *Canadian Journal of Chemistry*. 1975;53(4):610-5.

31. Anonymous. SHELXTL, version 6.14. Bruker AXS Inc., Madison, WI; 2000.

32. Farrugia LJ. ORTEP -3 for Windows - a version of ORTEP -III with a Graphical User Interface (GUI). *J Appl Crystallogr*. 1997 Oct 1;30(5):565-565. <DOI>.

33. Eğlence-Bakır S, Şahin M, Zahoor M, Dilmen-Portakal E, Ülküseven B. Synthesis and biological potentials of dioxomolybdenum(VI) complexes with ONS and ONN chelating thiosemicarbazones: DNA-binding, antioxidant and enzyme inhibition studies. *Polyhedron*. 2020 Nov;190:114754. <DOI>.

34. Kaya Y, Erçağ A, Kaya K. Synthesis, characterization and antioxidant activities of dioxomolybdenum(VI) complexes of new Schiff bases derived from substituted benzophenones. *Journal of Coordination Chemistry*. 2018 Oct 18;71(20):3364-80. <DOI>.

35. Çelen Ş, Eğlence-Bakır S, Şahin M, Deniz I, Celik H, Kizilcikli I. Synthesis and characterization of new thiosemicarbazonato molybdenum(VI) complexes and their in vitro antimicrobial activities. *Journal of Coordination Chemistry*. 2019 May 19;72(10):1747-58. <DOI>.

36. Plyler EK. Infrared spectra of methanol, ethanol, and n-propanol. *J Res Natl Bur Stand*. 1952;48(4):281-6.

37. Vrdoljak V, Cindrić M, Milić D, Matković-Čalogović D, Novak P, Kamenar B. Synthesis of five new molybdenum(VI) thiosemicarbazonato complexes. Crystal structures of salicylaldehyde and 3-methoxy-salicylaldehyde 4-methylthiosemicarbazones and their molybdenum(VI) complexes. *Polyhedron*. 2005 Sep;24(13):1717-26. <DOI>.

38. Novak P, Pičuljan K, Hrenar T, Smrečki V. Structure and Hydrogen Bonding Interactions in Methoxysalicylaldehyde Thiosemicarbazone Derivatives in Solution by NMR and DFT Methods. *Croatica Chemica Acta*. 2009;82(2):477-83.

Dioxomolybdenum(VI) Complexes of ONN-Chelating Thiosemicarbazones: Crystallographic and Spectroscopic (UV, IR, and NMR) Studies

Songül Eğlence-Bakır^{a*}

^aDepartment of Chemistry, Faculty of Science, Istanbul University, 34134, Istanbul, Turkey

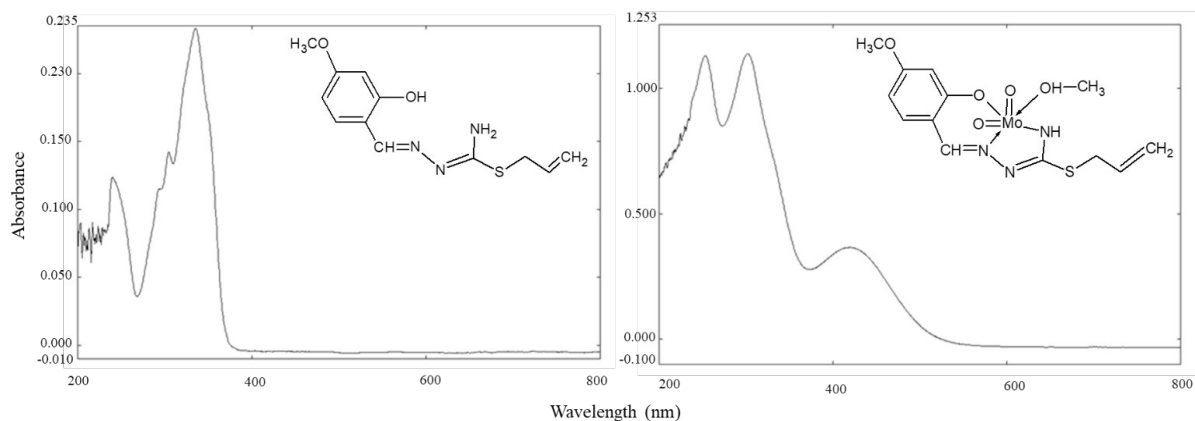


Figure S1: UV spectra of **L¹** and **1**

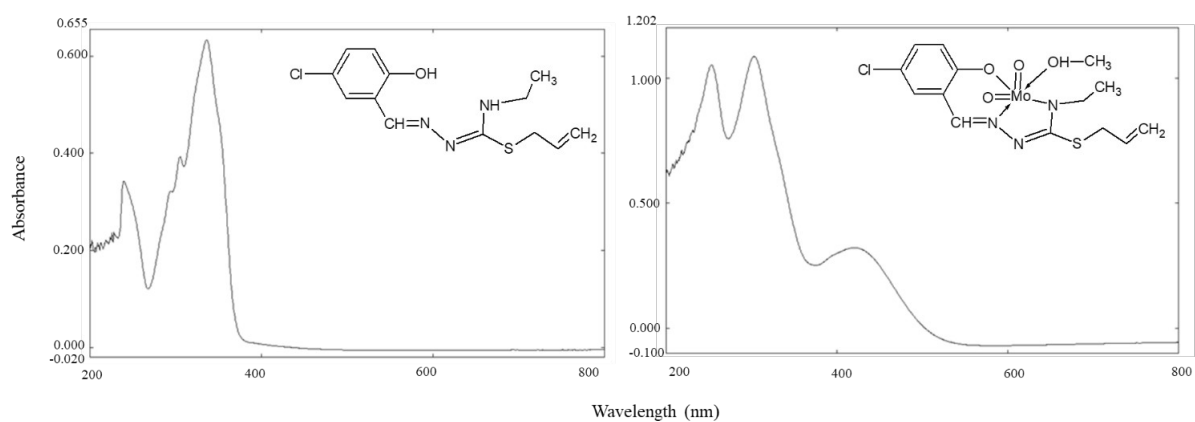
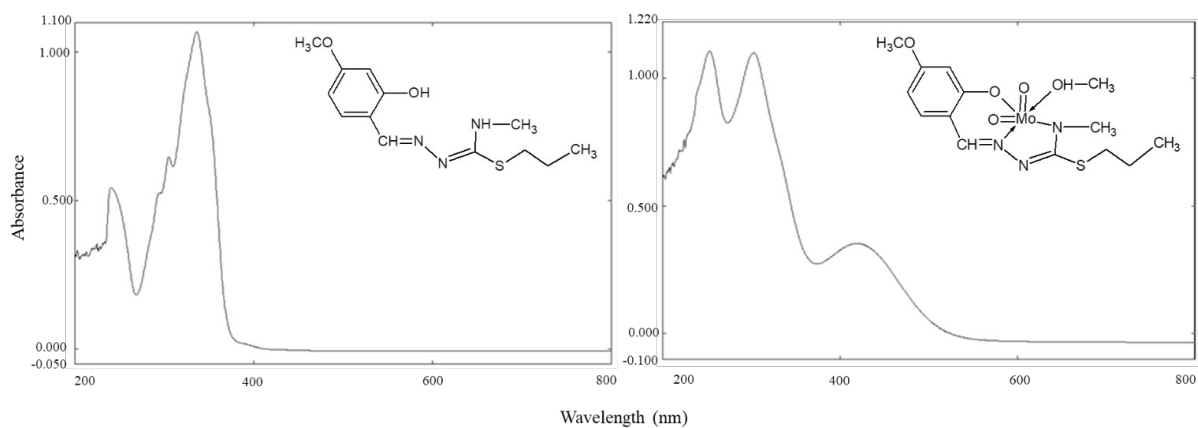
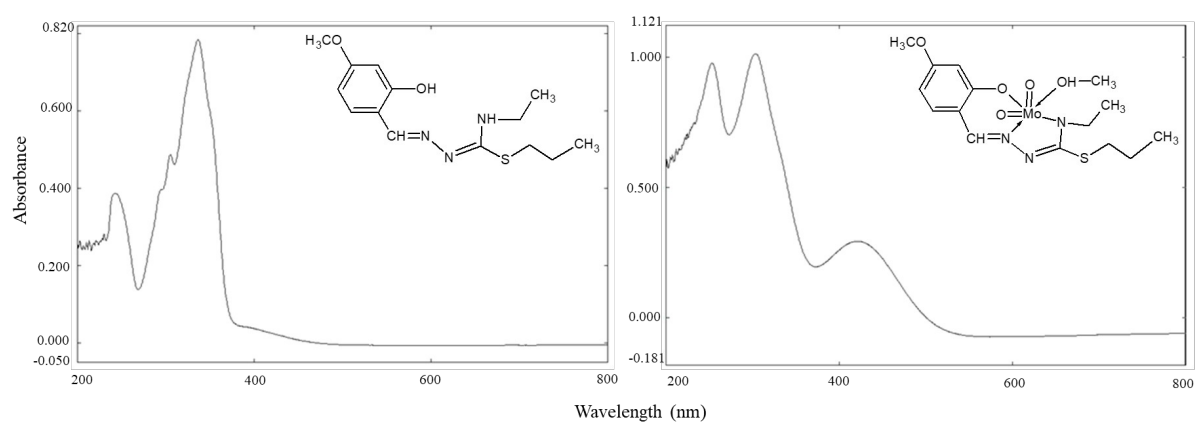
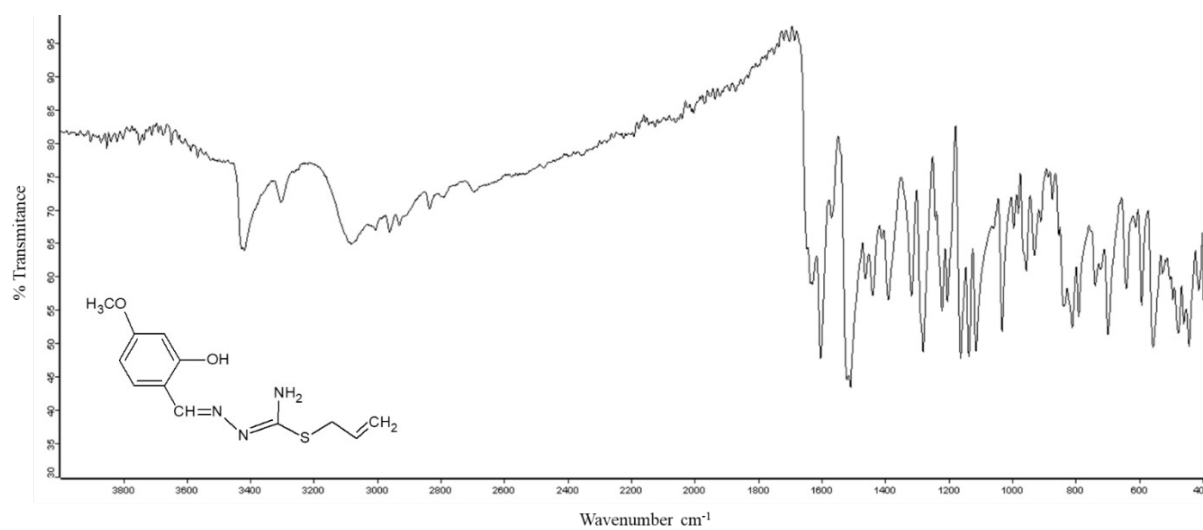
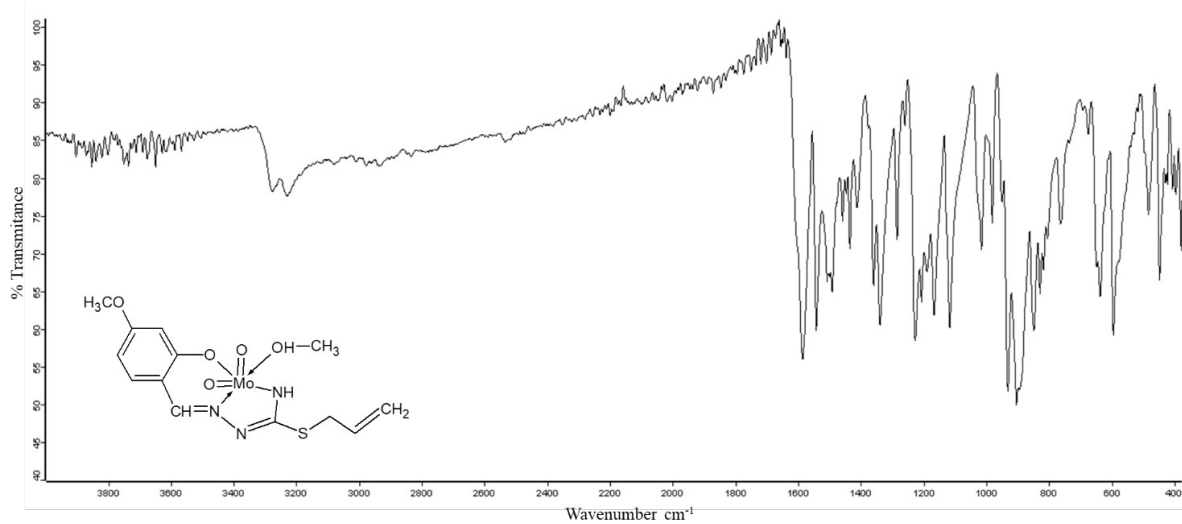
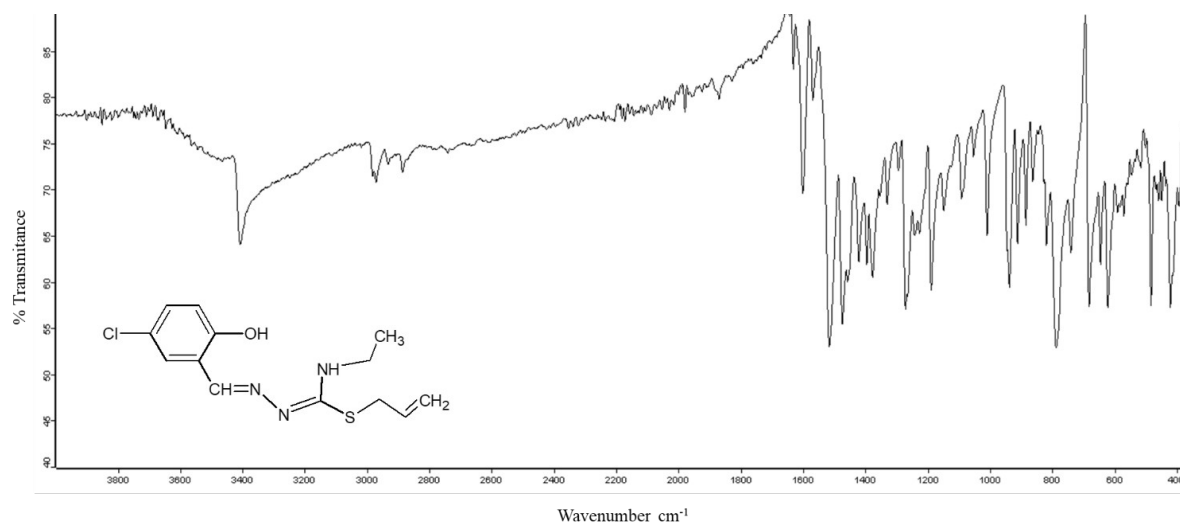
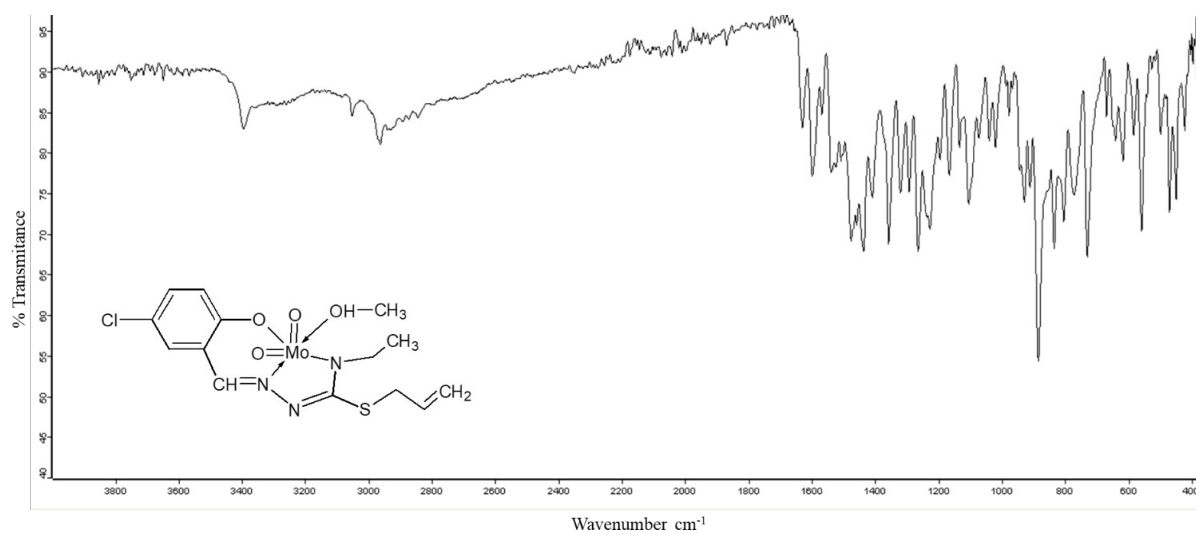
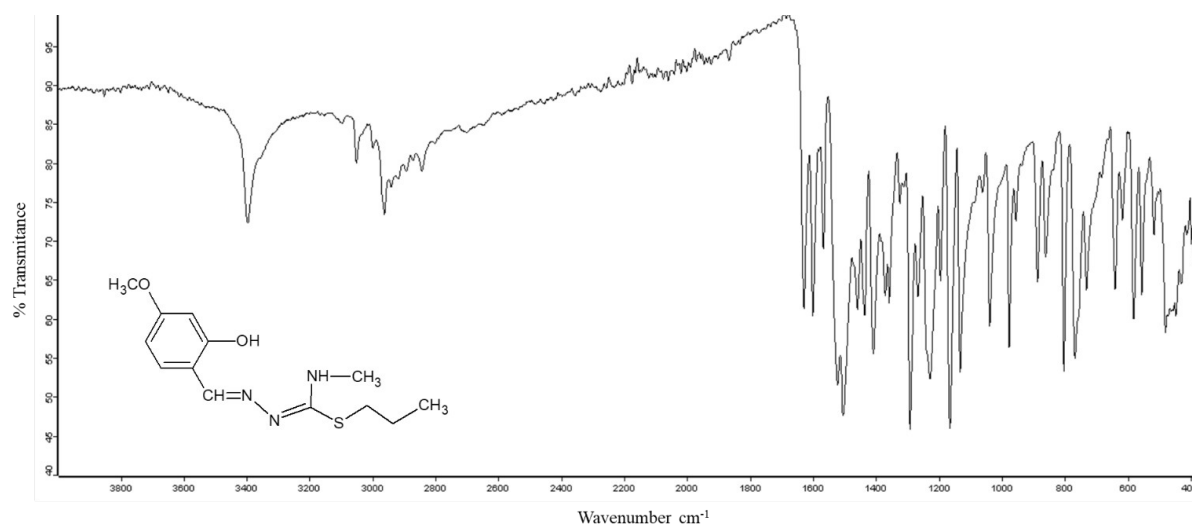
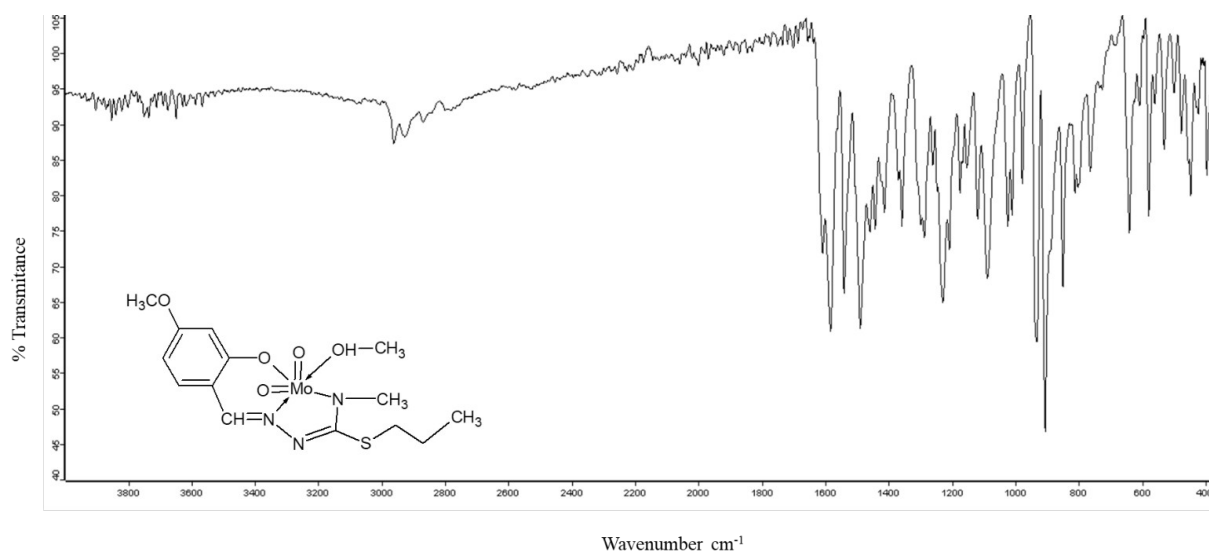


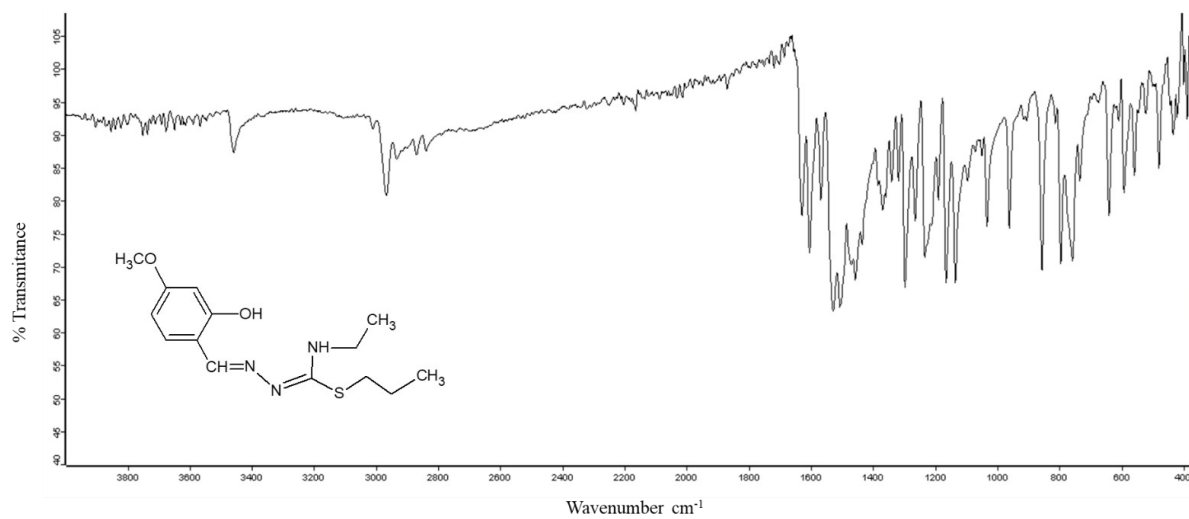
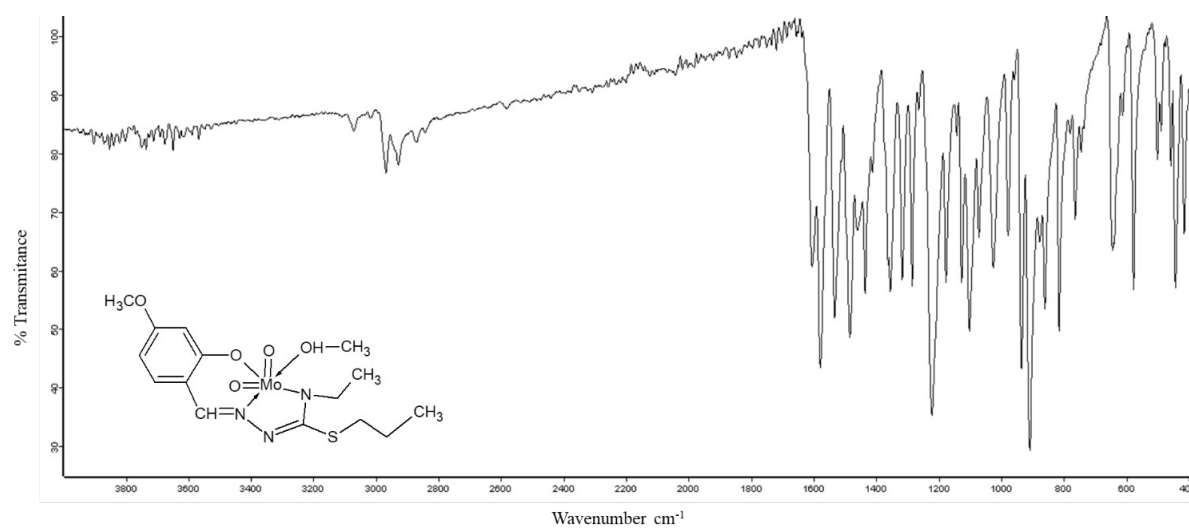
Figure S2: UV spectra of **L²** and **2**

**Figure S3:** UV spectra of **L³** and **3****Figure S4:** UV spectra of **L⁴** and **4**

**Figure S5:** IR spectrum of L¹**Figure S6:** IR spectrum of **1**

**Figure S7:** IR spectrum of L²**Figure S8:** IR spectrum of 2

**Figure S9:** IR spectrum of **L³****Figure S10:** IR spectrum of **3**

**Figure S11:** IR spectrum of L⁴**Figure S12:** IR spectrum of 4

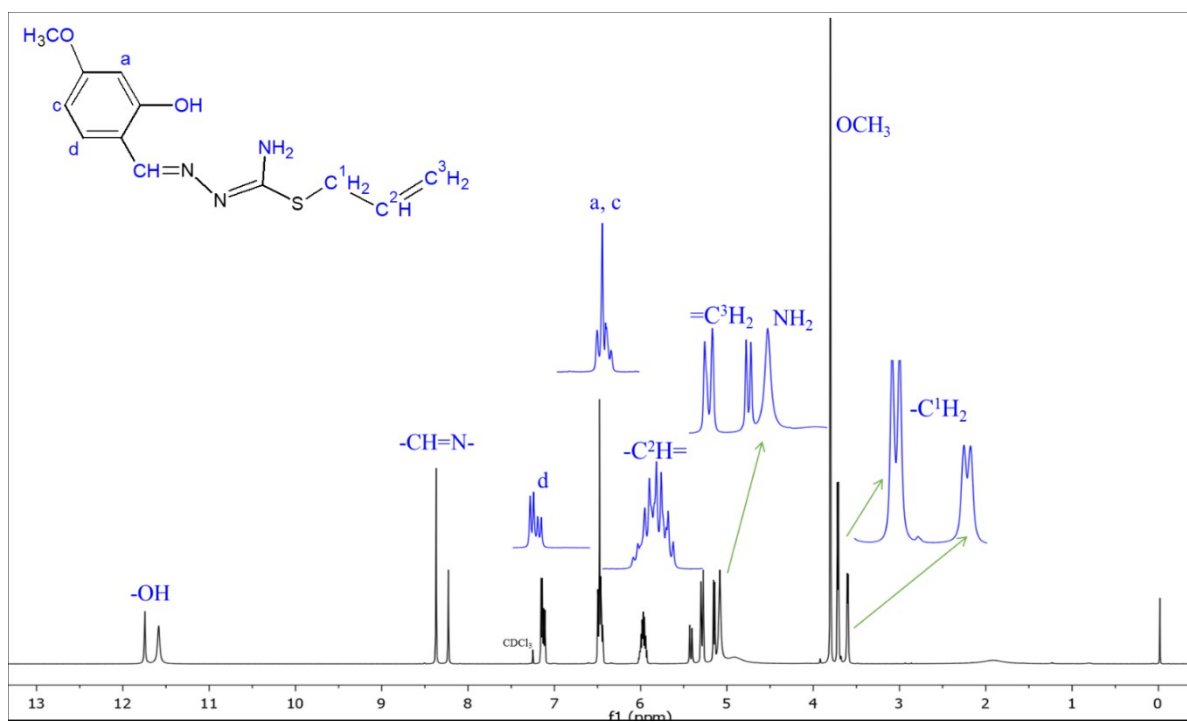


Figure S13: $^1\text{H-NMR}$ spectrum of L^1

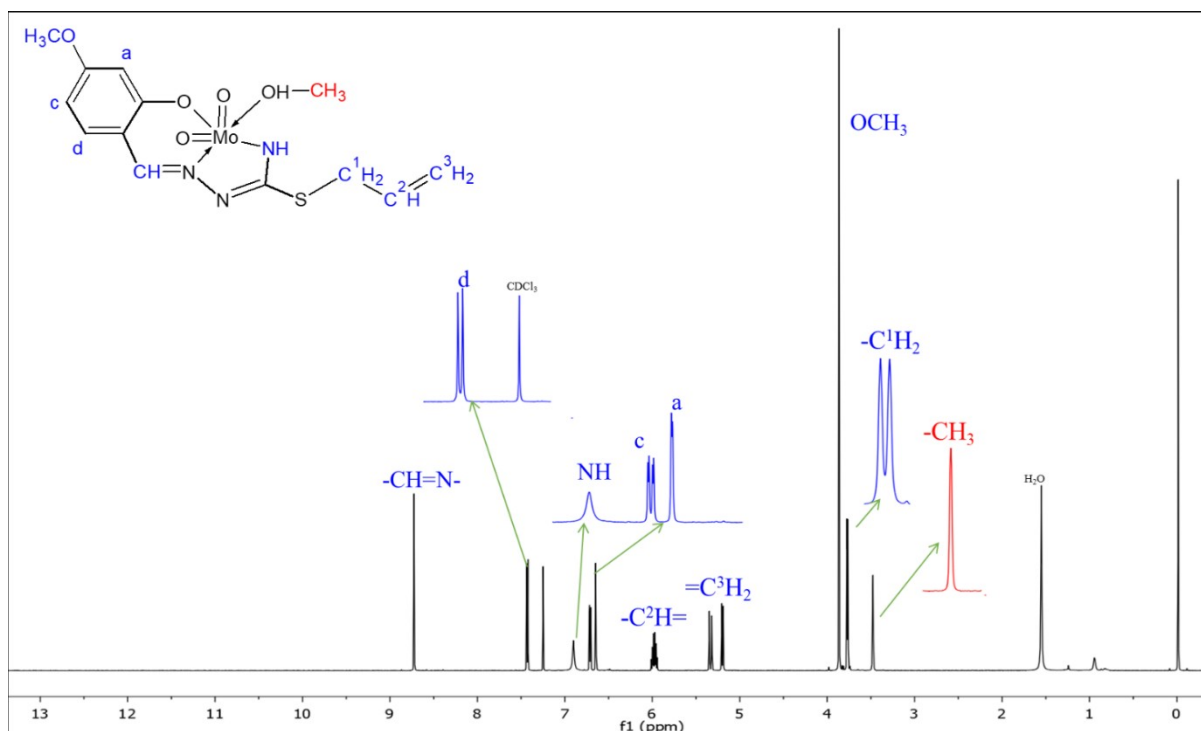
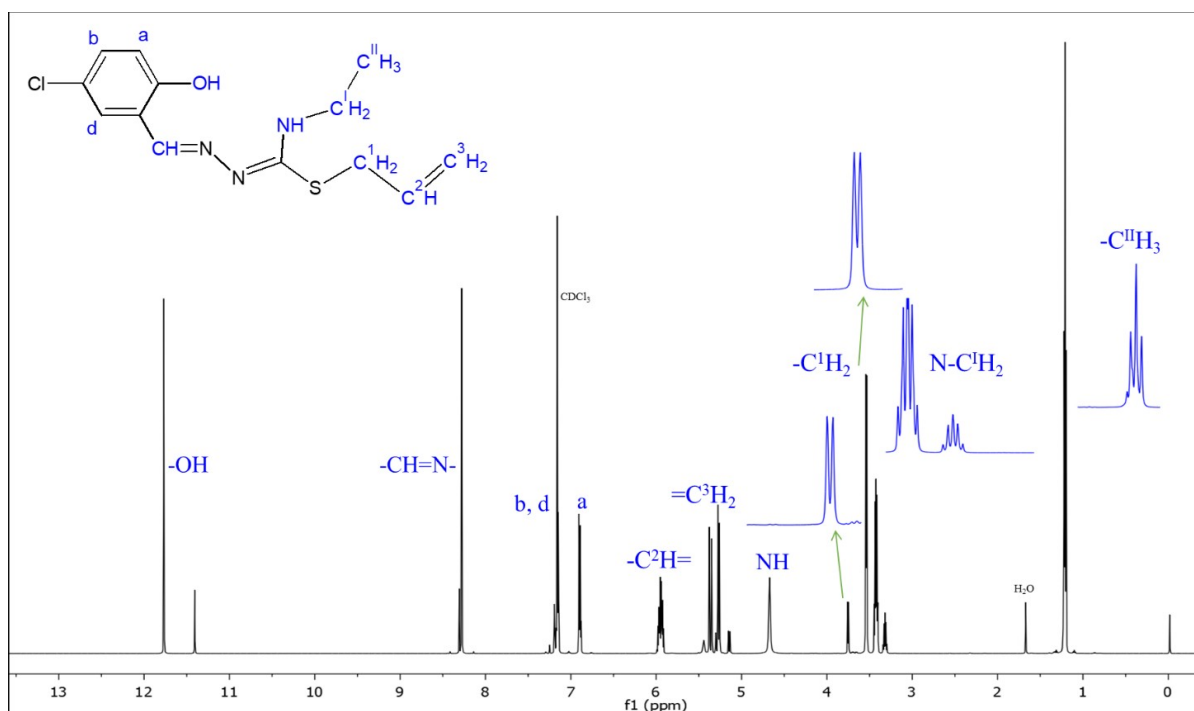
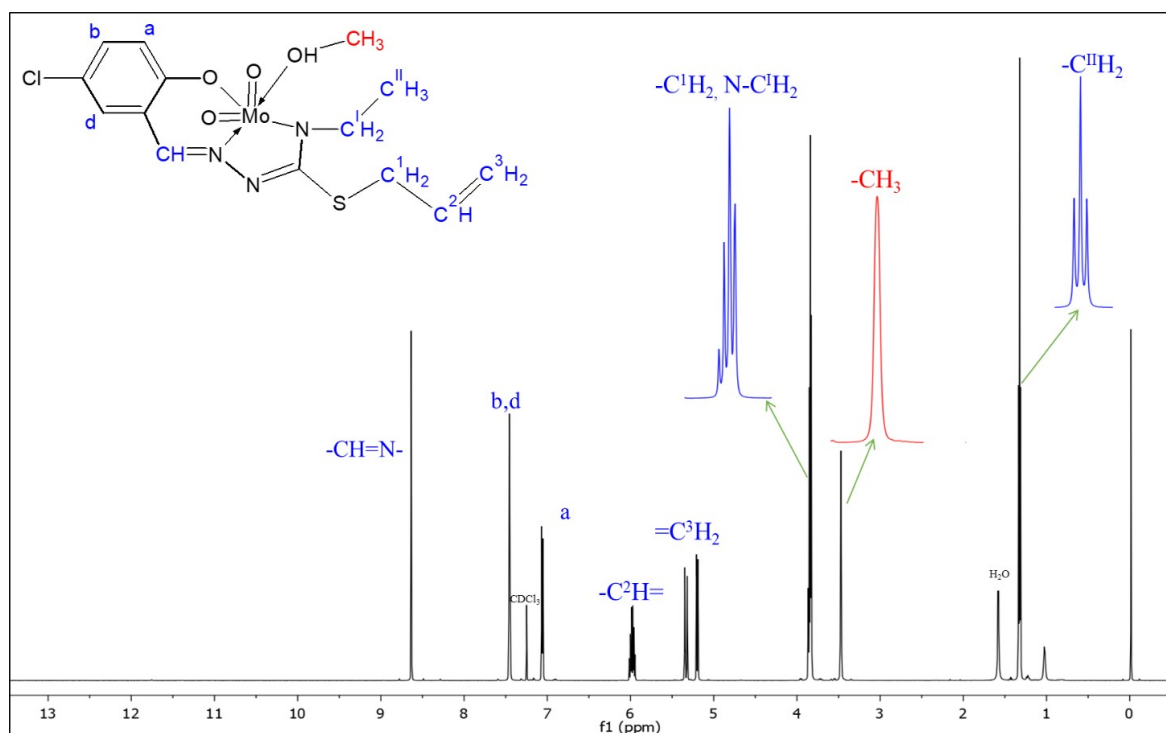
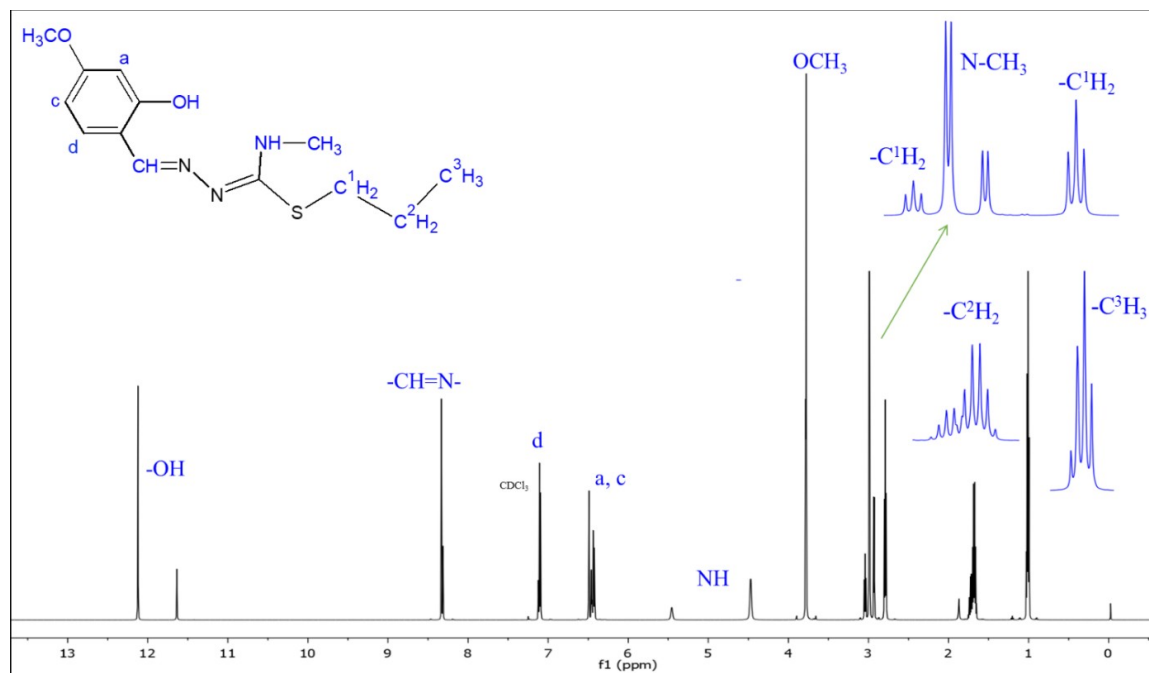
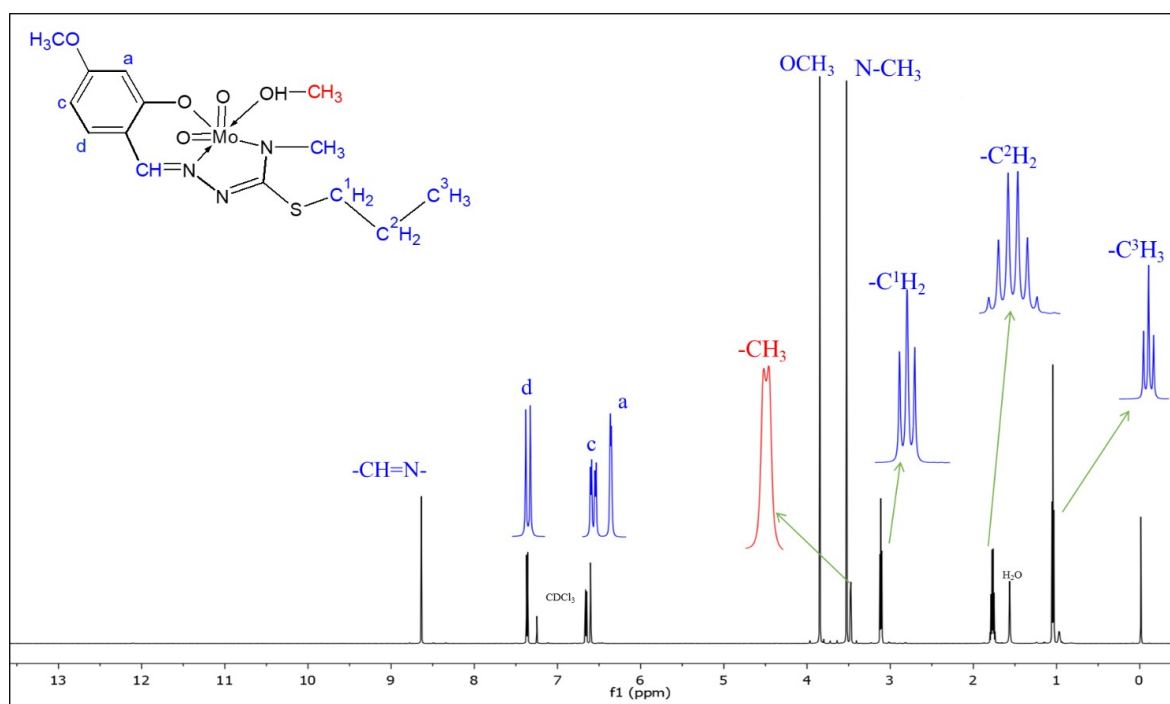
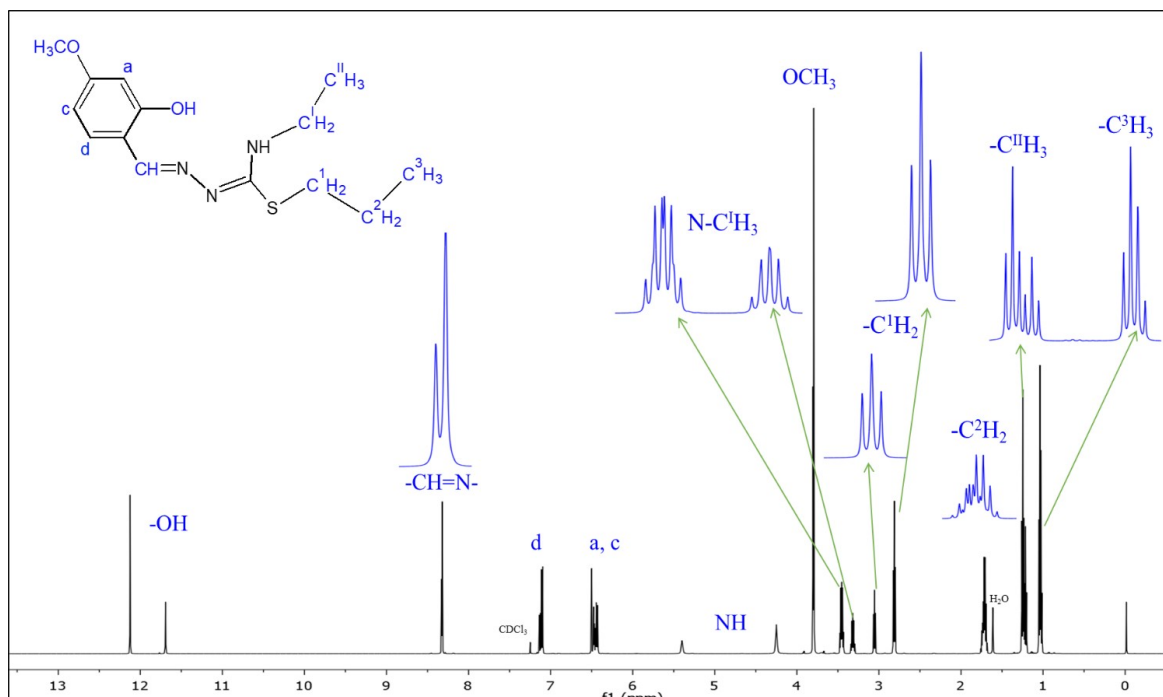
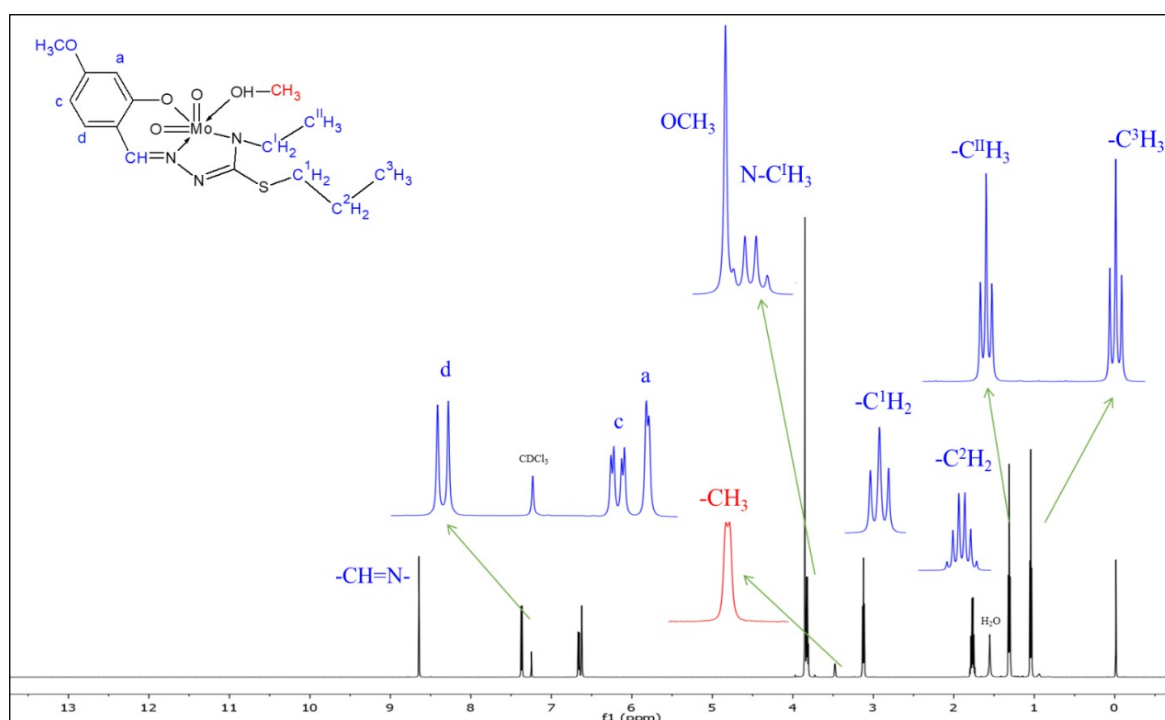
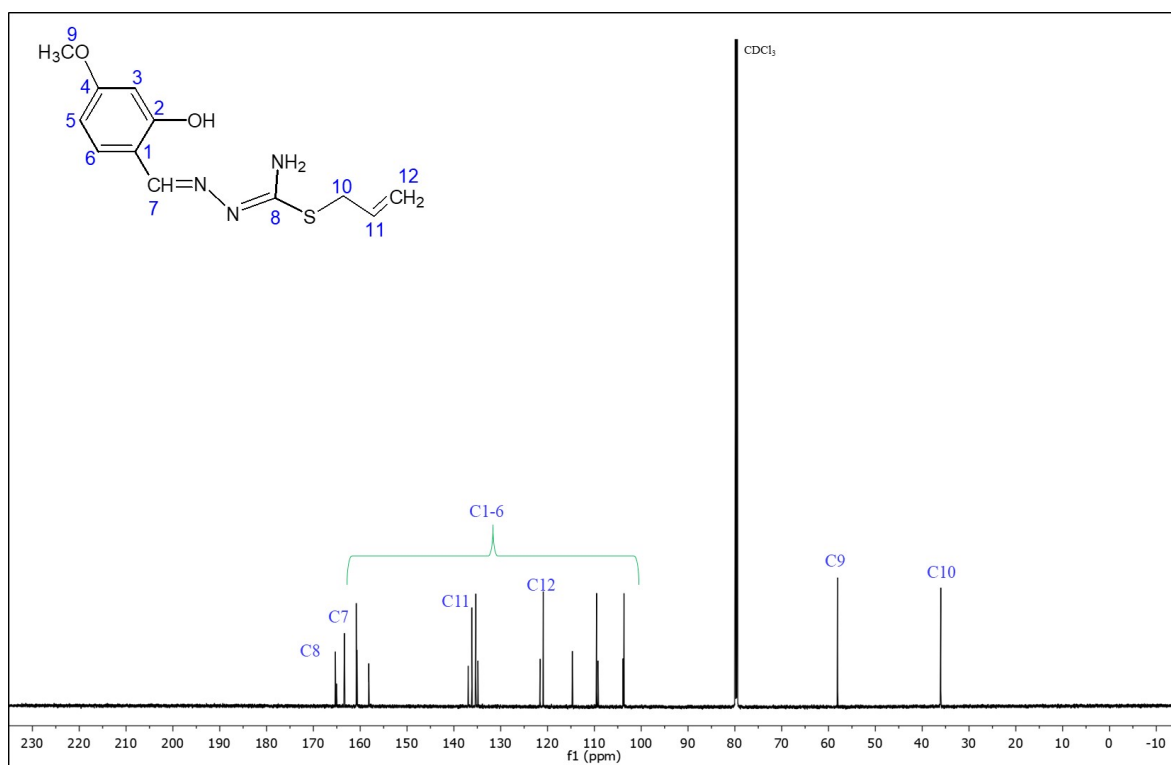
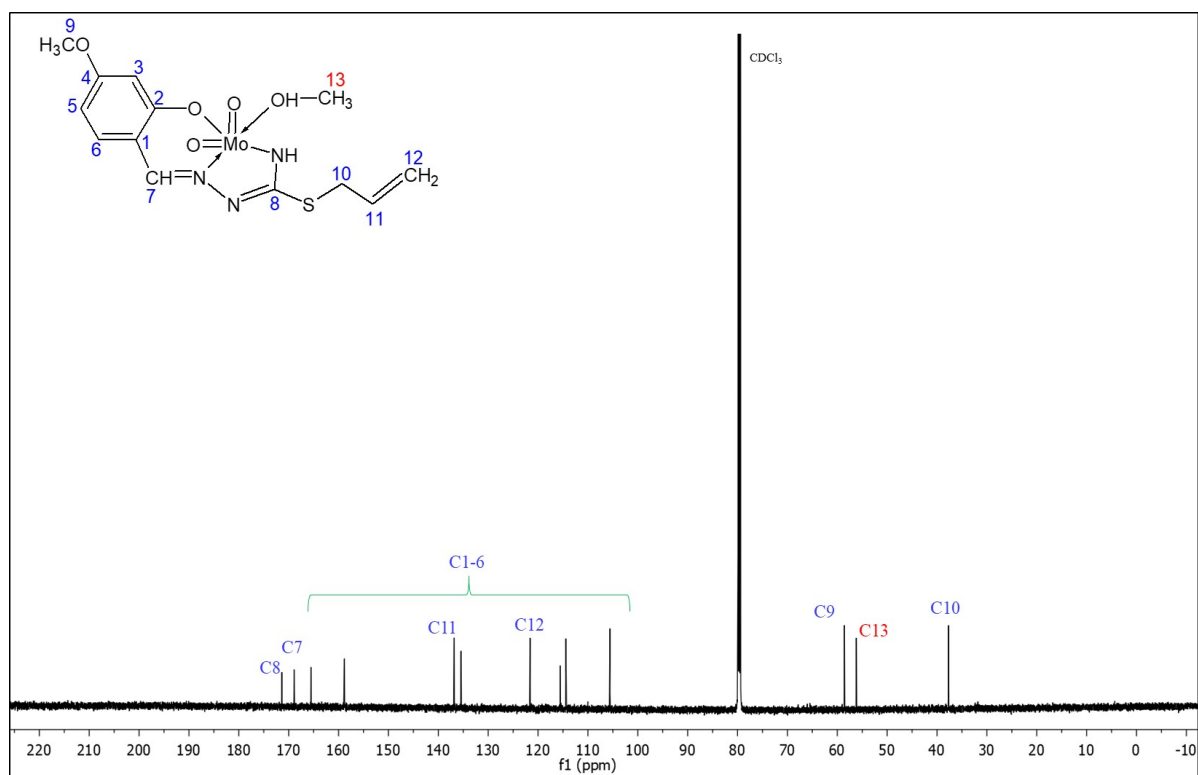


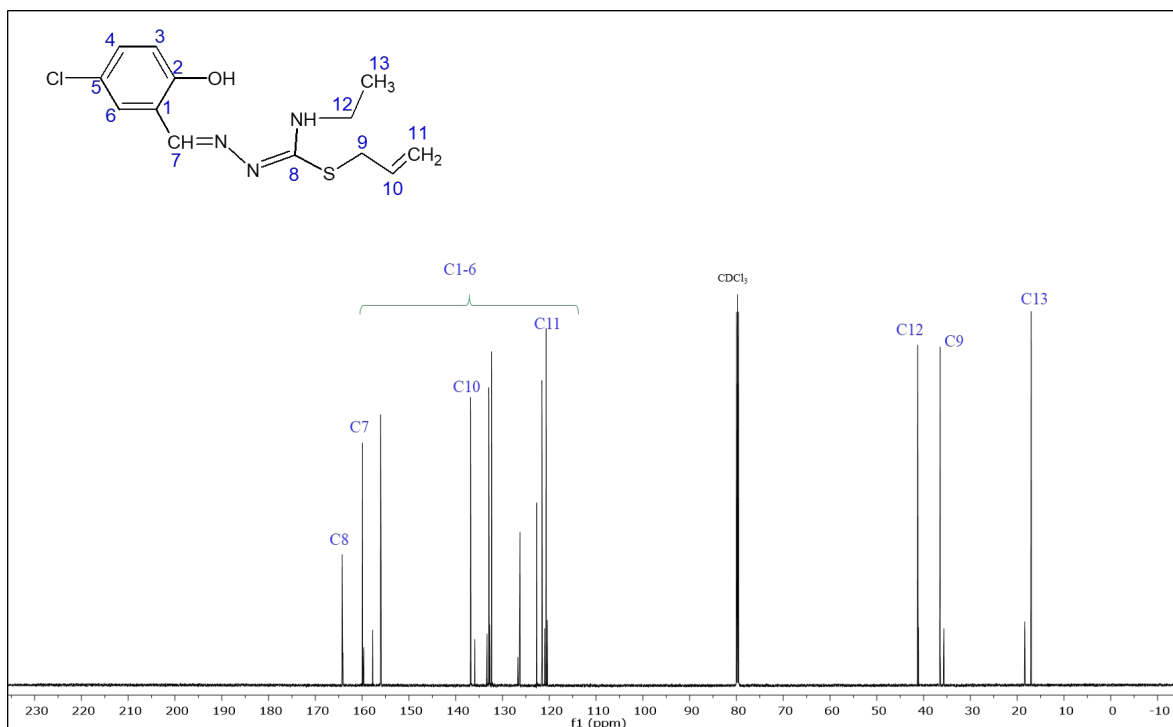
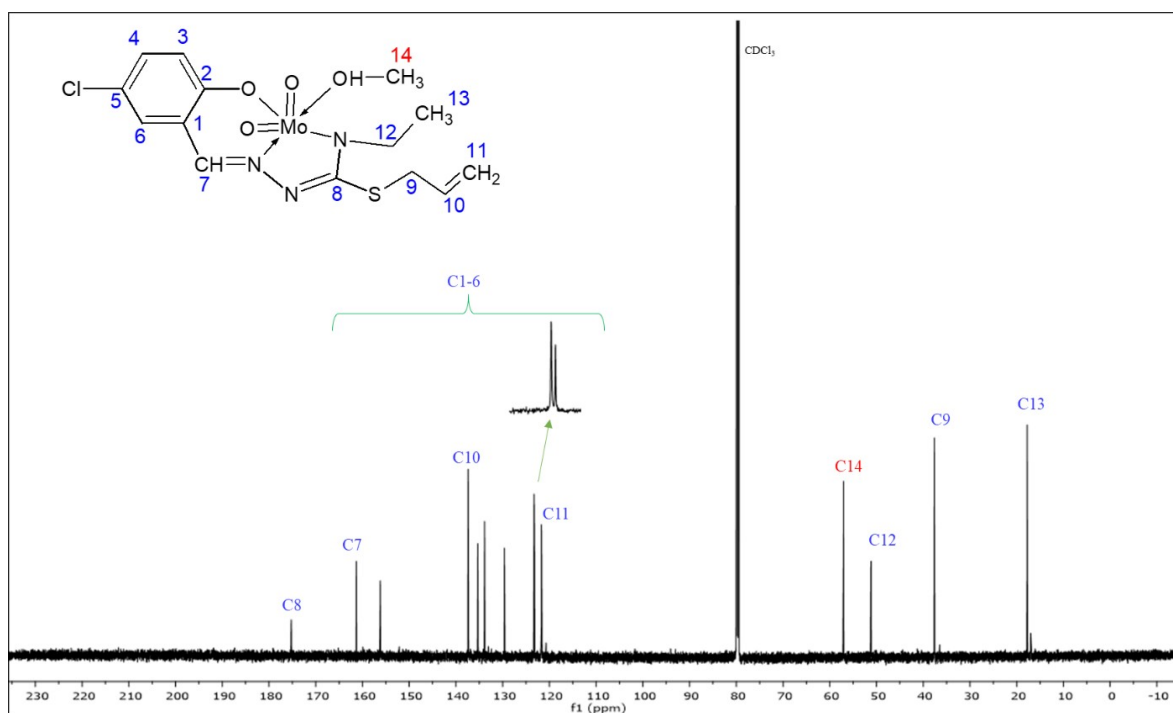
Figure S14: $^1\text{H-NMR}$ spectrum of **1**

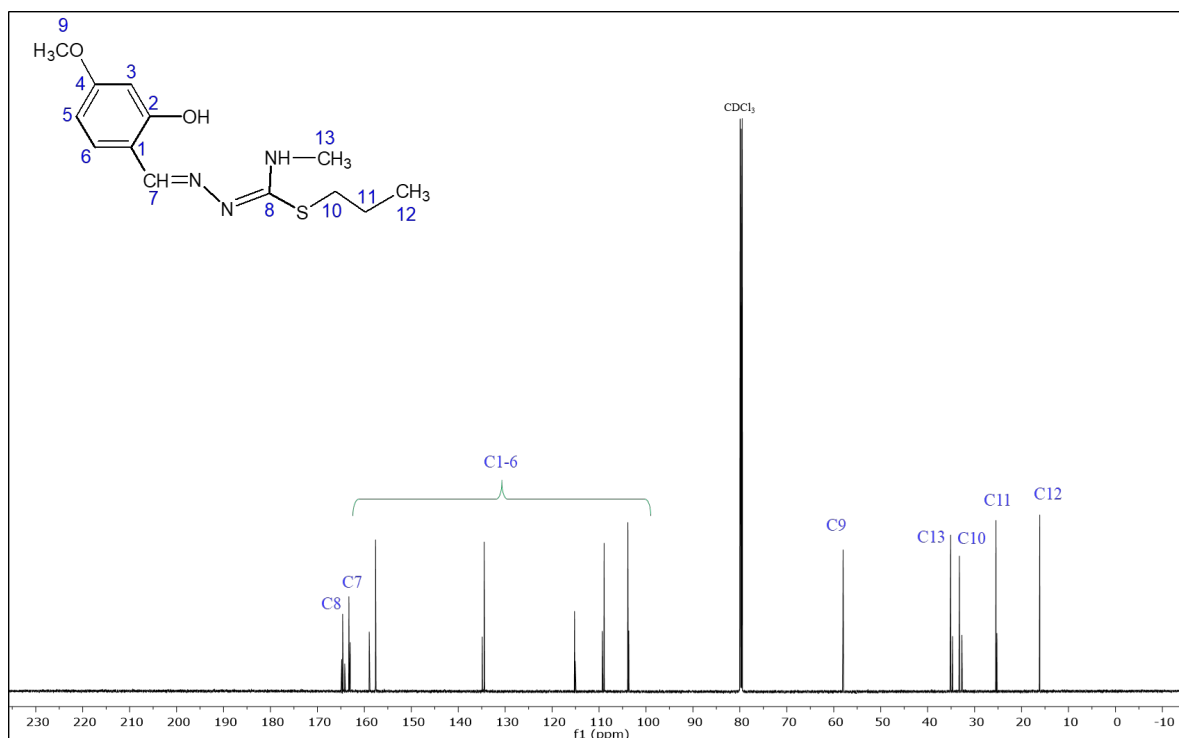
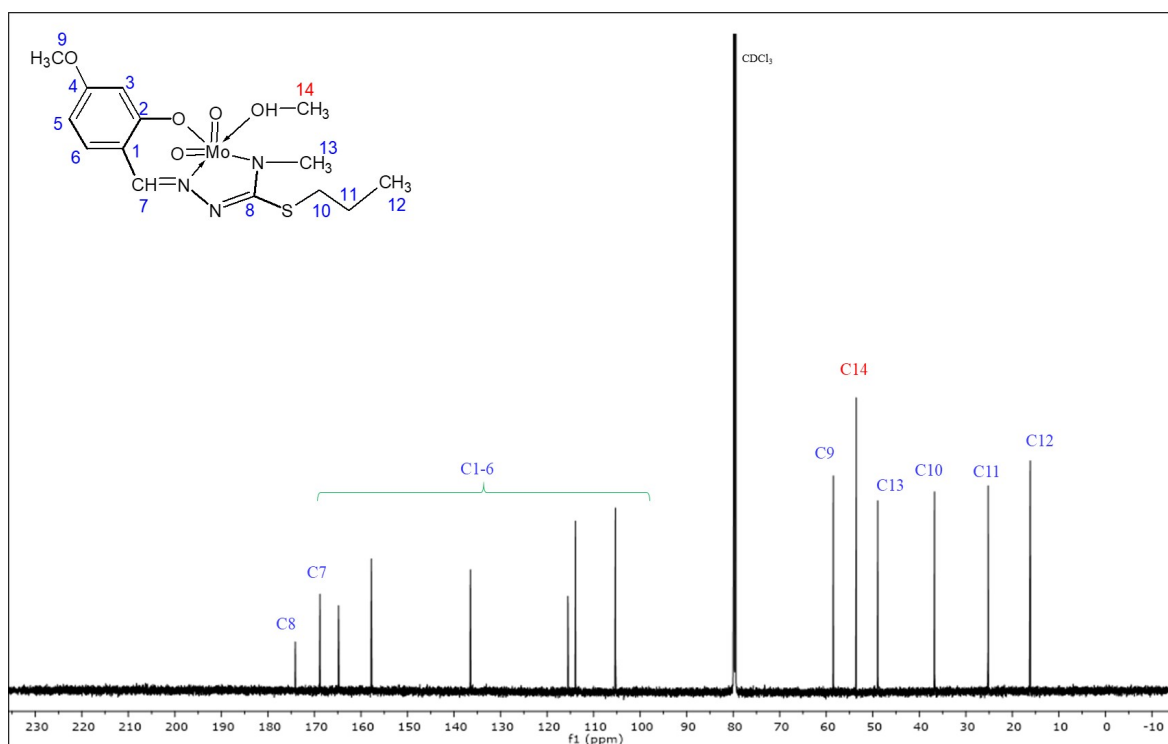
Figure S15: $^1\text{H-NMR}$ spectrum of L^2 Figure S16: $^1\text{H-NMR}$ spectrum of **2**

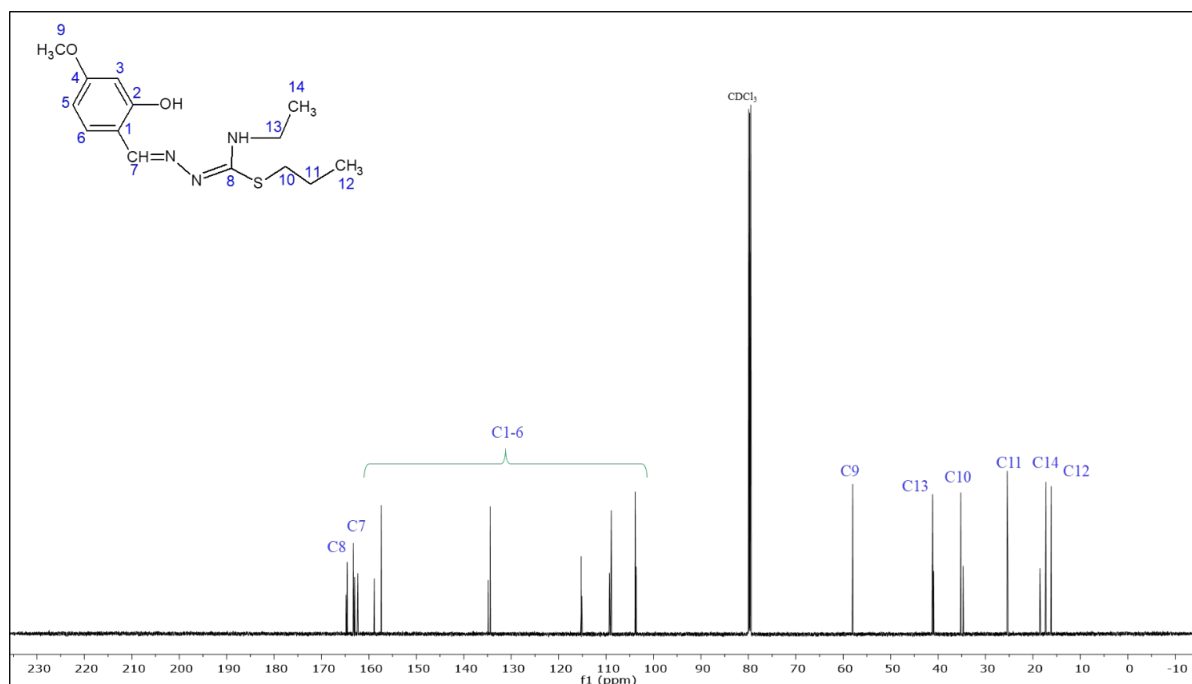
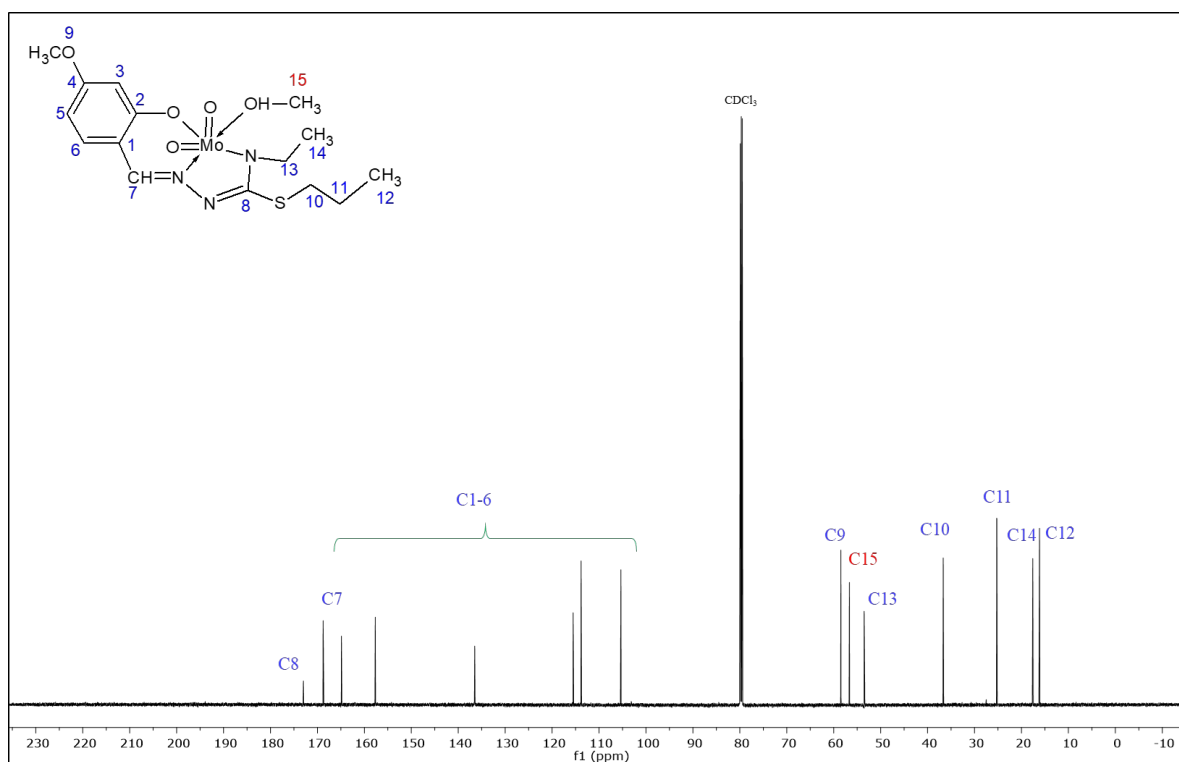
**Figure S17:** $^1\text{H-NMR}$ spectrum of L^3 **Figure S18:** $^1\text{H-NMR}$ spectrum of 3

Figure S19: $^1\text{H-NMR}$ spectrum of L^4 Figure S20: $^1\text{H-NMR}$ spectrum of 4

**Figure S21:** ¹³C-NMR spectrum of **L¹****Figure S22:** ¹³C-NMR spectrum of **1**

**Figure S23:** ¹³C-NMR spectrum of **L²****Figure S24:** ¹³C-NMR spectrum of **2**

**Figure S25:** ¹³C-NMR spectrum of **L³****Figure S26:** ¹³C-NMR spectrum of **3**

**Figure S27:** ¹³C-NMR spectrum of **L4****Figure S28:** ¹³C-NMR spectrum of **4**